

Functionalisation of Polymer Thin-Films towards their Application in Biosensing Organic Transistors

William G. Neal



Submitted in partial fulfilment of the requirements of the degree of

Doctor of Philosophy

Supervised by Dr Christian Nielsen & Professor Matteo Palma

Department of Chemistry

School of Physical and Chemical Sciences

Queen Mary University of London

Declaration

I, William George Neal, confirm that the research included within this thesis is my own work or that where it has been carried out in collaboration with, or supported by others, that this is duly acknowledged below and my contribution indicated. Previously published material is also acknowledged below.

I attest that I have exercised reasonable care to ensure that the work is original, and does not to the best of my knowledge break any UK law, infringe any third party's copyright or other Intellectual Property Right, or contain any confidential material. I accept that the College has the right to use plagiarism detection software to check the electronic version of the thesis. I confirm that this thesis has not been previously submitted for the award of a degree by this or any other university. The copyright of this thesis rests with the author and no quotation from it or information derived from it may be published without the prior written consent of the author.

Signature:

Initial submission Date: 22/12/2023

Revised submission date: May 2024

Publications

Publications resulting from collaborative works undertaken during PhD (not contributing to this thesis):

Published articles:

- C. J. Kousseff, F. E. Taifakou, **W. G. Neal**, M. Palma, C. B. Nielsen, Controlling morphology, adhesion, and electrochromic behavior of PEDOT films through molecular design and processing. *J. Polym. Sci.* **60**, 504–516 (2022).
- E. Jacobs, Y. Lin, Y. Huang, X. Ren, D. Simatos, C. Chen, D. Tjhe, M. Statz, L. Lai, P. A. Finn, **W. G. Neal**, G. D’Avino, V. Lemaure, S. Fratini, D. Beljonne, J. Strzalka, C. B. Nielsen, S. Barlow, S. R. Marder, I. McCulloch, H. Sirringhaus, High-Efficiency Ion-Exchange Doping of Conducting Polymers. *Adv. Mater.* **34**, 2102988 (2022).
- L. M. Cowen, P. A. Gilhooly-Finn, A. Giovannitti, G. LeCroy, H. Demetriou, **W. Neal**, Y. Dong, M. Westwood, S. Luong, O. Fenwick, A. Salleo, S. Heutz, C. B. Nielsen, B. C. Schroeder, Critical analysis of self-doping and water-soluble n-type organic semiconductors: structures and mechanisms. *J. Mater. Chem. C.* **10**, 8955–8963 (2022).
- L. Sun, L. Che, M. Li, **W. G. Neal**, X. Leng, Y. Long, Y. Jia, Y. Gao, M. Palma, Y. Lu, Zero-waste emission design of sustainable and programmable actuators. *SusMat.* **3**, 207–221 (2023).
- R. Marcial-Hernandez, S. Giacalone, **W. G. Neal**, C.-S. Lee, P. A. Gilhooly-Finn, G. Mastroianni, D. Meli, R. Wu, J. Rivnay, M. Palma, C. B. Nielsen, Aqueous processing of organic semiconductors enabled by stable nanoparticles with built-in surfactants. *Nanoscale.* **15**, 6793–6801 (2023).
- P. A. Gilhooly-Finn, I. E. Jacobs, O. Bardagot, Y. Zaffar, A. Lemaire, S. Guchait, L. Zhang, M. Freeley, **W. Neal**, F. Richard, M. Palma, N. Banerji, H. Sirringhaus, M. Brinkmann, C. B. Nielsen, Interplay between Side Chain Density and Polymer Alignment: Two Competing Strategies for Enhancing the Thermoelectric Performance of P3HT Analogues. *Chem. Mater.* (2023).

- T. Degousée, **W. G. Neal**, Z. Edwards, S. Singh, J. Selvarajah, T. Talha-Dean, M. Palma, B. C. Schroeder, J. A. Mol, One hour road to high-quality arrays of gold nanoparticles coated with organic ligands. *J. Mater. Chem. C* (2023), doi:10.1039/D3TC01497E.
- M. Tabassum, Q. Zia, H. Ye, **W. G. Neal**, S. Aslam, J. Zhang, L. Su, Fabrication of Potassium- and Rubidium-Doped Formamidinium Lead Bromide Nanocrystals for Surface Defect Passivation and Improved Photoluminescence Stability. *ACS Appl. Electron. Mater.* (2024), doi:10.1021/acsaelm.3c01542.

Acknowledgements

I would like to thank my supervisors Dr Christian Nielsen and Professor Matteo Palma for their guidance and support throughout this project. I would also like to thank all the current and past members of the Nielsen lab group, Palma lab group and Joseph Priestley building, for providing advice and socially stimulating conversations. A big thank you as well to all of my family members for their love and support.

Abstract

Point-of-care devices aim to improve medical treatment, by forecasting diseases before symptoms manifest. Multipurpose, portable and easy-to-use sensing devices would increase the accessibility of diagnostics, supporting the early detection and treatment of diseases. Integration into wearable technology would facilitate constant health monitoring, optimising diagnostic times. Biosensors based on organic transistors and those fabricated with functionalised organic semiconducting polymers, show potential in advancing healthcare towards this envisioned future. The scope of this thesis explores strategies to covalently interface biological receptors to semiconducting polymer thin-films, fabricate and characterise field-effect transistor devices utilising these thin-films, and explore their use as organic transistor biosensors.

The first research chapter (Chapter 3) identifies a foundational organic field-effect transistor (OFET) fabrication methodology incorporating a high-performance polymer (DPP-DTT). Assembly of large-area homogeneous thin-films, via a floating thin-film transfer method was emphasised. Influence of oxygen and nitrogen plasma treatment on the characteristics of OFETs were investigated. Nitrogen plasma modified thin-films observed exploitable chemical functionalities for receptor attachment.

In Chapter 4 thin-films composed of DPP-DTT blended with a cross-linking agent, glutaraldehyde, were incorporated into OFETs. The methodology facilitated the attachment of receptors onto the thin-film surface. Morphology, modified surface chemistry and preliminary OFET biosensing performance were investigated.

Chapter 5 details research on fabricating OFETs using an azide modified DPP-DTT polymer. Optimisation of the polymer solution and deposition are highlighted, to develop thin-films in OFETs. Receptor functionalisation, capitalising on strain-promoted azide-alkyne click chemistry, was explored. Morphology, modified surface chemistry and OFET performance were investigated. Additionally, research on the development of an organic electrochemical transistor (OECT), fabricated on a flexible substrate is presented. A novel dithienopyrrole

(DTP) derivative, endowed with a carboxyl group, was utilised as the channel material upon electropolymerisation. A receptor functionalisation strategy is discussed. Morphology, modified surface chemistry and OECT performance were investigated.

The strategies presented can enable the optimisation of organic transistor biosensors, further bridging a reality where such devices are integrated into medicine. As research in this field progresses, the integration of biosensors into medicine will significantly enhance the efficiency and accuracy of diagnostics, paving the way towards personalised and timely healthcare.

Table of Contents

Declaration	3
Publications	4
Acknowledgements	6
Abstract.....	7
Table of Contents	9
List of lists	14
i. List of Abbreviations, Acronyms and Symbols	14
ii. List of Figures	17
iii. List of Tables.....	29
1 Introduction	34
1.1 Organic electronics.....	34
1.2 Organic semiconducting polymers.....	35
1.3 Organic Field-effect Transistors	43
1.4 Biosensors	56
1.5 Organic Field-Effect Transistor Biosensors	59
1.6 Project outlines	69
2 Materials and Experimental Techniques	71
2.1 Device fabrication materials	71
2.1.1 Organic semiconducting materials	71
2.1.2 Substrates and substrate modifying chemicals	72
2.1.3 Deposition masks.....	73
2.1.4 Deposition materials.....	75
2.1.5 Solvents.....	75

2.1.6	Aptamer functionalisation chemicals	76
2.1.7	DNA sequences	77
2.2	Methodologies	78
2.2.1	Substrate cutting procedures	78
2.2.2	Substrate cleaning procedures	79
2.2.3	Octadecyltrichlorosilane SAM treatment of Si/SiO ₂ substrates	81
2.2.4	Thin-film deposition	82
2.2.5	Aptamer functionalisation	86
2.2.6	Sensing experiment solutions.....	90
2.3	Instrumentation background and methodologies.....	91
2.3.1	Atomic force microscopy	91
2.3.2	X-ray photoelectron spectrometry	95
2.3.3	Epifluorescence microscopy	98
2.3.4	OFET characterisation.....	100
2.3.5	Physical vapour deposition	102
2.3.6	Oxygen and nitrogen plasma generator	104
2.3.7	Miscellaneous equipment.....	105
3	Organic field-effect transistor fabrication and the effects of plasma modification ...	106
3.1	Acknowledgments.....	106
3.2	Introduction	106
3.3	Organic field-effect transistor fabrication	109
3.3.1	Thin-film deposition optimisation	109
3.3.2	ODTS SAM treatment of Si/SiO ₂ substrates.....	115
3.3.3	Contact electrode deposition	119

3.3.4	OFET electrical characterisation	121
3.4	Introducing exploitable chemical functionalities via O ₂ and N ₂ plasma treatment ..	124
3.4.1	The effects of O ₂ plasma treatment on thin-film morphologies	126
3.4.2	The effects of O ₂ plasma treatment on OFET performance	130
3.4.3	The introduction of exploitable chemical functionalities on O ₂ plasma treated thin-films.....	132
3.4.4	The effects of N ₂ plasma treatment on thin-film morphologies	136
3.4.5	The effects of N ₂ plasma treatment on OFET performance	140
3.4.6	The introduction of exploitable chemical functionalities on N ₂ plasma treated thin-films.....	145
3.4.7	Aptamer functionalisation of N ₂ plasma treated thin-films	149
3.5	Summary and conclusion	152
4	Investigation of DPP-DTT polymer blend with glutaraldehyde for receptor functionalisation and use in biosensing OFET devices	154
4.1	Acknowledgments.....	154
4.2	Introduction	154
4.3	Optimisation of DPP-DTT:GA thin-film deposition	157
4.4	Aptamer functionalisation of DPP-DTT:GA OFETs	161
4.4.1	Aptamer functionalisation of DPP-DTT:GA thin-films.....	161
4.4.2	Aptamer functionalisation of DPP-DTT:GA OFETs.....	164
4.5	Characterisation of aptamer functionalised DPP-DTT:GA OFET and the response to cortisol.....	176
4.5.1	Real-time response of aptamer functionalised DPP-DTT:GA OFET to cortisol	178
4.5.2	Transfer characteristic response of aptamer functionalised DPP-DTT:GA OFET to cortisol	183

4.5.3	Stabilising DPP-DTT:GA OFET sensitivity via source-drain electrode modification	187
4.6	Summary and conclusion	192
5	Investigation of chemically modified organic semiconducting materials for aptamer functionalisation and organic transistor fabrication	194
5.1	Acknowledgments.....	194
5.2	Introduction	194
5.3	Investigation of N ₃ -DPP polymer for functionalisation and use in OFET devices.....	198
5.3.1	N ₃ -DPP polymer thin-film deposition	198
5.3.2	Aptamer functionalisation of N ₃ -DPP polymer thin-film.....	201
5.3.3	Characterisation of N ₃ -DPP OFET.....	205
5.4	Investigation of a novel DTP carboxylic acid polymer for aptamer functionalisation and OECT devices	207
5.4.1	Aptamer functionalisation of PDTP-C4-acid thin-films.....	207
5.4.2	Fabrication and characterisation of a PDTP-C4-acid OECT.....	215
5.5	Summary and conclusion	223
6	Conclusions.....	225
7	Appendix	229
7.1	Organic field-effect transistor fabrication and the effects of plasma modification appendix.....	230
7.1.1	Thin-film deposition optimisation AFM.....	230
7.1.2	ODTS SAM treatment of Si/SiO ₂ substrates.....	248
7.1.3	Contact electrode deposition	251
7.1.4	The effects of O ₂ plasma treatment on thin-film morphologies appendix	253
7.1.5	The effects of O ₂ plasma treatment on OFET performance appendix	254

7.1.6	The introduction of exploitable chemical functionalities on O ₂ plasma treated thin-films appendix.....	258
7.1.7	The effects of N ₂ plasma treatment on thin-film morphologies appendix	259
7.1.8	The effects of N ₂ plasma treatment on OFET performance appendix	262
7.1.9	The introduction of exploitable chemical functionalities on N ₂ plasma treated thin-films appendix.....	278
7.1.10	Aptamer functionalisation of N ₂ plasma treated thin-films appendix.....	281
7.2	Investigation of glutaraldehyde DPP-DTT polymer blends for functionalisation and use in OFET devices appendix.....	284
7.2.1	DPP-DTT:GA AFM	284
7.2.2	DPP-DTT:GA Water contact angle measurements	298
7.2.3	DPP-DTT:GA epifluorescence microscopy	301
7.2.4	DPP-DTT:GA X-ray photoelectron spectroscopy.....	303
7.2.5	Preliminary sensing of Cortisol	304
7.3	Investigation of chemically modified organic semiconducting materials for aptamer functionalisation and organic transistor fabrication appendix.....	305
7.3.1	N ₃ -DPP AFM	305
7.3.2	N ₃ -DPP water contact angle.....	308
7.3.3	DTP-C4-acid AFM	309
7.3.4	DTP-C4-acid epifluorescence microscopy.....	313
8	References.....	316

List of lists

i. List of Abbreviations, Acronyms and Symbols

AFM	Atomic force microscopy
BCN-NHS	(1R,8S,9s)-Bicyclo[6.1.0]non-4-yn-9-ylmethyl N-succinimidyl carbonate
BE	binding energy
BGTC	bottom-gate top-contact
CB	chlorobenzene
CBA	cortisol binding aptamer
COMP-CBA	complimentary cortisol binding aptamer
CPS.eV	count per second per electron volt
CHCl ₃	chloroform
DBCO	Dibenzocyclooctyne
DI	deionised
DPBS	Dulbecco's Phosphate Buffered Saline
DPP	diketopyrrolopyrrole
DPP-DTT	poly[2,5-(2-octyldodecyl)-3,6-diketopyrrolopyrrole-alt-5,5-(2,5-di(thien-2-yl)thieno [3,2-b]thiophene)]
DPP-DTT:GA	DPP-DTT:GA (9:1) in chlorobenzene (5 mg mL ⁻¹)
DTP	dithieno[3,2-b:2',3'-d]pyrrole
EDC	1-ethyl-3-(3-dimethylaminopropyl) carbodiimide
EDOT	3,4-Ethylenedioxythiophene
EGOFET	electrolyte-gated organic field-effect transistor
FET	field-effect transistor
FFT	floating film transfer
FWHM	full width half maximum
GA	glutaraldehyde
HOMO	highest occupied molecular orbital
hrs	hours

IDE	interdigitated
I _{ds}	drain-source current
I _g	gate current
IPA	isopropyl alcohol
ITO	indium Tin Oxide
LUMO	lowest Unoccupied Molecular Orbital
MeCN	acetonitrile
MeOH	methanol
mins	minutes
MQ	milli-Q
N ₃ -CBA	azide terminated cortisol binding aptamer
N ₃ -DPP	azide functionalised DPP-DTT polymer
NH ₂ -CBA	amine terminated cortisol binding aptamer
NHS	<i>N</i> -hydroxysuccinimide
ODTS	octadecyltrichlorosilane
OECT	organic electrochemical transistor
OFET	organic field-effect transistor
OSC	organic semiconductor
PDMS	polydimethylsiloxane
PTFE	polytetrafluoroethylene
R _a	Average roughness
RPM	revolutions Per Minute
R _q	Root mean square roughness
RT	room temperature
s	seconds
S/D	source drain
SELEX	sequential evolution of ligands by exponential enrichment
SPAAC	strain promoted alkyne-azide cycloaddition
STD or SD or σ	standard deviation

Sulfo-NHS	N-hydroxysulfosuccinimide
Tris-HCl	tris hydrochloride
V _{gs}	gate-source voltage
V _{ds}	drain-source voltage
V _{th}	threshold voltage
W	power
WCA	water contact angle
XPS	X-ray photoelectron spectroscopy
μ	Charge carrier mobility

ii. List of Figures

Figure 1 Increasing conjugation length leading to a narrowing of band gap 35

Figure 2 Selected examples of generational organic semiconducting polymers: Polyacetylene (1st generation) P3HT (2nd generation) PBTTT (3rd generation) 37

Figure 3 Examples of common acceptor and donor monomer units in organic semiconducting polymers 38

Figure 4 Alternating structure of donor-acceptor polymers 39

Figure 5 Noncovalent conformational locking between S---O, in a diketopyrrolopyrrole monomer and flanking thiophene monomers 40

Figure 6 Chemical structure of Poly[2,5-(2-octyldodecyl)-3,6-diketopyrrolopyrrole-alt-5,5-(2,5-di(thien-2-yl)thieno [3,2-b]thiophene)] (DPP-DTT) 41

Figure 7 Schematic of an organic field-effect transistor. Image adapted with permission from {W.-Y. Lee, J. Mei, Z. Bao, "OFETs: BASIC CONCEPTS AND MATERIAL DESIGNS" in (2016; doi: 10.1142/9789813148611_0002), pp. 19–83}. Copyright {2024} World Scientific Publishing Co(64)..... 44

Figure 8 Operation of OFET including charge carrier density within the conductive channel and the output characteristics in (A) linear (B) pinch-off (C) saturation regime..... 45

Figure 9 OFET transfer characteristics (A) Linear regime (B) Saturation regime (C) output characteristics. Image adapted with permission from {Z. A. Lampert, H. F. Haneef, S. Anand, M. Waldrip, O. D. Jurchescu, Tutorial: Organic field-effect transistors: Materials, structure and operation. J. Appl. Phys. **124**, 071101 (2018).}. Copyright {2024} American Institute of Physics.(13) 46

Figure 10 Cross-sectional structural diagrams of an OFET, OECT and EGOFET 49

Figure 11 OFET configurations 1. bottom gate, bottom contact 2. bottom gate, top contact 3. top gate, bottom contact 4. top gate, top contact..... 49

Figure 12 OFET biosensor with the biorecognition layer at the organic semiconductor interface 59

Figure 13 DNA bases adenine, guanine, cytosine, thymine and RNA base uracil. 63

Figure 14 Strategies for the introduction of receptors and chemical binding sites to the organic semiconductor interface.....	66
Figure 15 Schematic of Ossila supplied high density 50 μm interdigitated source-drain deposition mask.....	73
Figure 16 Schematic of Ossila supplied low density variable (30, 40, 50, 60, 80 μm) channel length source-drain deposition mask	74
Figure 17 AFM instrument configuration a) photodetector b) piezoelectric scanner c) stage d) sample e) laser beam f) tip g) cantilever h) resulting AFM image of Hexane-AuNP-C8 network on interdigitated electrodes by Thibault Degousée is licensed under CC BY 3.0 Deed.(168) .	91
Figure 18 AFM image of NDI-OH film drop-cast at 45 °C by Lewis M. Cowen is licensed under CC BY 3.0 Deed.(169)	92
Figure 19 Force vs. Distance curve – depicting the effect of tip-to-sample distance on the force interaction between tip and sample. Image adapted with permission from {S. Caponi, C. Canale, O. Cavalleri, M. Vassalli, "Characterization Tools for Mechanical Probing of Biomimetic Materials" in <i>Nanotechnology Characterization Tools for Tissue Engineering and Medical Therapy</i> (2019) pp. 69–111.}. Copyright {2024} Springer Berlin Heidelberg(170)	92
Figure 20 Force vs. Time curve. Image adapted with permission from {S. Caponi, C. Canale, O. Cavalleri, M. Vassalli, "Characterization Tools for Mechanical Probing of Biomimetic Materials" in <i>Nanotechnology Characterization Tools for Tissue Engineering and Medical Therapy</i> (2019) pp. 69–111.}. Copyright {2024} Springer Berlin Heidelberg(170)	93
Figure 21 Bruker Dimension Icon AFM instrument.	94
Figure 22 ThermoFisher Nexsa X-ray Photoelectron Spectrometer.....	96
Figure 23 Epifluorescence microscope diagram. Image adapted with permission from {C. Stewart, J. Giannini, Inexpensive, Open Source Epifluorescence Microscopes. <i>J. Chem. Educ.</i> 93 , 1310–1315 (2016).}. Copyright {2024} American Chemical Society.(176)	98
Figure 24 Evaporation stack cross section a) mask holder b) shadow mask c) substrate d) magnetic sheet e) weight.....	102
Figure 25 Schematic of Plasma generator.	104

Figure 26 AFM topographical images (10 μm^2 and 3 μm^2) of a DPP-DTT thin-film spin coated from chlorobenzene (5 mg mL^{-1}).	109
Figure 27 FFT procedure: a) polymer solution deposited onto liquid substrate b) polymer solution spontaneously spreads across liquid substrate c) substrate stamped into dried polymer thin-film d) polymer thin-film lifted from liquid surface and transferred to substrate. Image adapted from ref. (75) "Principle and formation process of spontaneous spreading" by Jonghyeon Noh is licenced under CC BY 4.0 Deed.....	110
Figure 28 Camera image of a floating film transferred DPP-DTT thin-film on Si/SiO ₂ substrate (1.5 x 2 cm).....	111
Figure 29 AFM topographical images (10 μm x 10 μm) of DPP-DTT thin-films via FFT from 9:1 CHCl ₃ :CB a) 10 mg mL^{-1} b) 5 mg mL^{-1} c) 3 mg mL^{-1} , on Si/SiO ₂ substrates (polymer chain alignment indicated by white arrows).....	111
Figure 30 Roughness Ra and Rq values of DPP-DTT thin-films via FFT from 9:1 CHCl ₃ :CB (10, 5, 3 mg mL^{-1}) on Si/SiO ₂ substrates and a DPP-DTT thin-film via FFT from 9:1 CHCl ₃ :CB (3 mg mL^{-1}) on ODTs modified substrate.	113
Figure 31 Thicknesses of DPP-DTT thin-films via FFT from 9:1 CHCl ₃ :CB (10, 5, 3 mg mL^{-1}) on Si/SiO ₂ substrates and a DPP-DTT thin-film via FFT from 9:1 CHCl ₃ :CB (3 mg mL^{-1}) on ODTs modified substrate.....	114
Figure 32 Self-assembly reaction of octadecyltrichlorosilane with silicon dioxide dielectric surface.....	115
Figure 33 Water contact angle images of (left) ODTs modified Si/SiO ₂ substrate (104.8°) and (right) Si/SiO ₂ substrate (29.3°).....	116
Figure 34 AFM topographical images (10 μm x 10 μm) of (left) ODTs modified Si/SiO ₂ substrate and (right) Si/SiO ₂ substrate.	117
Figure 35 AFM roughness Ra and Rq values of ODTs modified Si/SiO ₂ surface and pre-modified Si/SiO ₂ surface.....	118
Figure 36 AFM topological image (50 μm x 50 μm) (top) and height profile (bottom) of physical vapour deposited gold (50 nm) S/D electrode on DPP-DTT thin-film via FFT from 9:1 CHCl ₃ :CB (3 mg mL^{-1}) on ODTs modified substrate.....	120

Figure 37 Transfer and output characteristics of bottom-gate top-contact configuration DPP-DTT OFET. Transfer characteristics in A) linear regime ($V_{ds} -1 V$) and B) saturation regime ($V_{ds} -50 V$), (blue) log scale (black) linear scale (red) gate current. C) Output characteristics. DPP-DTT thin-film via FFT from 9:1 $CHCl_3:CB$ (3 mg mL^{-1}) on ODTs modified Si/SiO_2 , with 50 nm gold deposited interdigitated S/D electrodes ($50 \mu\text{m}$ channel length).....	121
Figure 38 Introduction of chemical functionalities on DPP-DTT thin-film surfaces via (top) O_2 or (bottom) N_2 plasma treatment.....	124
Figure 39 AFM thicknesses of DPP-DTT thin-films before and after O_2 plasma treatment. Error bars represent the standard deviation between these values.....	127
Figure 40 AFM roughness values (A) R_q and (B) R_a of DPP-DTT thin-films before and after O_2 plasma treatment.	128
Figure 41 Formation processes of differing interface morphologies for a DPP-DTT thin-film deposited via FFT. Image adapted with permission from {G. Choi, K. Lee, S. Oh, J. Seo, C. Kim, T. K. An, J. Lee, H. S. Lee, Understanding Marangoni flow-driven solidification of polymer semiconducting films on an aqueous substrate. <i>J. Mater. Chem. C</i> . 8, 10010–10020 (2020).}. Copyright {2024} Royal Society of Chemistry.(211)	129
Figure 42 OFET performance (left) mobilities and (right) threshold voltages before and after O_2 plasma treatment. Drain voltage biased at $-1 V$	130
Figure 43 Oxygen peak areas of untreated and O_2 plasma treated DPP-DTT OFETs. Peak areas adjusted for SiO_2 contribution.	132
Figure 44 XPS $C1s$ high resolution scans of O_2 plasma treated DPP-DTT OFETs a) untreated b) 6 W, 90 s c) 12 W, 60 s d) 24 W, 30 s.	133
Figure 45 Carboxyl group component peak areas of untreated and O_2 plasma treated DPP-DTT OFETs.	134
Figure 46 AFM thicknesses of DPP-DTT OFETs before and after N_2 plasma treatment.....	136
Figure 47 AFM average roughness values (left) R_q and (right) R_a of DPP-DTT thin-films before and after N_2 plasma treatment.....	137
Figure 48 AFM thicknesses of DPP-DTT thin-films before and after N_2 plasma treatment. .	138

Figure 49 AFM average roughness values (left) Rq and (right) Ra of DPP-DTT thin-films before and after N ₂ plasma treatment.....	139
Figure 50 OFET performance (V _{ds} -1 V, -10 V) metrics (left) averaged threshold voltage (right) averaged mobility, before and after N ₂ plasma treatment.	141
Figure 51 Transfer characteristics a) V _{ds} -1 V b) V _{ds} -10 V and output characteristics of DPP-DTT OFETs before N ₂ plasma treatment (blue) log scale (black) linear scale (red) gate current, (upward arrow) forward sweeping voltages (downward arrow) reversed.	142
Figure 52 XPS high resolution N1s spectra nitrogen peak area of N ₂ plasma treated DPP-DTT thin-films.	145
Figure 53 XPS high resolution C1s scans of DPP-DTT thin-films (black) before and (red) after N ₂ plasma treatment (12 W for 30 s).	147
Figure 54 XPS C1s high resolution spectra C-N component peak area of N ₂ plasma treated DPP-DTT thin-films.	148
Figure 55 Aptamer attachment strategy of N ₂ plasma treated DPP-DTT thin-film: 1. N ₂ plasma treatment (12 W, 30 s) 2. BCN-NHS (1.0 mg mL ⁻¹) modification then washed with MQ water 3. N ₃ -CBA (1 μM) functionalisation then sequentially washed with 0.1 % tween20 solution and MQ water.	149
Figure 56 Hybridisation of aptamer functionalised thin-film with Cy3 labelled complimentary strand: 1. Cy3-comp-CBA (1 μM) hybridisation then sequentially washed with 0.1 % tween20 solution and MQ water.	150
Figure 57 Epifluorescence microscope image average pixel values: N ₂ plasma treated DPP-DTT thin-film functionalised with aptamers and hybridised with a Cy3 labelled complimentary strand. Average pixel values of thin-film controls also included.....	151
Figure 58 Spin coating series: Thicknesses of DPP-DTT:GA (9:1) thin-films from chlorobenzene (5 mg mL ⁻¹).	158
Figure 59 Spin coating series: Roughness Ra and Rq values of DPP-DTT:GA (9:1) thin-films from chlorobenzene (5 mg mL ⁻¹).	159
Figure 60 AFM topographical images (10 μm x 10 μm and 3 μm x 3 μm) of DPP-DTT:GA (9:1) thin-film spin coated (4K RPM) from chlorobenzene (5 mg mL ⁻¹).	160

Figure 61 Aptamer attachment strategy of DPP-DTT:GA thin-film: 1. NH ₂ -CBA (10 μM) functionalisation then sequentially washed with 0.1 % tween20 solution and MQ water. .	161
Figure 62 Hybridisation of aptamer functionalised DPP-DTT:GA thin-film with Cy3 labelled complimentary strand: 1. Cy3-comp-CBA (1 μM) hybridisation then washed with 0.1 % tween20 solution and MQ water.....	161
Figure 63 Epifluorescence microscope image pixel values: DPP-DTT:GA thin-film functionalised with aptamers and hybridised with a Cy3 labelled complimentary strand. Average pixel values of thin-film controls also included.	162
Figure 64 XPS high resolution O1s scans: (red) DPP-DTT thin-film spin coated from chlorobenzene (5 mg mL ⁻¹) and (black) DPP-DTT:GA thin-film spin coated from chlorobenzene (5 mg mL ⁻¹).	165
Figure 65 XPS high resolution C1s scans: DPP-DTT:GA thin-films functionalised with NH ₂ -CBA (1 μM, 5 μM and 10 μM) and a non-functionalised DPP-DTT:GA thin-film (black).	166
Figure 66 XPS high resolution scans (a) P2p and (c) N1s. Relative atomic content (%) (b) P2p, (d) N1s and (e) O1s. DPP-DTT:GA thin-films functionalised with NH ₂ -CBA (1 μM, 5 μM and 10 μM) and non-functionalised DPP-DTT:GA thin-film.	167
Figure 67 Water contact angles: DPP-DTT:GA thin-films functionalised with NH ₂ -CBA (1 μM, 5 μM and 10 μM) and a non-functionalised DPP-DTT:GA thin-film.....	169
Figure 68 XPS high resolution P2p scans: DPP-DTT:GA thin-film functionalised with NH ₂ -CBA (10 μM) and DPP-DTT:GA thin-film functionalisation controls.	170
Figure 69 XPS high resolution P2p scans: DPP-DTT:GA OFET functionalised with NH ₂ -CBA (10 μM) before S/D deposition (blue) and after S/D deposition (green). Non-functionalised DPP-DTT:GA OFET (red) and DPP-DTT:GA thin-film (black).....	172
Figure 70 XPS high resolution O1s scans: DPP-DTT:GA OFET functionalised with NH ₂ -CBA (10 μM) before S/D deposition (black) and after S/D deposition (red).....	173
Figure 71 Water contact angles (left) and AFM roughness Ra and Rq values (right): DPP-DTT:GA thin-film functionalised with NH ₂ -CBA (10 μM) with measurements performed before and after S/D deposition. Compared to measurements of a non-functionalised DPP-DTT:GA thin-film after S/D deposition.....	174

Figure 72 Transfer (A) and output (B) characteristics of BGTC configured aptamer functionalised DPP-DTT:GA OFET. Transfer characteristics measured in linear regime ($V_{ds} -10$ V), log scale (blue), linear scale (black) and gate current (red). DPP-DTT:GA OFET functionalised with NH_2 -CBA ($10 \mu M$) before 50 nm gold source-drain electrode deposition. $40 \mu m$ channel length measured. 177

Figure 73 Real-time (A) normalised (B) current response of aptamer functionalised DPP-DTT:GA OFET to cortisol (2 nM to 2 mM). OFET biased at $V_{gs} -1$ V and $V_{ds} -0.5$ V. $40 \mu m$ channel length measured. 179

Figure 74 Aptamer functionalised DPP-DTT:GA OFET sensing mechanism. Cortisol introduction induces a conformational change in the cortisol binding aptamer, causing surface negative charge density to increase. Positive charges are induced in the DPP-DTT:GA layer, detected as an increase in current. Image adapted with permission from {M. L. Hammock, A. N. Sokolov, R. M. Stoltenberg, B. D. Naab, Z. Bao, Organic Transistors with Ordered Nanoparticle Arrays as a Tailorable Platform for Selective, In Situ Detection. ACS Nano. 6, 3100–3108 (2012).}. Copyright {2024} American Chemical Society.(132) 180

Figure 75 $\Delta I/I_0$ (%) vs. cortisol concentration (M) sensing response of aptamer functionalised DPP-DTT:GA OFET to cortisol (2 nM to 2 mM). OFET biased at $V_{gs} -1$ V and $V_{ds} -0.5$ V. $40 \mu m$ channel length measured. 181

Figure 76 Transfer characteristic response of an aptamer functionalised DPP-DTT:GA OFET to Tris-HCl and cortisol (2nM to $20 \mu M$) incubation. OFET V_{gs} bias swept from 10 to -40 V, V_{ds} biased at -0.5 V. $40 \mu m$ channel length measured. 184

Figure 77 (top) Charge carrier mobilities (blue) and (bottom) threshold voltages (black) and on currents (red) of an aptamer functionalised DPP-DTT:GA OFET to Tris-HCl and cortisol (2nM to $20 \mu M$) incubation. OFET V_{gs} bias swept from 10 to -40 V, V_{ds} biased at -0.5 V. $40 \mu m$ channel length measured. 185

Figure 78 Transfer (A) and output (B) characteristics of BGTC configured DPP-DTT:GA OFET modified with MoO_3 . Transfer characteristics measured in linear regime ($V_{ds} -10$ V), log scale (blue), linear scale (black) and gate current (red). Source-drain electrode deposition layers: MoO_3 (5 nm) and Gold (50 nm). $40 \mu m$ channel length measured. 188

Figure 79 Normalised currents of BGTC configured MoO ₃ modified (red) and unmodified (black) DPP-DTT:GA OFETs. OFETs biased at V _{gs} -1 V and V _{ds} -0.5 V. 40 μm channel length measured.	189
Figure 80 Real-time current of a DPP-DTT:GA OFET modified with SiO. Source-drain electrode deposition layers: Gold (50 nm) and SiO (50 nm). OFET biased at V _{gs} -1 V and V _{ds} -0.5 V. 40 μm channel length measured and exposed to aqueous buffer.	190
Figure 81 Chemical structures of N ₃ -DPP polymer and polydithieno[3,2-b:2',3'-d]pyrrole acid (PDTP-C4-acid).	197
Figure 82 AFM topological images (5 μm x 5 μm) of N ₃ -DPP thin-films via FFT from chlorobenzene (5 mg mL ⁻¹) on ODTs modified Si/SiO ₂ substrate. N ₃ -DPP polymer solution probe tip sonicated before deposition.	199
Figure 83 Aptamer attachment strategy of N ₃ -DPP thin-film: 1. Incubation with DBCO-CBA solution in DPBS (1 μM), then sequentially washed with 0.1 % tween20 solution and MQ water.	201
Figure 84 (left) XPS high resolution N1s scans (No. scans = 5, scan size = 400 μm): N ₃ -DPP thin-film via FFT from chlorobenzene (5 mg mL ⁻¹) on ODTs modified Si/SiO ₂ substrate. (red) N1s experimental curve (dark blue line) Peak fitted curve (orange lines) Component peaks (green line) Background (light blue line) residual (right) N ₃ -DPP thin-film with N1 and N2 labelled azide nitrogens.	202
Figure 85 XPS high resolution P2p scans (top) and water contact angles (bottom) of N ₃ -DPP thin-films incubated with Cy3-comp-CBA, DBCO-CBA and DBCO-CBA + Cy3-comp-CBA.	204
Figure 86 Transfer (left) and output (right) characteristics of BGTC configured N ₃ -DPP OFET. Transfer characteristics measured in linear regime (V _{ds} -1 V), log scale (blue), linear scale (black) and gate current (red). N ₃ -DPP thin-film via FFT from CB (5 mg mL ⁻¹) on ODTs modified Si/SiO ₂ , with 50 nm gold deposited source-drain electrodes. 50 μm channel length measured.	205
Figure 87 Structures of the DTP-C4-acid monomer and DTP-C4-acid polymer (PDTP-C4-acid).	207

Figure 88 Camera image of PDTP-C4-acid thin-film deposited on ITO coated glass substrate by chronoamperometry (5 mM DTP-C4-acid, 0.85 V, 30 s, degassed MeCN). Clear blue area represents the DTP-C4-acid film, colourless area is the ITO-coated glass substrate. 208

Figure 89 AFM topographical images (10 μm x 10 μm , 2.5 μm x 2.5 μm) of PDTP-C4-acid thin-film deposited via chronoamperometry on ITO substrate. 209

Figure 90 XPS high resolution C1s spectrum of PDTP-C4-acid thin-film deposited via chronoamperometry on ITO substrate. Scan size = 400 μm . (Black line) C1s experimental curve, (Red line) Peak fitted curve. Component peak assignment (blue) C-C/C=C (turquoise) C-S/C-N and (magenta) COOH. 210

Figure 91 PDTP-C4-acid thin-film aptamer attachment strategy: 1. Incubation with $\text{NH}_2\text{-CBA}$ solution in DPBS (10 μM), then sequentially washed with 0.1 % tween20 solution and MQ water. 211

Figure 92 Hybridisation of aptamer functionalised PDTP-C4-acid thin-film with Cy3 labelled complimentary strand: 1. Cy3-comp-CBA (1 μM) hybridisation then washed with 0.1 % tween20 solution and MQ water. 212

Figure 93 Epifluorescence microscopy average pixel values of PDTP-C4-acid thin-films deposited via chronoamperometry. Thin-films functionalised with $\text{NH}_2\text{-CBA}$, via EDC/sulfo-NHS, and hybridised with COMP-CBA-Cy3 (sample 1). Control thin-films also presented (samples 2 – 7). 213

Figure 94 (A.) Scheme of DTP-C4-acid deposition on gold electrodes deposited onto polyimide substrate via chronoamperometry (0.85 V, 120 s) (B.) Microscope image of the electrodes (50 μm channel length) after the 1st PDTP-C4-acid deposition (C.) Microscope image of the electrodes (50 μm channel length) after the 2nd PDTP-C4-acid deposition (D.) Camera image of OECT after DTP-C4-acid deposition. 216

Figure 95 AFM topological images (5 μm x 5 μm , 2.5 μm x 2.5 μm) of PDTP-C4-acid thin-film deposited via chronoamperometry on gold electrodes on a polyimide substrate (50 μm channel length). 217

Figure 96 (left) Camera image showing probe station characterisation setup of PDTP-C4-acid OECT. 50 μm channel length. (blue oval) 20 μL of DPBS electrolyte solution overlapping PDTP-

C4-acid thin-film and gold gate electrode. (white) biasing positions of source/drain (yellow) biasing position of gate electrode. (right) Microscope image of DBPS electrolyte solution covering PDTP-C4-acid thin-film.	218
Figure 97 (A) Transfer and (B) output characteristics of PDTP-C4-acid OECT. Transfer characteristics measured V_g sweep 0.7 V to -0.7 V, V_{ds} -0.7 V. Output characteristics measured V_{ds} sweep 0.0 V to -0.7 V, V_g s 0.5 V to -0.7 V (-0.1 V intervals). (C) Real-time current V_g -0.7 V and V_{ds} -0.7 V and controls. DPBS electrolyte solution (20 μ L). 50 μ m channel length.	219
Figure 98 Polyimide tape isolated source-drain electrodes. Centre electrodes within Biopunctured hole are exposed. Electrode edges are insulated with polyimide tape.	220
Figure 99 (A.) Polydimethylsiloxane (PDMS) well transferred onto OECT substrate. Polyimide adhesive tape used to selectively expose source-drain electrode channel and contact pads. (B.) Scheme of chronoamperometry setup for selective DTP-C4-acid thin-film deposition. (C.) Microscope images of the source-drain electrodes (50 μ m channel length) after the 1 st (left) and 2 nd (right) PDTP-C4-acid thin-film depositions, via chronoamperometry (0.85 V, 120 s).	221
Figure 100 AFM topographical images (10 μ m x 10 μ m) of DPP-DTT thin-films via FFT from 9:1 CHCl_3 :CB (10 mg mL^{-1}) on Si/SiO ₂ substrates.	230
Figure 101 AFM topographical image and height profile (10 μ m x 10 μ m) of a DPP-DTT thin-film via FFT from 9:1 CHCl_3 :CB (10 mg mL^{-1}) on Si/SiO ₂ substrates.	231
Figure 102 AFM topographical images (10 μ m x 10 μ m) of a DPP-DTT thin-film spin coated from 9:1 CHCl_3 :CB (10 mg mL^{-1}) on Si/SiO ₂ substrate.	232
Figure 103 AFM topographical images (10 μ m x 10 μ m) of DPP-DTT thin-films via FFT from 9:1 CHCl_3 :CB (5 mg mL^{-1}) on Si/SiO ₂	233
Figure 104 AFM topographical images and height profiles (10 μ m x 10 μ m) of DPP-DTT thin-films via FFT from 9:1 CHCl_3 :CB (5 mg mL^{-1}) on Si/SiO ₂	236
Figure 105 AFM topographical images (10 μ m x 10 μ m) of DPP-DTT thin-films via FFT from 9:1 CHCl_3 :CB (3 mg mL^{-1}) on Si/SiO ₂	237

Figure 106 AFM topographical images and height profiles (20 μm x 20 μm) of DPP-DTT thin-films via FFT from 9:1 CHCl_3 :CB (3 mg mL^{-1}) on Si/SiO ₂	240
Figure 107 AFM topographical images (10 μm x 10 μm) of DPP-DTT thin-films via FFT from 9:1 CHCl_3 :CB (3 mg mL^{-1}) on ODTS modified Si/SiO ₂ substrates.....	241
Figure 108 AFM topographical images and height profiles (20 μm x 20 μm) of DPP-DTT thin-films via FFT from 9:1 CHCl_3 :CB (3 mg mL^{-1}) on ODTS modified Si/SiO ₂ substrates.	246
Figure 109 Water contact angle images of ODTS modified Si/SiO ₂ (300 nm) substrates.	248
Figure 110 Water contact angle image of pre-modified Si/SiO ₂ (300 nm) substrate.....	248
Figure 111 AFM topographical images (10 μm x 10 μm) of ODTS modified Si/SiO ₂ substrates.	249
Figure 112 AFM topographical images (10 μm x 10 μm) of Si/SiO ₂ substrates.	250
Figure 113 AFM topological images (50 μm x 50 μm) and height profiles of physical vapour deposited gold (50 nm) S/D electrodes on DPP-DTT thin-film via FFT from 9:1 CHCl_3 :CB (3 mg mL^{-1}).	252
Figure 114 Transfer characteristics ($V_{\text{ds}} -1$) of OFETs (left) before and (right) after O ₂ plasma treatment (blue) log scale (black) linear scale (red) gate current.	256
Figure 115 Transfer characteristics (left) $V_{\text{ds}} -1$ (right) $V_{\text{ds}} -10$ of DPP-DTT OFETs before N ₂ plasma treatment (blue) log scale (black) linear scale (red) gate current.....	263
Figure 116 Output characteristics of DPP-DTT OFETs before N ₂ plasma treatment.....	269
Figure 117 Transfer characteristics (left) $V_{\text{ds}} -1$ (right) $V_{\text{ds}} -10$ of DPP-DTT OFETs after N ₂ plasma treatment (blue) log scale (black) linear scale (red) gate current.....	271
Figure 118 Output characteristics of DPP-DTT OFETs after N ₂ plasma treatment.....	277
Figure 119 XPS N1s high resolution scan N ₂ plasma treated DPP-DTT thin-films.	279
Figure 120 XPS high resolution C1s scans of DPP-DTT OFETs N ₂ plasma treated.	280
Figure 121 Epifluorescence microscopy images (51.2 μm x 51.2 μm) of 1.0 mg mL^{-1} BCH-NHS, 1 μM N ₃ -CBA functionalised 12 W, 60 s N ₂ plasma treated DPP-DTT thin-films, fluorescently labelled with 1 μM Cy3-comp-CBA, and control thin-films.....	283
Figure 122 AFM topographical images and height profiles (50 μm x 50 μm) of spin coated 5 mg mL^{-1} in chlorobenzene DPP-DTT:GA thin-films on ODTS modified Si/SiO ₂ substrates. ...	291

Figure 123 AFM topographical images (10 μm x 10 μm) of 10 μM aptamer functionalised DPP- DTT:GA thin-films before and after S/D deposition.	294
Figure 124 AFM topological image and cross section of DPP-DTT:GA OFET with molybdenum trioxide (50 nm) and gold (50 nm) source-drain electrodes.....	295
Figure 125 AFM topological image and cross section of DPP-DTT:GA OFET with gold (50 nm) and silicon monoxide (50 nm) source-drain electrodes.	297
Figure 126 Water contact angle measurements of DPP-DTT:GA thin-film and NH ₂ -CBA functionalised (1 μM , 5 μM and 10 μM) thin-films.	298
Figure 127 Water contact angle measurements of 10 μM aptamer functionalised DPP-DTT:GA thin-films before and after S/D deposition.....	300
Figure 128 Epifluorescence microscopy images: DPP-DTT:GA thin-film functionalised with NH ₂ -CBA (10 μM) and hybridised with Cy3-comp-CBA (1 μM), and thin-film controls (51.2 μm x 51.2 μm).	301
Figure 129 Scaled real-time current response of functionalised DPP-DTT:GA OFET, V _{gs} -1 V, V _{ds} -0.5 V to cortisol (2 nM to 2 mM).	304
Figure 130 Real-time current response of non-functionalised DPP-DTT:GA OFET, V _{gs} -1 V, V _{ds} -0.5 V to cortisol (2 nM to 200 μM).	304
Figure 131 AFM thickness images (50 μm x 50 μm) of N ₃ -DPP thin-film via FFT from chlorobenzene (5 mg mL ⁻¹). Polymer solution probe sonicated.	307
Figure 132 Water contact angle measurements. N ₃ -DPP thin-films incubated with: Cy3-comp- CBA (1 μm), DBCO-CBA (1 μm) and DBCO-CBA (1 μm) + Cy3-comp-CBA (1 μm).....	308
Figure 133 AFM topographical images (10 μm x 10 μm) of ITO substrate.	309
Figure 134 AFM topographical image (10 μm x 10 μm) and height profiles of DTP-C4-acid thin- film deposited via chronoamperometry on ITO substrate.	310
Figure 135 AFM topological images and section height profiles (5 μm x 5 μm) of PDTP-C4-acid thin-film deposited via chronoamperometry onto gold electrodes on a polyimide substrate (50 μm channel length), white line indicates section analysed.	312

Figure 136 Epifluorescence microscopy images: DTP-C4-acid thin-films functionalised with NH₂-CBA (10 μM) and hybridised with Cy3-comp-CBA (1 μM), and thin-film controls (1.39 mm x 1.39 mm). 315

iii. List of Tables

Table 1 Introduction of chemical binding sites and receptor functionalisation strategies of organic semiconductors for OTFT biosensors. CuAAC = Copper-catalysed azide-alkyne cycloaddition, SPAAC = Strain-promoted alkyne-azide cycloaddition, BPA = bisphenol A, AFP = α-fetoprotein, CEA = carcinoembryonic antigen, ATP = adenosine triphosphate 67

Table 2 Names, abbreviations, structures and information of organic semiconducting materials 71

Table 3 Names, specifications and supplier information of substrates and substrate modifying materials 72

Table 4 Ossila supplied high density 50 μm channel length interdigitated source-drain deposition mask dimensions 73

Table 5 Ossila supplied low density variable (30, 40, 50, 60, 80 μm) channel length source-drain deposition mask dimensions 74

Table 6 Names, abbreviations, specifications and supplier information of deposition materials 75

Table 7 Names, specifications and supplier information of solvents..... 75

Table 8 Names, abbreviations, structures and supplier information of aptamer functionalisation chemicals 76

Table 9 Names, abbreviations and sequences of DNA strands used within thesis 77

Table 10 Spin coating conditions for 5 mg mL⁻¹ DPP-DTT:GA (25 % in H₂O), 9:1 in chlorobenzene polymer solution 83

Table 11 Physical vapour deposition settings and conditions of deposited materials 103

Table 12 Additional equipment details 105

Table 13 Transfer characteristic figures of merit from linear and saturation regimes. 122

Table 14 O₂ plasma exposure series conditions. 126

Table 15 N₂ plasma exposure series conditions (DPP-DTT038) 136

Table 16 AFM monitored changes in thin-film thickness of O ₂ and N ₂ plasma treated OFETs.	137
Table 17 Additional N ₂ plasma exposure series conditions.....	138
Table 18 Spin coating series conditions: DPP-DTT:GA (9:1) thin-films from chlorobenzene (5 mg mL ⁻¹) on ODTs modified Si/SiO ₂ substrates.	157
Table 19 DPP-DTT:GA NH ₂ -CBA functionalisation concentration series.	165
Table 20 Transfer characteristic figures of merit of aptamer functionalised DPP-DTT:GA OFET. DPP-DTT:GA OFET functionalised with NH ₂ -CBA (10 μM) before 50 nm gold source-drain electrode deposition. 40 μm channel length measured.	177
Table 21 OFET performance metrics V _{th} , μ and on/off ratio of DPP-DTT:GA OFET modified with MoO ₃	188
Table 22 Nitrogen ratios of N ₃ -DPP 80:20 copolymer. Expected nitrogen atomic % and actual nitrogen atomic % determined from XPS high resolution N1s scans.....	203
Table 23 Transfer characteristic figures of merit of an N ₃ -DPP OFET. N ₃ -DPP thin-film via FFT from CB (5 mg mL ⁻¹) on ODTs modified Si/SiO ₂ , with 50 nm gold deposited source-drain electrodes. 50 μm channel length measured.....	206
Table 24 Epifluorescence microscopy: Index of PDTP-C4-acid aptamer (NH ₂ -CBA) functionalisation and hybridisation (Cy3-comp-CBA) conditions. ✓ = present, X = absent..	212
Table 25 Averaged Roughness R _q and R _a values (3 x 2 μm x 2 μm areas) of DPP-DTT thin-films via FFT from 9:1 CHCl ₃ :CB (10 mg mL ⁻¹) on Si/SiO ₂ substrates.	231
Table 26 Averaged roughness R _q and R _a values (3 x 2 μm x 2 μm areas) of a DPP-DTT thin-film spin coated from 9:1 CHCl ₃ :CB (10 mg mL ⁻¹) on Si/SiO ₂ substrate.....	232
Table 27 Averaged roughness R _q and R _a values (3 x 2 μm x 2 μm ² areas) of DPP-DTT thin-films via FFT from 9:1 CHCl ₃ :CB (5 mg mL ⁻¹) on Si/SiO ₂	234
Table 28 Thickness values of DPP-DTT thin-films via FFT from 9:1 CHCl ₃ :CB (5 mg mL ⁻¹) on Si/SiO ₂	236
Table 29 Averaged roughness R _q and R _a values (3 x 2 μm x 2 μm ² areas) of DPP-DTT thin-films via FFT from 9:1 CHCl ₃ :CB (3 mg mL ⁻¹) on Si/SiO ₂	238

Table 30 Thickness values of DPP-DTT thin-films via FFT from 9:1 CHCl ₃ :CB (3 mg mL ⁻¹) on Si/SiO ₂	240
Table 31 Averaged roughness Rq and Ra values (3 x 2 μm x 2 μm areas) of DPP-DTT thin-films via FFT from 9:1 CHCl ₃ :CB (3 mg mL ⁻¹) on ODTS modified Si/SiO ₂ substrates.....	241
Table 32 Thickness values of DPP-DTT thin-films via FFT from 9:1 CHCl ₃ :CB (3 mg mL ⁻¹) on ODTS modified Si/SiO ₂ substrates.	247
Table 33 Water contact angles of ODTS modified Si/SiO ₂ substrate and pre-modified Si/SiO ₂ (300 nm) substrate.....	248
Table 34 AFM image roughness values Rq and Ra of ODTS modified Si/SiO ₂ substrates.	249
Table 35 AFM image roughness values Rq and Ra of Si/SiO ₂ substrates.	250
Table 36 Thickness values of physical vapour deposited gold (50 nm) S/D electrodes on DPP-DTT thin-film via FFT from 9:1 CHCl ₃ :CB (3 mg mL ⁻¹).	252
Table 37 Thin-film thickness values of DPP-DTT OFETs before O ₂ plasma treatment.	253
Table 38 Thin-film thickness values of DPP-DTT OFETs after O ₂ plasma treatment and change in thickness.....	253
Table 39 Thin-film roughness values of DPP-DTT OFETs before and after O ₂ plasma treatment.	253
Table 40 OFET transfer characteristics (V _{ds} -1) mobility and threshold voltage values before and after O ₂ plasma treatment.....	257
Table 41 XPS high resolution C1s scan component peak areas of DPP-DTT OFETs O ₂ plasma treated and untreated.	258
Table 42 XPS high resolution O1s, N1s, S2p, Si2p scan peak areas of DPP-DTT OFETs O ₂ plasma treated and untreated.	258
Table 43 Thin-film thicknesses of DPP-DTT OFETs before N ₂ plasma treatment.....	259
Table 44 Thin-film thicknesses of DPP-DTT OFETs after N ₂ plasma treatment and change in thin-film thickness.....	259
Table 45 Thin-film roughness Ra and Rq values of DPP-DTT OFETs before N ₂ plasma treatment.	259

Table 46 Thin-film roughness Ra and Rq values of DPP-DTT OFETs after N ₂ plasma treatment.	260
Table 47 Thin-film thickness values of DPP-DTT OFETs before N ₂ plasma treatment.	260
Table 48 Thin-film thickness values of DPP-DTT OFETs after N ₂ plasma treatment.	260
Table 49 Thin-film roughness Ra and Rq values of DPP-DTT OFETs before N ₂ plasma treatment.	261
Table 50 Thin-film roughness Ra and Rq values of DPP-DTT OFETs after N ₂ plasma treatment.	261
Table 51 OFET transfer characteristics (V _{ds} -1) mobility and threshold voltage values before N ₂ plasma treatment.....	264
Table 52 OFET transfer characteristics (V _{ds} -10) mobility and threshold voltage values before N ₂ plasma treatment.....	265
Table 53 OFET transfer characteristics (V _{ds} -1) mobility and threshold voltage values after N ₂ plasma treatment.	272
Table 54 OFET transfer characteristics (V _{ds} -10) mobility and threshold voltage values after N ₂ plasma treatment.....	273
Table 55 XPS high resolution C1s scan component peak areas of N ₂ plasma treated OFETs.	280
Table 56 Epifluorescence microscopy images average pixel value data of 1.0 mg mL ⁻¹ BCH-NHS, 1 μM N ₃ -CBA functionalised 12 W, 60 s N ₂ plasma treated DPP-DTT thin-films, fluorescently labelled with 1 μM Cy3-comp-CBA and control thin-films.....	283
Table 57 Spin coating thin-film thickness.	292
Table 58 AFM averaged roughness values Ra and Rq spin coating series.	292
Table 59 AFM averaged roughness values Ra and Rq of 10 μM aptamer functionalised DPP- DTT:GA thin-films before and after S/D deposition.	294
Table 60 Water contact angle measurement pristine, 1 μM, 5 μM and 10 μM functionalised DPP-DTT:GA thin-films.	299
Table 61 Water contact angle measurements of 10 μM aptamer functionalised DPP-DTT:GA thin-films before and after S/D deposition.....	300

Table 62 Epifluorescence microscopy image pixel values: DPP-DTT:GA thin-film functionalised with NH ₂ -CBA (10 μM) and hybridised with Cy3-comp-CBA (1 μM), and thin-film controls (51.2 μm x 51.2 μm).....	302
Table 63 XPS relative atomic % of DPP-DTT:GA control, 1 μM, 5 μM and 10 μM thin-films.	303
Table 64 Roughness Rq and Ra values of N ₃ -DPP thin-film via FFT from chlorobenzene (5 mg mL ⁻¹). Polymer solution probe sonicated.....	305
Table 65 Thin-film thicknesses of N ₃ -DPP thin-film via FFT from chlorobenzene (5 mg mL ⁻¹). Polymer solution probe sonicated.....	307
Table 66 AFM height profiles: vertical distance of masses on DTP-C4-acid thin-film deposited via chronoamperometry on ITO substrate.	310
Table 67 AFM roughness values Rq and Ra of DTP-C4-acid thin-film deposited via chronoamperometry on ITO substrate. Thin-film roughness measured at 250 nm x 250 nm areas, avoiding large masses.	311
Table 68 Epifluorescence microscopy average image pixel values: DTP-C4-acid thin-films functionalised with NH ₂ -CBA (10 μM) and hybridised with Cy3-comp-CBA (1 μM), and thin-film controls (1.39 mm x 1.39 mm).....	315

1 Introduction

1.1 Organic electronics

Organic electronics is a flourishing multidisciplinary field that capitalises on the fascinating properties of organic materials for applications in electronic devices. Overlapping several academic disciplines including chemistry, biology, physics and engineering; organic electronic researchers have been persistent in exploiting the advantageous qualities of organic materials for incorporation into existing technologies. Conventional silicon based technologies, which have defined and influenced the modern era, encounter specific limitations hindering further advancement due to the inherent characteristics and manufacturing processes associated with silicon. Organic materials address these limitations, as they possess favourable characteristics relating to flexibility, chemical tuneability, processability and low material cost. As such, organic materials have been explored to advance existing transistor, light emitting diode, photovoltaic and thermoelectric technologies.(1) Among these organic materials, those exhibiting semiconducting properties, referred to as organic semiconductors, have played a defining role in the field. Semiconductors are unique materials as they can be tuned to function as either an electrical insulator or conductor, through the influence of extrinsic factors. Conventional electrical conductors and insulators refer to materials with electrical conductivities $> 10^{-1} \text{ S m}^{-1}$ and $< 10^{-6} \text{ S m}^{-1}$, respectively. Semiconducting materials exhibit conductivities that range between the values of insulators and conductors.(2) Pure water is an example of an electrical insulator with a conductivity of $5.50 \times 10^{-6} \text{ S m}^{-1}$, where as copper metal is an electrical conductor with a conductivity of $5.84 \times 10^7 \text{ S m}^{-1}$.(3)

Progress with organic semiconductors accelerated in 1977, after Heeger, Shirakawa, and MacDiarmid discovered thin-films of polyacetylene, an organic semiconducting polymer, could achieve metallic electrical conductivities by doping with iodine.(4) Later, this serendipitous breakthrough would earn them the 2000 Noble Prize in chemistry.(5) Organic semiconductors have diversified from polyacetylene, yet polymers remain a significant material in organic electronics.

1.2 Organic semiconducting polymers

Organic semiconductors can be classified into a diverse range of carbon-rich materials. Overlapping different carbon allotropes such as graphene(6), buckminsterfullerene(7) and carbon nanotubes(8), as well as covalent organic frameworks (COFs)(9), organic small molecules and polymers.(10)

Organic semiconducting polymers are conjugated systems, simplified as a backbone containing a series of alternating single (σ -bonds) and double (π -bonds) carbon-carbon bonds. Semiconducting properties originate from this extended conjugated system, which enables the delocalisation of π electrons across the system through overlapping π orbitals. Elongating ethylene into polyacetylene demonstrates how an extended conjugation length transforms a previously insulating material into a semiconductor (Figure 1). π bonding and π^* anti-bonding orbitals within ethylene form discrete energy levels, which are referred to as the highest occupied molecular orbital (HOMO) and lowest unoccupied molecular orbital (LUMO), respectively. The HOMO and LUMO levels are separated by an energy gap, referred to as the bandgap. Additional single and double carbon bonds introduce additional energy levels which gradually reduce the bandgap between the HOMO and LUMO. Extending the conjugation to a semi-infinite length (polyacetylene) merges these discrete energy levels into bands, referred to as the valence band (HOMO) and conduction band (LUMO).(11)

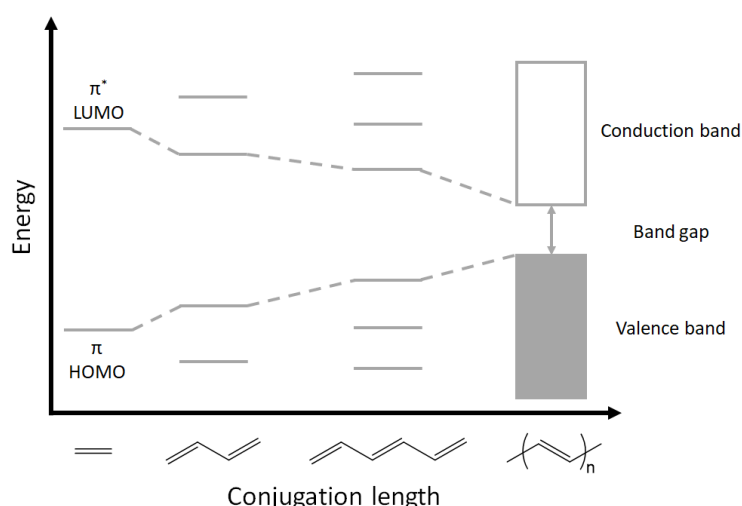


Figure 1 Increasing conjugation length leading to a narrowing of band gap

In their natural state, organic semiconductors act as insulators and are not intrinsically conducting, as the bandgap is too large for the excitation of an electron from the HOMO to the LUMO. However, conductivity can be controlled allowing charges to be transported through the material. The addition of an electron to the conduction band or the removal of an electron from the valence band, allows the resulting charge carrier (i.e. an electron or hole) to travel across the delocalised system. Charge carrier generation can be induced by chemical or electrochemical doping processes (12), as well as from the application of an electric field.(13)

The transport of charge carriers through a conjugated polymer is predominantly governed by two distinct mechanisms: intrachain charge transport and interchain charge transport. Intrachain charge transport occurs along the polymer backbone, whereas interchain charge transport occurs between neighbouring polymer chains, mediated through partially overlapping π orbitals.(14) Of these two, interchain charge transport is the limiting transport mechanism, with intrachain charge transport being roughly 1,000 times faster.(15) Though charge transport is strongly influenced by additional factors such as doping density, chemical impurities, dipole formation and morphological disorders.(16)

A figure of merit used to evaluate charge transport within an organic semiconductor is the charge carrier mobility ($\text{cm}^2 \text{V}^{-1} \text{s}^{-1}$), which can be extracted from an organic field-effect transistor (OFET). Charge carrier mobility (μ) measures the average drift velocity of charge carriers (holes or electrons) under a unit electric field.(17) Higher charge carrier mobilities are desired, as they indicate that charge carriers are transported more efficiently through the material. Charge carrier mobilities of organic semiconducting polymers have progressed from initial values of $10^{-5} \text{cm}^2 \text{V}^{-1} \text{s}^{-1}$ to values consistently greater than $10 \text{cm}^2 \text{V}^{-1} \text{s}^{-1}$.(18, 19) Values far exceeding this have been reported, but have been considered overestimated due to incorrect mobility extraction from non-ideal characteristics.(20) Charge carrier mobility is usually the main performance factor of organic semiconducting polymers, although other performance values exist in organic electronics for characterising materials, such as conductivity in thermoelectric materials.(21)

Organic semiconductor structures

Organic semiconducting polymers have increased in complexity since the study of first generation materials, such as polyacetylene (Figure 2). Second generation polymers (P3HT) introduced features such as solubilising side-chains, which improved the synthesis and deposition of the material. Third generation polymers, such as PBTTT, further improved the microstructure of thin-films, which increased the charge transport properties of the material.(22)

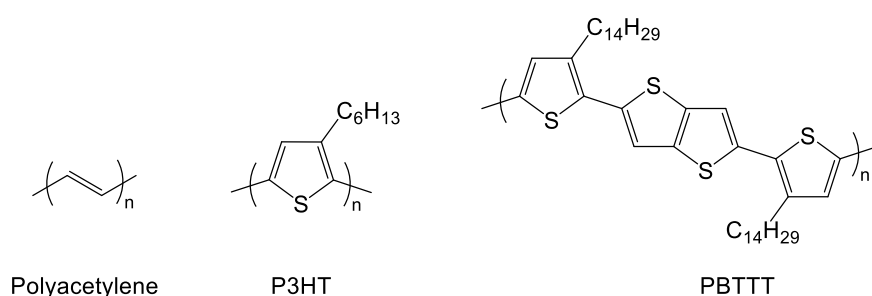


Figure 2 Selected examples of generational organic semiconducting polymers: Polyacetylene (1st generation) P3HT (2nd generation) PBTTT (3rd generation)

Organic semiconducting polymers consist of a chain of repeated aromatic monomer units, with the properties of the monomers influencing the polymer characteristics. Depending on the electron affinities of these monomers they are labelled as either acceptors or donors. Commonly reported examples of acceptor and donor monomers are presented in Figure 3. Donor monomers are electron rich, while acceptors are electron deficient. The monomer makeup of the polymer alters the HOMO/LUMO levels, which influences the preferred type of charge carrier (electron or hole) transported through the material. Polymers with high HOMO levels allow for the efficient removal of an electron and the transport of holes. Whereas, polymers with lowered LUMO levels allow for the addition of an electron and the efficient transport of electrons. Holes are charge carriers transported by materials referred to as p-type semiconductors, while electrons are transported by n-type semiconductors. Organic semiconducting polymers that can transport both holes and electrons also exist, which are referred to as ambipolar materials.(23)

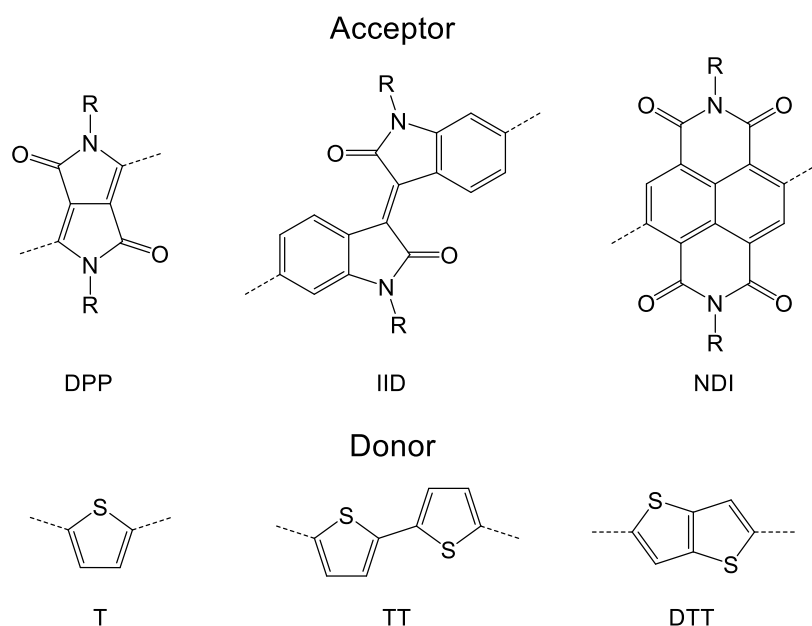


Figure 3 Examples of common acceptor and donor monomer units in organic semiconducting polymers

Generally, the bandgap restricts the type of charge carrier transported through a material, though other factors can overcome this.⁽²⁴⁾ The transport of electrons through a commonly understood p-type polymer (P3HT) in an organic field-effect transistor (OFET) has been reported. The OFET was fabricated with calcium source-drain electrodes and hydroxyl groups on the dielectric surface were passivated, which enabled electron transport.⁽²⁵⁾ HOMO and LUMO levels also influence the ambient stability of the material against oxidation and nucleophilic attack from oxygen and water molecules, respectively.⁽²⁶⁾ N-type materials have generally lagged behind the performance values of p-type materials, partly due to their poor air and aqueous stabilities. Additive blends and molecular design strategies have improved n-type stabilities, however the following sections will only discuss p-type materials.^(27, 28)

In polymer chemistry, polymers consisting of a single monomer unit repeated throughout the system are referred to as homopolymers. Organic semiconducting homopolymers containing either purely acceptor or donor monomers can influence the materials type (e.g. p-type or n-type). The polymer chains of p-type homopolymers contain an arrangement of donor monomers. Regioregular poly(3-hexylthiophene) (rr-P3HT) is a p-type organic semiconducting polymer, that is well researched due to its ease of synthesis, cost effectiveness and

processability. P3HT (Figure 2) is a model material that helped establish a lot of early general guidelines for high-performing conjugated polymers. Thin-films of rr-P3HT exhibit high levels of crystallinity, due to the highly ordered arrangement of the polymer chains.(29) Ordered packing was enabled by high backbone planarity, which maintains conjugation lengths along the polymer chains and avoids disrupting charge transport.(30, 31) These favourable properties increased charge carrier mobilities of rr-P3HT OFETs to $> 0.1 \text{ cm}^2 \text{ V}^{-1} \text{ s}^{-1}$. The design rules of P3HT influenced later higher performing thiophene based polymers, such as poly[2,5-bis(3-tetradecylthiophen-2-yl)thieno[3,2-b]thiophene] (PBTTT), which obtained charge carrier mobilities of $1.1 \text{ cm}^2 \text{ V}^{-1} \text{ s}^{-1}$.(32) Further enhancement of charge carrier mobility values in homopolymers were limited and eventually surpassed by donor-acceptor polymers. Despite this, P3HT is still ubiquitous in the literature, as its adaptability makes it useful for novel proof-of-concept studies.

Donor-acceptor polymers

Donor-acceptor (D-A) polymers often demonstrate higher charge carrier mobilities ($> 1.0 \text{ cm}^2 \text{ V}^{-1} \text{ s}^{-1}$), relative to polymers containing only donor or acceptor monomers. Unlike homopolymers, donor-acceptor polymers consist of an alternating arrangement of donor and acceptor monomers (Figure 4). The combination of various donor and acceptor monomers allows the HOMO and LUMO levels to be controlled through synthetic design, with some materials forming low bandgaps ($\sim 1 \text{ eV}$). This is possible as the LUMO is mainly sited at the acceptor, while the HOMO is sited at the donor. The tuneability of the HOMO/LUMO levels in D-A polymers has enabled the design of p-type, n-type and ambipolar transporting materials.(15)

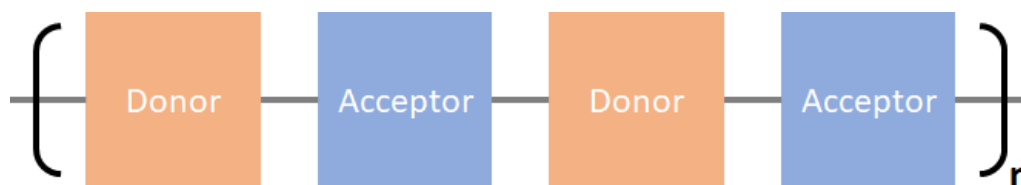


Figure 4 Alternating structure of donor-acceptor polymers

The exceptional charge carrier mobilities displayed by D-A polymers were initially unexpected, as they contradicted current charge transport guidelines. Thin-films of D-A polymers were noticeably less crystalline than homopolymer thin-films, which was thought to be a requirement for effective charge transport. The reason why D-A polymers can obtain such high mobilities with less optimal microstructures is still being understood. Instead, a separate set of design guidelines have been developed for high performing D-A polymers.(15)

Donor-acceptor polymers have highly planar and rigid backbones, enabling polymer chains to maintain tightly packed and flat conformations, through π - π stacking. Backbone conjugation lengths and π orbital overlap from neighbouring polymer chains are improved, which further enhances charge transport. Planarity and rigidity is further enhanced in D-A polymers by incorporating monomers that have fused aromatic ring structures, as well as those that can form noncovalent conformational locks with adjacent monomers, as shown in Figure 5.(33)

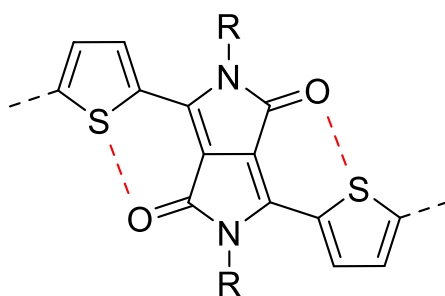


Figure 5 Noncovalent conformational locking between S---O, in a diketopyrrolopyrrole monomer and flanking thiophene monomers

The alternating D-A monomer arrangement also imparts beneficial qualities to the self-assembly of the polymer chains within a thin-film. Bulky groups within acceptor monomers, such as carbonyls, amides and imides, can sterically hinder polymer chains, leading to a twisted backbone. However, the regular alteration of donor and acceptor monomers allows the chains to pack in a more favourable and less sterically hindered conformation.(29)

Molecular weights of D-A polymers are also an important and controllable material parameter, as increased molecular weight correlates with higher charge carrier mobility. This dependence is explained by longer polymer chains more densely connecting ordered regions in thin-films, facilitating charge transport through less ordered regions.(34) Mobility

continues to increase until a saturation point is reached, when interchain charge transport becomes limited. For D-A polymers the charge carrier mobility tends to saturate at molecular weights $\sim 100 \text{ kg mol}^{-1}$.(15, 35) However, increasing the molecular weight of a polymer often lowers its solubility, making the solution processability of the material more challenging. A balance point needs to be found between insoluble-high molecular weight polymers and low mobility-low molecular weight polymers.(36)

Of these donor-acceptor polymer systems, those incorporating the accepting monomer diketopyrrolopyrrole (DPP) frequently report high charge carrier mobilities.(37) Additionally, the versatility of DPP polymers have seen their use in a range of applications within organic electronics, such as photovoltaics, thermoelectrics and bioelectronics.(38) Previously used as a pigment, the fused aromatic ring of DPP exhibits high planarity and strong electron deficiency.(39) The DPP core is usually flanked by aryl units, which improves the planarity and rigidity of resulting polymers, through chalcogen interactions (Figure 5).(40) Nitrogen atoms within the DPP core are available for the attachment of various side-chain groups, allowing the properties of DPP polymers to be finely tuned. Generally, linear or branched alkyl chains are attached to improve polymer solubility, as well as to control the molecular packing of the polymer chains. Alkyl chain length and branching point are factors that can influence the steric hinderance of the bulky chains and π - π stacking distances.(41) Incorporation of functionalised side-chains (e.g. siloxane) can further improve π - π stacking.(42, 43)

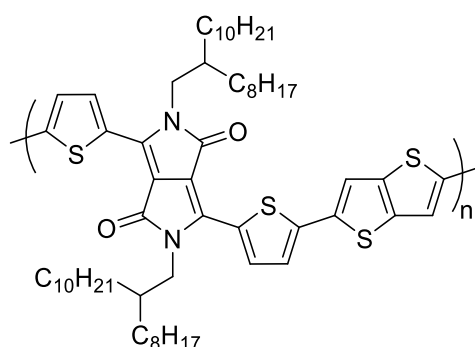


Figure 6 Chemical structure of Poly[2,5-(2-octyldodecyl)-3,6-diketopyrrolopyrrole-alt-5,5-(2,5-di(thien-2-yl)thieno [3,2-b]thiophene)] (DPP-DTT)

A range of donor monomers can be copolymerised with DPP. However, those copolymerised with thienothiophene (TT) to form the D-A polymer DPP-DTT (Figure 6), consistently report high charge carrier mobilities. The first reported synthesis of DPP-DTT demonstrated a charge carrier mobility of $0.94 \text{ cm}^2 \text{ V}^{-1} \text{ s}^{-1}$.⁽⁴⁴⁾ Through further optimisation DPP-DTT would later demonstrate mobilities $> 10 \text{ cm}^2 \text{ V}^{-1} \text{ s}^{-1}$, as well as excellent stability in ambient conditions.⁽⁴⁵⁾ The high performance of the polymer arises from the strong intermolecular interactions between the DPP and TT monomers. Consequently, the polymer chains observe short π - π stacking distances (3.4 \AA), resulting in enhanced charge transport. The short π - π stacking distances are also theorised to contribute to the high aqueous stability of DPP-DTT.⁽⁴⁶⁾ The high performance and solution processability of DPP-DTT has led to its commercial availability and wider success in organic electronics.

1.3 Organic Field-effect Transistors

Organic semiconducting polymers have multiple applications within organic electronics, such as in thermoelectric generators(47), photovoltaics(48) and light emitting diodes(49). With applications in organic field-effect transistors (OFETs) building considerable interest.(50, 51) Since the invention of the first metal-oxide field-effect transistor (MOSFET) by Kahng and Atalla at Bell Labs in 1960, FETs have become integral components within modern electronics.(52) Organic field-effect transistors were later realised in 1986, utilising an electrochemically polymerised film of polythiophene as the organic semiconductor.(53) In the following years, OFETs have been extensively researched and are achieving performances rivalling that of their inorganic counterparts.

The advantageous properties of organic semiconductors has majorly inspired and maintained the research appeal of OFETs. Properties that enable large-area fabrication of flexible OFETs, through the use of various solution processing and printing techniques, offer substantial cost benefits. Major milestones have since been realised and surpassed, through the development of high-performing organic semiconductors and interface engineering.(54) In particular, OFETs have experienced significant improvements to charge carrier mobilities, going from $10^{-5} \text{ cm}^2 \text{ V}^{-1} \text{ s}^{-1}$ to over $10 \text{ cm}^2 \text{ V}^{-1} \text{ s}^{-1}$.(55) Charge carrier mobilities of OFETs now exceed those of thin-film amorphous silicon FETs (0.5 to $1.0 \text{ cm}^2 \text{ V}^{-1} \text{ s}^{-1}$) and are within range of polycrystalline silicon FETs (1 to $1000 \text{ cm}^2 \text{ V}^{-1} \text{ s}^{-1}$), two current materials used in modern electronics.(19, 56) Through these improvements OFETs have been successfully utilised in applications including integrated circuits(57), for electronic memory storage(58) and as sensors.(59–61) Additionally, OFETs that consume low amounts of energy(19), have flexible and stretchable properties(62), as well as self-healing properties have been reported.(63) Continued research will lead to OFETs achieving further milestones and the discovery of novel applications.

Organic-field effect transistor operation

Organic-field effect transistors are three terminal electronic devices comprised of a gate electrode, dielectric layer, organic semiconductor layer and source-drain contacts, which are supported by a substrate (Figure 7). Charge carriers flow within a conductive channel (organic semiconductor) between two terminals (source and drain), which is modulated by the third terminal (gate). The distance between the source and drain electrodes is defined as the channel length (L), while the width is defined as the channel width (W).

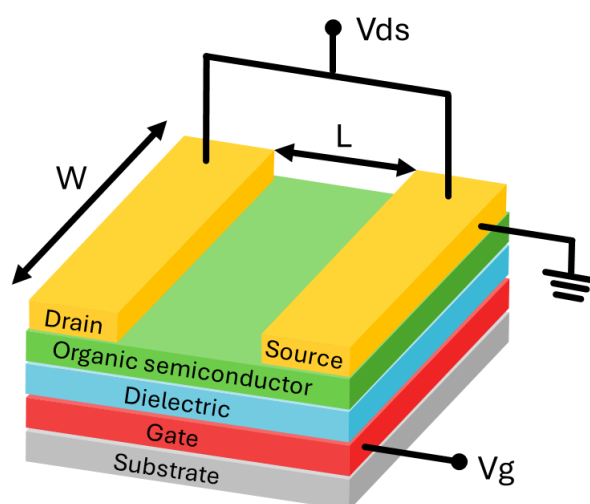


Figure 7 Schematic of an organic field-effect transistor. Image adapted with permission from {W.-Y. Lee, J. Mei, Z. Bao, "OFETs: BASIC CONCEPTS AND MATERIAL DESIGNS" in (2016; doi: 10.1142/9789813148611_0002), pp. 19–83}. Copyright {2024} World Scientific Publishing Co(64)

OFETs operate by applying a voltage bias between the source and gate electrodes (V_g). This accumulates charge carriers within the organic semiconductor at the dielectric interface, forming a conductive channel (accumulation layer) for charge transport. The polarity of V_g determines whether holes or electrons are accumulated as charge carriers within the conductive channel. A negative V_g induces holes in a p-type organic semiconductor and a positive V_g induces electrons in a n-type organic semiconductor. A second voltage bias, with the same polarity as V_g , is applied between the source (grounded) and drain electrodes (V_{ds}). This provides a voltage gradient, which drives the transport of charge carriers through the conductive channel leading to a flow and measure of drain current (I_{ds}). Charge carriers are

injected from the source electrode and into the organic semiconductor, which drift through the conductive channel and are collected by the drain electrode.

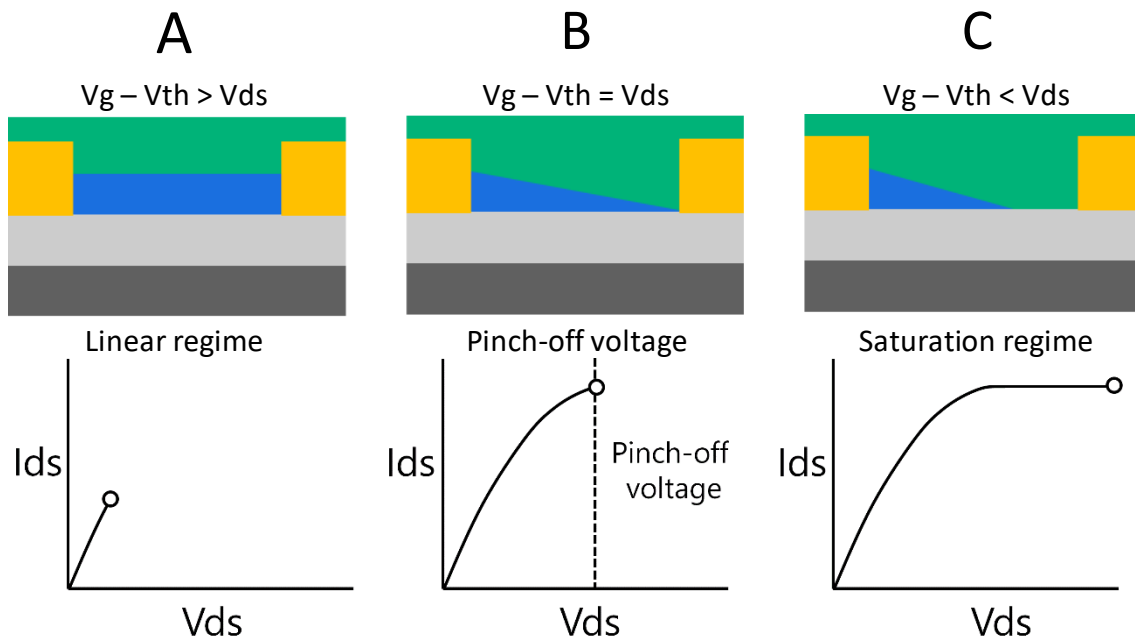


Figure 8 Operation of OFET including charge carrier density within the conductive channel and the output characteristics in (A) linear (B) pinch-off (C) saturation regime.

Organic semiconductors are not intrinsically conductive and in the absence of a gate voltage bias are in an off state. Application of a gate voltage switches the OFET to its on state, but only when a minimum gate voltage is applied defined as the threshold voltage (V_{th}). The operation of an OFET is characterized by two regimes, the linear regime and saturation regime (Figure 8). These regimes relate the uniformity of charge density within the conductive channel with the magnitude of applied voltages (V_g and V_{ds}). The combined application of V_g and V_{ds} is required to drive the transport of charge carriers. At a constant gate voltage that is greater than the threshold voltage ($V_g > V_{th}$) a uniform conductive channel forms at the organic semiconductor/dielectric interface. Application of a small source-drain voltage ($V_g - V_{th} > V_{ds}$) causes charge carriers to flow through the conductive channel, from the source to the drain electrode. Here the drain current (I_{ds}) increases proportionally to the source-drain voltage (V_{ds}) and is in the linear regime. As V_{ds} increases and approaches V_{gs} the shape of the conductive channel changes due to the two interacting potentials, which reduces the rate of current increase. At $V_g - V_{th} = V_{ds}$ the pinch-off voltage is reached, forming a depleted

region of charge carriers near the drain electrode. A limited number of charge carriers can flow through this depleted region which limits I_{ds} . Further increase in V_{ds} ($V_g - V_{th} < V_{ds}$) increases the depletion region and I_{ds} saturates, termed the saturation regime. (13, 65)

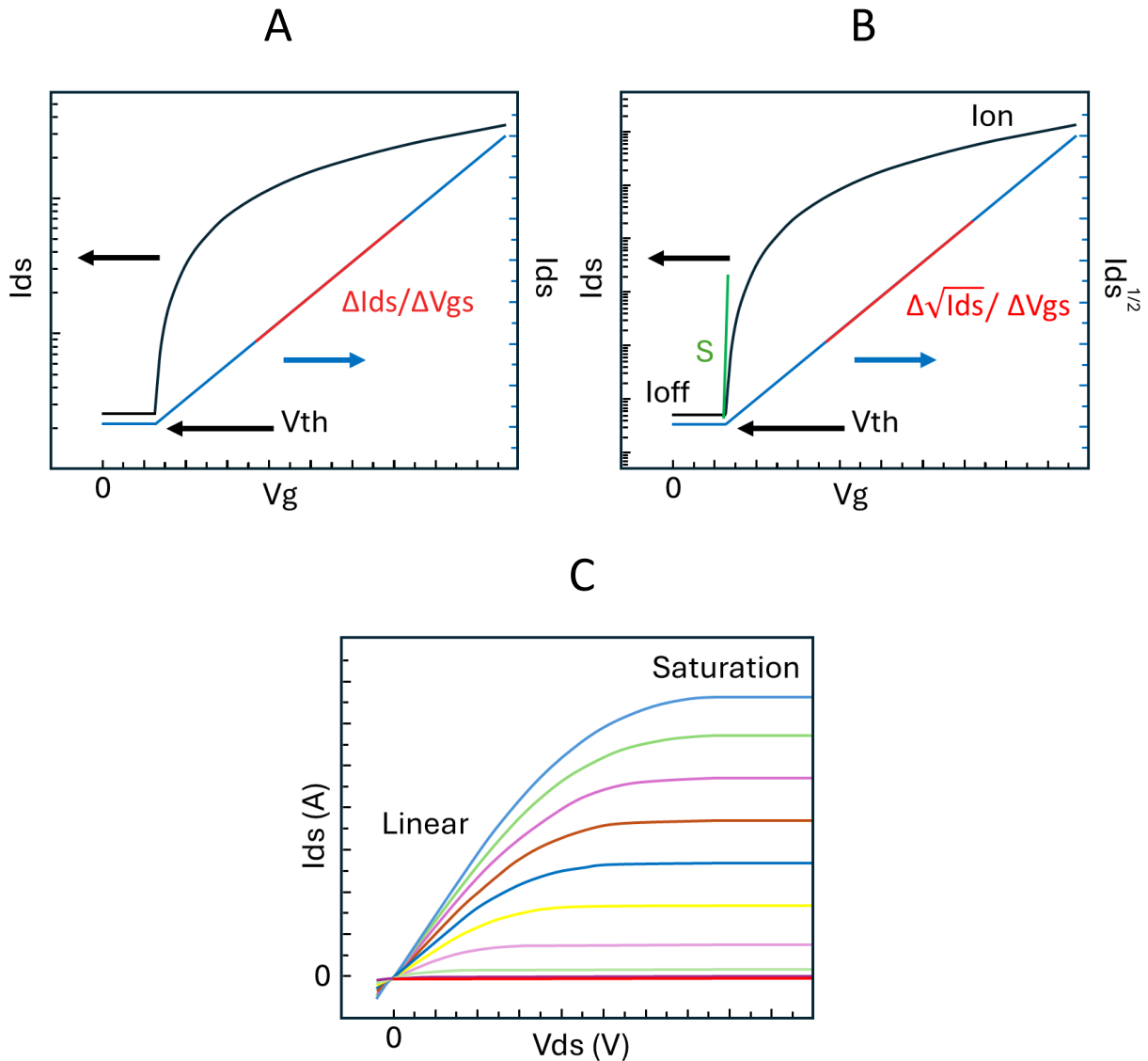


Figure 9 OFET transfer characteristics (A) Linear regime (B) Saturation regime (C) output characteristics. Image adapted with permission from {Z. A. Lamport, H. F. Haneef, S. Anand, M. Waldrip, O. D. Jurchescu, Tutorial: Organic field-effect transistors: Materials, structure and operation. J. Appl. Phys. 124, 071101 (2018)}. Copyright {2024} American Institute of Physics.(13)

OFETs are evaluated through two I-V characteristics, defined as the output and transfer characteristics (Figure 9). The output characteristics are obtained by sweeping the source-

drain voltage (V_{ds}) at a constant gate voltage (V_g). The transfer characteristics are obtained by sweeping the gate voltage at a constant source-drain voltage. From the transfer characteristics several parameters can be extracted, which include charge carrier mobility (μ), on/off current ratio (on/off), threshold voltage (V_{th}) and sub-threshold swing (S).

The charge carrier mobility (μ) indicates how fast the charge carriers are moving through the conductive channel in the organic semiconductor, and is expressed as $\text{cm}^2 \text{V}^{-1} \text{s}^{-1}$. Charge carrier mobility can be extracted from the slope of either the linear or saturation regime. In the linear regime, where $V_g - V_{th} > V_{ds}$, the charge carrier mobility can be expressed with Equation 1:

$$\text{Equation 1} \quad \mu_{lin} = \frac{\delta I_{ds,lin}}{\delta V_g} \frac{L}{WC_i V_{ds}}$$

Where $\frac{\delta I_{ds,lin}}{\delta V_g}$ is the slope of the transfer curve, referred to as the transconductance. L and W are the channel length and width, respectively. C_i is the capacitance of the dielectric layer. In the saturation regime, where $V_g - V_{th} < V_{ds}$, the charge carrier mobility is expressed with Equation 2:

$$\text{Equation 2} \quad \mu_{sat} = \left(\frac{\delta \sqrt{I_{ds,sat}}}{\delta V_g} \right)^2 \frac{2L}{WC_i}$$

The threshold voltage (V_{th}) can also be obtained from either the linear or saturation regimes, and is the point at which the linear fit of a slope intercepts the x-axis (V_g). Threshold voltage is the minimum gate voltage required to induce the conductive channel, for low-voltage applications the V_{th} should be as close to 0 as possible. A nonzero V_{th} is usually required to form the conductive channel and this value can be influenced by different factors. (13) Charge traps present at the organic semiconductor/dielectric interface and within the bulk of the semiconductor need to be filled before the channel can form, which increases V_{th} . In addition, alignment of the source-drain contact work function with the HOMO level shifts V_{th} . (66) Bias stress can also shift the threshold voltage, which occurs during OFET continuous operation causing charges to immobilise in the organic semiconductor, the gate dielectric and at the interface between the two layers. (67)

The on/off current ratio (on/off) is the ratio of the drain current (I_{ds}) in the on state (I_{ds} at a specific V_g) and the off state (the lowest measured I_{ds}). On/off ratios of $>10^3$ are generally required for most OFET applications. The on/off ratio can be increased using dielectrics with high dielectric constants, a thin organic semiconductor layer and patterned channel areas.(16)

The subthreshold slope (S) is measured between the off current and the threshold voltage, indicating the point where all charge traps have been filled and the conducting channel starts to form. This is reflected in the transfer curve as the region where the drain current starts to increase exponentially. Subthreshold slope is defined as the gate voltage required to increase the drain current by one order of magnitude (V/decade), which highlights how fast the device switches from the off to the on state, i.e. how fast I_{ds} increases with V_g at a constant V_{ds} . OFETs used in applications where high switching speeds are required, such as integrated circuits, need low subthreshold slope values.(11, 57)

Organic transistor architectures

Organic field-effect transistors are a type of organic thin-film transistor (OTFT), which includes organic electrochemical transistors (OECTs) and electrolyte-gated field-effect transistors (EGOFETs). The structures of these OTFTs in their operating state are presented in Figure 10. The basic structure of these OTFTs can be broken down into the following components: substrate layer, organic semiconductor layer, source and drain electrodes, gate electrode and dielectric layer.(68) Instead of a solid dielectric layer OECTs and EGOFETs use a liquid dielectric layer, in the form of an electrolyte solution, which could be aqueous or even honey based.(69) Generally, the permeability of the organic semiconductor to the electrolyte solution determines if the device operates as an OECT or as an EGOFET. OECTs are permeable to the solution, whereas EGOFETs are impermeable and the electrolyte solution. The high capacitance of the electrolyte solution allow OECTs and EGOFETs to operate at much lower voltages, relative to OFETs.(70) The simplicity of OFET fabrication makes them advantageous, as OECTs and EGOFETs require additional structures to contain the electrolyte solution during operation. OFETs with relatively low operating voltages can be fabricated using optimised dielectric layers.(71)

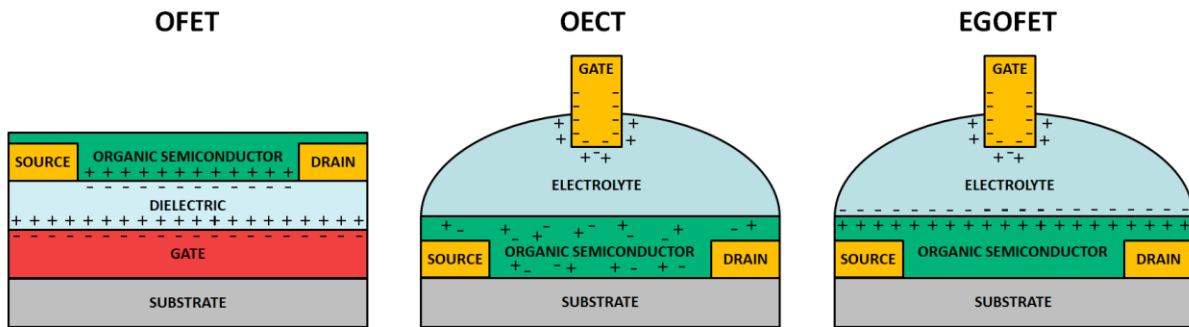


Figure 10 Cross-sectional structural diagrams of an OFET, OEET and EGOFET

The components of an OFET can be rearranged into four possible structures, which are illustrated in Figure 11: bottom gate, bottom contact (BGBC), bottom gate, top contact (BGTC), top gate, bottom contact (TGBC) and top gate, top contact (TGTC).⁽¹³⁾ The chosen OFET structure is usually dependent on the intended application, with each structure displaying certain advantages and disadvantages. In applications where the organic semiconductor needs to be protected from the environment then TGBC or TGTC structures can be used. Whereas, components of BGBC and BGTC can be fabricated in advance, allowing novel organic semiconductors to be quickly characterised.⁽¹³⁾

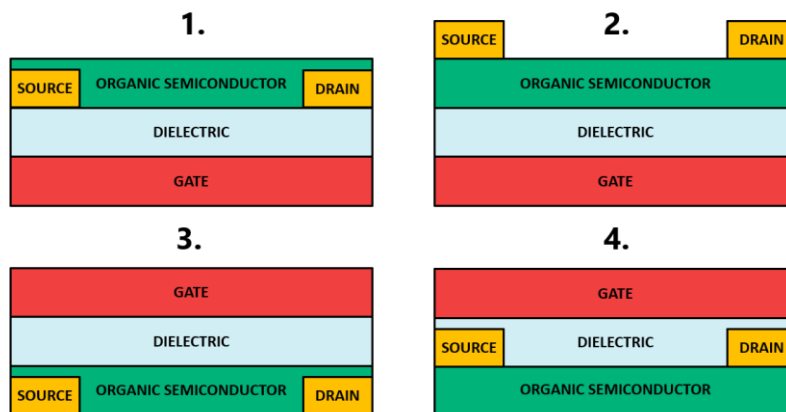


Figure 11 OFET configurations 1. bottom gate, bottom contact 2. bottom gate, top contact 3. top gate, bottom contact 4. top gate, top contact

OFETs can be fabricated under atmospheric laboratory conditions, though resulting devices usually demonstrate poorer performances relative to those fabricated in inert conditions. The increased performance of OFETs fabricated in inert conditions is due to the absence of contaminants, such as from oxygen and water, which induce non-ideal behaviours and charge

traps.(67, 72) However, it has been recently highlighted that OFET fabrication under inert conditions (e.g. glovebox) introduces other unique contaminants, that reduce OFET performance and reproducibility. Contaminant sources, such as vacuum pumps and off-gassing materials, can introduce oil mist and reactive chemicals as contaminants, respectively.(73)

Organic semiconductor deposition methods

The morphology of the organic semiconducting polymer layer can significantly influence the performance of an OFET. Optimised organic semiconducting materials can be hindered by the quality of the resulting thin-film, which is indicated by the surface morphology. Surface defects in the form of pin holes and embedded masses can introduce charge traps, which limit charge transport through the film.(74) Thin-films with high crystallinity can indicate higher charge carrier mobilities, however this is also dependent on the interconnection of ordered regions.(35) The organic semiconducting polymers is usually deposited from solution as a solid-state thin-film. The solution processability of these materials is an attractive quality for large-scale manufacturing techniques, such as roll-to-roll printing and ink jet printing.

Numerous research-based methods have been developed for the deposition of organic semiconducting polymers, which can control and alter the thin-film morphology. Popular techniques include: drop-casting, spin-coating, floating film transfer(75), meniscus guided coating(76) and electrohydrodynamic printing.(77) Drop-casting is a simple and convenient thin-film deposition technique. A droplet of the polymer solution is spread across a substrate and the thin-film forms as the solvent evaporates. However, the simplicity often limits its reproducibility, with variations in film thickness and uniformity often displayed between batches.

Spin-coating involves dispensing the polymer solution onto the centre of a substrate, which is then spun to a determined rotation speed. Centrifugal force causes the solution to spread outwards across the substrate, the thin-film forms as the solvent evaporates. Control over the spin speed, acceleration and spin time allows reproduceable thin-films to be formed, that show consistent thicknesses and morphologies.(78) Off-centre spin-coating is a variation

which forms thin-films with highly aligned polymer chains. The centripetal and centrifugal forces induced by the rotation can drive the polymer chains to align along the radial direction. Polymer chain alignment is desirable as it improves charge transport and OFET performance. Higher charge carrier mobilities have been measured in highly aligned off-centre spin-coated DPP-DTT OFETs ($2.05 \text{ cm}^2 \text{ V}^{-1} \text{ s}^{-1}$), relative to centre spin-coated thin-films ($0.66 \text{ cm}^2 \text{ V}^{-1} \text{ s}^{-1}$).⁽⁷⁹⁾

Parameters such as polymer concentration and solvent selection are also important to consider during deposition. Reported are the charge carrier mobilities for DPP-DTT polymers ranging in molecular weight (100 kg mol^{-1} to 300 kg mol^{-1}), that were deposited at different concentrations (1 mg mL^{-1} to 12 mg mL^{-1}). The highest charge carrier mobility obtained for each polymer occurred at a different concentration. With the optimal concentration decreasing as polymer molecular weight increased.⁽⁸⁰⁾ Reportedly, changing the solvent in a DPP polymer solution could control the edge-on (chlorobenzene) or face-on (chloroform) orientation of the polymer in the thin-film. The edge-on orientation is more desirable in OFETs, with edge-on charge carrier mobilities ($2.12 \text{ cm}^2 \text{ V}^{-1} \text{ s}^{-1}$) outperforming the face-on orientation ($0.76 \text{ cm}^2 \text{ V}^{-1} \text{ s}^{-1}$).⁽⁸¹⁾ Additionally, balancing solvent factors such as boiling point, solubility and molecular interactions for controlling charge carrier mobilities of DPP-DTT OFETs have been highlighted.⁽⁸²⁾

Organic semiconductor layer post-deposition methods

After depositing the organic semiconducting polymer thin-film post-deposition techniques can be utilised to improve and control the morphology of the thin-film, further enhancing OFET performance. Examples of post-deposition techniques include thermal annealing (TA), solvent vapor annealing (SVA) and mechanical rubbing. TA subjects the polymer thin-film to elevated temperatures and enables the polymer chains to reorganise and form more crystalline regions. Thermally annealed OFETs observe higher charge carrier mobilities, as well as lower contact resistances due to improved polymer/electrode interface.^(83, 84) SVA exposes the polymer thin-film to an atmosphere of solvent vapor, which reorganises the polymer morphology into more crystalline regions. Water filled voids within the polymer thin-

film, which induce charge trapping, can also be removed using SVA.(85) Mechanical rubbing of the polymer thin-film, achieved using by rubbing the thin-film with a rotating cloth covered cylinder, aligns the polymer chains in the rotation direction.(86) If this done perpendicular to the source/drain electrodes, then an increase in OFET charge carrier mobility is realised.(87)

Dielectric layer

The OFET dielectric layer accumulates charges and forms the conductive channel at the interface with the organic semiconductor layer. Application of a voltage bias at the gate electrode causes the dielectric layer to polarise. In the case of a p-type semiconductor, a negative voltage is applied to the gate electrode, which causes positive charges to form within the dielectric at the gate interface. Negative charges form within the dielectric at the opposite interface with the organic semiconductor. Once the gate voltage has reached the required threshold voltage, where trap states have been filled, then enough charges accumulate within the semiconductor for the conductive channel to form.

In addition to electrically insulating the organic semiconductor from the gate electrode, the capacitance of the dielectric material greatly influences OFET performance. Low-voltage OFETs require high capacitance dielectrics, with the capacitance (C_i) of a material described with the following Equation 3:

Equation 3
$$C_i = \varepsilon_0 \left(\frac{k}{d} \right)$$

Where ε_0 is the vacuum permittivity, k is the dielectric constant, and d is the dielectric thickness. The capacitance of a material is proportional to its dielectric constant and inversely proportional to the dielectric thickness. Therefore, high material capacitance can be achieved by increasing the dielectric constant or by decreasing the dielectric thickness. Generally, dielectric constants are categorised as being high- k ($k > 3.9$) or low- k ($k < 3.9$), relative to the dielectric constant of silicon dioxide (SiO_2), which has a $k = 3.9$.(88) High- k and low- k dielectric materials have separate advantages within OFETs. OFETs fabricated from high- k materials display higher on-currents and lower threshold voltages, where as OFETs using low-

k materials display higher charge carrier mobilities, lower subthreshold slope and low hysteresis.(16)

Thinner dielectric layers are desirable for low-voltage OFETs, as reducing the thickness increases the capacitance. However, reducing the thickness can decrease the density of dielectric coverage, which can form defects and pinholes leading to higher gate leakage. The surface properties are also an important factor in OFET performance, as it has been reported that increased dielectric surface roughness leads to a significant decrease in charge carrier mobility, as well as increasing charge traps.(89)

A dielectric layer frequently utilised for low-voltage OFET fabrication is SiO₂, as it can be conveniently grown onto a doped silicon gate, which combined acts as the substrate layer. However, the intrinsic properties of SiO₂ often present problems for OFET performance. Silanol groups on the surface of the SiO₂ dielectric can act as charge traps at the interface with the organic semiconductor layer. For p-type organic semiconductors filling of these traps leads to a depletion in charge carriers and a negative shift in threshold voltage.(90) Passivation of these charge traps is required for low-voltage OFET applications, which is achieved using self-assembled monolayers (SAMs) of an alkylsilane such as octadecyltrichlorosilane (ODTS). In addition to passivating traps, SAMs can also improve charge carrier mobility by promoting molecular ordering of the channel semiconductor and used for organic non-volatile memory purposes.(91, 92)

The rigidity of SiO₂ restricts applications in flexible and wearable OFETs, however there are many examples of polymer based dielectric materials compatible with flexible substrates.(93–95) Both high-k and low-k polymer dielectrics have been developed for low-voltage OFET fabrication, such as PMMA, CYTOP and PMSQ/PAN bilayers. In addition to flexibility, polymer dielectrics show controllable thickness, solution processability and patternability.

Source-drain electrodes

OFET source-drain contacts are conductive materials used to inject/extract charges through the conductive channel in the organic semiconductor during operation. Ohmic contacts are

required for the efficient injection of charge carrier into the organic semiconductor.(96) The HOMO/LUMO levels of the organic semiconductor generally determine the material used for the source-drain contacts. p-type organic semiconductors require materials with work functions that align with the HOMO level. Misalignment of these levels creates a charge carrier injection barrier or contact resistance at the interface between the organic semiconductor and contacts. Overcoming this misalignment results in a negative shift in the threshold voltage.(66)

Most donor acceptor polymers have HOMO levels in the range of 5.0 to 5.5 eV, which require materials with high work functions such as gold (~5.1 eV), palladium (~5.2 eV) or platinum (~5.6 eV), for the efficient injection of holes.(50, 97) However, work function is a surface property and can vary substantially with surface preparation and cleanliness. The work function of gold has been shown to vary between 4.4 and 5.4 eV.(98, 99) Despite this, D-A polymer based OFETs are usually fabricated with gold contacts, as the material forms a better interface with the organic semiconductor layer.

Conventionally, the contact material is deposited onto a pattern of the source-drain contacts, via evaporation or sputtering techniques. The patternable area can be formed through lithographic techniques (e.g. photolithography) or as a stencil (e.g. shadow mask).(100) Lithographic techniques can pattern source-drain contacts with smaller features (< 1 μm), relative to shadow masks. Shadow masks limit channel lengths to 10's of μm , as features below this can experience shadowing effects.(101) However, most lithographic techniques use aggressive chemicals which are not suitable for patterning on top of the organic semiconductor layer.

The deposition technique utilised is dependant on what OFET structure is being fabricated. Deposition for bottom-gate bottom-contact (BGBC) and bottom-gate top-contact (BGTC) OFET structures, occurs before or after the organic semiconductor, respectively. BGTC OFETs generally benefit from lower contact resistances and higher charge carrier mobilities, relative to BGBC OFETs.(102) Though, BGBC OFETs are more suitable for large-scale manufacture as they can utilise lithography based techniques.(51)

Gold source-drain contacts can function in flexible OFETs, however the cost and energy intensive deposition process makes gold less favourable in commercial applications.(103) The conductive polymer PEDOT:PSS is an attractive alternative material for source-drain contacts. The work function of PEDOT:PSS can be tuned between 4.5 eV and 5.3 eV, by varying the ratio of the two components. Additionally, PEDOT:PSS source-drain electrodes can be deposited using electrohydrodynamic printing and homemade 3D printers, to fabricate OFETs.(104, 105)

1.4 Biosensors

Of the numerous applications organic field-effect transistors can be used for, the utilisation of OFETs as biosensors is of great importance. A biosensor is defined as “a device that uses specific biochemical reactions mediated by isolated enzymes, immunosystems, tissues, organelles or whole cells to detect chemical compounds usually by electrical, thermal or optical signals”, according to the International Union of Pure and Applied Chemistry.(106) Put simply, a biosensor is an analytical device composed of a biorecognition layer and a transducer. Interactions between the analyte and the biorecognition layer are translated into a measurable signal by the transducer.(107)

Biosensors allow for the detection of various clinically relevant targets, which are referred to as biomarkers, a portmanteau of “biological marker”. Biomarkers are broadly defined as “any substance, structure, or process that can be measured in the body or its products and influence or predict the incidence of outcome or disease”, by the World Health Organization and the United Nations.(108) Detectable biomarkers of interest include antibodies, hormones, DNA, volatile gases and many other biological small molecules. Biomarker detection can be achieved in a wide range of biological mediums such as blood, sweat, saliva, urine, and tears. Additionally, biosensors possess several attractive features and qualities such as low production cost, high sensitivity and specificity, rapid response time, ease of operation and a reduced need for additional equipment.(109, 110) As such, biosensors are playing a pivotal role in shaping the future of healthcare and the treatment of disease. A particular focus on progressing the areas of personalised medicine and early detection within healthcare, are key motivations for developing biosensing technologies. The former is a defined medical model where a patient receives the correct treatment at the right time. The latter involves detecting a disease as early as possible, ideally before the development of symptoms and at most before it reaches a terminal stage.(111) Both concepts look to improve a patient’s prognosis, by enabling more effective medical decisions and interventions to be performed. The effectiveness of personalised medicine and early detection are both reliant on the ability to diagnose specific aspects underlying a condition.(112) Ideally, a diagnosis

should be determined before symptoms manifest, which can require the detection and tracking of multiple biomarkers to identify patterns correlating to a specific disease, while minimising diagnostic delay. However, such practices can be hindered by conventional medical technology, which often increase diagnosis times. Current diagnostic medical equipment is usually complex and only operated by skilled personnel in dedicated facilities that are located away from the patient. Biosensing platforms developed for point-of-care testing allow non-skilled users to perform tests where the patient is located, thereby reducing diagnostic delay.(107) The development of digital biosensors that are portable, wearable or implantable enable continuous real-time diagnostics to be performed, maximising early diagnosis of health conditions.(113)

Biosensors can be initially categorised depending on if the analyte generated signal is either quantitative or qualitative. Glucometers used by diabetics to monitor blood glucose levels are an example of a quantitative biosensor, where a measurable blood glucose concentration is determined.(114) Lateral flow tests used to detect COVID-19 are an example of a qualitative biosensor, where a visual signal is induced upon detection.(115) The former is preferred as the analyte can be quantified into numerical data, allowing for more precise measurements and therefore more informed decisions to be made.

Biosensors can be further categorised based on label-based or label-free detection mechanisms. Label-based detection involves the attachment of a label to the biomarker or biorecognition layer, where the target analyte is indirectly measured by measuring the number of labels. Popular label-based approaches use fluorescent, chemiluminescent or radioactive labels to detect biomarkers. However, label-based approaches introduce specific limitations that are associated with the label properties and the labelling process. Labelling is usually laborious and the labels can alter interactions between the biomarker and the biorecognition layer.(116, 117) Label-free approaches do not require labels and instead utilise the physical properties of the biomarker for detection. Label-free detection is preferred over label-based due to the relative simplicity of the approach.

The core components of a biosensor are the biorecognition layer and the transducer. The biorecognition layer is generally formed of bioreceptors, which are discussed in more detail later in this chapter. Numerous platforms can function as the transducer within a biosensor. Electrochemical, field-effect transistor, optical, photoelectrochemical, quartz crystal microbalance and cantilever based transducers have all been used for biosensing applications.*(109, 118, 119)*

Of these, biosensors that use field-effect transistors as the transducer observe several advantages for health monitoring applications, such as label-free detection quantitative signal generation, increased sensitivity from signal amplification, multiparameter detection, and low voltage/power consumption.*(120, 121)* Combined with the flexible and biocompatible properties of organic semiconducting polymers, OFET biosensors enable the development of wearable and implantable sensors fulfilling the criteria of future continuous health monitoring devices.*(59, 68)*

1.5 Organic Field-Effect Transistor Biosensors

Biosensing OFETs transduce binding interactions between target biomarkers and the biorecognition layer, through changes in charge density. Upon binding, charge density at the organic semiconductor surface is altered, which can either induce or deplete charge carriers in the conductive channel. (122) This is detected through multiple parameters such as the threshold voltage, on/off ratio, charge carrier mobility and output characteristics. Real-time monitoring, with the continuous application of voltage biases (V_g and V_{ds}) can detect biomarkers through changes in drain current (I_{ds}).

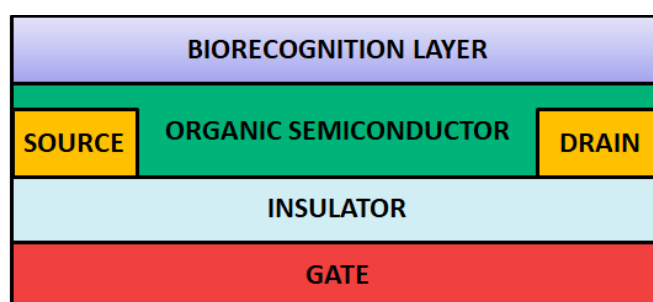


Figure 12 OFET biosensor with the biorecognition layer at the organic semiconductor interface

A general structure of an OFET biosensor is illustrated in Figure 12, where the biorecognition layer is coupled to the organic semiconductor layer. Other geometries are possible, such as gate(123) or dielectric(124) coupled biorecognition layers, however the simplicity of this arrangement offers several advantages. Firstly, the biorecognition layer is in close proximity to the organic semiconductor layer, allowing biomarker interactions to directly influence the conductive channel, which is desired for increased sensing performance.(125) Secondly, the organic semiconductor layer provides a range of strategies for the covalent attachment of the biorecognition layer, preserving the long-term stability and sensitivity of the biosensor. Additionally, the organic semiconductor layer offers a large-area for biorecognition layer attachment, which is required for fast single-molecule detection.(126) Passivation of the organic semiconductor layer to reduce non-specific analyte interactions is generally not required, unlike gate functionalised devices.(127, 128) Finally, deposition of the biorecognition layer happens last, which avoids exposure to harsh conditions (high temperatures, aggressive solvents, etc) during fabrication.

Organic semiconductors lack the specificity/selectivity necessary for biosensing applications. A biorecognition layer is coupled to the semiconductor to impart these desired levels of selectivity and specificity. The biorecognition layer is composed of bioreceptors, which are naturally occurring biomolecules such as enzymes, antibodies and DNA strands. Bioreceptors can also be synthetically produced (e.g. aptamers and hydrogels), which allow receptors to be designed to interact with a range of target species.(129) Chemical functionalities, such as carboxylic acid groups, can serve as the biorecognition layer, but are less selective to a specific target.(130, 131)

Target biomarkers are introduced to the biorecognition layer (a.k.a. the sensing channel) in solution (e.g. an aqueous buffered solution or physiological fluid), which is either kept during sensing or removed after a period of incubation. Depending on the type of bioreceptor or species of biomarker detected the sensing mechanism can change. Charged bioreceptors, such as DNA, exploit changes in charge density to detect biomarkers. Interactions between DNA and a target alter charge density at the organic semiconductor surface, which either induce or deplete charge carriers within the conductive channel.(132) The detection of charged biomarkers works in a similar fashion.(133) Interactions between enzymes and biomarkers also increases charge density at the surface, but they can also generate protons that accumulate near the conductive channel, which fill charge traps and increase charge carrier mobility.(134)

A biosensors performance can be assessed through several figures of merit, such as sensitivity, selectivity, limit of quantification, limit of identification and limit of detection.(135) Limit of detection is defined as the minimum detectable amount of a target biomarker, and is a critical metric for sensitive biosensors. Lower limits of detection are desired for biosensing applications, with OFET biosensors currently demonstrating attomolar limits of detection.(136)

OFET biosensor requirements:

Certain performance criteria should be met before sensing with the mentioned OFET biosensor configuration. Low-voltage OFET operation is needed for portable and wearable biosensing applications, which is dictated by the threshold voltage (V_{th}). A V_{th} near 0 V is therefore essential, requiring the removal of charge traps within the organic semiconductor thin-film bulk and at the dielectric interface.

Furthermore, the organic semiconductor should exhibit high environmental and aqueous stability, since this interface is exposed to both the atmosphere and the biomarker solution. Poor stability reduces OFET performance, as oxygen and water can penetrate into the thin-film between polymer chains and form charge traps.⁽²⁶⁾ To avoid this it has been reported that organic semiconducting polymers thin-films with small π - π stacking ($< 3.6 \text{ \AA}$) and thicknesses of 30 nm enable long-term environmental and aqueous stability.⁽⁴⁶⁾ A deep HOMO level ($> 5.1 \text{ eV}$) can also prevent air oxidation and long alkyl side chains can form hydrophobic surfaces that shield the polymer backbone from water.⁽¹³⁷⁾ Donor-acceptor polymers (such as DPP-DTT) often demonstrate small π - π stacking due to their planarity and rigidity, as well as deep HOMO levels, making them ideal materials for biosensors.

Enhancing OFET biosensor performance:

Improved biosensing sensitivity can be achieved with several optimisation strategies. Factors relating to receptor density, sensing channel dimensions, charge carrier mobility and thin-film thickness can improve sensitivity. High charge carrier mobilities, while not essential for OFET biosensors, are necessary for achieving high sensitivity, as they enable faster response speeds and superior signal amplification.^(138, 139) Therefore, responsive and sensitive biosensors should aim to utilise high performing materials, such as donor-acceptor organic semiconducting polymers.

Receptor density and the area of the sensing channel are important factors for single-molecule sensing. The importance of large-area receptor functionalised interfaces for single-molecule detection at very fast time-scales has been studied. In nanometric biosensing

devices, the probability of a single target molecule (dispersed in a 10-100 μL volume) interaction through diffusion is extremely unlikely, referred to as the diffusion-barrier issue. A simulated timescale of several days was required for ten molecules in a 100 μL femtomolar solution to interact with a nanometric device. The diffusion-barrier issue could be overcome with micrometric to millimetric sized interfaces, that were densely functionalised with immunoglobulin G antibodies ($\times 10^{12}$ receptors). Immunoglobulin G antigens (target analyte) could be reliably detected in 100 μL volumes at $39 \pm 6 \times 10^{-21}$ M, within 10 minutes.(126)

Thin-film thickness also correlates with biosensing sensitivity. Minimising the gap between the receptor and the conductive channel has been shown to enhance sensitivity, as receptor interactions have a greater influence on charge carriers within the channel. Reducing the thickness of the thin-film to ~ 10 nm minimises this gap, however this should be done without compromising the stability of the organic semiconductor layer.(125, 134)

Biosensing considerations:

Biomarker detection in physiologically relevant fluids is a key target for OFET biosensors. However, counterions within these solutions can screen the effect of charged biomolecules on the conductive channel. In solution, charged biomolecules are surrounded by charged counterions due to electrostatic interactions. The number of net charges approaches the number of counter-charges, on a certain length scale. This results in a screening effect, where the influence of a charged biomolecule decays exponentially towards zero with distance. This physical distance is referred to as the Debye length (λ_D) and varies with ionic strength, where solutions with high ionic strengths have shorter Debye lengths.(140) For OFET biosensors, if the biomolecule is at a distance $> \lambda_D$, then the charge is screened and the influence on the conductive channel is negligible.

The influence of Debye length on biomarker detection in OFETs has been investigated.(133) Biomarker sensing was performed in a series of diluted buffer solutions, with ranging ionic strengths. The Debye lengths of the solutions were 0.8 nm, 8 nm and 80 nm, while the distance between the receptor and the surface was ~ 7 nm. Biosensor sensitivity was shown to decrease with decreasing Debye length and demonstrated a negligible response with a

Debye length of 0.8 nm. Therefore, Debye length needs to be considered for improved biosensor sensitivity. Reducing the ionic strength of a solution through dilution does overcome the Debye length. However, this is often not applicable for physiological samples, as high ion concentrations are needed to stabilise biomolecular conformations and maintain receptor binding affinity.(141, 142) Alternatively, some receptors (e.g. DNA aptamers) have been shown to interact with biomarkers below Debye lengths under physiological conditions.(143)

Aptamers as receptors for OFET biosensors

Receptor choice for the biorecognition layer is usually influenced by the target biomarker, i.e. specific antibodies are used to detect specific antigens. The high specificity of these receptors endow biosensors with high sensitivity, however they also limit the range of detectable biomarker species. Future health monitoring devices should detect a diverse range of targets for effective diagnoses to be made.

Aptamers are tailorable and highly specific receptors capable of interacting with a versatile range of biomarkers. They are short single strands of DNA or RNA bases (Figure 13), usually ranging from 10 to 100 base pairs in length. Similar to DNA strands found in nature, the sequence of bases are structurally supported by a sugar-phosphate backbone. The base sequence within the aptamer is screened through a SELEX process (Systematic evolution of ligands by exponential enrichment), which identifies strands that demonstrate high binding affinity and specificity to a target biomarker. A range of biomarker species can be targeted including: metal ions, small molecules, oligonucleotides, proteins, viruses and cells.(144)

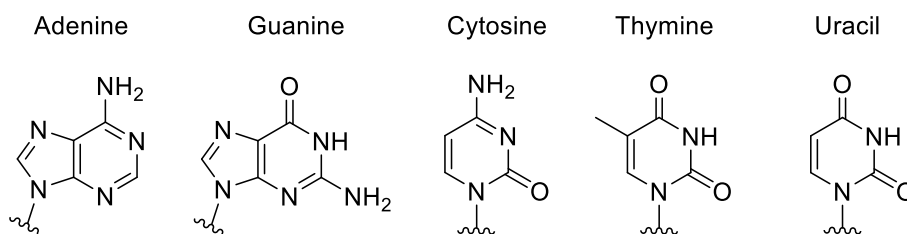


Figure 13 DNA bases adenine, guanine, cytosine, thymine and RNA base uracil.

Aptamers bind to biomarkers through noncovalent interactions, such as hydrogen bonding, electrostatic interactions, and π stacking, causing the structure of the aptamer to undergo a conformational change.(145, 146) This conformational change is exploited by aptamer functionalised OFETs to detect target biomarkers, through changes in negative charge density at the organic semiconductor surface. Phosphate groups within the sugar-phosphate backbone are negatively charged, providing a level of negative charge density at the surface. Upon binding with a target biomarker the conformation of the aptamer strand changes, which reorientates the aptamer strand either closer or further away from the surface. If the aptamer moves closer then negative charge density increases near the surface, which induces holes in the conductive channel. Whereas, holes are depleted from the conductive channel if the aptamer orientates away from the surface. An increase or decrease in mobile holes manifests as an increase or decrease in drain current, respectively.(143) Biosensing OFETs functionalised with aptamers at the organic semiconductor interface, have detected mercury ions (Hg^{2+})(132), thrombin proteins(133) and DNA strands (147), with respective detection limits of 1 μM , 1 nM and 1 nM.

In addition to biomarker versatility, high binding affinity and specificity, aptamers provide additional advantages. Aptamers can be readily synthesised and demonstrate greater stability across a range of environmental conditions (temperature, pH, chemically harsh), relative to other receptors.(148) Increased chemical resistance enables aptamers to be chemically modified with various functional groups (such as azide, carboxylic acid, amine), which further enables their covalent attachment to the organic semiconductor layer through several strategies.(145) Due to their small size relative to other bioreceptors sensing below the Debye screening lengths can also occur.(144) Sensing in physiological fluids (i.e. blood, sweat and tears) with high ionic strengths is therefore possible.(133) For instance, OFETs functionalised with aptamers have detected mercury ions (Hg^{2+}) in undiluted samples of seawater.(46) Aptamers can also be regenerated after binding with a target biomarker, allowing biosensors to be reused.(149) The multiplexed capabilities of aptamers in a biosensing FET have also demonstrated.(150)

Organic semiconductor receptor attachment strategies

Aptamers used as the biorecognition layer in biosensing OFETs need to be coupled to the organic semiconductor interface. So far, two strategies for the effective attachment of aptamers to the organic semiconductor layer have been reported. Both strategies introduced exploitable chemical functionalities to the OFET surface prior to aptamer functionalisation, as the organic semiconductor layer intrinsically lacked these functionalities.

One approach deposited a layer of poly-maleic anhydride onto the organic semiconductor layer (DDFTTF), via plasma-enhanced chemical vapor deposition. Surface anhydride groups were then hydrolysed into carboxylic acids groups in the presence of an aqueous environment. Subsequently, amine-terminated aptamers were covalently attached to the carboxylic acids, via EDC/NHS chemistry.⁽¹⁴⁷⁾ An alternative approach formed an ordered array of gold nanoparticles (AuNP) onto the organic semiconductor layer (DDFTTF). First, hydrogen tetrachloroaurate (HAuCl₄) suspended in a polymer matrix (PS-b-P4VP) was deposited onto the organic semiconductor. Oxygen plasma was used to remove the polymer matrix and convert HAuCl₄ into metallic gold nanoparticles. Thiol-terminated aptamers were then attached to the gold nanoparticles, via gold-thiol chemistry.⁽¹³²⁾

The above strategies were effective at attaching aptamers to the organic semiconductor layer. However, the additional steps required for functionalization increase the complexity of the biosensor, limiting its general applicability and wider adoption. Other aptamer functionalisation strategies exist for EGOFETs where the gate electrode is functionalised, however these devices lack the outlined advantages of OFETs.⁽¹²⁷⁾ Despite this, alternative strategies used to attach other receptors could be modified and exploited for aptamers. Novel strategies for coupling biological materials to organic thin-film transistors are frequently reported.^(151–153)

Strategies for attaching bioreceptors to OFETs generally fall into two categories: non-covalent functionalisation and covalent functionalisation. Non-covalent functionalisation is reliant on adsorption of the receptor onto an OFET interface via intermolecular forces. This approach is convenient, however OFETs functionalised this way incur stability and repeatability issues, as

the bioreceptor can detach from the interface during operation.(154) Covalent functionalisation relies on the formation of chemical bonds between the bioreceptor and the OFET interface, which securely anchors the bioreceptor to the interface. Covalent attachment mitigates the issues presented by non-covalent approaches and is viewed as a more optimal functionalisation approach. However, it requires specific chemical functionalities on both the organic semiconductor layer and bioreceptor.

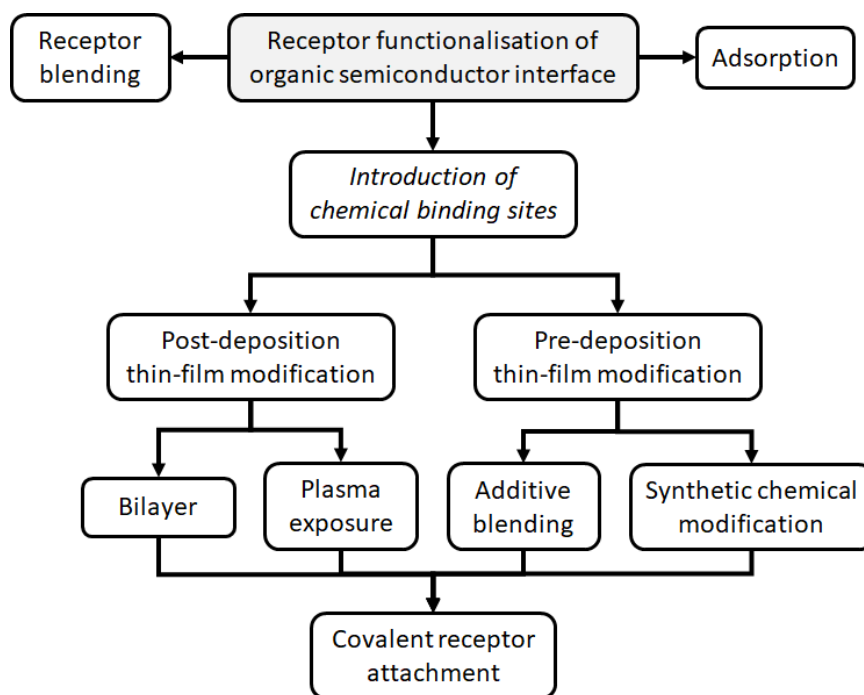


Figure 14 Strategies for the introduction of receptors and chemical binding sites to the organic semiconductor interface

Multiple pathways have been developed for covalently functionalising organic semiconductor thin-films with bioreceptors, through the introduction of chemical binding sites. A flow diagram of binding site introduction and receptor functionalisation to the organic semiconductor layer is illustrated in Figure 14, with the details of these strategies presented in Table 1. Chemical binding sites can be introduced to the organic semiconducting polymer thin-film in several ways, occurring at different points of fabrication. Usually, occurring before or after thin-film deposition. Synthetic chemical modification of the material and blending are two strategies that introduce chemical binding sites before thin-film deposition. Plasma

treatment and the addition of an interfacing bilayer introduce chemical binding sites to the thin-film after deposition.

OTFT	Modification	Introduced functionality	Receptor/attached functionality	Target biomarker and LOD	Reference
Post-deposition					
<i>Synthetic</i>					
OECT	DPP-DTT	Azide	Enzyme /alkyne (CuAAC)	Glucose (1 μ M)	(155)
OECT	PEDOT	Azide	Aptamer /DBCO (SPAAC)	Thrombin (31 nM / 22 nM)	(156, 157)
OECT	PEDOT	Carboxylic acid	Antibody /amine (EDC/NHS)	Cortisol (8.8 μ g mL ⁻¹)	(158)
EGOFET	C8-BTBT-C8	Biotin	Aptamer /streptavidin	Influenza A virus (6 μ g mL ⁻¹)	(159)
<i>Blending</i>					
OFET	Glutaraldehyde	Aldehyde	Antibody/amine	Antigens: AFP (0.176 pM) and CEA (65 fM)	(160)
OFET	DMP[5]-COOH	Carboxylic acid	Antibody /amine (EDC/NHS)	CEA (aM)	(136)
Pre-deposition					
<i>Plasma</i>					
OFET	Oxygen plasma	Carboxylic acid	Enzyme /amine (EDC/NHS)	ATP (0.1 nM)	(134)
<i>Bilayer</i>					
OFET	HAuCl ₄	Au nanoparticles	Aptamer/thiol	Hg ²⁺ (1 μ M/10 μ M), Thrombin (100 pM)	(46, 132, 133)
OFET	Poly-maleic anhydride	Carboxylic acid	Aptamer /amine (EDC/NHS)	DNA (1 nM)	(147)
OFET	BFPA	Aldehyde	Antibody/amine	Antigen AFP (45 fM)	(161)
EGOFET	pdEthAA	Carboxylic acid	Antibody/biotin	Protein (CRP)	(162)
Receptor blend					
OECT	p(EDOT-ran-EDOTOH)	N/A	Enzyme	Glucose (10 μ M)	(163)
EGOFET	pBTTT	N/A	Modified antigen (alkyl-BPA)	BPA (2 μ g mL ⁻¹)	(164)

Table 1 Introduction of chemical binding sites and receptor functionalisation strategies of organic semiconductors for OTFT biosensors. CuAAC = Copper-catalysed azide–alkyne cycloaddition, SPAAC = Strain-promoted alkyne-azide cycloaddition, BPA = bisphenol A, AFP = α -fetoprotein, CEA = carcinoembryonic antigen, ATP = adenosine triphosphate

One of the key advantages of organic materials is the ease of modification through chemical synthesis. Synthetic modification of the material with certain exploitable chemical groups facilitate the attachment of bioreceptors. Chemical groups that enable crosslinking to bioreceptors under mild conditions are desired, so that the integrity of the organic semiconductor and the bioreceptor is preserved. Carboxylic acid and azide chemical groups are notable examples, which facilitate bioreceptor attachment through mild EDC/NHS coupling and click chemistry reactions (CuAAC, SPAAC), respectively. However, this strategy often leads to performance reduction of chemically modified organic semiconducting polymers. The introduced functionalities often disrupt the π -stacking within the thin-film, which impairs charge transport. Maintaining high charge carrier mobilities required for sensitive biosensors is therefore difficult to balance with this strategy.^(61, 135)

Blending, plasma and bilayer receptor attachment strategies are also reported. The advantages of these strategies are that they enable high performing organic semiconducting polymers (e.g. DPP-DTT) to be utilised. High performing materials lack exploitable functionalities for receptor attachment, so methods of introducing chemical binding sites without altering their performance are advantageous. The high performance of these materials are generally retained using these identified strategies. The mentioned receptor attachment strategies provide several exploitable pathways for aptamer functionalisation. Aptamers can be chemically modified with desired functionalities making many of these strategies plausible. Selected strategies can be applied to functionalising organic semiconducting polymers for biosensing OFET applications.

1.6 Project outlines

OFETs incorporating organic semiconducting polymers have emerged as favourable transducers for portable and wearable biosensing applications. Interfacing OFETs with DNA aptamers as the receptor layer would enable high sensitivity and high biomarker versatility. Resulting OFET biosensors would fulfil requirements desired in future health monitoring devices, expediting point of care and personalised medicine. The organic semiconducting polymer layer is an attractive interface for large-area aptamer functionalisation, though reported pathways for covalently attaching aptamers to this interface remain limited. A key challenge involves introducing chemical binding sites to high performing organic semiconducting polymers without significantly reducing performance. Diversifying aptamer covalent attachment strategies is essential for their wider implementation and should be expanded.

The research aims of this thesis revolve around a central theme, which focuses on developing strategies for covalently attaching DNA aptamers to organic semiconducting polymer thin-films, for applications in biosensing OFETs. The following work is structured into three sections, each highlighting a strategy for aptamer functionalisation under ambient conditions. Modification of thin-films containing a model high performing organic semiconducting polymer (DPP-DTT) for aptamer attachment is explored in the first two research chapters. Derivatives of existing materials modified with functionalities for aptamer attachment are explored in the final chapter. The utility of the materials within organic transistors for low-voltage biosensing applications is also explored.

The first research chapter (Chapter 3) begins with establishing methods for fabricating OFETs that are viable platforms for low-voltage biosensing investigations. Subsequently, thin-film surfaces are exposed to either oxygen or nitrogen plasma, as techniques of introducing exploitable chemical functionalities. OFETs exposed to either plasma approaches are characterised and the exploitability of plasma-induced chemical binding sites for aptamer attachment is compared.

Research methods learnt from the preceding chapter are utilised and expanded upon in Chapter 4. Chemical binding sites are introduced to DPP-DTT polymer thin-films through small molecule blending. The utility of this blended system for aptamer attachment and OFET biosensing applications is explored.

The final research chapter (Chapter 5) looks at two systems, which are derivatives of existing materials. Synthetic chemical modification has endowed these materials with functionalities known to facilitate receptor attachment. Aptamer attachment strategies are investigated for both materials, as well as the fabrication of organic transistors for biosensing applications.

2 Materials and Experimental Techniques

Outlined below are materials and experimental techniques utilised throughout this thesis.

2.1 Device fabrication materials

2.1.1 Organic semiconducting materials

A list of organic semiconducting materials used within this thesis is presented in Table 2. The organic semiconducting polymer DPP-DTT was purchased from Ossila Ltd and used within chapter 3 and chapter 4 of this thesis. The organic semiconducting polymer N₃-DPP was synthesised by Dr Raymundo Marcial Hernandez and used within chapter 5 of this thesis. The organic semiconducting small molecule DTP-COOH was synthesised by Dr Christina Kousseff and used within chapter 5 of this thesis.

Name and abbreviations	Structure	Information
Poly[2,5-(2-octyldodecyl)-3,6-diketopyrrolopyrrole-alt-5,5-(2,5-di(thien-2-yl)thieno [3,2-b]thiophene)], DPP-DTT		Manufacturer: Ossila Ltd Batch code: M0311A2 Mw: 204 kg mol ⁻¹ Mn: 66 kg mol ⁻¹ PDI: 3.09
N₃-DPP polymer		Synthesised by Dr Raymundo Marcial Hernandez Mw: 50.6 kg mol ⁻¹ Mn: 54.7 kg mol ⁻¹ PDI: 1.08
4-(4H-Dithieno[3,2-b:2',3'-d]pyrrol-4-yl)butanoic acid, DTP-C4-acid, DTP-COOH		Synthesised by Dr Christina Kousseff

Table 2 Names, abbreviations, structures and information of organic semiconducting materials

2.1.2 Substrates and substrate modifying chemicals

A list of substrates and substrate modifying materials used within this thesis is presented in Table 3. Si/SiO₂ substrates were used in chapter 3 chapter 4 and chapter 5 of this thesis. ITO and polyimide substrates were used in chapter 5 of this thesis. Polyimide tape and PDMS were used to modify polyimide substrates in chapter 5. ODTs was used to modify Si/SiO₂ substrates.

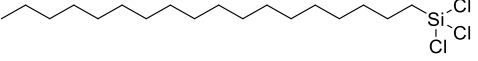
Substrate	Specifications/structure	Supplier
Silicon/Silicon oxide (Si/SiO ₂) (300 nm) wafers	100 mm wafer, oxide 2950 Å, Czochralski method Silicon, p-type doped (Boron), orientation <1-0-0>, grade Prime, thickness min 500 mm, thickness max 550 mm, resistivity min 0.01 Ω·cm, resistivity max 0.02 Ω·cm, front side finish Polished, Back side finish Etched	Silicon Quest International
Indium Tin Oxide (ITO) coated glass	15 ohms/sq, Polished OLED Soda Lime	VisionTek Systems
Polyimide sheets	300 mm x 320 mm x 125 mm	RS Components Ltd.
Polyimide silicon adhesive coated tape	33 m x 25 mm x 60 mm.	RS Components Ltd.
Octadecyltrichlorosilane (ODTS)		FluoroChem Ltd
Polydimethylsiloxane (PDMS)	SYLGARD™ 184 Silicone Elastomer Kit	Farnell Limited

Table 3 Names, specifications and supplier information of substrates and substrate modifying materials

2.1.3 Deposition masks

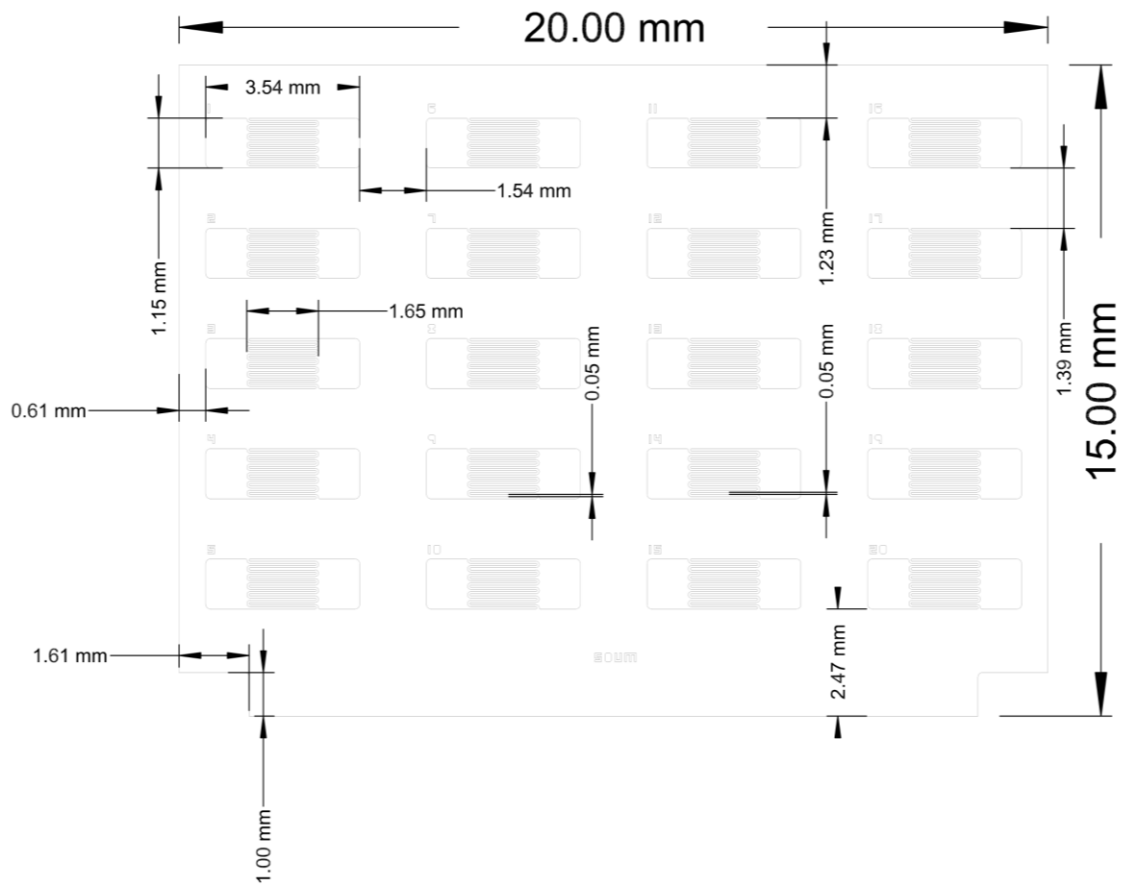


Figure 15 Schematic of Ossila supplied high density 50 μm interdigitated source-drain deposition mask

Channel Geometry	Interdigitated
Channel lengths	50 μm
Channel width	18.23 mm
Contact pad size	1.15 mm x 0.945 mm
Channel bar tolerance	± 7 μm
Mask dimensions	20 mm x 15 mm x 30 μm
Mask material	Electroformed nickel
Mask Thickness	30 μm
Number of OFETs	20

Table 4 Ossila supplied high density 50 μm channel length interdigitated source-drain deposition mask dimensions

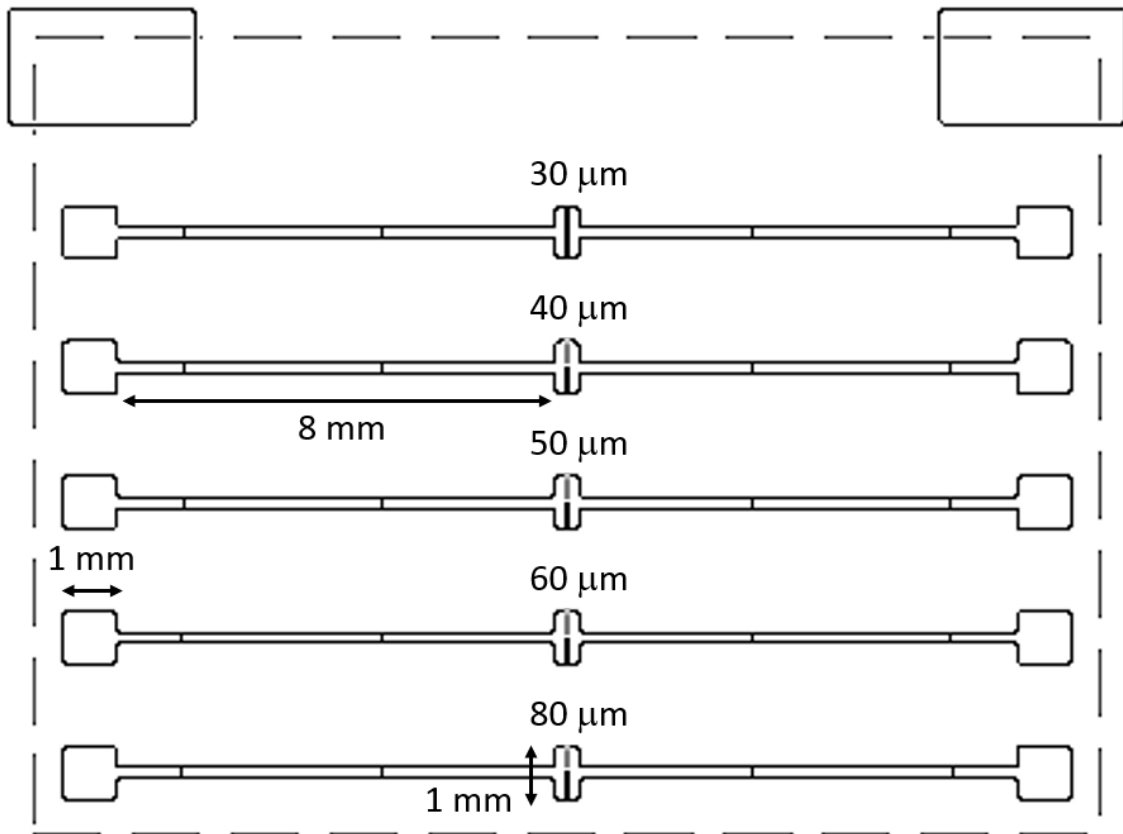


Figure 16 Schematic of Ossila supplied low density variable (30, 40, 50, 60, 80 μm) channel length source-drain deposition mask

Channel Geometry	Linear
Channel lengths	30, 40, 50, 60, 80 μm
Channel width	1 mm
Contact pad size	1 mm x 1 mm
Channel bar tolerance	± 10 μm
Mask dimensions	20 mm x 15 mm x 35 μm
Mask material	Electroformed nickel
Mask Thickness	30 μm
Number of OFETs	5

Table 5 Ossila supplied low density variable (30, 40, 50, 60, 80 μm) channel length source-drain deposition mask dimensions

2.1.4 Deposition materials

Material	Specifications	Supplier
Gold (Au)	Wire, 1.0 mm diameter, purity 99.999 %	Goodfellow
Chromium (Cr)	Solid irregular sized pieces, purity 99 %	Fisher Scientific
Silicon monoxide (SiO)	Purity 99.9 %	Glentham Life Sciences Ltd
Molybdenum trioxide (MoO ₃)		

Table 6 Names, abbreviations, specifications and supplier information of deposition materials

2.1.5 Solvents

Solvent name	Specifications	Supplier
Acetone	>= 99 %	Fisher Scientific UK Ltd
Acetonitrile	>= 99.9 %	Fisher Scientific UK Ltd
Chloroform	Anhydrous, ≥ 99 %	Merck Life Science UK Limited
Chlorobenzene	Anhydrous, 99.8 %	Sigma aldrich
Dulbecco's Phosphate Buffered Saline	Potassium chloride (2.7 mM), potassium phosphate monobasic (1.5 mM), sodium chloride (137.9 mM), sodium phosphate dibasic (8.1 mM)	Thermo Fisher Scientific (Gibco)
Isopropanol		Honeywell
Ethanol		Honeywell
Toluene	Anhydrous, 99.85 %	Thermo Scientific
Methanol		Honeywell
Sulfuric acid	95 – 97 %	Merck Life Science UK Limited
Hydrogen peroxide	30 %	Fisher Scientific UK Ltd

Table 7 Names, specifications and supplier information of solvents

2.1.6 Aptamer functionalisation chemicals

A list of aptamer functionalisation chemicals used within this thesis is presented in Table 8. BCN-NHS was used in chapter 3 of this thesis. GA was used in chapter 4 of this thesis. EDC and sulfo-NHS were used in chapter 5 of this thesis.

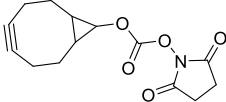
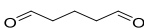
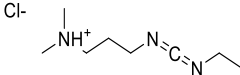
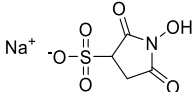
Chemical name	Structure	Supplier
(1R,8S,9s)-Bicyclo[6.1.0]non-4-yn-9-ylmethyl N-succinimidyl carbonate (BCN-NHS)		Sigma Aldrich
Glutaraldehyde (GA) 25 % in H ₂ O		Sigma Aldrich
1-ethyl-3-(3-dimethylaminopropyl)carbodiimide hydrochloride (EDC)		Sigma Aldrich
N-hydroxysulfosuccinimide (Sulfo-NHS)		Sigma Aldrich

Table 8 Names, abbreviations, structures and supplier information of aptamer functionalisation chemicals

2.1.7 DNA sequences

A list of DNA sequences used within this thesis is presented in Table 9, along with the sequence name/abbreviation and sequence of bases + functionalities. All sequences were ordered and prepared by Integrated DNA Technologies. DNA sequences arrived in a dehydrated state and were resuspended to a concentration of either 100 μM or 1000 μM , with Milli-Q water. Stock DNA solutions were stored in a freezer, and thawed for 15 minutes before use.

DNA sequence name	DNA sequence abbreviation	DNA sequence
Amine terminated cortisol binding aptamer	NH ₂ -CBA	5'-amine-GGA ATG GAT CCA CAT CCA TGG ATG GGC AAT GCG GGG TGG AGA ATG GTT GCC GCA CTT CGG CTT CAC TGC AGA CTT GAC GAA GCT T-3'
Amine terminated dehydroepiandrosterone sulphate binding aptamer	NH ₂ -DHEAS	5'-amine-CTG CTC TCG GGA CGT GGA TTT TCC GCA TAC GAA GTT GTC CCG AG-3'
Azide terminated cortisol binding aptamer	N ₃ -CBA	5'-azide-GGA ATG GAT CCA CAT CCA TGG ATG GGC AAT GCG GGG TGG AGA ATG GTT GCC GCA CTT CGG CTT CAC TGC AGA CTT GAC GAA GCT T-3'
Azide terminated neuropeptide Y (DPP- DTT043 N ₂ plasma)	N ₃ -NPY	5'-azide-AGC AGC ACA GAG GTC AGA TGC AAA CCA CAG CCT GAG TGG TTA GCG TAT GTC ATT TAC GGA CCT ATG CGT GCT ACC GTG AA-3'
Cy3 labelled complimentary cortisol binding aptamer	Cy3-comp-CBA	5'-Cy3-AA GCT TCG TCA AGT CTG CAG TGA AGC CGA AGT GCG GCA ACC ATT CTC CAC CCC GCA TTG CCC ATC CAT GGA TGT GGA TCC ATT CC- 3'
DBCO terminated cortisol binding aptamer	DBCO-CBA	5'-DBCO-GGA ATG GAT CCA CAT CCA TGG ATG GGC AAT GCG GGG TGG AGA ATG GTT GCC GCA CTT CGG CTT CAC TGC AGA CTT GAC GAA GCT T-3'

Table 9 Names, abbreviations and sequences of DNA strands used within thesis

2.2 Methodologies

Outlined below are procedures that have been repeated frequently throughout this thesis.

2.2.1 Substrate cutting procedures

Cutting of Si/SiO₂ (300 nm) wafers

100 mm Si/SiO₂ (300 nm) wafers were mechanically diced into 15 mm x 20 mm substrates. A PELCO FlexScribe 200 Front-Side Scribing Tool was used to scribe the dimensions onto the wafers. Mechanical pressure was then applied to the scribed wafer, causing the wafer to break along the scribe line.

Cutting of Indium tin oxide (ITO) coated glass sheets

Indium tin oxide (ITO) coated glass sheets were scribed using a PELCO Flexscribe into 20 mm x 15 mm sections. The scribed ITO sheets were then divided into individual substrates with glass breaking pliers. The cut edges of the ITO substrates were smoothed with a disc polisher.

Cutting of polyimide sheets

Polyimide sheets, measuring 300 mm x 320 mm x 125 μm, were divided into individual substrates measuring 20 mm x 15 mm with scissors.

2.2.2 Substrate cleaning procedures

Cleaning of Si/SiO₂ (300 nm) substrates (20 mm x 15 mm)

Substrates were added to a PTFE substrate holder, which was transferred to a 100 mL glass beaker. The substrates were cleaned via sonication, in a bath sonicator (supplied by Ultrawave), by immersing the substrates successively in piranha solution (3:1, H₂SO₄:30 % H₂O₂) for 1 hour, MQ water for 30 minutes, acetone for 30 minutes, MQ water for 30 minutes, IPA for 30 minutes. Cleaned substrates were then stored in IPA.

Cleaning of ODTs modified Si/SiO₂ (300 nm) substrates (20 mm x 15 mm)

Substrates were added to a PTFE substrate holder, which was transferred to a 100 mL glass beaker. The substrates were cleaned via sonication, in a bath sonicator, in IPA for 15 minutes. Cleaned substrates were removed from the IPA and pressurised air was used to remove excess IPA from the substrates. The substrates were dried using a 100 °C hotplate, under N₂ atmosphere, for 15 minutes.

Cleaning of No. 1.5 glass coverslip substrates (22 mm x 22 mm)

Substrates were added to a PTFE substrate holder, which was transferred to a 100 mL glass beaker. The substrates were cleaned via sonication, in a bath sonicator, by immersing the substrates successively in piranha solution (3:1, H₂SO₄:30 % H₂O₂) for 1 hour, MQ water for 30 minutes, acetone for 30 minutes, MQ water for 30 minutes, IPA for 30 minutes. Cleaned substrates were then stored in IPA. Stored substrates were dried with pressurised air, before use.

Cleaning of ITO coated glass substrates (20 mm x 15 mm x 1.1 mm)

Substrates were added to a PTFE substrate holder, which was transferred to a 100 mL glass beaker. The substrates were cleaned via sonication, in a bath sonicator, by immersing the substrates successively in soapy MQ water for 1 x 15 minutes, MQ water for 3 x 15 minutes, acetone for 2 x 10 minutes and IPA for 2 x 5 minutes. Cleaned substrates were stored in IPA.

Stored substrates removed from the IPA and dried with pressurised air. Air plasma was used for 15 minutes, to further clean the substrates before use.

Cleaning of polyimide substrates (20 mm x 15 mm x 125 μ m)

Substrates were added to a PTFE substrate holder, which was transferred to a 100 mL glass beaker. The substrates were cleaned via sonication, in a bath sonicator, by immersing the substrates in IPA for 15 minutes. Cleaned substrates were then dried with pressurised air.

2.2.3 Octadecyltrichlorosilane SAM treatment of Si/SiO₂ substrates

Procedure adapted from Kang et al., 2014.(165)

Si/SiO₂ (300 nm) substrates, stored in IPA, were removed and dried with a pressurised air hose. Substrates were then placed in an air plasma cleaner (High setting = 18 W) and treated with air plasma to activate the SiO₂ surface, for 1 hour. 100 mL oven dried glass beaker charged with 40 mL dry toluene and 157.7 µL octadecyltrichlorosilane, giving a 0.01 M ODTs solution, and was clamped onto a hotplate. Air plasma treated substrates were then transferred to a PTFE substrate holder, which was then lowered into the 0.01 M ODTs solution. Aluminium foil was then used to seal the opening of the glass beaker. A syringe needle, attached to a Schlenk line, was pierced through the aluminium foil and secured with a clamp. N₂ gas was then streamed into the beaker above the solvent line. The surface of the hotplate was set to 60 °C and the reaction was left for 2 hours. After the reaction, the substrate holder containing the modified substrates was transferred to a 100 mL beaker containing toluene. The beaker was then placed into a sonication bath and sonicated for 15 minutes. The process was then repeated once more, in a beaker containing IPA. After 15 minutes, the substrates were removed from the IPA solution and dried with a pressurised air hose. Finally, the modified substrates were dried further on a 100 °C hotplate under nitrogen for 15 minutes. 20 µL of Milli-Q water was used to observe the more hydrophobic properties of the substrates. Confirming that the functionalisation reaction was successful. The ODTs substrates were stored under vacuum prior to use.

2.2.4 Thin-film deposition

2.2.4.1 Deposition of 3 mg mL⁻¹ DPP-DTT in chlorobenzene polymer solution, via floating thin-film transfer

A 3 mg mL⁻¹ DPP-DTT polymer solution in a CHCl₃:CB 9:1, prepared in an amber vial with a magnetic stir bar. The vial was wrapped in aluminium foil and inserted into a heating block, which was then placed on a hotplate. The polymer solution was heated to 45 °C and stirred at 250 RPM for 4 hours. 70 cm³ of RT MQ water, was measured using a graduated measuring cylinder and poured into a 9 cm diameter glass petri dish. The petri dish was placed onto a hotplate with the temperature set to 25 °C. The petri dish was then surrounded with a 20 cm high screen, in order to shield the surface of the MQ water from turbulent air. A ~5 cm wide break in the screen was allowed, so that the pipette could access the surface of the MQ water. Using a 2-20 µL pipette, 20 µL of the 45 °C polymer solution was pipetted in the centre of the MQ water surface. The position of the pipette tip was maintained at a constant height, that was < 1 cm above the surface of the MQ water. The floated thin-film was dried for between 3-5 minutes. The floated thin-film was then transferred onto a substrate, by stamping the substrate into the thin-film. The transferred thin-film was dried with an air hose and then thermally annealed on a hotplate at 100 °C, under a N₂ atmosphere, for 1 hour.

2.2.4.2 Deposition of 5 mg mL⁻¹ DPP-DTT:GA solution, 9:1 in chlorobenzene and glutaraldehyde (25 % in H₂O), via Spin coating

A 5 mg mL⁻¹ DPP-DTT:GA solution, blended in a 9:1 volume ratio with chlorobenzene and a 25 % solution of glutaraldehyde (GA) in H₂O, was prepared in an amber vial containing a magnetic stir bar. The vial was wrapped in aluminium foil and inserted into a heating block, which was then placed onto a hotplate. The polymer solution was stirred at 250 RPM for 24 hours at RT. The polymer solution was heated to 50 °C, prior to spin coating. 100 µL of the DPP-DTT:GA solution was pipetted onto the centre of the substrate, and spin coated using the settings in Table 10.

Step	RPM	Acceleration	Time
1st step	4K	1K	120 s
2nd step	8K	1K	30 s

Table 10 Spin coating conditions for 5 mg mL⁻¹ DPP-DTT:GA (25 % in H₂O), 9:1 in chlorobenzene polymer solution

The spin coated thin-film was then thermally annealed on a hotplate at 100 °C, under a N₂ atmosphere, for 1 hour.

2.2.4.3 Floating thin-film transfer of 5 mg mL⁻¹ N₃-DPP in chlorobenzene polymer solution

A 5 mg mL⁻¹ N₃-DPP polymer solution in chlorobenzene, prepared in an amber vial. The mixture was then probe sonicated to produce a homogenous polymer solution. Probe tip sonicator conditions are described in section 2.3.7. 70 cm³ of RT MQ water, was measured using a graduated measuring cylinder and poured into a 9 cm diameter glass petri dish. The petri dish was placed onto a hotplate with the temperature set to 25 °C. The petri dish was then surrounded with a 20 cm high screen, in order to shield the surface of the MQ water from turbulent air. A ~5 cm wide break in the screen was allowed, so that the pipette could access the surface of the MQ water. Using a 2-20 µL pipette, 20 µL of the RT polymer solution was pipetted in the centre of the MQ water surface. The position of the pipette tip was maintained at a constant height, that was < 1 cm above the surface of the MQ water. The floated thin-film was dried between 3-5 minutes. The floated thin-film was then transferred onto a substrate, by stamping the substrate into the thin-film. The transferred thin-film was dried with an air hose and then thermally annealed on a hotplate at 110 °C, under a N₂ atmosphere, for 30 minutes.

2.2.4.4 Chronoamperometry polymerisation of DTP-C4-acid monomer solution

A solution of 5 mM DTP-C4-acid monomer and 0.1 M TBAClO₄ in degassed MeCN was prepared in a volumetric flask. The mixture was inverted repeatedly, until a clear solution was obtained. The solution was then filtered into a glass cell, using a 0.45 µm pore size syringe filter. Following this, a Ag/AgNO₃ electrode (reference electrode), platinum wire (counter electrode) and ITO coated glass substrate (working electrode) were inserted into the solution, with the ends of the electrodes spaced equally apart within the solution. The electrodes were then connected to a PalmSens EmStat4 potentiostat. Polymerisation of DTP-C4-acid was achieved by applying a potential of 0.85 V for 30 s, with an interval of 0.1 s. DTP-C4-acid polymer thin-films on ITO coated glass were removed from the solution. Excess solution was removed by submerging the thin-films into degassed MeCN, this process was repeated 4 times. The thin-films were then dried with an air hose for 30 s.

2.2.5 Aptamer functionalisation

2.2.5.1 N₂ plasma treated DPP-DTT thin-film aptamer functionalisation

DPP-DTT thin-film via FFT from 9:1 CHCl₃:CB (3 mg mL⁻¹) on No. 1.5 glass coverslips (22 mm + 22 mm) was prepared as described in section 2.2.4.1. A 3 mg mL⁻¹ DPP-DTT thin-film was N₂ plasma treated with the following treatment conditions; 12 W/0.3 mbar/30 s. The N₂ plasma treated thin-film was transferred to a 6-well plate, along with a moist Kimwipe. A 1.0 mg mL⁻¹ solution of BCN-NHS in DPBS was prepared. 50 μL of the BCN-NHS solution was pipetted onto the surface of the N₂ plasma treated thin-film. The thin-film was covered, placed onto a platform shaker and shaken at 250 RPM/30 mins/25 °C. The thin-film was then rinsed with MQ water. A 1 μM solution of N₃-CBA in DPBS was prepared. 50 μL of the N₃-CBA solution was pipetted onto the surface of the BCN-NHS modified thin-film. The thin-film was covered, placed onto a platform shaker and shaken at 250 RPM/30 mins/25 °C. The N₃-CBA functionalised thin-film was rinsed sequentially with a 0.1 % solution of tween20 and MQ water, then dried with an argon gas hose.

Cy3-comp-CBA hybridisation:

Aptamer functionalisation carried out the same as before, with the following additional steps performed after aptamer functionalisation.

A 1 μM solution of Cy3-comp-CBA in DPBS was prepared. A NH₂-CBA functionalised DPP-DTT thin-film was placed in a 6-well plate, along with a moist Kimwipe. 50 μL of the Cy3-comp-CBA solution was pipetted onto the thin-film. The thin-film was covered, placed onto a platform shaker and shaken at 250 RPM/1 hr/25 °C. The Cy3-comp-CBA hybridised thin-film was rinsed sequentially with a 0.1 % solution of tween20 and MQ water, then dried with an argon gas hose.

2.2.5.2 5 mg mL⁻¹ DPP-DTT:glutaraldehyde (25 % in H₂O) 9:1 in chlorobenzene thin-film aptamer functionalisation

DPP-DTT:GA thin-film was deposited onto No. 1.5 glass coverslips (22 mm + 22 mm) as described in section 2.2.4.2. A 10 μM solution of NH₂-CBA in DPBS was prepared. A DPP-DTT:GA thin-film was placed in a 6-well plate, along with a moist Kimwipe. 50 μL of the NH₂-CBA solution was pipetted onto the thin-film. The thin-film was covered, placed onto a platform shaker and shaken at 250 RPM/3 hrs/25 °C. The NH₂-CBA functionalised thin-film was rinsed sequentially with a 0.1 % solution of tween20 and MQ water, then dried with an argon gas hose.

Cy3-comp-CBA hybridisation:

Aptamer functionalisation carried out the same as before, with the following additional step performed after aptamer functionalisation.

A 1 μM solution of Cy3-comp-CBA in DPBS was prepared. A NH₂-CBA functionalised DPP-GA thin-film was placed in a 6-well plate, along with a moist Kimwipe. 50 μL of the Cy3-comp-CBA solution was pipetted onto the thin-film. The thin-film was covered, placed onto a platform shaker and shaken at 250 RPM/1 hr/25 °C. The Cy3-comp-CBA hybridised thin-film was rinsed sequentially with a 0.1 % solution of tween20 and MQ water, then dried with an argon gas hose.

2.2.5.3 N₃-DPP thin-film aptamer functionalisation

Following procedure was adapted from Fenoy et al., 2022.(156)

A 1 μ M solution of DBCO-CBA in DPBS was prepared. A N₃-DPP thin-film was placed in a 6-well plate, along with a moist Kimwipe. 50 μ L of the DBCO-CBA solution was pipetted onto the thin-film. The thin-film was covered, placed onto a platform shaker and shaken at 200 RPM/1 hr/25 °C. The DBCO-CBA functionalised thin-film was rinsed sequentially with a 0.1 % solution of tween20 and MQ water, then dried with an argon gas hose.

Cy3-comp-CBA hybridisation:

Aptamer functionalisation carried out the same as before, with the following additional steps performed after aptamer functionalisation.

A 1 μ M solution of Cy3-comp-CBA in DPBS was prepared. A DBCO-CBA functionalised N₃-DPP thin-film was placed in a 6-well plate, along with a moist Kimwipe. 50 μ L of the Cy3-comp-CBA solution was pipetted onto the thin-film. The thin-film was covered, placed onto a platform shaker and shaken at 250 RPM/1 hr/25 °C. The Cy3-comp-CBA hybridised thin-film was rinsed sequentially with a 0.1 % solution of tween20 and MQ water, then dried with an argon gas hose.

2.2.5.4 DTP-C4-acid thin-film aptamer functionalisation

Procedure adapted from Aerathupalathu et al., 2022.(158)

A solution of 0.4 M 1-ethyl-3-(3-dimethylaminopropyl)-carbodiimide (EDC) and 0.1 M N-hydroxysulfosuccinimide (sulfo-NHS) in DPBS was prepared. A chronoamperometry polymerised DTP-C4-acid thin-film, on ITO, was placed in a 6-well plate, along with a moist Kimwipe. 100 μL of the EDC/sulfo-NHS solution was pipetted onto the thin-film. The thin-film was covered, placed onto a platform shaker and shaken at 250 RPM/6 hrs/25 °C. The thin-film was then rinsed with MQ water. A 10 μM solution of NH_2 -CBA in DPBS was prepared. 100 μL of the NH_2 -CBA solution was pipetted onto the EDC/sulfo-NHS activated DTP-C4-acid thin-film. The thin-film was covered, placed onto a platform shaker and shaken at 250 RPM/1 hr/25 °C. The NH_2 -CBA functionalised thin-film was rinsed sequentially with a 0.1 % solution of tween20 and MQ water, then dried with an argon gas hose.

Cy3-comp-CBA hybridisation:

Aptamer functionalisation carried out the same as before, with the following additional step performed after aptamer functionalisation.

A 1 μM solution of Cy3-comp-CBA in DPBS was prepared. 100 μL of the Cy3-comp-CBA solution was pipetted onto the NH_2 -CBA functionalised DTP-C4-acid thin-film. The thin-film was covered, placed onto a platform shaker and shaken at 250 RPM/1 hr/25 °C. The Cy3-comp-CBA hybridised thin-film was rinsed sequentially with a 0.1 % solution of tween20 and MQ water, then dried with an argon gas hose.

2.2.6 Sensing experiment solutions

Tris-HCl buffer solution preparation:

A solution of Tris-HCl 50 mM, NaCl 100 mM, MgCl₂ 5 mM in MQ water was prepared and the pH adjusted to 7.4 at 25 °C.(150)

Cortisol sensing solutions preparation:

A 50 mM stock solution of hydrocortisone (supplied by Sigma Aldrich) in methanol, was prepared in a graduated microcentrifuge tube. Part of the stock cortisol solution was diluted to 2 mM with Tris-HCl buffer solution. A series of dilutions were performed with Tris-HCl buffer solution, giving a range of cortisol solution concentrations from 2 nM to 2 mM.

2.3 Instrumentation background and methodologies

2.3.1 Atomic force microscopy

Atomic force microscopy (AFM) is a type of scanning probe microscopy (SPM). Developed by Binnig et al., in 1986, the atomic force microscope combined the basics of a stylus profilometer with the theoretical concepts of scanning tunneling microscopy.(166) The technique allows the surface of a thin-film to be mapped three-dimensionally, enabling morphological features and other mechanical properties to be measured. AFM shows a high degree of flexibility in terms of its methodology. Making it an applicable technique for thin-films with varying properties and under different environmental conditions. Additionally, vertical and horizontal resolutions of sub-nanometre and several nanometres can be achieved by the instrument, respectively.(167)

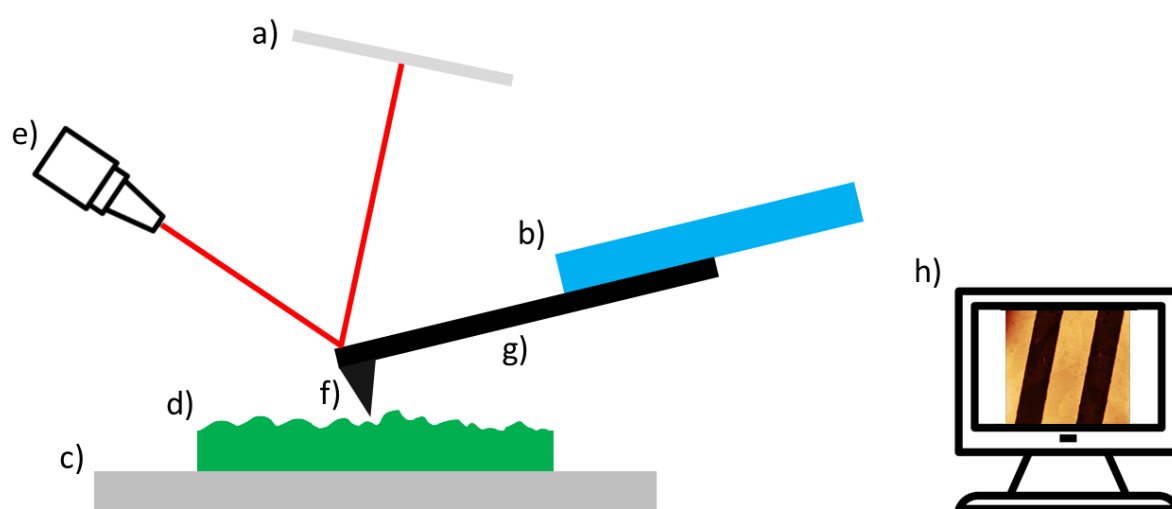


Figure 17 AFM instrument configuration a) photodetector b) piezoelectric scanner c) stage d) sample e) laser beam f) tip g) cantilever h) resulting AFM image of [Hexane-AuNP-C8 network on interdigitated electrodes](#) by [Thibault Degousée](#) is licensed under CC BY 3.0 Deed.(168)

AFM instrument configuration is depicted in Figure 17, where a laser beam is aligned to the back of the cantilever which reflects into a quadrant-photodetector (photodiode detector). During operation the cantilever flexes due to interacting forces between the tip and the thin-film. Deflection alters the position of the laser beam reflected into the photodetector. The change in the laser position is transduced and generated into a map of the surface (Figure

18). During scanning, a feedback loop is implemented to maintain the desired interaction between the tip and the thin-film.

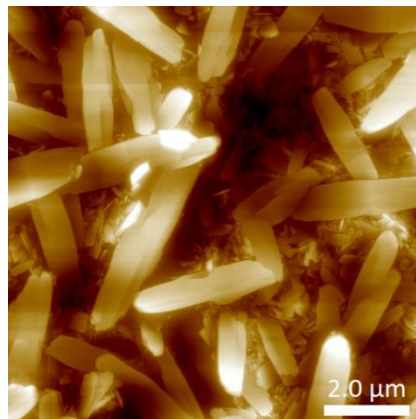


Figure 18 AFM image of [NDI-OH film drop-cast at 45 °C](#) by [Lewis M. Cowen](#) is licensed under CC BY 3.0 Deed.(169)

AFM can be conducted in different modes, with mode selection dependent on the intrinsic properties of the thin-film surface. The specific modes are referred to as contact, non-contact and tapping mode. Each mode operates within a different regime of the force vs. distance curve illustrated in Figure 19, where the distance between the tip and the thin-film determines the type of force experienced. Contact and non-contact modes operate in repulsive force and attractive force regimes, respectively. Tapping mode is considered a hybrid between contact and non-contact modes, where the tip is oscillated at a set frequency and makes periodic contact with the thin-film surface.

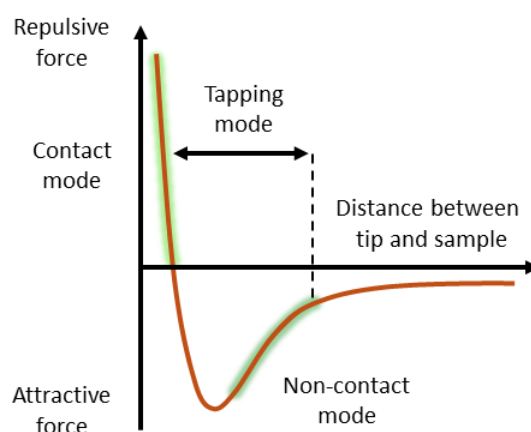


Figure 19 Force vs. Distance curve – depicting the effect of tip-to-sample distance on the force interaction between tip and sample. Image adapted with permission from {S. Caponi, C.

Canale, O. Cavalleri, M. Vassalli, "Characterization Tools for Mechanical Probing of Biomimetic Materials" in *Nanotechnology Characterization Tools for Tissue Engineering and Medical Therapy* (2019) pp. 69–111.}. Copyright {2024} Springer Berlin Heidelberg(170)

The interaction between the tip and the thin-film surface is described by the Lennard-Jones potential, which is approximated by the following Equation 4:

$$\text{Equation 4} \quad V = 4\varepsilon \left[\left(\frac{\sigma}{r} \right)^{12} - \left(\frac{\sigma}{r} \right)^6 \right]$$

Where V is the potential, ε is the minimum potential, σ is the distance at which the potential is zero and r is the distance between the tip and the surface. $\left(\frac{\sigma}{r} \right)^{12}$ models short range repulsive forces and $\left(\frac{\sigma}{r} \right)^6$ models long range attractive forces. A timeline of attractive and repulsive forces experienced by the tip is illustrated in Figure 20. Where the Z position is the height of the tip. A and E denote the force of approaching and withdrawing from the thin-film, respectively. B and D denote the occurrence of attractive forces, while C is the point at which the tip is engaged with the thin-film surface and repulsive forces arise.

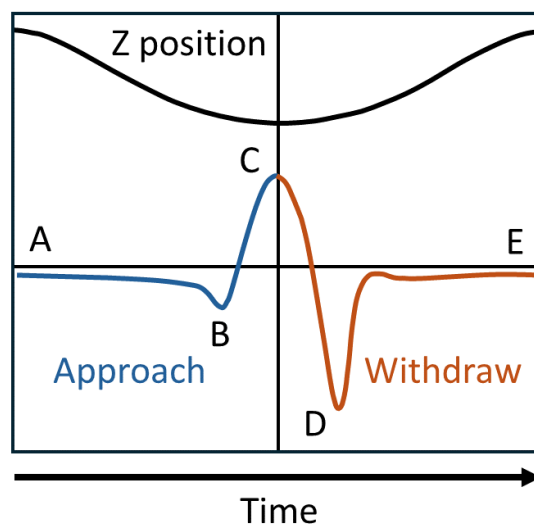


Figure 20 Force vs. Time curve. Image adapted with permission from {S. Caponi, C. Canale, O. Cavalleri, M. Vassalli, "Characterization Tools for Mechanical Probing of Biomimetic Materials" in *Nanotechnology Characterization Tools for Tissue Engineering and Medical Therapy* (2019) pp. 69–111.}. Copyright {2024} Springer Berlin Heidelberg(170)

The quality of an AFM image is influenced by balancing the setpoint, feedback gain and scan rate. The setpoint is the amplitude which is maintained by the feedback loop during scanning. The feedback gain determines how quickly the feedback loop reacts to maintaining the setpoint. The scan rate determines the speed at which the probe travels over the thin-film surface.

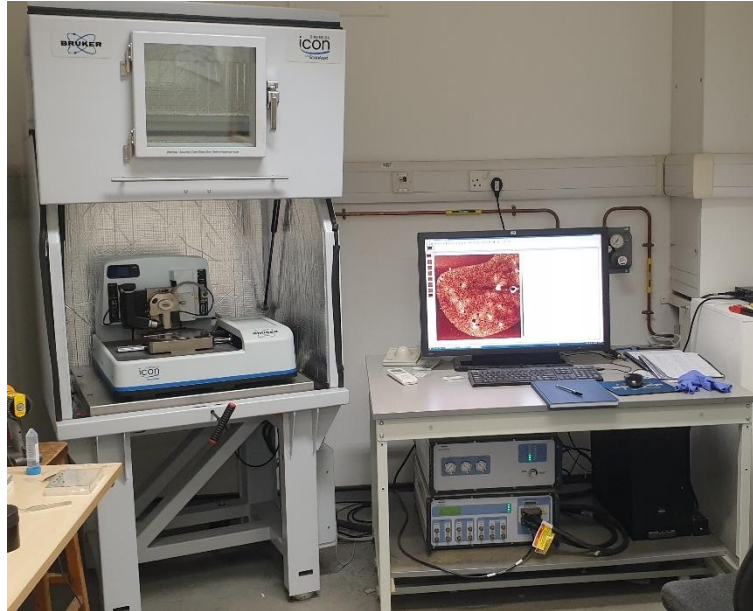


Figure 21 Bruker Dimension Icon AFM instrument.

In this work atomic force microscopy (AFM) images were captured on a Bruker Dimension Icon system (Figure 21), running NanoScope software. Measurements were carried out in a climate controlled room, in air, using Bruker ScanAsyst-AIR model silicon nitride tips. With reflective aluminium coating the back side of the tips. AFM images were acquired using PeakForce QNM, a variant of Peak Force Tapping mode. In general, Images were scanned with a frequency of between 0.5 – 1.0 Hz/line, a setpoint between 0.05 – 0.15 V and feedback gain between 5.0 – 20.0. Captured AFM images were processed and analysed with NanoScope Analysis 1.7 software.

2.3.2 X-ray photoelectron spectrometry

X-ray photoelectron spectroscopy (XPS) is a frequently used technique for the sensitive analysis of a surfaces chemical composition. A majority of the theory and instrumentation of XPS was developed by Kai Siegbahn and colleagues in the 1950s and 1960s. XPS involves irradiating the surface of a material with X-rays, which cause the atoms within the surface to eject an electron. The kinetic energy (KE) of the emitted electron is detected by an analyser. Elemental characterisation is determined by the binding energy (BE) of the electron, which is calculated with the following Equation 5, if the energy of the X-ray ($h\nu$) and kinetic energy (KE) of the electron is known:

Equation 5
$$BE = h\nu - KE$$

Counting these electrons and measuring their energies allows the identification of the elemental composition and relative quantities of a surface. Making XPS both a qualitative and quantitative technique. The binding energy of the electron can also determine the chemical environment, which shifts depending on oxidation state and electronegativity of neighbouring elements. Allowing functional groups to be discerned and the chemical composition of a surface to be determined. XPS has a surface sensitivity of 10 nm allowing composition of both the surface and underlying material to be determined. XPS is also flexible with conductive or insulating materials.(171–173)

All XPS experiments were performed using a ThermoFisher Nexsa X-ray Photoelectron Spectrometer (Figure 22). The software Thermo Advantage v5.9925, was used to process all resulting XPS spectra.



Figure 22 ThermoFisher Nexsa X-ray Photoelectron Spectrometer

XPS experiments were undertaken using the following conditions and parameters. The time between sample preparation and analysis was minimised, to prevent adventitious carbon contribution to the spectra. Samples were mounted onto a stage with metal clips. The stage was then loaded into an ultra-high vacuum (UHV) analysis chamber. XPS scans were started when the analysis chamber achieved a vacuum of $\sim 3.0 \text{ E}^{-8}$ mbar. A charge gun was enabled during all XPS analysis scans, to avoid sample charging. XPS survey spectra were captured within a binding energy range between -10.000 and 1350.000 eV, pass energy 200.000 eV, number of scans 20, dwell time 10 ms, energy step size 1.000 eV. High resolution scans pass energy 50.000 eV, number of scans 30, dwell time 50 ms, energy step size 0.100 eV. Spot sizes were set to either 30 μm , 100 μm or 400 μm .(173)

Survey ID tool processed XPS survey spectra, which automatically identifies and peak fits elements within the spectrum. High resolution scan background addition and component peak fitting were applied using the following parameters. High resolution scans were fitted with a Smart background and then charge corrected using the C1s peak shift. Peak fitting

binding energies were obtained from literature sources. The following constraints were used during peak fitting of high resolution C1s spectra; tolerance of peak binding energies were set to ± 0.2 eV. Full Width Half Maximum (FWHM) of the C-C peak was used as an approximate reference value for the other chemical peaks, with a ± 10 % tolerance.⁽¹⁷⁴⁾ For known materials the Area CPS.eV was constrained to the expected ratio of the minor elements within the material. Peak fitting was carried out iteratively, using the defined constraints. Until the residual, defined as the difference between the experimental and fitted curves, was minimised and while still being chemically/physically reasonable.

2.3.3 Epifluorescence microscopy

Epifluorescence microscopy is an imaging technique utilised in a diverse range of scientific fields. The general structure of an epifluorescence microscope is depicted in Figure 23. Fluorophores present on the sample are excited with a specific excitation wavelength, causing the fluorophore to emit an emission wavelength. The emission wavelength is filtered through a dichromatic mirror and observed through the eyepiece. However, a limitation of epifluorescence is that a high background fluorescence can be observed.(175, 176)

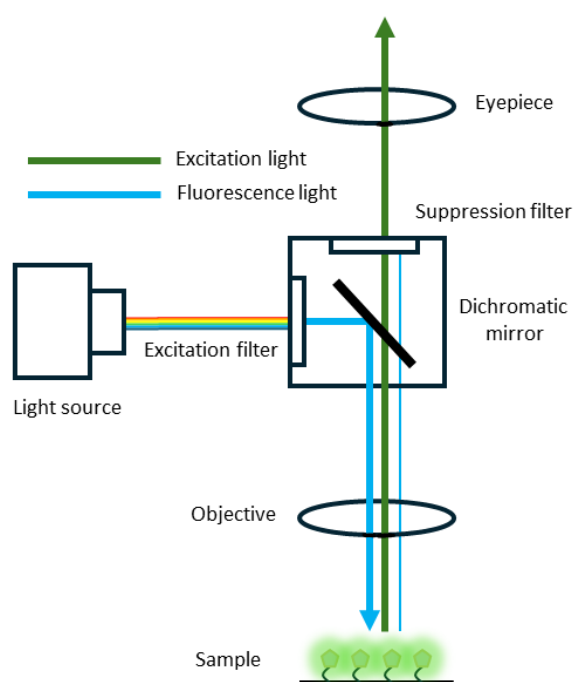


Figure 23 Epifluorescence microscope diagram. Image adapted with permission from {C. Stewart, J. Giannini, Inexpensive, Open Source Epifluorescence Microscopes. J. Chem. Educ. 93, 1310–1315 (2016).}. Copyright {2024} American Chemical Society.(176)

In this work epifluorescence microscopy images were captured using the following instruments and related software:

Zeiss Super resolution LSM 710 ELYRA PS.1 microscope, images were collected with Zen 2012 software, images were processed using ImageJ software.

Nikon CSU-W1 SoRA Super-Resolution Spinning Disk Confocal microscope, CFI Plan Fluor 10x/0.3/WD 16mm objective, CoolLED pE-4000 MultiLaser, Photometrics Prime BSI back-illuminated sCMOS cameras

The images were processed using the software ImageJ. The average pixel value for each image was determined through Image J and recorded. Graph of average pixel values were plotted in OriginPro 2021.

Epifluorescence microscopy was used to analyse Cy3 fluorescently labelled complimentary cortisol binding aptamer strands. The excitation wavelength and emission wavelength of the microscope was set to 555 nm and 569 nm, respectively. Under the epifluorescence microscopy conditions, the fluorescent dye Cy3, when present is excited by the excitation wavelength and emits an emission wavelength. Thereby, increasing the average pixel density of the images, above the background fluorescence.

2.3.4 OFET characterisation

OFET characterisation equipment was composed of two interconnected parts; a Lake Shore Cryotronics Inc. TTPX Probe Station and a Kiethley Model 4200-SCS Semiconductor Characterization System.

All OFET measurements were performed in ambient conditions. Patterning of the thin-films around the source drain electrode pairs was performed, before OFET characterisation. A soft pointed instrument was used to divide the individual devices into separate areas of thin-film. The process was performed to prevent leakage currents reducing OFET performances.(177) Probe station probes were lowered onto the gate, source and drain electrodes. The probe contacting the gate electrode was positioned onto an exposed area of doped silicon. Probes contacting the source/drain electrodes were positioned onto the respectful electrode pads. Source electrode was set to common. The transfer characteristics were measured by sweeping the gate (V_{gs}) at a constant drain bias (V_{ds}). The output characteristics were measured by sweeping the drain at a constant gate bias, which was repeated sequentially changing the gate bias. I_{ds} vs. Time studies were accomplished by applying constant gate and drain biases.

OFET figures of merit were extracted from the transfer curves. Transfer characteristics extracted from OFETs measured in the linear regime, where $V_{ds} < V_{gs} - V_{th}$, uses Equation 6 as follows:

$$\text{Equation 6} \quad I_{ds,lin} = \frac{W}{L} \mu_{lin} C_i (V_{gs} - V_{th}) V_{ds}$$

In the equation, W is defined as the channel width, L is the channel length, μ_{lin} is the mobility, C_i is the capacitance per unit area of the dielectric, V_{gs} is gate voltage bias, V_{th} is the threshold voltage and is the V_{ds} drain voltage bias.

Taking the derivative(13) with respect to V_{gs} and rearrangement of the equation calculates the saturation mobility (μ_{lin}), as shown in Equation 7:

$$\text{Equation 7} \quad \mu_{lin} = \frac{\delta I_{ds,lin}}{\delta V_{gs}} \frac{L}{WC_i V_{ds}}$$

Transfer characteristics extracted from OFETs measured in the saturation regime, where $V_{ds} > V_{gs} - V_{th}$, uses Equation 8 as follows:

$$\text{Equation 8} \quad I_{ds, sat} = \frac{W}{2L} \mu_{sat} C_i (V_{gs} - V_{th})^2$$

In the equation, W is defined as the channel width, L is the channel length, μ_{lin} is the mobility, C_i is the capacitance per unit area of the dielectric, V_{gs} is gate voltage bias and V_{th} is the threshold voltage.

Taking the derivative(13) with respect to V_{gs} and rearrangement of the equation calculates the saturation mobility (μ_{sat}), as shown in Equation 9:

$$\text{Equation 9} \quad \mu_{sat} = \left(\frac{\delta \sqrt{I_{ds, sat}}}{\delta V_{gs}} \right)^2 \frac{2L}{WC_i}$$

Threshold voltage (V_{th}) was calculated by (linear regression fit) extrapolating the transfer curve to the value that intercepts the x axis. Equation 10 was used:

$$\text{Equation 11} \quad y = mx + c$$

Where y (I_{ds}) is set to 0, c is the y axis intercept and m is the gradient. Rearrangement of the equation calculates the V_{th} , which is equal to x as shown in Equation 12:(13)

$$\text{Equation 12} \quad x = \frac{(y-c)}{m}$$

A reference value for C_i , of 11.5 nF cm^{-2} , was set as the approximate areal gate capacitance of the SiO_2 dielectric layer.(92) The dielectric layer is modified with a ODTS SAM, so it is acknowledged that the effective capacitance is altered by the combined in-series capacitances of the SAM and dielectric layer. However, the thickness of the ODTS SAM is considered negligible (1.55 nm, dielectric constant of 3) relative to the thickness of the SiO_2 layer (300 nm, dielectric constant of 3.9), with the capacitance of the thicker SiO_2 layer dominate of the two.(90)

2.3.5 Physical vapour deposition

Electrode deposition of materials was achieved using a physical vapour depositor. The vacuum pressure was monitored using an Edwards 1005 Pirani Penning Controller. Material deposition rate and thickness was monitored with a Inficon SQM-160 Rate/Thickness Monitor connected to a quartz crystal microbalance (QCM) crystal (6 MHz Gold, Clean-room compatible, 14 mm). Solid and powdery evaporation materials were loaded into tungsten boats.

Substrates were assembled into an evaporation stack, before insertion into the physical vapour depositor. The evaporation stack is illustrated in Figure 24, where a magnetic sheet was used to maintain flush mask contact with the substrate, reducing shadowing effects.

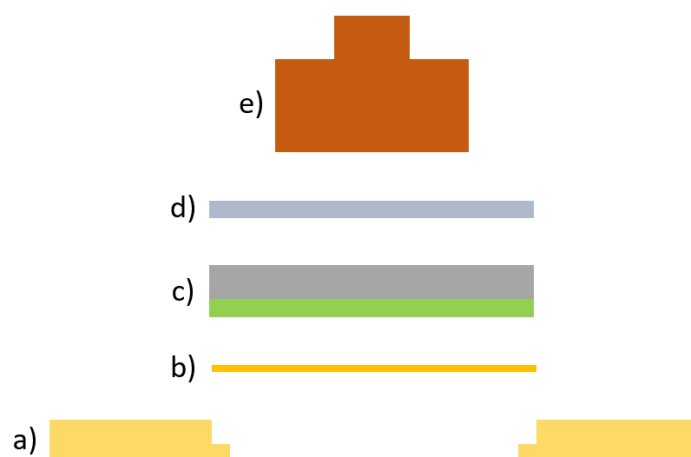


Figure 24 Evaporation stack cross section a) mask holder b) shadow mask c) substrate d) magnetic sheet e) weight

To achieve reported vacuum pressures and to prevent substrate overheating, a metal liquid nitrogen cooled lid was utilised. Before materials deposition, liquid nitrogen was fed into a reservoir attached to the lid. The liquid nitrogen cooled a metal plate that extended into the vacuum chamber. The metal plate was positioned above the evaporation stack, which cooled the area surrounding the evaporation stack. Liquid nitrogen was added continually until material deposition was complete. Materials were deposited using the conditions and settings listed in Table 11.

Material	Abbreviation	Z-Ratio	Deposition rate Å s ⁻¹	Pressure mbar
Chromium	Cr	0.305	1.0	~5.0 E ⁻⁶
Gold	Au	0.381	0.5	~5.0 E ⁻⁶
Molybdenum trioxide	MoO ₃	0.529	0.5	~5.0 E ⁻⁶
Silicon monoxide	SiO	0.870	1.0	~5.0 E ⁻⁶

Table 11 Physical vapour deposition settings and conditions of deposited materials

2.3.6 Oxygen and nitrogen plasma generator

Oxygen (O_2) and nitrogen (N_2) plasma were generated within a Diener Femto Plasma Etcher. A schematic representation of plasma generation is illustrated in Figure 25. A high electric field is used to generate O_2 or N_2 plasma, by applying a 40 kHz voltage to an electrode. The electric field accelerates electrons, which collide with gas molecules. If the collision occurs with sufficient energy, the molecule can transform into an excited species, such as a radical or ion. The excited species is also accelerated in the electric field and can react with a surface, creating new chemical species on the surface. If this doesn't occur, the excited species can relax by emitting a photon.

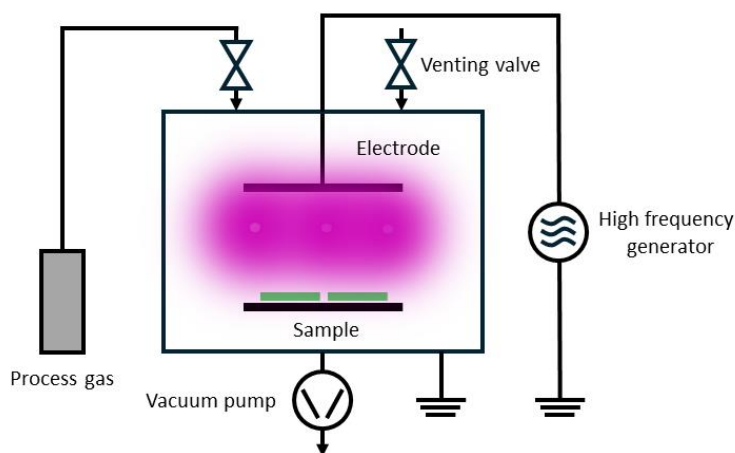


Figure 25 Schematic of plasma generator.

O_2 and N_2 plasma treatment procedure:

Samples were positioned onto the centre of a grated metal holder, which was inserted into the plasma generator chamber. The chamber was sealed and evacuated of air. A flow of oxygen or nitrogen gas was pumped into the chamber to purge the remaining air from the system, for 5 minutes. The gas flow rate was then adjusted until the chamber pressure measured 0.3 mbar.

2.3.7 Miscellaneous equipment

Equipment	Specification details										
Air plasma cleaner	Harrick Plasma PDC-32G-2 plasma cleaner										
Data processing software	Microsoft Excel Spreadsheet Software OriginPro 2021 (64-bit) version 9.8.0.200										
Milli-Q water dispenser	Millipore Milli-Q Integral 3 Water Purification System										
Electrochemistry	PalmSens EmStat4 potentiostat										
Platform Shaker	Fisherbrand Incubating Mini Platform Shaker										
Probe tip sonicator	<p>Benchmark Pulse 150 Ultrasonic Homogenizer. Equipped with a 2 mm titanium horn. Horn cleaned with acetone prior to use. Horn positioned into sample solution. Sample clamped into an ice bath.</p> <table border="1"> <thead> <tr> <th>Parameter</th> <th>Value</th> </tr> </thead> <tbody> <tr> <td>Power rate</td> <td>35 %</td> </tr> <tr> <td>On time</td> <td>4 s</td> </tr> <tr> <td>Off time</td> <td>4 s</td> </tr> <tr> <td>Total sonication time</td> <td>2 minutes</td> </tr> </tbody> </table>	Parameter	Value	Power rate	35 %	On time	4 s	Off time	4 s	Total sonication time	2 minutes
Parameter	Value										
Power rate	35 %										
On time	4 s										
Off time	4 s										
Total sonication time	2 minutes										
Spin coater	Laurell Technologies Operations WS-650-Lite Series Spin Processor										
Vortex mixer	VWR Analog Vortex Mixer										
Wafer dicing scribe	PELCO® FlexScribe™ 200 Front-Side Scribing Tool										
Water contact angle	Kruss-scientific Advance Drop Shape Analyser. Water contact angles were obtained by a numerical fitting algorithm using the side view of a 4 – 6 μ L deionized water drop										

Table 12 Additional equipment details

3 Organic field-effect transistor fabrication and the effects of plasma modification

3.1 Acknowledgments

The author would like to acknowledge Dr Mark Freeley for capturing epifluorescence microscopy images, captured at Queen Mary University. All other experiments were conducted by the author.

3.2 Introduction

Organic field-effect transistors (OFETs) have been extensively researched for biosensing applications, effectively bridging electronic devices with biological interfaces.^(59, 60, 107, 178, 179) Among these, OFETs utilising organic semiconducting polymers stand out as favourable candidates for healthcare applications, since these materials exhibit high biocompatibility, offer flexibility, and lower production costs.^(178, 180) OFET sensing capabilities include the detection of various biomarkers, such as physical indicators like pulse, blood pressure and nerve impulses.^(181–183) Chemical biomarkers are also detectable, which include antigens, antibodies, hormones, pH, DNA, volatile gases and other biologically relevant small molecules.^(107, 184) Furthermore, organic semiconducting polymers are highly versatile and effective at sensing in various mediums like blood, sweat, saliva, urine, and tears.^(154, 181) This, in combination with the flexibility of organic semiconducting polymers, holds great promise for the future development of wearable biosensing devices.^(122, 185, 186)

To date, these biosensors have attained single-molecule detection limits within respectable detection times (~minutes), by creating large interfaces (micrometre to millimetre) densely populated with biological receptors.^(126, 139, 187–189) Specific sensing responses require receptors tailored to analytes, attached to the sensing interface.⁽¹⁸¹⁾ Strategies of receptor attachment can influence resulting biosensing performances. Immobilising receptors through

physical adsorption is simple but incurs stability and sensitivity degradation.⁽¹⁵⁴⁾ Alternatively, receptor immobilisation through covalent bonding can overcome these issues.

Covalent attachment of receptors, through chemical bonding, is primarily performed at the gate electrode or semiconductor interface.⁽¹⁷⁹⁾ Gate receptor functionalisation is popular, especially if gold is utilised as the gate material. However, the viability of this method is hindered by the price of gold, which is further compounded by the need for large-area receptor functionalised interfaces. Therefore, the organic semiconductor polymer is a preferable receptor attachment site, providing a large interface for maintaining receptor stability. However, high-performing and environmentally stable organic semiconducting polymers generally lack intrinsic chemical functionalities, making the covalent attachment of receptors problematic. Attempts at chemical modification have been made, but resulting materials often exhibit impaired performances, such as reduced charge carrier mobilities, relative to the original material.⁽⁶¹⁾ Exploring strategies for modifying the organic semiconducting polymer, while maintaining high performances are therefore important.

A method of introducing chemically exploitable functionalities localised on the surface layer of a material, has been demonstrated through plasma treatment. This technique is frequently utilised to modify the surface properties of materials, including polymers, for convenient biomolecule attachment strategies.^(190–194) Plasma treated polymer surfaces have been investigated for sensor fabrication in various biomedical applications.⁽¹⁹⁵⁾ Additionally, interface modification of organic semiconducting materials in OFETs, via plasma-enhanced chemical vapour deposition, has been reported.^(147, 196) Plasma treatment of organic semiconducting polymer thin-film surfaces has also been reported to improve both air stability and performance metrics of OFETs.^(197, 198) Specifically, the modification of organic semiconducting polymers for biosensing OFET applications has been reported. In this context, Shen et al., utilised oxygen plasma treatment to introduce carboxylic acid groups to the surface of a high performance PDPP3T polymer thin-film OFET.⁽¹³⁴⁾ Carboxylic acid groups were subsequently exploited through EDC/NHS chemistry to covalently attach enzymes specific to adenosine triphosphate (ATP) to the thin-film surface. The technique was

successful at retaining significant OFET performance, while sensing ATP at a low detection limit of 0.1 nM. Expanding upon this approach, it is advantageous to explore the use of an environmentally stable and higher performing polymer, DPP-DTT, coupled with more favourable receptors such as DNA aptamers, as they provide analyte tunability and exhibit high affinity and stability, making them promising receptors for investigation.^(45, 199)

In this chapter, we explore the influence of plasma treatment on the characteristics of DPP-DTT OFETs. Initially an optimised method of fabricating OFETs, incorporating DPP-DTT, as the active material, as a platform for low-voltage biosensing devices is discussed. Following this, an exploration into plasma induced surface modification of DPP-DTT polymer thin-films, for applications in aptamer functionalisation is studied. Plasma treatment is explored in two approaches: oxygen and nitrogen plasma treatment. The degree of control over thin-film morphology, surface chemistry and OFET performance, via plasma modification is explored. Subsequently, a novel aptamer functionalisation strategy is identified, facilitated by nitrogen plasma treatment.

3.3 Organic field-effect transistor fabrication

3.3.1 Thin-film deposition optimisation

The characteristics of an organic semiconducting polymer thin-film greatly influences the performance of the fabricated OFET. Key characteristics involving the surface morphology and thickness need to be controlled. Surface morphology needs to be controlled to minimise thin-film disorders, such as structural defects, which can affect charge transport within the material.^(16, 200) Controlling the thin-film thickness is necessary to increase device sensitivity, without compromising the threshold voltage or charge carrier mobility.^(18, 125, 201) Therefore, homogeneous thin-films exhibiting smooth and consistent surface morphologies, as well as uniform thicknesses, are required.

In our work toward this end we initially faced issues forming DPP-DTT thin-films, when using spin coating as a thin-film deposition method. An example illustrating the morphology of a spin coated thin-film can be seen in Figure 26, revealing a dense array of large aggregates extending beyond the surface. In contrast, a defined crystalline morphology with densely stacked fibrillar bundles is observed between the aggregates.

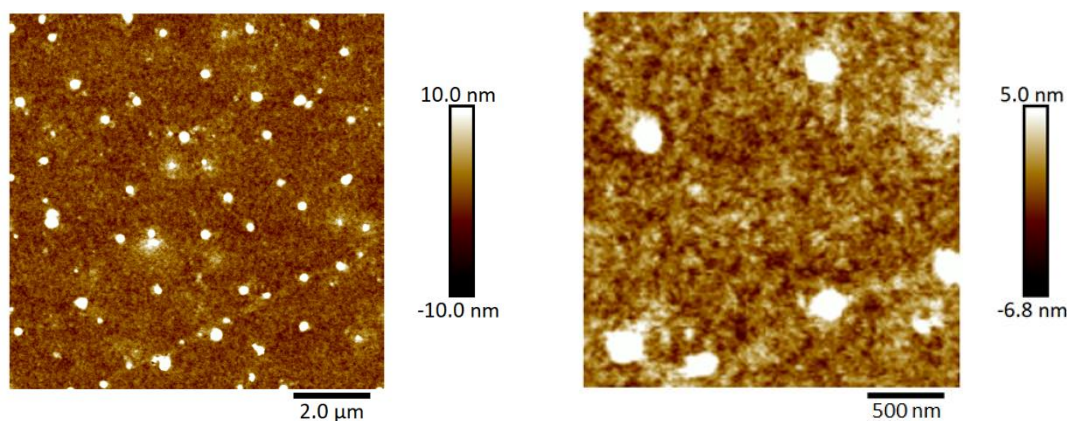


Figure 26 AFM topographical images ($10 \mu\text{m}^2$ and $3 \mu\text{m}^2$) of a DPP-DTT thin-film spin coated from chlorobenzene (5 mg mL^{-1}).

The high molecular weight (Mw) of the commercial DPP-DTT polymer, $M_w > 200 \text{ kg mol}^{-1}$, will influence the morphology of the thin-film. Higher Mw polymers typically observe lower solubilities and aggregate more readily in solution, which influences the solid-state

morphology.(81, 202) Strategies were explored to control this, including: varying solvent systems, varying polymer solution temperature ranges, off-centre/dynamic spin coating and thermal/solvent vapour thin-film annealing. However, the resulting thin-film morphologies observed no significant improvements.

A technique referred to as floating film transfer (FFT), synonymously known as floating film transfer method (FTM),(203) was explored as a thin-film deposition technique. The technique provides several advantages including: alignment of the polymer chains, conservation of the material, adaptability of the substrate and formation of large-area thin-films.(75, 103, 204–206) Additionally, FFT DPP-DTT thin-films often afford higher OFET performances relative to spin coated thin-films.(204)

A predetermined 9:1 chloroform and chlorobenzene solvent mixture was utilised for the polymer solution. This solvent system has been proven effective in producing DPP-DTT thin-films exhibiting high degrees of polymer chain alignment and high mobilities, via the FFT methodology.(103) A DPP-DTT polymer solution concentration series was prepared at 10, 5 and 3 mg mL⁻¹. Other parameters relating to the polymer solution deposition volume, liquid substrate composition, and temperature of the polymer solution/liquid substrate were controlled. Polymer solutions were deposited using FFT methodology (see section 2.2.4.1), with the process illustrated in Figure 27.

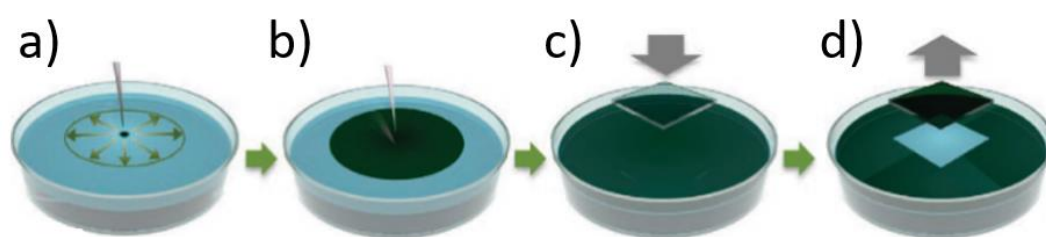


Figure 27 FFT procedure: a) polymer solution deposited onto liquid substrate b) polymer solution spontaneously spreads across liquid substrate c) substrate stamped into dried polymer thin-film d) polymer thin-film lifted from liquid surface and transferred to substrate. Image adapted from ref. (75) "[Principle and formation process of spontaneous spreading](#)" by [Jonghyeon Noh](#) is licenced under CC BY 4.0 Deed

An example of a DPP-DTT thin-film transferred to a substrate, via FFT, is depicted in Figure 28. The image highlights FFT as an advantageous method for producing large area uniform thin-

films with low volumes of polymer solution (20 μL). In comparison, obtaining an equivalent spin coated thin-film would require 100 μL of polymer solution, consuming five times more material.

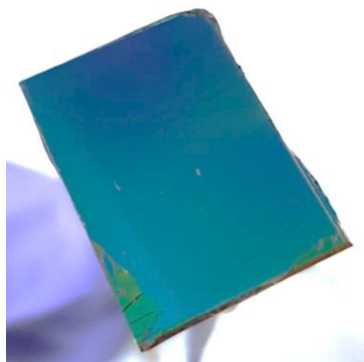


Figure 28 Camera image of a floating film transferred DPP-DTT thin-film on Si/SiO₂ substrate (1.5 x 2 cm).

The morphology of the thin-films were examined using AFM. Representative thin-film surface morphologies are depicted in Figure 29. Further AFM topographical images of thin-films prepared from 10, 5, 3 mg mL⁻¹ solutions are provided in the appendix Figure 100, Figure 103 and Figure 105, respectively (see appendix section 7.1.1).

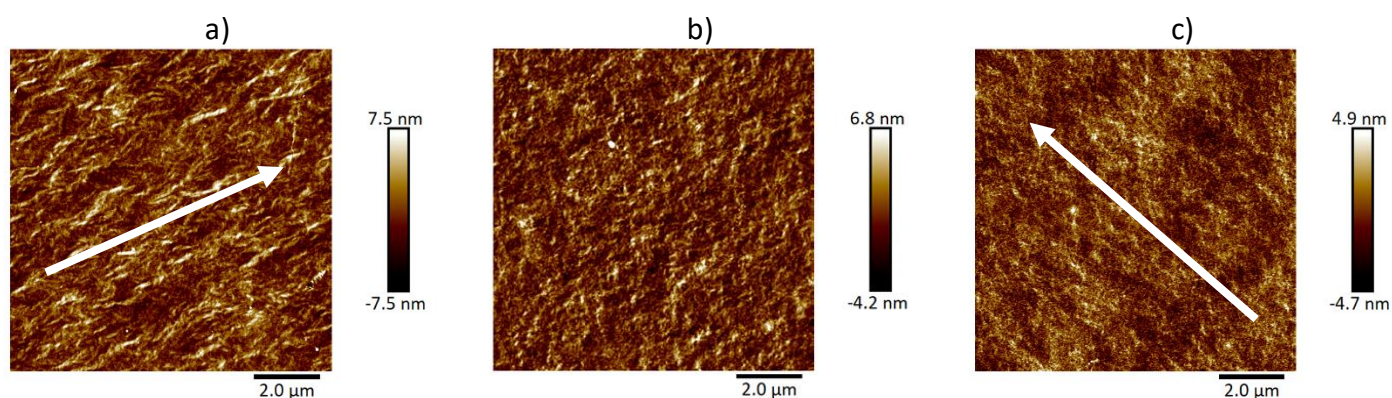


Figure 29 AFM topographical images (10 μm x 10 μm) of DPP-DTT thin-films via FFT from 9:1 CHCl₃:CB a) 10 mg mL⁻¹ b) 5 mg mL⁻¹ c) 3 mg mL⁻¹, on Si/SiO₂ substrates (polymer chain alignment indicated by white arrows).

The FFT DPP-DTT thin-films display large areas of homogeneity, a characteristic observed across the concentration series. The surface morphologies of the thin-films are free of prominent structures and other defects that could impede charge transport. Regions of

polymer chain alignment can be observed in the AFM images of the thin-films cast from 10 and 3 mg mL⁻¹ solutions, the direction of the alignment is highlighted by white arrows. However, polymer chain alignment was not ubiquitously observed across the thin-film, which was attributed to nonuniform solvent evaporation during thin-film drying.⁽¹⁰³⁾ Thin-film averaged roughness Ra and Rq values are presented in Figure 30, with observed Rq values consistent with previously reported values of thin-films deposited via FFT.⁽¹⁰³⁾ The concentration of the polymer solution did not significantly influence thin-film roughnesses.

A DPP-DTT thin-film spin coated from 9:1 CHCl₃:CB (10 mg mL⁻¹) was also prepared, AFM images and extracted Ra and Rq values are depicted in Figure 102 and Table 26 (see appendix section 7.1.1). Averaged Ra and Rq values for FFT thin-films are larger than spin coated thin-films (Ra 0.99, Rq 1.25). This is consistent with literature observations, where FFT thin-films are rougher relative to spin coated thin-films. The increase in roughness is correlated with the improved molecular ordering observed in FFT thin-films.⁽²⁰⁶⁾ A comparison of Ra and Rq values between FFT thin-films on Si/SiO₂ and ODTS modified Si/SiO₂ substrates shows small variations. However, this is assumed to be due to small changes in FFT reproducibility rather than influence from the substrate. ODTS modification of Si/SiO₂ substrates is detailed in the following section (see section 3.3.2).

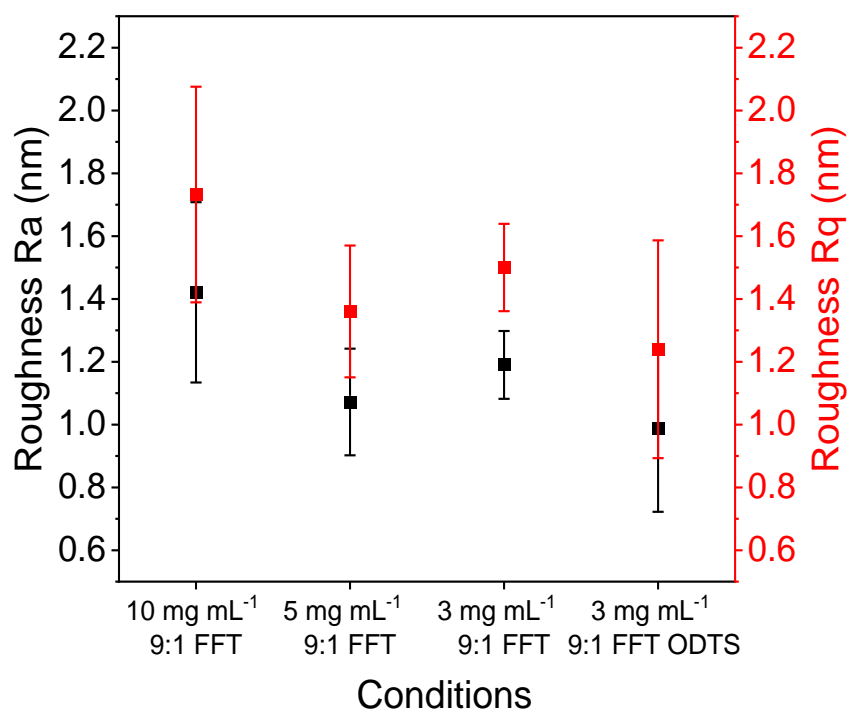


Figure 30 Roughness Ra and Rq values of DPP-DTT thin-films via FFT from 9:1 CHCl₃:CB (10, 5, 3 mg mL⁻¹) on Si/SiO₂ substrates and a DPP-DTT thin-film via FFT from 9:1 CHCl₃:CB (3 mg mL⁻¹) on ODTs modified substrate.

Thin-film thicknesses were measured using AFM, with AFM images and height profiles provided in appendix section 7.1.1. Thicknesses of the thin-film concentration series are presented in Figure 31. A trend of decreasing polymer solution concentration with decreasing thickness is observed. Thin-films cast from 10 and 5 mg mL⁻¹ solutions observed thickness considered too large for biosensing OFET devices, with 5 mg mL⁻¹ observing a large variation in thicknesses. The large standard deviation of the 5 mg mL⁻¹ thin-films may have resulted from inconsistencies when performing the FFT technique. Thin-films cast from 3 mg mL⁻¹ solution have small and uniform thicknesses of around 20 nm, which is considered optimal for biosensing OFET devices. A 3 mg mL⁻¹ FFT thin-film was prepared and transferred onto ODTs modified substrates, which gave rise to slightly thinner thin-films (~15 nm) relative to thin-films on Si/SiO₂ substrates (~20 nm).

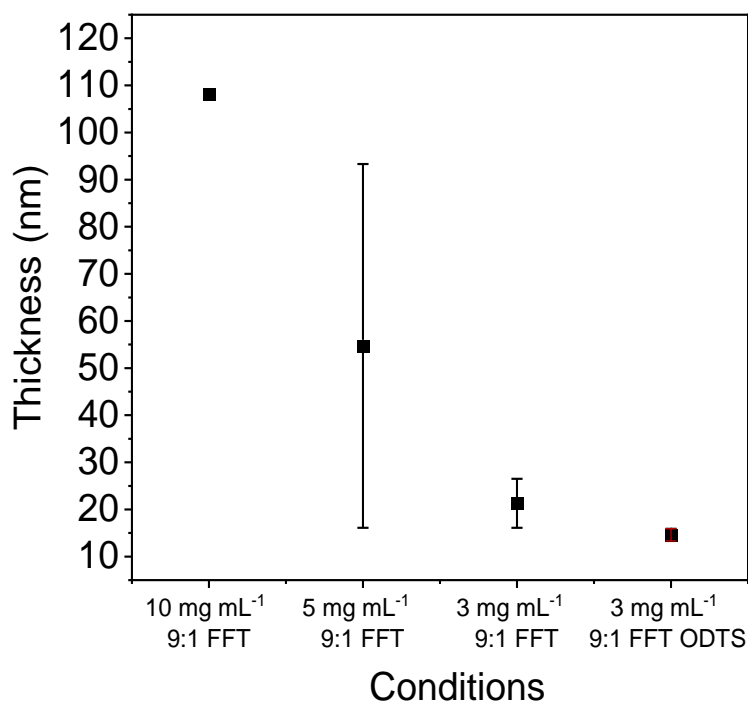


Figure 31 Thicknesses of DPP-DTT thin-films via FFT from 9:1 CHCl₃:CB (10, 5, 3 mg mL⁻¹) on Si/SiO₂ substrates and a DPP-DTT thin-film via FFT from 9:1 CHCl₃:CB (3 mg mL⁻¹) on ODTs modified substrate.

In summary, a technique referred to as floating film transfer (FFT), was utilised to produce thin-films with optimised morphological and thickness characteristics. The thin-films observed continuous homogeneous morphologies, with minimal structural defects. Regions of polymer chain alignment were also observed. Roughness values (Rq) in the range of 0.9 nm to 1.6 nm were consistent with values observed in the literature. The thicknesses of the thin-films were also controlled by changing the concentration of the polymer solution. 3 mg mL⁻¹ thin-films with thicknesses in the range of 15 nm were determined optimal and suitable for incorporation into OFET devices.

3.3.2 ODTS SAM treatment of Si/SiO₂ substrates

Heavily p-type doped silicon wafers with a 300 nm thermally grown silicon dioxide layer, were utilised as the gate electrode and dielectric layer, respectively. Si/SiO₂ in its pristine state can lead to undesirable OFET performance issues, relating to increased threshold voltages. The surface of the dielectric layer (SiO₂) introduces charge traps at the dielectric-semiconductor interface. Charge traps cause a shift in the threshold voltage of the device, as larger biases are required to fill the traps before the conducting channel can begin to form within the organic semiconducting polymer layer.(207) This issue is problematic for biosensing devices requiring low operating voltages.(208)

Modification of the SiO₂ surface was required for our system, to passivate potential charge traps interfacing with the organic semiconducting polymer layer. Treatment of the SiO₂ surface with self-assembled monolayers (SAMs) was explored as a method for improving the surface properties of the dielectric layer. Specifically, the molecule octadecyltrichlorosilane (ODTS) was employed, as it has been demonstrated as the most effective SAM on SiO₂ at enhancing OFET performances.(90) A modified methodology (see section 2.2.3) for ODTs functionalisation of Si/SiO₂ substrates was adapted from a procedure reported by Kang et al.(165) ODTs modification of silicon dioxide dielectric surface is illustrated in Figure 32.

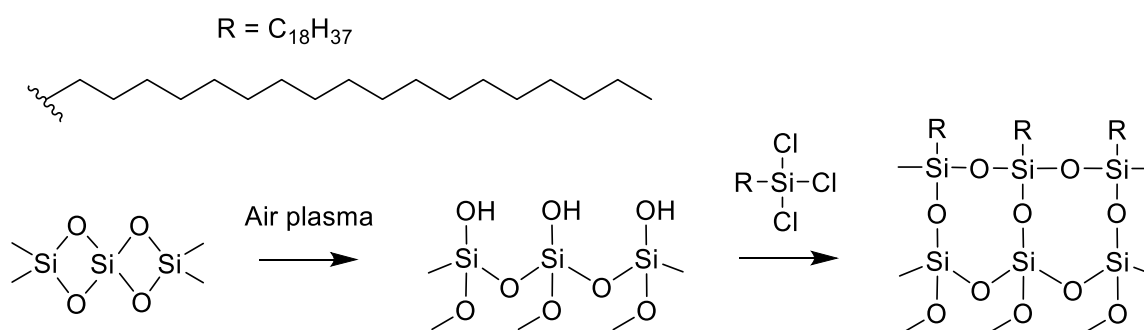


Figure 32 Self-assembly reaction of octadecyltrichlorosilane with silicon dioxide dielectric surface.

Characterisation of the ODTs modified substrates was performed using a combination of water contact angle (WCA) analysis and AFM imaging. Details on WCA measurements are presented in section 2.3.7. WCA measurements were performed on ODTs modified Si/SiO₂

substrates to verify the introduction of the SAM and assess the uniformity of SAM coverage. ODTs modification introduces alkyl chains onto the dielectric layer surface, consequently increasing the hydrophobicity and the water contact angle of the surface.(207) SAM coverage can also be verified by the WCA, with values below expected ranges suggestive of incomplete coverage. Representative WCA images of the pre- and post-modified ODTs Si/SiO₂ substrates, are depicted in Figure 33. A difference in the WCAs between the pre- and post-modified ODTs Si/SiO₂ substrates is observed. Additional WCA images are presented in Figure 109, alongside tabulated WCA values presented in Table 33 (see appendix section 7.1.2).

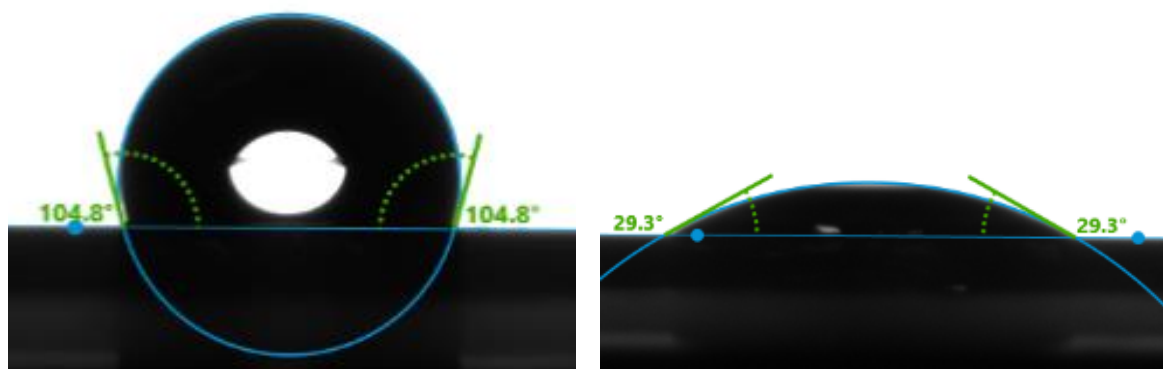


Figure 33 Water contact angle images of (left) ODTs modified Si/SiO₂ substrate (104.8°) and (right) Si/SiO₂ substrate (29.3°).

The WCA of the dielectric surface increases from 29.3° to an average of 104.8° ± 0.46°, after ODTs modification. The obtained WCA values are consistent with reported values of ODTs treated surfaces observing high surface coverages.(91)

Characterisation of the SAM surface morphology of the pre- and post-modified ODTs Si/SiO₂ surfaces was performed using AFM. Representative AFM images of the surfaces are depicted in Figure 34. Additional AFM images of pre- and post-modified ODTs Si/SiO₂ surfaces are provided in Figure 111 and Figure 112, with tabulated roughness values Ra and Rq shown in Table 34 and Table 35 (see appendix section 7.1.2). Extracted roughness values Ra and Rq are presented in Figure 35.

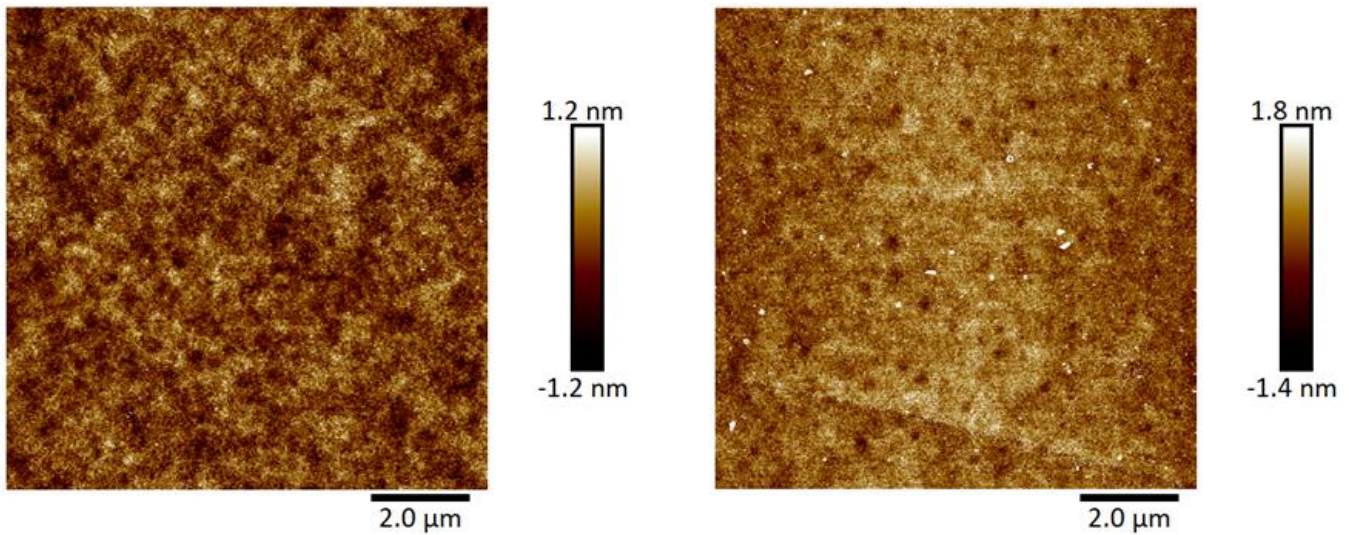


Figure 34 AFM topographical images (10 μm x 10 μm) of (left) ODTS modified Si/SiO₂ substrate and (right) Si/SiO₂ substrate.

The AFM images of the ODTS modified substrate observe homogeneous morphologies, free of large particles or defects. A change in the AFM roughness values, between the pre- and post-modified surfaces is observed, indicating a change in the surface morphology. Further confirming the successful modification of the dielectric layer surface. A decrease in average Ra and Rq values for the ODTS modified surface, relative to the pre-modified surface, is observed. The roughness values of the ODTS modified surfaces, are consistent with reported ranges (0.34 nm to 1.50 nm).^(91, 209, 210)

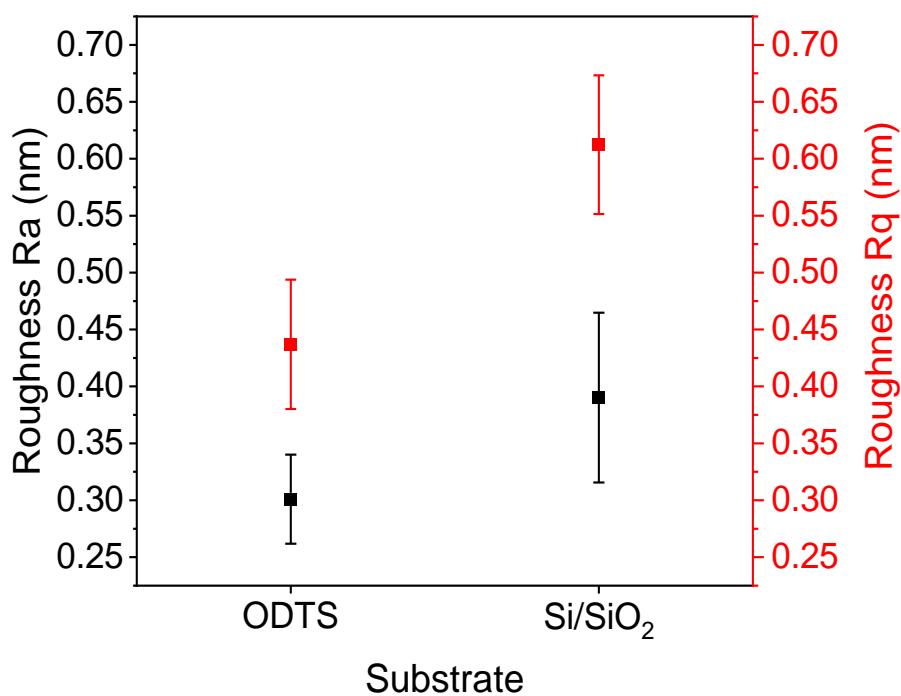


Figure 35 AFM roughness Ra and Rq values of ODTs modified Si/SiO₂ surface and pre-modified Si/SiO₂ surface.

In summary, an optimised methodology for modifying the dielectric surface of Si/SiO₂ substrates with a self-assembled monolayer of ODTs has been developed. The quality of the ODTs SAM was verified by WCA and AFM measurements, indicating that a dense and homogeneous SAM had formed. Accordingly, a high degree of potential charge trapping sites on the SiO₂ surface are passivated by the SAM. The modified dielectric layer and gate electrode substrates are now suitable for low-voltage OFET investigations.

3.3.3 Contact electrode deposition

Fabrication of the OFET source/drain (S/D) electrodes was performed using a combination of physical vapour deposition and shadow masking. Physical vapour deposition methodology is described in section 2.3.5. Dimensional properties of the deposition mask are detailed in Figure 15 and Table 4 in section 2.1.3. Gold was utilised as the S/D electrode contact material due to the work function (~ 5.2 eV) closely aligning with the HOMO (~ 5.2 eV) of DPP-DTT ensuring efficient charge injection.^(44, 98) Additionally, gold observes improved interfacial properties with the semiconducting material.⁽⁹⁸⁾ Before S/D contacts were evaporated, a DPP-DTT thin-film via FFT from 9:1 CHCl_3 :CB (3 mg mL^{-1}) on ODTS modified substrate was prepared using FFT (see section 2.2.4.1) and ODTS (see section 2.2.3) methods. 50 nm gold contacts were evaporated on top of the DPP-DTT thin-film, as this configuration (bottom-gate top-contact) exhibits lower contact resistances relative to bottom-gate bottom-contact.⁽¹⁰²⁾ A representative AFM image of gold deposited onto the DPP-DTT thin-film is presented in Figure 36, additional images and tabulated data are presented in Figure 113 and Table 36, respectively (see appendix section 7.1.3). An average thickness of $49.8 \text{ nm} \pm 1.54 \text{ nm}$ was determined for the deposited gold layer, consistent with the expected value.

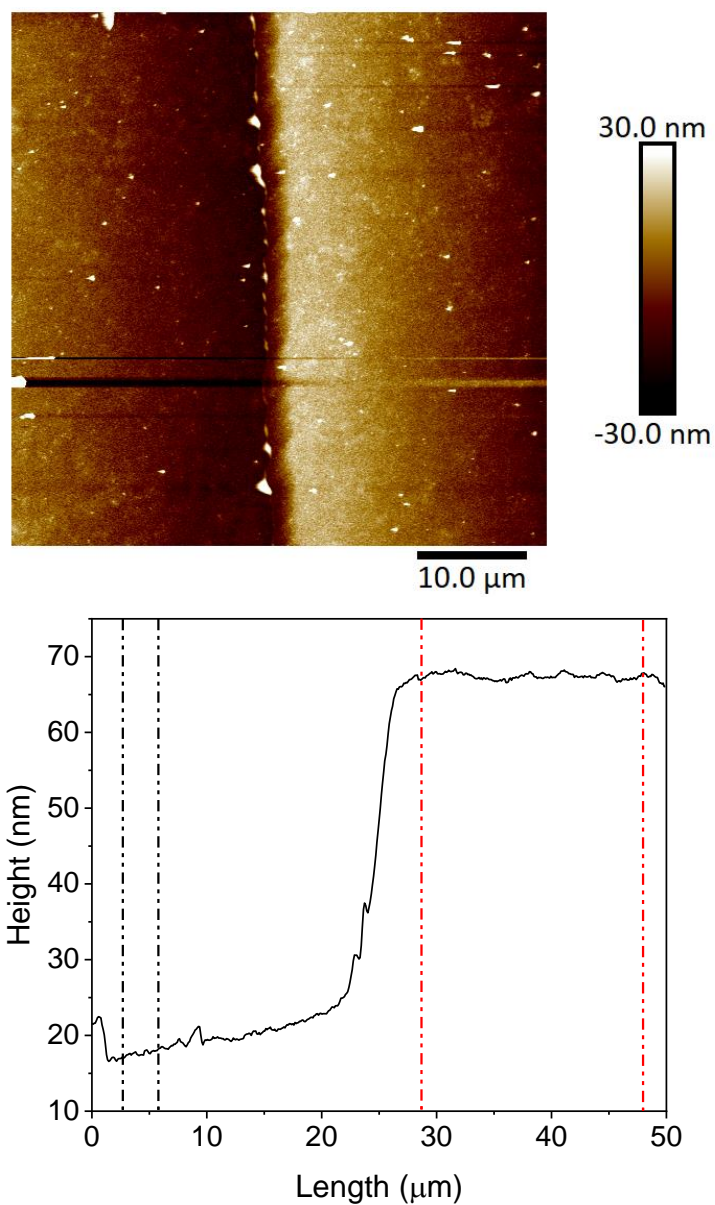


Figure 36 AFM topographical image (50 μm x 50 μm) (top) and height profile (bottom) of physical vapour deposited gold (50 nm) S/D electrode on DPP-DTT thin-film via FFT from 9:1 CHCl₃:CB (3 mg mL⁻¹) on ODTS modified substrate.

3.3.4 OFET electrical characterisation

The optimised methodologies outlined in the previous sections were utilised to fabricate an organic field-effect transistor (OFET). The subsequent transistor was characterised to determine OFET performance metrics using the methodology outlined in section 2.3.4. Transfer curves measured in linear and saturation regimes are presented in Figure 37 a) and b), respectively. Output curves are presented in Figure 37 c). Transfer characteristics were extracted and used to calculate OFET performance figures of merit, depicted in Table 13.

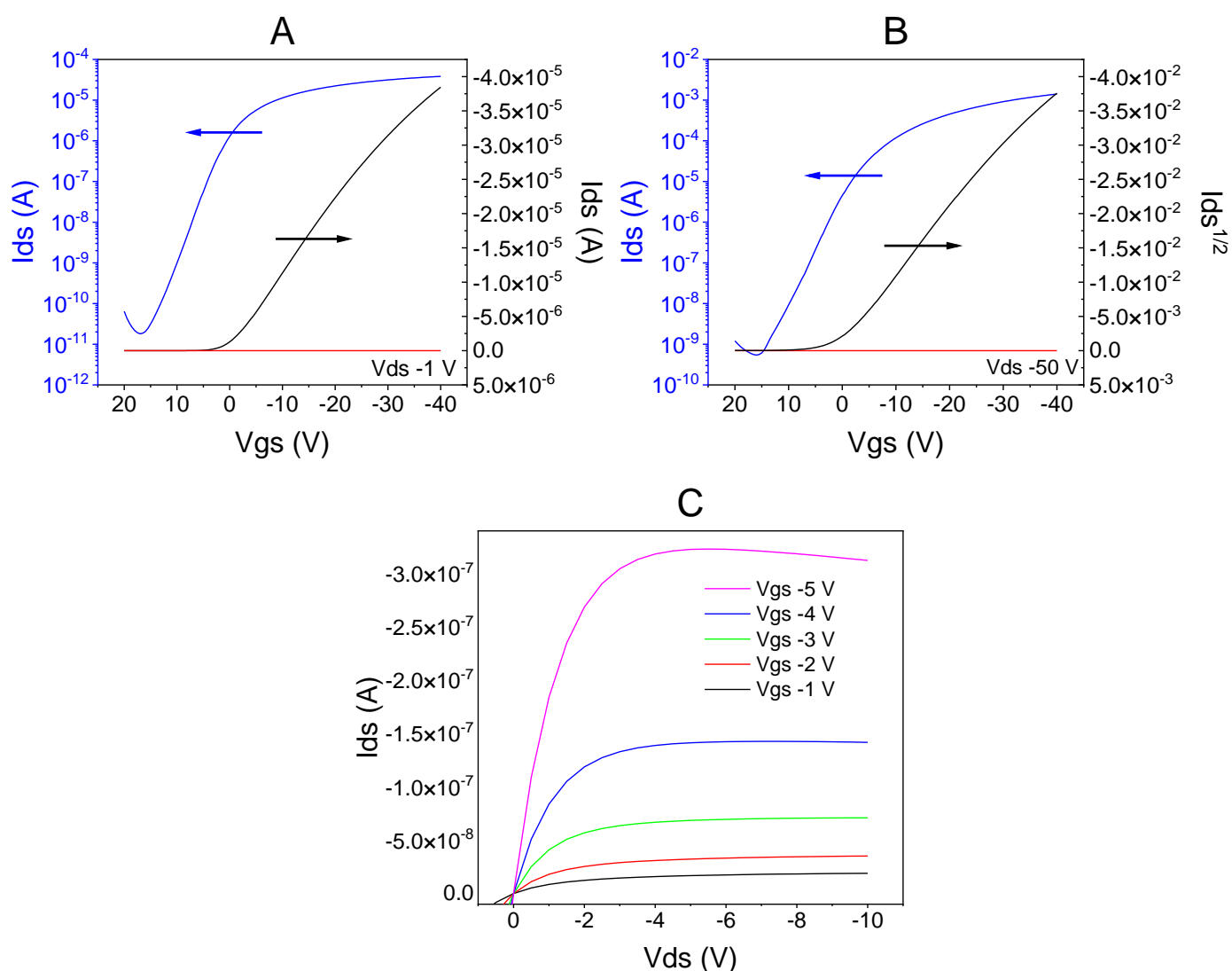


Figure 37 Transfer and output characteristics of bottom-gate top-contact configuration DPP-DTT OFET. Transfer characteristics in A) linear regime ($V_{ds} -1$ V) and B) saturation regime ($V_{ds} -50$ V), (blue) log scale (black) linear scale (red) gate current. C) Output characteristics. DPP-

DTT thin-film via FFT from 9:1 CHCl₃:CB (3 mg mL⁻¹) on ODTS modified Si/SiO₂, with 50 nm gold deposited interdigitated S/D electrodes (50 μm channel length).

Figure of merit	Linear regime	Saturation regime
μ (cm ² V ⁻¹ s ⁻¹)	0.268	0.516
V _{th} (V)	0.06	0.53
On/Off	2.1x10 ⁶	2.6x10 ⁶

Table 13 Transfer characteristic figures of merit from linear and saturation regimes.

The OFET exhibits clear p-type behaviour in the transfer and output characteristics. The OFET obtained a linear regime mobility (μ_{lin}) of 0.268 cm² V⁻¹ s⁻¹ and a saturation regime mobility (μ_{sat}) of 0.516 cm² V⁻¹ s⁻¹. The saturated mobility value is in good agreement with those of reported literature devices, also fabricated in ambient conditions.(103, 211) A difference between μ_{lin} and μ_{sat} is observed. Both values are within the same magnitude, but the μ_{lin} is almost half of the μ_{sat} .

The observed difference in calculated mobility values can be explained by contact effects. In an ideal system, where contacts observe ohmic behaviour, μ_{lin} and μ_{sat} would be equivalent. However, in non-ideal systems a resistance between the contacts and the material exists. Linear and saturation regimes experience the effect of contact resistance differently, resulting in differing μ_{lin} and μ_{sat} values.(212) Low threshold voltages in the linear and saturation regimes were demonstrated by the OFET. Additionally, high on/off ratios $\sim 2 \times 10^6$ and low gate currents (I_{gs}) $\sim x 10^{-10}$ A were obtained. Output curves observe linear and saturation regions at V_{gs} biases of -1 to -5 V, with linear curves intersecting at V_{ds} 0 V, indicating low contact resistance.(83)

In summary, a methodology for fabricating OFETs observing performances suitable for potential low-voltage biosensing device applications has been developed. OFETs were fabricated in ambient conditions, composed of a DPP-DTT 3 mg mL⁻¹ thin-film deposited by floating film transfer method, an ODTS modified Si/SiO₂ substrate and 50 nm gold interdigitated source-drain electrodes. Optimisation of the OFET components proved advantageous, resulting in acceptable OFET mobility values, low threshold voltage values and high on/off ratio. The fabrication methodology produces OFETs as suitable initial platforms

for further investigating covalent strategies for the functionalisation of DPP-DTT thin-films with aptamers.

3.4 Introducing exploitable chemical functionalities via O₂ and N₂ plasma treatment

In the following sections O₂ and N₂ plasma treatment are individually utilised to introduce new chemical functionalities onto the surface of DPP-DTT polymer thin-films. Chemical functionalities introduced from O₂ and N₂ plasma exposure are depicted in Figure 38. The introduction of chemically exploitable functionalities, such as carboxylic acid and primary amine groups, assists multiple potential pathways for the covalent attachment of aptamers under physiological conditions.(134, 213, 214)

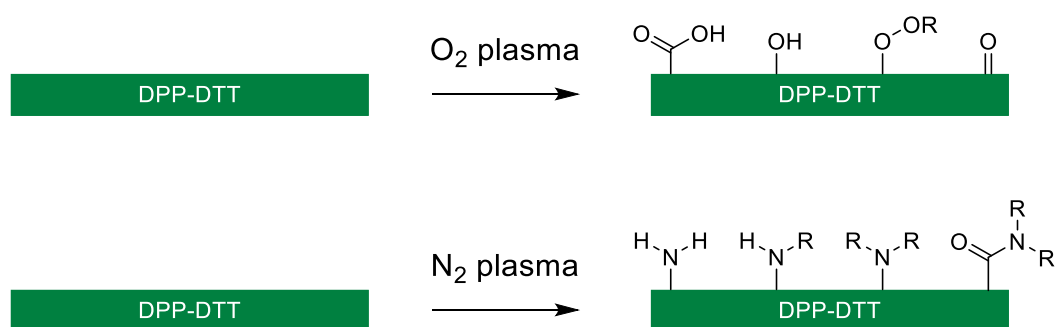


Figure 38 Introduction of chemical functionalities on DPP-DTT thin-film surfaces via (top) O₂ or (bottom) N₂ plasma treatment.

Variations in plasma conditions favouring either etching or chemical modification of the polymer thin-film need to be considered. Particularly as the chemical composition of the polymer material can influence either preference. With plasma etching favouring polymers containing oxygen functionalities along the backbone, whereas chemical modification favours aromaticity within the backbone.(195) Since the backbone of DPP-DTT contains both oxygen containing functionalities and aromaticity, predicting the influence of the plasma on thin-film properties is complicated. Nevertheless, minimising plasma etching whilst maximising plasma induced chemical modification is prioritised. A balance point between the two factors needs to be established, by controlling plasma conditions such as power and exposure time. In order to isolate this balance point a variation of plasma conditions will be investigated.

Additionally, the specificity of plasma treatment is another factor to consider. Plasma treatment does not introduce a single type of chemical functionality to a surface.(191)

Instead, it introduces a range of different functionalities, with some formed during plasma treatment and others as a result of post-plasma-induced aging processes. However, resulting plasma conditions can influence the selectivity of the introduced functionalities, which will be considered.

The influence of O₂ and N₂ plasma treatment on the properties of DPP-DTT OFETs is investigated. To identify optimised plasma treatment conditions, properties relating to thin-film morphology, surface chemistry and OFET performance will be monitored. Further, a method of attaching aptamers to plasma exposed thin-films is demonstrated.

3.4.1 The effects of O₂ plasma treatment on thin-film morphologies

The effect of O₂ plasma treatment on the thin-film morphology of DPP-DTT OFETs was investigated. Morphological attributes relating to thin-film thickness and roughness were monitored with AFM (see section 2.3.1). OFET devices were prepared using the fabrication methodology outlined in section 3.3. O₂ plasma treatment was conducted using the methodology detailed in section 2.3.6. A series of O₂ plasma treatment conditions were investigated, details for which are presented in Table 14.

Power (W)	Time (s)
6	90
12	60
24	30

Table 14 O₂ plasma exposure series conditions.

DPP-DTT thin-film thicknesses before and after O₂ plasma treatment are presented in Figure 39. Tabulated data is provided in Table 37 and Table 38 (see appendix section 7.1.4). A decrease in average thin-film thickness across the series was observed, as plasma exposure is an etching process this can be expected to a degree.⁽¹⁹⁰⁾ The degree of etching under relatively milder plasma conditions was more significant than what was observed by Shen et al.⁽¹³⁴⁾ A difference can be expected, due to intrinsic reproducibility problems between plasma generator chambers. Chamber conditioning, chamber dimensions and sample position relative to the plasma influence resulting outcomes.⁽⁷²⁾ The thickness of the thin-film exposed to 12 W, 60 s plasma experienced the lowest amount of surface etching, retaining 95 % of its original thickness. A balance point between power and time, on minimising thin-film etching rate was established. Conditions at 12 W, 60 s approach this balance point, suggesting that the integrity of the underlying DPP-DTT polymer chains are retained. Further preserving charge transport and resulting OFET performance.⁽¹³⁴⁾

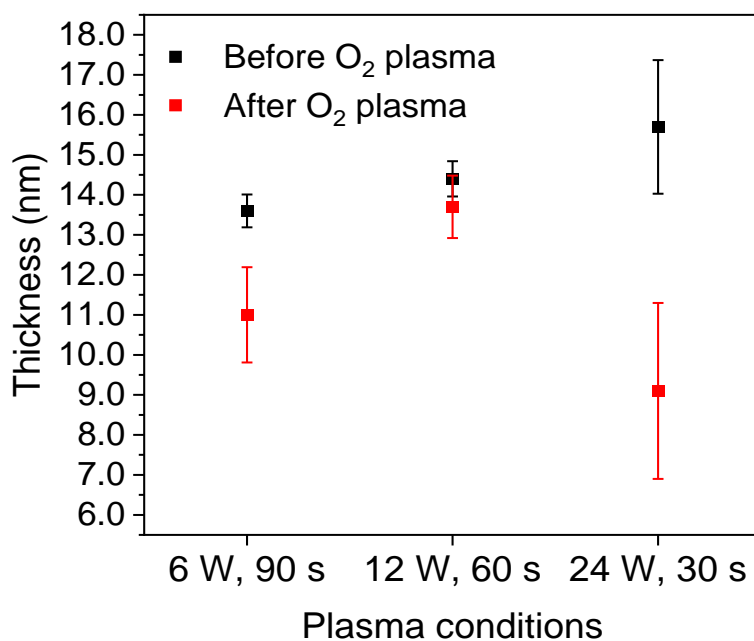


Figure 39 AFM thicknesses of DPP-DTT thin-films before and after O₂ plasma treatment. Error bars represent the standard deviation between these values.

DPP-DTT thin-film roughnesses (R_q and R_a) before and after O₂ plasma treatment are presented in Figure 40. Tabulated data is provided in Table 39 (see appendix section 7.1.4). A change in the surface morphology is observed, indicated by a change in the average thin-film roughnesses. A decrease in average thin-film roughness was observed across the series upon plasma treatment, with similar roughnesses observed across the series. However, this observation is less significant for thin-films with overlapping standard deviations. The decrease in roughness was considered anomalous, as an increase in surface roughness was expected after plasma exposure.⁽¹⁹¹⁾ The unexpected observation could be explained when considering the morphology of the thin-film deposited via floating film transfer (FFT) method.

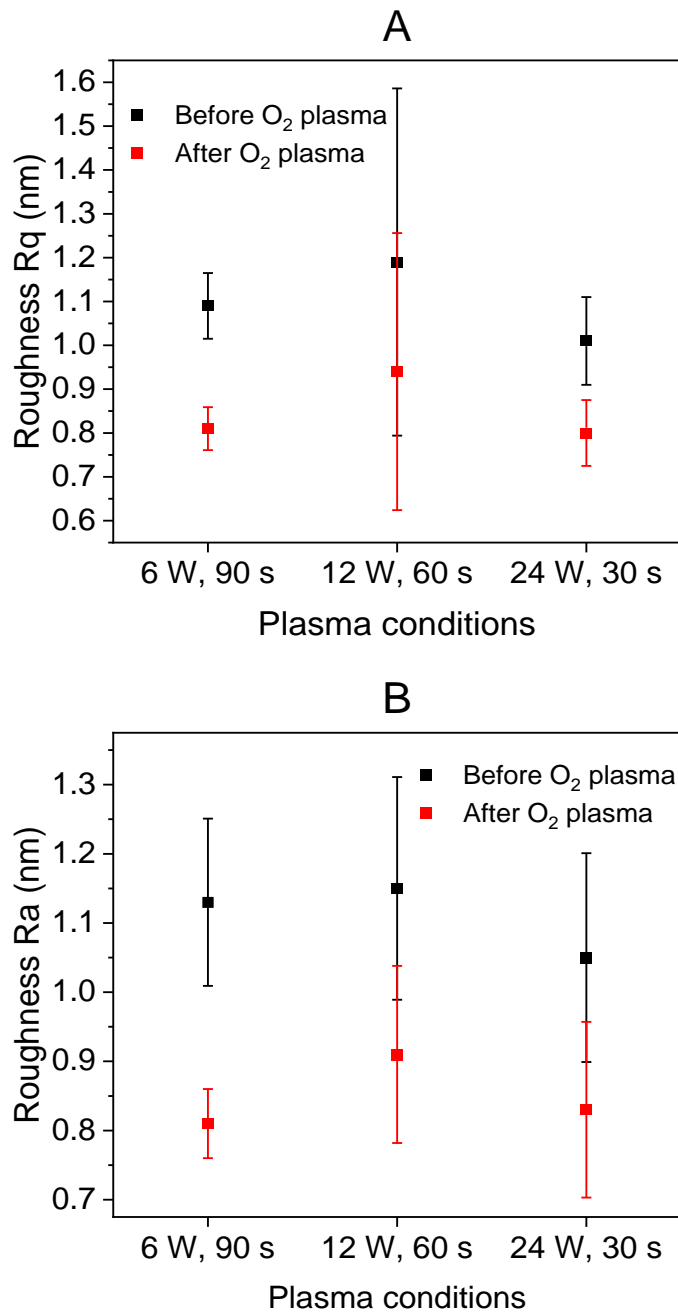


Figure 40 AFM roughness values (A) Rq and (B) Ra of DPP-DTT thin-films before and after O₂ plasma treatment.

The FFT method produces thin-films with differing morphologies at the two deposition interfaces, i.e. the atmosphere and liquid substrate interfaces. The formation process of the two differing morphologies is illustrated in Figure 41. The surface roughness of the thin-film interfacing with the liquid substrate is typically rougher than the surface interfacing with the

atmosphere.(46) The smoother thin-film surface interfacing with the atmosphere is transferred onto the substrate surface, now forming part of the dielectric-semiconductor interface. Plasma treatment occurs at the rougher thin-film surface that interfaced with the liquid substrate. Etching of the thin-film surface exposes the smoother thin-film bulk, resulting in lower roughness values of plasma exposed thin-films.

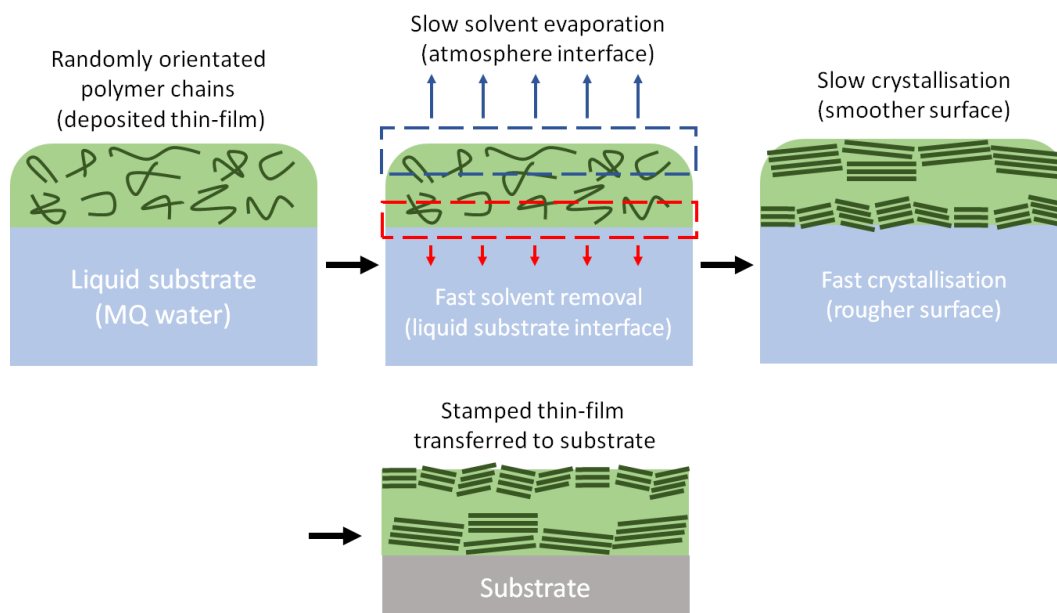


Figure 41 Formation processes of differing interface morphologies for a DPP-DTT thin-film deposited via FFT. Image adapted with permission from {G. Choi, K. Lee, S. Oh, J. Seo, C. Kim, T. K. An, J. Lee, H. S. Lee, Understanding Marangoni flow-driven solidification of polymer semiconducting films on an aqueous substrate. J. Mater. Chem. C. 8, 10010–10020 (2020)}. Copyright {2024} Royal Society of Chemistry.(211)

3.4.2 The effects of O₂ plasma treatment on OFET performance

Following the thin-film morphological characterisation of O₂ plasma treated DPP-DTT OFETs, the effects on OFET performance was investigated. OFET characterisation was conducted using the procedure described in section 2.3.4. Transfer characteristics of OFETs before and after O₂ plasma treatment are presented in Figure 114 and Figure 117 (see appendix section 7.1.5). O₂ plasma treatment conditions are presented in Table 14 (see section 3.4.1). Three source-drain electrode pairs were measured per OFET, and the calculated OFET performance metrics were averaged. Averaged OFET mobilities (μ) and threshold voltages (V_{th}) before and after O₂ plasma, are presented in Figure 42. Tabulated data is provided in Table 40 (see appendix section 7.1.5).

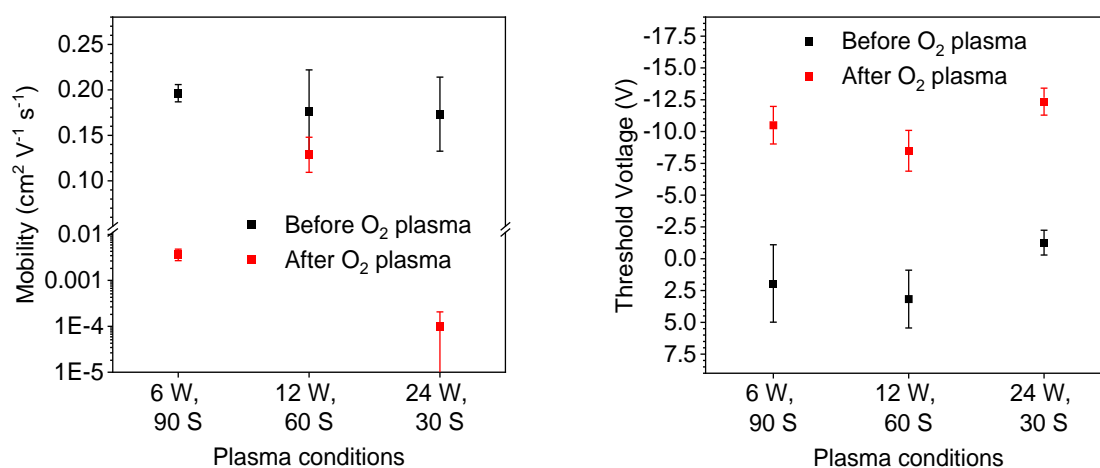


Figure 42 OFET performance (left) mobilities and (right) threshold voltages before and after O₂ plasma treatment. Drain voltage biased at -1 V.

A decrease in μ and an equivalent negative shift (\sim -12 V) in V_{th} was observed across the series. Decreasing μ was ascribed to etching of the conductive channel.⁽¹³⁴⁾ The OFET exposed to 12 W, 60 s plasma retained the highest initial μ (73 %). Which is attributed to the thin-film mostly retaining its initial thickness and therefore observing less etching of the conducting channel (see section 3.4.1). Shifting of the V_{th} indicates a change in the contact resistance at the polymer/contact interface, as well as the introduction of charge traps in the polymer.⁽²⁰⁰⁾ Since the contacts isolate the polymer/contact interface, the latter is considered more plausible. The equal shift in V_{th} and unequal change in μ suggests the

generated traps are likely deep charge traps.(200, 215) Considering the thin-films were exposed to plasma, the introduction of charge traps to the polymer thin-film could occur in several ways. However, the potential source wasn't investigated further. Ionisation of the surface and the resulting newly introduced chemical species have been observed to act as local defects, which introduce charge traps.(215) Oxygen diffusion into the thin-film has been observed inducing gap states within the thin-film morphology, which introduce charge traps.(216, 217) Plasma treatment also increases the hydrophilicity of the thin-film, which can facilitate the diffusion of water into the thin-film, acting as charge traps. Finally, surface rearrangement of the plasma exposed polymer thin-film is to be expected. A mechanism for charge trap generation can be explained as follows; plasma induces surface rearrangement in polymers facilitating the formation of structural inhomogeneities, which in turn form intrinsic traps.(190, 192, 200)

The OFET exposed to 12 W, 60 s O₂ plasma retained the highest amount of its initial performance. However, the large shift in V_{th} observed in O₂ plasma exposed OFETs makes them less suitable for low-voltage I_{ds} vs. time sensing investigations. Instead, the resulting OFETs could be applied to alternative sensing experiments using higher voltage biases, such as transfer characteristic based sensing.(107)

3.4.3 The introduction of exploitable chemical functionalities on O₂ plasma treated thin-films

Following the OFET characterisation of O₂ plasma treated DPP-DTT OFETs, the effects on thin-film surface chemistry was investigated. O₂ plasma treatment conditions are presented in Table 14 (see section 3.4.1). X-ray photoelectron spectroscopy (XPS) was conducted and resulting spectra processed using methodology detailed in section 2.3.2. XPS was used to quantify the introduction of oxygen containing species on the surface of O₂ plasma exposed thin-films. High resolution O1s scans of O₂ plasma treated thin-films were run to identify changes in thin-film surface oxygen content. Peak areas of fitted and SiO₂ adjusted O1s spectra are depicted in Figure 43. SiO₂ will contribute to the total oxygen content. Data for which is presented in Table 42 (see appendix 7.1.6).

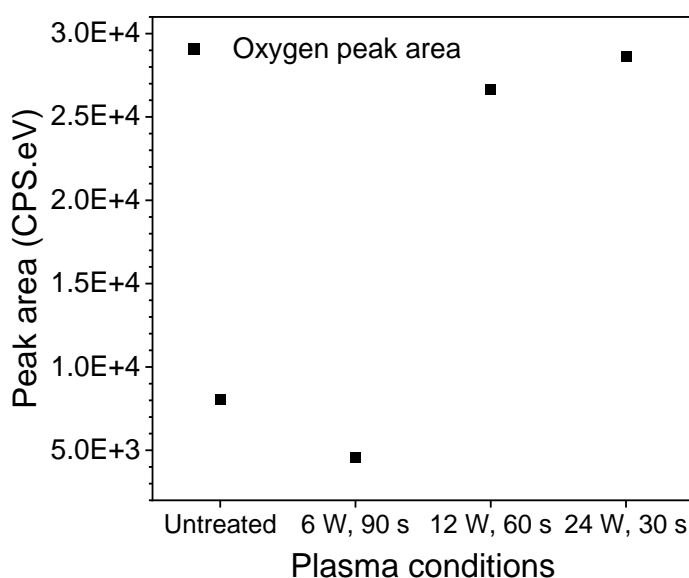


Figure 43 Oxygen peak areas of untreated and O₂ plasma treated DPP-DTT OFETs. Peak areas adjusted for SiO₂ contribution.

Compared to the untreated reference sample, an increase in oxygen content was observed for thin-films exposed to 12 W plasma for 60 s and 24 W for 30 s, suggesting that more oxygen containing species were introduced to the surface. A decrease in oxygen content is observed for 6 W, 90 s plasma exposed thin-film, suggesting these conditions favour thin-film etching

rather than chemical modification. An interesting trend is observed, however more data points are required to further validate this.

C1s high resolution scans were run to further identify the oxygen containing chemical groups covalently bonded to carbon. C1s high resolution scan spectra of the untreated and N₂ plasma treated thin-films are presented in Figure 44. Tabulated peak fittings for C1s spectra and elemental spectra are presented in Table 41 and Table 42, respectively (see appendix section 7.1.6). Within the C1s high resolution spectra of O₂ plasma exposed thin-films, an extension of the shoulder on the main peak is noticed. The shoulder extends to higher binding energies, which is consistent with plasma-induced surface oxidation.(134)

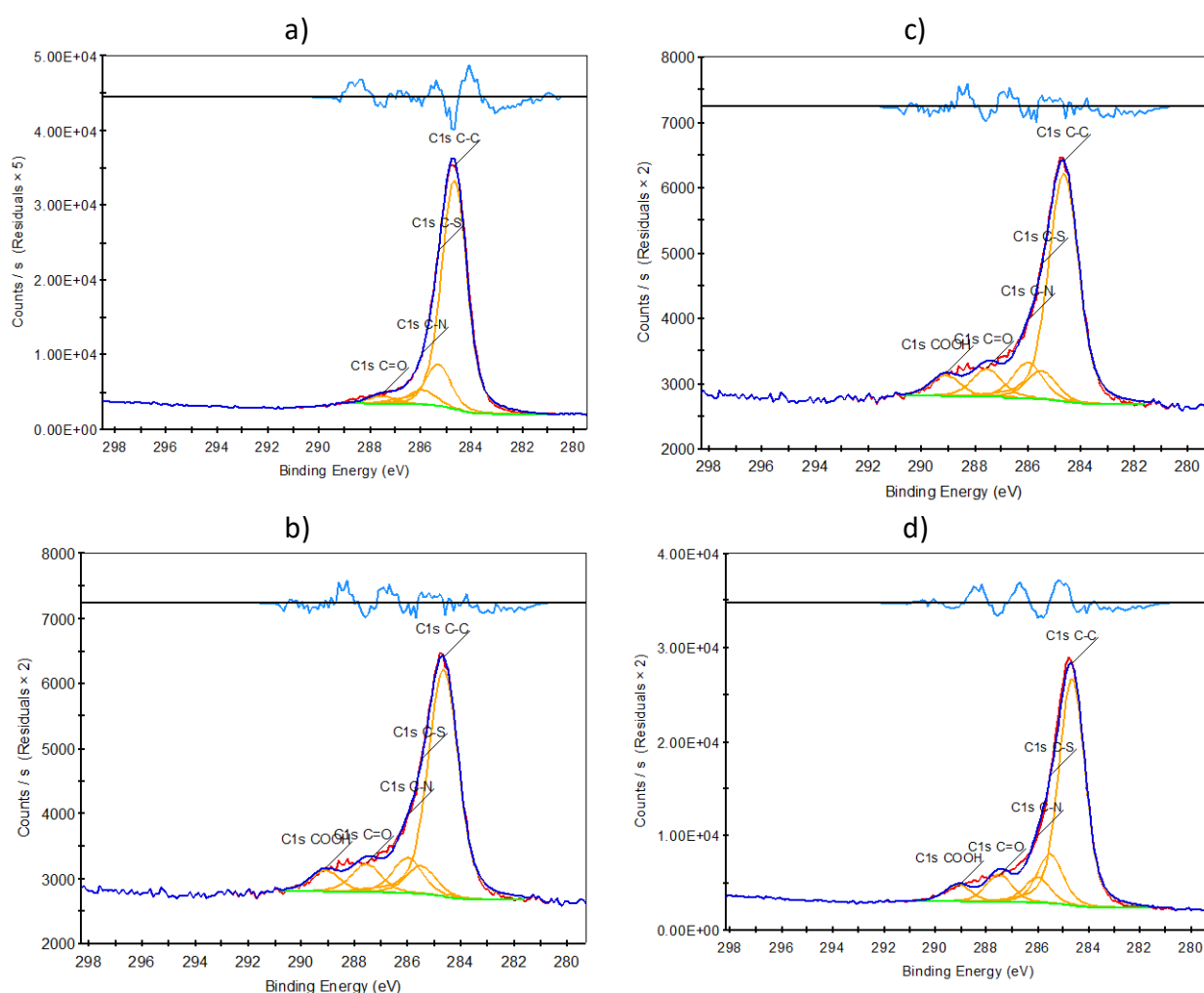


Figure 44 XPS C1s high resolution scans of O₂ plasma treated DPP-DTT OFETs a) untreated b) 6 W, 90 s c) 12 W, 60 s d) 24 W, 30 s.

A new component (~ 289.3 eV) within this shoulder is introduced to the plasma exposed C1s spectra, assigned to carboxylic acid groups. The number of carboxylic acid groups was extracted from the component peak area, given in counts per second per electron volt (CPS.eV), where the area of the peak is proportional to number of atoms per unit volume. Carboxylic acid component peak area is presented in Figure 45. The thin-film exposed to 12 W, 60 s O_2 plasma observed the highest quantity of carboxylic acid groups (~ 2862). Equating to 4 carboxylic acid groups per $10 \mu m^2$, when factoring the scan area (scan area = $7,855 \mu m^2$, calculated through $3.142 \times r^2$, where $r = 50 \mu m$), calculated through size radius ($r = 50 \mu m$, $3.142 \times r^2 = 7,855 \mu m^2$) and assuming a negligible XPS probing depth. The density of exploitable receptor attachment sites (carboxylic acid groups) was considered relatively low, when compared to the densities obtained through alternative OFET receptor functionalisation strategies. One approach utilising an array of 40 nm spaced gold nanoparticles, for attaching thiol terminated receptors, observed binding site densities of 250,000 per $10 \mu m^2$.(133)

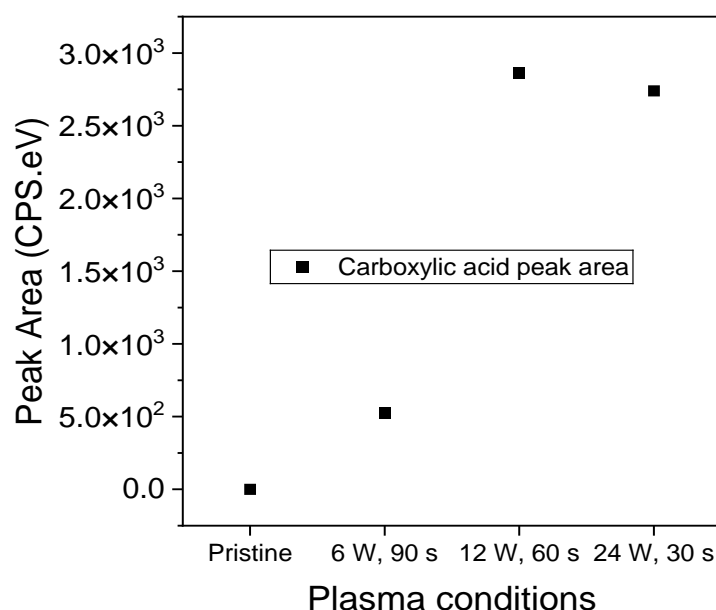


Figure 45 Carboxyl group component peak areas of untreated and O_2 plasma treated DPP-DTT OFETs.

The low amount of carboxyl groups on the thin-film surface may be due to inadequate O_2 plasma treatment conditions or through plasma-induced surface restructuring effects.

Surface restructuring occurs in response to changes in enthalpy and entropy. The plasma exposed surface experiences energy differences at the air interface and entropy differences with the thin-film bulk.⁽¹⁹²⁾ Surface restructuring stabilises these differences, which can drive newly introduced chemical functionalities away from the surface and in towards the bulk of the thin-film. This leads to a decrease in the density of functional groups on the surface, which can be substantial for plasma treated surfaces.⁽¹⁹²⁾ The comparable number of carboxylic acid groups observed between 12 W for 60 s and 24 W for 30 s suggests a saturation point is reached. This saturation point may indicate an equilibrium in surface restructuring between the number of carboxylic groups on the surface and those within the bulk. However, without the use of crosslinks between polymer chains, surface restructuring effects are unavoidable.

O₂ plasma exposure was successful at introducing carboxylic acid groups onto the thin-film surface. Further, strategies of functionalising O₂ plasma exposed surfaces with cortisol binding aptamers, via EDC/NHS crosslinking chemistries, were attempted. However, validating the success of these strategies could not be achieved, in either XPS or epifluorescence microscopy experiments. The low density of newly introduced carboxylic acid groups was deemed to be the limiting factor. Additional experimentation to increase the density of carboxylic acid groups was considered, but not attempted. Considering the already optimised methodology, minimal improvement to the carboxylic acid density was expected.

Overall, O₂ plasma exposure conditions 12 W, 60 s achieved an optimised balance between thin-film etching and chemical modification. This results in low thin-film etching as confirmed by AFM analysis, while retaining the highest OFET performance and observing the highest density of carboxylic acid groups according to XPS data. Ultimately, an alternative receptor functionalisation strategy similar to O₂ plasma treatment was explored, utilising N₂ plasma.

3.4.4 The effects of N₂ plasma treatment on thin-film morphologies

In order to overcome the limitations observed in O₂ plasma treated thin-films, N₂ plasma treatment was studied. The effects of N₂ plasma treatment on the thin-film morphology of DPP-DTT OFETs were investigated. Morphological attributes relating to thin-film thickness and roughness were monitored with AFM (see section 2.3.1). OFET devices were prepared using the fabrication methodology outlined in section 3.3. N₂ plasma treatment was conducted using the methodology detailed in section 2.3.6. Initially, a comparative series of N₂ plasma conditions similar to O₂, were investigated. Conditions for which are presented in Table 15.

Power (W)	Time (s)
6	90
12	60
24	30

Table 15 N₂ plasma exposure series conditions (DPP-DTT038)

DPP-DTT thin-film thicknesses before and after N₂ plasma treatment, are presented in Figure 46. Tabulated data is provided in Table 43 and Table 44 (see appendix section 7.1.7).

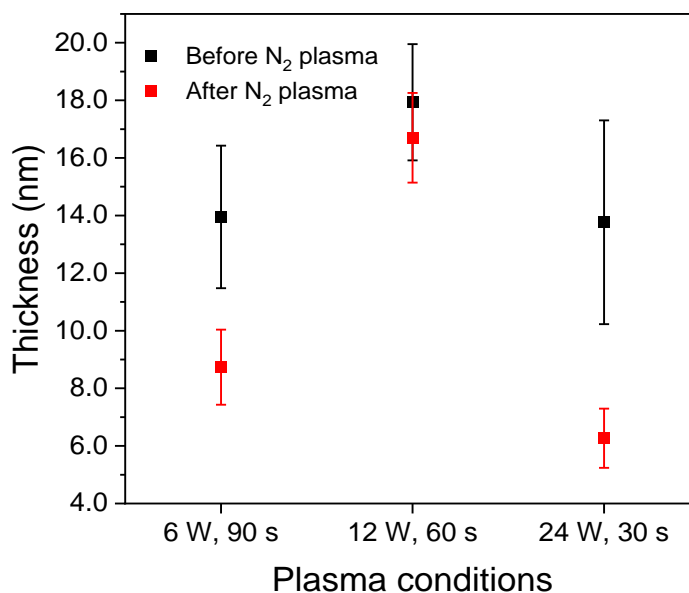


Figure 46 AFM thicknesses of DPP-DTT OFETs before and after N₂ plasma treatment.

A decrease in average thin-film thickness across the series is observed, which was similarly observed in O₂ plasma treated samples. However, N₂ plasma exposed thin-films observed a higher degree of etching, relative to O₂ plasma thin-films (Table 16). This suggests that N₂ plasma exposure is more intense than O₂ plasma under comparable conditions. Similar to what was found for O₂ plasma treatment, 12 W, 60 s plasma exposed thin-film observed the smallest amount of thin-film etching.

Plasma conditions	O ₂ plasma Δ thickness nm	N ₂ plasma Δ thickness nm
6 W, 90 s	2.6	5.3
12 W, 60 s	0.7	1.2
24 W, 30 s	5.6	7.5

Table 16 AFM monitored changes in thin-film thickness of O₂ and N₂ plasma treated OFETs.

DPP-DTT thin-film roughnesses (R_q and R_a) before and after N₂ plasma treatment are presented in Figure 47. Tabulated data is provided in Table 45 and Table 46 (see appendix section 7.1.7). A change in the surface morphology is observed, indicated by a change in the average thin-film roughnesses. The average roughness of N₂ plasma exposed thin-films expectedly increased, apart from 12 W, 60 s which observed a decrease.⁽¹⁹¹⁾ However, the observed differences were probably not significant when considering the large-overlapping standard deviations. Thin-film roughnesses were less affected by N₂ plasma exposure relative to O₂ plasma exposed thin-films.

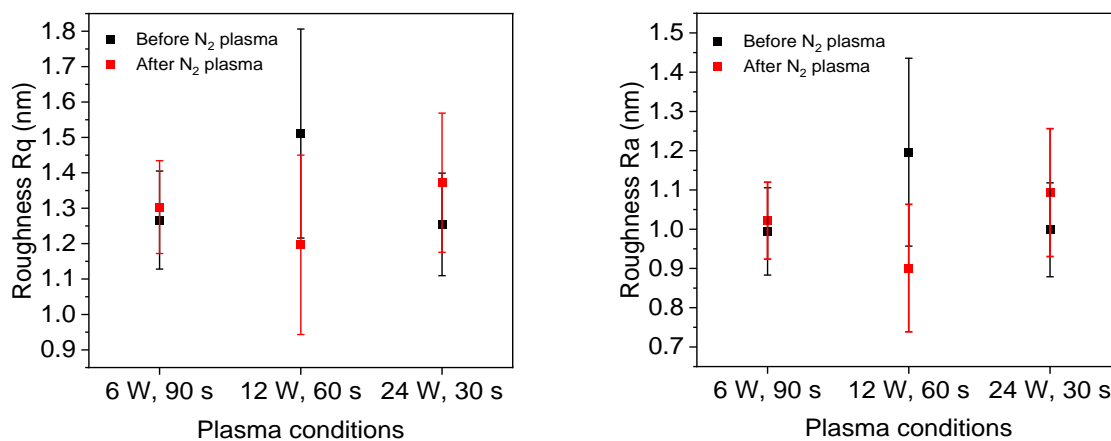


Figure 47 AFM average roughness values (left) R_q and (right) R_a of DPP-DTT thin-films before and after N₂ plasma treatment.

Given the increased etching rate of N₂ plasma, which could significantly diminish initial OFET performance, a series of 6 W and 12 W powers were further explored. Thin-films were exposed to a range of times at 6 W and 12 W. Series conditions are presented in Table 17.

Power (W)	Time (s)
6	30
	60
	90
12	30
	60
	90

Table 17 Additional N₂ plasma exposure series conditions.

DPP-DTT thin-film thicknesses before and after N₂ plasma are presented in Figure 48. Tabulated data is provided in Table 47 and Table 48 (see appendix section 7.1.7). Thin-films exposed to 6 W, 90 s, 12 W, 30 s and 12 W, 90 s plasma observed a significant decrease in average thickness. Thin-films exposed to 6 W, 30 s, 6 W, 60 s and 12 W 60 s observed no decrease in average thin-film thickness. Suggesting the integrity of the thin-films are retained more so under those conditions.

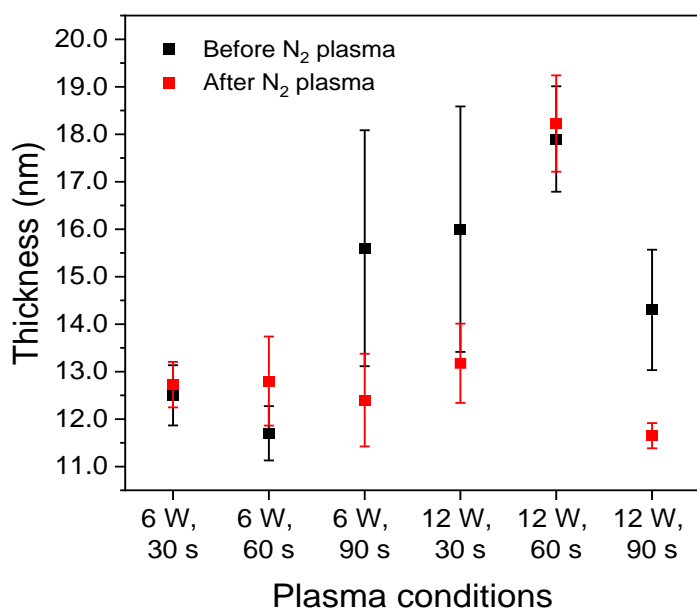


Figure 48 AFM thicknesses of DPP-DTT thin-films before and after N₂ plasma treatment.

DPP-DTT thin-film roughnesses (R_q and R_a) before and after N_2 plasma treatment are presented in Figure 49. Tabulated data is supplied in Table 49 and Table 50 (see appendix section 7.1.7).

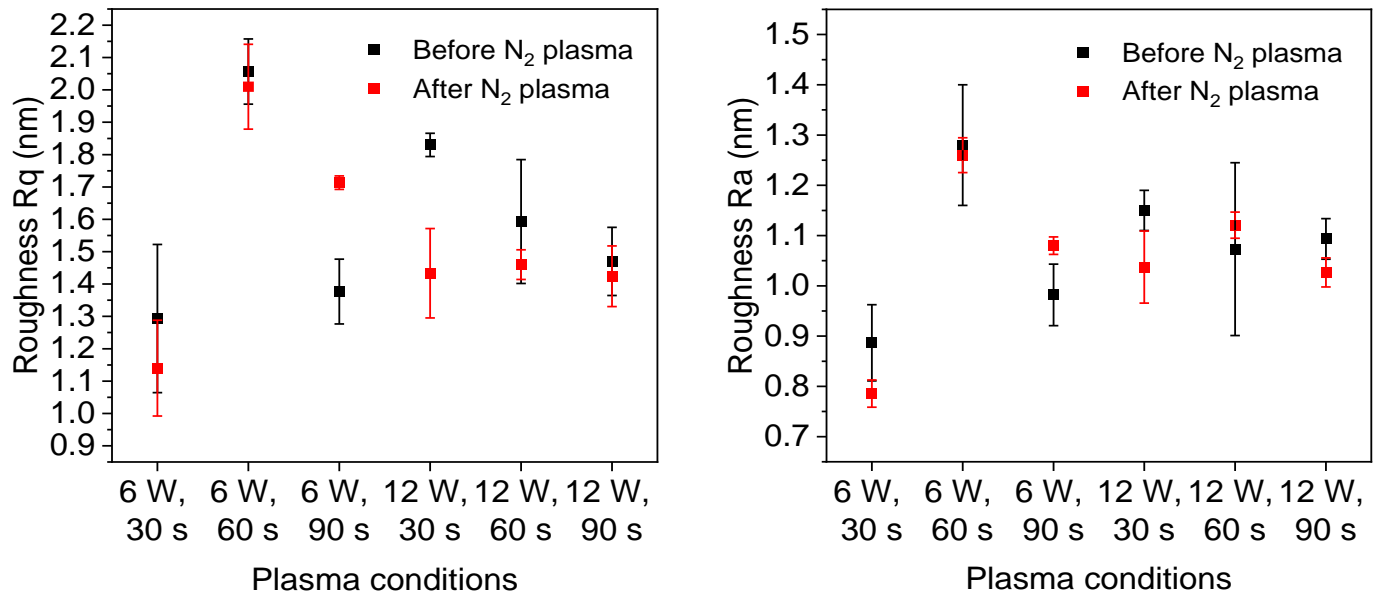


Figure 49 AFM average roughness values (left) R_q and (right) R_a of DPP-DTT thin-films before and after N_2 plasma treatment.

Overall, average thin-film roughness decreases after N_2 plasma treatment, although some exceptions to this trend are noted. The magnitude in change to roughness values showed little consistency and was independent of exposure time or power. Therefore, N_2 plasma introduces a high degree of variation in the resulting thin-film morphology.

3.4.5 The effects of N₂ plasma treatment on OFET performance

Following the thin-film morphological characterisation of N₂ plasma treated DPP-DTT OFETs, the effects on OFET performance were investigated. OFET characterisation was conducted using the procedure described in section 2.3.4. Transfer characteristics of OFETs before and after N₂ plasma treatment are presented in Figure 115 and Figure 117 (see appendix section 7.1.8). Output characteristics of OFETs before and after N₂ plasma treatment are presented in Figure 116 and Figure 118 (see appendix section 7.1.8). N₂ plasma treatment conditions are presented in Table 17 (see section 3.4.4).

OFET performance metrics V_{th} and μ , were extracted from the transfer characteristics of pre- and post-plasma exposed OFETs (Figure 50). Three source-drain electrode pairs were measured per OFET and the data averaged. Averaged V_{th} and μ values are presented in (before) Table 51 and Table 52 (after) Table 53 and Table 54 (see appendix section 7.1.8). Transfer characteristics were measured at two drain-source voltages (V_{ds}), -1 V and -10 V. A higher V_{ds} (-10 V) was utilised in response to the large V_{th} shift observed in O₂ plasma exposed OFETs, which impeded low-voltage I_{ds} vs. time sensing experiments. A higher V_{ds} was selected to facilitate stabler transfer characteristic based sensing experiments.

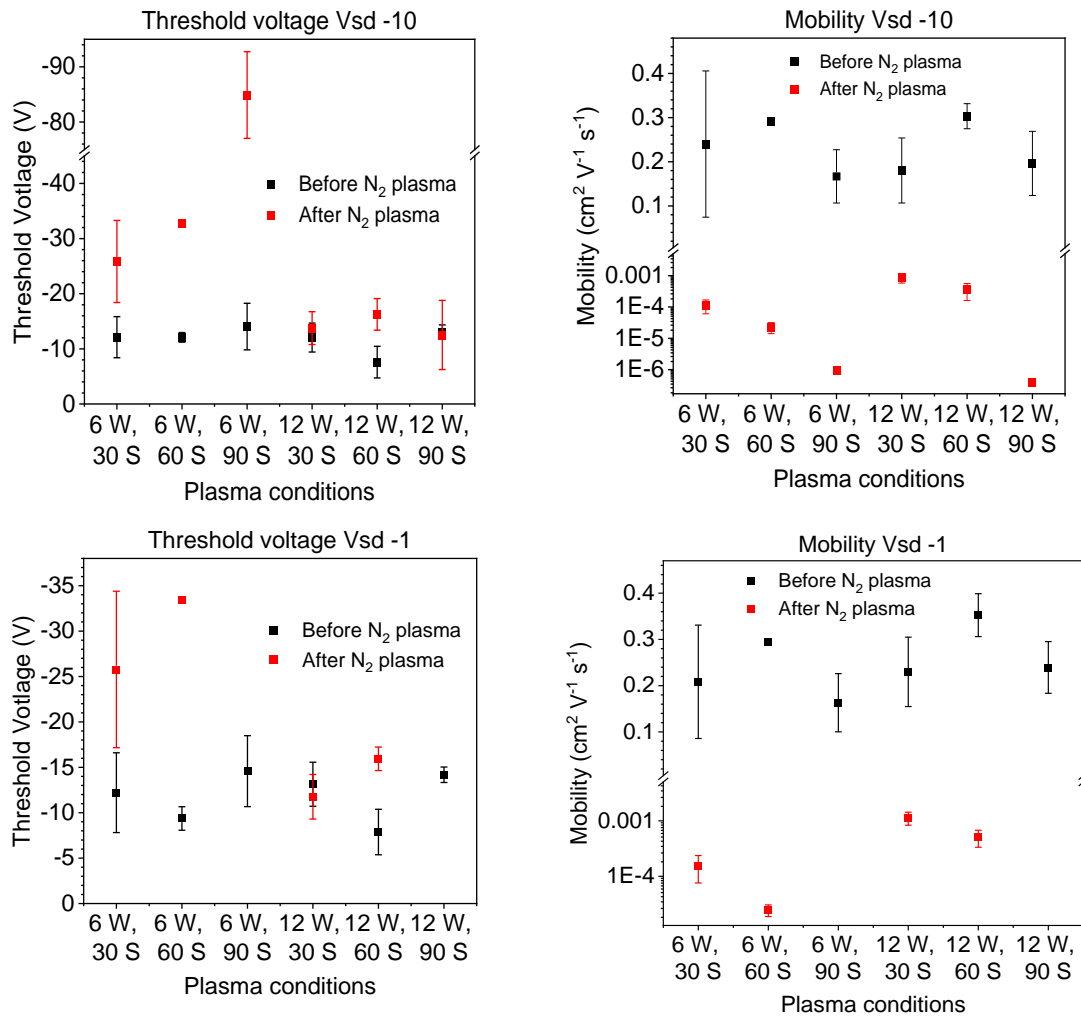


Figure 50 OFET performance ($V_{ds} = -1$ V, -10 V) metrics (left) averaged threshold voltage (right) averaged mobility, before and after N_2 plasma treatment.

An initial threshold voltage (V_{th}) of around -10 V for OFETs is observed, which is a negative shift relative to the V_{th} of OFETs measured in previous chapter sections (< -1 V). However, a discrepancy in the extracted threshold voltages is identified in the output characteristics. OFET output curves were observed for gate-source voltages (V_{gs}) ranging from 0 V to -5 V were measured, which contradict V_{th} values extracted from the transfer characteristics. The source of the V_{th} discrepancy was considered to be from hysteresis effects. The effects were observed in the transfer and output characteristics, when the sweeping voltages were measured in the forward and reversed plasma direction. (218) OFET hysteresis is present in transfer

and output characteristics depicted in Figure 51, where a shift in I_{ds} at corresponding V_{gs}/V_{ds} is observed between the forward and reverse voltage sweeps.

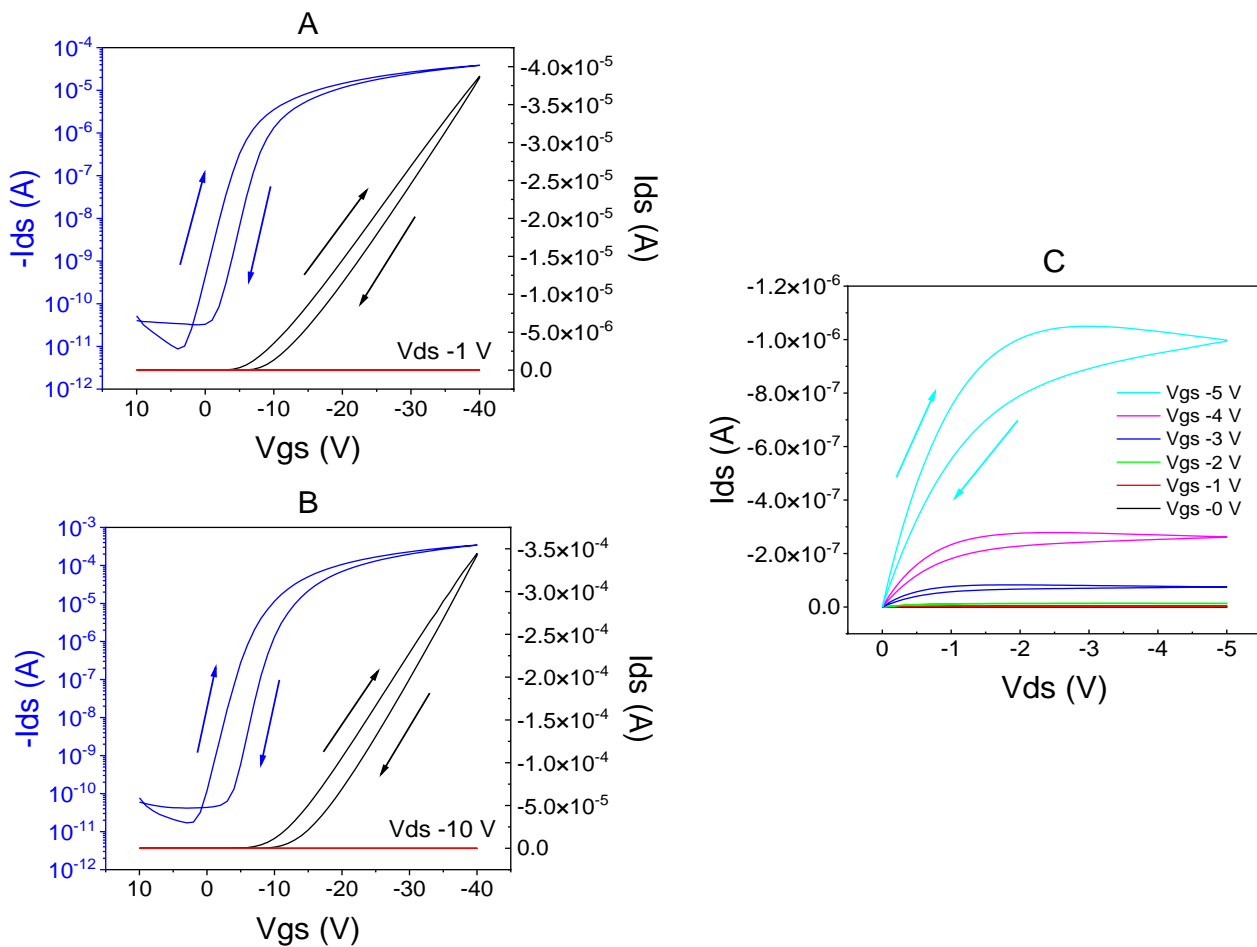


Figure 51 Transfer characteristics a) $V_{ds} -1 V$ b) $V_{ds} -10 V$ and output characteristics of DPP-DTT OFETs before N_2 plasma treatment (blue) log scale (black) linear scale (red) gate current, (upward arrow) forward sweeping voltages (downward arrow) reversed.

Hysteresis effects are commonly observed in OFETs and originate in various ways.(219) However, the origin of the hysteresis was not further identified. In addition, the observed mobility (μ) values were representative of previous OFETs. Despite this difference, the results were seen as contextually relevant and the effects of N_2 plasma treatment on OFET performance continued.

Compared to O_2 plasma treatment, the etching rate of thin-films exposed to N_2 plasma was more profound, as evident from the AFM thickness data (section 3.4.4). This observation

extends to the OFET performance, where a greater reduction in performance metrics is observed. The diminished performance is particularly highlighted in the output characteristics, only the OFETs exposed to 12 W for 30 s and 12 W for 60 s N₂ plasma exhibit output curves, with reduced drain-source currents (I_{ds}). Generally, an increase in V_{th} and a decrease in μ is observed after N₂ plasma exposure, across the series. Gate current remained in the sub-nanoamp range, and considered not a contributing factor to reduced OFET performances. Among the N₂ plasma conditions tested, the OFET exposed to 12 W, 30 s plasma retained the highest performance. Preserving a similar initial V_{th} and the highest retained μ , however the resulting μ was 0.47 % of its original value. The impact on mobility and V_{th} is apparent in the output characteristics, as the majority of the N₂ plasma exposed OFETs did not exhibit output curves. OFETs exposed to N₂ plasma, which exhibited output curves, saw a significant decrease in I_{ds} , indicating a reduction in μ .

The μ decreases as the exposure time increases for both 6 W and 12 W exposed OFETs. This significant decrease in mobility can be partly attributed to etching of the conductive channel. However, even in OFET thin-films that experienced minimal etching, there were still substantial decreases in mobility, more pronounced than in O₂ plasma exposed OFETs. Furthermore, OFETs exposed to either 6 W or 12 W N₂ plasma, which had similar levels of thin-film etching, displayed differing shifts in V_{th} . This substantial decrease in mobility, along with the variations in the shift in V_{th} , suggests that other influences induced by N₂ plasma are impacting the performance metrics of the OFETs.

These observations can be explained by the increasing density of nitrogen-containing chemical functionalities introduced to the thin-film surface as exposure time increases. Plasma treated surfaces with higher chemical group densities tend to undergo more extensive polymer surface restructuring, as discussed above. The variations in reduced OFET performance observed at both 12 W and 6 W could be attributed to differences in the selectivity of nitrogen containing functionalities. With some functionalities being less influential on OFET performance than others. This possibility is supported by evidence

discussed in the XPS data. A combination of these factors, along with the effects discussed in the O₂ plasma treatment section, contribute to the overall reduction in OFET performance.

Characterisation of N₂ plasma exposed OFETs observed a significant decrease in performance metrics V_{th} and μ , relative to O₂ plasma exposed OFETs. N₂ plasma treatment conditions 12 W, 30 s were identified as less influential on OFET performance.

3.4.6 The introduction of exploitable chemical functionalities on N₂ plasma treated thin-films

Following the OFET characterisation of N₂ plasma treated DPP-DTT OFETs, the effects on thin-film surface chemistry were investigated. N₂ plasma treatment conditions are presented in Table 17 (see section 3.4.4). X-ray photoelectron spectroscopy (XPS) was conducted and resulting spectra processed using methodology detailed in section 2.3.2.

N₂ plasma treatment is expected to introduce various nitrogen containing chemical groups, such as amines (R-NH₂, R₂-N-H and R₃-N), amides (R₂-N-C=O), imines (R-N=C) and nitriles (C≡N) onto the thin-film surface.^(190, 191, 220) N1s high resolution scans of N₂ plasma treated thin-films were run to identify changes in nitrogen content on the thin-film surface, spectra for which are presented in Figure 119 (see appendix section 7.1.9). All spectra observe a peak at a binding energy of ~400.0 eV, which is assigned to nitrogen. Peak areas of the fitted N1s spectra are presented in Figure 52.

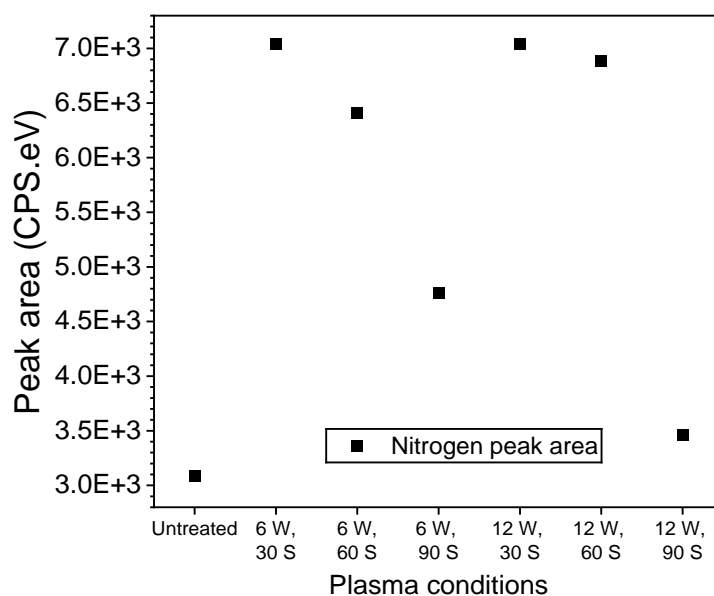


Figure 52 XPS high resolution N1s spectra nitrogen peak area of N₂ plasma treated DPP-DTT thin-films.

An increase in N1s peak area corresponds to an increase in nitrogen content. The N1s peak areas of N₂ plasma exposed thin-films are increased, relative to the unexposed thin-film. This

indicates that N₂ plasma introduces nitrogen containing chemical species onto the surface of the thin-films. A general trend of decreasing nitrogen content with increasing exposure time is observed for 6 W and 12 W plasma exposed thin-films. The trend is more evident in 6 W plasma exposed thin-films. A correlation between the degree of thin-film etching (see section 3.4.4) and resulting nitrogen content, couldn't be identified. Nitrogen containing species introduced to the surface appear to saturate within the first 30 seconds of N₂ plasma exposure. For thin-films exposed to 6 W and 12 W, 30 s exposure times observe the highest amount of nitrogen containing species. Saturation of oxygen content on O₂ plasma exposed PMMA surfaces with increased exposure time has been observed.⁽²²¹⁾ However, this saturation point isn't maintained throughout the series. Instead a decrease in nitrogen content with increasing exposure time is followed. Two mechanisms can facilitate the reduction of nitrogen content with increasing exposure time. Processes relating to the restructuring of the plasma exposed thin-film surface and hydrolysis of imines into volatile ammonia, result in lowering surface nitrogen content. Plasma induced surface restructuring, which was explained further in section 3.4.5, can cause new nitrogen containing functionalities on the surface to move in towards the thin-film bulk. Resulting in a decrease of nitrogen content on the surface. Surface restructuring was thought to have contributed to the reduced OFET performances of N₂ plasma treated thin-films (section 3.4.5). With lower nitrogen content N₂ plasma exposed thin-films observing a higher degree of surface restructuring, due to an initial increased nitrogen surface content with increased exposure time. Additionally, imine hydrolysis with atmospheric moisture into volatile ammonia, can facilitate the elimination of surface nitrogen species.⁽¹⁹²⁾ Further, it's reported that shorter exposure times favour higher densities of primary amine groups. Other nitrogen containing species, such as imines, may be favoured at longer exposure times. Elimination of nitrogen containing groups on the thin-film surface, via imine hydrolysis, might occur to a greater extent with longer exposure times. However, the final surface nitrogen content is a complex relationship between multiple factors, which could lead to ambiguity in findings.⁽¹⁹¹⁾

To further identify the nitrogen containing chemical groups, XPS high resolution C1s scans were run. C1s spectra were run to distinguish between different nitrogen containing species

covalently bonded to carbon. Representative spectra of thin-films before and after N₂ plasma exposure are depicted in Figure 53, additional series spectra are presented in Figure 120 (see appendix section 7.1.9). Similar to what was observed with O₂ plasma treatment, the shoulder of N₂ plasma exposed thin-films extends to higher binding energies, which is consistent with plasma-induced surface oxidation.

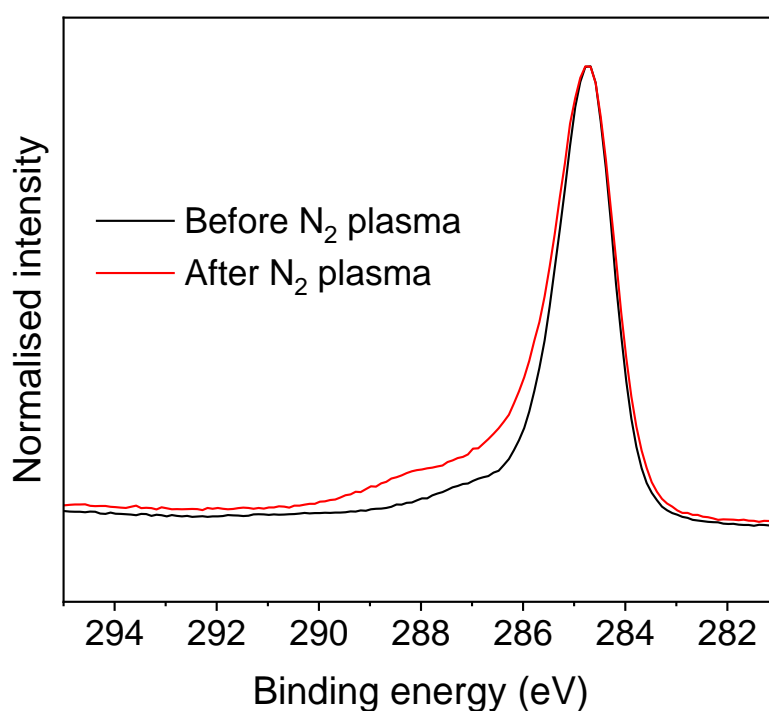


Figure 53 XPS high resolution C1s scans of DPP-DTT thin-films (black) before and (red) after N₂ plasma treatment (12 W for 30 s).

A new component (~288.3 eV) within this shoulder is seen in the C1s spectra for the N₂ plasma treated thin-films, assigned to amide groups.⁽¹³⁴⁾ An increase in the C-N component peak is also observed. Thin-film C-N and amide group component peak areas are presented in Figure 54. The C-N component could not be resolved into individual amino or imine functionalities, due to XPS constraints and chemical groups sharing identical binding energies.^(173, 190) A trend in decreasing number of C-N chemical groups with increasing exposure time is observed, which closely follows the N1s nitrogen content trend. Similarly, the thin-films exposed to 6 W, 30 s and 12 W, 30 s N₂ plasma observe the largest increase in C-N content.

An interesting trend is observed, however more data points are required to further validate this.

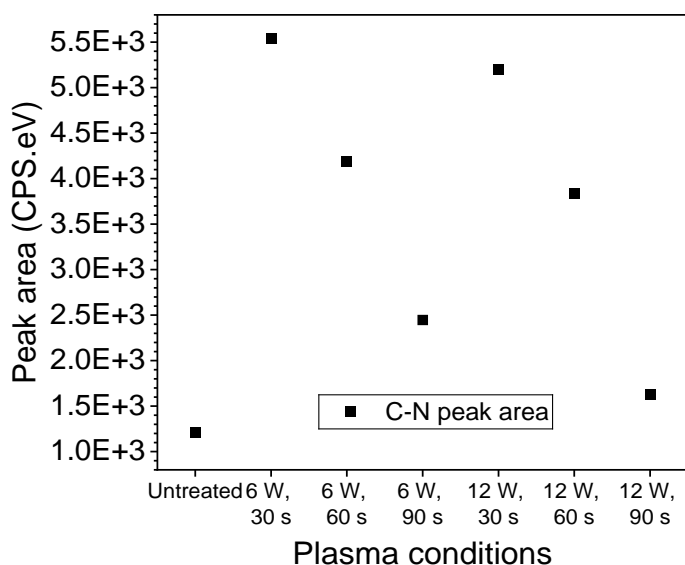


Figure 54 XPS C1s high resolution spectra C-N component peak area of N₂ plasma treated DPP-DTT thin-films.

The thin-film surface exposed to 6 W, 30 s N₂ plasma observed the highest increased C-N peak area (5538.05 CPS.eV). In comparison to thin-films exposed to O₂ plasma, the C-N peak area is nearly double that of the carboxylic acid peak area. However, XPS analysis did not provide the necessary resolution to distinguish individual amino and imine groups within the C-N component peak. The target amino group, primary amines, is assumed to be a contributing functionality in the C-N component peak area, but a definitive density was not determined.

3.4.7 Aptamer functionalisation of N₂ plasma treated thin-films

In order to demonstrate the exploitability of newly introduced amine groups on N₂ plasma modified DPP-DTT surfaces, an aptamer functionalisation strategy was developed (see section 2.2.5.1 and Figure 55). An aptamer sequence identified as binding specifically to cortisol was used.⁽²²²⁾ A methodology was adapted from established methods previously developed within the Palma group.^(150, 223) The strategy utilised cross-linking and strain-promoted alkyne-azide cycloaddition (SPAAC) chemistries, facilitated by (1R,8S,9s)-Bicyclo[6.1.0]non-4-yn-9-ylmethyl N-succinimidyl carbonate (BCN-NHS) (see section 2.1.6) and azide terminated cortisol binding aptamers (N₃-CBA) (see section 2.1.7).

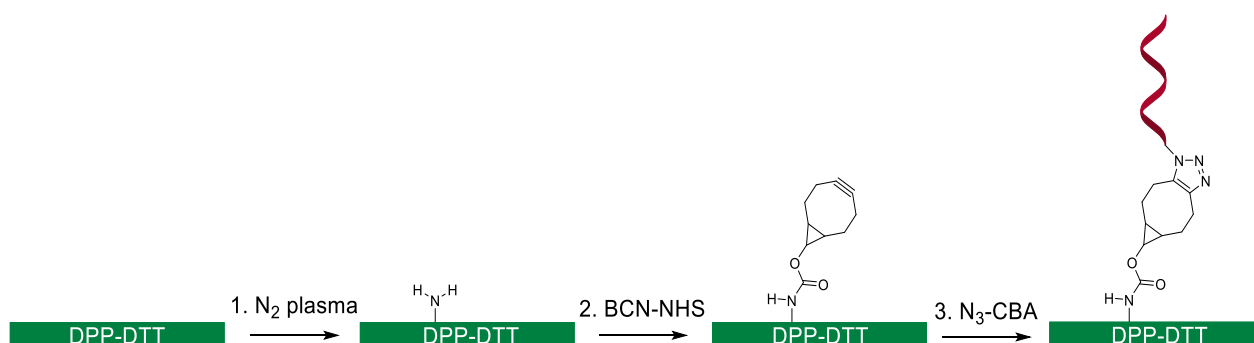


Figure 55 Aptamer attachment strategy of N₂ plasma treated DPP-DTT thin-film: 1. N₂ plasma treatment (12 W, 30 s) 2. BCN-NHS (1.0 mg mL⁻¹) modification then washed with MQ water 3. N₃-CBA (1 μM) functionalisation then sequentially washed with 0.1 % tween20 solution and MQ water.

Thin-films were N₂ plasma treated at 12 W for 30 s, guided by preceding OFET performance and XPS data. N₂ plasma exposed DPP-DTT thin-film surfaces were initially modified with BCN-NHS. N-hydroxysuccinimide esters react readily with amine groups, facilitating the covalent attachment of BCN groups to the modified DPP-DTT surface. Subsequently, BCN-DPP-DTT surfaces were functionalised with N₃-CBA, via a SPAAC click reaction.

Verifying the successful surface functionalisation involved labelling the aptamers with a Cy3 labelled DNA strand, that was complimentary to the cortisol binding aptamer sequence (Cy3-comp-CBA). Cy3-comp-CBA (see section 2.1.7) was hybridised to the covalently attached aptamer on the DPP-DTT thin-film surface (see Figure 56).

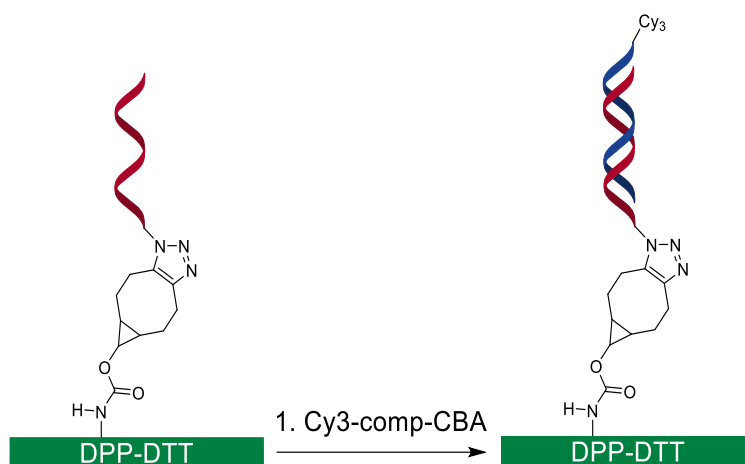


Figure 56 Hybridisation of aptamer functionalised thin-film with Cy3 labelled complimentary strand: 1. Cy3-comp-CBA ($1 \mu\text{M}$) hybridisation then sequentially washed with 0.1 % tween20 solution and MQ water.

Several controls were employed, including the absence of $\text{N}_3\text{-CBA}$, Cy3-comp-CBA and N_2 plasma. Additionally, a control functionalised with an aptamer composed of a differing sequence was used. The non-complementary azide terminated aptamer sequence was specific to the analyte neuropeptide Y ($\text{N}_3\text{-NYP}$, see section 2.1.7).

Detection of Cy3 hybridised thin-films was achieved with epifluorescence microscopy, using a Zeiss Elyra PS1 super resolution microscope (see section 2.3.3). Epifluorescence images are depicted in Figure 121 (see appendix section 7.1.10), with extracted fluorescence data presented in Figure 57. The thin-film functionalised with $\text{N}_3\text{-CBA}$ and hybridised with Cy3-comp-CBA shows a significant increase in fluorescence, relative to the control samples. This suggests an increased amount of Cy3 on the thin-film surface, facilitated by hybridisation of the aptamer with the Cy3 labelled strand. Further support from control thin-films, which mainly observe background fluorescence, strengthens the evidence of successful hybridisation. The $\text{N}_3\text{-NYP}$ control observed a slight increase above the background fluorescence, caused by partial hybridisation with the Cy3-comp-CBA strand. However, the magnitude of the increase wasn't significant.

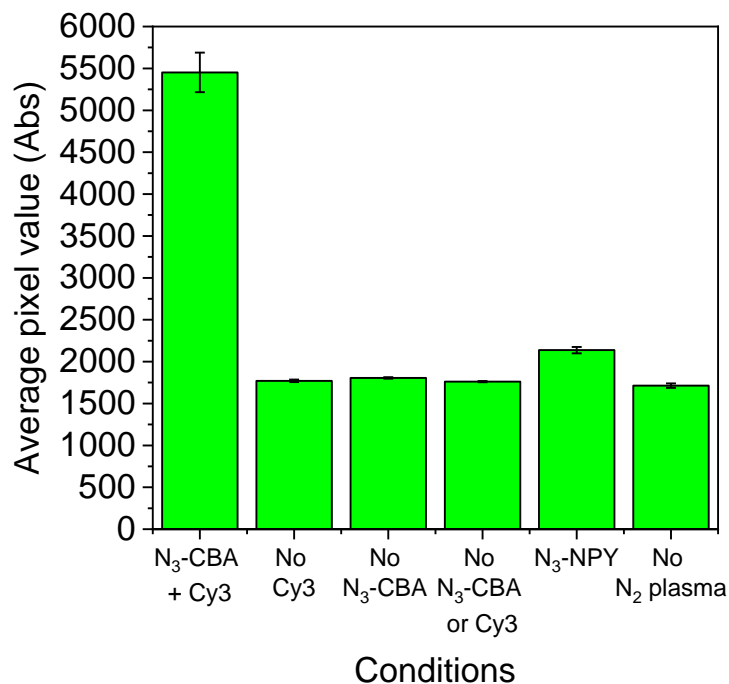


Figure 57 Epifluorescence microscope image average pixel values: N₂ plasma treated DPP-DTT thin-film functionalised with aptamers and hybridised with a Cy3 labelled complimentary strand. Average pixel values of thin-film controls also included.

Hybridisation of the Cy3 labelled complimentary strand confirms the attachment of the aptamer to the N₂ plasma modified DPP-DTT surface. Additionally, hybridisation confirms the preservation of the aptamers binding affinity and mobility (i.e. the aptamers ability to move and reconfigure). A novel aptamer attachment strategy utilising N₂ plasma treated thin-films has been developed.

3.5 Summary and conclusion

In summary, this chapter presents a foundational methodology for fabricating organic field-effect transistors (OFET) incorporating the high performance organic semiconducting polymer DPP-DTT. Further, O₂ and N₂ plasma treatment of DPP-DTT OFET platforms were investigated as a method of introducing exploitable chemical functionalities on the thin-film surface, for strategies in aptamer attachment.

Optimisation of the DPP-DTT thin-film utilised floating film transfer (FFT) as a deposition methodology. Thin-film morphology and thickness was optimised by controlling the concentration of the DPP-DTT polymer solution. Thin-films exhibited continuous areas of homogeneity, free of defects and large aggregates. Additionally, evidence of polymer chain alignment was observed in AFM images. Modification of the SiO₂ dielectric surface was conducted to passivate surface charge traps. A self-assembled monolayer of octadecyltrichlorosilane (ODTS) was formed on the dielectric surface. A dense and uniform layer of ODTS was confirmed by water contact angle measurements and AFM imaging. The optimised methodologies were assembled into a bottom-gate top-contact OFET, incorporating gold deposited interdigitated source-drain electrodes. OFETs fabricated under ambient laboratory conditions exhibited acceptable mobilities and low threshold voltages, suitable for low-voltage biosensing applications.

Following this, O₂ and N₂ plasma treatments of DPP-DTT thin-films were investigated individually, as methods of introducing exploitable chemical functionalities to the thin-film surface. A series of conditions varying plasma exposure powers and times were explored. The balance between thin-film etching and chemical modification, was monitored with AFM and XPS measurements. The influence of plasma treatment on OFET performance was also monitored. An optimised balance between O₂ plasma power and exposure time (12 W, 60 s) was identified. The OFET exposed to O₂ plasma under these conditions experienced minimal etching, maximal chemical modification and retained the highest performance. However, the limited density of carboxylic acid groups, possibly due to plasma-induced surface restructuring, restricted further aptamer functionalisation.

Subsequently, the exploration of N₂ plasma treatment was considered as an alternative aptamer functionalisation strategy. N₂ plasma was discovered to etch thin-films more intensely under similar conditions relative to O₂ plasma. The increased intensity of N₂ plasma was reflected in the OFET performance, which observed a significant reduction in the charge carrier mobilities. However, an increase in exploitable functional groups was apparent in XPS spectra. N₂ plasma treatment conditions 12 W, 30 s were identified as the optimal balance between chemical modification and OFET performance retention. Further, an aptamer functionalisation strategy was employed and verified by epifluorescence microscopy. The strategy modified amine functional groups on a N₂ plasma exposed thin-film surface with BCN-NHS, followed by a SPAAC click reaction between surface attached BCN groups and N₃-aptamers. Despite the promising result, the fabrication of an aptamer functionalised N₂ plasma treated OFET was not pursued. Instead, the attention of this thesis was directed to an alternative aptamer functionalisation strategy with improved OFET performance: the foundational methods and knowledge learnt from this chapter were further utilised in the following chapters.

Continuation of this research chapter should focus on measuring a sensing response with an aptamer functionalised OFET. The aptamer functionalisation strategy developed using nitrogen plasma should be applied to a DPP-DTT OFET with a low starting threshold voltage (< 1 V). The sensing response to cortisol should then be determined through real-time current or transfer curve sensing experiments.

4 Investigation of DPP-DTT polymer blend with glutaraldehyde for receptor functionalisation and use in biosensing OFET devices

4.1 Acknowledgments

The author acknowledges Dr Mark Freeley for capturing epifluorescence microscopy images, at Queen Mary University. All other experiments were conducted by the author.

4.2 Introduction

In Chapter 3 O₂ and N₂ plasma were used to introduce chemically exploitable functionalities to the surface interface of DPP-DTT OFETs. Desired functionalities could be identified, however plasma exposed OFETs were limited either by the density of exploitable chemical groups or a reduction in OFET performance. The following chapter endeavours to address these highlighted issues by opting for a modified OFET fabrication approach, involving an organic semiconducting polymer and small molecule blended system.

Blending polymers or small molecules with organic semiconducting materials has found numerous applications within organic electronics.^(224–227) Particularly in the fields of organic photovoltaics and organic thermoelectrics, where respective blended systems are employed for bulk-heterojunction thin-film formation and thin-film conductivity enhancement.^(228–230) The prominent conductive polymer blend PEDOT:PSS, composed of the organic conductor poly(3,4-ethylenedioxythiophene) (PEDOT) blended with polyanion poly(styrene sulfonate) (PSS), is recognised for its remarkable versatility in several areas of organic electronics.^(231, 232)

In particular, OFETs incorporating blended systems have displayed enhanced properties: improvements to OFET air, thermal, and mechanical stabilities, as well as stretchability and performance figures of merit have been reported.^(233–236) In addition, these improvements also extend to OFET based sensors, with blended systems enabling sensing capabilities or

providing sites for receptor functionalisation. Examples of the former have enabled OFET gas sensors to detect gases such as ammonia or superoxide.(237, 238) Instances of blended systems facilitating receptor functionalisation of biosensing organic transistors have been reported, including the attachment of antibodies and aptamers.(159, 164) Notable work by Sun et al., reported the single molecule detection of carcinoembryonic antigen (CEA), with OFETs functionalised with antibodies.(136) A blended system comprising of DPP-DTT and a derivative of pillar[5]arene containing carboxylic groups (DMP[5]-COOH) was employed as the channel material. Antibodies specific to CEA were attached to the OFET channel surface, by exploiting carboxylic acid groups on DMP[5]-COOH through the use of EDC/NHS crosslinking chemistry. CEA was incubated on the sensing channel and detected through changes in threshold voltage from the transfer characteristics, achieving an attomolar limit of detection. Additionally, the same research group demonstrated a facile yet effective receptor functionalisation approach, by blending DPP-DTT with a small molecule dialdehyde, glutaraldehyde (GA).(160) Antibodies specific to α -fetoprotein (AFP) and carcinoembryonic antigen (CEA), were attached to the surface of respective OFET channels, via a condensation reaction. The reaction was facilitated by aldehyde groups in GA reacting with primary amine groups in the antibodies. Antigens AFP and CEA were incubated on respective OFET sensing channels and responses were detected through shifting threshold voltages. Detection limits of 0.176 pM and 65 fM were obtained for AFP and CEA, respectively. In addition to facilitating receptor attachment, GA blending also improved the overall OFET performance. The optimised DPP-DTT:GA (9:1) blend observed an average charge carrier mobility and threshold voltage of $2.07 \text{ cm}^2 \text{ V}^{-1} \text{ s}^{-1}$ and -0.29 V , respectively. Asserting that GA improves the OFET by:

1. Enhancing the thin-film morphology by suppressing DPP-DTT gelation
2. The strong polar groups are conducive to charge accumulation and transportation in the channel.

Additionally, instances of glutaraldehyde facilitating the attachment of amine terminated ss-DNA to silicon nanowires and graphene FETs have also been reported.(239, 240) Combined with the commercial availability, low cost and high reactivity with amine groups at neutral pH, glutaraldehyde demonstrates promising attributes for effectively attaching aptamers to DPP-DTT OFETs, while preserving OFET performance.(241)

Building upon the foundational BGTC OFET fabrication and characterisation methods learnt in Chapter 3, OFETs incorporating DPP-DTT:GA thin-film blends were investigated. The following chapter presents research into the fabrication of aptamer functionalised DPP-DTT:GA OFETs, followed by the evaluation of initial biosensing capabilities. First DPP-DTT:GA thin-film deposition methodology was optimised, followed by the identification of an optimised strategy for functionalising DPP-DTT:GA OFETs, with amine terminated cortisol binding aptamers. Aptamer functionalised DPP-DTT:GA OFETs were characterised and the initial biosensing capabilities determined. Additionally, techniques for addressing OFET sensitivities and stabilities were identified.

4.3 Optimisation of DPP-DTT:GA thin-film deposition

Optimisation of the DPP-DTT:GA thin-film deposition process was initially investigated. Reportedly, the DPP-DTT:GA (9:1) in chlorobenzene (5 mg mL^{-1}) blend that was spin coated onto ODTS modified Si/SiO₂ substrates, displayed optimised OFET performance values. Therefore, these established polymer solution deposition conditions were adopted. Control of thin-film thickness while maintaining uniform surface coverage of the substrate, was explored by varying the initial spin coating speed (RPM). DPP-DTT:GA thin-films were deposited onto ODTS modified Si/SiO₂ substrates, under a series of spin coating conditions presented in Table 18, as described in section 2.2.4.2. Morphological attributes relating to thin-film thickness and roughness were monitored with AFM (see section 2.3.1). Averaged DPP-DTT:GA thin-film thicknesses are presented in Figure 58, with AFM images and tabulated data provided in Figure 122 and Table 57 (see appendix section 7.2.1), respectively.

Step	RPM	Acceleration	Time
1	2K, 4K, 5K, 6K, 7K	1K	120 s
2	8K	1K	30 s

Table 18 Spin coating series conditions: DPP-DTT:GA (9:1) thin-films from chlorobenzene (5 mg mL^{-1}) on ODTS modified Si/SiO₂ substrates.

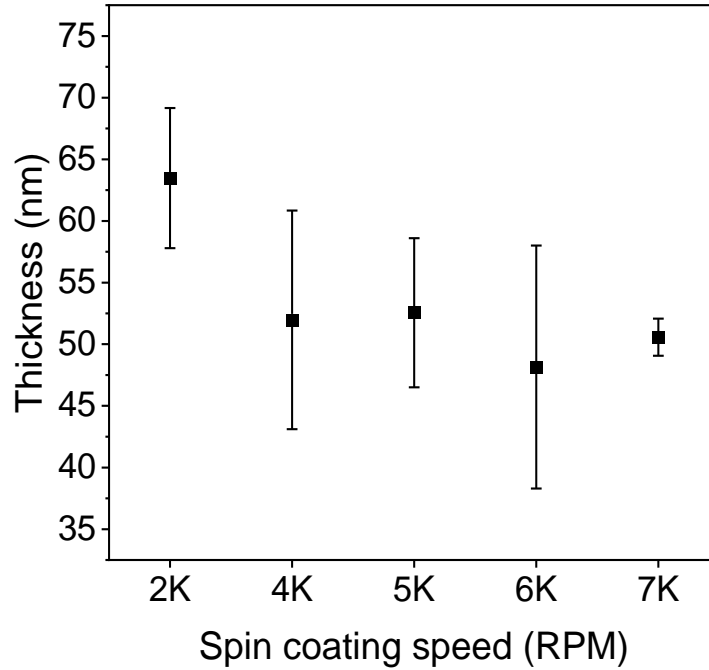


Figure 58 Spin coating series: Thicknesses of DPP-DDT:GA (9:1) thin-films from chlorobenzene (5 mg mL^{-1}).

Spin coating the DPP-DDT:GA solution at 2K RPM resulted in a thin-film observing the largest average thickness, while the thin-films spin coated at speeds > 2K RPM observed smaller average thicknesses. However, a noticeable reduction in thin-film thickness with increasing RPM was not observed. Instead, similar values in average thin-film thickness were obtained, with the values thicker than the reported value of 34.25 nm. The impact of spin coating speed with RPMs greater than 2K appear less influential on the resulting thickness of DPP-DDT:GA thin-films. The variation in thin-film thicknesses between the obtained and reported values is attributed to differences in the molecular weights of the DPP-DDT polymers.(242) However, the average thickness of the thin-films were in range of previously reported OFET biosensors.(46)

Insight into thin-film roughness across the spin coating series was also determined. Average roughness values R_a and R_q of thin-films across the spin coating series are provided in Figure 59. Average thin-film roughness remains consistent across the spin coating series.

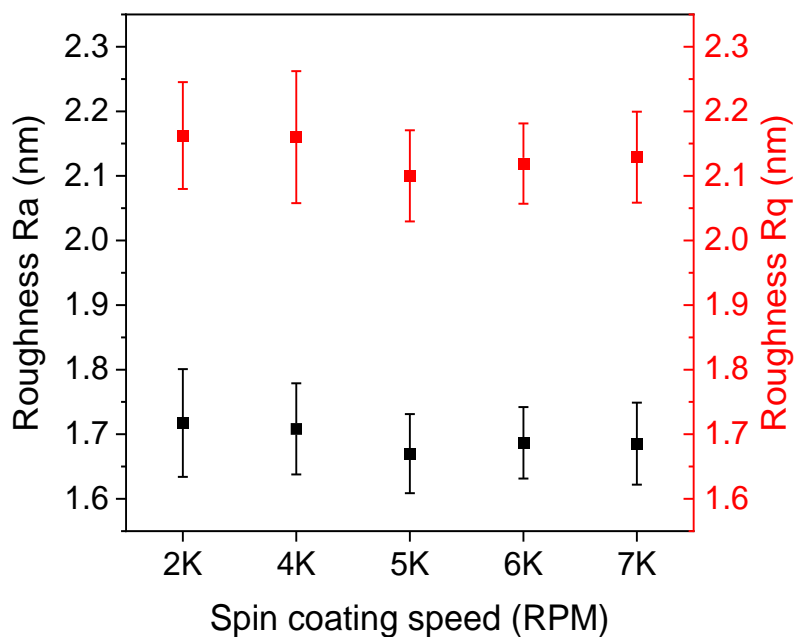


Figure 59 Spin coating series: Roughness Ra and Rq values of DPP-DTT:GA (9:1) thin-films from chlorobenzene (5 mg mL^{-1}).

Overall, the average Rq value obtained is lower than the reported value of 4.48 nm, suggesting a reduction in thin-film crystallinity. A decrease in Rq with increasing GA content was reported. However, the difference in roughness is attributed to the difference in molecular weight of the DPP-DTT polymers.⁽⁸¹⁾ Given the limited controllability of thin-film thickness and roughness uniformity, variations in substrate coverage became the determining factor in selecting spin coating conditions. The DPP-DTT:GA spin coating conditions at 4K RPM achieved greater coverage, relative to the other thin-films with comparable thicknesses.

The thin-film morphology of the 4K RPM spin coated DPP:GA thin-film was investigated. Topographical AFM images of the 4K RPM spin coated DPP:GA thin-film are presented in Figure 60. The thin-film exhibits sizable areas of homogeneity, as well as a fibrillar morphology resembling that of reported DPP polymer blends.^(243, 244) Some large aggregates are observed on the surface, but at a lower density, relative to thin-films without the addition of GA (see section 3.3.1, Figure 26). The addition of GA was claimed to improve the morphology of the DPP-DTT:GA thin-film, by suppressing the gelation of the polymer. Gelation of Donor-Acceptor polymers, such as DPP-DTT, in solution is a recurring issue that affects the deposition

process of thin-films. Suppressing polymer solution gelation has been reported with other blended systems as being effective.(36)

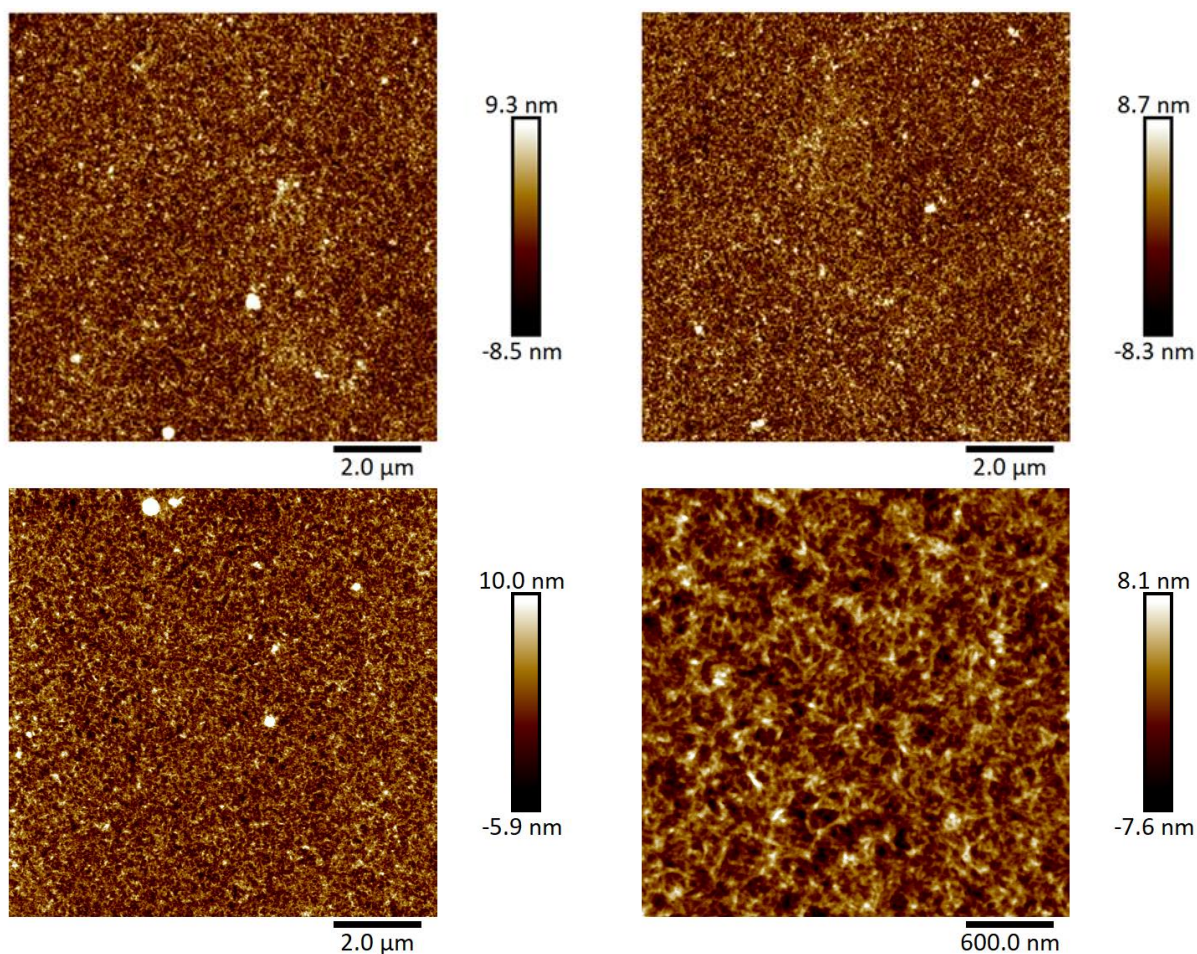


Figure 60 AFM topographical images (10 μm x 10 μm and 3 μm x 3 μm) of DPP-DTT:GA (9:1) thin-film spin coated (4K RPM) from chlorobenzene (5 mg mL⁻¹).

In summary, a series of spin coating conditions were investigated for depositing DPP-DTT:GA (9:1) in chlorobenzene (5 mg mL⁻¹) blended thin-films. Spin coating RPM was found to be less influential on thin-film thickness and roughness, but more impactful on substrate surface coverage. Greater substrate coverage was observed by the DPP-DTT:GA thin-film spin coated at 4K RPM, while demonstrating an average thickness of 52.0 nm. Additionally, the 4K RPM spin coated thin-film observed a fibrillar morphology and large areas of homogeneity. DPP-DTT:GA thin-films spin coated at 4K RPM were considered suitable for further investigations in aptamer functionalisation, as well as incorporation into OFET devices.

4.4 Aptamer functionalisation of DPP-DTT:GA OFETs

4.4.1 Aptamer functionalisation of DPP-DTT:GA thin-films

In order to demonstrate the exploitability and reactivity of aldehyde groups on glutaraldehyde (GA) blended DPP-DTT surfaces, a functionalisation strategy for attaching cortisol binding aptamers (CBA) was investigated. The strategy is illustrated in Figure 61 and detailed in section 2.2.5.2. Aptamer attachment was facilitated by a condensation reaction between surface aldehyde groups and amine terminated cortisol binding aptamers (NH₂-CBA). DPP-DTT:GA thin-films were deposited as described in section 2.2.4.2.

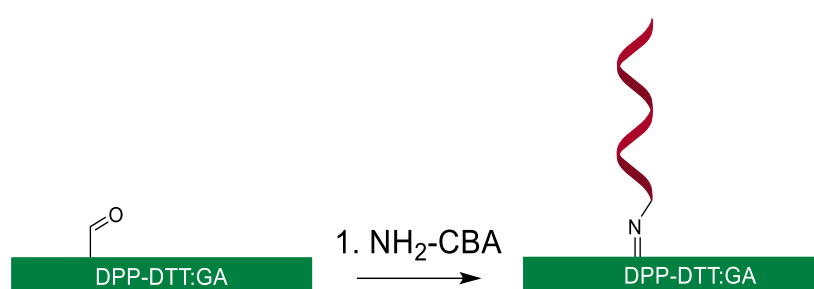


Figure 61 Aptamer attachment strategy of DPP-DTT:GA thin-film: 1. NH₂-CBA (10 μM) functionalisation then sequentially washed with 0.1 % tween20 solution and MQ water.

Verifying the successful surface functionalisation involved hybridising the attached aptamers with a complimentary Cy3 labelled DNA strand (Cy3-comp-CBA). Cy3-comp-CBA (see section 2.1.7) was hybridised to the covalently attached CBA on the DPP-DTT:GA thin-film surface (see Figure 62).

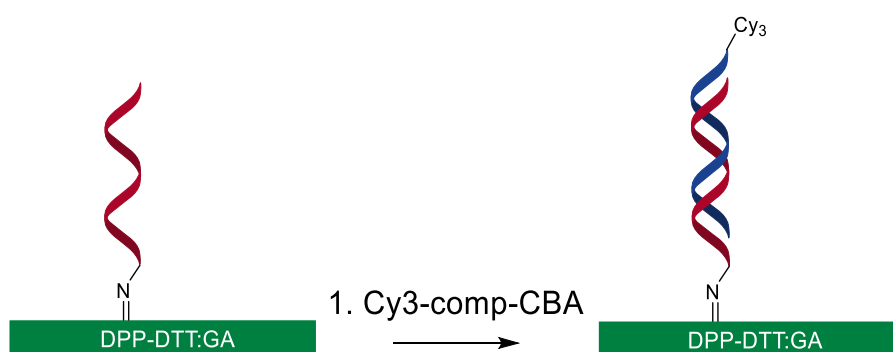


Figure 62 Hybridisation of aptamer functionalised DPP-DTT:GA thin-film with Cy3 labelled complimentary strand: 1. Cy3-comp-CBA (1 μM) hybridisation then washed with 0.1 % tween20 solution and MQ water.

Several controls experiments were carried out to further verify hybridisation, including the absence of NH₂-CBA (No NH₂-CBA), Cy3-comp-CBA (No Cy3) and both NH₂-CBA/Cy3-comp-CBA (No NH₂-CBA or Cy3). Additionally, a control functionalised with an aptamer composed of a differing sequence was used. The non-complementary amine terminated aptamer sequence (NH₂-DHEAS) was specific to the analyte dehydroepiandrosterone-sulphate (see section 2.1.7). Detection of Cy3 hybridised thin-films was performed through epifluorescence microscopy, using a Zeiss Elyra PS1 super resolution microscope (see section 2.3.3). Pixel values were extracted from the images, which are presented in Figure 63. Epifluorescence images are depicted in Figure 128, with tabulated average pixel values in Table 62 (see appendix section 7.2.3).

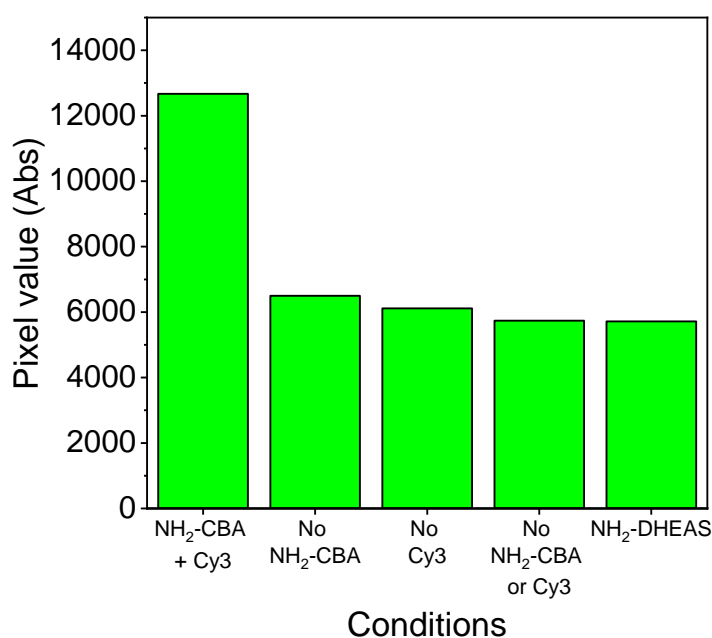


Figure 63 Epifluorescence microscope image pixel values: DPP-DTT:GA thin-film functionalised with aptamers and hybridised with a Cy3 labelled complimentary strand. Average pixel values of thin-film controls also included.

The thin-film functionalised with NH₂-CBA and hybridised with Cy3-comp-CBA observes a significant increase in fluorescence, relative to the control samples. Indicating an increased amount of Cy3 on the thin-film surface, facilitated by hybridisation of the aptamer with the Cy3 labelled strand. Further supported by control thin-films, which mainly observe

background fluorescence, strengthening the evidence of successful hybridisation. Glutaraldehyde can react with primary amine groups in adenine, guanine and cytosine DNA bases, which is a process exploited in applications utilising DNA.(245, 246) Therefore, the aptamer could react with the DPP-DTT:GA thin-film surface at multiple points along the strand. In turn, restricting the aptamer and preventing analyte binding. Hybridisation of the strand can indicate that the reaction between GA and the DNA bases is mitigated. This suggests that analyte-aptamer binding events are free to occur within the system.

Hybridisation of the Cy3 labelled complimentary strand to the NH₂-CBA strand confirms the covalent attachment of the aptamer to the DPP-DTT:GA thin-film surface. Additionally, hybridisation confirms the preservation of both the binding affinity and mobility of the attached aptamer. A trend confirming aptamer attachment and hybridisation is observed, however more data points should be collected to further validate this. The following section investigates the influence of aptamer concentration on DPP-DTT:GA thin-film functionalisation.

4.4.2 Aptamer functionalisation of DPP-DTT:GA OFETs

Following the epifluorescence microscopy investigation of aptamer functionalised DPP-DTT:GA thin-films, X-ray photoelectron spectroscopy (XPS) was performed to further confirm and optimise the aptamer functionalisation strategy. DPP-DTT:GA thin-films were deposited as described in section 2.2.4.2. X-ray photoelectron spectroscopy (XPS) was conducted and resulting spectra processed using methodology detailed in section 2.3.2.

To confirm the presence of glutaraldehyde GA within the thin-film surface, DPP-DTT thin-films blended with glutaraldehyde (GA) and without (No GA), were characterised via XPS high resolution O1s scans (Figure 64). According to Sun et al., GA introduces a peak into the O1s spectrum at 531.36 eV. A peak was introduced to the spectra, which can be attributed to the carbonyl group in GA. However this is disputed, as the binding energy of the aliphatic (GA) carbonyl groups are expected to be higher than the aromatic (DPP-DTT) carbonyl groups.(236, 247) Alternatively, the peak could result from shifting of the aromatic carbonyl peak, caused by electron enrichment from the aliphatic carbonyl groups in GA.(236) Sun et al., identified a peak shift in the UV-Vis spectrum of DPP-DTT:GA blended thin-films, induced by charge-transfer between GA and the DPP-DTT polymer. Charge transfer could also shift the aromatic carbonyl peak to a lower binding energy. Despite this a change in the O1s spectrum is observed between DPP-DTT thin-films blended with and without GA, which is consistent with literature findings.(160)

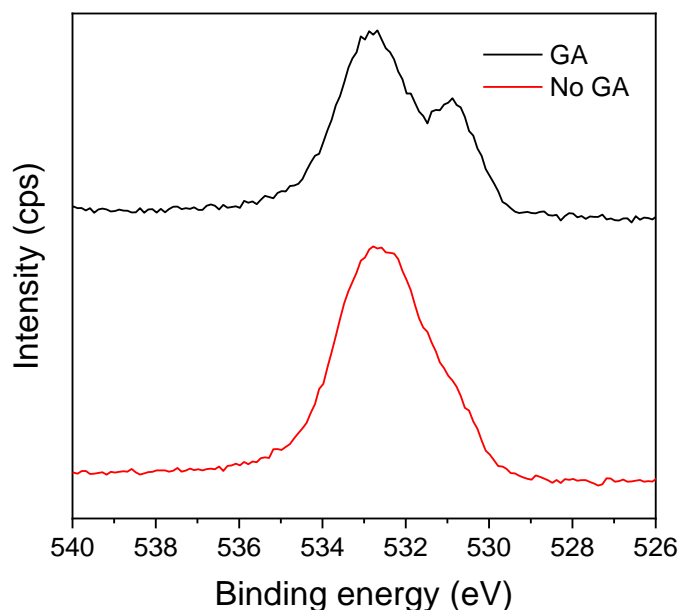


Figure 64 XPS high resolution O1s scans: (red) DPP-DTT thin-film spin coated from chlorobenzene (5 mg mL^{-1}) and (black) DPP-DTT:GA thin-film spin coated from chlorobenzene (5 mg mL^{-1}).

Following the confirmation of GA within the DPP-DTT:GA thin-film surface, further optimisation of the aptamer functionalisation strategy was conducted. A series of NH_2 -CBA concentrations, presented in Table 19, were investigated. Aptamer functionalisation of DPP-DTT:GA thin-films is detailed in section 2.2.5.2. The aptamer concentration range was determined from previously reported concentrations.(147, 248)

Concentration
1 μM
5 μM
10 μM

Table 19 DPP-DTT:GA NH_2 -CBA functionalisation concentration series.

Aptamer functionalisation was verified in high resolution carbon (C1s), phosphorus (P2p), oxygen (O1s) and nitrogen (N1s) spectra. Overlaid and normalised high resolution C1s spectra of the DPP-DTT:GA concentration series are presented in Figure 65. A change in the shoulder region of the C1s peak is observed for NH_2 -CBA functionalised DPP-DTT:GA thin-films. The intensity of the shoulder increases, indicating an increase in the component peaks

contributing to this region. Component peaks present in the aptamer, relating to -C-O and C-N (286.2 eV), C-C(=O), N-C(=N) and N-C-O (287.5 eV) and N-C(=O) (288.5 eV), have binding energies within this increased region.(249) This increase in intensity further supports the presence of the aptamer on the DPP-DTT:GA thin-film surface. Additionally the intensity increases with increasing NH₂-CBA concentration, suggesting aptamer attachment can be controlled.

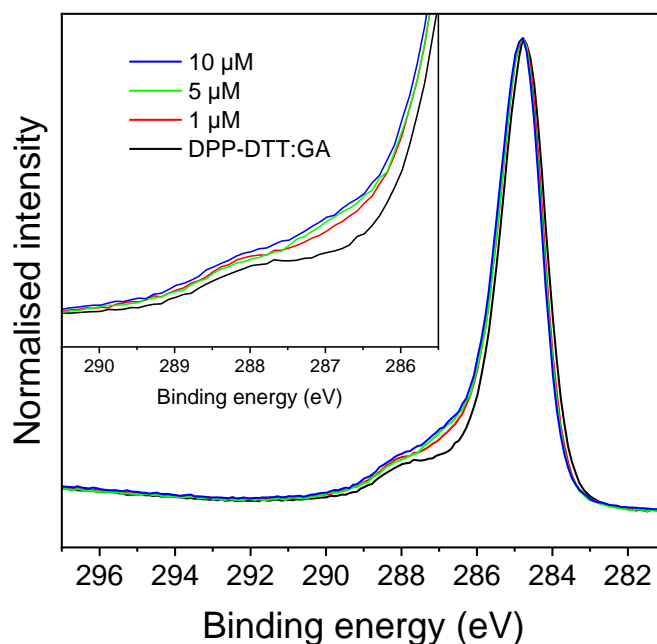


Figure 65 XPS high resolution C1s scans: DPP-DTT:GA thin-films functionalised with NH₂-CBA (1 μM, 5 μM and 10 μM) and a non-functionalised DPP-DTT:GA thin-film (black).

Aptamer functionalisation of DPP-DTT:GA thin-films can be further validated by detecting the introduction of phosphorus, as well as additional oxygen and nitrogen species.(132, 133) Phosphorus is a component of the aptamer's phosphate backbone, but is not present within the chemical structure of either DPP-DTT or GA. A phosphate peak in the P2p spectrum is expected to appear after aptamer functionalisation. Furthermore, aptamers are also rich in oxygen and nitrogen species, so a peak intensity in both O1s and N1s spectra is also expected to increase after aptamer functionalisation.(160)

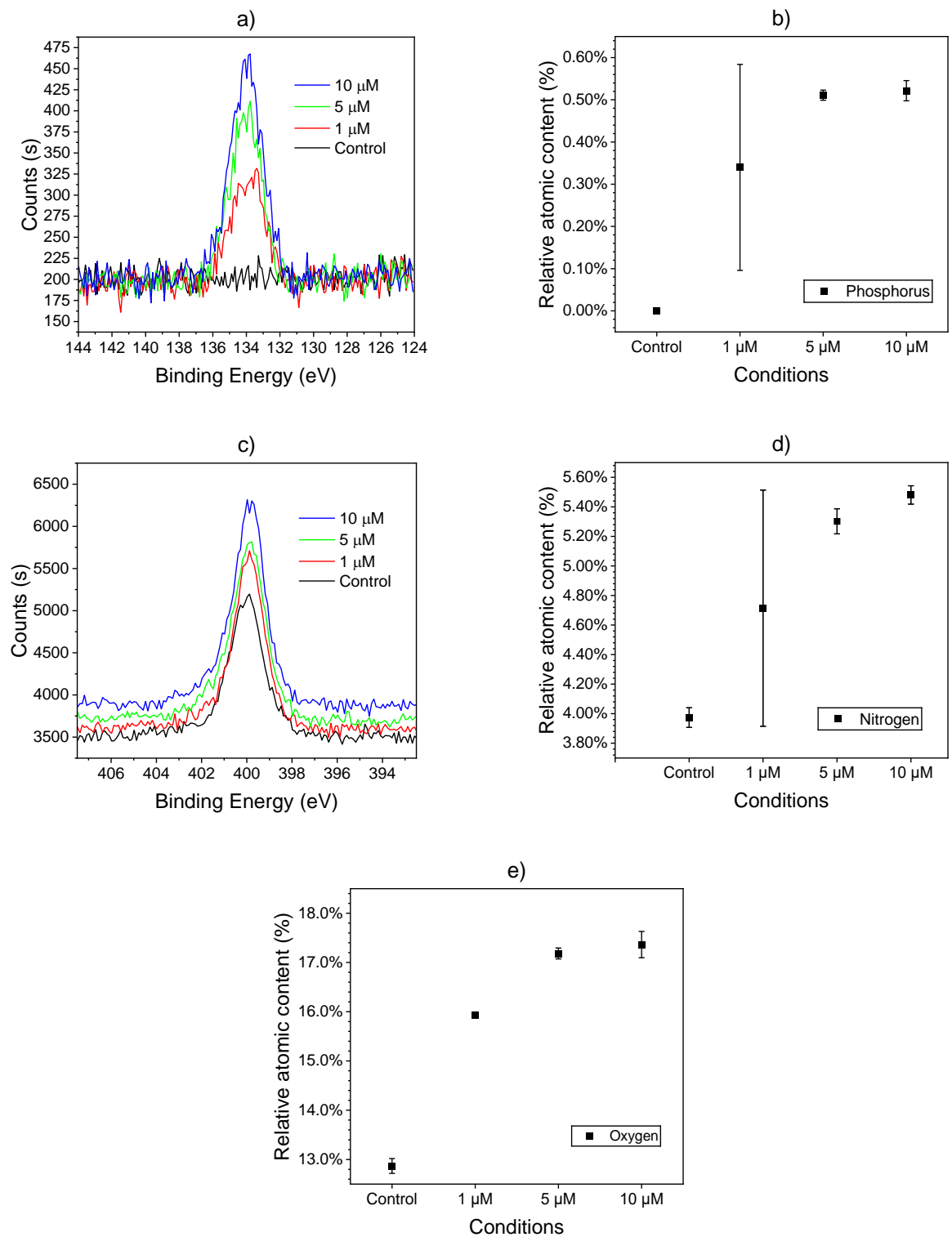


Figure 66 XPS high resolution scans (a) P2p and (c) N1s. Relative atomic content (%) (b) P2p, (d) N1s and (e) O1s. DPP-DTT:GA thin-films functionalised with NH₂-CBA (1 μM , 5 μM and 10 μM) and non-functionalised DPP-DTT:GA thin-film.

Phosphorus peaks in the overlaid P2p spectra, presented in Figure 66, a), are observed for NH₂-CBA incubated DPP-DTT:GA thin-films, indicating the presence of the aptamer on the surface. A P2p peak is absent in the non-functionalised DPP-DTT:GA thin-film. The intensity of the P2p peak increases as the aptamer concentration increases, this trend is also observed in the N1s spectra, presented in Figure 66, c). Due to oxygen from the SiO₂ layer contributing to the O1s spectra, increased peak intensity could not be distinguished. The atomic % of phosphorus on the functionalised DPP-DTT:GA thin-film surfaces is presented in Figure 66, b), with tabulated data presented in Table 63 (see appendix section 7.2.4). The atomic % was calculated relative to the high resolution CPS.eV of the other elements (C1s, O1s, N1s, S2p). The atomic % of phosphorus increases with increasing aptamer concentration until appearing to saturate at 10 μM. Increasing atomic percentage of nitrogen (Figure 66, d) and oxygen (Figure 66, e) with increasing aptamer concentration is similarly observed. The atomic percentage of oxygen was corrected for SiO₂ contribution. A saturation point at 10 μM is also evident in the atomic percentage of both nitrogen and oxygen spectra. Phosphorus, nitrogen and oxygen atomic percentages indicate that a saturation point is reached when a 10 μM aptamer concentration is utilised.

Further evidence of aptamer functionalisation was corroborated by water contact angle (WCA) measurements, which are presented in Figure 67. Details on WCA measurements are presented in section 2.3.7. WCA images and tabulated data are presented in Figure 126 and Table 60, respectively (see appendix section 7.2.2).

A decrease in WCA occurs between the non-functionalised (DPP-DTT:GA) and functionalised (1 μM, 5 μM, 10 μM) DPP-DTT:GA thin-films, with the surface becoming more hydrophilic. The hydrophilicity of the surface increases due to the hydrophilic phosphate backbone within the aptamer. A decrease in WCA indicates the aptamer is present on the DPP-DTT:GA thin-film surface. Further, WCA angle decreases as aptamer concentration increases. The DPP-DTT:GA thin-film incubated with 10 μM NH₂-CBA solution observed the lowest WCA, as well as the narrowest standard deviation. Indicating a higher aptamer density and more uniform surface coverage, relative to the 1 μM and 5 μM solutions.

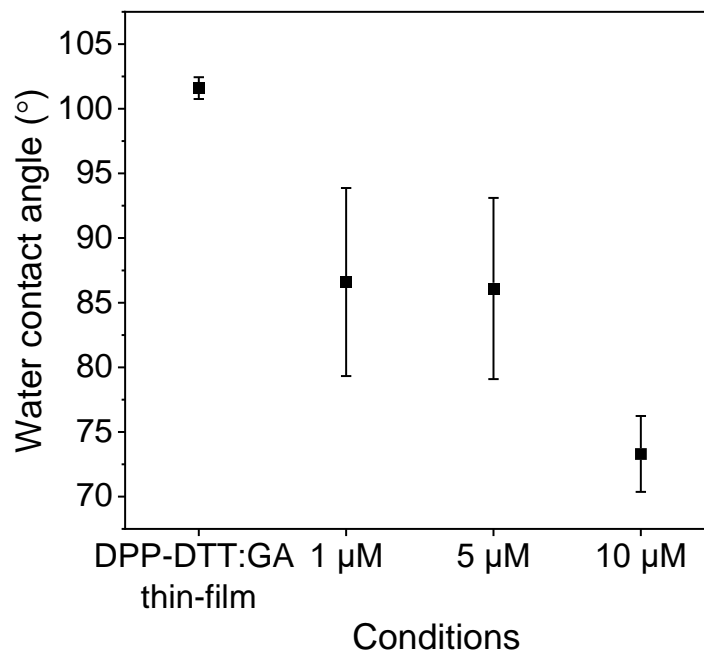


Figure 67 Water contact angles: DPP-DDT:GA thin-films functionalised with $\text{NH}_2\text{-CBA}$ (1 μM , 5 μM and 10 μM) and a non-functionalised DPP-DDT:GA thin-film.

Further evidence of aptamer attachment was investigated through a series of control studies. Several control thin-films were prepared including; a DPP-DDT thin-film incubated with 10 μM $\text{NH}_2\text{-CBA}$ (No GA), a DPP-DDT:GA thin-film incubated with Dulbecco's Phosphate-Buffered Saline (DPBS), and a DPP-DDT:GA thin-film incubated with an azide terminated cortisol binding aptamer ($\text{N}_3\text{-CBA}$). Control thin-films were compared to a DPP-DDT:GA thin-film incubated with 10 μM $\text{NH}_2\text{-CBA}$ (10 μM) and a non-functionalised DPP-DDT:GA thin-film (DPP-DDT:GA). P2p spectra are stacked vertically for ease of visualisation which is presented in Figure 68.

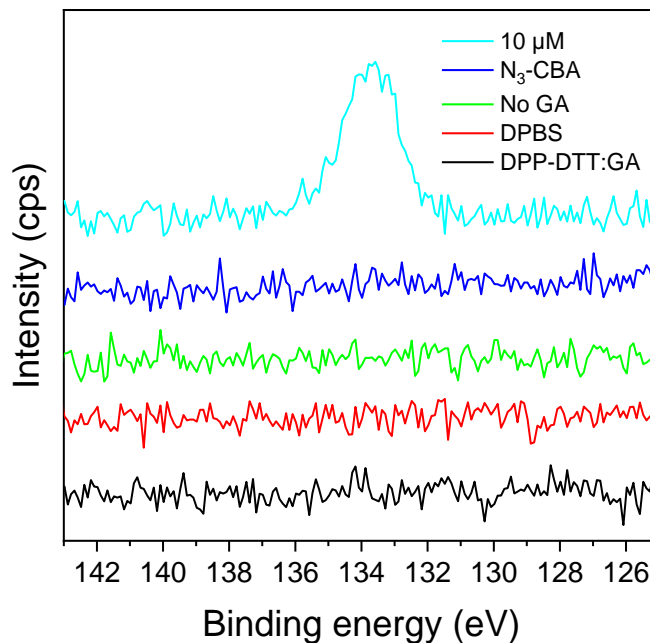


Figure 68 XPS high resolution P2p scans: DPP-DTT:GA thin-film functionalised with NH₂-CBA (10 μM) and DPP-DTT:GA thin-film functionalisation controls.

The absence of P2p peaks in the control scans is evident, indicating the absence of phosphorus on the thin-film surfaces. Only the DPP-DTT:GA thin-film incubated with 10 μM NH₂-CBA observed a P2p peak. The GA control indicates that GA is required to facilitate aptamer attachment to the thin-film surface. The absence of phosphorus in the N₃-CBA control spectra indicates several things. Firstly, the terminal amine group on the cortisol binding aptamer is required to facilitate the attachment of the aptamer to the thin-film surface. Secondly, interactions between GA and amine groups within the DNA bases are also mitigated. Finally, any potential physisorbed DNA on the thin-film surface is not significantly contributing to the P2p peak. The DPBS control indicates that residual DPBS isn't significantly contributing to the P2p peak. Control spectra provides further support that cortisol binding aptamers are attached to the DPP-DTT:GA thin-film surface.

The following section details a strategy for functionalising BGTC DPP-DTT:GA OFETs. After developing an aptamer functionalisation method, the influence of OFET fabrication was investigated. So far, bottom-gate top-contact (BGTC) organic field-effect transistors (OFETs)

have been explored within this thesis. A BGTC device architecture was utilised previously in chapter 3, with fabricated OFETs demonstrating comparable performances to reported values. Subsequently, the BGTC methodology was to be applied to fabricate DPP-DTT:GA OFETs. However, this fabrication procedure differs from that reported by Sun et al. Reported was the fabrication of bottom-gate top-contact (BGBC) OFETs, which were then functionalised with receptors.⁽¹⁶⁰⁾ Functionalisation of BGTC OFETs can potentially occur at two stages within the fabrication process, either before or after source-drain (S/D) deposition. Typically, BGTC OFETs are functionalised with receptors after S/D deposition.^(46, 133, 134, 147) This route avoids exposing biological receptors to elevated temperatures that are generated during the deposition process, which may denature receptors and disrupt receptor binding activity. However, if the area surrounding the aptamer functionalised thin-films was cooled during deposition, then receptor activity could be preserved. Considering this, aptamer functionalisation of DPP-DTT:GA OFETs was attempted before and after S/D deposition.

BGTC OFETs were fabricated using the following methods. DPP-DTT:GA thin-films were deposited onto ODTS modified Si/SiO₂ substrates as described in sections 2.2.4.2. ODTS modified Si/SiO₂ substrates were prepared as described in section 2.2.3. Gold (50 nm) source-drain electrodes were deposited using a combination of physical vapour deposition and shadow masking. Physical vapour deposition was performed as described in section 2.3.5. Source-drain electrodes with extended contact pads were utilised, to allow for improved accessibility during potential sensing channel experiments. Dimensional properties of the deposition mask are detailed in Figure 16 and Table 5 in methodologies section 2.1.3. Both OFETs functionalised before and after S/D deposition were incubated with aptamers using the methodology detailed in section 2.2.5.2.

XPS high resolution P2p and O1s scans were performed to confirm aptamer functionalisation on DPP-DTT:GA OFETs functionalised before S/D deposition (Before S/D) and after S/D deposition (After S/D). In addition, two controls were prepared and analysed: 1. A non-functionalised DPP-DTT:GA thin-film (DPP-DTT:GA) 2. A non-functionalised DPP-DTT:GA OFET

(DPP-DTT:GA S/D). P2p scans of the functionalised OFETs and controls are presented in Figure 69.

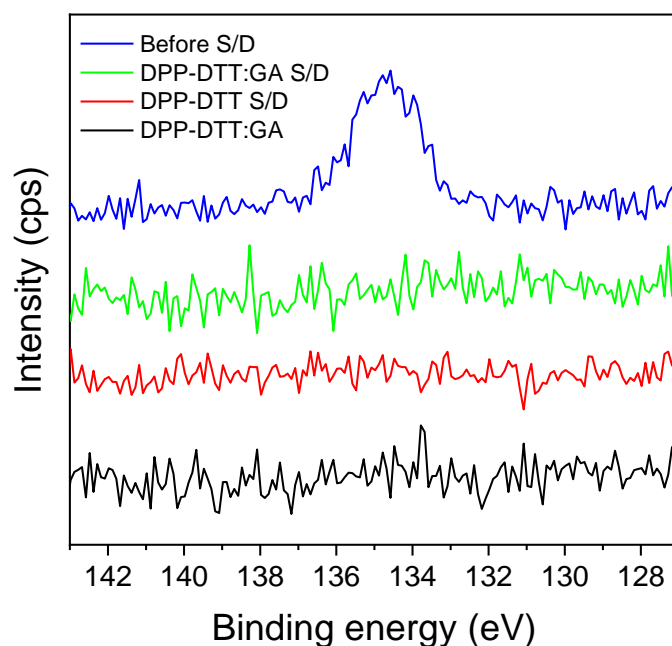


Figure 69 XPS high resolution P2p scans: DPP-DTT:GA OFET functionalised with $\text{NH}_2\text{-CBA}$ ($10 \mu\text{M}$) before S/D deposition (blue) and after S/D deposition (green). Non-functionalised DPP-DTT:GA OFET (red) and DPP-DTT:GA thin-film (black).

The DPP-DTT:GA OFET functionalised before S/D deposition was the only surface that observed a peak in the P2p scans. A P2p peak was not observed in the OFET functionalised after S/D deposition, suggesting that the deposition process inhibits the attachment of aptamers to the thin-film. A difference in XPS high resolution O1s scan peaks (Figure 70) of the functionalised DPP-DTT:GA OFETs before and after S/D deposition is observed. The characteristic O1s peak for DPP-DTT:GA is not observed for the functionalised DPP-DTT:GA OFET after S/D deposition. This suggests that GA is potentially removed from the DPP-DTT:GA thin-film surface during the S/D deposition process.

Functionalising before S/D deposition appears to negate this removal process, as the characteristic O1s peak is maintained. Aptamers are known for having higher thermal stability, relative to other biological receptors⁽²⁵⁰⁾. With the addition of being cooled during

S/D deposition aptamer binding ability may be preserved. However, verifying this claim could not be substantiated in time.

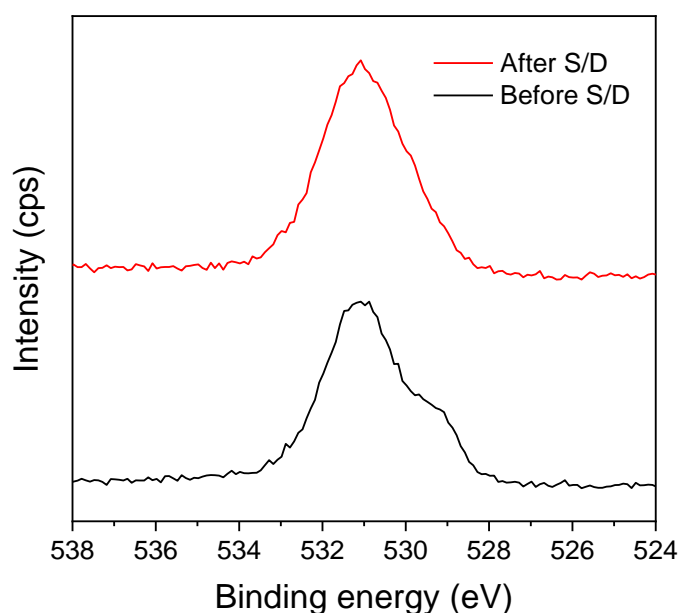


Figure 70 XPS high resolution O1s scans: DPP-DTT:GA OFET functionalised with $\text{NH}_2\text{-CBA}$ ($10 \mu\text{M}$) before S/D deposition (black) and after S/D deposition (red).

Further evidence of aptamer preservation on the DPP-DTT:GA OFET after S/D deposition was supported by water contact angle (WCA) and AFM measurements (Figure 71). WCA images and tabulated data are presented in Figure 127 and Table 61, respectively. AFM images and tabulated roughness data are presented in Figure 123 and Table 59, respectively. DPP-DTT:GA thin-films were analysed during the aptamer functionalisation and OFET fabrication processes. A non-functionalised DPP-DTT:GA thin-film OFET was fabricated as a comparison. Similar WCAs are observed between functionalised DPP-DTT:GA thin-films before and after S/D deposition. Whereas, the non-functionalised DPP-DTT:GA OFET observes a higher WCA than both functionalised thin-films. Similar WCAs between the functionalised thin-films suggests the aptamer is still present after S/D deposition. Similar evidence is observed in the AFM roughness values, where both functionalised DPP-DTT:GA thin-films observe comparative R_a and R_q values. Increase in roughness after aptamer functionalisation, can be expected. DNA deposited onto polymer and gold surfaces have reported increases in

roughness.(127, 251) Additionally, an increase in roughness was reported for the antibody functionalised DPP-DTT:GA thin-films.

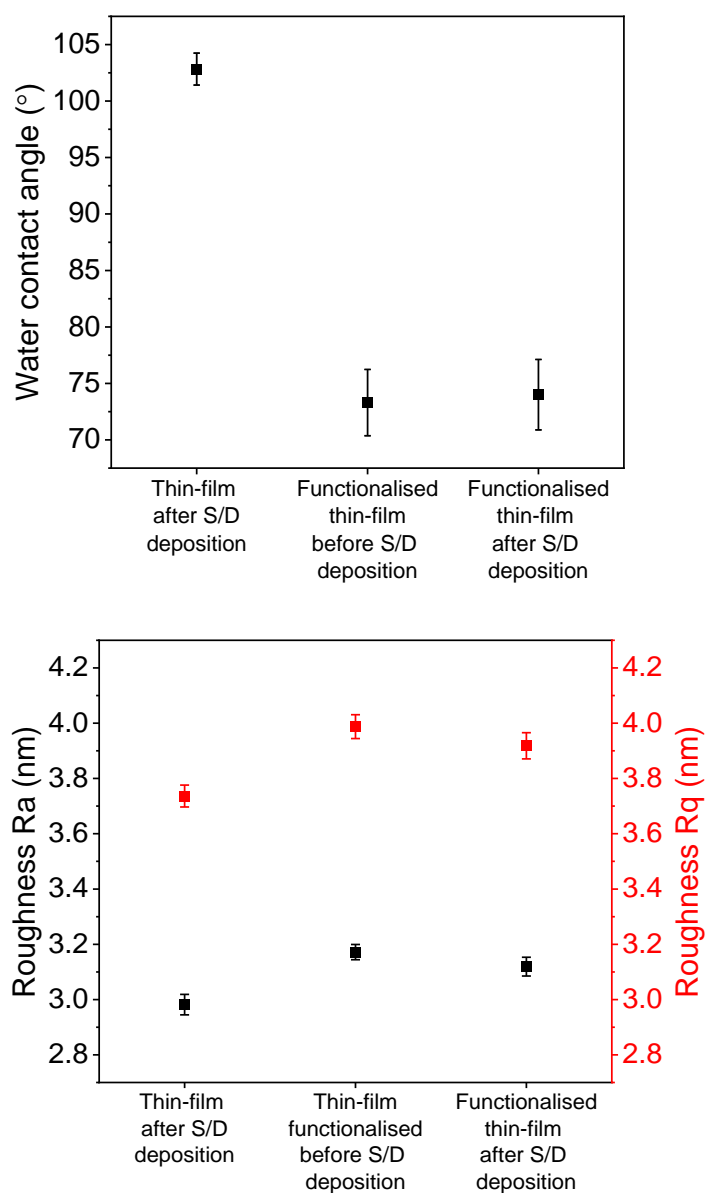


Figure 71 Water contact angles (left) and AFM roughness Ra and Rq values (right): DPP-DTT:GA thin-film functionalised with NH₂-CBA (10 μM) with measurements performed before and after S/D deposition. Compared to measurements of a non-functionalised DPP-DTT:GA thin-film after S/D deposition.

This section identified a method of functionalising DPP-DTT:GA OFETs with cortisol binding aptamers. The functionalisation strategy was optimal with a 10 μM NH₂-CBA solution,

determined through XPS and WCA measurements. XPS further identified that aptamer functionalisation of DPP-DTT:GA OFETs was possible if the performed before S/D deposition. The following section will characterise the functionalised DPP-DTT:GA OFETs.

4.5 Characterisation of aptamer functionalised DPP-DTT:GA OFET and the response to cortisol

The following section characterises aptamer functionalised DPP-DTT:GA OFETs to assess the performance for low-voltage sensing studies. Fabrication of aptamer functionalised DPP-DTT:GA OFETs and subsequent characterisation were performed with the following procedures. DPP-DTT:GA thin-films were deposited onto ODTS modified Si/SiO₂ substrates and functionalised with aptamers as described in sections 2.2.4.2 and 2.2.5.2, respectively. ODTS modified Si/SiO₂ substrates were prepared as described in section 2.2.3. Source-drain electrodes (gold 50 nm) were deposited using a combination of physical vapour deposition and shadow masking. Physical vapour deposition was performed as described in section 2.3.5. Source-drain electrodes with extended contact pads were utilised, to allow for improved accessibility of sensing channel with target analyte solution. Dimensional properties of the deposition mask are detailed in Figure 16 and Table 5 in section 2.1.3, respectively. OFET characterisation was conducted using the procedure described in section 2.3.4.

The deposition mask fabricates five source-drain electrode pairs with extended contact pads and variable channel lengths (30 μm , 40 μm , 50 μm , 60 μm and 80 μm). For clarity, data for the 40 μm channel length is presented. Transfer and output curves are presented in Figure 37. Hysteresis was monitored by sweeping the voltage forwards and backwards. OFET performance figures of merit extracted from the transfer characteristics are presented in Table 20.

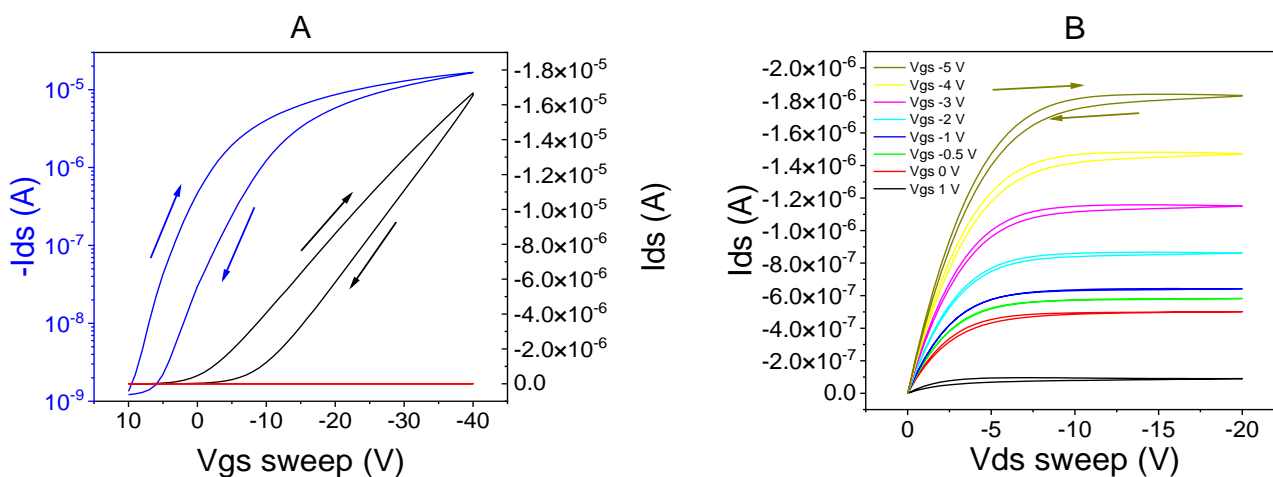


Figure 72 Transfer (A) and output (B) characteristics of BGTC configured aptamer functionalised DPP-DTT:GA OFET. Transfer characteristics measured in linear regime ($V_{ds} -10$ V), log scale (blue), linear scale (black) and gate current (red). DPP-DTT:GA OFET functionalised with $\text{NH}_2\text{-CBA}$ ($10 \mu\text{M}$) before 50 nm gold source-drain electrode deposition. $40 \mu\text{m}$ channel length measured.

Figure of merit	Linear regime
μ_{lin} ($\text{cm}^2 \text{V}^{-1} \text{s}^{-1}$)	0.147
V_{th} (V)	0.10
On/Off	1.4×10^4

Table 20 Transfer characteristic figures of merit of aptamer functionalised DPP-DTT:GA OFET. DPP-DTT:GA OFET functionalised with $\text{NH}_2\text{-CBA}$ ($10 \mu\text{M}$) before 50 nm gold source-drain electrode deposition. $40 \mu\text{m}$ channel length measured.

The OFET exhibits p-type behaviour in both the transfer and output characteristics. The OFET obtained a linear mobility (μ_{lin}) of $0.147 \text{ cm}^2 \text{V}^{-1} \text{s}^{-1}$, as well as a low threshold voltage of 0.10 V. Additionally, the OFET demonstrates an acceptable on/off ratio (1.4×10^4) and gate current ($\sim 10^{-10}$ A). The measured charge carrier mobility is lower than the reported value ($2.07 \text{ cm}^2 \text{V}^{-1} \text{s}^{-1}$) for a DPP-DTT:GA OFET, but is consistent with values measured from DPP-DTT OFETs in previous sections. The transfer and output characteristics observed hysteresis, though a comparison with reported characteristics can not be determined. Output curves demonstrate linear and saturation regions at low gate biases (V_{gs}), with the curves intersecting at $V_{ds} 0$ V indicating low contact resistance. The OFET performance metrics of the aptamer functionalised DPP-DTT:GA OFET demonstrate suitability for low-voltage sensing investigations, which are discussed in the following section.

4.5.1 Real-time response of aptamer functionalised DPP-DTT:GA

OFET to cortisol

After characterising the aptamer functionalised DPP-DTT:GA OFET, the sensing response to cortisol was investigated. Cortisol solutions were prepared in Tris-HCl buffer, as described in section 2.2.6. Tris-HCl buffer served as the sensing medium to preserve the binding ability of the aptamer, having previously proven effective for this specific aptamer sequence.^(150, 252) The aptamer functionalised DPP-DTT:GA OFET was biased at the gate electrode (V_{gs}) and drain electrode (V_{ds}) with voltage biases of -1 V and -0.5 V, respectively.

The real-time and normalised current response of the aptamer functionalised DPP-DTT:GA OFET to cortisol solutions (2 nM to 2 mM) is presented in Figure 73. Currents were normalised by dividing I_{ds} by the baseline current (I_0). I_0 is the initial current after bias-stress had reduced, the average of which was taken as the baseline. Increasingly concentrated solutions of cortisol were added to the sensing channel, at 5 minute intervals. Additionally, the responses to Tris-HCl buffer and Milli-Q (MQ) water are also presented. Initially, a continuous decrease in I_{ds} was observed, before plateauing at around 1300 s. The continuous decrease in I_{ds} is also observed before and after the addition of Tris-HCl buffer to the sensing channel (see appendix section 7.2.5, Figure 129). Decreasing I_{ds} during OFET operation is referred to as the bias-stress effect, which results in a negative shifting of the threshold voltage (V_{th}). Bias-stress is attributed to the prolonged application of the gate voltage bias (V_{gs}).⁽²⁵³⁾ To mitigate the bias-stress effect the OFET was biased for 25 minutes, before the addition of the cortisol solutions.⁽²⁵⁴⁾ After 25 minutes I_{ds} begins to plateau allowing for clearer sensing observations. Additionally, during this 25 minute period Tris-HCl buffer was added to the sensing channel at 5 minute intervals, in order to maintain an aqueous environment for the subsequent introduction of the cortisol solutions. The addition of Tris-HCl and cortisol solutions are marked by sharp fluctuations and recovery of I_{ds} , this is attributed to mechanical noise caused by solution pipetting.

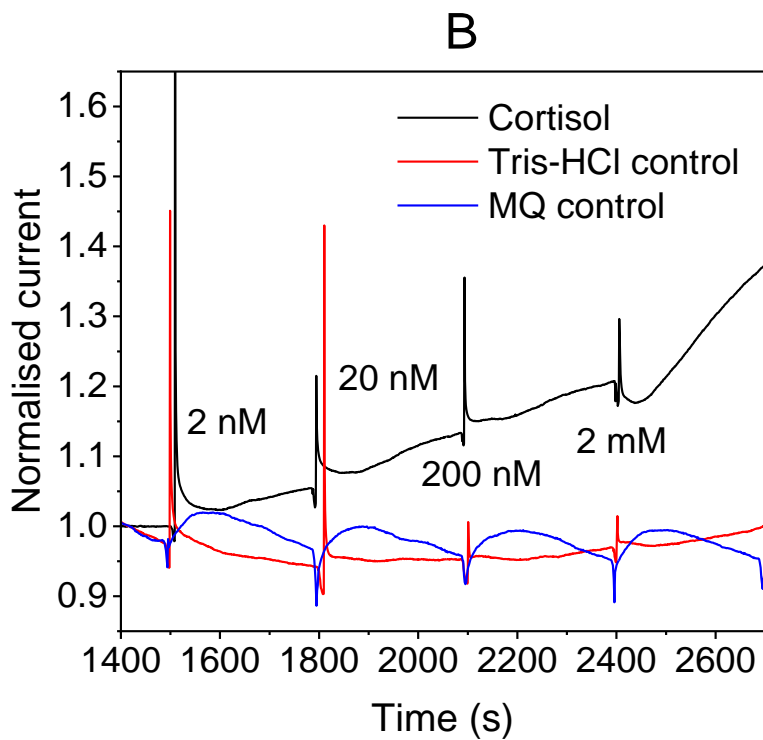
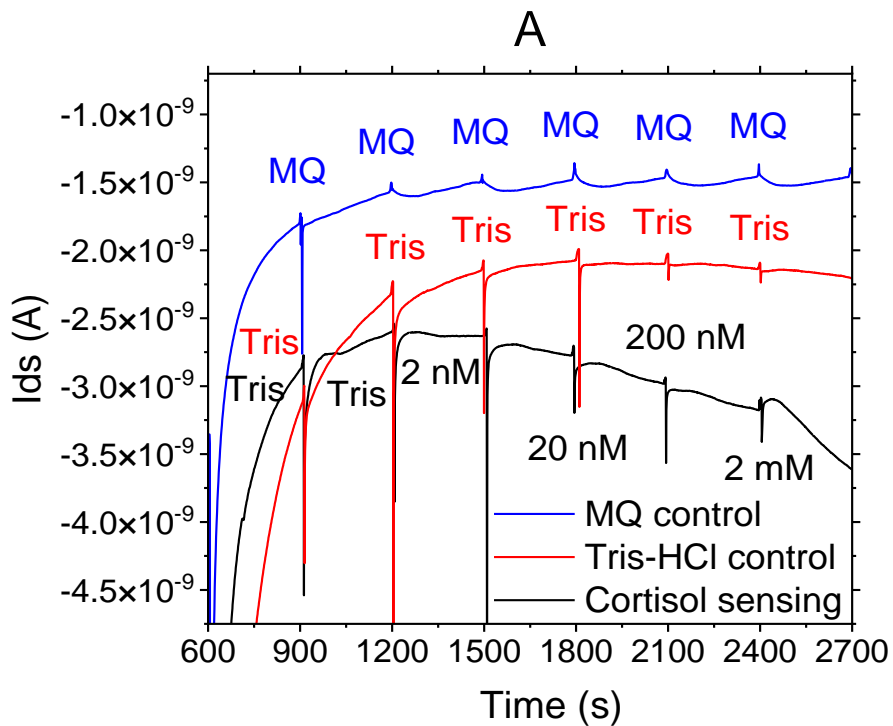


Figure 73 Real-time (A) normalised (B) current response of aptamer functionalised DPP-DTT:GA OFET to cortisol (2 nM to 2 mM). OFET biased at $V_{gs} -1$ V and $V_{ds} -0.5$ V. 40 μ m channel length measured.

After introducing cortisol to the sensing channel a gradual increase in the normalised current is observed. An increase in I_{ds} does not occur when only Tris-HCl or MQ water is added to the sensing channel. Instead, the normalised current for Tris-HCl and MQ water fluctuates around unity. Increasing current after the addition of cortisol to the sensing channel can be expected, with details of the sensing mechanism illustrated in Figure 74. The introduction of cortisol to the cortisol binding aptamer induces a conformational change upon binding, where the aptamer is positioned closer to the thin-film surface. The conformational change increases negative charge density closer to the thin-film surface. Positive charges are subsequently induced in the semiconductor by the increased negative charge density, manifested as an increase in current.^(46, 132) Considering cortisol is charge neutral under these conditions, changes in the current result from changes in aptamer conformation, which is corroborated by the absence of a comparable response in a non-functionalised OFET (see appendix section 7.2.5 Figure 130).⁽²⁵⁵⁾

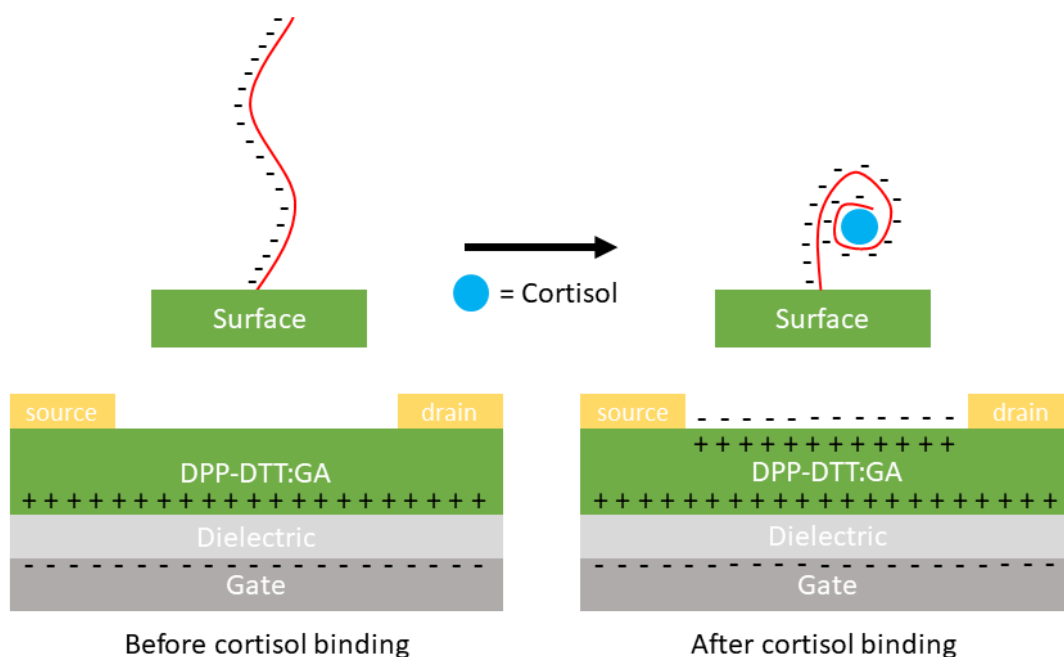


Figure 74 Aptamer functionalised DPP-DTT:GA OFET sensing mechanism. Cortisol introduction induces a conformational change in the cortisol binding aptamer, causing surface negative charge density to increase. Positive charges are induced in the DPP-DTT:GA layer, detected as an increase in current. Image adapted with permission from {M. L. Hammock, A. N. Sokolov, R. M. Stoltenberg, B. D. Naab, Z. Bao, Organic Transistors with Ordered Nanoparticle Arrays as a Tailorable Platform for Selective, In Situ Detection. ACS Nano. 6, 3100–3108 (2012)}. Copyright {2024} American Chemical Society.⁽¹³²⁾

Following this, the percentage change in current response to cortisol was determined. The percentage change in I_{ds} ($\Delta I/I_0$) was calculated and plotted against cortisol concentration, which is presented in Figure 75. $\Delta I/I_0$ was calculated for each cortisol concentration using Equation 13:

$$\text{Equation 13} \quad \Delta I/I_0 = \frac{|I-I_0|}{I_0} \times 100 \%$$

Where I is the drain current (I_{ds}) after 300 s had elapsed. I_0 is the initial current (I_{ds}) plateau after bias stress effect had reduced, the average of which is taken as the baseline value (I_0). (150)

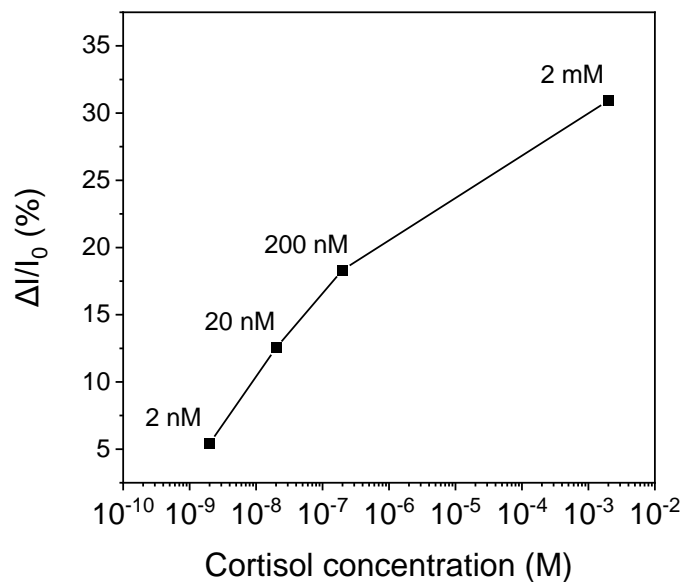


Figure 75 $\Delta I/I_0$ (%) vs. cortisol concentration (M) sensing response of aptamer functionalised DPP-DTT:GA OFET to cortisol (2 nM to 2 mM). OFET biased at V_{gs} -1 V and V_{ds} -0.5 V. 40 μm channel length measured.

A change in $\Delta I/I_0$ is observed across the cortisol concentration range, with $\Delta I/I_0$ increasing as concentration increases. A response to a 2 nM cortisol solution suggests the OFET can detect cortisol below physiological ranges found in sweat (51.4 nM to 3.0 nM) and blood (690 nM to 55 nM). (256)

The response to cortisol is promising but remains preliminary, as issues were encountered regarding the repeatability of the biosensing OFET. Reproducing the sensing response under identical conditions was not successful. Similarly, a response was not observed after regenerating the cortisol bound aptamers by incubating the sensing channel with an 8 M urea solution. Urea has been previously reported effective at unbinding cortisol from aptamers, enabling the reuse of the biosensor.(257) Additionally, adjacent aptamer functionalised source-drain electrodes (50 μm and 60 μm) were investigated, as well as the fabrication of additional devices, but a response was not observed. More control experiments are also required to validate the selectivity and specificity of the biosensing OFET. Unfortunately, these controls could not be conducted on the cortisol responsive channel due to degradation of the source-drain electrodes from subsequent testing.

Furthermore, the stability of the imine group (Schiff base) formed during aptamer attachment to the thin-film surface, can be questioned under aqueous sensing conditions. Imine formation, between the amine terminated aptamer and aldehyde in glutaraldehyde, is a reversible reaction and in the presence of an aqueous buffer can be hydrolysed back into amine and aldehyde groups.(258) The reaction reversibility suggests the aptamer can become detached from the channel during sensing measurements, and removed entirely after washing steps. The issue is further compounded from a competitive reaction between the amine group in Tris-HCl and the regenerated aldehyde, fully displacing the aptamer. Detachment and removal of the aptamer from the channel between washing stages would explain why the observed sensing response was not repeatable.

Mitigating this in future work can be addressed through two options. Firstly, a different aqueous buffer, that doesn't contain amine groups (e.g. PBS), should be used when preparing the cortisol solutions.(158) Secondly, the imine group can be converted into an amine by using the reducing agent sodium cyanoborohydride (NaCNBH_3), through reductive amination. Reduction of the imine group into an amine stabilises the bond anchoring the aptamer to the sensing channel surface, preventing aptamer detachment and removal.(259)

4.5.2 Transfer characteristic response of aptamer functionalised DPP-DTT:GA OFET to cortisol

In addition to investigating the real-time response of an aptamer functionalised DPP-DTT:GA OFET, the influence of cortisol on the transfer characteristics was also investigated. A significant advantage of OFETs is that multiple parameters (μ , V_{th} and I_{on}) can be used to determine sensing responses, which are extracted from the transfer characteristics. Sun et al., immobilised antibodies on the surface of DPP-DTT:GA thin-films and measured a positive change in the threshold voltage (V_{th}), achieving a detection limit of 65 fM.

Transfer characteristics were measured by sweeping the gate voltage (V_{gs}) from 10 V to -40 V, with a drain-source voltage bias (V_{ds}) of -10 V. The transfer characteristics of the OFET were repeatedly measured until consecutive transfer curves overlapped, to obtain a stable baseline. Following this, Tris-HCl buffer and cortisol solutions were pipetted onto the sensing channel and incubated for 10 minutes. The sensing channel was then rinsed with MQ water (5 s) and dried with nitrogen (30 s). Afterward, the transfer characteristics of the OFET were measured and compared with the baseline, wherein changes to charge carrier mobility (μ), threshold voltage (V_{th}) and I_{on} current were determined. Transfer characteristics of the baseline and incubated sensing channel are presented in Figure 76. Sensing parameters μ , V_{th} and I_{on} current extracted from the transfer characteristics are presented in Figure 77.

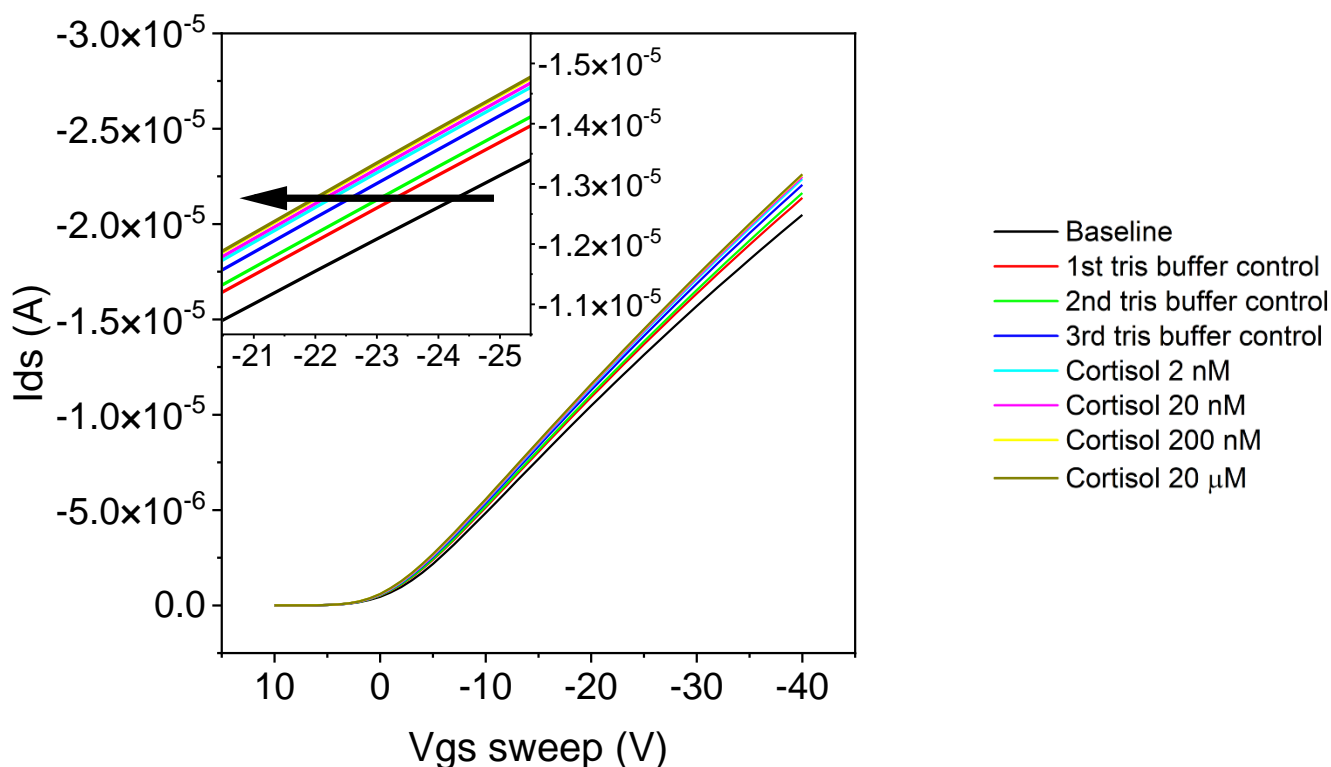


Figure 76 Transfer characteristic response of an aptamer functionalised DPP-DTT:GA OFET to Tris-HCl and cortisol (2nM to 20 μ M) incubation. OFET Vgs bias swept from 10 to -40 V, Vds biased at -0.5 V. 40 μ m channel length measured.

The sensing channel was first incubated with Tris-HCl buffer, before incubating with cortisol solutions. Tris-HCl buffer incubation was repeated successively three times, to determine if the transfer characteristics deviated from the initial baseline. A consistent change in both V_{th} and I_{on} current is observed after each Tris-HCl incubation, with V_{th} increasing and I_{on} current decreasing. Tris-HCl evidently influenced the sensing channel, and while this effect could have been mitigated, a discernible change in V_{th} or I_{on} current after cortisol incubation could not be distinguished. Further, the μ remained comparatively stable after Tris-HCl incubation, making it a more suitable metric for cortisol sensing. However, a significant change in μ is not observed after incubating with cortisol solutions.

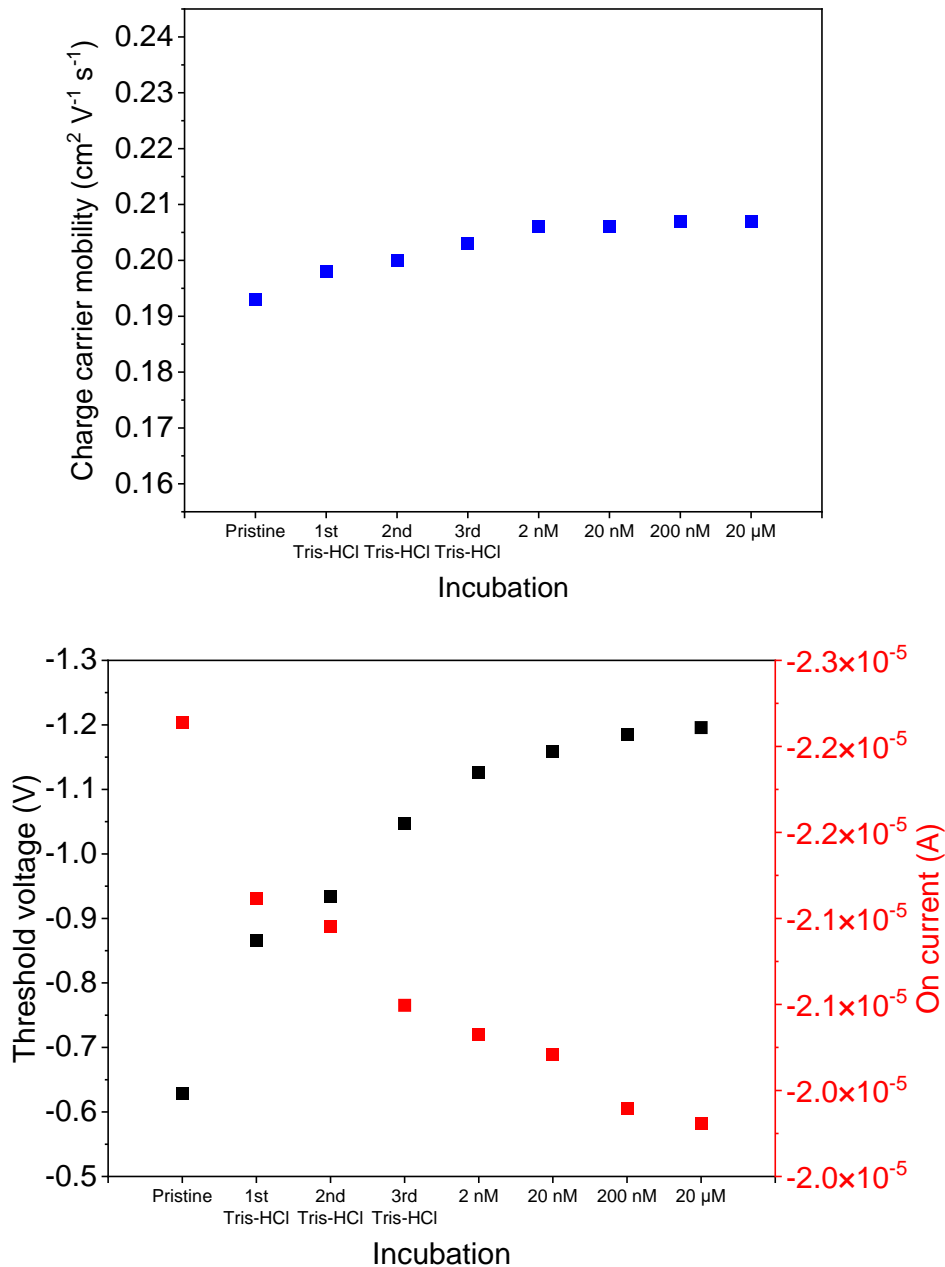


Figure 77 (top) Charge carrier mobilities (blue) and (bottom) threshold voltages (black) and on currents (red) of an aptamer functionalised DPP-DTT:GA OFET to Tris-HCl and cortisol (2nM to 20 mM) incubation. OFET V_{gs} bias swept from 10 to -40 V, V_{ds} biased at -0.5 V. 40 mm channel length measured.

The sensing strategy was reportedly effective with antibodies, however the applicability for aptamers can be questioned. Wang et al., reported that gate voltage can influence the local electronic environment of aptamers. Further stating that sweeping the gate voltage can

modulate the aptamer conformation, thereby releasing the target analyte.(260) Transfer characteristics of an aptamer functionalised metal oxide FET were measured by Nakatsuka et al., to detect a range of target analytes, using a mV gate voltage sweeping range. Considering this, the gate voltage sweep (10 to -40 V) utilised may have exceeded the limit tolerable to the aptamer, inducing a conformational change and affecting negative surface charge density. However, this was not investigated further.

4.5.3 Stabilising DPP-DTT:GA OFET sensitivity via source-drain electrode modification

The following section highlights efforts at stabilising the bias-stress effect and improving OFET sensitivity, through modification of the source-drain (S/D) electrodes with molybdenum trioxide (MoO_3) and silicon monoxide (SiO).

Bias-stress driven instability was previously observed in real-time cortisol sensing experiments (see section 4.5.1). Which was observed as a continuous decrease in drain current upon constant gate (V_g) and drain (V_{ds}) electrode biasing of the DPP-DTT:GA OFET. Bias-stress is assigned to the trapping of charge carriers (holes) during OFET operation, resulting in a continuous decrease in current and a negative shift in threshold voltage (V_{th}). Sources of charge traps from multiple OFET sites have been identified, including: intrinsic defect states in the organic semiconductor layer, surface states at the organic semiconductor/dielectric interface, water penetration into the organic semiconductor layer and minority charge carrier (electrons) injection from the drain electrode.⁽⁶⁷⁾ Several solutions have been identified at mitigating bias-stress instabilities, including: SAM modification of the dielectric surface⁽⁹⁰⁾, addition of molecular additives to organic semiconductor⁽²⁶¹⁾, OFET encapsulation ⁽²⁶²⁾ and source-drain contact modification⁽⁷²⁾. The latter was identified as an appropriate solution to integrate into the OFET. MoO_3 has been previously used to modify the S/D contacts in DPP-DTT OFETs.^(72, 263) S/D contacts were modified with a MoO_3 layer (5 nm – 15 nm), which was inserted between the DPP-DTT thin-film and Au contact. The modified S/D contacts were able to suppress electron injection from the negatively biased drain electrode, by imposing a greater energy barrier. Electron injection suppression reduced electron trapping during OFET operation, which consequently reduced bias-stress.

Reduction of the bias-stress effect was realised by depositing a layer of molybdenum trioxide (MoO_3) between the DPP-DTT:GA thin-film and the gold S/D electrodes. DPP-DTT:GA thin-films were deposited onto ODTs modified Si/ SiO_2 substrates as described in section 2.2.4.2. ODTs modified Si/ SiO_2 substrates were prepared as described in section 2.2.3. Molybdenum

trioxide (5 nm) and gold (50 nm) were deposited through physical vapour deposition, which was performed as described in section 2.3.5. AFM images confirmed the combined thickness (55.9 nm) and alignment of the MoO₃:Au layer (see appendix section 7.2.1, Figure 124). Transfer and output characteristics of the DPP-DTT:GA modified MoO₃ OFET were performed using the procedure described in section 2.3.4.

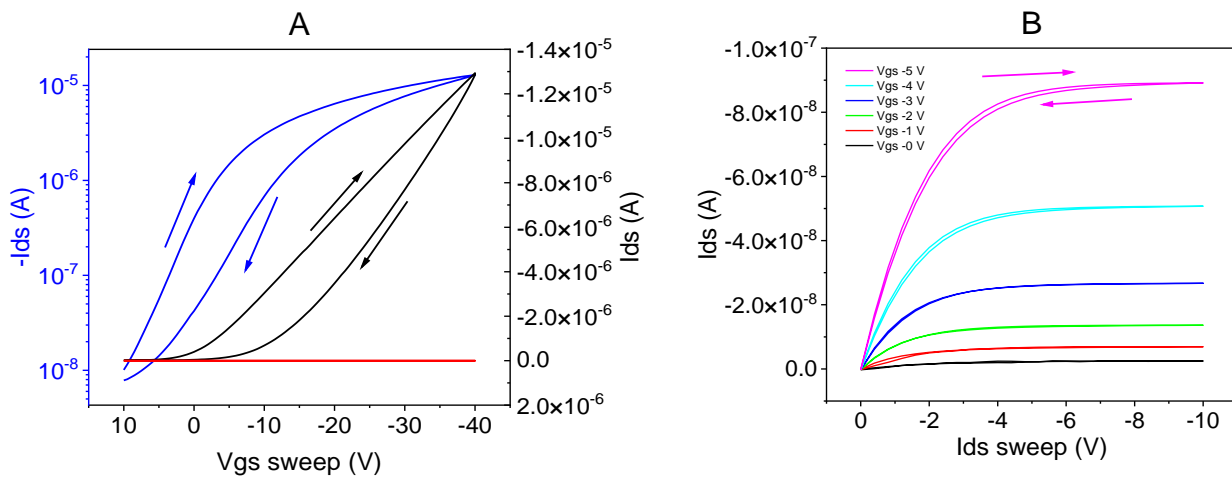


Figure 78 Transfer (A) and output (B) characteristics of BGTC configured DPP-DTT:GA OFET modified with MoO₃. Transfer characteristics measured in linear regime (V_{ds} -10 V), log scale (blue), linear scale (black) and gate current (red). Source-drain electrode deposition layers: MoO₃ (5 nm) and Gold (50 nm). 40 μm channel length measured.

Threshold voltage V	-0.73
$\mu \text{ cm}^2 \text{ V}^{-1} \text{ s}^{-1}$	0.173
On/Off	1.7E+03

Table 21 OFET performance metrics V_{th}, μ and on/off ratio of DPP-DTT:GA OFET modified with MoO₃.

OFET characteristics and performance metrics V_{th}, μ and on/off ratio are presented in Figure 78 and Table 21, respectively. The OFET with MoO₃ layer observes comparable performance metrics to DPP-DTT:GA OFETs seen previously. However a decrease in I_{ds} in the output curves is observed, potentially due to the quality of the MoO₃ layer interfacing with the thin-film. Following this the effects on bias-stress in current vs. time studies were investigated. The OFET was biased with V_g -1 V and V_{ds} -1 V, for 5 minutes. The drain current was measured

and then normalised to the initial starting current, for MoO₃ unmodified (No MoO₃) and modified (MoO₃) OFETs (Figure 79).

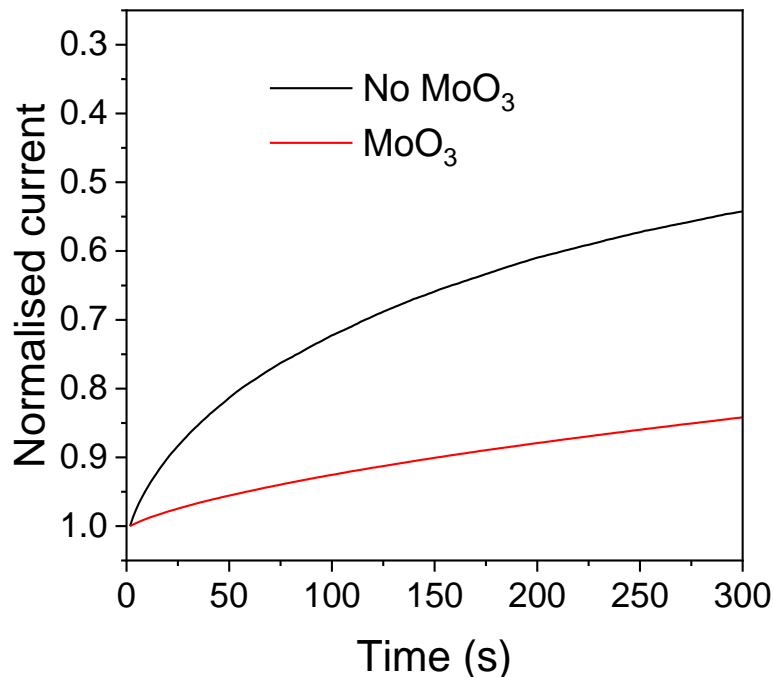


Figure 79 Normalised currents of BGTC configured MoO₃ modified (red) and unmodified (black) DPP-DTT:GA OFETs. OFETs biased at V_{gs} -1 V and V_{ds} -0.5 V. 40 μm channel length measured.

A difference in the normalised currents is demonstrated between the MoO₃ modified and unmodified OFETs. The OFET with MoO₃ observes a stabler drain current over time, relative to the OFET without MoO₃. Indicating that MoO₃ is suppressing electron injection from the drain electrode into the DPP-DTT:GA thin-film. Reducing electron injection reduces charge trapping during OFET operation, leading to a reduction in bias-stress and stabler drain current. Further optimisation of the MoO₃ layer thickness may reduce the impact of bias-stress, however this can only be minimised so much as other sources are still potentially inducing this effect.

Further efforts were made to improve the sensitivity of the DPP-DTT:GA OFET, through passivation of the gold source-drain (S/D) electrodes with silicon monoxide. (SiO references) The gold source-drain (S/D) electrodes were passivated with silicon monoxide to form an

insulating layer between the gold layer and the aqueous buffer solution. Insulating with silicon monoxide would allow the OFET to operate at greater drain (V_{ds}) voltage biases. In turn increasing device sensitivity, without the S/D electrodes degrading from exceeding the electrochemical window of the aqueous buffer solution.(133) Additionally, insulation of the electrodes has been reported to lower signal noise caused by target analyte interactions.(147)

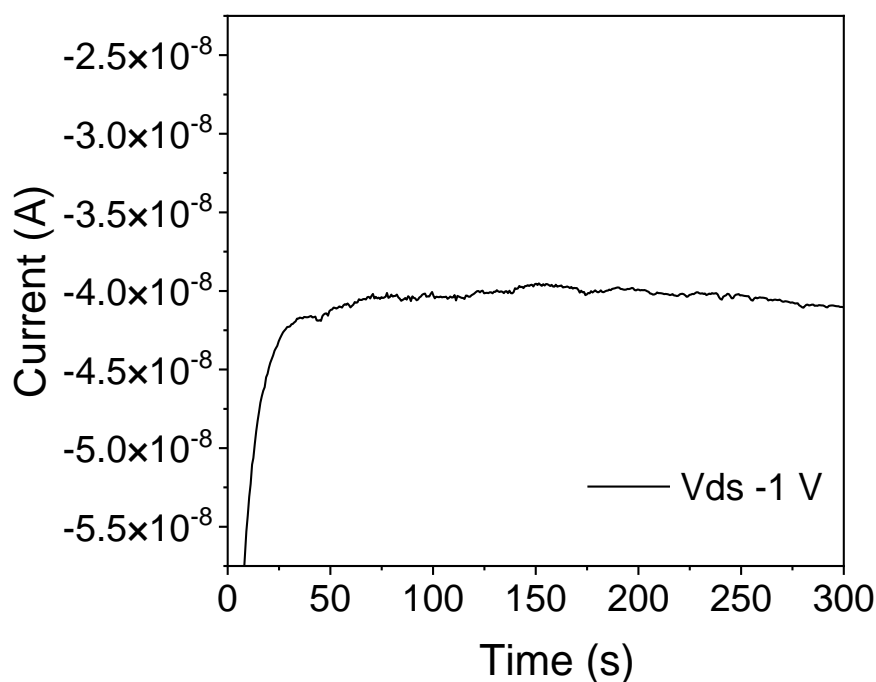


Figure 80 Real-time current of a DPP-DTT:GA OFET modified with SiO. Source-drain electrode deposition layers: Gold (50 nm) and SiO (50 nm). OFET biased at V_{gs} -1 V and V_{ds} -0.5 V. 40 μm channel length measured and exposed to aqueous buffer.

DPP-DTT:GA thin-films were deposited onto ODTs modified Si/SiO₂ substrates as described in section 2.2.4.2. ODTs modified Si/SiO₂ substrates were prepared as described in section 2.2.3. Gold (50 nm) and silicon monoxide (50 nm) were deposited by physical vapour deposition, which was performed as described in section 2.3.5. Source-drain electrodes with extended contact pads were utilised. AFM images confirmed the combined thickness (100 nm) and alignment of the Au:SiO layers (see appendix section 7.2.1, Figure 125). Aqueous buffer solution was deposited onto the sensing channel before OFET biasing, with the solution overlapping the silicon monoxide insulated S/D electrodes. Subsequently, the DPP-DTT:GA

OFET was biased with V_g -1 V and V_{ds} -1 V, for 5 minutes (see Figure 80). The OFET observes stable operation in an aqueous environment during biasing. Insulation of the S/D electrodes with silicon monoxide seems effective at operating the OFET at biases outside the electrochemical window of the aqueous buffer solution.

Initial efforts at reducing the bias-stress effect and improving device sensitivity were successful. Reduction of the bias-stress effect was realised by inserting a 5 nm layer of MoO_3 , between the DPP-DTT:GA thin-film and the Au S/D electrodes. The MoO_3 layer was effective at reducing the bias-stress during OFET operation, mitigating the continuous decrease in drain current. Efforts to increase OFET sensitivity during real-time current response studies, were conducted by insulating the S/D electrodes with silicon monoxide. Insulation of the S/D electrodes allowed the DPP-DTT:GA OFET to operate at higher V_{ds} voltage biases, while exposed to an aqueous environment. However, combining the two methods into an OFET and determining the improvement to the sensing response could not be completed in time.

4.6 Summary and conclusion

In summary, this chapter explores the fabrication and characterisation of an aptamer functionalised biosensing OFET. Building on the OFET fabrication work discussed in chapter 3, a receptor functionalisation strategy that did not compromise OFET performance was identified. The adapted functionalisation methodology involved blending the high performance DPP-DTT polymer with the small molecule glutaraldehyde (GA).

The thin-film forming properties of an established DPP-DTT:GA (9:1) in chlorobenzene (5 mg mL⁻¹) blend were investigated via spin coating. Optimised thin-film deposition conditions were determined, with resulting DPP-DTT:GA thin-films displaying suitable thickness and morphology. Following this, a strategy for attaching aptamers (specific to cortisol) to DPP-DTT:GA thin-films was developed and qualified by epifluorescence microscopy. Aptamer functionalisation was facilitated by a condensation reaction, occurring between amine terminated aptamers and GA aldehyde groups blended within the thin-film surface. A combination of XPS and WCA measurements were performed to further optimise the aptamer functionalisation strategy, by varying the aptamer concentration. Furthermore, by monitoring the thin-film surface during OFET fabrication, it was revealed that aptamer functionalisation could not occur after source-drain electrode deposition. However, the successful fabrication of aptamer-functionalized DPP-DTT:GA OFETs could only be verified when the aptamer attachment occurred before S/D deposition.

Characterisation of the aptamer functionalised DPP-DTT:GA OFET confirmed its suitability for low-voltage sensing applications, with the blending of GA facilitating aptamer attachment without impeding OFET performance. Subsequently, the biased OFET demonstrated a preliminary real-time current response to a physiological relevant range of cortisol concentrations. Minor controls supported the observation, however further validation of the sensing response is required. Additionally, reducing OFET bias-stress and increasing OFET drain voltage bias under aqueous conditions were realised through the modification of source-drain contacts with MoO₃ and SiO, respectively.

Overall, a promising biosensing platform has been fabricated. However, more experiments are required to replicate the sensing response, as well as to further validate the specificity of the biosensor. The reversibility of the imine group formed during aptamer attachment may introduce reproducibility problems during aqueous sensing experiments. Reducing the imine into an amine through reductive amination with sodium cyanoborohydride should be explored, in order to stabilise the bond anchoring the aptamer to the sensing channel surface. Preparation of the cortisol solutions in an alternative buffer (e.g. PBS) that doesn't contain competitive amine groups should also be investigated. Implementation of the as discussed source-drain contact modifications could also improve the real-time current response. Furthermore, attempts should be made to explore the versatility of the biosensing platform with aptamers specific to other target analytes. Additionally, replacing glutaraldehyde with small molecule aromatic aldehydes may improve device performance by intercalating with the DPP-DTT polymer and enhance charge transport.

5 Investigation of chemically modified organic semiconducting materials for aptamer functionalisation and organic transistor fabrication

5.1 Acknowledgments

The author would like to acknowledge the following researchers for contributing to this work. Dr Raymundo Marcial Hernandez for synthesising the N₃-DPP polymer. Dr Christina Kousseff for synthesising the DTP-C4-acid material.(264) Epifluorescence microscopy images were captured by Caoimhe O'Neill at Queen Mary University.

5.2 Introduction

So far, the research chapters within this thesis have focused on methods of introducing chemical binding sites to DPP-DTT thin-films for receptor attachment, either through plasma treatment or small molecule blending. Alternative approaches involving the chemical modification of established materials are also reported, endowing them with exploitable chemical functionalities for receptor attachment.

Organic semiconducting materials are renowned for their chemical tuneability, providing advantages in tailoring and directing their properties towards specific applications. Chemical modification of materials can induce many beneficial properties, both physical and electrical. Tunable physical properties of organic semiconductors include solubility(265), environmental stability(46) and adhesiveness(266). Chemical modification is also influential on the materials' electrical properties, which can affect the charge transport mode (electronic and ionic)(267, 268), type of charge carrier transported (electrons and holes)(269), as well as OFET performance metrics (charge carrier mobility)(270). Additionally, added chemical functionalities enable crosslinking within thin-films.(271)

In the context of sensing, chemical modification of organic semiconductors serves two purposes. Firstly, it can endow the material with sensing capabilities, enabling the detection of specific analytes. Secondly, it can facilitate the attachment of receptors to the material during the biosensor fabrication process. An example of the former was reported by Minamiki et al., fabricating an electrolyte-gated field-effect transistor incorporating an organic semiconducting polymer P3CPT, a derivative of P3HT containing carboxylic acid groups. The chemically modified material was capable of detecting biogenic amines, such as histamine, achieving a limit of detection of 1.6 mM.(131)

For facilitating receptor attachment, a small yet effective toolkit of chemical groups is available, with azide(156), alkyne(272), and carboxylic acid groups(158, 273) as notable examples. Li et al. reported a derivative of the high performing material DPP-DTT, which was chemically modified to contain azide functional groups (N_3 -DPP).(155) Several polymers were synthesised through the copolymerisation of DPP monomers containing branched alkyl chains or linear alkyl chains terminated with azide groups, with the monomer ratios and alkyl chain lengths varied. The synthesised N_3 -DPP polymers were interesting as they maintained charge carrier mobilities similar to the original DPP-DTT polymer ($> 0.1 \text{ cm}^2 \text{ V}^{-1} \text{ s}^{-1}$). The N_3 -DPP polymer labelled C10-10a, copolymerised with 10 % azide DPP monomers containing a ten-carbon alkyl linker, demonstrated a versatile range of applications through post-synthesis modifications. Multiple alkyne-modified functional groups could be clicked onto the azide end groups, mediated through copper-catalysed azide-alkyne cycloaddition click chemistry. Attachment could also occur in solution or on the thin-film surface. The attached functionalities could increase thin-film biocompatibility, enable photopatterning via UV-activated interchain cross-linking or facilitate bioconjugation with receptors. An OECT material was also synthesised, by copolymerising the azide-functionalised DPP monomer with a glycolated 2,2'-bithiophene monomer. The fabricated OECT was functionalised with enzymes specific to glucose and was capable of detecting glucose at 1 μM .

The azide-modified DPP-DTT polymer shows opportunity for expansion, through aptamer functionalisation and operation as a biosensing OFET. Modifying the material with azide

groups enabled the attachment of different functional units, broadening its range of applications. However, the reported functionalisation method utilises a copper catalyst, which is a known cytotoxin that can damage DNA.(274) Instead, the attachment could be achieved through copper-free click chemistry, which uses a strain-promoted azide-alkyne click reaction, eliminating the need for a copper catalyst. A reported example of this has been used to attach DNA to a derivative of P3HT terminated with an azide group.(275) Additionally, an undertested (potentially due to its solubility) N₃-DPP polymer containing twice as many azide groups was also synthesised, labelled C10-20a (Figure 81). The material afforded equivalent OFET charge carrier mobilities, while providing more potential receptor attachment sites. For these reasons the C10-20a material should be explored for aptamer functionalisation and OFET fabrication.

The organic semiconductor dithieno[3,2-b:2',3'-d]pyrrole (DTP) has been extensively modified with chemical groups for organic electronic applications in OFETs, OLEDs and OPVs.(276, 277) Alkynylated DTP derivatives have been reported to facilitate the attachment of a range of functionalities to deposited thin-films, mediated through azide click chemistry.(272, 278) A novel dithieno[3,2-b:2',3'-d]pyrrole derivative containing a carboxylic acid moiety (DTP-C4-acid) has been synthesised within the Nielsen research group. The carboxylic acid group within the DTP-C4-acid makes it a viable material for exploring functionalisation strategies with aptamers, as similar DNA attachment strategies have been reported.(147) Deposition of the material through electropolymerisation and subsequent aptamer functionalisation, would result in the fabrication of a biosensing OECT.(163)

The following chapter is divided into two sections, each investigating a derivative of an existing material containing a known chemical functional group exploitable for receptor functionalisation. The first material is a reported derivative of DPP-DTT containing azide moieties (N₃-DPP), while the second is a novel derivative of dithieno[3,2-b:2',3'-d]pyrrole containing a carboxylic acid moiety (DTP-C4-acid) which can be polymerised into polydithieno[3,2-b:2',3'-d]pyrrole (PDTP-C4-acid). Structures of the two polymers are presented in Figure 81.

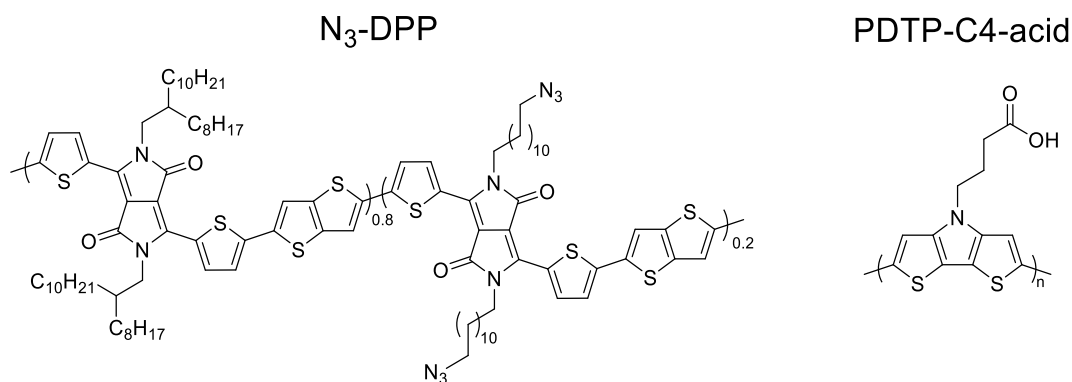


Figure 81 Chemical structures of N₃-DPP polymer and polydithieno[3,2-b:2',3'-d]pyrrole acid (PDTP-C4-acid).

The opening section presents research on the N₃-DPP polymer. Initially, the thin-film deposition methodology is optimised, with the morphology and surface chemistry characterised. Following this, a strategy for attaching aptamers to the thin-film surface through a strain-promoted azide-alkyne click chemistry reaction is explored. An N₃-DPP OFET is fabricated using previously identified methodologies within this thesis and the suitability of the OFET for low-voltage biosensing applications is discussed.

The final section presents research investigating the small molecule DTP-C4-acid. First, electrodeposition of the DTP-C4-acid as a polymer thin-film is explored, with the morphology and surface chemistry of the deposited thin-film characterised. A strategy of exploiting the carboxylic acid groups on the thin-film surface for the attachment of aptamers is explored through EDC/NHS coupling chemistry. A proof of concept OECT is fabricated on a flexible substrate, which is further characterised and the suitability of the OECT for low-voltage biosensing applications is discussed.

5.3 Investigation of N₃-DPP polymer for functionalisation and use in OFET devices

5.3.1 N₃-DPP polymer thin-film deposition

Optimisation of the N₃-DPP thin-film deposition process was initially investigated. The reported N₃-DPP polymer solution deposition conditions were initially explored, where N₃-DPP in chlorobenzene (5 mg mL⁻¹) was spin coated (1,000 rpm, 60 s) onto ODTs modified Si/SiO₂ substrates. However, issues were encountered when replicating these established deposition conditions. The synthesised N₃-DPP polymer was poorly soluble in chlorobenzene, resulting in a transparent solution containing undissolved masses of polymer. The poor solubility was attributed to the higher molecular weight of the N₃-DPP polymer (M_n 50.6 kDa, M_w 54.7 kDa, PDI 1.08) relative to the reported N₃-DPP polymer (20 % azide monomer) (M_n 15 kDa M_w 19 kDa, PDI 1.3). Additionally, the resulting N₃-DPP polymer solution adhered poorly to ODTs modified Si/SiO₂ substrates. Consequently, a spin-coated thin-film could not be obtained.

Initial deposition problems were resolved using a combination of probe tip sonication to prepare a homogenous N₃-DPP polymer solution and the floating film transfer (FFT) method to transfer the thin-films onto ODTs modified Si/SiO₂ substrates. Probe tip sonication is commonly used for exfoliating 2D materials, such as graphene and MoS₂, from bulk powder in solution.^(279, 280) The 2D material layers are kept together by van der Waals forces making them challenging to disperse and isolate in solution. The solubility of donor-acceptor polymers such as N₃-DPP, are influenced by intermolecular forces with π - π stacking contributing significantly. Additionally, reducing the number of solubilising branched alkyl chains within the polymer, with azide terminated linear alkyl chains, will exacerbate the solubility difficulties. The proposed probe tip sonication conditions (see section 2.3.7) utilized were suggested by Dr Raymundo Marcial Hernandez from The Nielsen Lab group. After sonication, the N₃-DPP in chlorobenzene (5 mg mL⁻¹) polymer solution was opaque and free

from undissolved masses of polymer, indicating more of the polymer had dissolved into solution.

N₃-DPP thin-films were deposited using the FFT method and transferred onto ODTs modified Si/SiO₂ substrates, the conditions used are described in section 2.2.4.3. ODTs modified Si/SiO₂ substrates were prepared as described in section 2.2.3. Morphological attributes relating to thin-film thickness and roughness were monitored with AFM (see section 2.3.1), with topographical AFM images of the N₃-DPP thin-film presented in Figure 82. The thin-films exhibit smooth morphologies with sizeable areas of homogeneity. Regions of polymer chain alignment could not be identified, which were exhibited by DPP-DTT thin-films deposited by the FFT method.

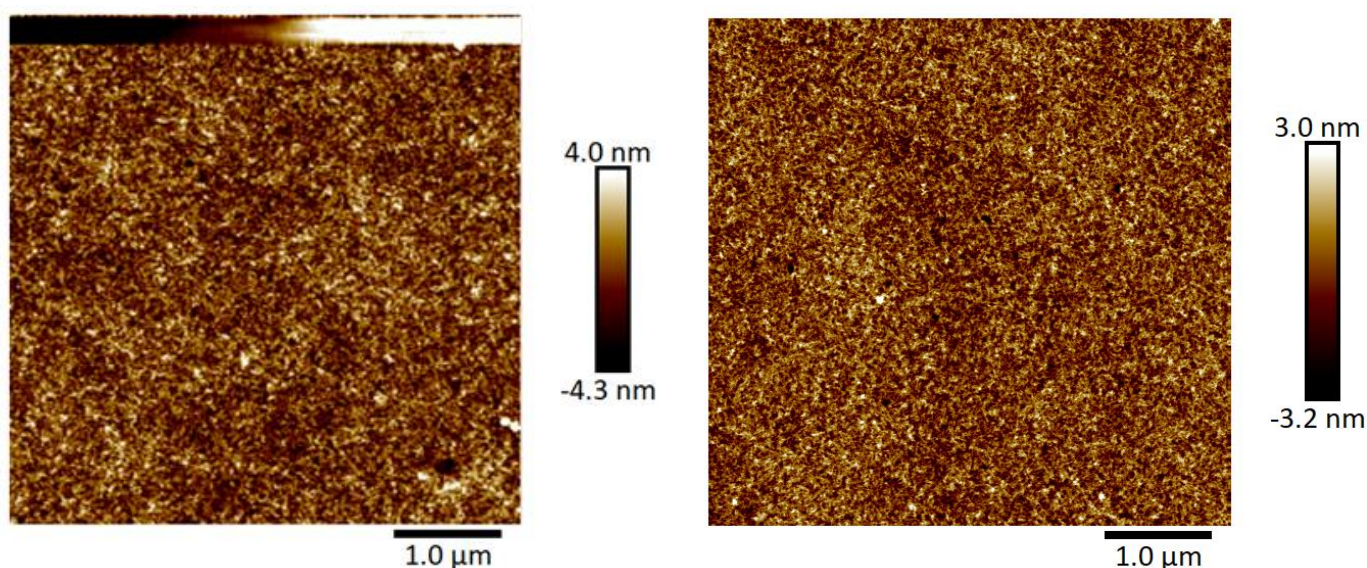


Figure 82 AFM topological images (5 μm x 5 μm) of N₃-DPP thin-films via FFT from chlorobenzene (5 mg mL⁻¹) on ODTs modified Si/SiO₂ substrate. N₃-DPP polymer solution probe tip sonicated before deposition.

Average roughness values Rq 0.99 nm ± 0.021 nm and Ra 0.78 nm ± 0.016 nm, as well as average thin-film thickness of 15.5 nm ± 0.54 nm were determined for the N₃-DPP thin-films. Tabulated roughness data is presented in Table 64 (see appendix section 7.3.1). AFM images and tabulated data relating to thin-film thickness are presented in Figure 131 and Table 65 (see appendix section 7.3.1), respectively. The average thickness of the N₃-DPP thin-films obtained via FFT were thinner than the reported thickness range (30 – 40 nm). However, as

discussed previously the thinner thickness is advantageous for biosensing OFETs. Roughness values for the N₃-DPP thin-film were not reported, so a direct comparison could not be made. Though, the roughness values are similar to those obtained for DPP-DTT thin-films deposited via FFT, as mentioned in section 3.3.1. In summary, a method of depositing N₃-DPP polymer thin-films with suitable morphology and thickness for incorporation into biosensing OFETs has been developed. Probe tip sonication was used to form a homogenous N₃-DPP polymer solution. N₃-DPP thin-films were deposited via the FFT method and transferred onto ODTS modified Si/SiO₂ substrates.

5.3.2 Aptamer functionalisation of N₃-DPP polymer thin-film

In order to demonstrate the exploitability of the azide groups on N₃-DPP thin-film surfaces, a functionalisation strategy for attaching cortisol binding aptamers (CBA) was investigated. The adapted strategy is illustrated in Figure 83, with the procedure detailed in section 2.2.5.3. Aptamer attachment was facilitated by a strain-promoted azide-alkyne click reaction between surface azide groups and dibenzocyclooctyne (DBCO), with DBCO attached to the terminal end of the cortisol binding aptamer strand (DBCO-CBA). The strategy differs from the reported N₃-DPP polymer functionalisation method, which used a copper catalyst to catalyse the azide-alkyne cycloaddition reaction. Copper catalysts are known cytotoxins that can interact and damage DNA, this is prevented by using DBCO and avoids further contaminating the thin-film surface.⁽²⁷⁴⁾ N₃-DPP thin-films were deposited onto ODTs modified Si/SiO₂ substrates as described in section 2.2.4.3. ODTs modified Si/SiO₂ substrates were prepared as described in section 2.2.3. X-ray photoelectron spectroscopy (XPS) was conducted and resulting spectra processed using methodology detailed in section 2.3.2. Five scans were collected using a 400 μm X-ray spot size.

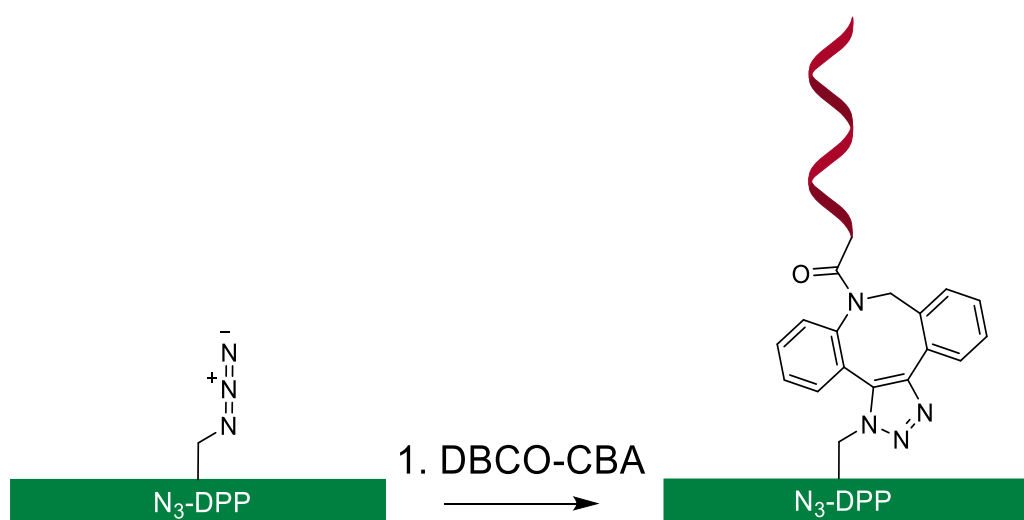


Figure 83 Aptamer attachment strategy of N₃-DPP thin-film: 1. Incubation with DBCO-CBA solution in DPBS (1 μM), then sequentially washed with 0.1 % tween20 solution and MQ water.

XPS analysis began by confirming the azide groups on the N₃-DPP thin-film surface. A high resolution N1s spectrum was run to determine the nitrogen environment, which is presented

in Figure 84. Two peaks are seen in the N1s spectrum, which are fitted with three components labelled N1s, N1 azide and N2 azide. N1 azide and N2 azide are attributed to azide nitrogen atoms, while N1s is attributed to the nitrogen atoms within the DPP core. The azide component peak at the highest binding energy (~404 eV) is assigned to the central electron deficient nitrogen (N2) and the two lateral nitrogen atoms (N1) are assigned to the peak at a lower binding energy (~401 eV).⁽²⁸¹⁾ The azide group is observable in the N1s spectrum and therefore present on the thin-film surface.

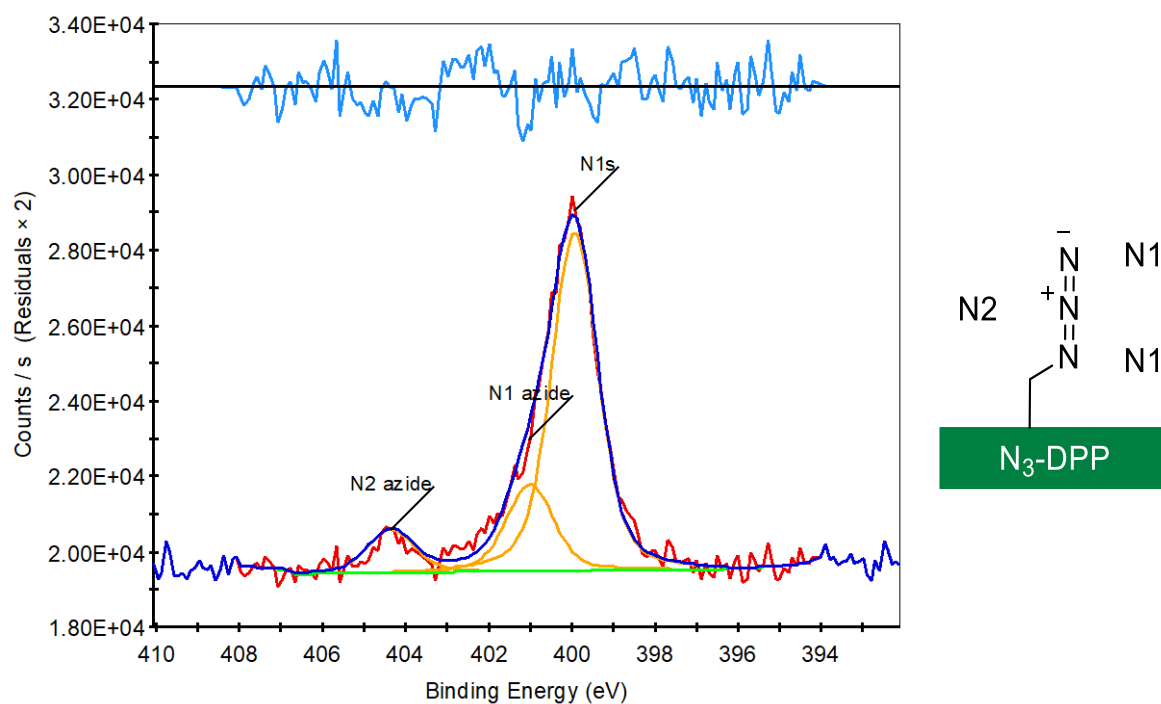


Figure 84 (left) XPS high resolution N1s scans (No. scans = 5, scan size = 400 μm): N₃-DPP thin-film via FFT from chlorobenzene (5 mg mL⁻¹) on ODTs modified Si/SiO₂ substrate. (red) N1s experimental curve (dark blue line) Peak fitted curve (orange lines) Component peaks (green line) Background (light blue line) residual (right) N₃-DPP thin-film with N1 and N2 labelled azide nitrogens.

The atomic % of the different nitrogen species determined by XPS, were compared with the expected atomic % for the synthesised N₃-DPP polymer (Table 22). Synthesis of the N₃-DPP polymer involved the copolymerisation of alky-DPP and azide-DPP monomers at a respective 80:20 ratio. The polymer is expected to contain an 80:20 ratio of these monomers, but due to the controllability of copolymerisation the actual monomer ratios could vary from the

expected. The actual atomic % of the azide group agrees closely with the expected, suggesting the N₃-DPP copolymer contains the expected ratio of azide monomers.

Nitrogen species	Expected average nitrogen atom ratio	Expected nitrogen atomic %	Actual nitrogen atomic %
N DPP	2.0	62.5	64.0
N1 azide	0.8	25	24.0
N2 azide	0.4	12.5	12.0

Table 22 Nitrogen ratios of N₃-DPP 80:20 copolymer. Expected nitrogen atomic % and actual nitrogen atomic % determined from XPS high resolution N1s scans.

Following the confirmation of the azide functionality on the N₃-DPP thin-film surface DBCO-CBA functionalised N₃-DPP thin-films were analysed via XPS and water contact angle (WCA) measurements (Figure 85). High resolution P2p scans were run to identify phosphorous on the thin-film surface, an indicator of the DNA aptamer strand. A control N₃-DPP thin-film was incubated with a DNA strand that did not contain an azide functionality (Cy3-comp-CBA). Additionally, an N₃-DPP thin-film was incubated with DBCO-CBA and hybridised with a strand that is complimentary to the cortisol binding aptamer strand (DBCO-CBA + Cy3-comp-CBA). A non-functionalised N₃-DPP thin-film was also prepared (N₃-DPP). A phosphorous peak can be seen for the DBCO-CBA functionalised thin-film, indicating the presence of the aptamer. However, a phosphorous peak is also observed for the Cy3-comp-CBA incubated thin-film. However, the intensity of the DBCO-CBA thin-film peak is greater than the Cy3-comp-CBA thin-film, indicating Cy3-comp-CBA was physically adsorbed onto the surface. The intensity of the DBCO-CBA + Cy3-comp-CBA hybridised thin-film is greater than the other thin-films, which is expected after successful hybridisation of the DNA strands.

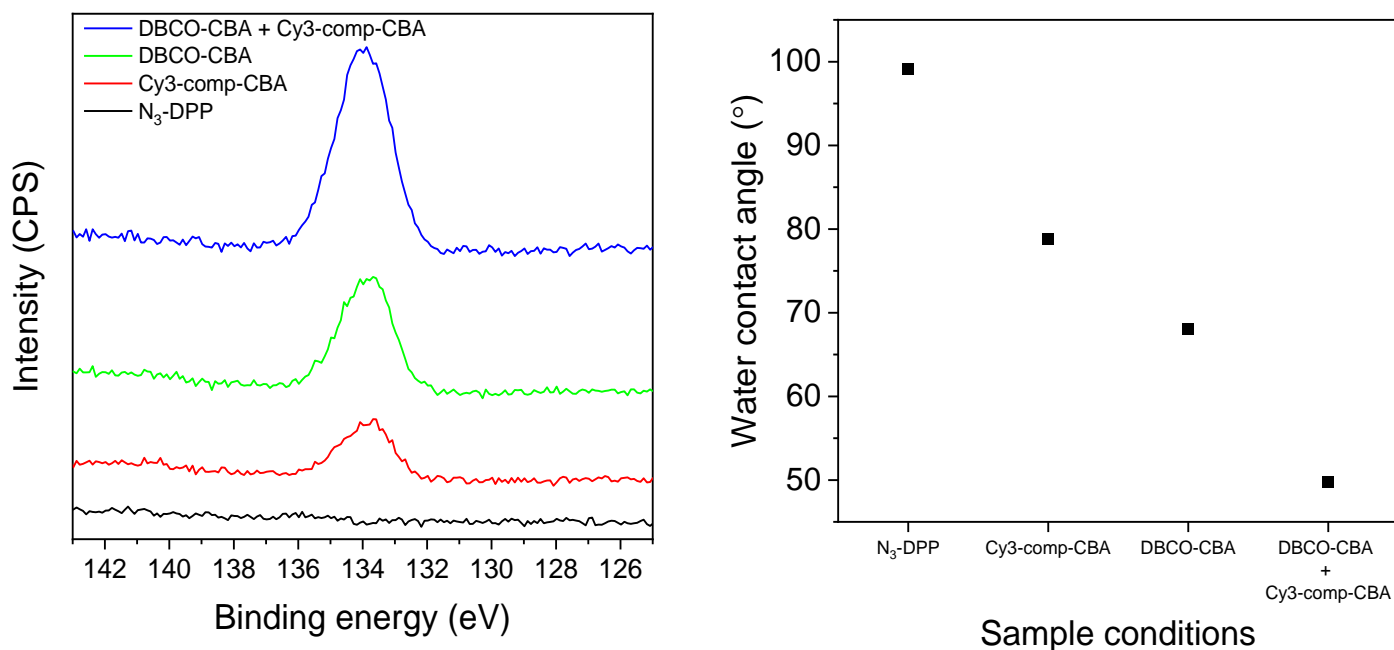


Figure 85 XPS high resolution P2p scans (top) and water contact angles (bottom) of N₃-DPP thin-films incubated with Cy3-comp-CBA, DBCO-CBA and DBCO-CBA + Cy3-comp-CBA.

XPS observations were additionally qualified by WCA measurements (Figure 85). WCA images and tabulated data are presented in Figure 132 (see appendix section 7.3.2). The WCA of the non-functionalised N₃-DPP thin-film was determined to be 99.1°, which is reasonable as it is close to the reported WCA of the 10% N₃-DPP polymer (98°).⁽¹⁵⁵⁾ The WCA decreases between the non-functionalised and Cy3-comp-CBA incubated N₃-DPP thin-films, suggesting that physical adsorption of Cy3-comp-CBA is occurring. The WCA decreases further for the DBCO-CBA functionalised thin-film, as well as for the DBCO-CBA + Cy3-comp-CBA hybridised thin-film. Suggesting binding of the aptamer strand to the N₃-DPP thin-film is occurring.

5.3.3 Characterisation of N₃-DPP OFET

The following section characterises an N₃-DPP OFET to assess the performance for applications in low-voltage biosensing studies. Fabrication and subsequent characterisation of the N₃-DPP OFET were performed with the following procedures. An N₃-DPP thin-film was deposited onto an ODTS modified Si/SiO₂ substrate, using floating film transfer methods described in sections 2.2.4.3 and 2.2.3. Source-drain electrodes (gold, 50 nm) were deposited using a combination of physical vapour deposition and shadow masking. Physical vapour deposition was performed as described in section 2.3.5. Dimensional properties of the deposition mask are detailed in Figure 15 and Table 4 in section 2.1.3. OFET characterisation was conducted using the procedure described in section 2.3.4. Transfer and output curves are presented in Figure 86, with OFET performance figures of merit extracted from the transfer characteristics presented in Table 23.

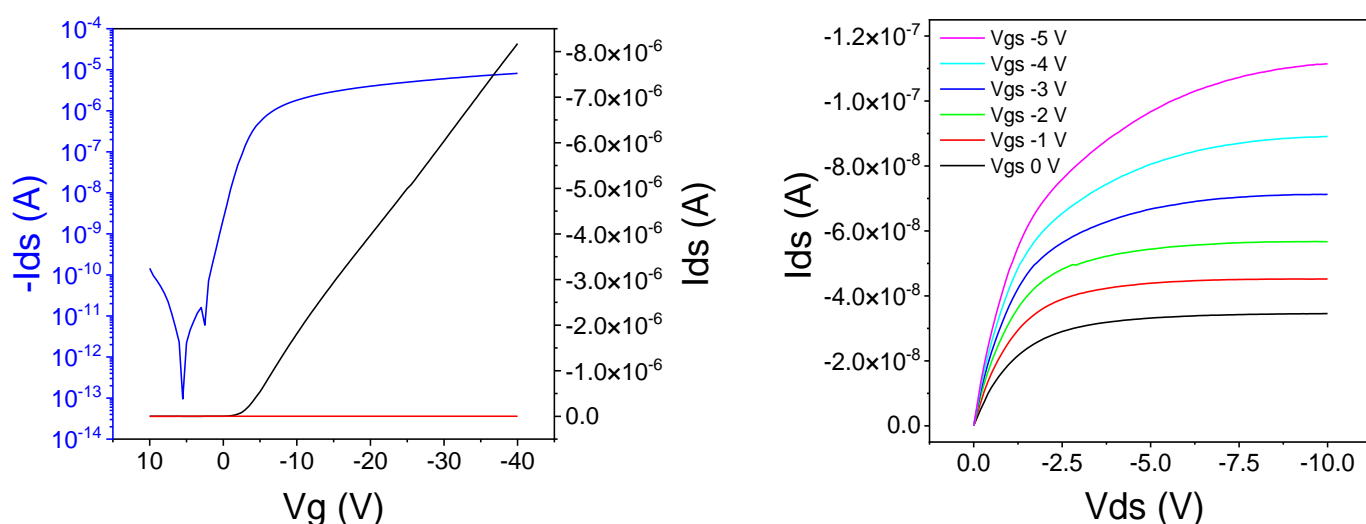


Figure 86 Transfer (left) and output (right) characteristics of BGTC configured N₃-DPP OFET. Transfer characteristics measured in linear regime ($V_{ds} -1$ V), log scale (blue), linear scale (black) and gate current (red). N₃-DPP thin-film via FFT from CB (5 mg mL^{-1}) on ODTS modified Si/SiO₂, with 50 nm gold deposited source-drain electrodes. $50 \mu\text{m}$ channel length measured.

Figure of merit	Linear regime
μ_{lin} (cm ² V ⁻¹ s ⁻¹)	0.05
Threshold voltage (V)	-0.98
On/Off	8.6x10 ⁷

Table 23 Transfer characteristic figures of merit of an N₃-DPP OFET. N₃-DPP thin-film via FFT from CB (5 mg mL⁻¹) on ODTs modified Si/SiO₂, with 50 nm gold deposited source-drain electrodes. 50 μm channel length measured.

The OFET exhibits p-type behaviour in both the transfer and output characteristics. The OFET afforded a linear mobility (μ_{lin}) of 0.05 cm² V⁻¹ s⁻¹ and a threshold voltage of -0.98 V. Additionally, the OFET demonstrates a high on/off ratio (8.6x10⁷) and low gate current (~x10⁻¹⁰ A). The measured charge carrier mobility is lower than the reported value (0.29 cm² V⁻¹ s⁻¹) for a N₃-DPP OFET, which is also lower than values determined for DPP-DTT OFETs in previous sections. A lower mobility can be expected for a chemically modified material based off an existing high performing material, such as DPP-DTT. However, the charge carrier mobility isn't the determining factor in the overall sensing capabilities of a biosensing OFET, as examples of biosensing OFETs with lower mobilities are reported.(282) Therefore, the measured mobility of the N₃-DPP OFET is acceptable for exploring biosensing applications, but performances such as sensitivity may be reduced. Output curves demonstrate linear and saturation regions at low gate biases (V_{gs}), with the curves intersecting at V_{ds} 0 V indicating low contact resistance. The OFET performance metrics of the N₃-DPP OFET demonstrate suitability for low-voltage sensing investigations. However, due to problems later encountered with the deposition of the N₃-DPP thin-films, further experiments could not be continued. Instead of forming a continuous large-area film, the N₃-DPP thin-film would spread across the liquid substrate surface and then quickly disintegrate. The small thin-film fragments could be stamped onto a substrate, although it was assumed the discontinuous morphology of the film would not function in an OFET. Attempts at reoptimising the FFT conditions were made, but a large-area film could not be produced. It's speculated that the N₃-DPP polymer degraded over time, due to the reactivity of the azide groups. The material was stored in ambient conditions, which may have accelerated degradation. Regardless, improving the stability of the material is something to be explored.

5.4 Investigation of a novel DTP carboxylic acid polymer for aptamer functionalisation and OECT devices

5.4.1 Aptamer functionalisation of PDTP-C4-acid thin-films

PDTP-C4-acid thin-film deposition on ITO

The following section explores the deposition and aptamer functionalisation of DTP-C4-acid. Thin-films of DTP-C4-acid were initially required before aptamer functionalisation strategies could be investigated, as well as incorporating DTP-C4-acid into an OECT. In its present form DTP-C4-acid exists as a small molecule (see Figure 87), but can be deposited as a polymer thin-film (PDTP-C4-acid) through a method of electropolymerisation known as chronoamperometry.

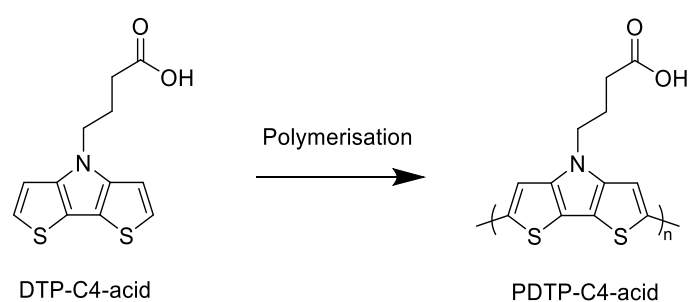


Figure 87 Structures of the DTP-C4-acid monomer and DTP-C4-acid polymer (PDTP-C4-acid).

Established chronoamperometry conditions previously developed within the Nielsen research group by Dr Christina Kousseff, were used to deposit DTP-C4-acid polymer thin-films. PDTP-C4-acid thin-films were prepared on indium tin oxide (ITO) coated glass substrates via chronoamperometry, as described in section 2.2.4.4. A representative PDTP-C4-acid thin-film deposited on ITO coated glass by chronoamperometry is presented in Figure 88. PDTP-C4-acid deposition results in a blue transparent thin-film on the ITO surface. A distinct boundary between the thin-film and the ITO is formed indicating where the substrate was submerged in the solution.

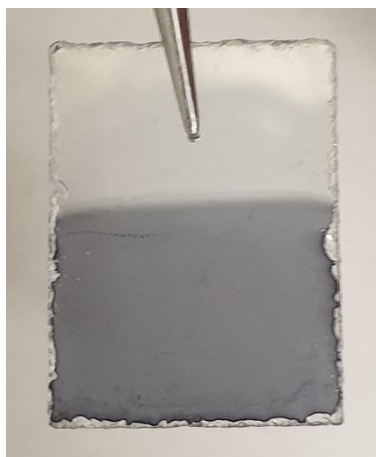


Figure 88 Camera image of PDTP-C4-acid thin-film deposited on ITO coated glass substrate by chronoamperometry (5 mM DTP-C4-acid, 0.85 V, 30 s, degassed MeCN). Clear blue area represents the DTP-C4-acid film, colourless area is the ITO-coated glass substrate.

The morphology of the DTP-C4-acid thin-film was investigated with AFM (see section 2.3.1). Topographical AFM images of the DTP-C4-acid thin-film are presented in Figure 89. The thin-film is populated with a dense array of large masses extending out of the surface. Height profiles of the masses reveal that they are upwards of 600 nm in height (see appendix section 7.3.3, Figure 134 and Table 66). The masses are formed during the deposition process and do not originate from the ITO surface (see appendix section 7.3.3, Figure 133). A smooth morphology between the masses is revealed in the 2.5 μm x 2.5 μm image, with averaged roughness R_q and R_a values of 1.81 nm \pm 0.236 nm and 1.45 nm \pm 0.199 nm, respectively (see appendix section 7.3.3, Table 67). The PDTP-C4-acid morphology was acceptable for initial aptamer functionalisation investigations, as the thin-film morphology on ITO may differ from the fabricated OECT morphology.

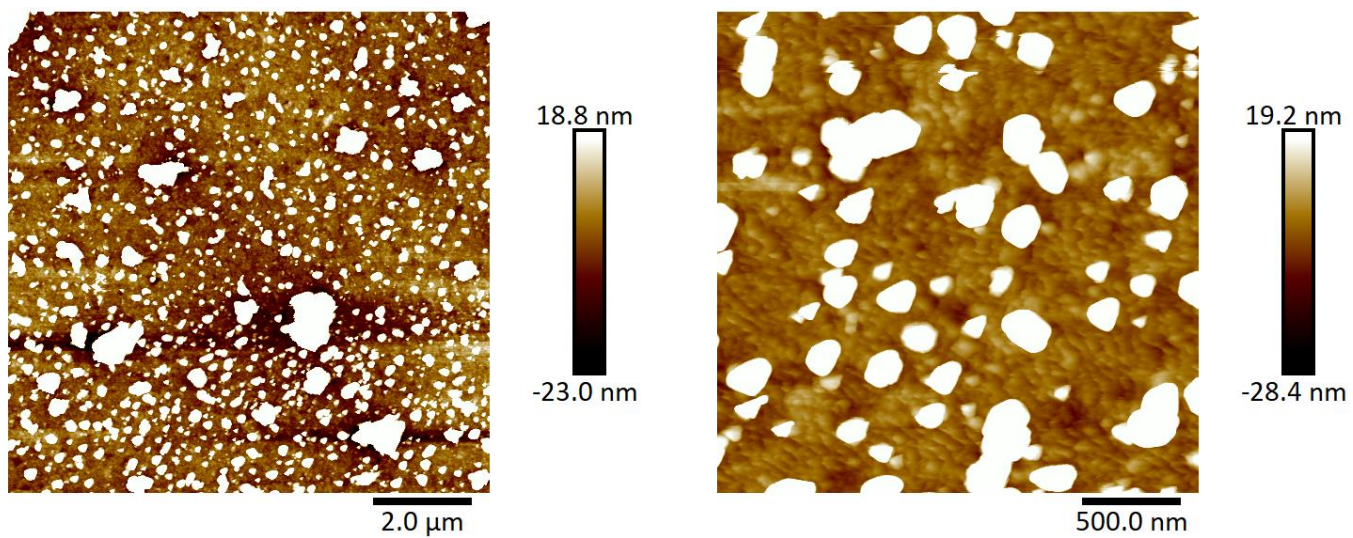


Figure 89 AFM topographical images (10 μm x 10 μm, 2.5 μm x 2.5 μm) of PDTP-C4-acid thin-film deposited via chronoamperometry on ITO substrate.

X-ray photoelectron spectroscopy of the PDTP-C4-acid thin-film

Verification of the carboxylic groups on the surface of the PDTP-C4-acid thin-film was achieved through X-ray photoelectron spectroscopy. XPS was conducted and the resulting spectrum processed using methods detailed in section 2.3.2. In addition, a 400 μm X-ray spot size was used. High resolution C1s scans were run to characterise the carbon environment on the thin-film surface, the C1s spectrum is presented in Figure 90. Three component peaks can be fitted to the experimental C1s scan, which are assigned to -C/C=C, C-S/C-N and COOH environments within PDTP-C4-acid. The fitted component peak at the highest binding energy (~ 289 eV) can be assigned to the carbon within the carboxylic acid group.⁽²⁴⁷⁾ Comparing the experimental C1s spectrum to a spectrum reported by Li et al., of a DTP polymer that substitutes the carboxylic acid group for an alkyl chain, reveals that the component peak at 289 eV is absent. The absence of this region supports the presence of carboxylic groups on the surface of the PDTP-C4-acid thin-film.⁽²⁸³⁾

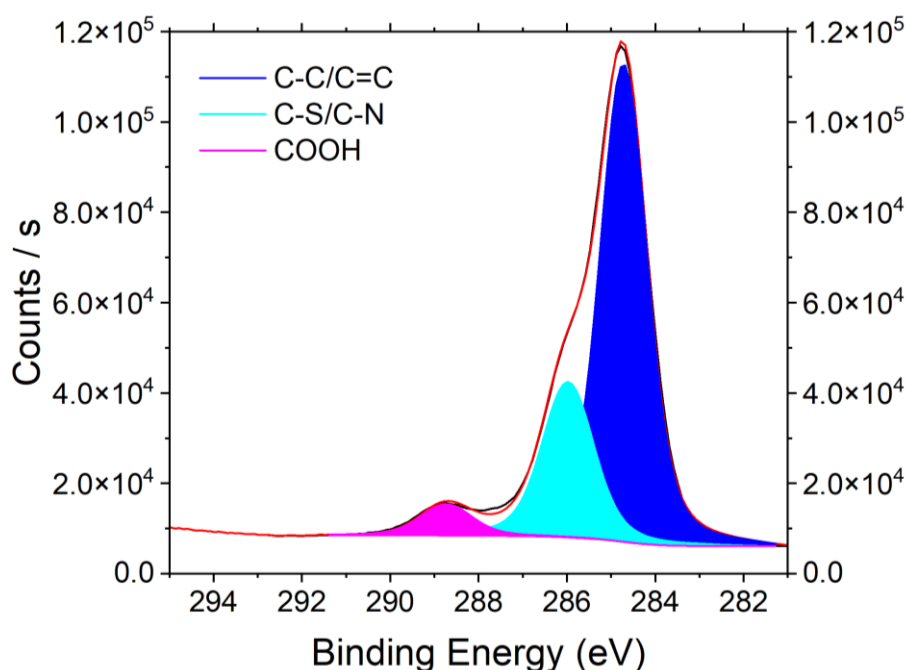


Figure 90 XPS high resolution C1s spectrum of PDTP-C4-acid thin-film deposited via chronoamperometry on ITO substrate. Scan size = 400 μm . (Black line) C1s experimental curve, (Red line) Peak fitted curve. Component peak assignment (blue) C-C/C=C (turquoise) C-S/C-N and (magenta) COOH.

Aptamer functionalisation of PDTP-C4-acid thin-films

In order to demonstrate the exploitability and reactivity of carboxylic acid groups on PDTP-C4-acid surface, a functionalisation strategy for attaching cortisol binding aptamers (CBA) was investigated. The developed strategy is illustrated in Figure 91, with the procedure details described in section 2.2.5.4. Aptamer attachment was facilitated by activating the carboxylic acid groups with EDC/sulfo-NHS forming amine-reactive NHS esters, which can then react with amine terminated cortisol binding aptamers (NH₂-CBA). DTP-COOH thin-films were prepared on indium tin oxide (ITO) coated glass substrates via chronoamperometry, as described in section 2.2.4.4.

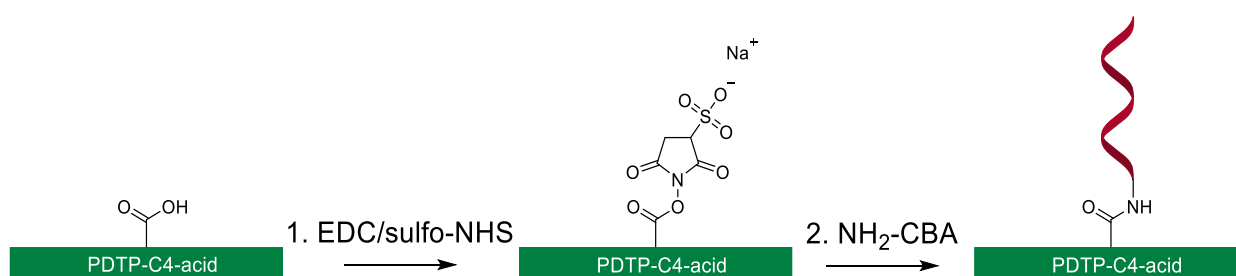


Figure 91 PDTP-C4-acid thin-film aptamer attachment strategy: 1. Incubation with NH₂-CBA solution in DPBS (10 μM), then sequentially washed with 0.1 % tween20 solution and MQ water.

Qualifying the successful surface functionalisation involved labelling the attached aptamers with a Cy3 labelled DNA strand (Cy3-comp-CBA), which was complimentary to the CBA sequence. Cy3-comp-CBA (see section 2.1.7) was hybridised to the covalently attached aptamer on the PDTP-C4-acid surface (see Figure 92).

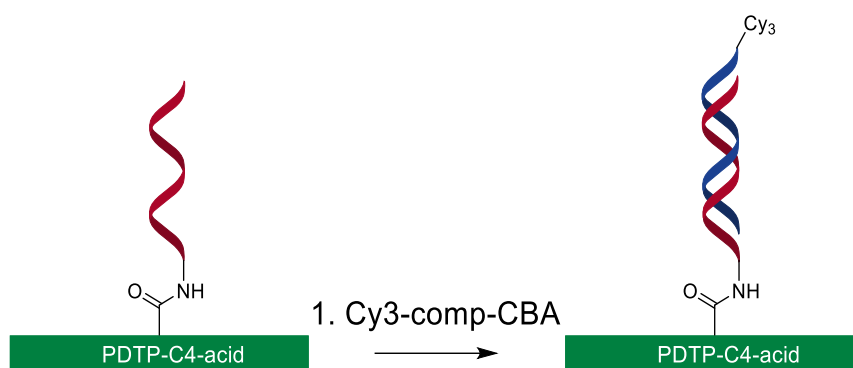


Figure 92 Hybridisation of aptamer functionalised PDTP-C4-acid thin-film with Cy3 labelled complementary strand: 1. Cy3-comp-CBA ($1 \mu\text{M}$) hybridisation then washed with 0.1 % tween20 solution and MQ water.

Alongside the functionalised and hybridised thin-films several controls were employed to further verify attachment and hybridisation. Control thin-films include the absence of EDC/sulfo-NHS, $\text{NH}_2\text{-CBA}$ /Cy3-comp-CBA (No EDC/sulfo-NHS or $\text{NH}_2\text{-CBA}$ or Cy3), Cy3-comp-CBA (No Cy3), $\text{NH}_2\text{-CBA}$ (No CBA), $\text{NH}_2\text{-CBA}$ and Cy3-comp-CBA (No CBA or Cy3), EDC/sulfo-NHS (No EDC/sulfo-NHS) and EDC/NHS or CBA (No EDC/sulfo-NHS or CBA). An index of PDTP-C4-acid incubation conditions and figure labels are provided in Table 24.

Sample No.	EDC/sulfo-NHS	$\text{NH}_2\text{-CBA}$	Cy3-comp-CBA
1	✓	✓	✓
2	X	X	X
3	✓	✓	X
4	✓	X	✓
5	✓	X	X
6	X	✓	✓
7	X	X	✓

Table 24 Epifluorescence microscopy: Index of PDTP-C4-acid aptamer ($\text{NH}_2\text{-CBA}$) functionalisation and hybridisation (Cy3-comp-CBA) conditions. ✓ = present, X = absent.

Detection of CBA functionalised and Cy3 hybridised thin-films was performed through epifluorescence microscopy, using a Nikon CSU-W1 SoRA Super-Resolution microscope (see section 2.3.3). Due to instrument restrictions the images were captured using an emission wavelength filter specific to the fluorescent label GFP, instead of Cy3. However, the range of the filtered wavelength overlaps with the emission wavelength range of the fluorescent label (Cy3). Average pixel values were extracted from the images, which are presented in Figure

93. Epifluorescence images are depicted in Figure 136, with tabulated average pixel values in Table 68 (see appendix section 7.3.4).

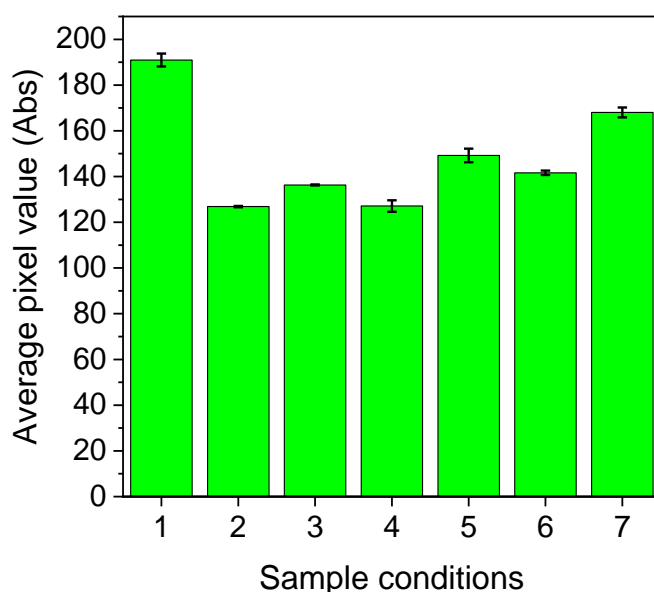


Figure 93 Epifluorescence microscopy average pixel values of PDTP-C4-acid thin-films deposited via chronoamperometry. Thin-films functionalised with NH₂-CBA, via EDC/sulfo-NHS, and hybridised with COMP-CBA-Cy3 (sample 1). Control thin-films also presented (samples 2 – 7).

The thin-film, functionalized with NH₂-CBA via EDC/sulfo-NHS and hybridized with Cy3-comp-CBA, exhibits increased fluorescence compared to the control samples. Representing an increased presence of the fluorescent label on the thin-film surface. The increase was facilitated by the hybridisation of the aptamers attached to the thin-film with the Cy3 labelled strand. Lower levels of fluorescence were measured for the control thin-films, with samples 2 and 4 observing background levels of fluorescence. Attachment of the aptamer to the thin-film via EDC/sulfo-NHS coupling chemistry is supported by comparing sample 6, where EDC/sulfo-NHS is controlled for. The fluorescence of sample 1 is higher than sample 6, highlighting the need for EDC/sulfo-NHS to activate the thin-film carboxylic acid groups prior to introducing NH₂-CBA. The thin-film incubated with Cy3-comp-CBA (Sample 7) obtained a fluorescence value higher than the background fluorescence of sample 2, suggesting that Cy3-comp-CBA may be physically adsorbed on the surface. The large protruding masses on the thin-film surface identified in AFM images, may have facilitated the physical adsorption of the

Cy3-comp-CBA strand. Considering sample 4 was incubated with EDC/sulfo-NHS and Cy3-comp-CBA and obtained a fluorescence value near to background, the higher fluorescence value of sample 7 may have resulted from imperfect washing. The small difference in fluorescence intensity is partly due to the GFP filter on the microscope, which allowed wavelengths emitted by Cy3 but at a lower intensities than the maximum emission wavelength. Sample 1, which was both functionalised and hybridised, achieved the highest fluorescence value suggesting the aptamer is attached to the PDTP-C4-acid thin-film.

5.4.2 Fabrication and characterisation of a PDTP-C4-acid OECT

Following the development of an aptamer functionalisation strategy, a proof of concept DTP-C4-acid OECT was fabricated. Source-drain electrodes (chromium 10 nm and gold 100 nm) were deposited using a combination of physical vapour deposition and shadow masking onto flexible polyimide substrates. A thin layer of chromium was deposited first onto the polyimide substrate, which improves the adhesion of the deposited gold layer on the polyimide substrate. Physical vapour deposition was performed as described in section 2.3.5. Source-drain electrodes with extended contact pads were utilised to allow for improved accessibility of the electrodes during DTP-C4-acid deposition. Dimensional properties of the deposition mask are detailed in Figure 16 and Table 5 in section 2.1.3, respectively. A PDTP-C4-acid thin-film was deposited onto gold source-drain electrodes (50 μm channel length) by adapting the methods described in section 2.2.4.4. The thin-film deposition time was increased to 120 s and the source-drain electrode on polyimide substrate used as the working electrode.

PDTP-C4-acid thin-film deposition on gold source-drain electrodes

Figure 94 A. illustrates the process of depositing a PDTP-C4-acid thin-film onto a pair of source-drain electrodes, via chronoamperometry. Deposition proceeded according to the following steps: **1.** The source-drain electrode patterned polyimide substrate, platinum wire counter electrode and silver/silver nitrate (Ag/AgNO_3) reference electrode were inserted equally spaced into the DTP-C4-acid solution (5 mM DTP-C4-acid and 0.1 M TBAClO_4 in degassed MeCN). **2.** The air exposed contact pad of the electrode was biased at 0.85 V for 120 s. A PDTP-C4-acid thin-film was deposited onto the submerged part of the biased electrode (Figure 94 B.). **3.** The substrate was rotated 180° and reinserted into the solution. Once more, the air exposed contact pad of the electrode was biased at 0.85 V for 120 s. A 2nd PDTP-C4-acid thin-film was deposited onto the submerged part of the biased electrode. **4.** Bridging of the PDTP-C4-acid thin-films across the electrode channel length occurs, which was indicated by thin-film deposition on the submerged contact pad (Figure 94 C.). The fabricated OECT after PDTP-C4-acid deposition is shown in Figure 94 D.

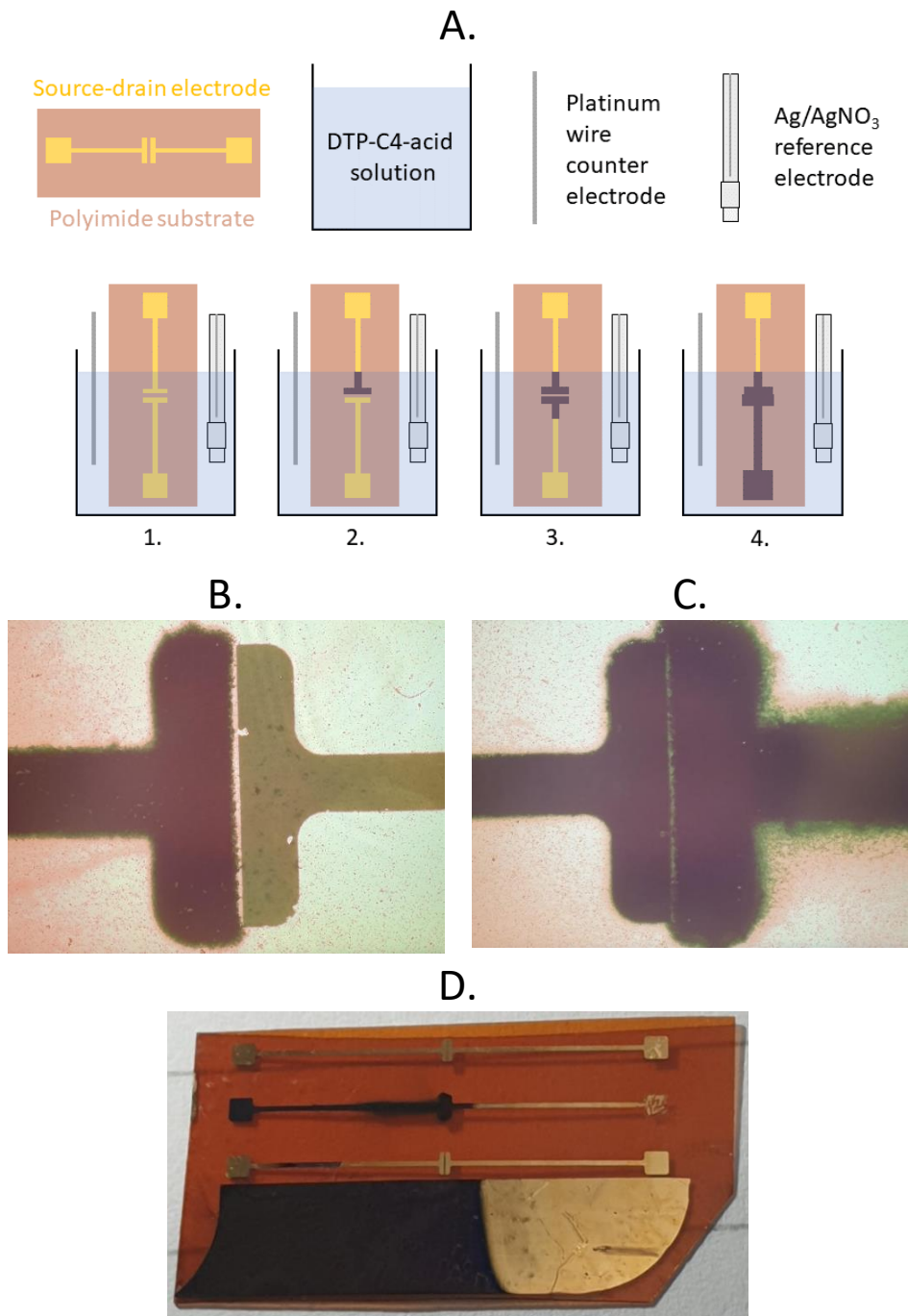


Figure 94 (A.) Scheme of DTP-C4-acid deposition on gold electrodes deposited onto polyimide substrate via chronoamperometry (0.85 V, 120 s) (B.) Microscope image of the electrodes (50 μm channel length) after the 1st PDTP-C4-acid deposition (C.) Microscope image of the electrodes (50 μm channel length) after the 2nd PDTP-C4-acid deposition (D.) Camera image of OECT after DTP-C4-acid deposition.

The morphology of the DTP-C4-acid thin-film was investigated with AFM (see section 2.3.1). Topographical AFM images of the DTP-C4-acid thin-film are presented in Figure 95. Large masses extending out of the surface can be seen, similar to those seen in AFM images of PDTP-C4-acid thin-film deposited on ITO. However, a different surface morphology between the masses is exhibited. A morphology composed of defined globular grains is exhibited, with grain diameters ranging from 200 nm to 1.5 μm and a vertical range of 230 nm (see appendix section 7.3.3, Figure 135). The morphology is common for electrodeposited DTP or PEDOT materials on gold.(284, 285)

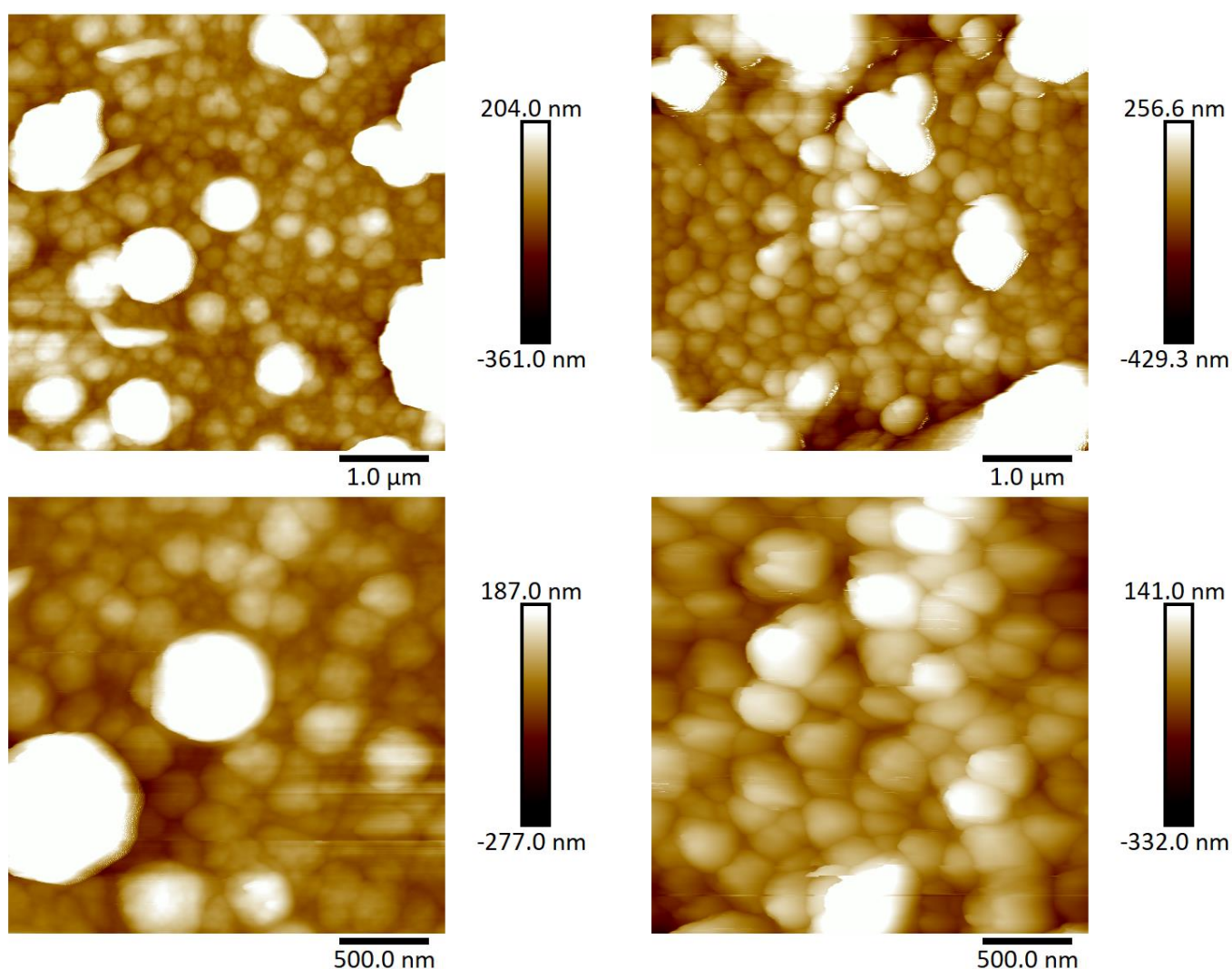


Figure 95 AFM topographical images (5 μm x 5 μm , 2.5 μm x 2.5 μm) of PDTP-C4-acid thin-film deposited via chronoamperometry on gold electrodes on a polyimide substrate (50 μm channel length).

Following the deposition of the PDTP-C4-acid thin-film on the source-drain electrodes the transistor was characterised. Dulbecco's Phosphate-Buffered Saline (DPBS) was used as the electrolyte solution interfacing both the channel and the gate electrode. The electrolyte solution (20 μL) was deposited onto the device, covering both the thin-film channel and the gold gate, as illustrated in Figure 96.



Figure 96 (left) Camera image showing probe station characterisation setup of PDTP-C4-acid OECT. 50 μm channel length. (blue oval) 20 μL of DPBS electrolyte solution overlapping PDTP-C4-acid thin-film and gold gate electrode. (white) biasing positions of source/drain (yellow) biasing position of gate electrode. (right) Microscope image of DPBS electrolyte solution covering PDTP-C4-acid thin-film.

Transfer characteristics were measured by sweeping the gate voltage (V_g) from 0.7 V to -0.7 V, while applying a drain-source voltage (V_{ds}) bias of -0.7 V. Output characteristics were measured by sweeping V_{ds} from 0.7 V to -0.7 V, while applying V_g biases of 0.5 V to -0.7 V at -0.1 V intervals. The transfer and output characteristics, as well as the real-time current of the PDTP-C4-acid OECT are presented in Figure 97. The OECT shows p-type accumulation mode operation, the conductivity of the channel increases as ions are injected into the material, stabilising mobile holes, at greater gate voltage biases. The real-time current of the biased PDTP-C4-acid OECT outputs in the microamp range. Control measurements demonstrate the requirement for applied negative biases at the gate and drain electrodes for the OECT to operate. The results from the proof of concept device indicate that the novel DTP-C4-acid polymer can operate as an OECT material.

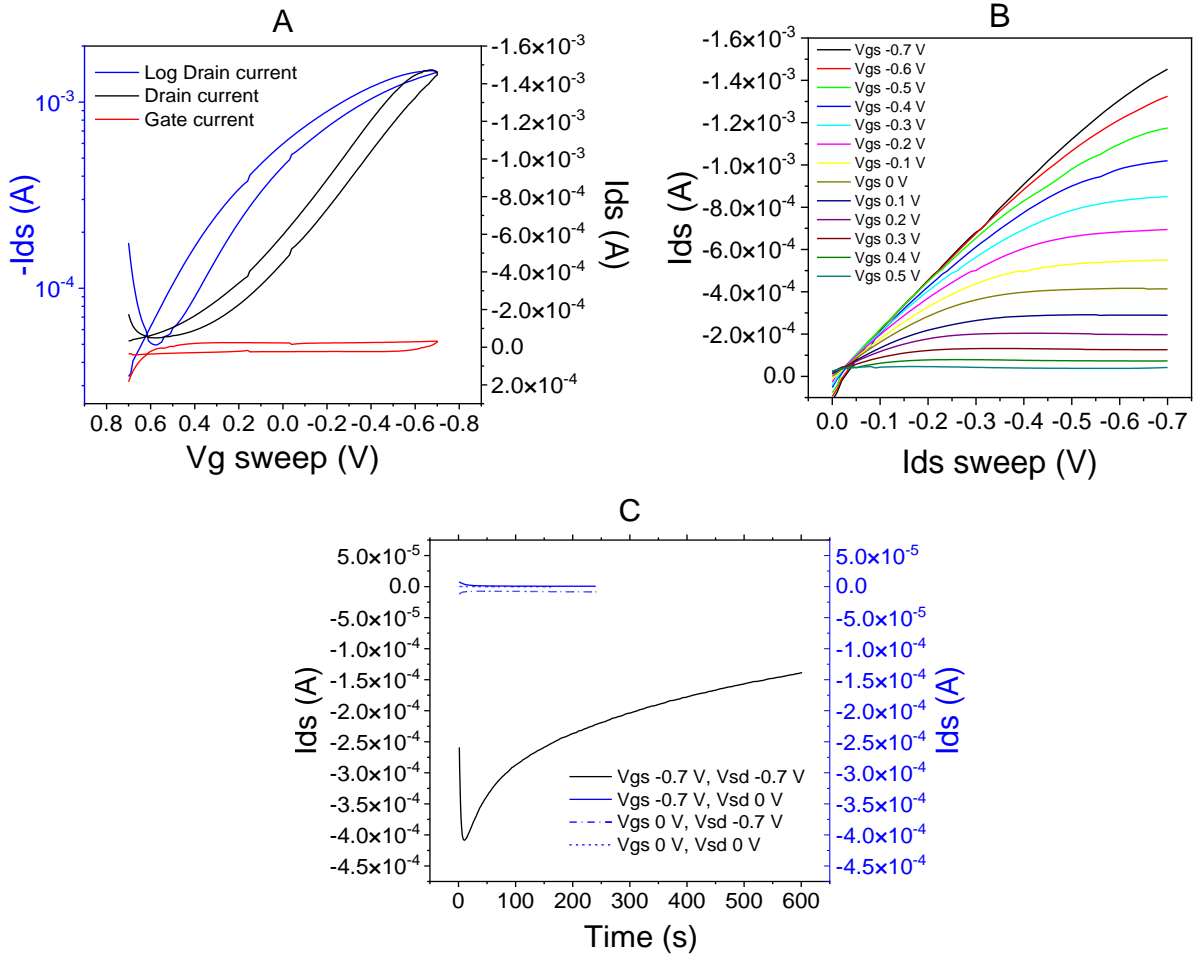


Figure 97 (A) Transfer and (B) output characteristics of PDTP-C4-acid OECT. Transfer characteristics measured V_g sweep 0.7 V to -0.7 V, $V_{ds} = -0.7$ V. Output characteristics measured V_{ds} sweep 0.0 V to -0.7 V, V_{gs} 0.5 V to -0.7 V (-0.1 V intervals). (C) Real-time current $V_g = -0.7$ V and $V_{ds} = -0.7$ V and controls. DPBS electrolyte solution (20 μ L). 50 μ m channel length.

Controlling the deposition of PDTP-C4-acid thin-film

Efforts were made to improve the PDTP-C4-acid thin-film deposition methodology, by controlling where the electropolymerisation occurs on the source-drain electrodes. Previously, thin-film deposition wasn't controlled and occurred at any point along the biased electrode exposed to the DTP-C4-acid solution. Generally, control over OECT thin-film deposition is preferred, where the material is isolated within the length of the source-drain electrode channel.

A simple method of selectively depositing the thin-film to a smaller area of the source-drain electrodes was achieved using polyimide adhesive tape and a PDMS well. Areas of the polyimide adhesive tape were removed using a 1 mm and 3 mm Bio-puncture. The polyimide adhesive tape was transferred onto a polyimide substrate patterned with source-drain electrodes (Figure 98). The source-drain electrode channel and electrode pads were aligned with the 1 mm and 3 mm holes in the polyimide tape, respectively. Deposition of the polymer thin-film could now be confined to a smaller area, with the contact pads still accessible for applying a voltage bias during chronoamperometry.



Figure 98 Polyimide tape isolated source-drain electrodes. Centre electrodes within Biopunctured hole are exposed. Electrode edges are insulated with polyimide tape.

The DTP-C4-acid solution was also contained within a PDMS well, further restricting thin-film deposition to the exposed electrode area. The PDMS well was prepared using the following procedure: Chemicals from SYLGARD™ 184 Silicone Elastomer Kit were combined in a 50 mL falcon tube at a 9:1 ratio and mixed together with a glass rod. The mixture was poured into a glass petri dish to a height of 10 mm. The mixture was then placed inside a vacuum oven. A

vacuum was applied until all air bubbles within the PDMS mixture were removed. The mixture was then baked on a hotplate at 90 °C for 10 minutes. A scalpel blade was used to divide the cured PDMS into a rectangular well. The PDMS well was then transferred onto the substrate, illustrated in Figure 99 C.

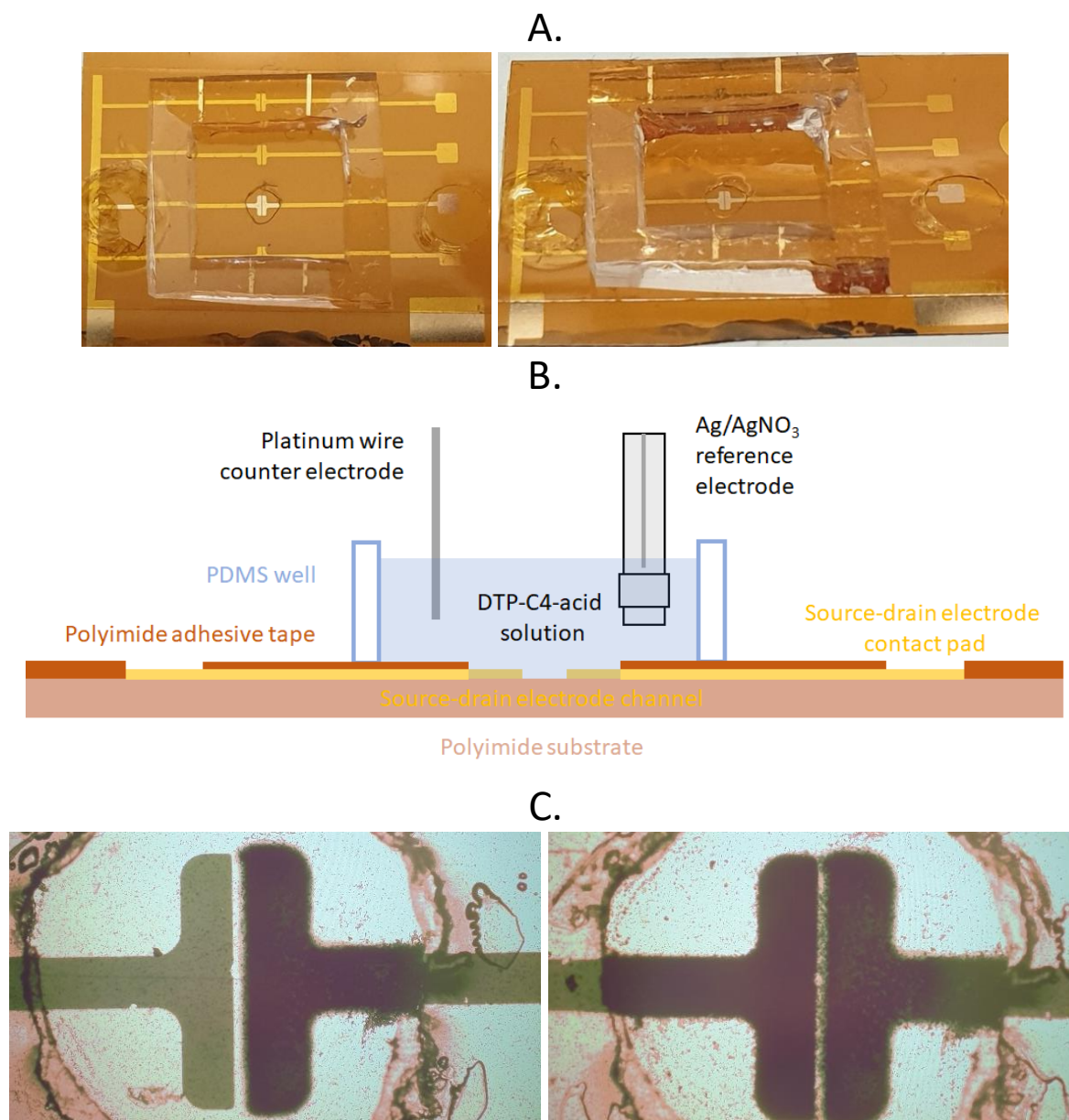


Figure 99 (A.) Polydimethylsiloxane (PDMS) well transferred onto OECT substrate. Polyimide adhesive tape used to selectively expose source-drain electrode channel and contact pads. (B.) Scheme of chronoamperometry setup for selective DTP-C4-acid thin-film deposition. (C.) Microscope images of the source-drain electrodes (50 μm channel length) after the 1st (left) and 2nd (right) PDTP-C4-acid thin-film depositions, via chronoamperometry (0.85 V, 120 s).

A scheme illustrating the setup for the selective deposition of the PDTP-C4-acid thin-film is presented in Figure 99 B. Polyimide adhesive tape exposes part of the source-drain electrode and contact pads, while encapsulating the remaining electrode. The PDMS well contains the DTP-C4-acid solution so that it is in contact with the exposed electrode. A PDTP-C4-acid thin-film was deposited onto gold source-drain electrodes (40 μm channel length) by adapting the methods described in section 2.2.4.4. The thin-film deposition time was increased to 120 s and performed on both source-drain electrodes in two stages, with the source-drain electrodes on polyimide substrate used as the working electrode. Microscope images of the deposited thin-film are presented in Figure 99 C. The PDTP-C4-acid thin-film is deposited onto the exposed electrode, while the electrode under the polyimide tape is isolated during deposition. After the 2nd deposition part of the PDTP-C4-acid thin-film can be seen crossing the channel length, bridging the source-drain electrodes. Further characterisation of the deposited thin-film was not performed due to time restrictions.

5.5 Summary and conclusion

In summary, this chapter explores the fabrication and characterisation of two organic transistors, utilising chemically modified materials containing functional groups that are exploitable for receptor attachment. A reported DPP-DTT derivative containing azide functional groups (N_3 -DPP) was initially investigated. N_3 -DPP polymer thin-films with morphologies and thicknesses suitable for biosensing OFETs could be deposited, using a combination of probe tip sonication and the floating film transfer method. Probe tip sonication enabled the preparation of a homogenous polymer solution, while the FFT method facilitated the transfer of deposited N_3 -DPP thin-films onto ODTS modified Si/SiO₂ substrates. Azide groups on the N_3 -DPP thin-film surface were identified in the XPS high resolution N1s spectrum. The N_3 -DPP thin-film surface was functionalised with DBCO terminated aptamers, through a strain-promoted azide-alkyne click chemistry reaction, evident in XPS and WCA measurements. Finally, an N_3 -DPP OFET was fabricated and characterised using previously established methods. Performance characteristics identified the fabricated OFET as a suitable platform for further biosensing applications.

A novel dithienopyrrole (DTP) derivative, endowed with a carboxyl group (DTP-C4-acid) was also explored. The DTP-C4-acid monomer could be deposited as a polymer (PDTP-C4-acid) thin-film onto ITO coated glass via chronoamperometry. Characterisation of the resulting thin-film with AFM revealed a smooth surface morphology between an array of large protruding masses. The thin-films on ITO could be functionalised with amine terminated aptamers through EDC/sulfo-NHS coupling chemistry, which was qualified by epifluorescence microscopy. A proof of concept OECT was fabricated on a flexible polyimide substrate via chronoamperometry. Gold source-drain electrodes were patterned onto the substrate and a PDTP-C4-acid thin-film bridging the channel length was deposited. Transfer and output curves were obtained for the OECT using DPBS as the electrolyte solution, with the device exhibiting p-type accumulation mode operation. Real-time current of the biased OECT was also obtained, demonstrating the materials suitability for biosensing applications.

Overall, strategies for functionalising two chemically modified materials (N₃-DPP and DTP-C4-acid) with aptamers were identified. Organic transistors fabricated with these materials showed promise as low-voltage biosensing platforms. Further research is required to explore the biosensing capabilities of these platforms. Aptamer functionalisation of the N₃-DPP OFET and PDTP-C4-acid OECT should be carried out and respective responses to cortisol determined.

The proof-of-concept PDTP-C4-acid OECT demonstrated the materials suitability for future biosensing applications. However, refinement of the deposition process and use of more sophisticated fabrication methods should be explored. Generally, OECT thin-film deposition is controlled in order to isolate the material within the length of the source-drain electrode channel. Control of the polymer thin-film was partly addressed by selectively exposing desired areas of the source-drain electrodes with patterned polyimide tape. A technique known as thermal scanning probe lithography (t-SPL), would enable higher resolution patterning of the thin-film.⁽²⁸⁶⁾ By coating the source-drain electrodes with a thermally sensitive resist, such as polyphthalaldehyde (PPA), t-SPL, performed on a NanoFrazor, could be used to selectively ablate areas of resist exposing specific areas of the electrodes, with micrometre tolerances. Polymer thin-film electrodeposition would be restricted to areas on the source-drain electrodes patterned via t-SPL, with the remaining PPA layer encapsulating the non-patterned electrodes.

In addition to performing biosensing experiments with the aptamer functionalised DTP-C4-acid thin-film, it would be interesting to compare the response against a gate-functionalised OECT. Biosensing OECTs have previously attached thiol terminated aptamers to gold gate electrodes, which demonstrated low detection limits (10 pM).⁽²⁸⁷⁾ In future work, it would be interesting to compare the sensitivity of the novel DTP-C4-acid material with these two functionalisation strategies.

6 Conclusions

Organic electronics exhibit significant potential in surpassing contemporary electronics, with the advantages of organic semiconducting materials currently being utilised in modern OLED technologies. A reality of wearable continuous health monitoring devices, based on biosensing OFETs, seems to be imminently upon us. However, this reality still requires some challenges to be overcome. Rapid single-molecule biomarker detection require biosensors with large-area interfaces that are densely functionalised with receptors. The OFET organic semiconductor layer represents a convenient interface for receptor functionalisation and transduction of biomarker binding interactions into a measurable signal. Additionally, aptamers are receptors that can interact with a versatile range of biomarker species, with high specificity and in under physiological conditions. This work identifies and develops strategies to functionalise organic semiconducting polymers with aptamers for biosensing applications.

A foundational method was developed for fabricating low-voltage organic field-effect transistors (OFET) incorporating the high performance organic semiconducting polymer DPP-DTT. Following this, DPP-DTT OFETs were exposed to O₂ or N₂ plasma as strategies for introducing exploitable chemical functionalities (carboxylic acid or amine) to the thin-film surface, to facilitate aptamer attachment.

Optimisation of the DPP-DTT thin-film utilised floating film transfer (FFT) as a deposition method. Thin-film morphology and thickness was optimised by controlling the concentration of the DPP-DTT polymer solution. Thin-films exhibited continuous areas of homogeneity, that were free of defects and large aggregates. Additionally, evidence of polymer chain alignment was demonstrated in AFM images. Modification of the SiO₂ dielectric surface was conducted to passivate surface charge traps, using a self-assembled monolayer of octadecyltrichlorosilane (ODTS). A bottom-gate top-contact OFET, incorporating gold deposited interdigitated source-drain electrodes, was fabricated under ambient laboratory conditions. The OFETs exhibited comparable mobilities and low threshold voltages, making them suitable initial platforms for biosensing applications.

Following this, O₂ and N₂ plasma treatment of DPP-DTT thin-films were investigated individually, as methods of introducing exploitable chemical functionalities to the thin-film surface. A series of conditions varying plasma exposure powers and times were explored. The balance between thin-film etching and chemical modification, was monitored with AFM and XPS measurements. The influence of plasma treatment on OFET performance was also monitored. An optimised balance between O₂ plasma power and exposure time (12 W, 60 s) was identified. The OFET exposed to O₂ plasma under these conditions experienced minimal etching, maximal chemical modification and retained the highest performance. However, the limited density of carboxylic acid groups, possibly due to plasma-induced surface restructuring, restricted aptamer functionalisation.

Subsequently, the exploration of N₂ plasma treatment was considered as an alternative aptamer functionalisation strategy. N₂ plasma was discovered to etch thin-films more intensely under similar conditions relative to O₂ plasma. The increased intensity of N₂ plasma was reflected in the OFET performance, which observed a significant reduction in the charge carrier mobilities. However, an increase in exploitable functional groups was apparent in XPS spectra. N₂ plasma treatment conditions 12 W, 30 s were identified as the optimal balance between chemical modification and OFET performance retention. Further, a novel aptamer functionalisation strategy was developed and confirmed by epifluorescence microscopy. The strategy modified amine functional groups on the N₂ plasma exposed thin-film surface with BCN-NHS. Followed by a SPAAC click reaction between surface attached BCN groups and N₃-aptamers. Despite the promising result, the fabrication of an aptamer functionalised N₂ plasma treated OFET was not pursued. Instead, the attention of this thesis was directed to an alternative aptamer functionalisation strategy with improved OFET performance.

A receptor functionalisation strategy that did not compromise OFET performance was later identified and exploited. The adapted functionalisation methodology involved blending the high performance DPP-DTT polymer with the small molecule glutaraldehyde (GA).

The thin-film forming properties of an established DPP-DTT:GA (9:1) in chlorobenzene (5 mg mL⁻¹) blend were investigated via spin coating. Optimised thin-film deposition conditions

were determined, with resulting DPP-DTT:GA thin-films displaying suitable thicknesses and morphologies. Following this, a strategy for attaching aptamers (specific to cortisol) to DPP-DTT:GA thin-films was developed and qualified by epifluorescence microscopy. Aptamer functionalisation was facilitated by a condensation reaction, occurring between amine terminated aptamers and GA aldehyde groups blended within the thin-film surface. A combination of XPS and WCA measurements were performed to further optimise the aptamer functionalisation strategy, by varying the aptamer concentration. Furthermore, by monitoring the thin-film surface during OFET fabrication, it was revealed that aptamer functionalisation could not occur after source-drain electrode deposition. However, the successful fabrication of aptamer-functionalized DPP-DTT:GA OFETs could only be verified if aptamer attachment occurred before S/D deposition.

Characterisation of the aptamer functionalised DPP-DTT:GA OFET confirmed its suitability for low-voltage sensing applications, with the blending of GA facilitating aptamer attachment without impeding OFET performance. Subsequently, the biased OFET demonstrated a preliminary real-time current response to a physiological relevant range of cortisol concentrations. Minor controls supported the observation, however further validation of the sensing response is required. The reversibility of the imine group formed during aptamer attachment may introduce reproducibility problems during aqueous sensing experiments. Reducing the imine into an amine through reductive amination with sodium cyanoborohydride should be explored, in order to stabilise the bond anchoring the aptamer to the sensing channel surface. Preparation of the cortisol solutions in an alternative buffer (e.g. PBS) that doesn't contain competitive amine groups should also be investigated.

A reported DPP-DTT derivative containing azide groups (N_3 -DPP) was explored. Homogenous N_3 -DPP thin-films could be deposited using probe tip sonication to form the polymer solution and the FFT method to transfer thin-films onto substrates. The azide group could be identified on the N_3 -DPP thin-film surface in the XPS high resolution N1s (nitrogen) spectrum. The N_3 -DPP thin-film surface could be functionalised with DBCO terminated aptamers, through a strain-promoted azide-alkyne click chemistry reaction, with evidence from XPS and WCA

measurements. Finally, an N₃-DPP OFET was fabricated which demonstrated performances making it suitable for biosensing applications. Unfortunately, further work could not be conducted to assess the biosensing capabilities of a functionalised OFET, due to the potential degradation of the N₃-DPP polymer. Resolving this potential issues should be explored in future work.

A novel dithienopyrrole (DTP) derivative, endowed with a carboxyl group (DTP-C4-acid) was also explored. The DTP-C4-acid monomer could be deposited as a polymer (PDTP-C4-acid) thin-film onto ITO coated glass via chronoamperometry. Characterisation of the resulting thin-film with AFM revealed a smooth surface morphology between an array of large protruding masses. The thin-films on ITO could be functionalised with amine terminated aptamers through EDC/sulfo-NHS coupling chemistry, which was qualified by epifluorescence microscopy. A proof of concept OECT was fabricated on a flexible polyimide substrate via chronoamperometry. Gold source-drain electrodes were patterned onto the substrate and a PDTP-C4-acid thin-film bridging the channel length was deposited. Transfer and output curves were obtained for the OECT by using DPBS as the electrolyte solution, with device exhibiting p-type accumulation mode operation. Real-time current of the biased OECT were also obtained which demonstrated the materials suitability for biosensing applications. In future work, sensing experiments should be conducted with aptamer functionalised OECTs, to assess the response to target biomarkers.

Further progress is required before a future of commercially available and wearable health monitoring devices can be used to further develop personal healthcare. A more unified understanding on how organic semiconductors work and methods of improving their environmental and electrical stabilities are required. Successfully adapting laboratory fabrication techniques to large-scale manufacturing is also critical. The field of organic bioelectronics will continue to be full of impactful discoveries with meaningful applications.

7 Appendix

7.1 Organic field-effect transistor fabrication and the effects of plasma modification appendix

7.1.1 Thin-film deposition optimisation AFM

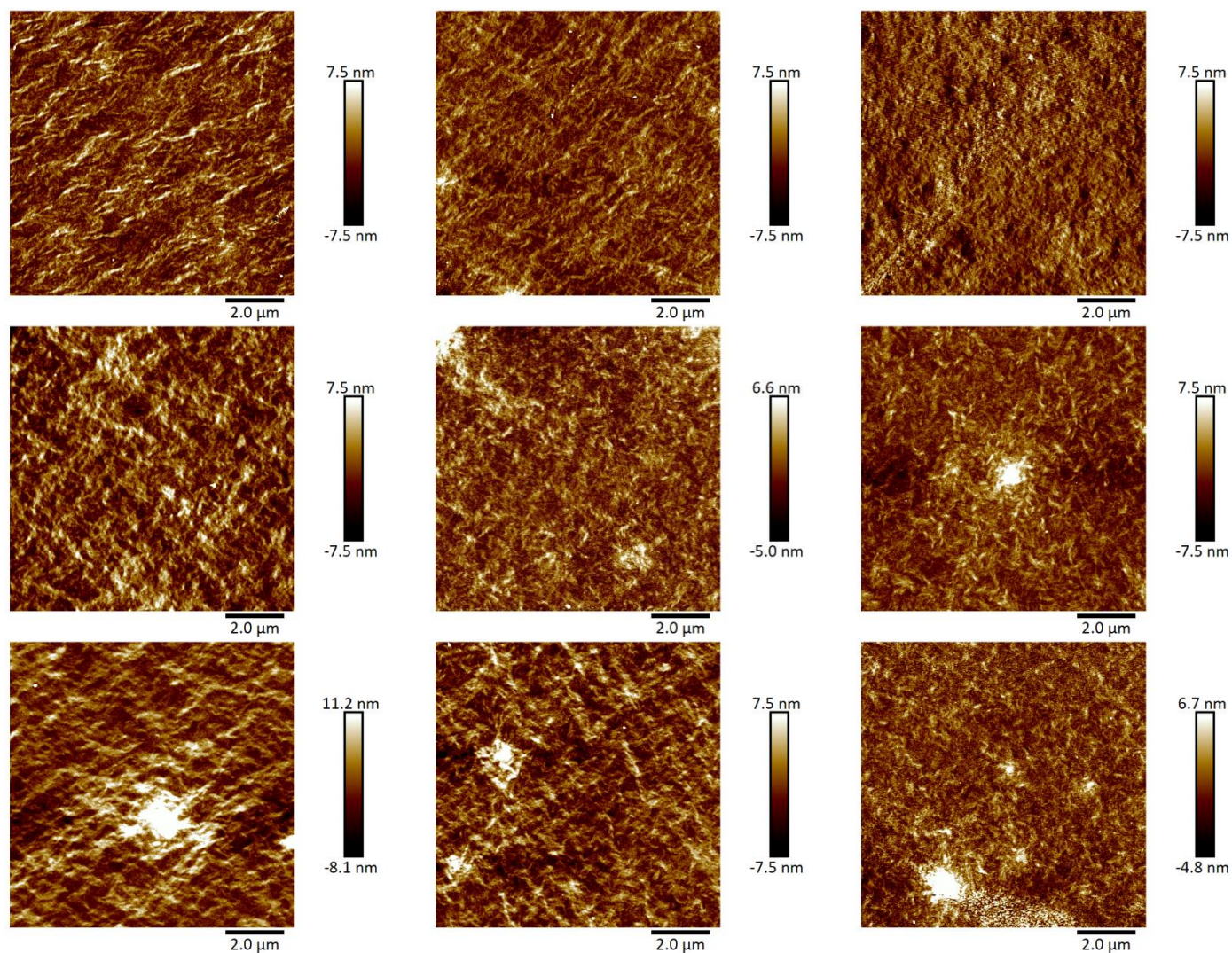


Figure 100 AFM topographical images ($10\ \mu\text{m} \times 10\ \mu\text{m}$) of DPP-DTT thin-films via FFT from 9:1 CHCl_3 :CB ($10\ \text{mg mL}^{-1}$) on Si/SiO₂ substrates.

Image No. and Roughness	1 nm	2 nm	3 nm	4 nm	5 nm	6 nm	7 nm	8 nm	9 nm	Average nm	STD nm
1 Rq	2.08	1.58	1.87	2.03	1.45	1.52	2.21	1.77	1.44	1.78	0.343
2 Rq	1.65	1.63	1.73	1.95	1.31	1.51	2.69	1.92	1.29		
3 Rq	1.99	1.63	1.81	2.12	1.49	1.62	2.36	2.11	1.34		
1 Ra	1.65	1.26	1.5	1.62	1.16	1.2	1.79	1.42	1.15	1.42	0.282
2 Ra	1.3	1.31	1.37	1.58	1.04	1.2	2.14	1.53	1.03		
3 Ra	1.57	1.28	1.44	1.69	1.18	1.28	1.92	1.73	1.03		

Table 25 Averaged Roughness Rq and Ra values ($3 \times 2 \mu\text{m} \times 2 \mu\text{m}$ areas) of DPP-DTT thin-films via FFT from 9:1 $\text{CHCl}_3:\text{CB}$ (10 mg mL^{-1}) on Si/SiO_2 substrates.

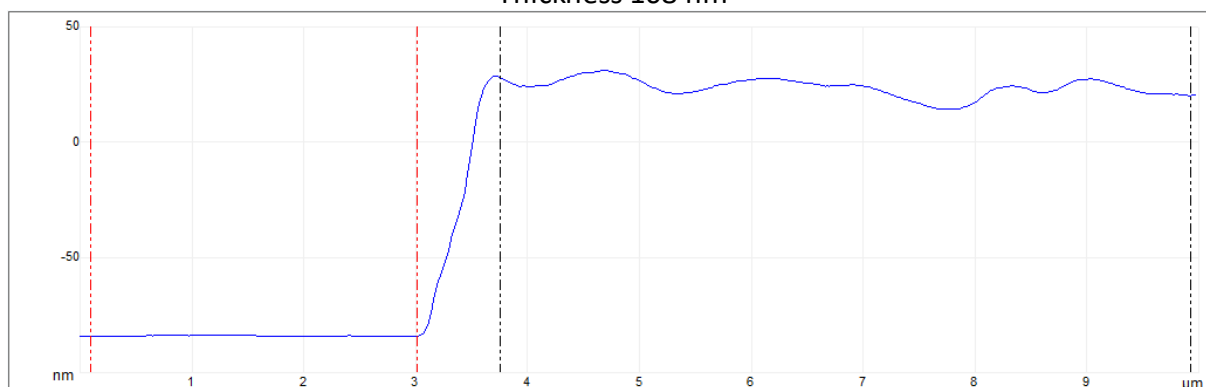
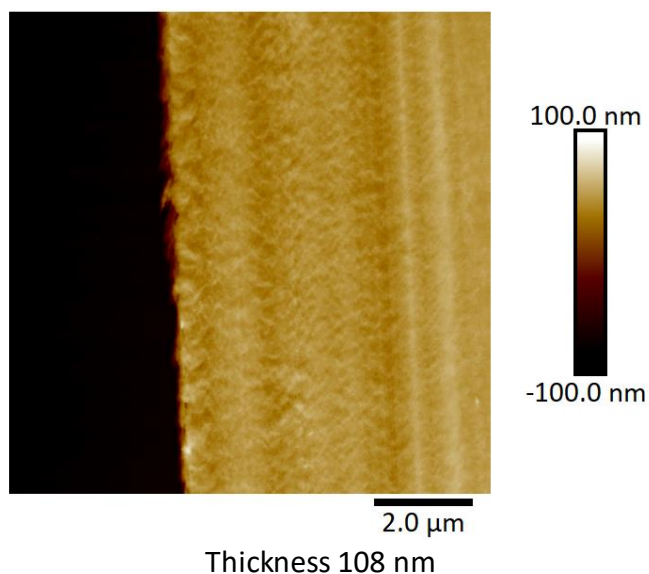


Figure 101 AFM topographical image and height profile ($10 \mu\text{m} \times 10 \mu\text{m}$) of a DPP-DTT thin-film via FFT from 9:1 $\text{CHCl}_3:\text{CB}$ (10 mg mL^{-1}) on Si/SiO_2 substrates.

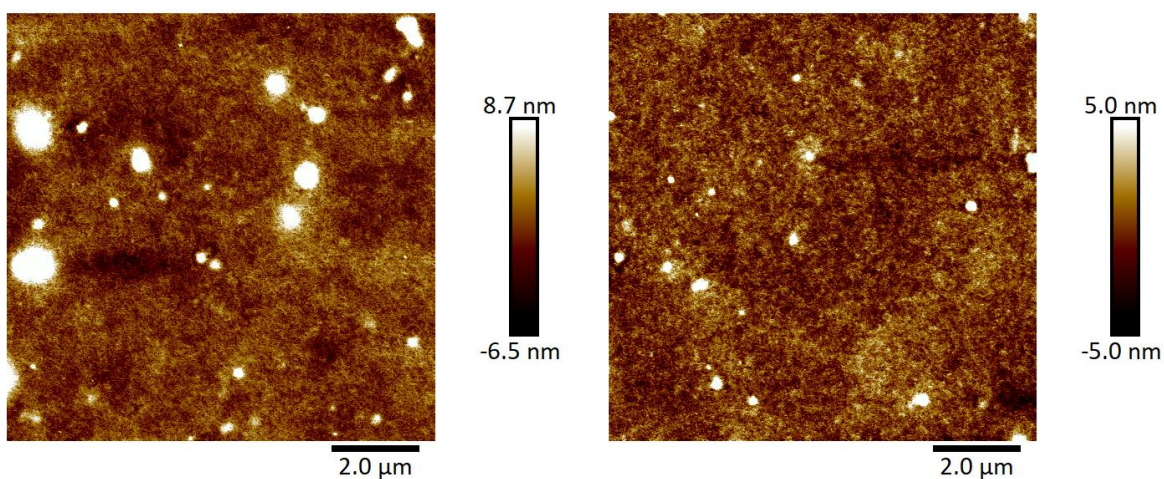


Figure 102 AFM topographical images ($10\ \mu\text{m} \times 10\ \mu\text{m}$) of a DPP-DTT thin-film spin coated from 9:1 CHCl_3 :CB ($10\ \text{mg mL}^{-1}$) on Si/SiO₂ substrate.

Image No. and Roughness	1 nm	2 nm	3 nm	Average nm	STD nm
1 Rq	1.38	1.36	1.40	1.25	0.143
2 Rq	1.15	1.14	1.08		
1 Ra	1.10	1.08	1.10	0.99	0.110
2 Ra	0.91	0.92	0.86		

Table 26 Averaged roughness Rq and Ra values ($3 \times 2\ \mu\text{m} \times 2\ \mu\text{m}$ areas) of a DPP-DTT thin-film spin coated from 9:1 CHCl_3 :CB ($10\ \text{mg mL}^{-1}$) on Si/SiO₂ substrate.

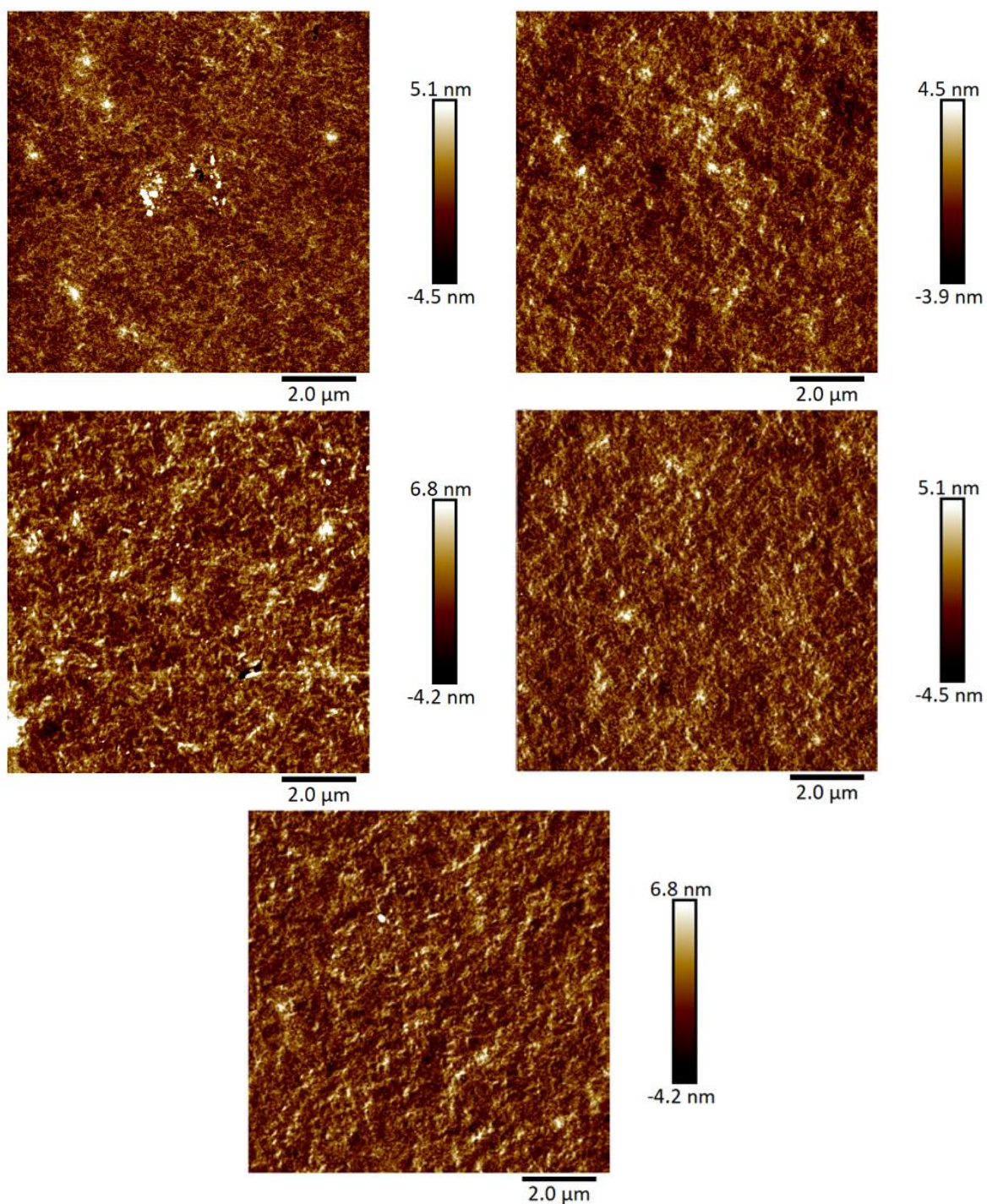
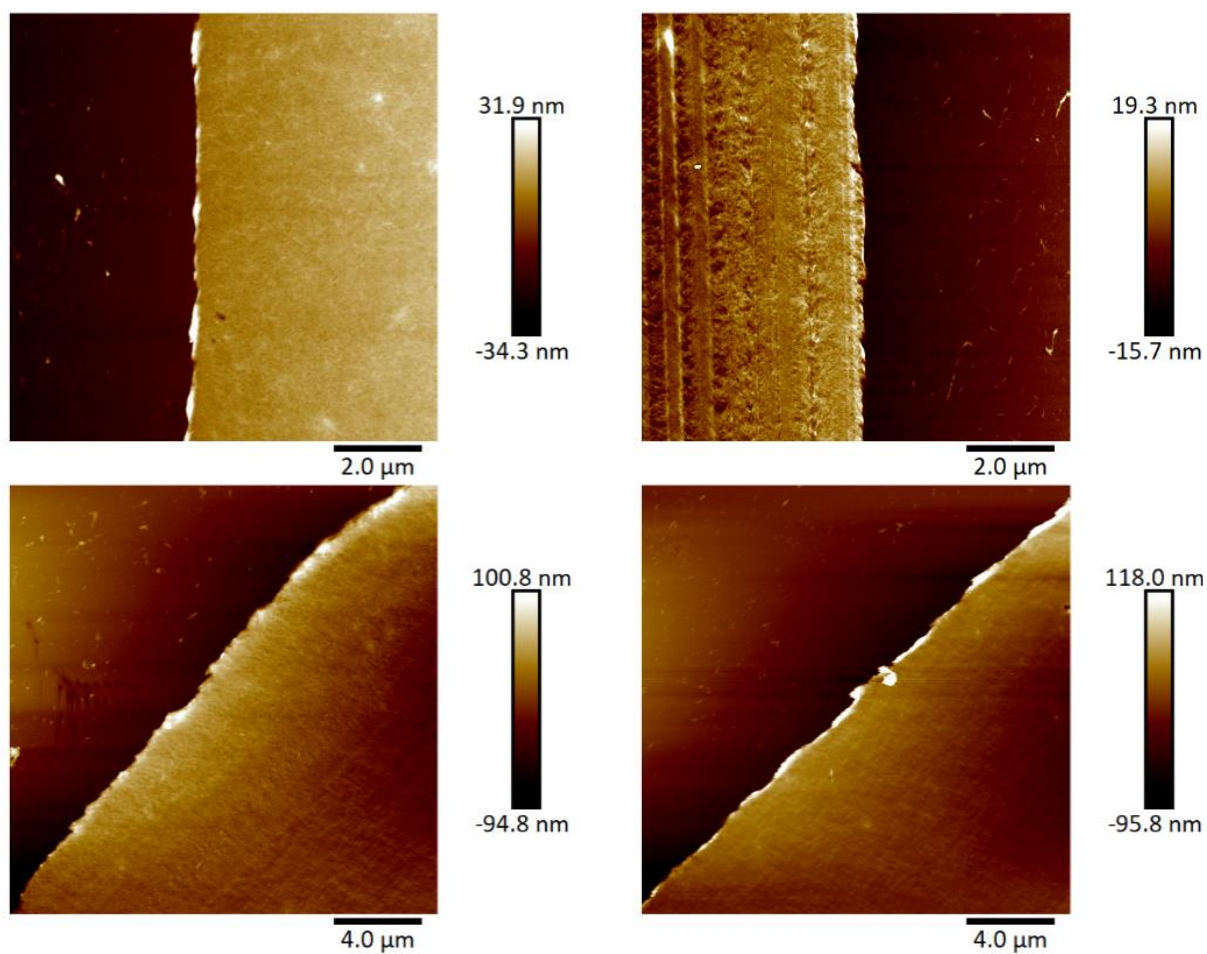
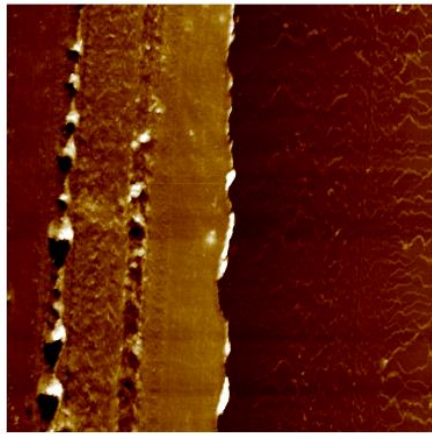


Figure 103 AFM topographical images (10 μm x 10 μm) of DPP-DTT thin-films via FFT from 9:1 CHCl₃:CB (5 mg mL⁻¹) on Si/SiO₂.

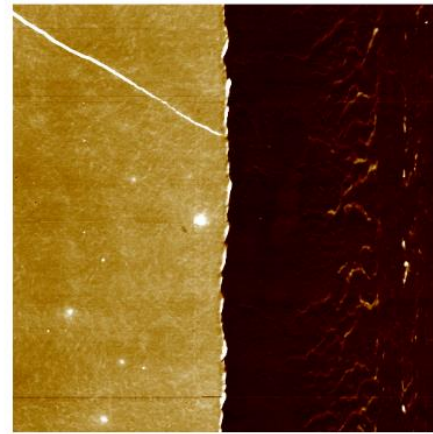
Image No. and Roughness	1 nm	2 nm	3 nm	4 nm	5 nm	Average nm	STD nm
1 Rq	1.24	1.06	1.50	1.36	1.64	1.36	0.210
2 Rq	1.21	1.07	1.53	1.33	1.56		
3 Rq	1.22	1.13	1.65	1.40	1.50		
1 Ra	0.98	0.84	1.19	1.06	1.30	1.07	0.170
2 Ra	0.96	0.84	1.20	1.06	1.23		
3 Ra	0.95	0.87	1.31	1.10	1.19		

Table 27 Averaged roughness Rq and Ra values ($3 \times 2 \mu\text{m} \times 2 \mu\text{m}^2$ areas) of DPP-DTT thin-films via FFT from 9:1 CHCl_3 :CB (5 mg mL^{-1}) on Si/SiO₂.



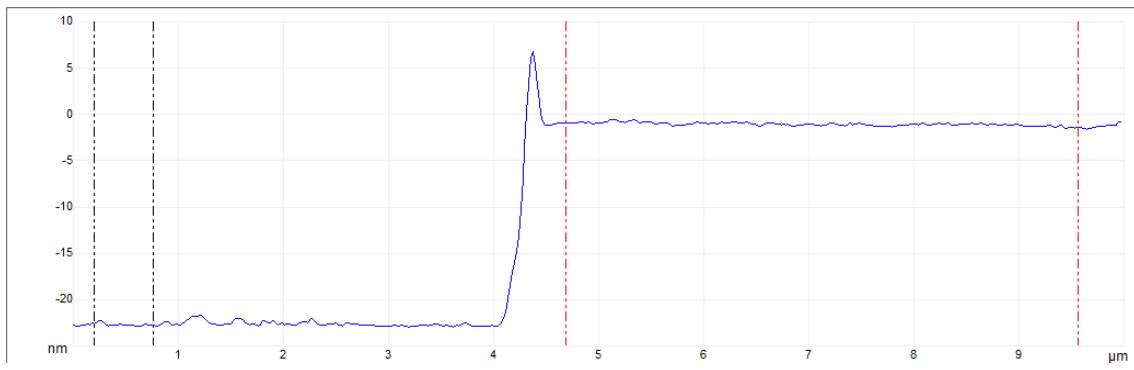


4.0 μm

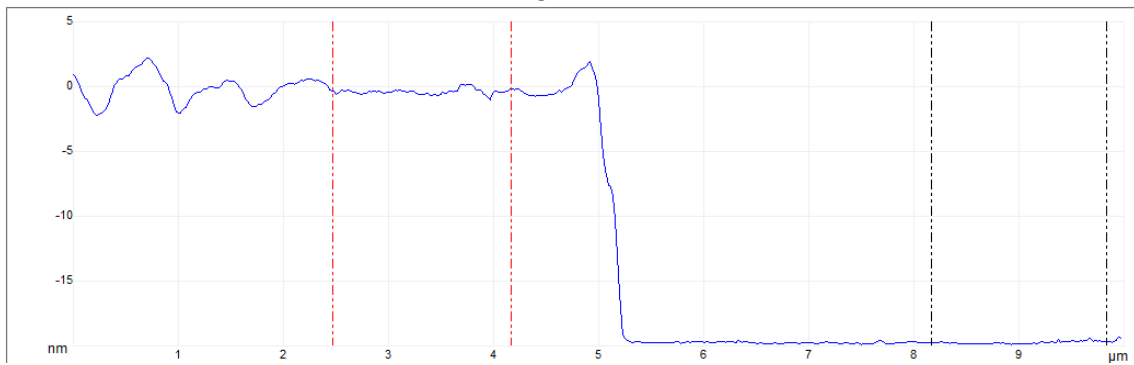


4.0 μm

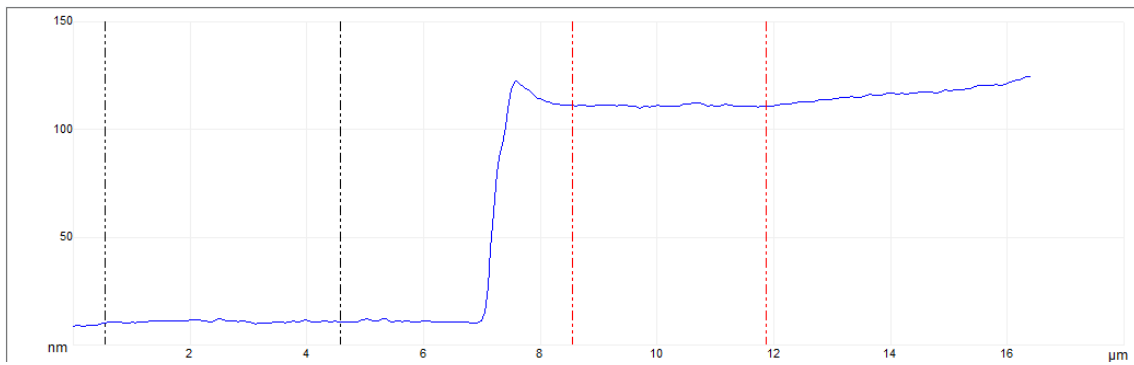
21.6 nm



19.4 nm



100 nm



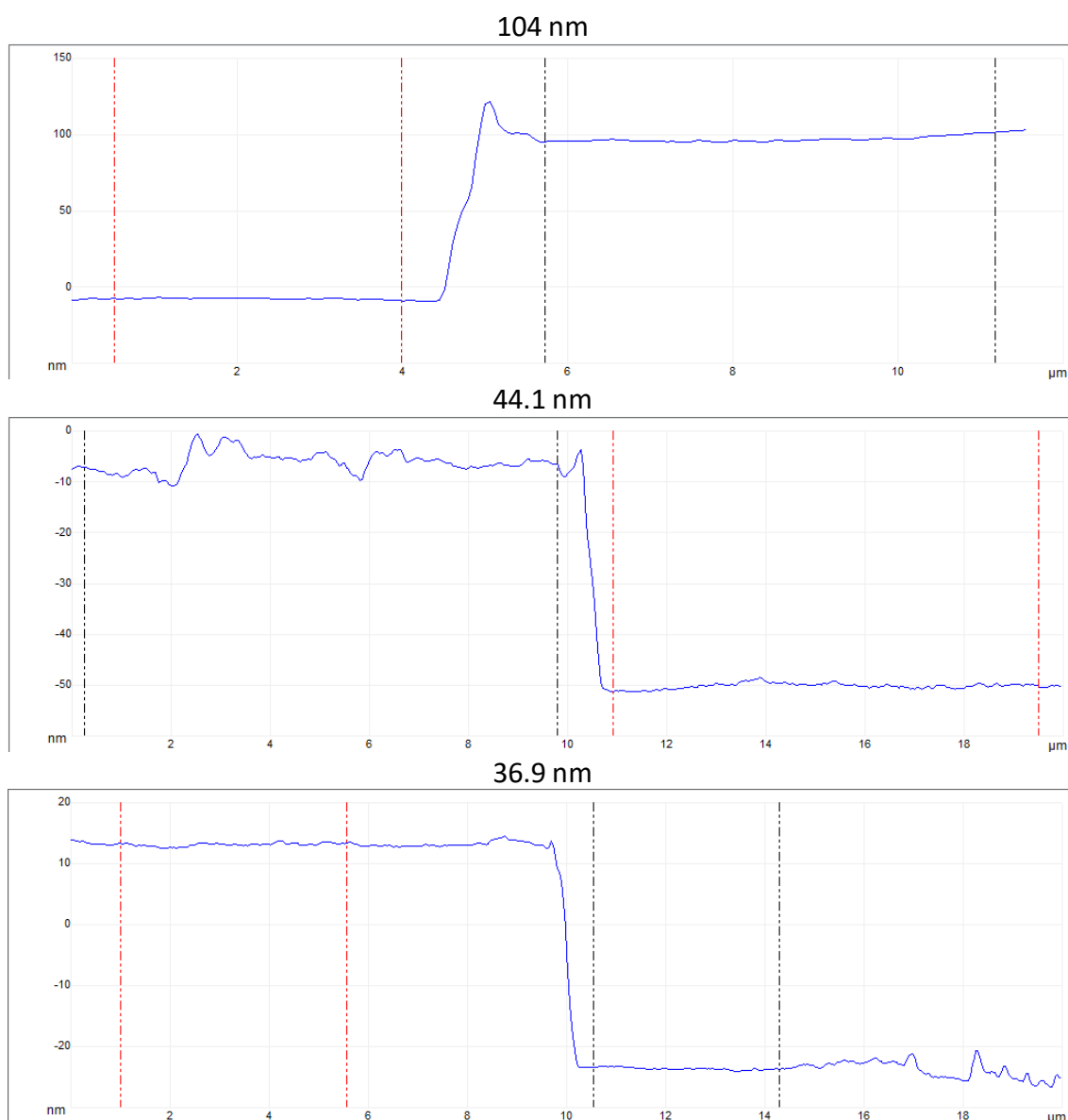


Figure 104 AFM topographical images and height profiles ($10\ \mu\text{m} \times 10\ \mu\text{m}$) of DPP-DDT thin-films via FFT from 9:1 CHCl_3 :CB ($5\ \text{mg mL}^{-1}$) on Si/SiO_2 .

Sample 1	Sample 2	Sample 3	Average nm	STD nm
21.6 nm	104 nm	44.1 nm	54.7 nm	38.6 nm
19.4 nm	102 nm	36.9 nm		

Table 28 Thickness values of DPP-DDT thin-films via FFT from 9:1 CHCl_3 :CB ($5\ \text{mg mL}^{-1}$) on Si/SiO_2 .

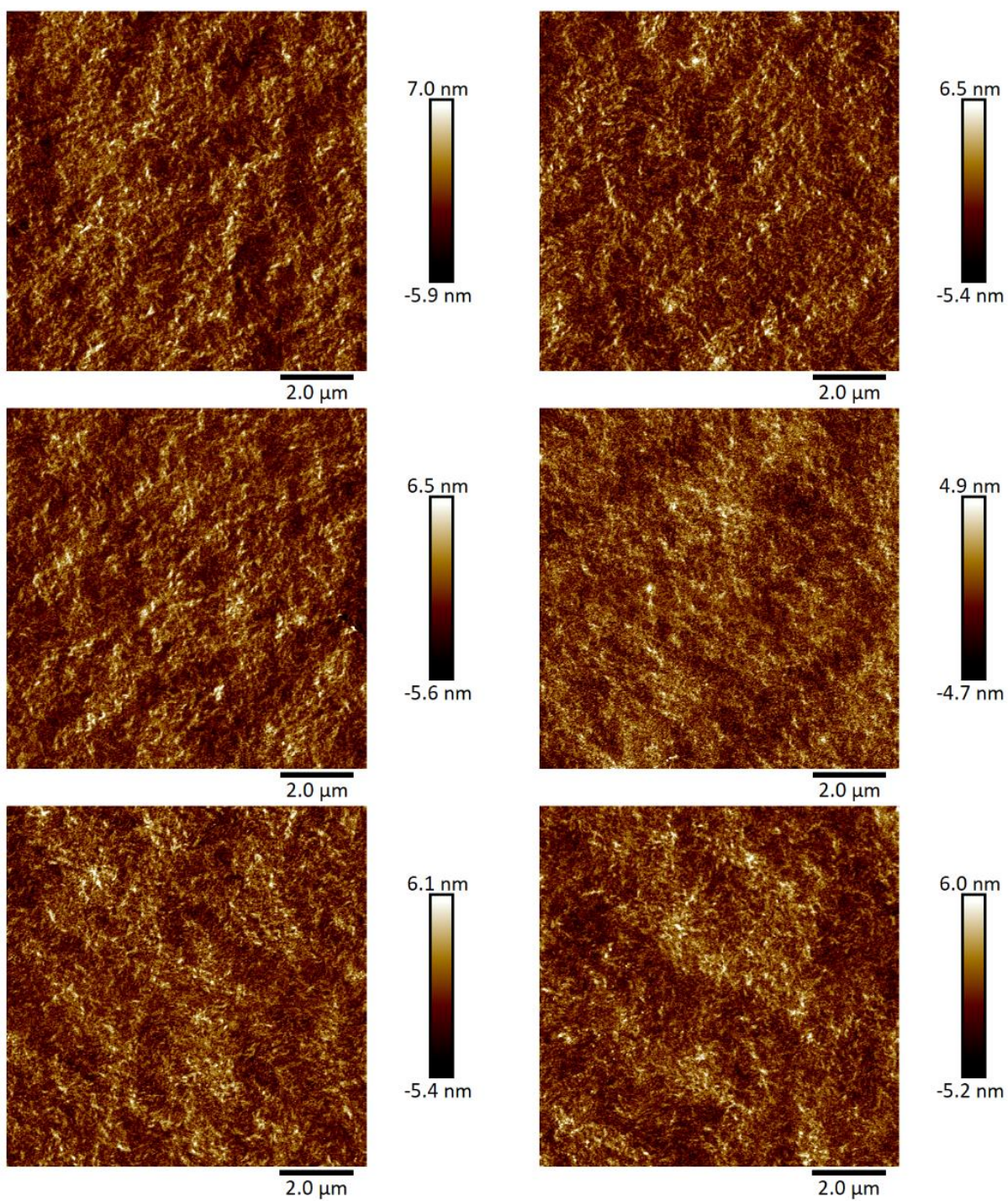
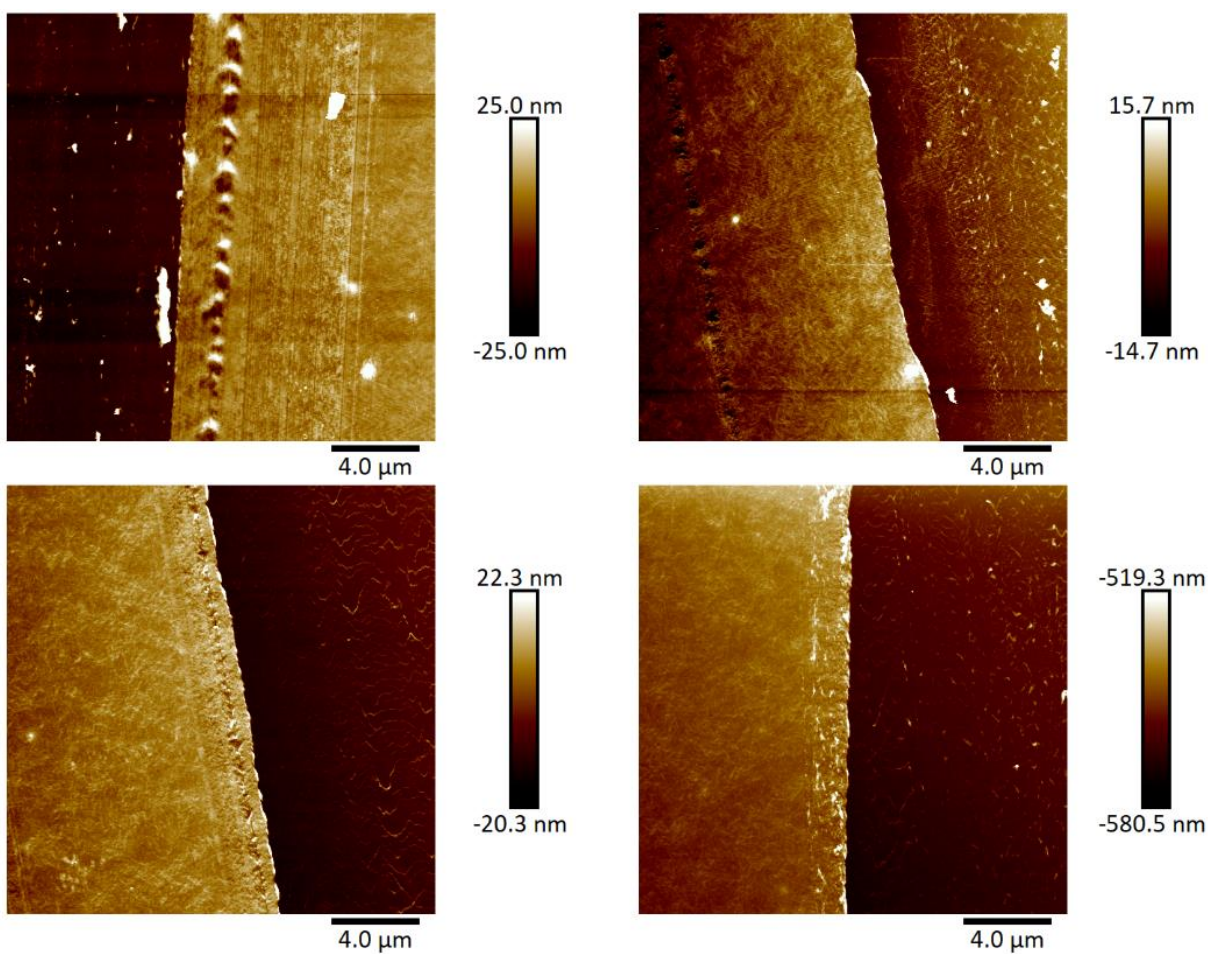
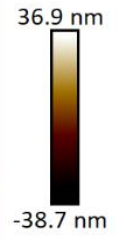
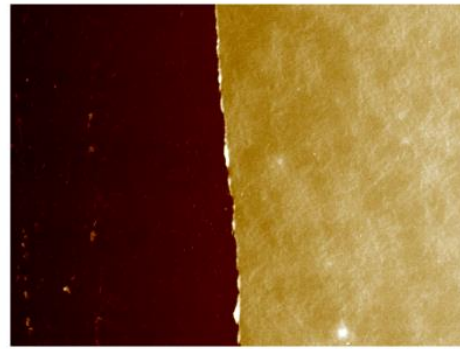
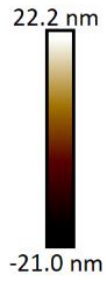
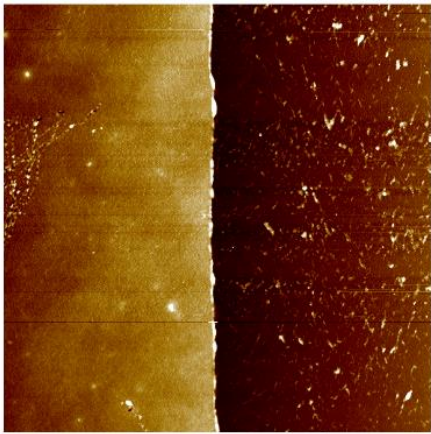


Figure 105 AFM topographical images (10 μm x 10 μm) of DPP-DTT thin-films via FFT from 9:1 CHCl₃:CB (3 mg mL⁻¹) on Si/SiO₂.

Image No. and Roughness	1 nm	2 nm	3 nm	4 nm	5 nm	6 nm	Average nm	STD nm
1 Rq	1.60	1.52	1.64	1.29	1.40	1.37	1.50	0.139
2 Rq	1.73	1.42	1.51	1.24	1.52	1.35		
3 Rq	1.66	1.58	1.55	1.33	1.50	1.47		
1 Ra	1.26	1.21	1.28	1.03	1.10	1.08	1.19	0.108
2 Ra	1.36	1.13	1.20	0.98	1.21	1.07		
3 Ra	1.31	1.25	1.24	1.05	1.20	1.17		

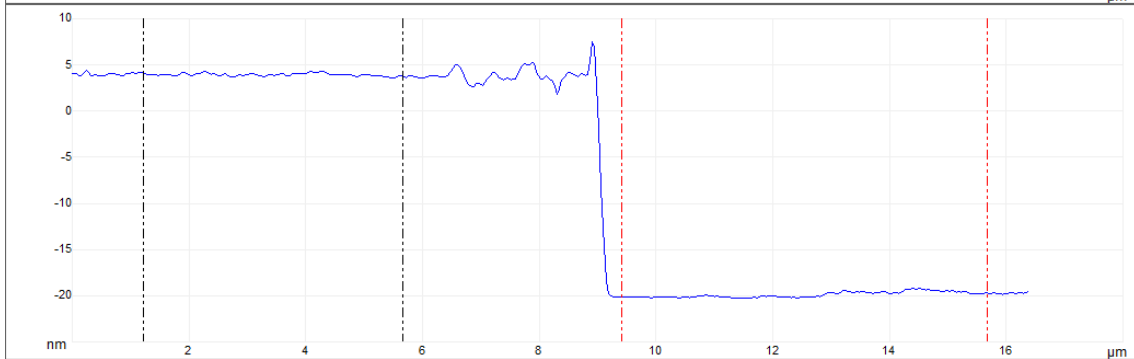
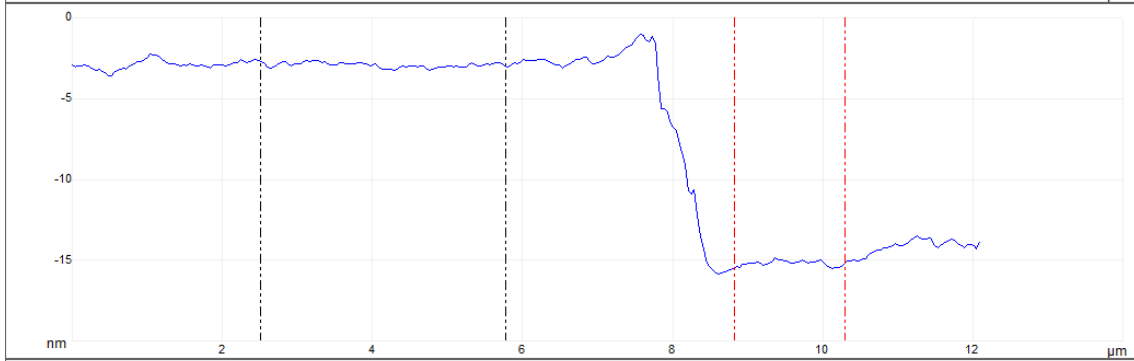
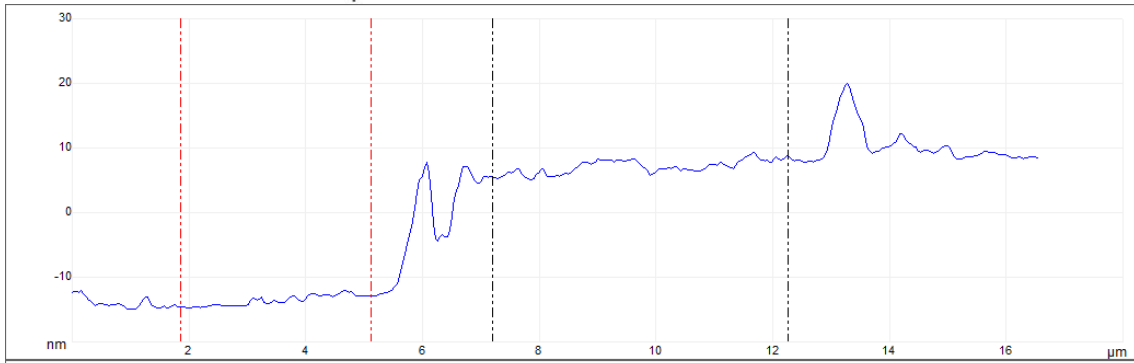
Table 29 Averaged roughness Rq and Ra values ($3 \times 2 \mu\text{m} \times 2 \mu\text{m}^2$ areas) of DPP-DTT thin-films via FFT from 9:1 CHCl_3 :CB (3 mg mL^{-1}) on Si/SiO₂.





4.0 μm

4.0 μm



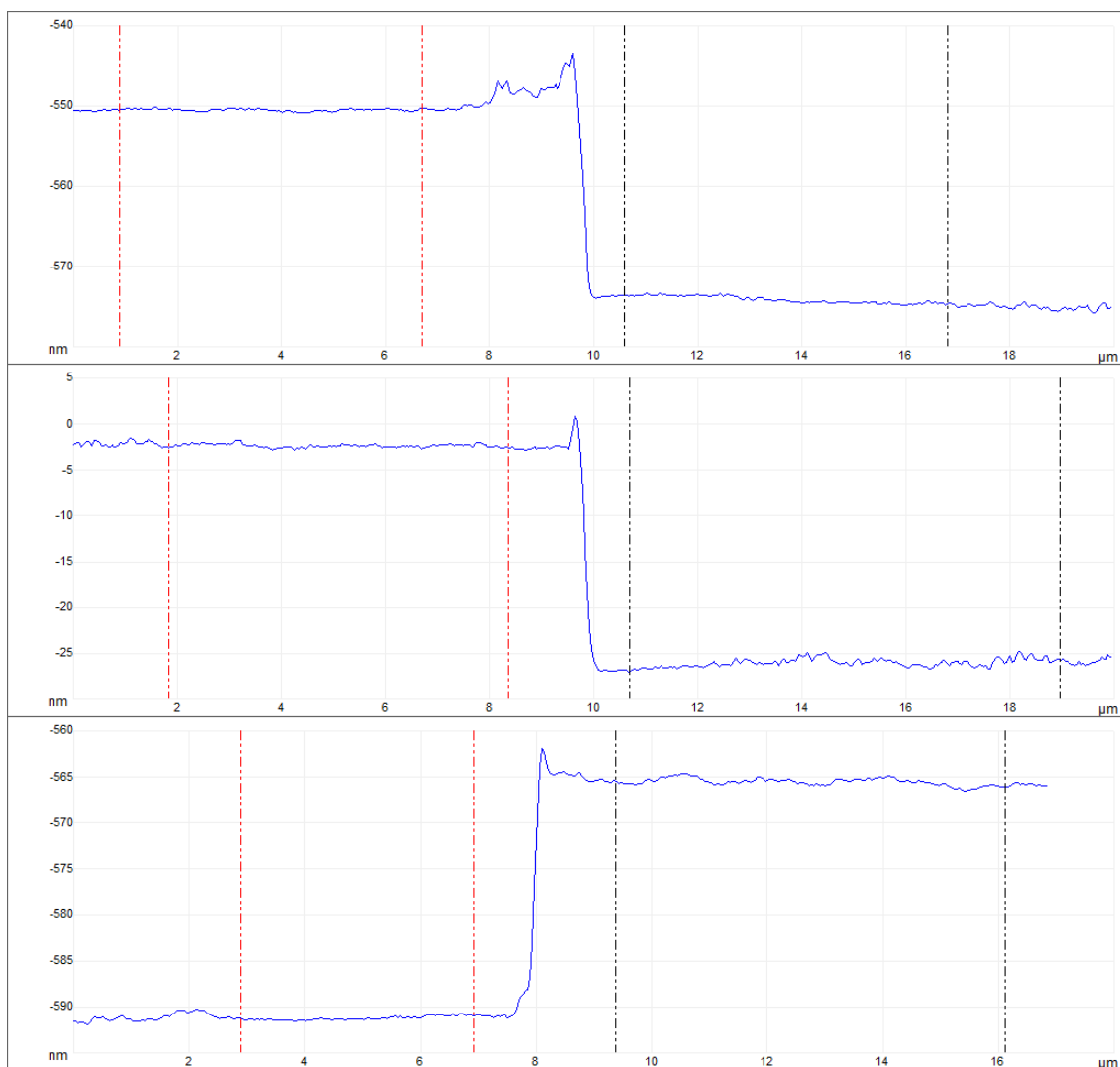


Figure 106 AFM topographical images and height profiles (20 μm x 20 μm) of DPP-DDT thin-films via FFT from 9:1 CHCl_3 :CB (3 mg mL^{-1}) on Si/SiO₂.

1 nm	2 nm	3 nm	Average nm	STD nm
19.2	23.9	23.4	21.3	5.2
12.2	21.6	27.4		

Table 30 Thickness values of DPP-DDT thin-films via FFT from 9:1 CHCl_3 :CB (3 mg mL^{-1}) on Si/SiO₂.

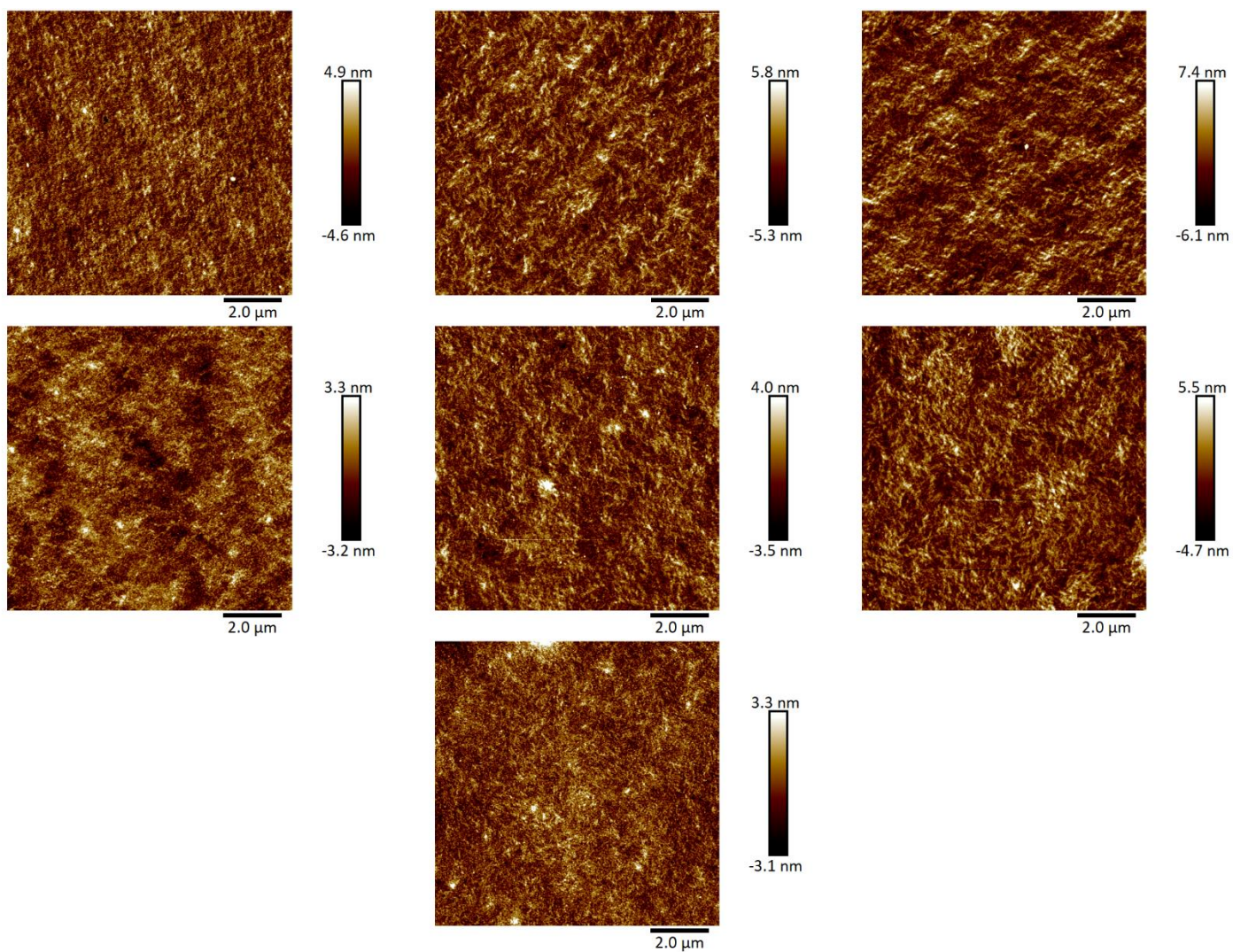
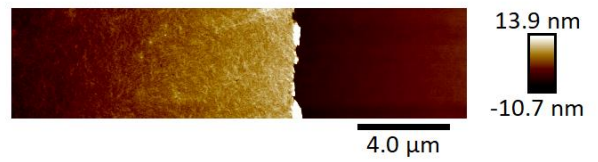
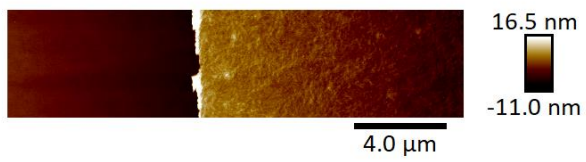
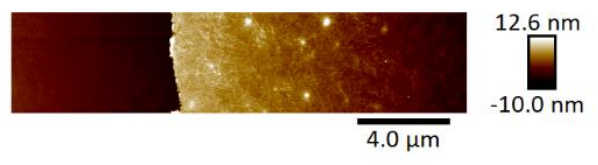
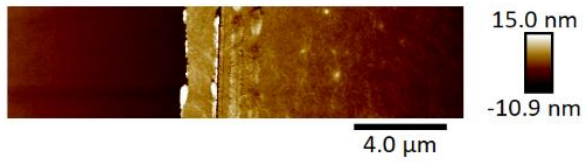
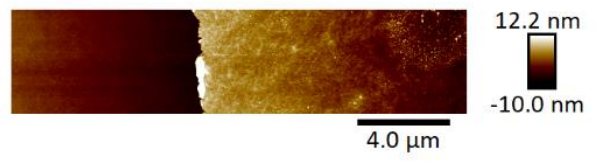
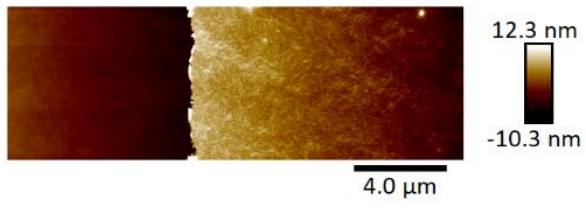
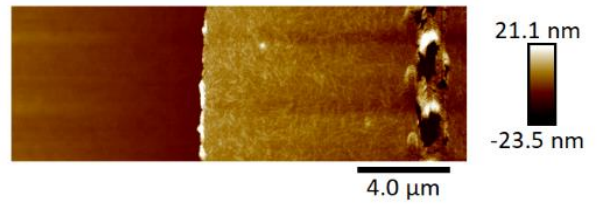
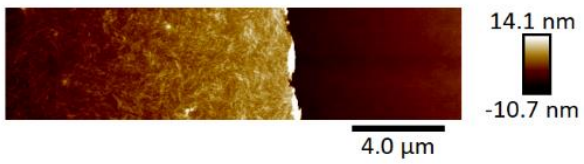
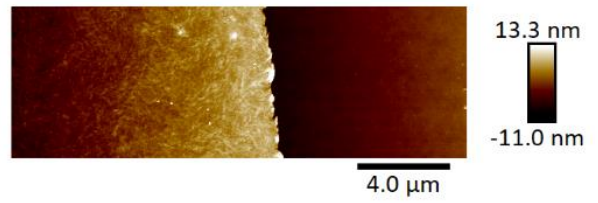
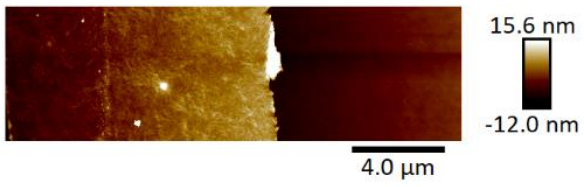
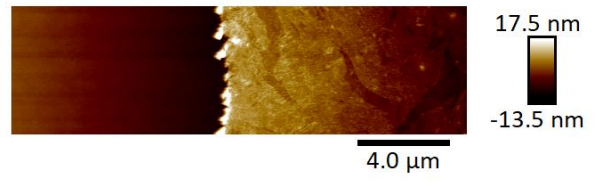
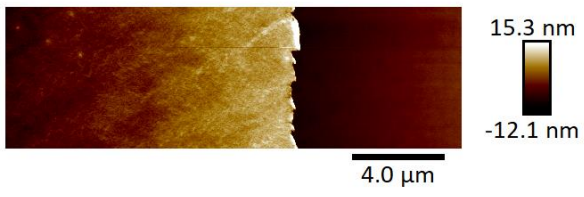


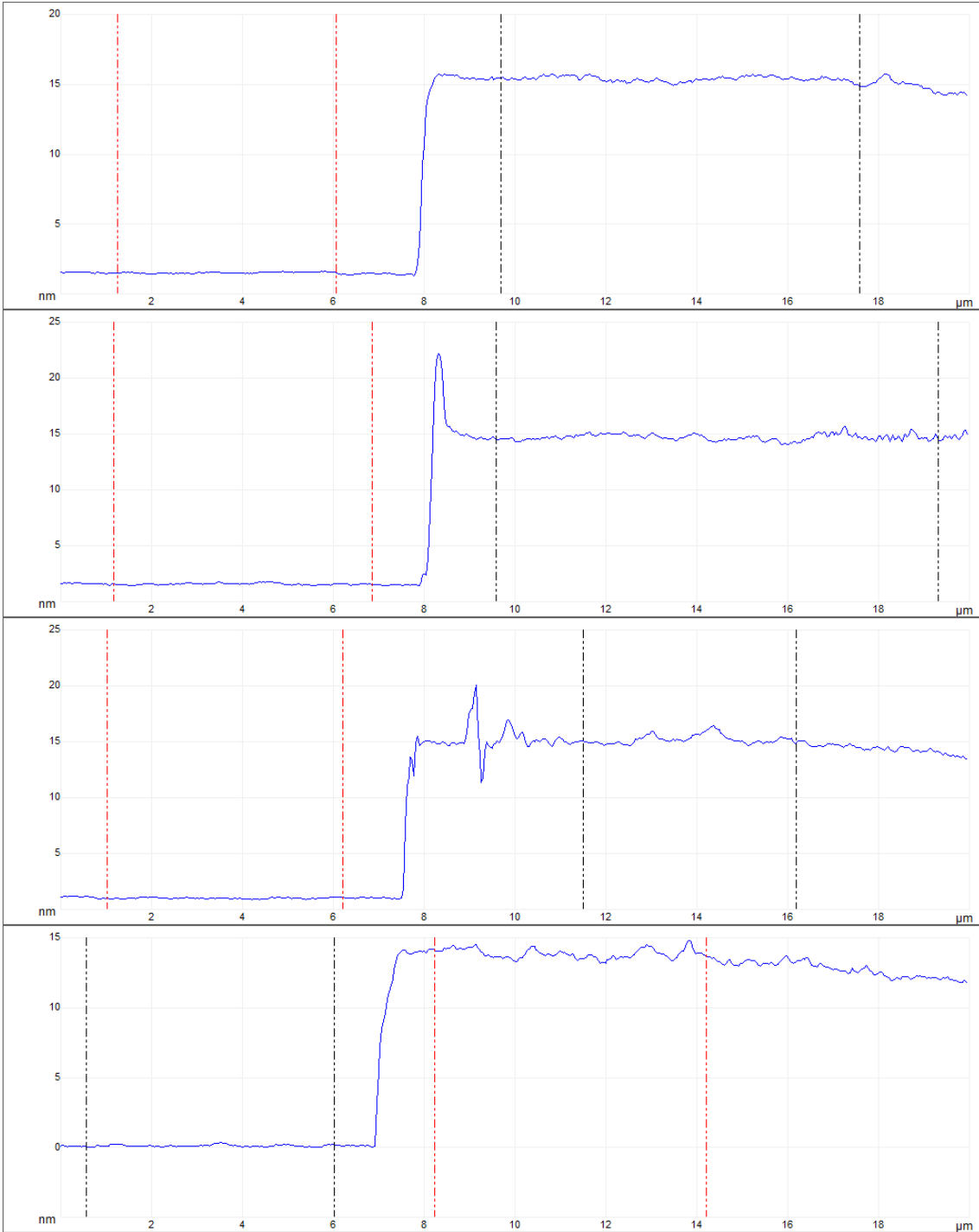
Figure 107 AFM topographical images ($10 \mu\text{m} \times 10 \mu\text{m}$) of DPP-DTT thin-films via FFT from 9:1 $\text{CHCl}_3:\text{CB}$ (3 mg mL^{-1}) on ODTS modified Si/SiO_2 substrates.

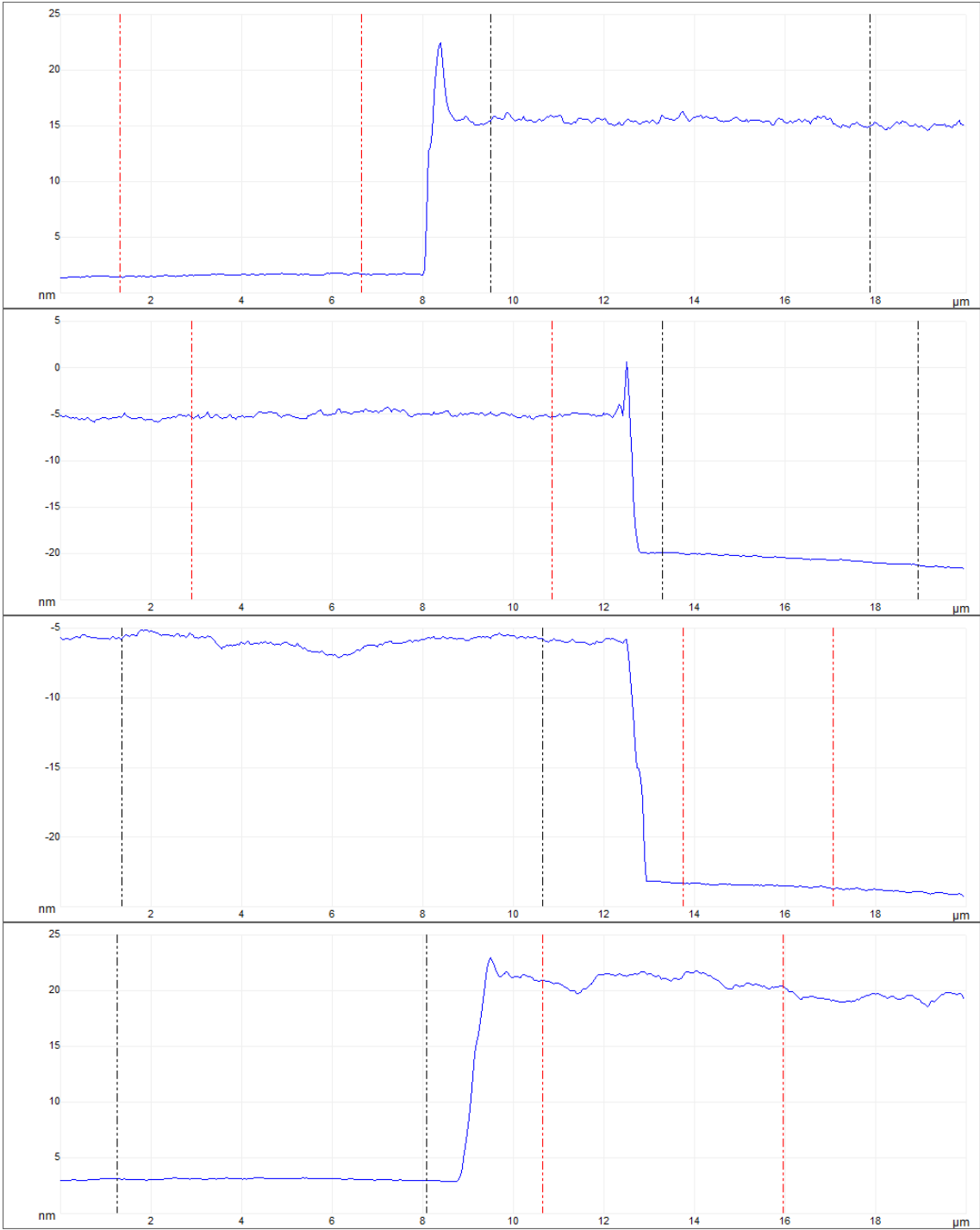
Image No. and Roughness	1 nm	2 nm	3 nm	4 nm	5 nm	6 nm	7 nm	Average nm	STD nm
1 Rq	1.32	1.45	1.78	0.89	1.01	1.35	0.81	1.24	0.331
2 Rq	1.32	1.62	1.76	0.83	0.95	1.36	0.86		
3 Rq	1.30	1.50	1.72	0.95	1.03	1.42	0.82		
1 Ra	1.05	1.16	1.43	0.70	0.80	1.09	0.64	0.99	0.266
2 Ra	1.05	1.30	1.40	0.66	0.76	1.09	0.68		
3 Ra	1.03	1.20	1.37	0.75	0.83	1.12	0.65		

Table 31 Averaged roughness Rq and Ra values ($3 \times 2 \mu\text{m} \times 2 \mu\text{m}$ areas) of DPP-DTT thin-films via FFT from 9:1 $\text{CHCl}_3:\text{CB}$ (3 mg mL^{-1}) on ODTS modified Si/SiO_2 substrates.









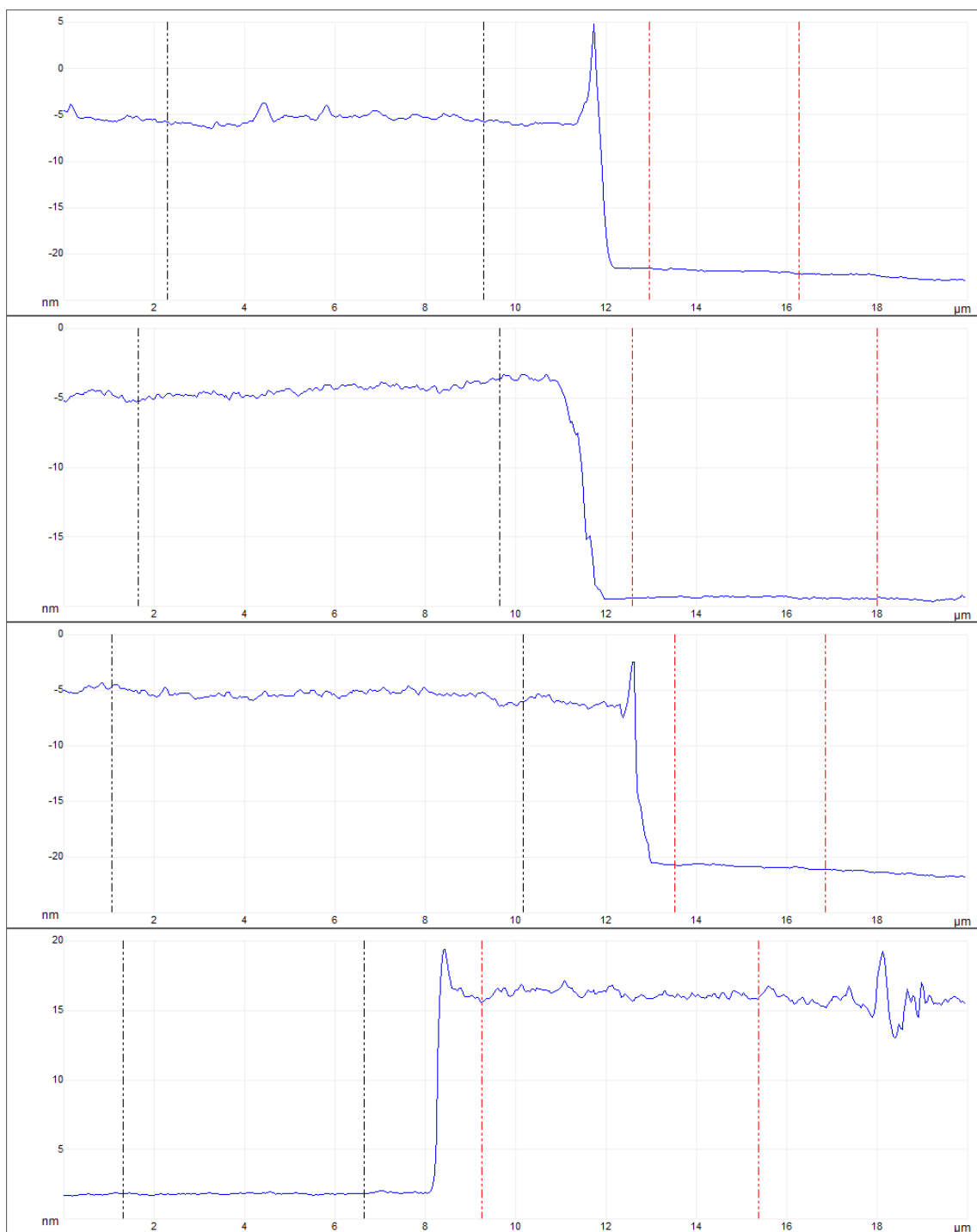


Figure 108 AFM topographical images and height profiles ($20 \mu\text{m} \times 20 \mu\text{m}$) of DPP-DDT thin-films via FFT from 9:1 CHCl_3 :CB (3 mg mL^{-1}) on ODTS modified Si/SiO₂ substrates.

1 nm	2 nm	3 nm	4 nm	Average nm	STD nm
13.9	13.2	14.0	13.3	14.6	1.30
13.4	15.8	16.4	17.3		
14.8	14.6	13.8	14.2		

Table 32 Thickness values of DPP-DTT thin-films via FFT from 9:1 CHCl₃:CB (3 mg mL⁻¹) on ODTS modified Si/SiO₂ substrates.

7.1.2 ODTs SAM treatment of Si/SiO₂ substrates

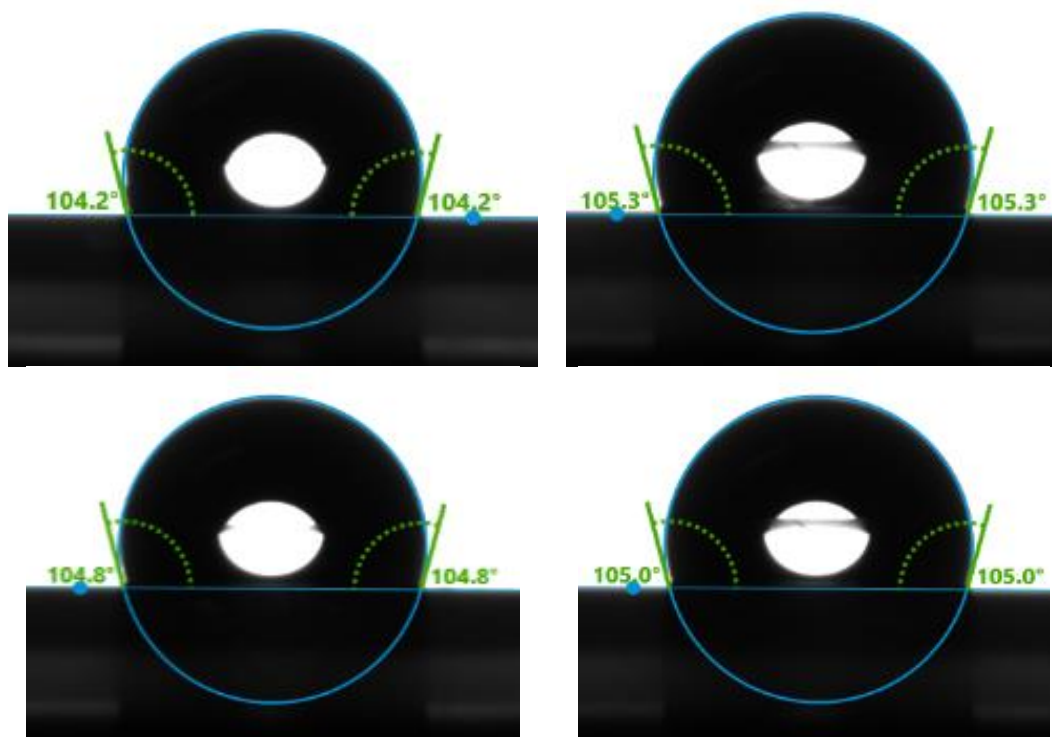


Figure 109 Water contact angle images of ODTs modified Si/SiO₂ (300 nm) substrates.

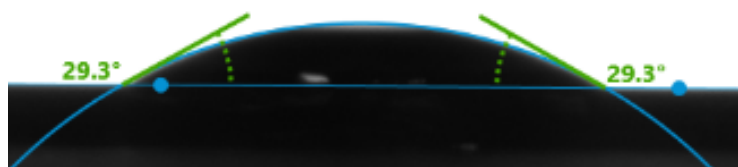


Figure 110 Water contact angle image of pre-modified Si/SiO₂ (300 nm) substrate.

Sample	1	2	3	4	Average	STD	Si/SiO ₂ (300 nm)
WCA	104.2°	105.3°	104.8°	105.0°	104.8°	0.46°	29.3°

Table 33 Water contact angles of ODTs modified Si/SiO₂ substrate and pre-modified Si/SiO₂ (300 nm) substrate.

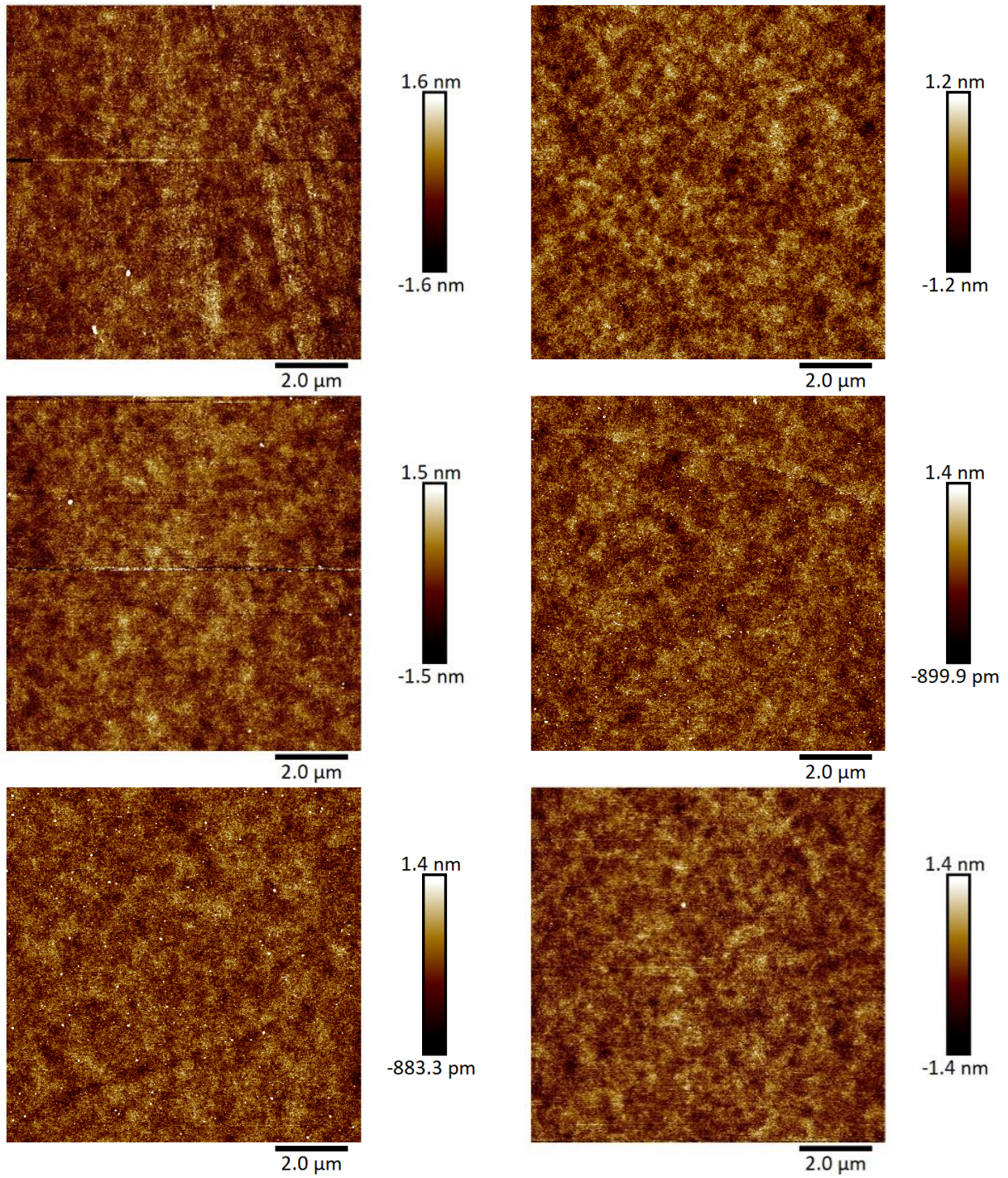


Figure 111 AFM topographical images ($10\ \mu\text{m} \times 10\ \mu\text{m}$) of ODTS modified Si/SiO₂ substrates.

Roughness	1 nm	2 nm	3 nm	4 nm	5 nm	6 nm	Average nm	STD nm
Rq	0.481	0.346	0.461	0.432	0.501	0.402	0.437	0.0568
Ra	0.361	0.272	0.323	0.262	0.270	0.316	0.301	0.0391

Table 34 AFM image roughness values Rq and Ra of ODTS modified Si/SiO₂ substrates.

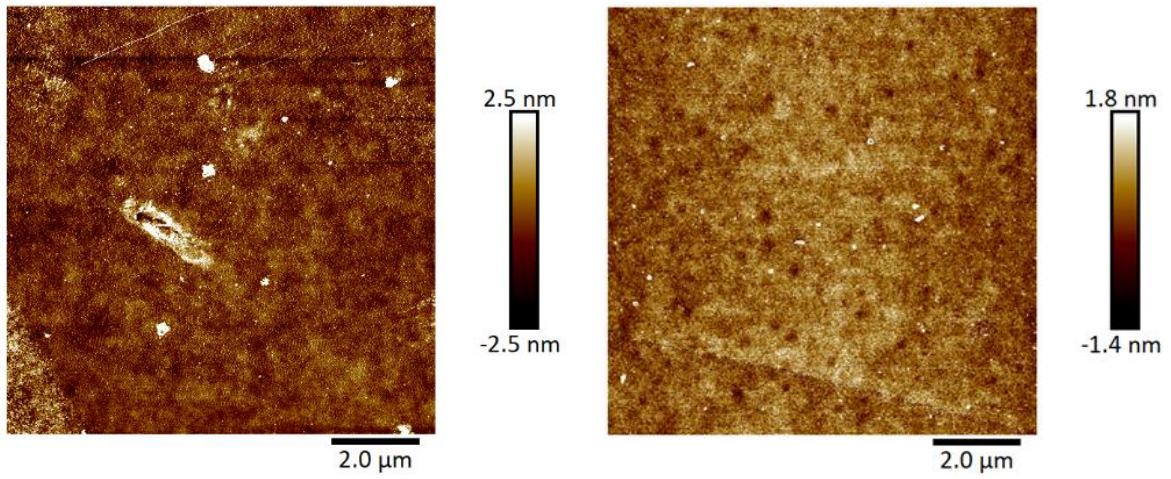
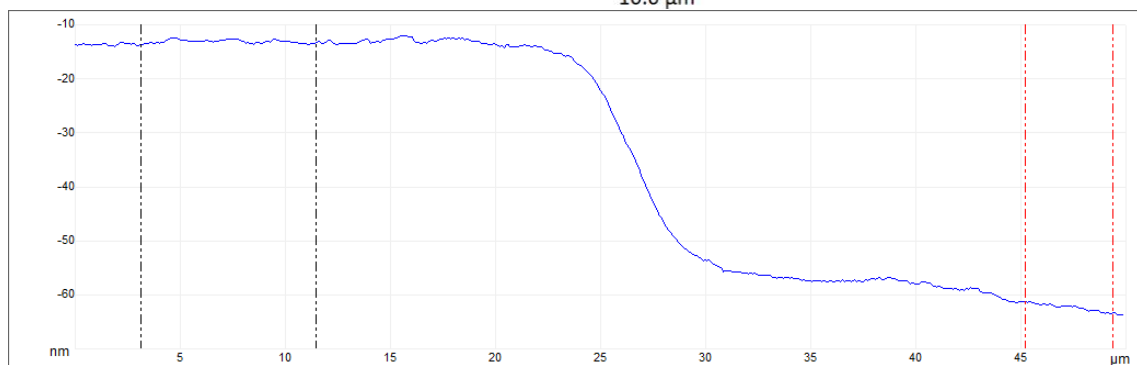
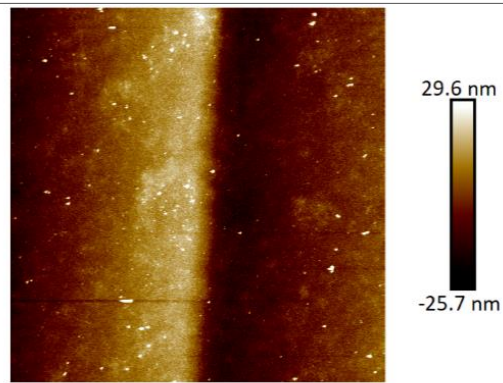
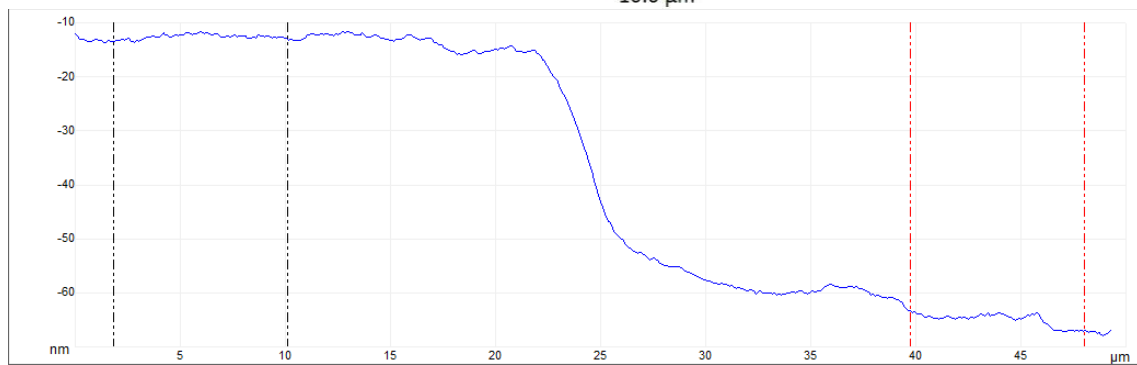
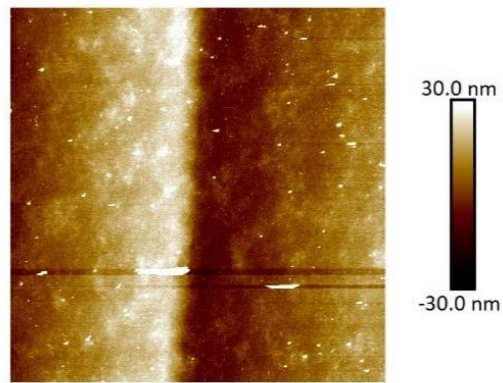


Figure 112 AFM topographical images (10 μm x 10 μm) of Si/SiO₂ substrates.

Roughness	1 nm			2 nm			Average nm	STD nm
Rq	0.621	0.561	0.651	0.600	0.583	0.668	0.614	0.0407
Ra	0.459	0.422	0.486	0.310	0.311	0.318	0.384	0.0808

Table 35 AFM image roughness values Rq and Ra of Si/SiO₂ substrates.

7.1.3 Contact electrode deposition



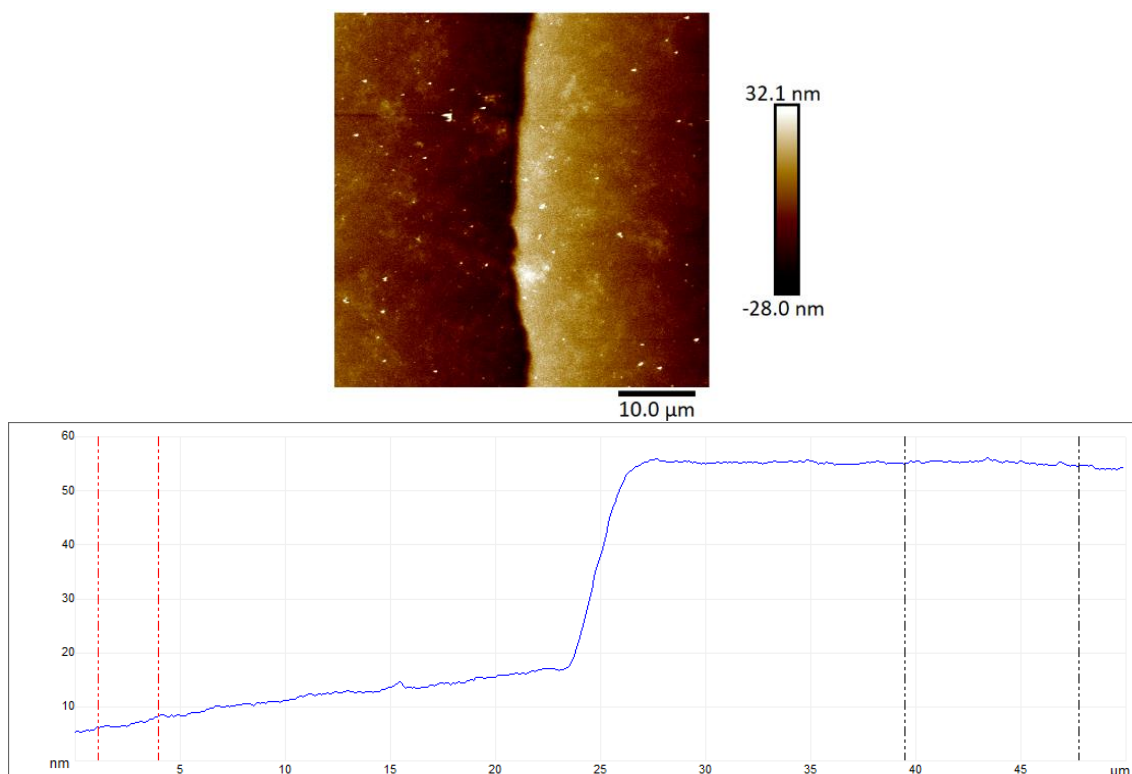


Figure 113 AFM topological images ($50 \mu\text{m} \times 50 \mu\text{m}$) and height profiles of physical vapour deposited gold (50 nm) S/D electrodes on DPP-DTT thin-film via FFT from 9:1 CHCl_3 :CB (3 mg mL^{-1}).

1 nm	2 nm	3 nm	4 nm	Average nm	STD nm
52.4	49.2	48.4	49.2	49.8	1.54

Table 36 Thickness values of physical vapour deposited gold (50 nm) S/D electrodes on DPP-DTT thin-film via FFT from 9:1 CHCl_3 :CB (3 mg mL^{-1}).

7.1.4 The effects of O₂ plasma treatment on thin-film morphologies

appendix

Conditions	Before O ₂ plasma					
	1 nm	2 nm	3 nm	4 nm	Average nm	σ nm
6 W, 0.3 mbar, 90 s	13.9	13.2	14.0	13.3	13.6	0.41
12 W, 0.3 mbar, 60 s	14.8	14.6	13.8	14.2	14.4	0.44
24 W, 0.3 mbar, 30 s	13.4	15.8	16.4	17.3	15.7	1.67

Table 37 Thin-film thickness values of DPP-DTT OFETs before O₂ plasma treatment.

Conditions	After O ₂ plasma						
	1 nm	2 nm	3 nm	4 nm	Average nm	σ nm	Δ nm
6 W, 0.3 mbar, 90 s	12.0	9.8	10.2	12.1	11.0	1.19	2.6
12 W, 0.3 mbar, 60 s	14.7	13.7	12.8	13.5	13.7	0.78	0.7
24 W, 0.3 mbar, 30 s	9.9	6.9	7.8	11.8	9.1	2.20	5.6

Table 38 Thin-film thickness values of DPP-DTT OFETs after O₂ plasma treatment and change in thickness.

Conditions	Before O ₂ plasma				After O ₂ plasma			
	Rq nm	σ nm	Ra nm	σ nm	Rq nm	σ nm	Ra nm	σ nm
6 W, 0.3 mbar, 90 s	1.09	0.075	0.81	0.049	1.13	0.121	0.81	0.050
12 W, 0.3 mbar, 60 s	1.19	0.396	0.94	0.316	1.15	0.161	0.91	0.128
24 W, 0.3 mbar, 30 s	1.01	0.100	0.80	0.075	1.05	0.151	0.83	0.127

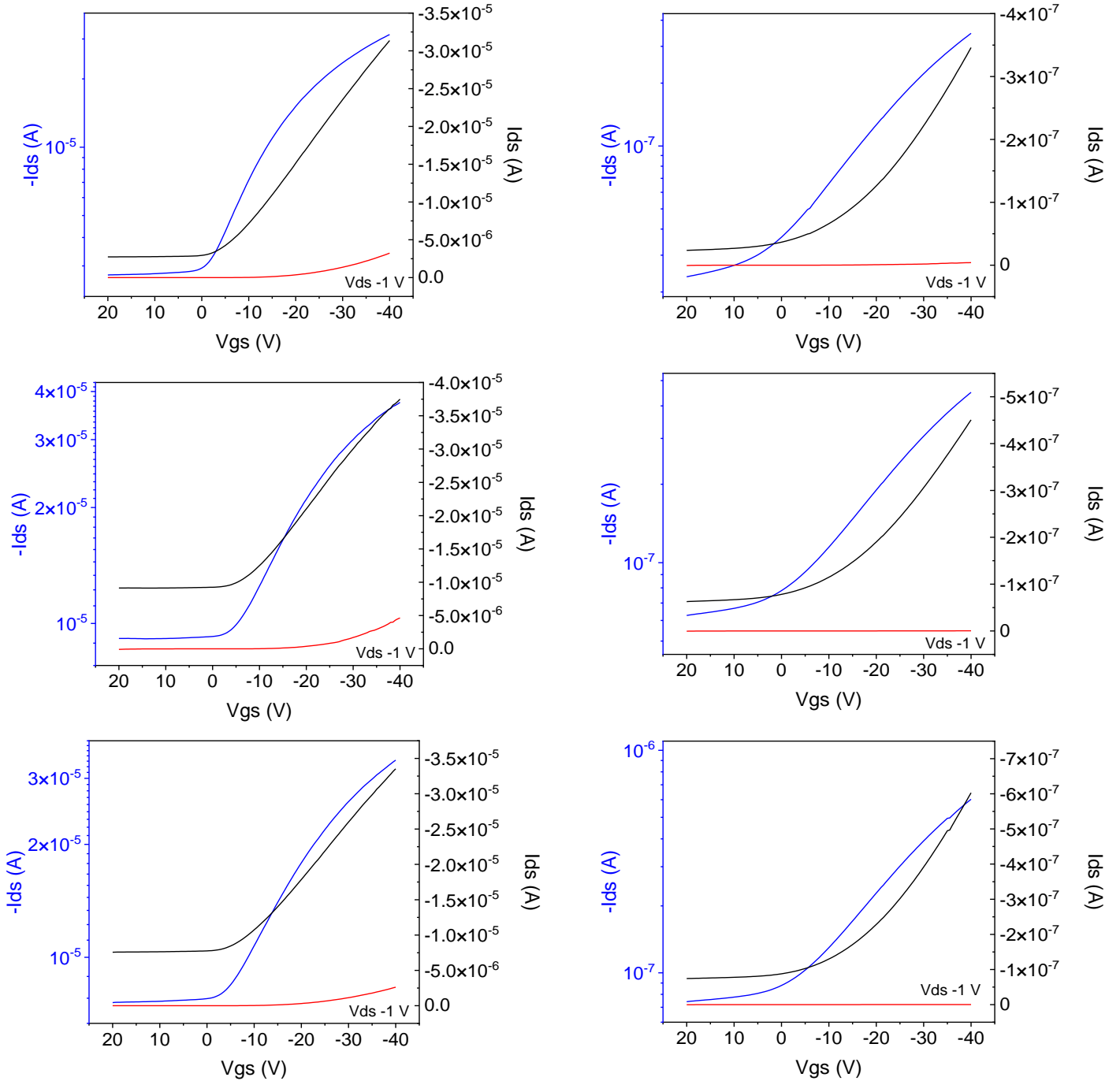
Table 39 Thin-film roughness values of DPP-DTT OFETs before and after O₂ plasma treatment.

7.1.5 The effects of O₂ plasma treatment on OFET performance

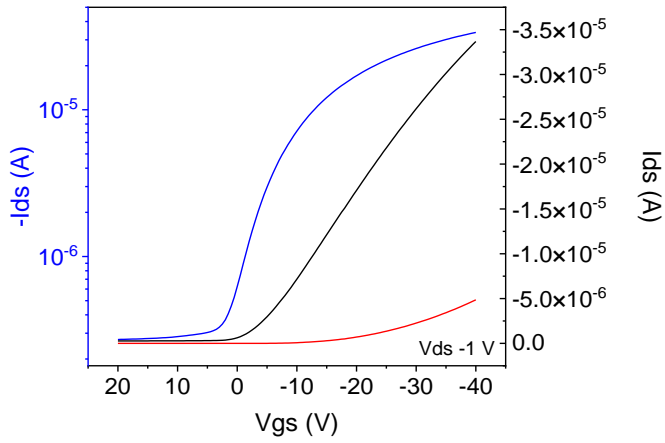
appendix

Before 6 W, 90 s

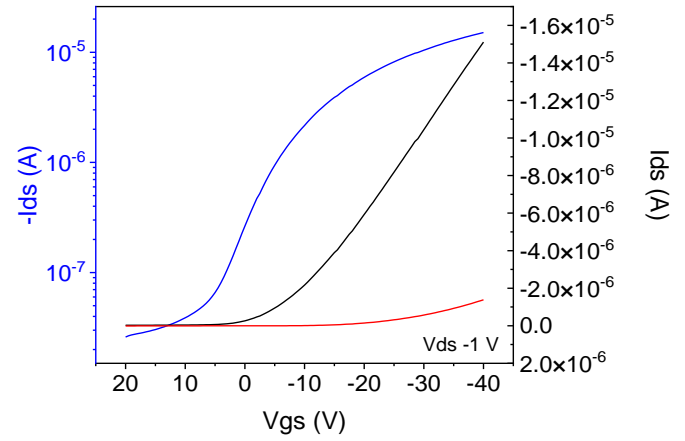
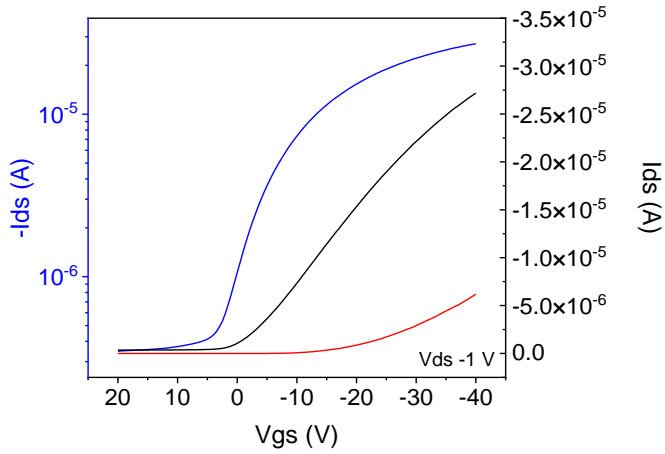
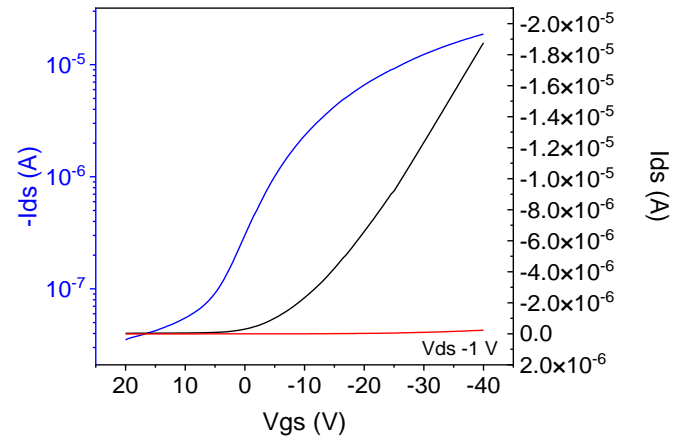
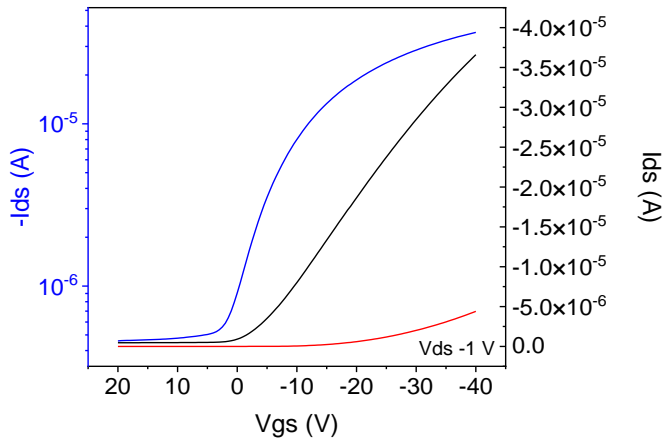
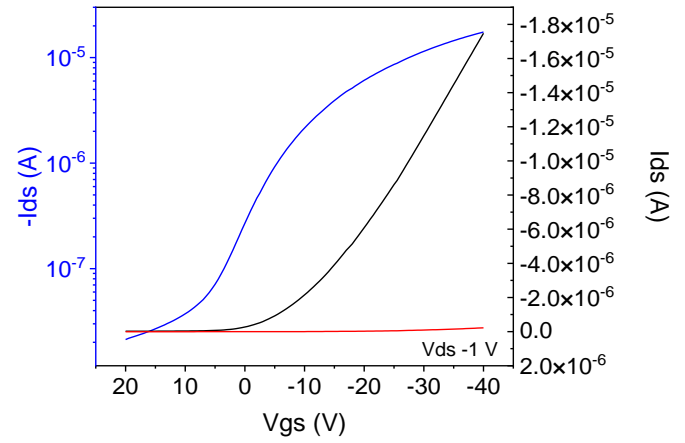
After 6 W, 90 s



Before 12 W, 60 s



After 12 W, 60 s



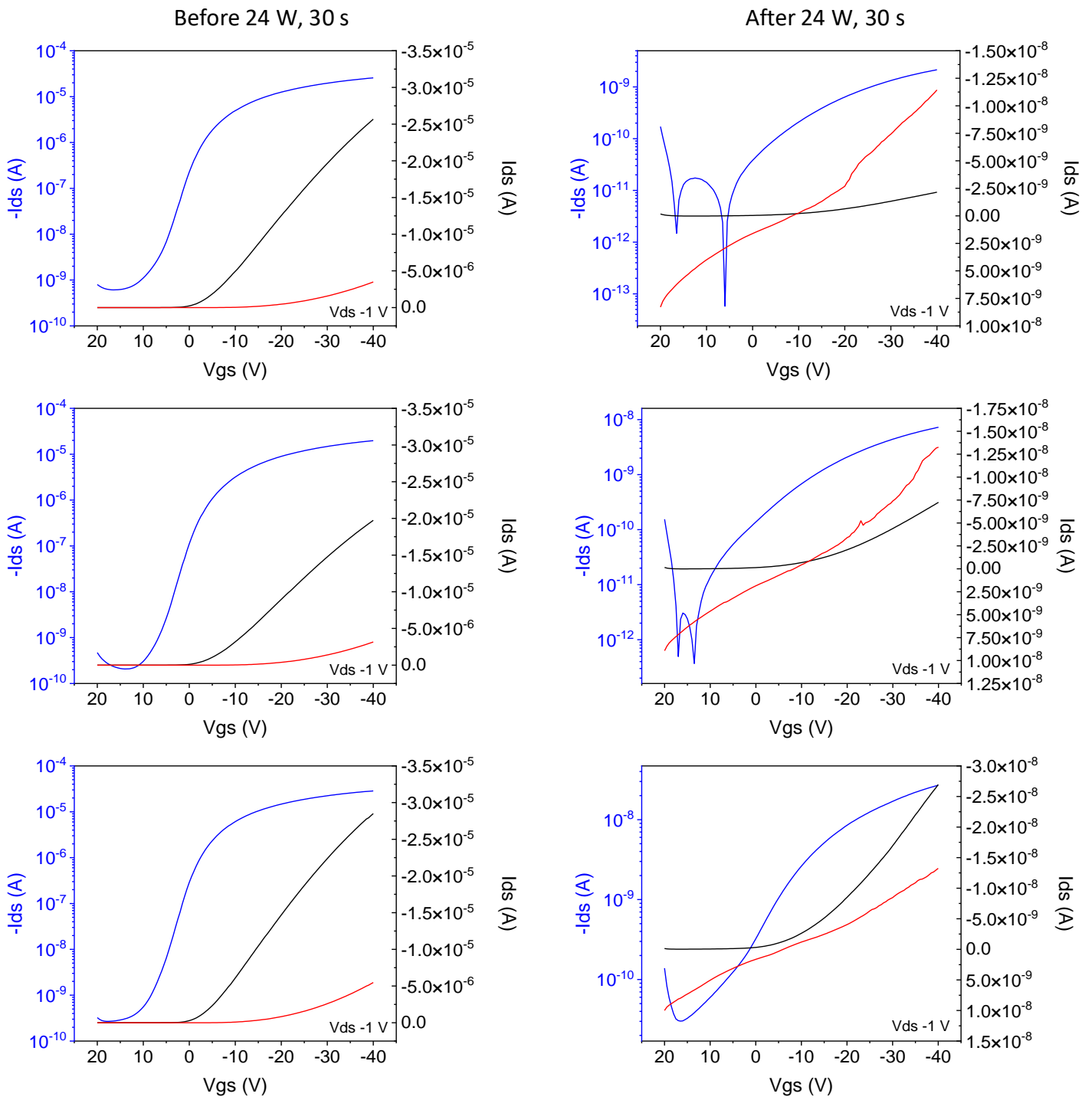


Figure 114 Transfer characteristics ($V_{ds} = -1$) of OFETs (left) before and (right) after O_2 plasma treatment (blue) log scale (black) linear scale (red) gate current.

Conditions		Threshold voltage (V)	σ (V)	Mobility ($\text{cm}^2 \text{V}^{-1} \text{s}^{-1}$)	σ ($\text{cm}^2 \text{V}^{-1} \text{s}^{-1}$)
6 W, 90 s	Before	1.94	3.041	1.96E-01	9.50E-03
	After	-10.47	1.474	3.74E-03	1.05E-03
12 W, 60 s	Before	3.17	2.273	1.76E-01	4.57E-02
	After	-8.49	1.600	1.29E-01	1.93E-02
24 W, 30 s	Before	-1.27	0.977	1.73E-01	4.07E-02
	After	-12.35	1.059	1.00E-04	1.05E-04

Table 40 OFET transfer characteristics ($V_{ds} = -1$) mobility and threshold voltage values before and after O_2 plasma treatment.

7.1.6 The introduction of exploitable chemical functionalities on O₂ plasma treated thin-films appendix

Sample conditions	Functional group Area CPS.eV					Abbe criterion
	C1s C-C	C1s C-S	C1s C-N	C1s C=O	C1s COOH	
Untreated	41595.78	7087.67	3490.32	1483.9	0	0.1847
6 W, 90 s	5011.16	714.31	1248.56	732.14	525.61	0.4688
12 W, 60 s	38221.22	5434.48	4332.1	4318.29	2861.66	0.1525
24 W, 30 s	37132.51	4433.98	3443.14	4336.98	2740.05	0.1647

Table 41 XPS high resolution C1s scan component peak areas of DPP-DTT OFETs O₂ plasma treated and untreated.

Sample conditions	Element Area CPS.eV				
	O1s	N1s	S2p	Si2p	SiO ₂ adjusted O1s
Untreated	10470.67	3183.57	7008.46	1204.44	8061.79
6 W, 90 s	6587.18	1414.50	812.32	1016.34	4554.50
12 W, 60 s	28558.53	4041.10	5312.48	939.04	26680.45
24 W, 30 s	34344.14	3680.57	4895.14	2870.29	28603.56

Table 42 XPS high resolution O1s, N1s, S2p, Si2p scan peak areas of DPP-DTT OFETs O₂ plasma treated and untreated.

7.1.7 The effects of N₂ plasma treatment on thin-film morphologies

appendix

Plasma conditions	Before N ₂ plasma				
	1 nm	2 nm	3 nm	Average nm	σ nm
6 W, 90 s	12.2	15.7	14.0	14.0	1.75
12 W, 60 s	19.1	15.6	19.1	17.9	2.02
24 W, 30 s	12.3	17.8	11.2	13.8	3.54

Table 43 Thin-film thicknesses of DPP-DTT OFETs before N₂ plasma treatment.

Plasma conditions	After N ₂ plasma					
	1 nm	2 nm	3 nm	Average nm	σ nm	Δ
6 W, 90 s	8.3	7.7	10.2	8.7	1.31	5.3
12 W, 60 s	15.8	15.8	18.5	16.7	1.56	1.2
24 W, 30 s	7.4	6.0	5.4	6.3	1.03	7.5

Table 44 Thin-film thicknesses of DPP-DTT OFETs after N₂ plasma treatment and change in thin-film thickness.

Plasma conditions	Ra										
	1 nm			2 nm			3 nm			Average nm	σ nm
6 W, 90 s	0.99	0.82	0.89	1.12	0.97	1.10	0.91	1.14	1.01	0.99	0.111
12 W, 60 s	0.96	1.26	0.85	1.48	1.45	1.49	1.05	1.04	1.19	1.20	0.239
24 W, 30 s	1.14	0.93	0.95	1.06	1.18	0.94	0.97	1.04	0.79	1.00	0.120
Plasma conditions	Rq										
	1 nm			2 nm			3 nm			Average nm	σ nm
6 W, 90 s	1.28	1.03	1.13	1.44	1.22	1.38	1.21	1.44	1.27	1.27	0.138
12 W, 60 s	1.24	1.57	1.07	1.87	1.83	1.87	1.34	1.32	1.49	1.51	0.295
24 W, 30 s	1.44	1.17	1.18	1.32	1.47	1.22	1.20	1.29	1.00	1.25	0.145

Table 45 Thin-film roughness Ra and Rq values of DPP-DTT OFETs before N₂ plasma treatment.

Plasma conditions	Ra										
	1 nm			2 nm			3 nm			Average nm	σ nm
6 W, 90 s	0.96	1.08	1.04	1.16	1.11	1.02	1.05	0.83	0.94	1.02	0.098
12 W, 60 s	1.05	0.99	1.14	0.76	0.83	0.62	1.01	0.89	0.82	0.90	0.162
24 W, 30 s	1.02	1.02	1.12	1.37	0.95	1.05	0.94	1.01	1.36	1.09	0.163
Plasma conditions	Rq										
	1 nm			2 nm			3 nm			Average nm	σ nm
6 W, 90 s	1.21	1.39	1.30	1.48	1.41	1.36	1.33	1.05	1.20	1.30	0.131
12 W, 60 s	1.35	1.31	1.67	1.00	1.17	0.78	1.31	1.14	1.04	1.20	0.253
24 W, 30 s	1.30	1.28	1.40	1.65	1.20	1.34	1.17	1.27	1.74	1.37	0.197

Table 46 Thin-film roughness Ra and Rq values of DPP-DTT OFETs after N₂ plasma treatment.

Plasma conditions	1 nm	2 nm	3 nm	4 nm	Average nm	σ nm
6 W, 30 s	12.7	11.7	12.3	13.2	12.5	0.63
6 W, 60 s	10.9	11.7	12.2	12.0	11.7	0.57
6 W, 90 s	12.8	18.8	15.0	15.9	15.6	2.49
12 W, 30 s	14.3	19.8	14.4	15.6	16.0	2.59
12 W, 60 s	18.0	18.6	18.7	16.3	17.9	1.11
12 W, 90 s	15.8	14.2	12.7	14.4	14.3	1.27

Table 47 Thin-film thickness values of DPP-DTT OFETs before N₂ plasma treatment.

Plasma conditions	1 nm	2 nm	3 nm	4 nm	Average nm	σ nm
6 W, 30 s	12.5	12.2	12.9	13.3	12.7	0.48
6 W, 60 s	13.4	13.2	11.4	13.2	12.8	0.94
6 W, 90 s	12.2	11.1	13.2	13.1	12.4	0.98
12 W, 30 s	13.5	12.4	12.6	14.2	13.2	0.83
12 W, 60 s	18.0	17.4	17.8	19.7	18.2	1.01
12 W, 90 s	12.0	11.4	11.5	11.7	11.7	0.26

Table 48 Thin-film thickness values of DPP-DTT OFETs after N₂ plasma treatment.

Plasma conditions	Rq					Ra				
	1 nm	2 nm	3 nm	Average nm	STD nm	1 nm	2 nm	3 nm	Average nm	STD nm
6 W, 30 s	1.22	1.11	1.55	1.29	0.229	0.92	0.80	0.94	0.89	0.076
6 W, 60 s	2.15	2.07	1.95	2.06	0.101	1.40	1.28	1.16	1.28	0.120
6 W, 90 s	1.48	1.37	1.28	1.38	0.100	1.05	0.97	0.93	0.98	0.061
12 W, 30 s	1.79	1.86	1.84	1.83	0.036	1.19	1.15	1.11	1.15	0.040
12 W, 60 s	1.62	1.77	1.39	1.59	0.191	1.27	1.00	0.95	1.07	0.172
12 W, 90 s	1.57	1.48	1.36	1.47	0.105	1.10	1.13	1.05	1.09	0.040

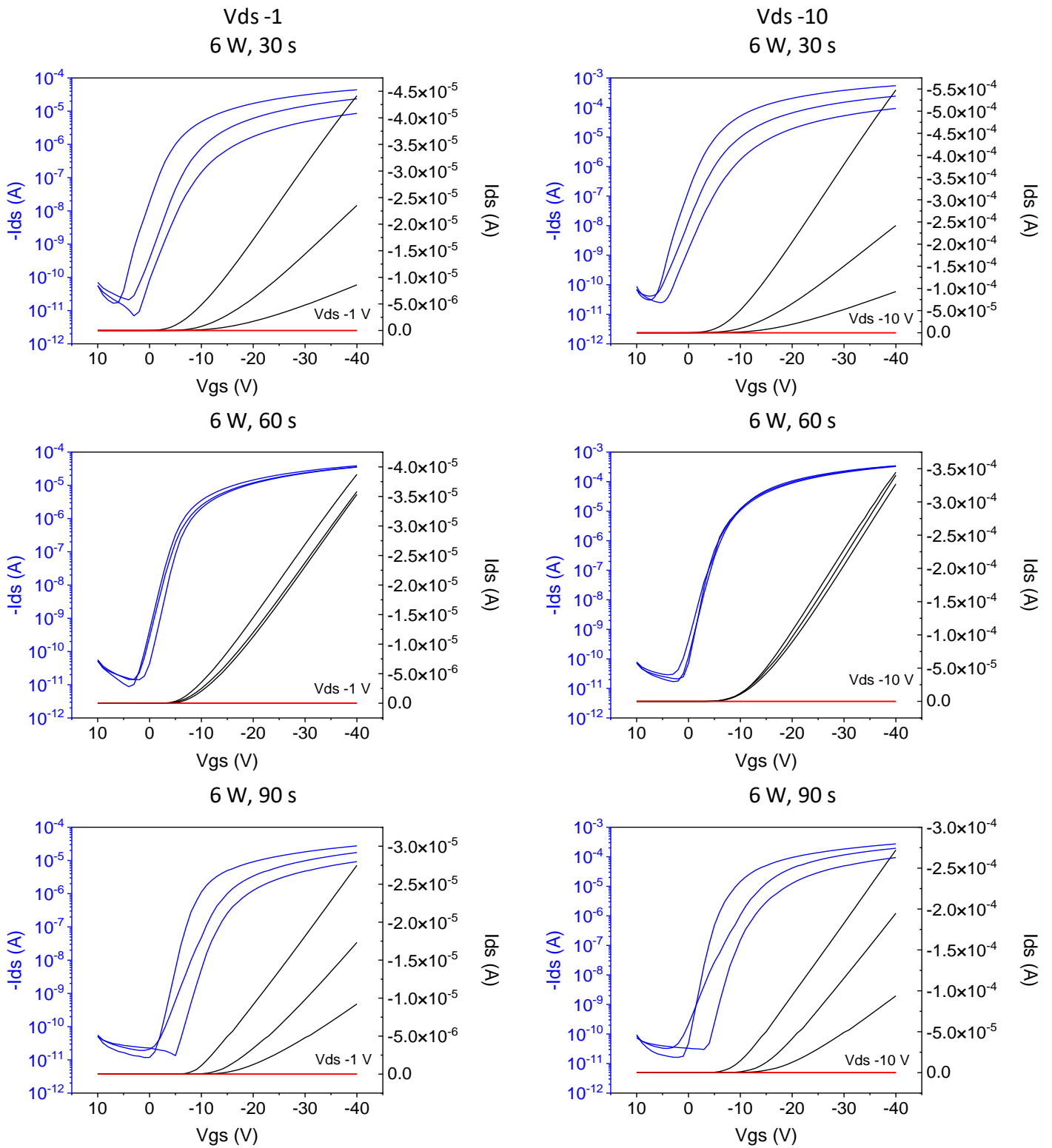
Table 49 Thin-film roughness Ra and Rq values of DPP-DTT OFETs before N₂ plasma treatment.

Plasma conditions	Rq					Ra				
	1 nm	2 nm	3 nm	Average nm	STD nm	1 nm	2 nm	3 nm	Average nm	STD nm
6 W, 30 s	1.07	1.04	1.31	1.14	0.148	0.79	0.76	0.81	0.79	0.025
6 W, 60 s	1.87	2.03	2.13	2.01	0.131	1.22	1.28	1.28	1.26	0.035
6 W, 90 s	1.69	1.72	1.73	1.71	0.021	1.09	1.06	1.09	1.08	0.017
12 W, 30 s	1.59	1.33	1.38	1.43	0.138	1.12	0.99	1.00	1.04	0.072
12 W, 60 s	1.41	1.50	1.47	1.46	0.046	1.10	1.15	1.11	1.12	0.026
12 W, 90 s	1.53	1.37	1.37	1.42	0.092	1.06	1.01	1.01	1.03	0.029

Table 50 Thin-film roughness Ra and Rq values of DPP-DTT OFETs after N₂ plasma treatment.

7.1.8 The effects of N₂ plasma treatment on OFET performance

appendix



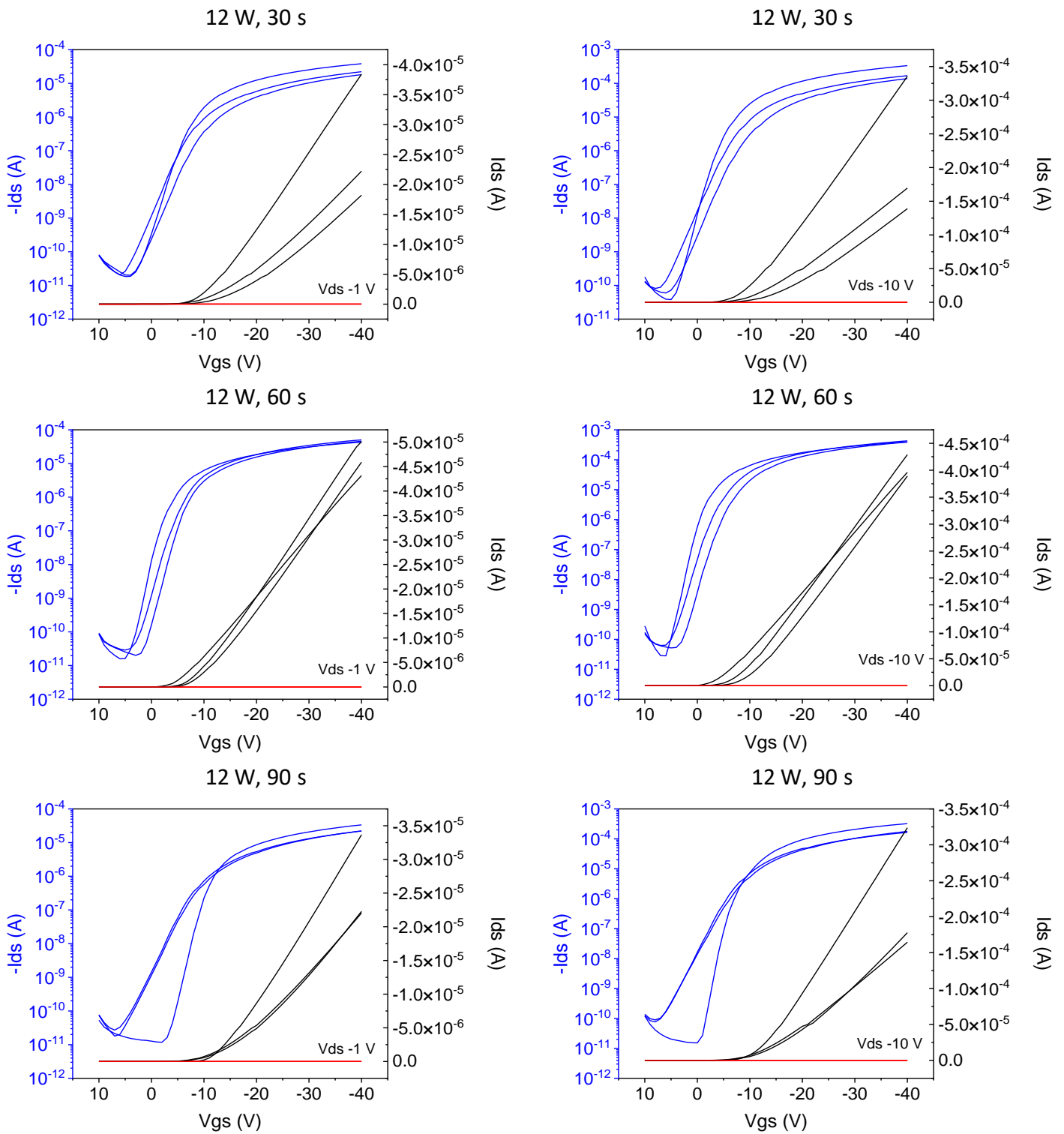


Figure 115 Transfer characteristics (left) $V_{ds} = -1$ (right) $V_{ds} = -10$ of DPP-DTT OFETs before N_2 plasma treatment (blue) log scale (black) linear scale (red) gate current.

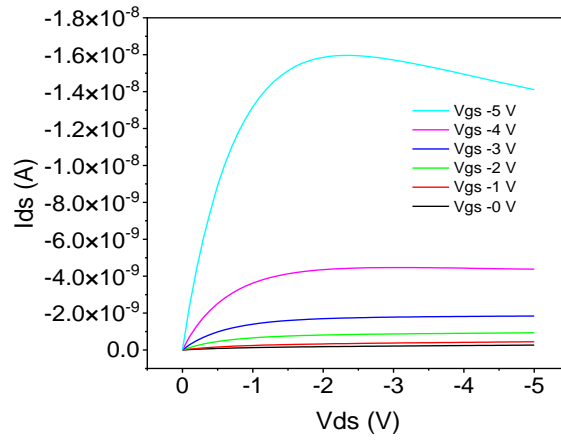
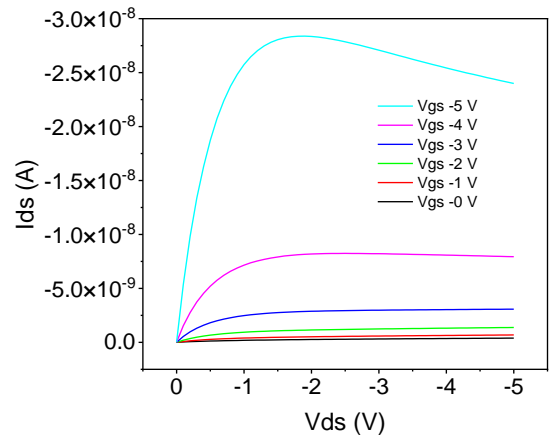
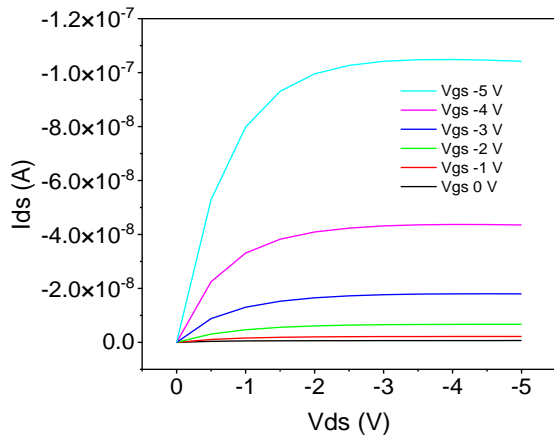
Before 6 W, 30 s, Vds -1					
S/D	1	2	3	Average	σ
Vth (V)	-7.3	-13.5	-15.8	-12.2	4.39
μ (cm ² V ⁻¹ s ⁻¹)	-3.29E-01	-2.13E-01	-8.38E-02	-2.1E-01	1.22E-01
Before 6 W, 60 s, Vds -1					
S/D	1	2	3	Average	σ
Vth (V)	-7.9	-10.0	-10.2	-9.4	1.30
μ (cm ² V ⁻¹ s ⁻¹)	-2.9E-01	-3.0E-01	-3.0E-01	-2.9E-01	3.00E-03
Before 6 W, 90 s, Vds -1					
S/D	1	2	3	Average	σ
Vth (V)	-10.2	-15.8	-17.7	-14.6	3.91
μ (cm ² V ⁻¹ s ⁻¹)	-2.2E-01	-1.7E-01	-9.7E-02	-1.6E-01	6.29E-02
Before 12 W, 30 s, Vds -1					
S/D	1	2	3	Average	σ
Vth (V)	-10.6	-13.5	-15.4	-13.1	2.42
μ (cm ² V ⁻¹ s ⁻¹)	-3.2E-01	-2.0E-01	-1.7E-01	-2.3E-01	7.51E-02
Before 12 W, 60 s, Vds -1					
S/D	1	2	3	Average	σ
Vth (V)	-5.1	-8.6	-9.9	-7.9	2.51
μ (cm ² V ⁻¹ s ⁻¹)	-3.0E-01	-3.9E-01	-3.7E-01	-3.5E-01	4.63E-02
Before 12 W, 90 s, Vds -1					
S/D	1	2	3	Average	σ
Vth (V)	-13.4	-14.1	-15.1	-14.2	0.85
μ (cm ² V ⁻¹ s ⁻¹)	-3.0E-01	-2.0E-01	-2.1E-01	-2.4E-01	5.60E-02

Table 51 OFET transfer characteristics (Vds -1) mobility and threshold voltage values before N₂ plasma treatment.

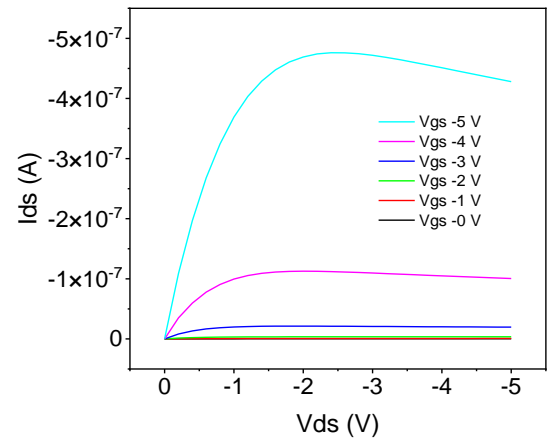
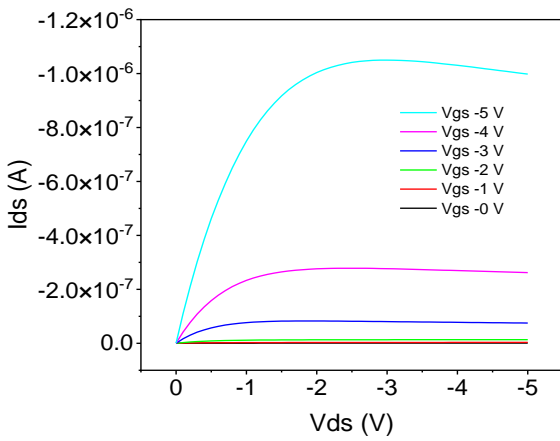
Before 6 W, 30 s, Vds -10					
S/D	1	2	3	Average	σ
Vth (V)	-8.1	-12.9	-15.4	-12.1	3.72
μ (cm ² V ⁻¹ s ⁻¹)	-4.2E-01	-2.1E-01	-8.9E-02	-2.4E-01	1.66E-01
Before 6 W, 60 s, Vds -10					
S/D	1	2	3	Average	σ
Vth (V)	-11.1	-12.3	-12.8	-12.1	0.86
μ (cm ² V ⁻¹ s ⁻¹)	-2.9E-01	-3.0E-01	-2.9E-01	-2.9E-01	3.49E-03
Before 6 W, 90 s, Vds -10					
S/D	1	2	3	Average	σ
Vth (V)	-9.4	-15.0	-17.7	-14.0	4.23
μ (cm ² V ⁻¹ s ⁻¹)	-2.1E-01	-1.9E-01	-9.9E-02	-1.7E-01	6.04E-02
Before 12 W, 30 s, Vds -10					
S/D	1	2	3	Average	σ
Vth (V)	-9.5	-11.9	-14.7	-12.0	2.62
μ (cm ² V ⁻¹ s ⁻¹)	-2.6E-01	-1.5E-01	-1.3E-01	-1.8E-01	7.36E-02
Before 12 W, 60 s, Vds -10					
S/D	1	2	3	Average	σ
Vth (V)	-4.6	-7.9	-10.3	-7.6	2.87
μ (cm ² V ⁻¹ s ⁻¹)	-2.7E-01	-3.2E-01	-3.2E-01	-3.0E-01	2.84E-02
Before 12 W, 90 s, Vds -10					
S/D	1	2	3	Average	σ
Vth (V)	-12.0	-12.6	-14.5	-13.0	1.29
μ (cm ² V ⁻¹ s ⁻¹)	-2.8E-01	-1.4E-01	-1.7E-01	-2.0E-01	7.26E-02

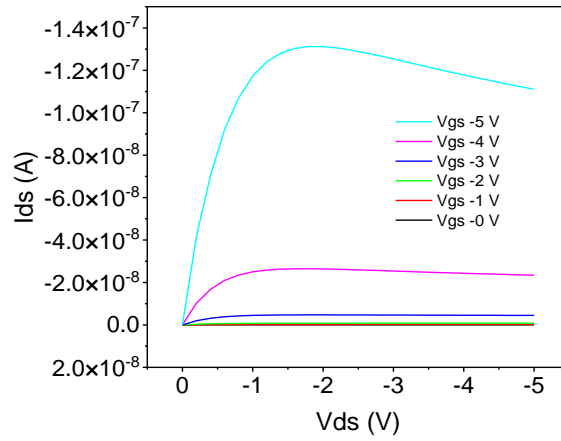
Table 52 OFET transfer characteristics (Vds -10) mobility and threshold voltage values before N₂ plasma treatment.

6 W, 30 s

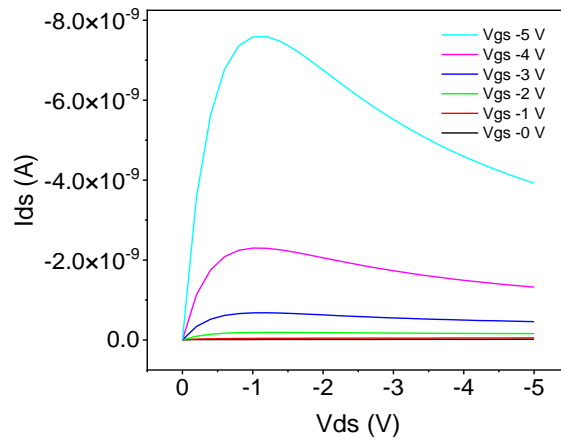
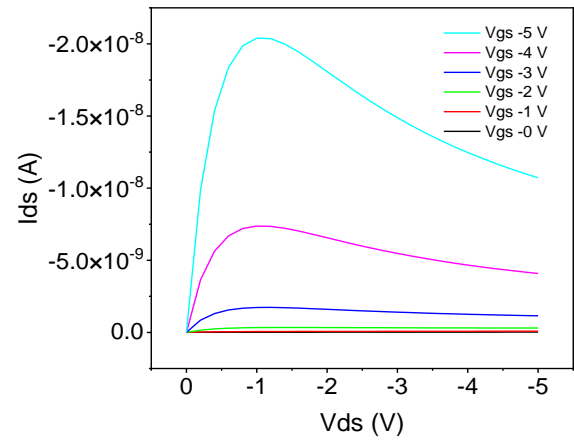
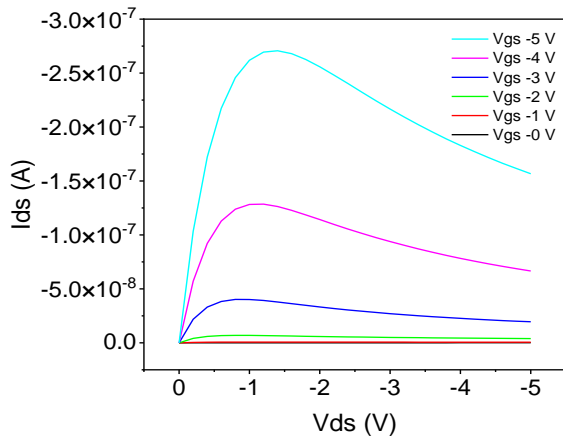


6 W, 60 s

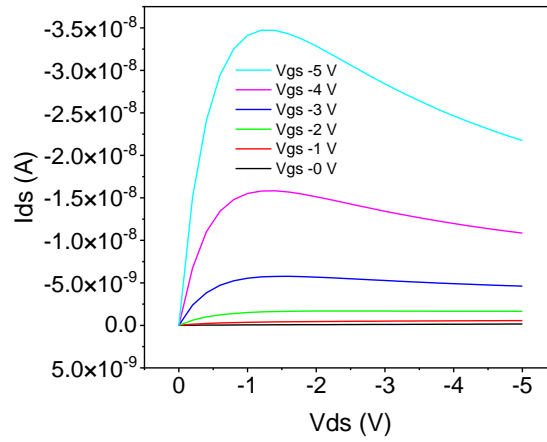
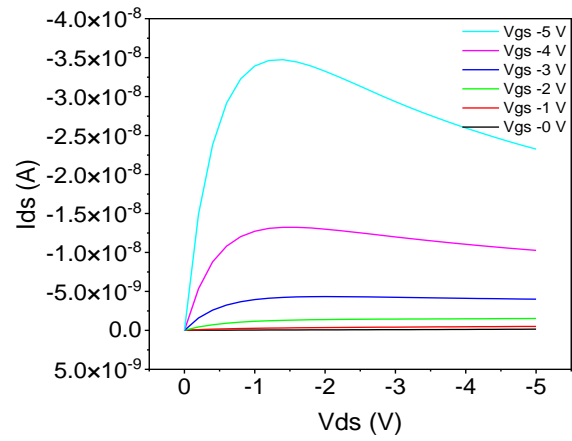
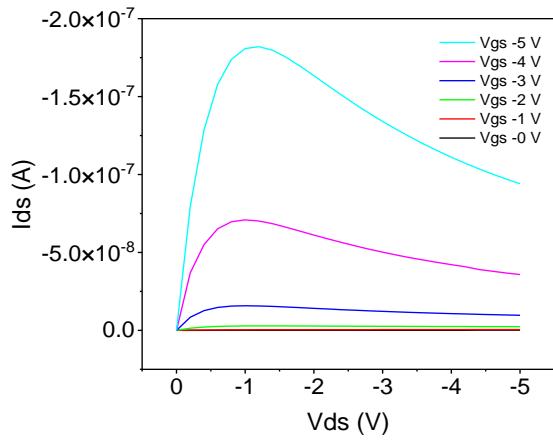




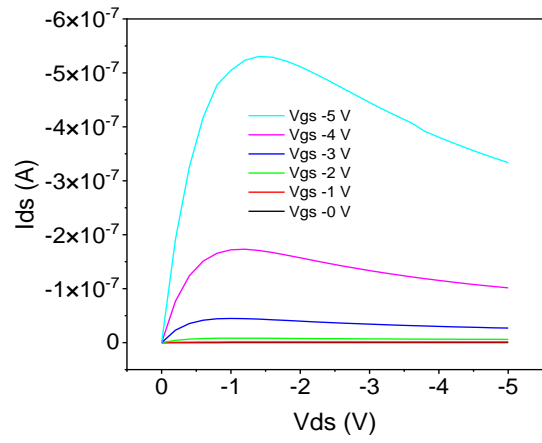
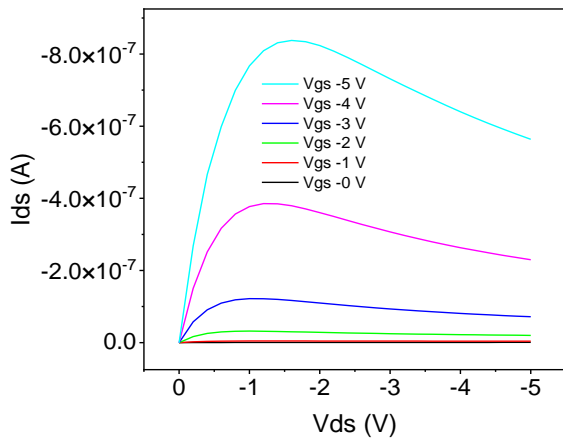
6 W, 90 s



12 W, 30 s



12 W, 60 s



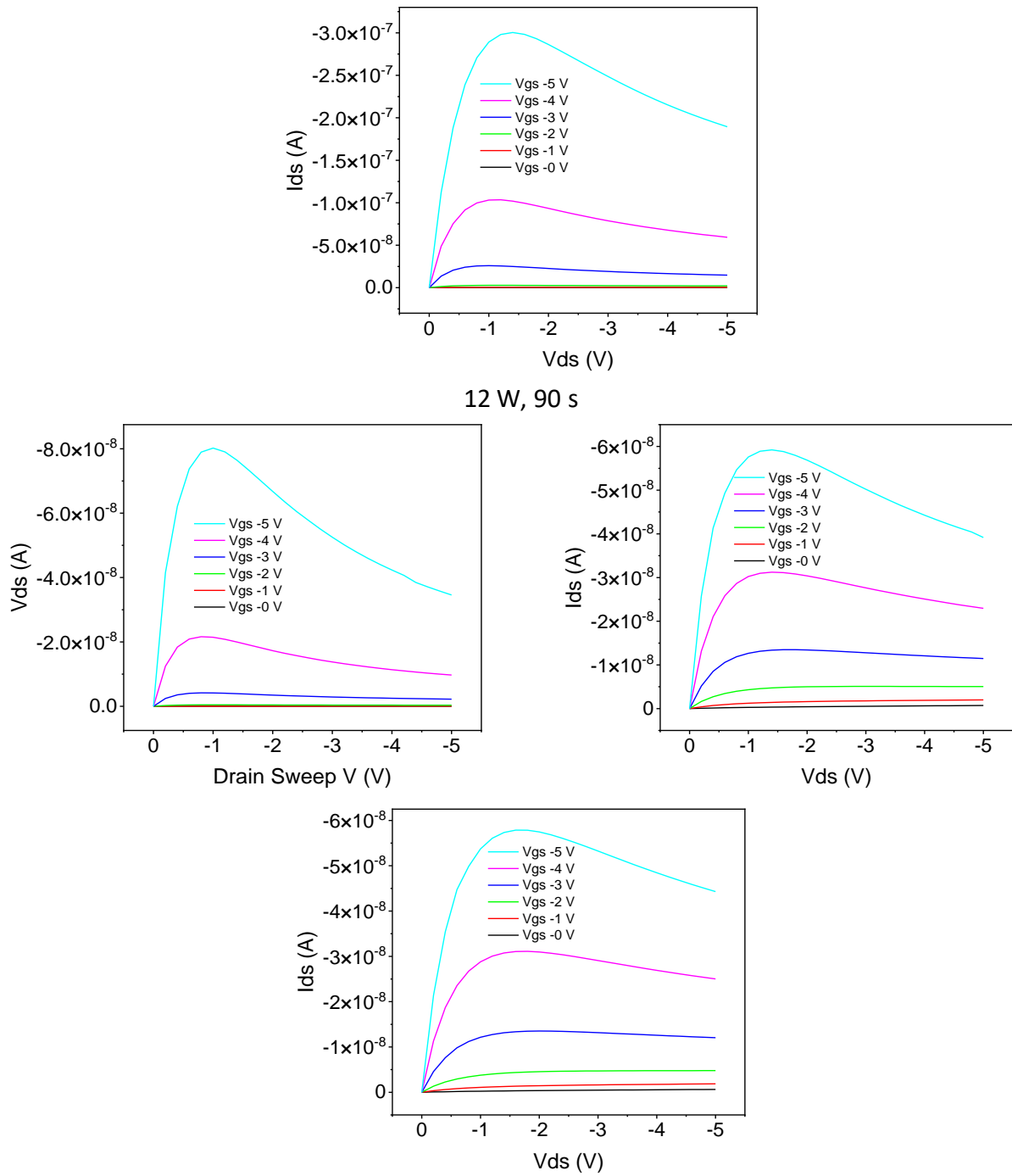
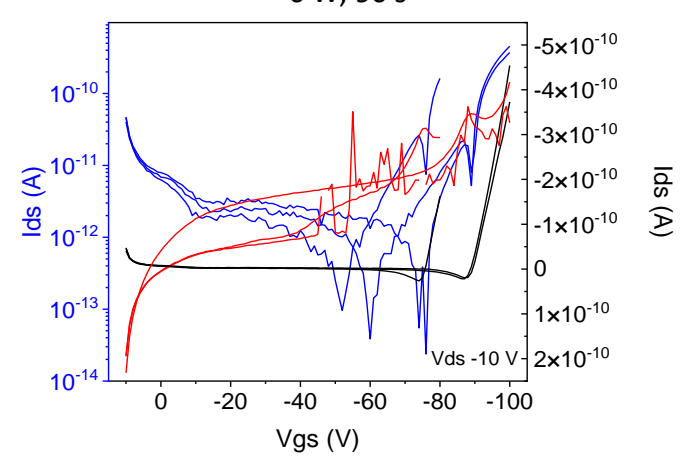
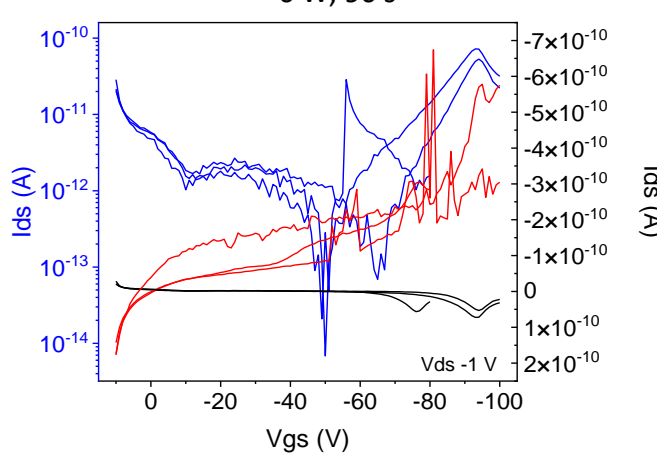
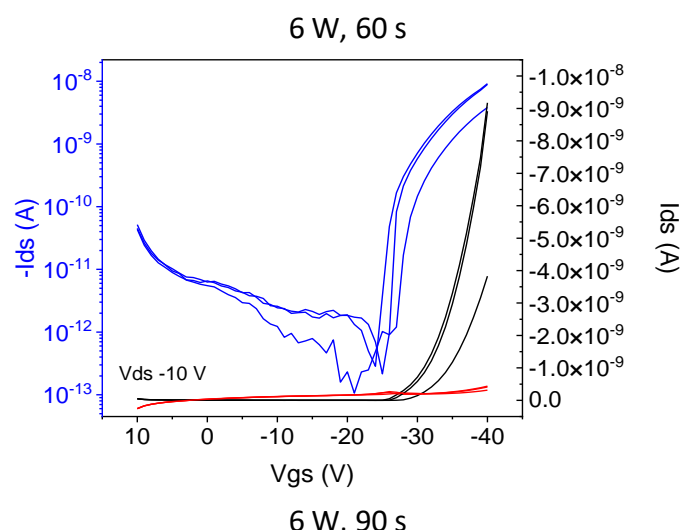
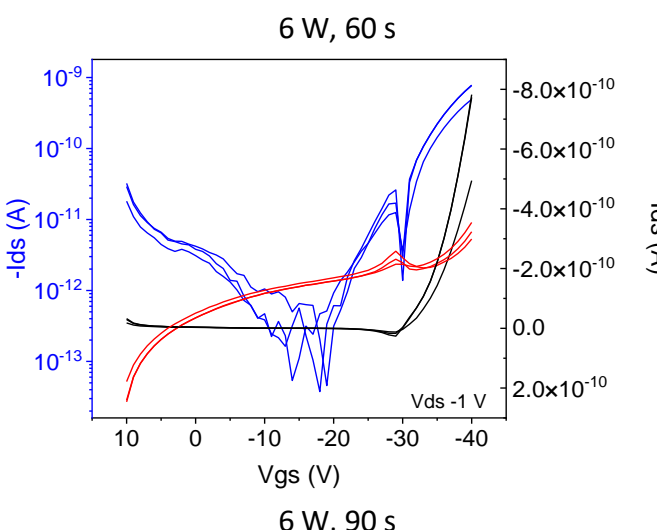
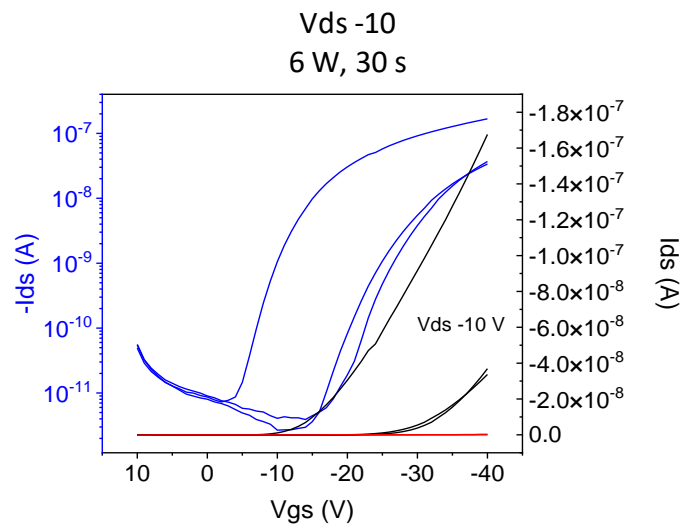
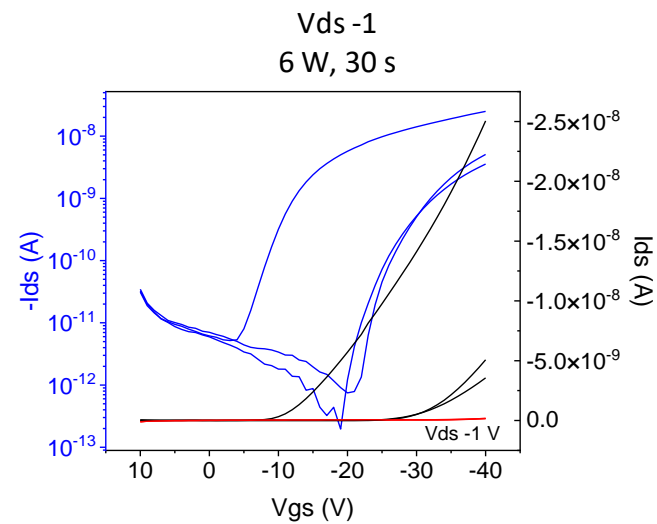


Figure 116 Output characteristics of DPP-DTT OFETs before N_2 plasma treatment.



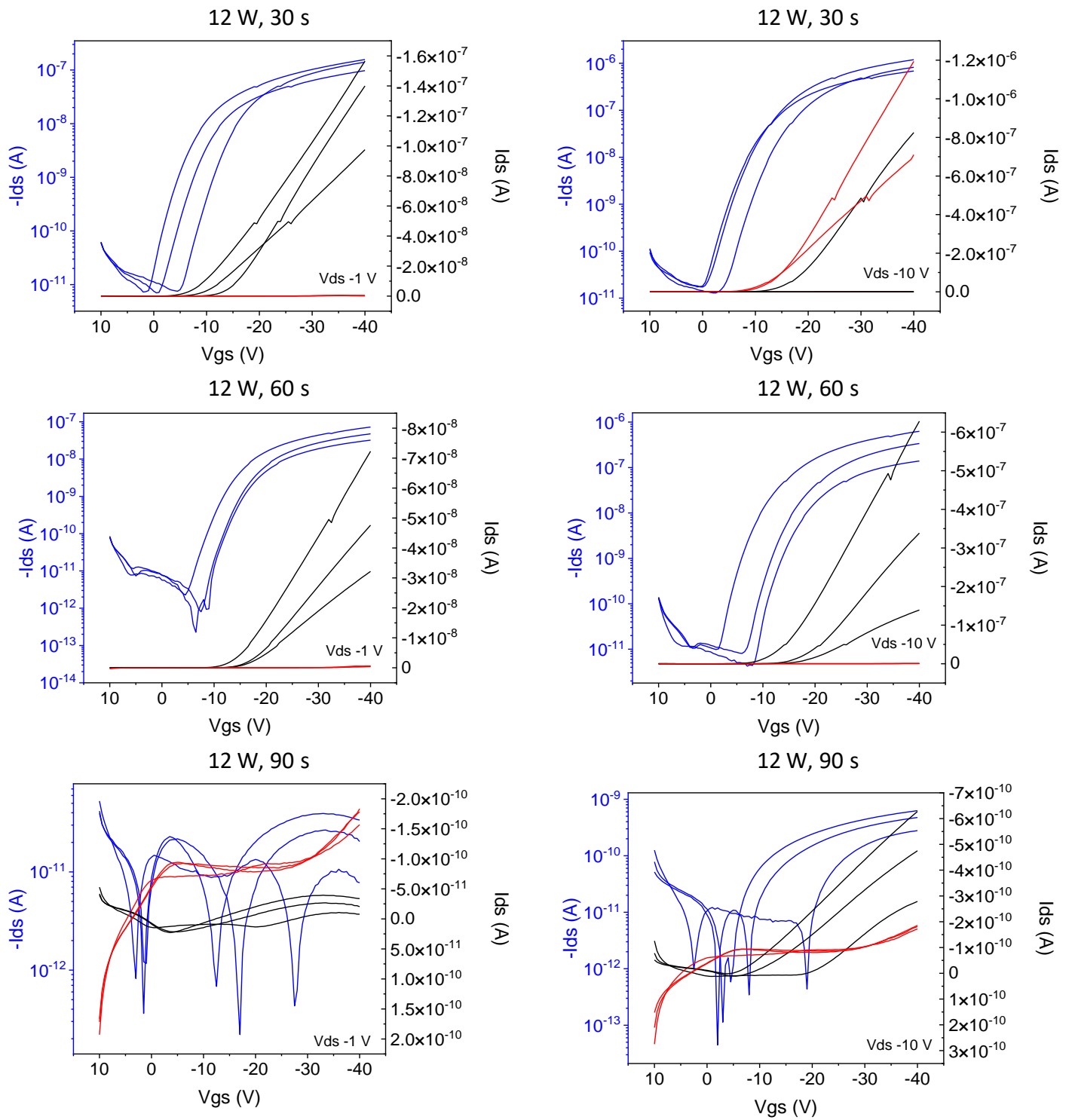


Figure 117 Transfer characteristics (left) $V_{ds} -1$ (right) $V_{ds} -10$ of DPP-DTT OFETs after N_2 plasma treatment (blue) log scale (black) linear scale (red) gate current.

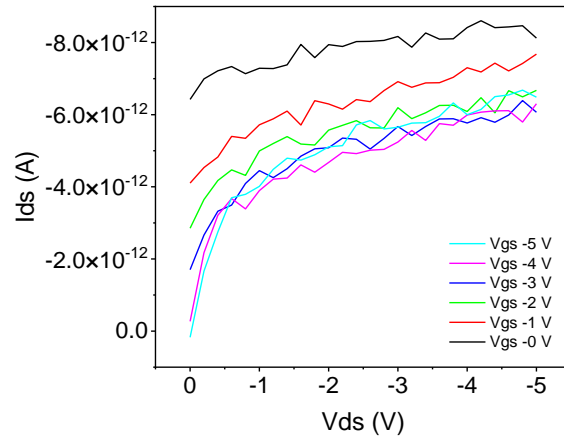
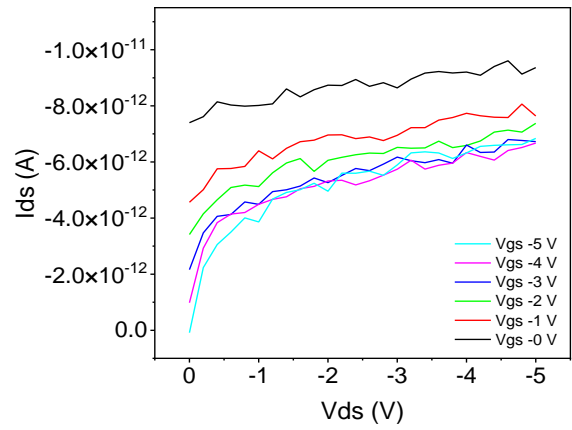
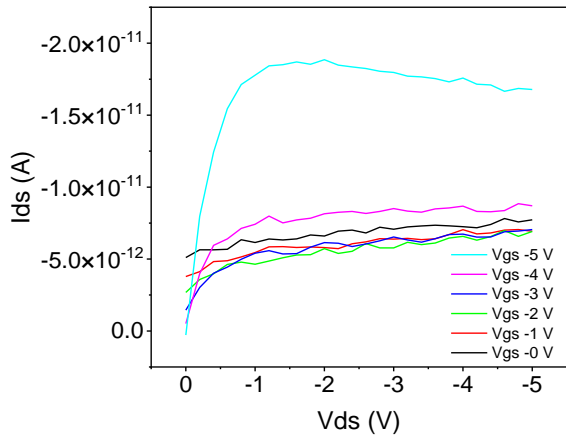
After 6 W, 30 s, Vds -1					
S/D	1	2	3	Average	σ
Vth (V)	-15.8	-31.2	-30.3	-25.8	8.61
μ (cm ² V ⁻¹ s ⁻¹)	-2.4E-04	-1.4E-04	-8.7E-05	-1.6E-04	8.04E-05
After 6 W, 60 s, Vds -1					
S/D	1	2	3	Average	σ
Vth (V)	-33.5	-33.2	-33.6	-33.4	0.21
μ (cm ² V ⁻¹ s ⁻¹)	-1.8E-05	-2.7E-05	-2.9E-05	-2.5E-05	5.81E-06
After 6 W, 90 s, Vds -1					
S/D	1	2	3	Average	σ
Vth (V)	Not measurable				
μ (cm ² V ⁻¹ s ⁻¹)	Not measurable				
After 12 W, 30 s, Vds -1					
S/D	1	2	3	Average	σ
Vth (V)	-14.6	-10.5	-10.2	-11.8	2.45
μ (cm ² V ⁻¹ s ⁻¹)	-1.3E-03	-7.9E-04	-1.3E-03	-1.1E-03	2.98E-04
After 12 W, 60 s, Vds -1					
S/D	1	2	3	Average	σ
Vth (V)	-16.5	-16.9	-14.5	-15.9	1.30
μ (cm ² V ⁻¹ s ⁻¹)	-3.4E-04	-5.0E-04	-6.8E-04	-5.0E-04	1.71E-04
After 12 W, 90 s, Vds -1					
S/D	1	2	3	Average	σ
Vth (V)	Not measurable				
μ (cm ² V ⁻¹ s ⁻¹)	Not measurable				

Table 53 OFET transfer characteristics (Vds -1) mobility and threshold voltage values after N₂ plasma treatment.

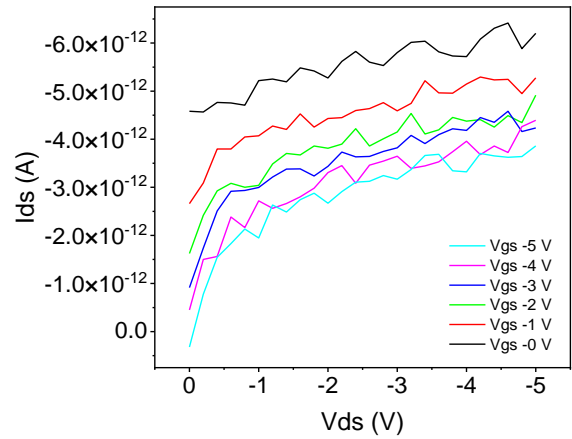
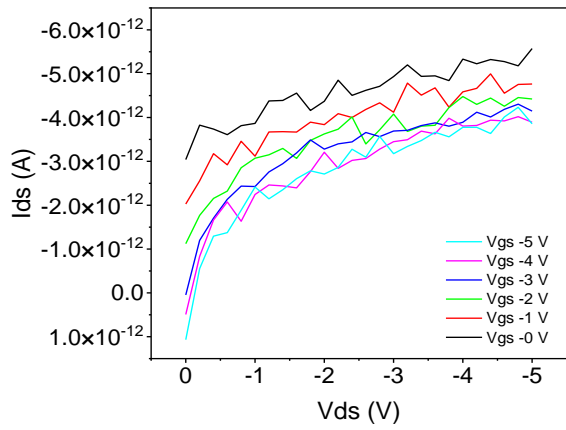
After 6 W, 30 s, Vds -10					
S/D	1	2	3	Average	σ
Vth (V)	-17.3	-29.3	-30.9	-25.8	7.44
μ (cm ² V ⁻¹ s ⁻¹)	-1.8E-04	-7.4E-05	-9.4E-05	-1.1E-04	5.38E-05
After 6 W, 60 s, Vds -10					
S/D	1	2	3	Average	σ
Vth (V)	-33.0	-32.4	-32.7	-32.7	0.32
μ (cm ² V ⁻¹ s ⁻¹)	-1.3E-05	-2.8E-05	-2.8E-05	-2.3E-05	8.81E-06
After 6 W, 90 s, Vds -10					
S/D	1	2	3	Average	σ
Vth (V)	-75.8	-89.6	-89.3	-84.9	7.87
μ (cm ² V ⁻¹ s ⁻¹)	-9.4E-07	-8.5E-07	-9.9E-07	-9.3E-07	7.04E-08
After 12 W, 30 s, Vds -10					
S/D	1	2	3	Average	σ
Vth (V)	-16.6	-10.7	-14.1	-13.8	2.97
μ (cm ² V ⁻¹ s ⁻¹)	-8.6E-04	-5.8E-04	-1.1E-03	-8.5E-04	2.67E-04
After 12 W, 60 s, Vds -10					
S/D	1	2	3	Average	σ
Vth (V)	-17.6	-18.2	-13.0	-16.3	2.87
μ (cm ² V ⁻¹ s ⁻¹)	-1.5E-04	-3.8E-04	-5.6E-04	-3.6E-04	2.03E-04
After 12 W, 90 s, Vds -10					
S/D	1	2	3	Average	σ
Vth (V)	-19.5	-10.6	-7.4	-12.5	6.27
μ (cm ² V ⁻¹ s ⁻¹)	-3.5E-07	-4.0E-07	-4.7E-07	-4.0E-07	6.24E-08

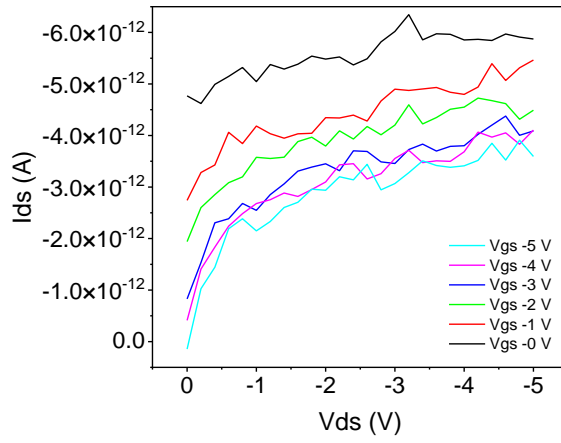
Table 54 OFET transfer characteristics (Vds -10) mobility and threshold voltage values after N₂ plasma treatment.

6 W, 30 s

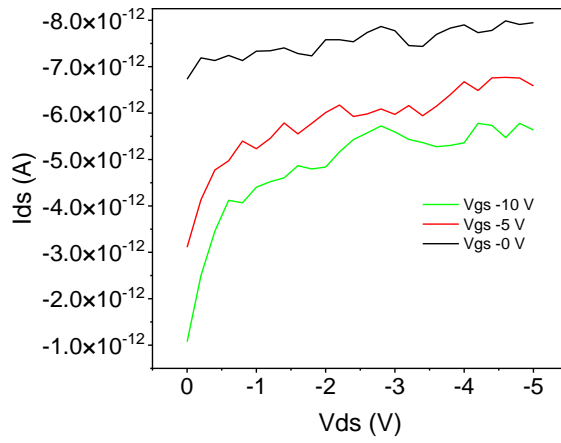
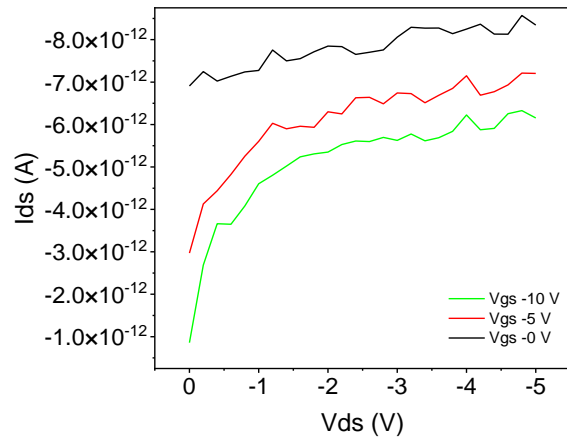
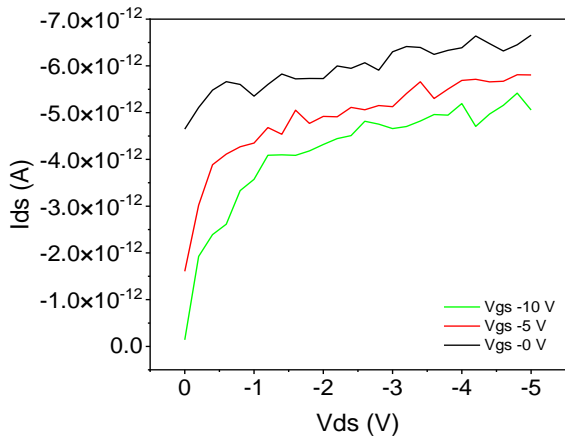


6 W, 60 s

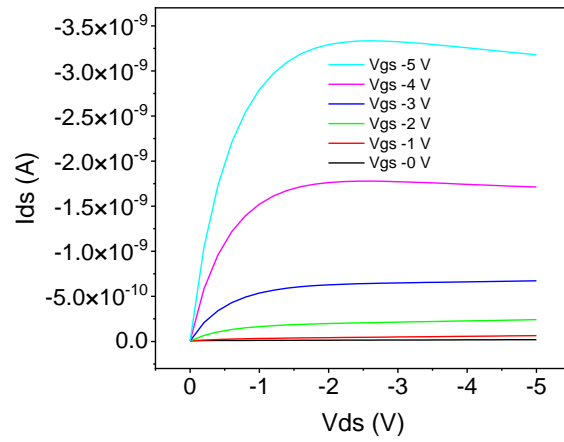
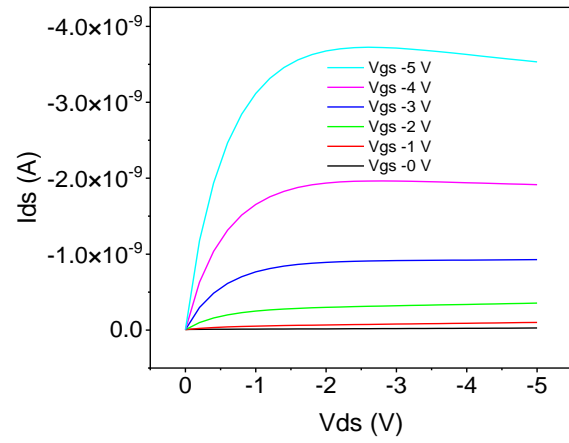
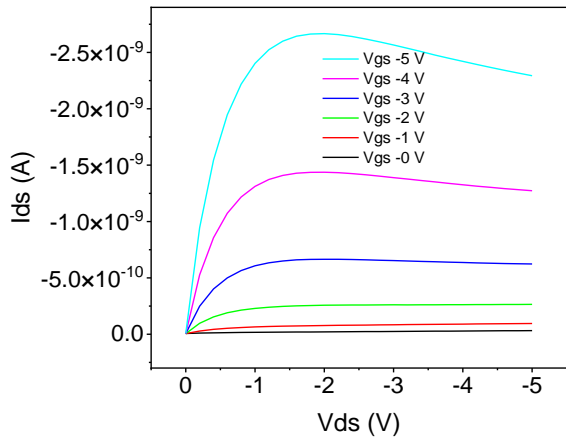




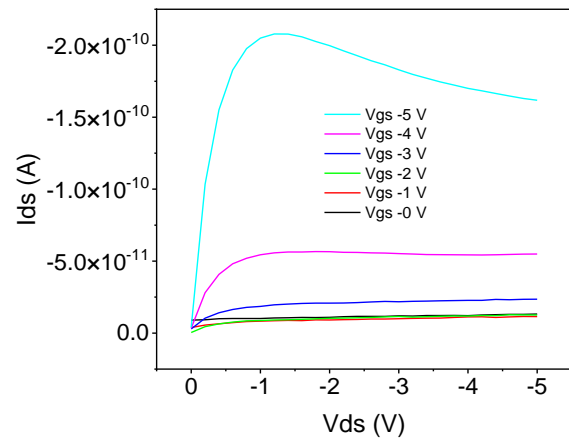
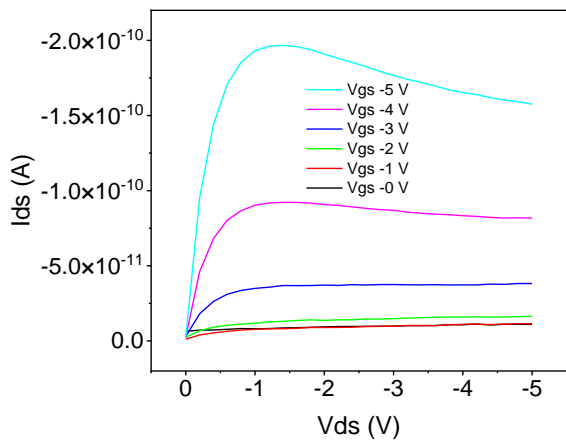
6 W, 90 s



12 W, 30 s



12 W, 60 s



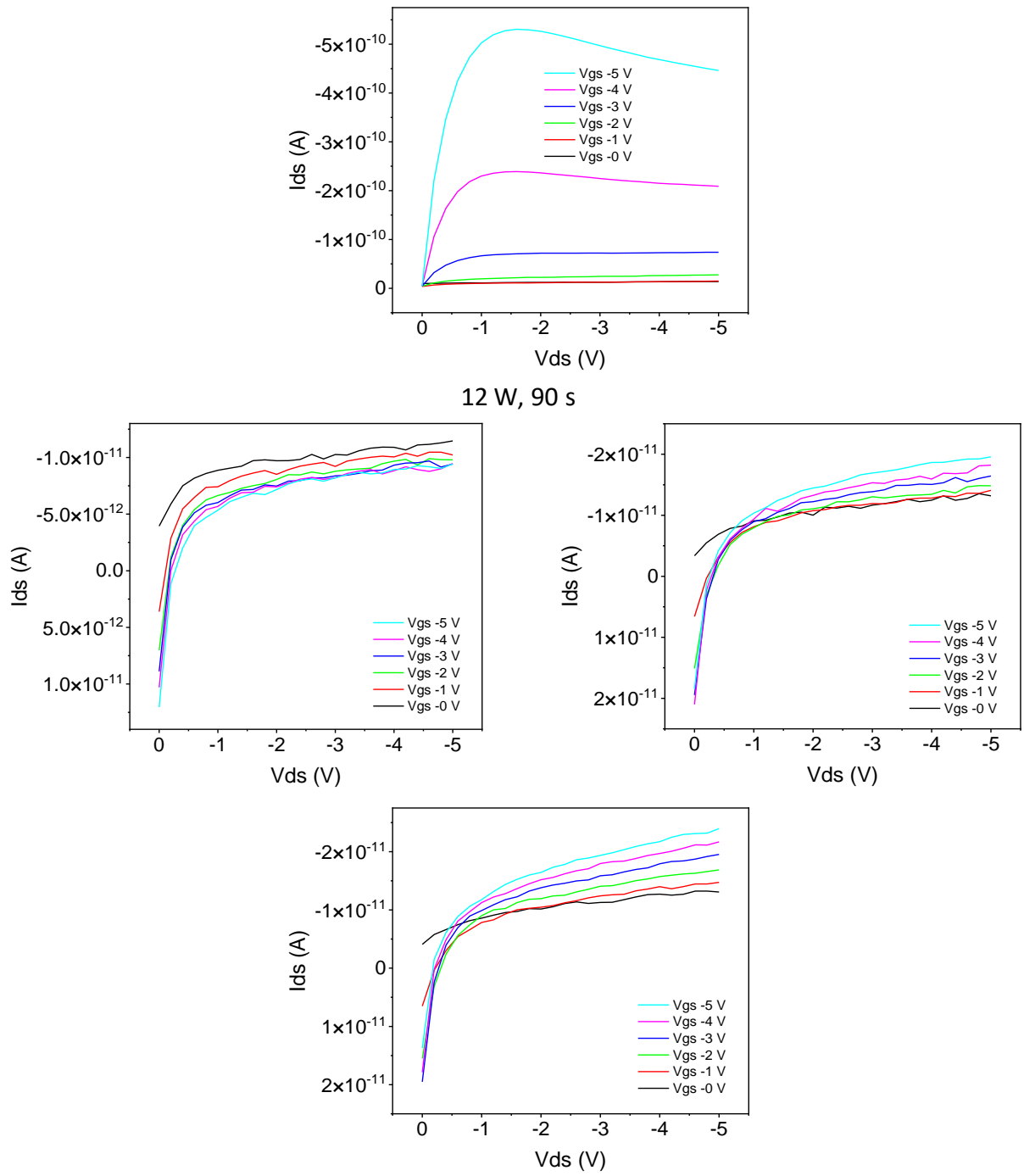
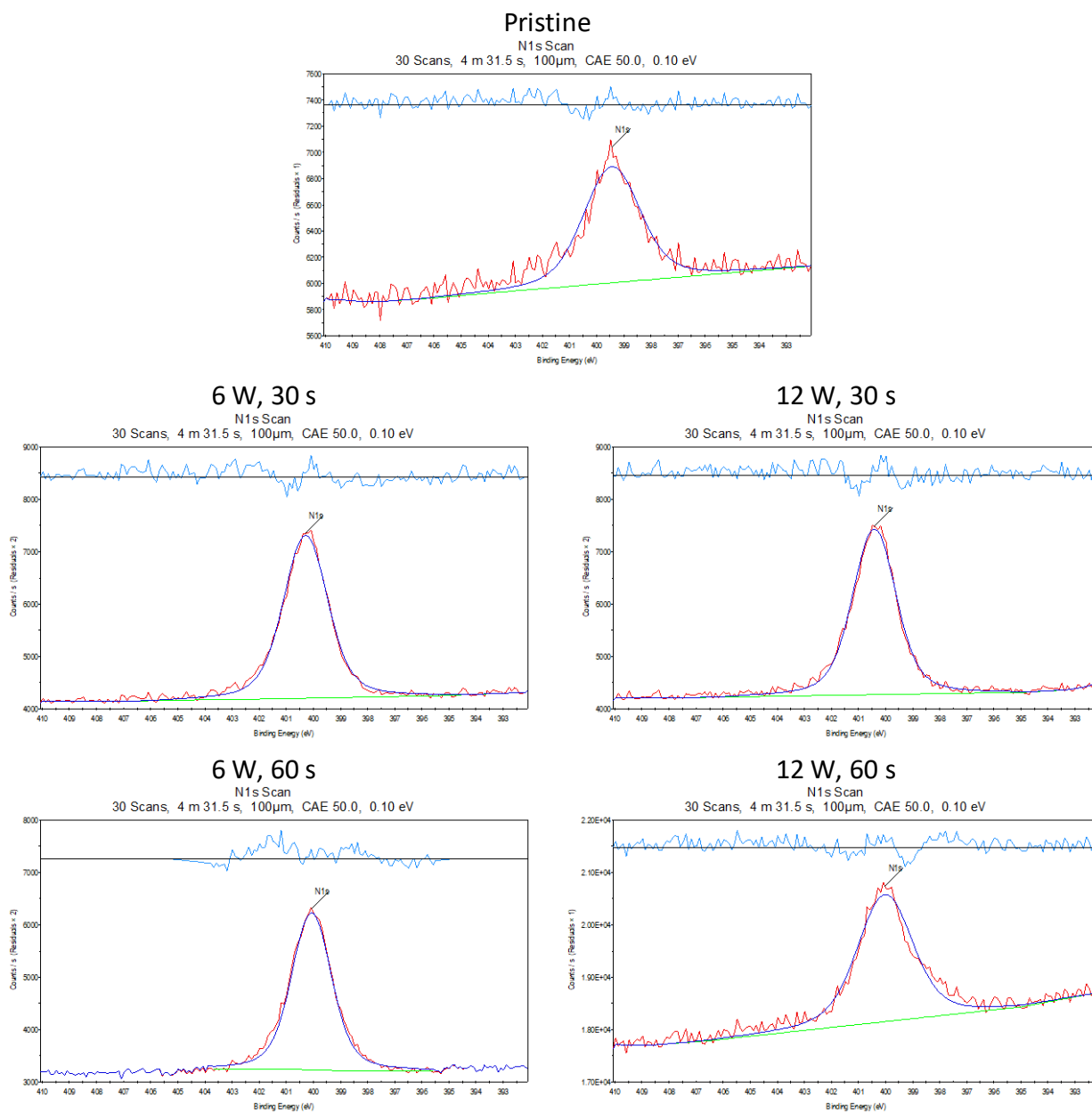


Figure 118 Output characteristics of DPP-DTT OFETs after N₂ plasma treatment.

7.1.9 The introduction of exploitable chemical functionalities on N₂ plasma treated thin-films appendix



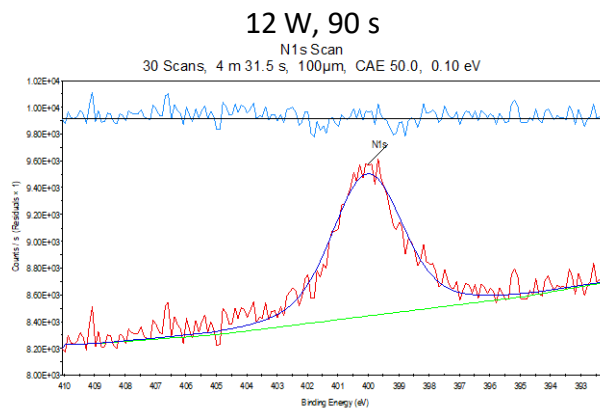
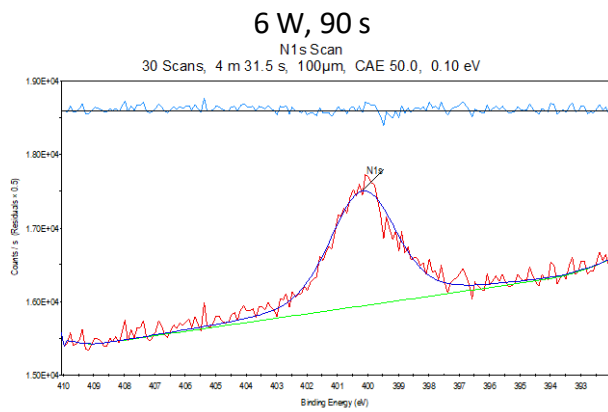
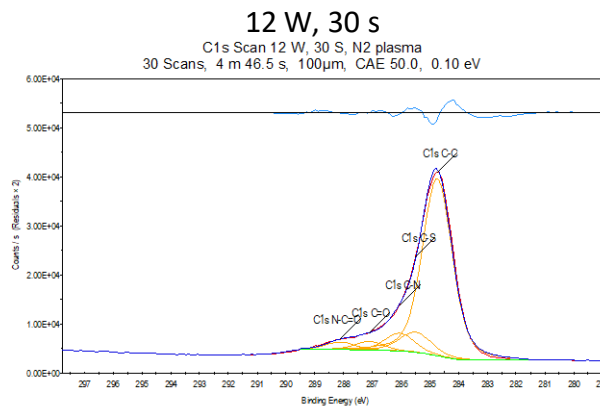
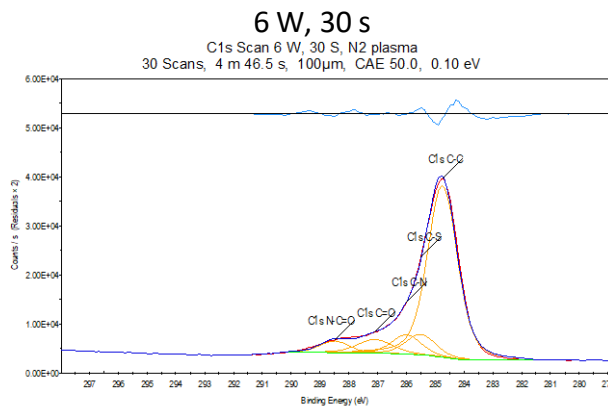
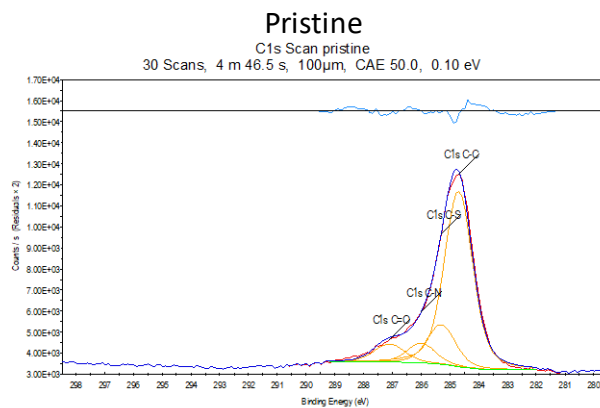


Figure 119 XPS N1s high resolution scan N₂ plasma treated DPP-DTT thin-films.



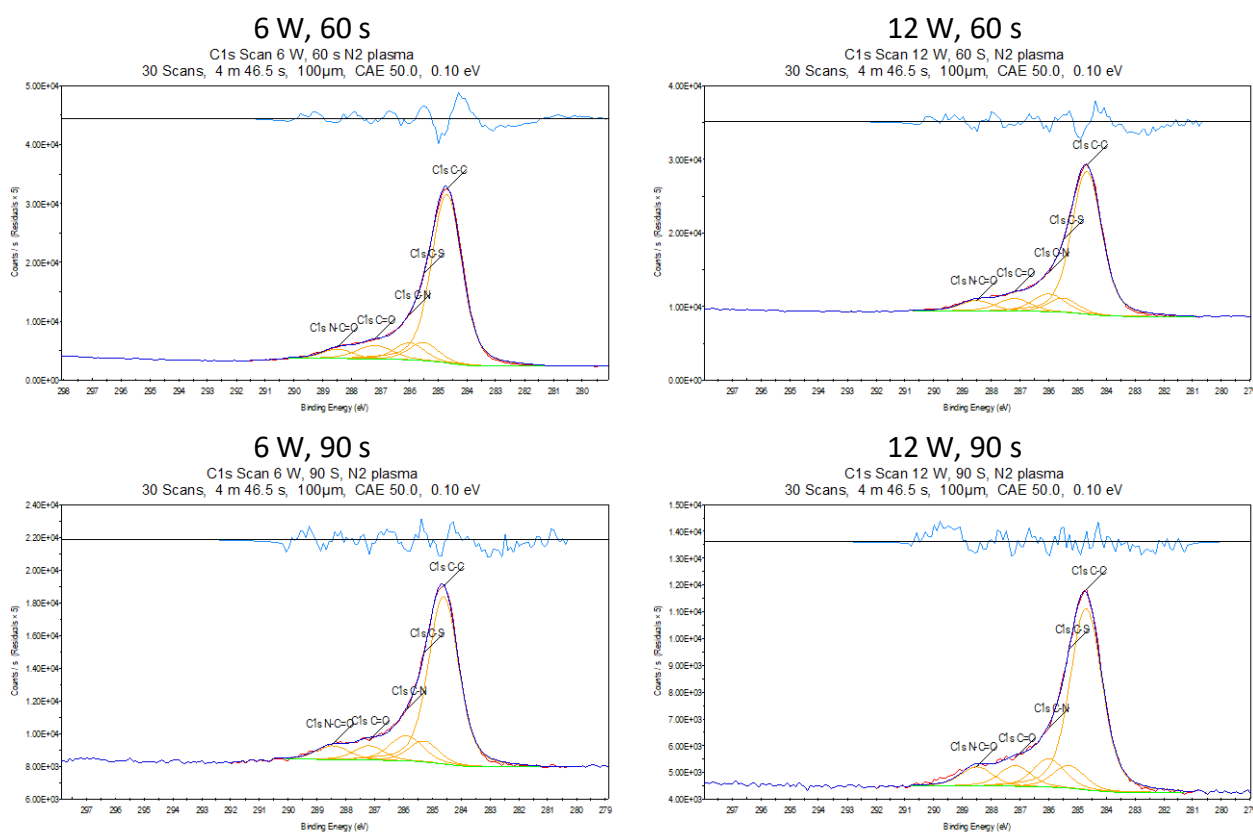
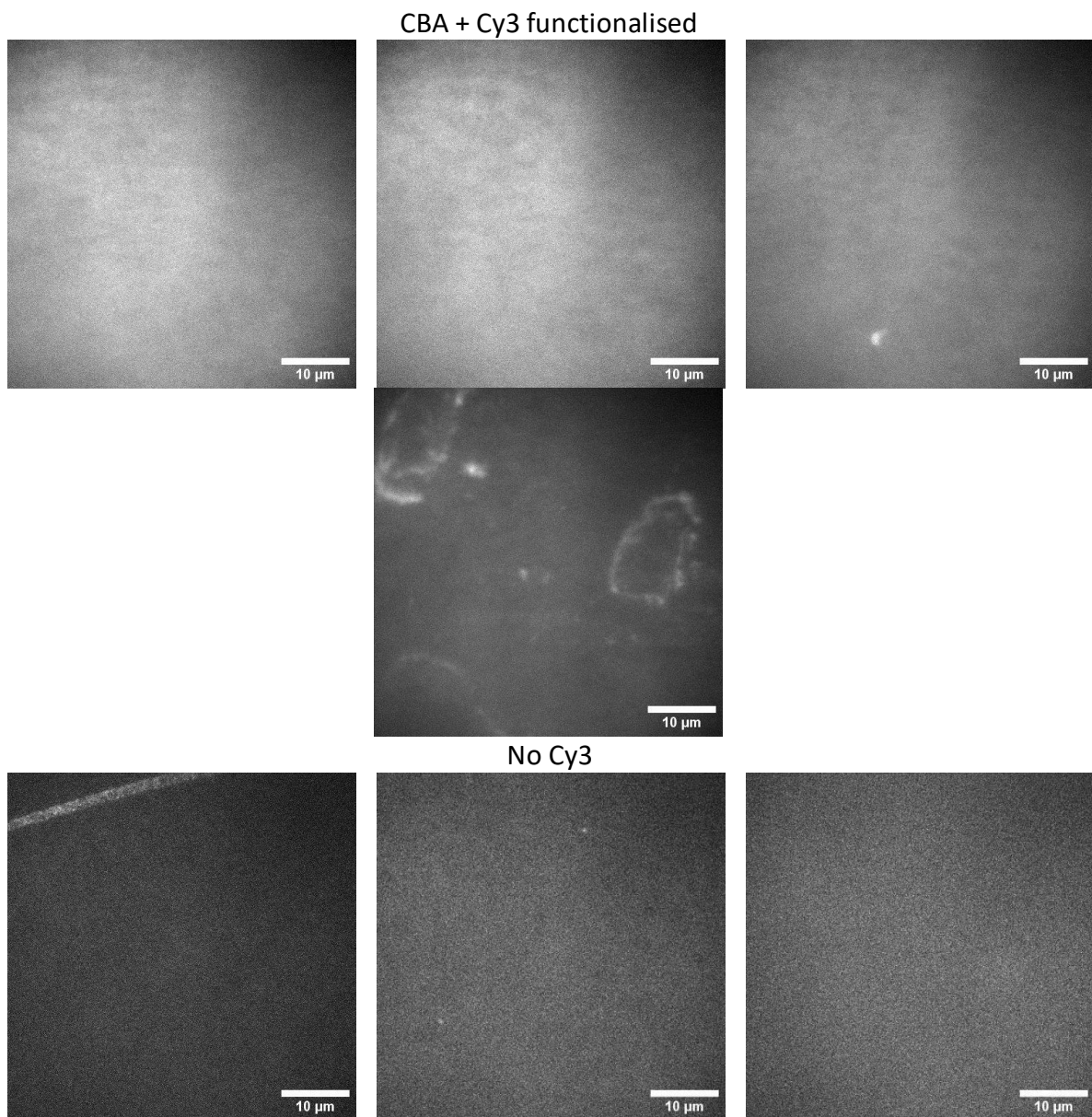


Figure 120 XPS high resolution C1s scans of DPP-DTT OFETs N₂ plasma treated.

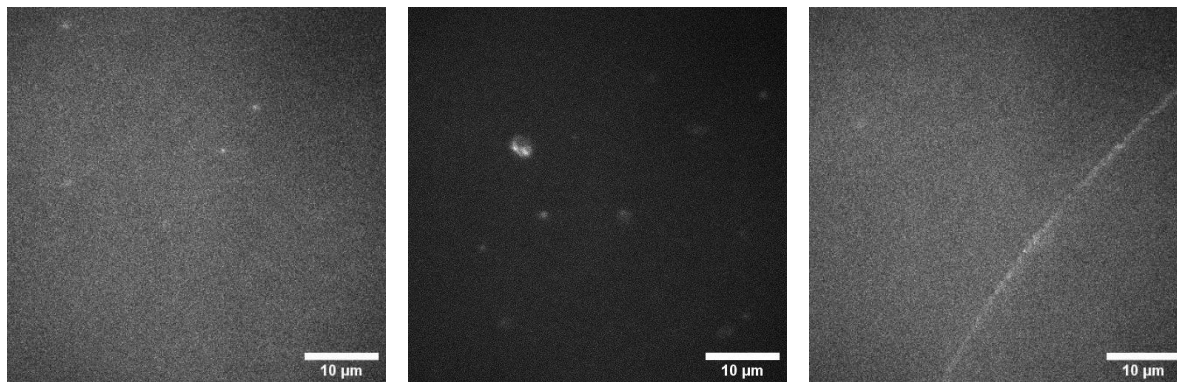
Sample conditions	Element Area CPS.eV		C1s components Area CPS.eV					Combined C-N and O=C-N	C1s Abbe criterion
	N1s	S2p	C-C	C-S	C-N	C=O	O=C-N		
6 W, 30 s	7045.64	6308.34	49706.97	5912.05	5538.05	4760.23	3375.55	8913.60	0.1131
6 W, 60 s	6404.73	4832.24	41415.9	4425.68	4188.75	4019.58	2335.99	6524.74	0.1478
6 W, 90 s	4757.46	1849.32	14715.61	1837.25	2447.03	1256.10	1311.2	3758.23	0.4184
12 W, 30 s	7039.75	6370.13	51214.13	6375.42	5204.48	2490.80	2217.62	7422.10	0.1104
12 W, 60 s	6882.53	3274.84	27906.01	2802.1	3842.5	2747.28	2205.96	6048.46	0.2505
12 W, 90 s	3465.86	1411.41	10419.56	1301.61	1630.23	1187.25	1090.81	2721.04	0.4743
Pristine	3082.23	2166.27	11545.55	2432.13	1216.07	1216.08	0	1216.07	0.2048

Table 55 XPS high resolution C1s scan component peak areas of N₂ plasma treated OFETs.

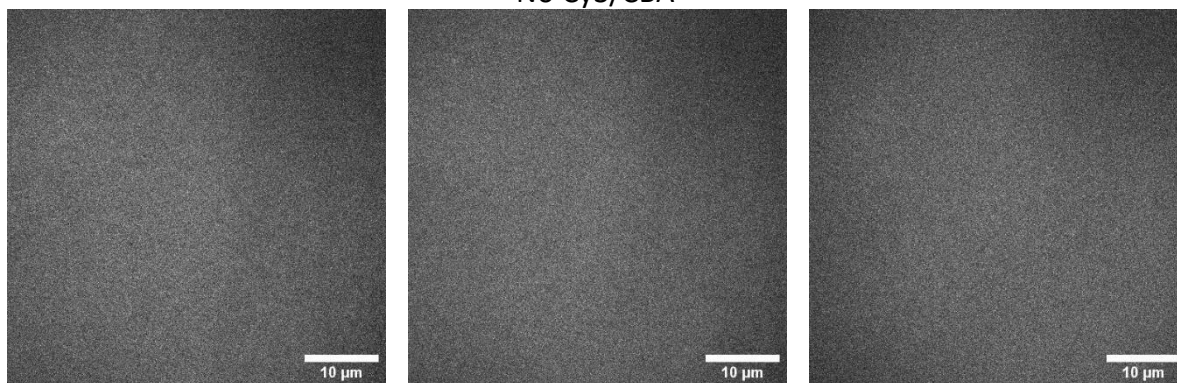
7.1.10 Aptamer functionalisation of N₂ plasma treated thin-films
appendix



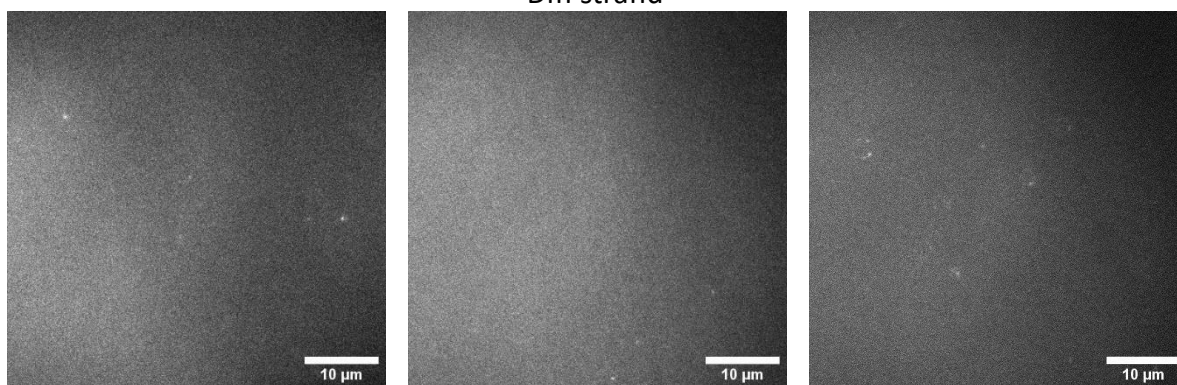
No CBA



No Cy3/CBA



Diff strand



No plasma

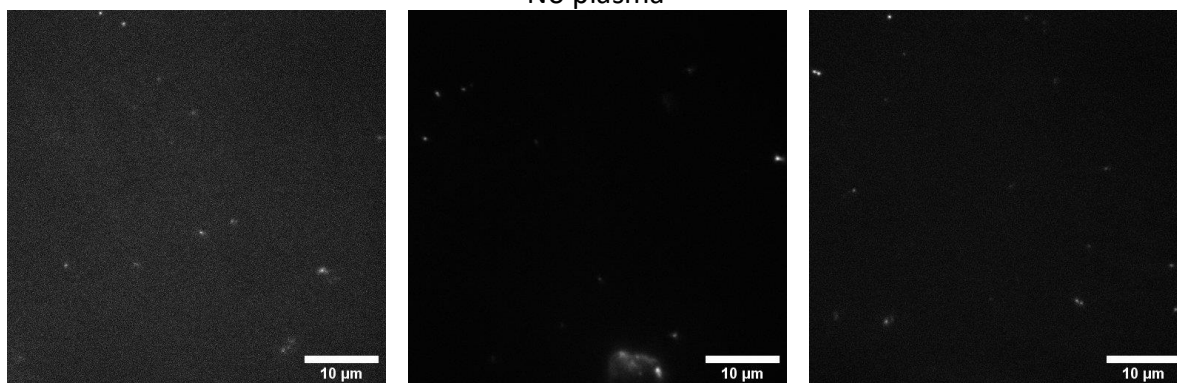


Figure 121 Epifluorescence microscopy images (51.2 μm x 51.2 μm) of 1.0 mg mL^{-1} BCH-NHS, 1 μM N_3 -CBA functionalised 12 W, 60 s N_2 plasma treated DPP-DTT thin-films, fluorescently labelled with 1 μM Cy3-comp-CBA, and control thin-films.

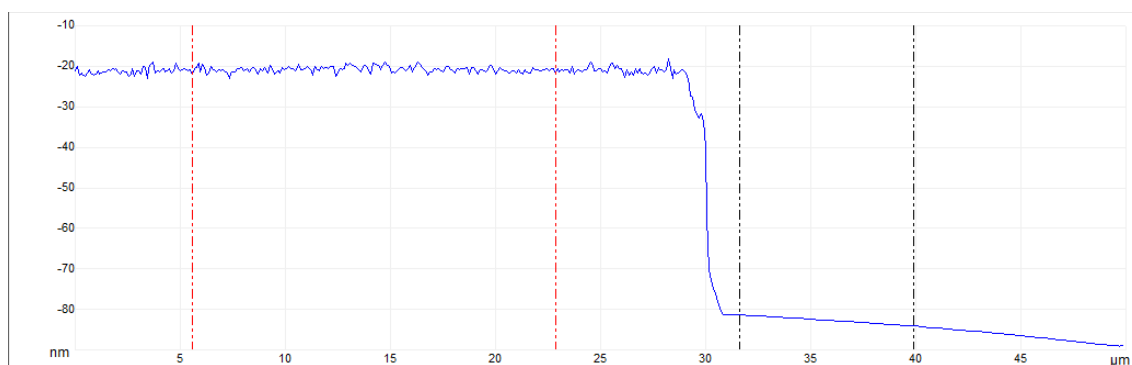
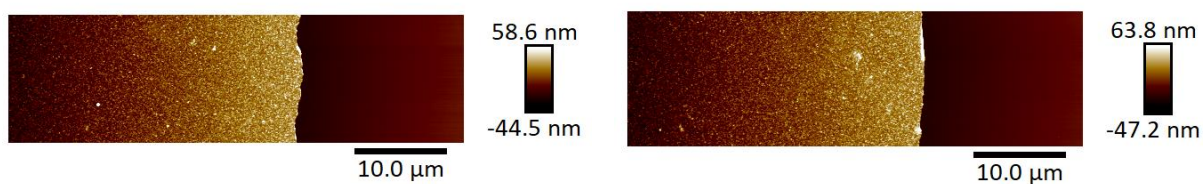
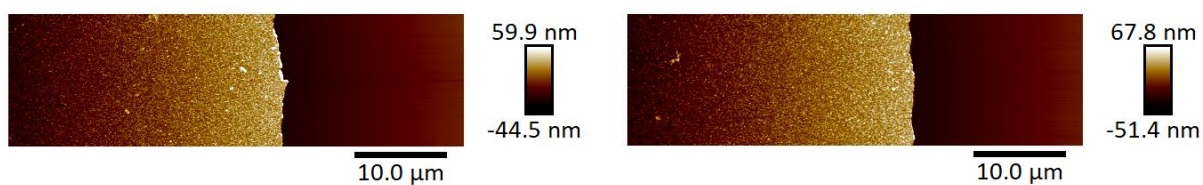
Thin-film conditions	Average pixel value (Abs)	Average (Abs)	STD (Abs)
CBA + Cy3 functionalised	5761.660	5452.684	236.8553
	5480.936		
	5196.962		
	5371.178		
No Cy3	1775.799	1770.738	15.25894
	1782.824		
	1753.592		
No CBA	1795.204	1805.039	8.6218
	1808.621		
	1811.293		
No Cy3/CBA	1762.663	1761.335	6.6748
	1754.096		
	1767.246		
Diff strand	2176.992	2137.368	38.0775
	2134.059		
	2101.053		
No plasma	1695.459	1713.629	26.5940
	1744.153		
	1701.275		

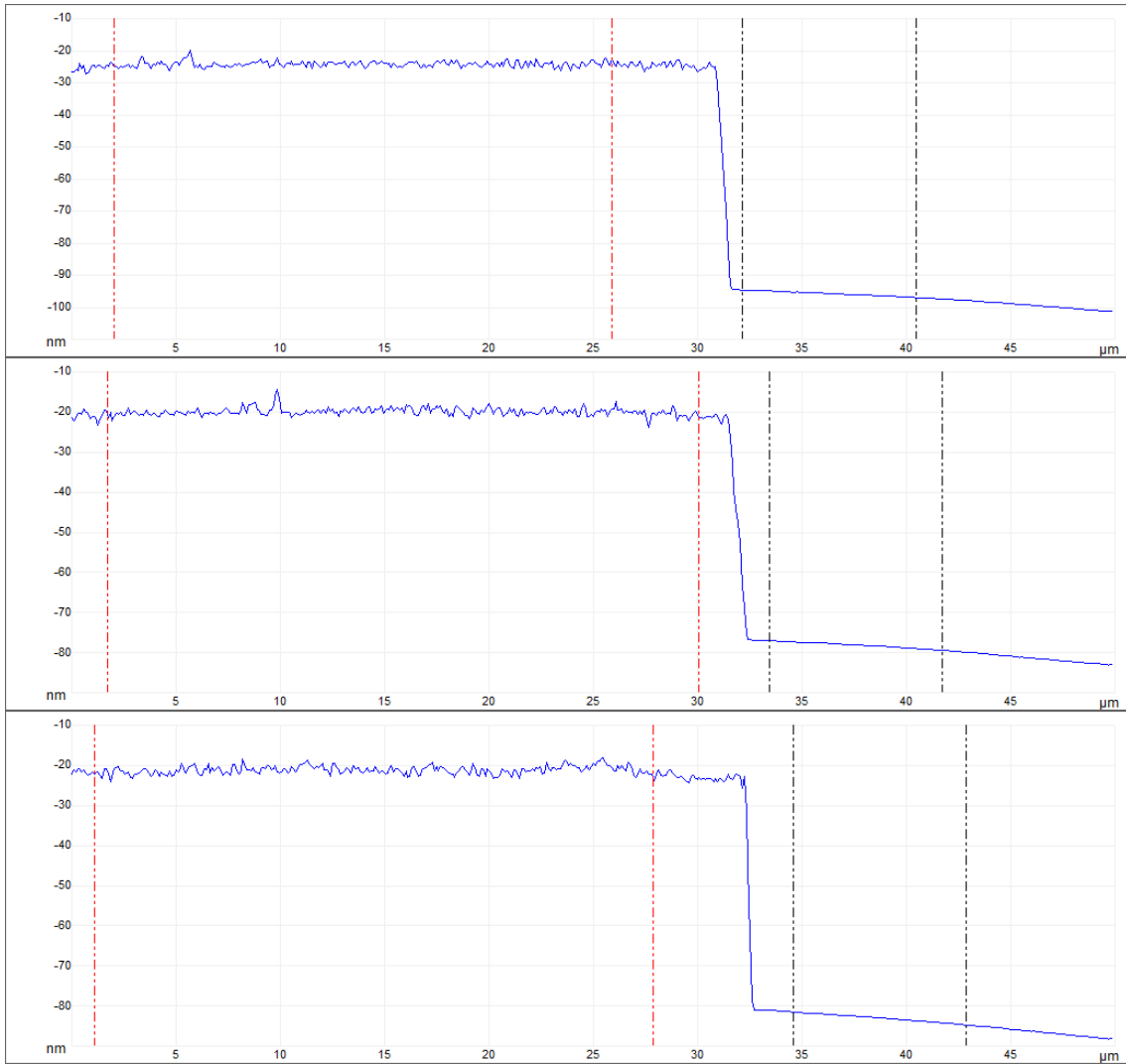
Table 56 Epifluorescence microscopy images average pixel value data of 1.0 mg mL^{-1} BCH-NHS, 1 μM N_3 -CBA functionalised 12 W, 60 s N_2 plasma treated DPP-DTT thin-films, fluorescently labelled with 1 μM Cy3-comp-CBA and control thin-films.

7.2 Investigation of glutaraldehyde DPP-DTT polymer blends for functionalisation and use in OFET devices appendix

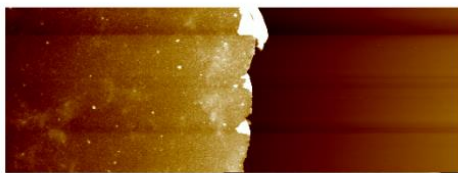
7.2.1 DPP-DTT:GA AFM

2K

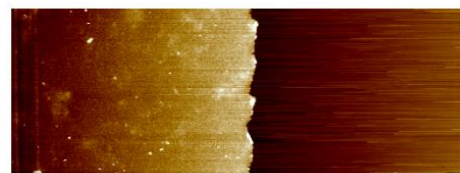




4K

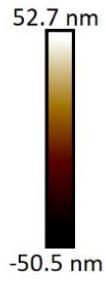
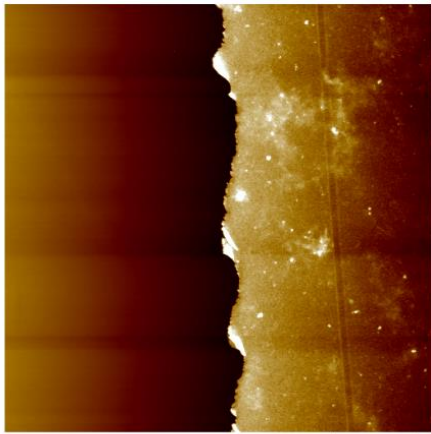


10.0 μm

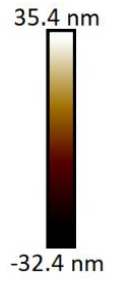
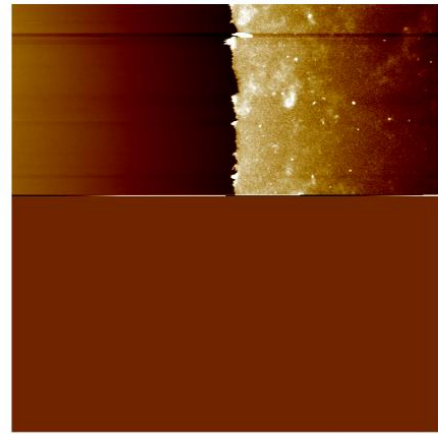


10.0 μm

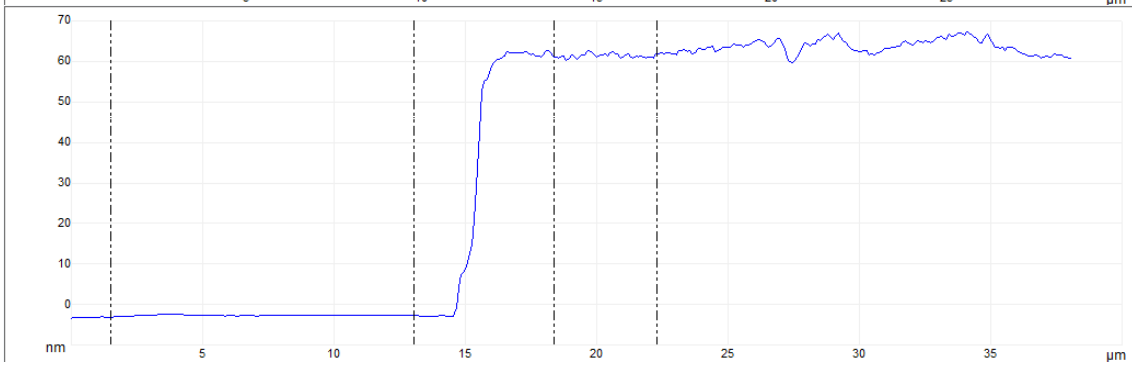
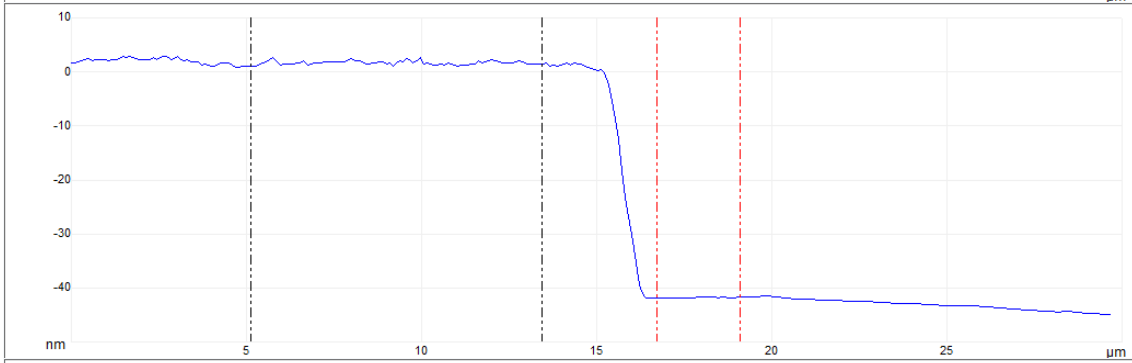
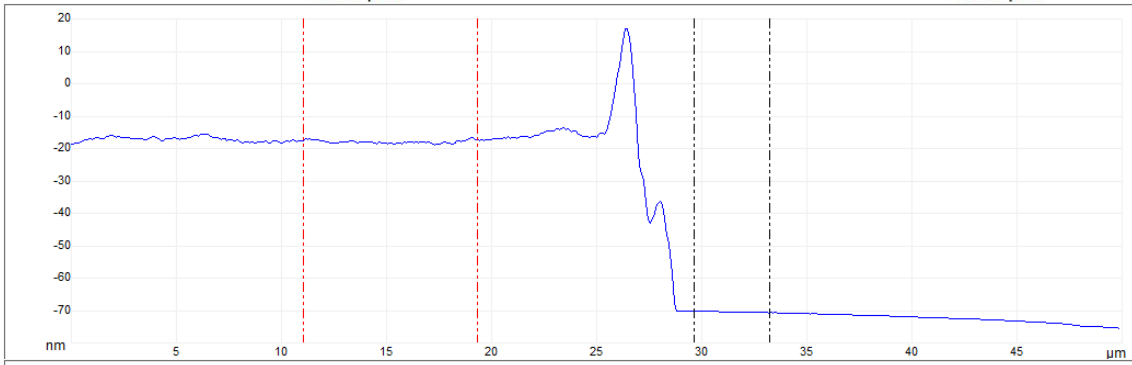
285

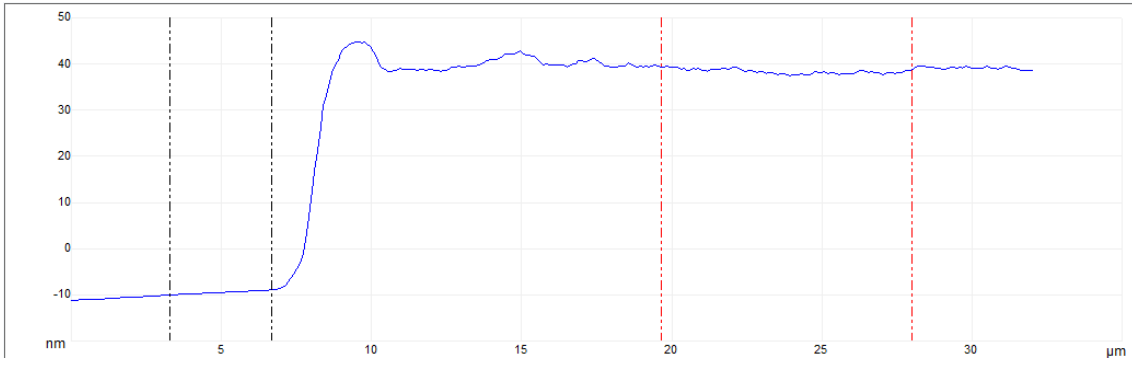


10.0 μm

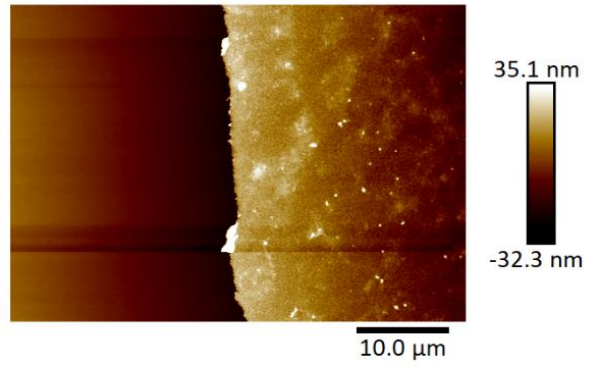
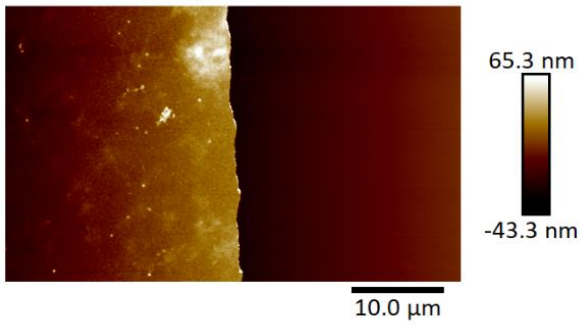
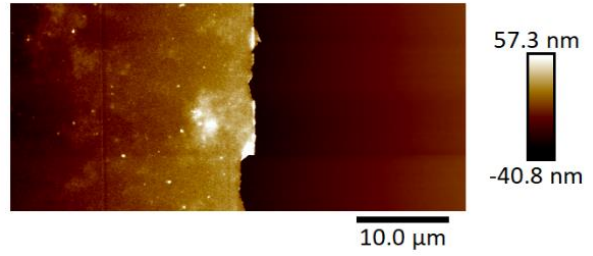
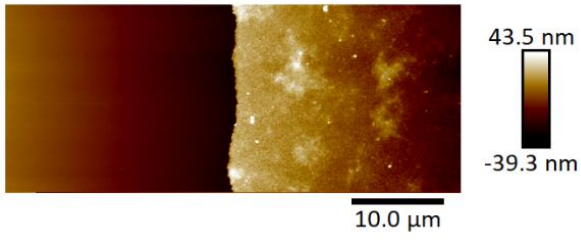


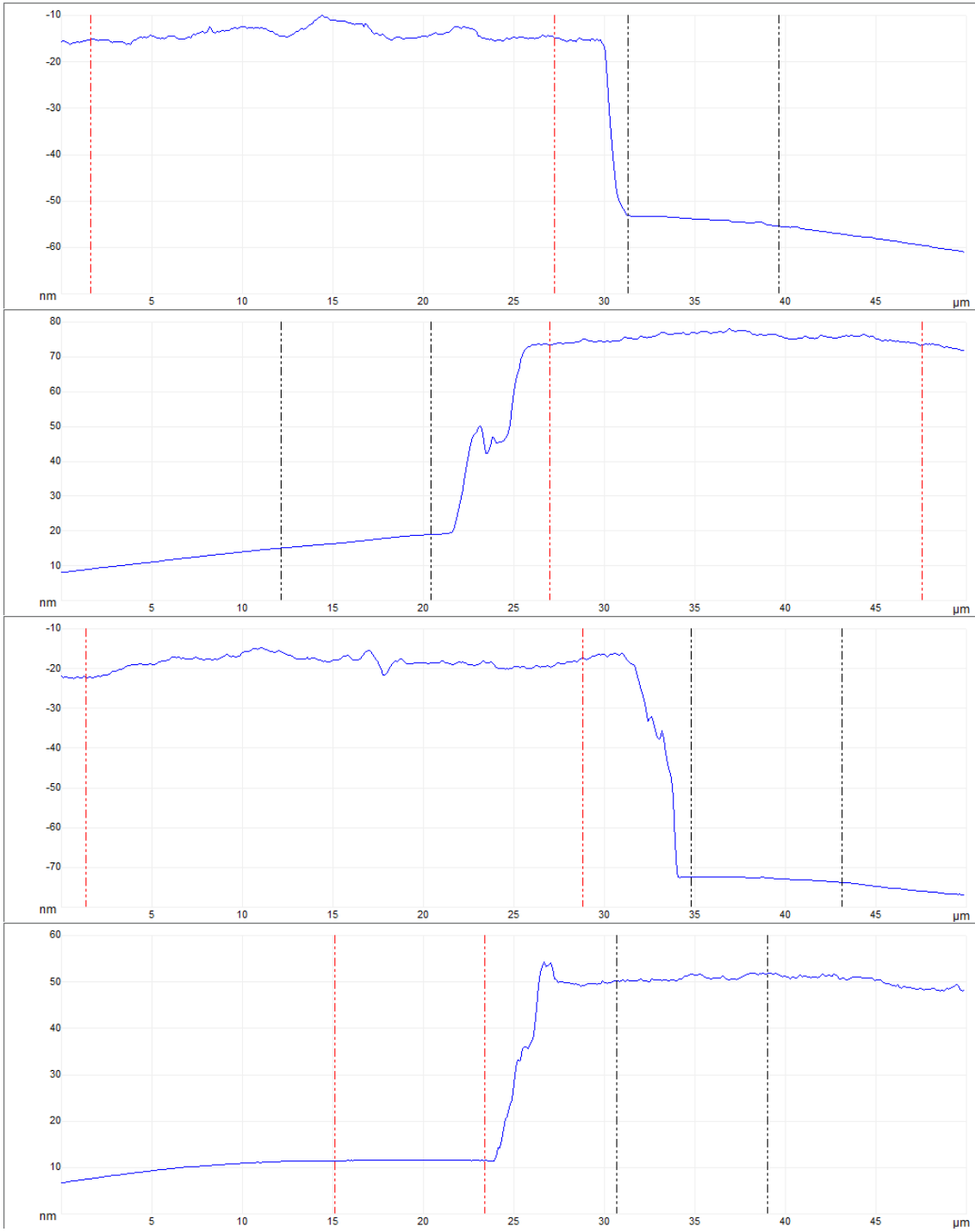
10.0 μm



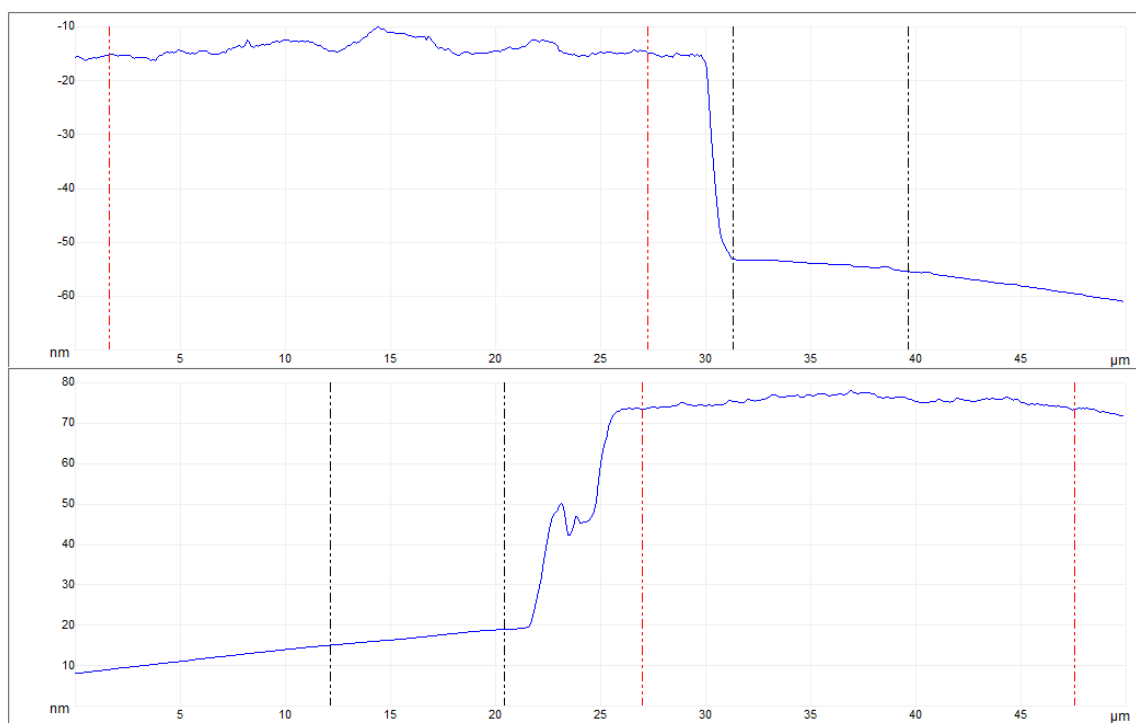
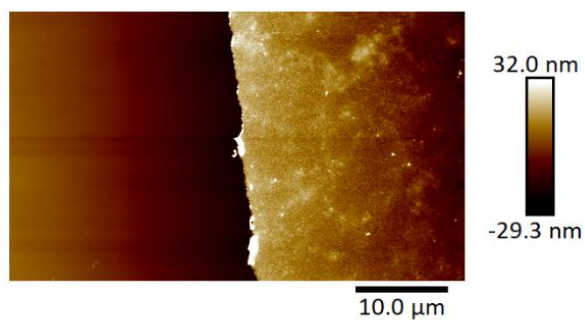
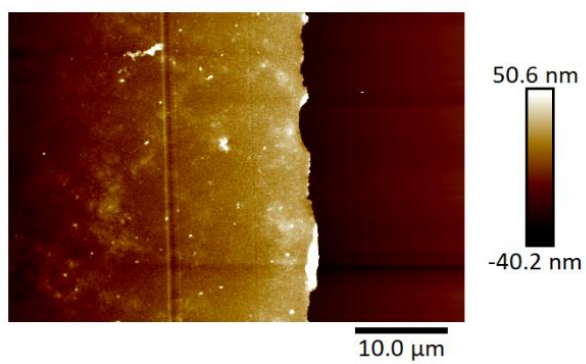
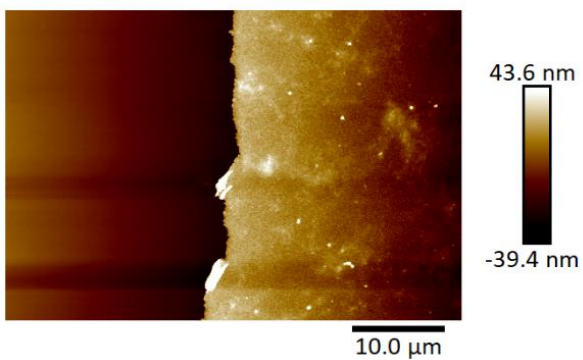
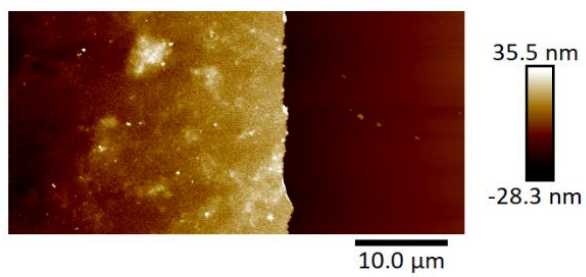


5K

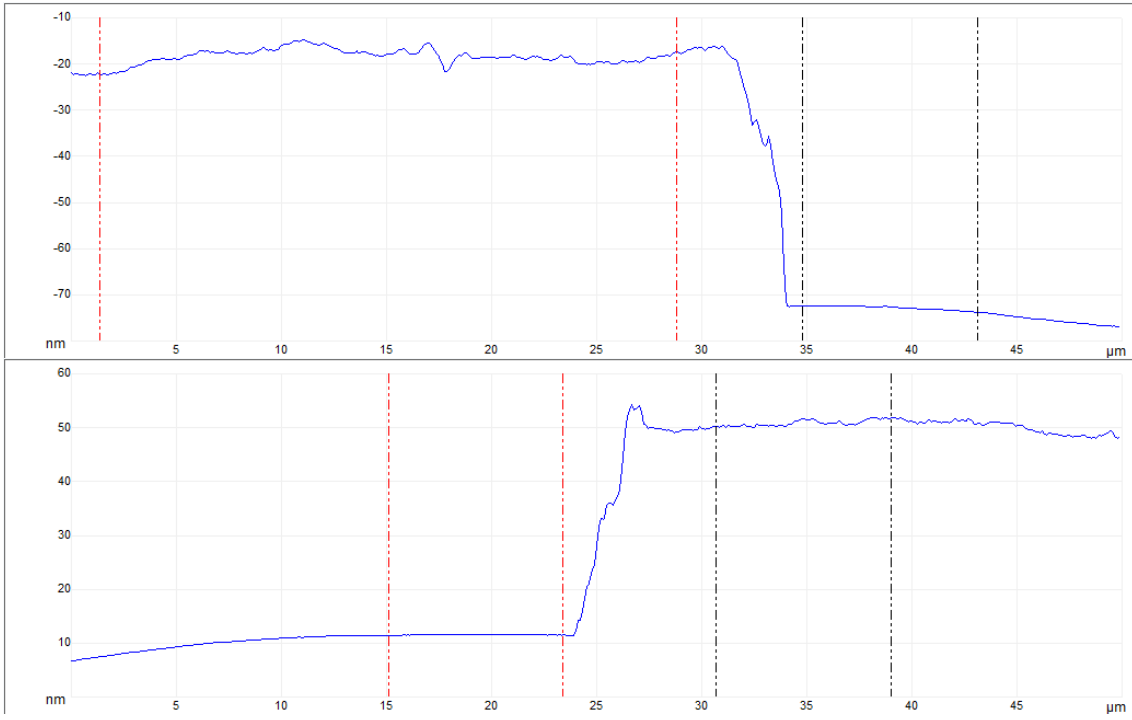




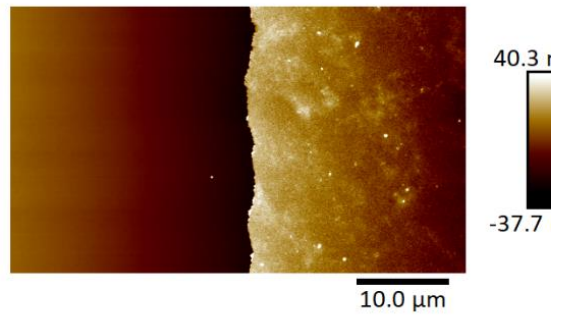
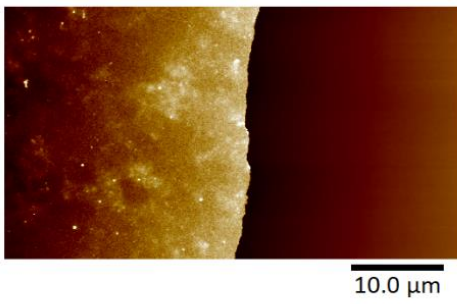
6K



289



7K



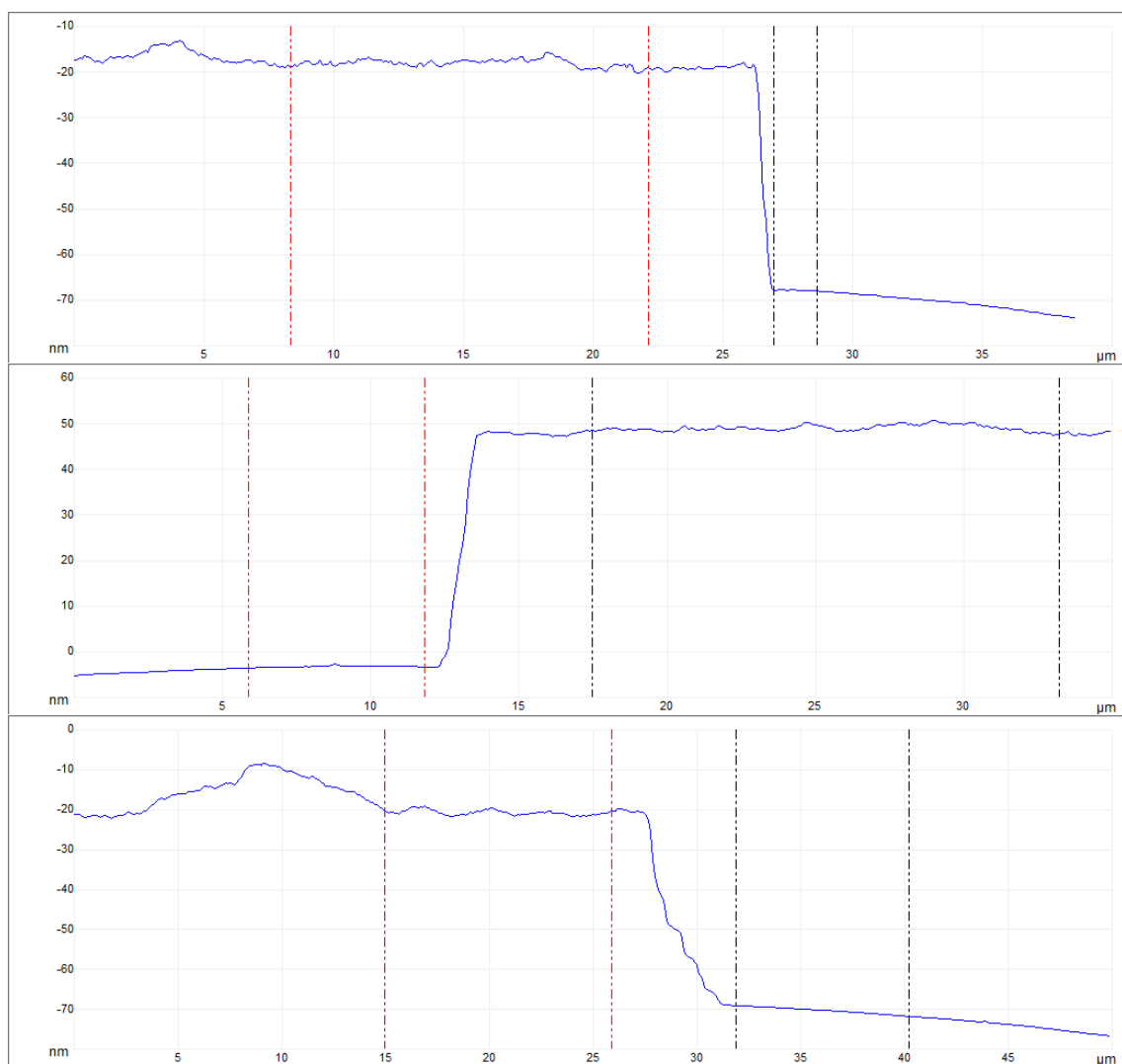
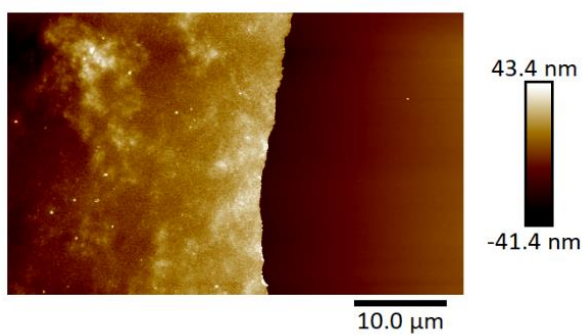


Figure 122 AFM topographical images and height profiles ($50\ \mu\text{m} \times 50\ \mu\text{m}$) of spin coated $5\ \text{mg mL}^{-1}$ in chlorobenzene DPP-DTT:GA thin-films on ODTs modified Si/SiO₂ substrates.

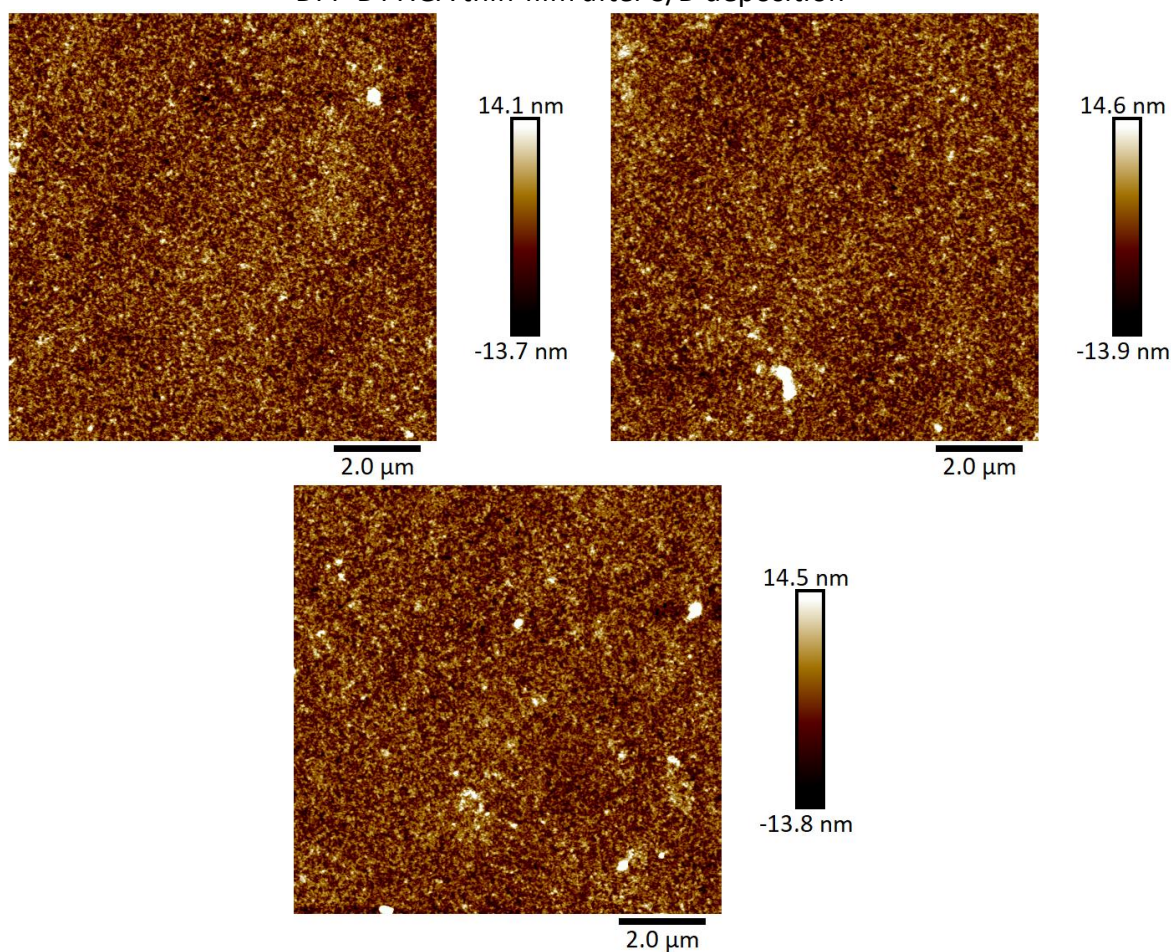
RPM	1 nm	2 nm	3 nm	4 nm	Average nm	STD nm
2K	61.8	71.7	58.6	61.8	63.5	5.69
4K	52.4	43.5	64.1	47.9	52.0	8.86
5K	51.7	56.0	58.1	44.4	52.6	6.05
6K	40.2	58.6	54.5	39.3	48.2	9.85
7K	49.8	52.3	49.6		50.6	1.50

Table 57 Spin coating thin-film thickness.

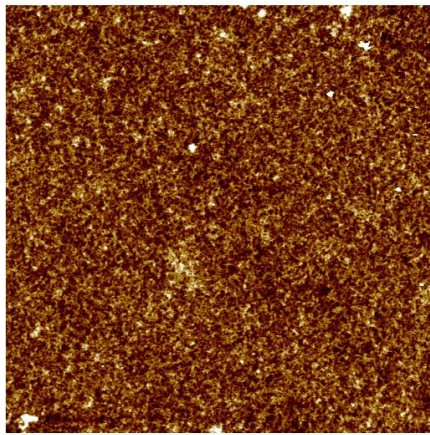
Spin coating conditions RPM	Ra		Rq	
	Average nm	STD nm	Average nm	STD nm
2K	1.72	0.083	2.16	0.083
4K	1.71	0.071	2.16	0.102
5K	1.67	0.061	2.10	0.071
6K	1.69	0.055	2.12	0.062
7K	1.69	0.063	2.13	0.070

Table 58 AFM averaged roughness values Ra and Rq spin coating series.

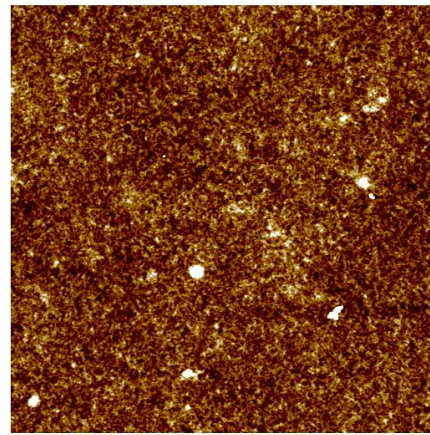
DPP-DTT:GA thin-film after S/D deposition



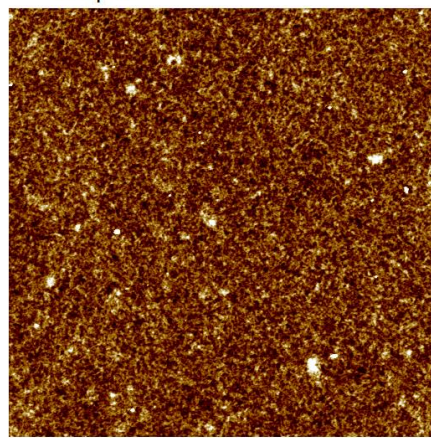
Functionalised before S/D deposition



2.0 μm

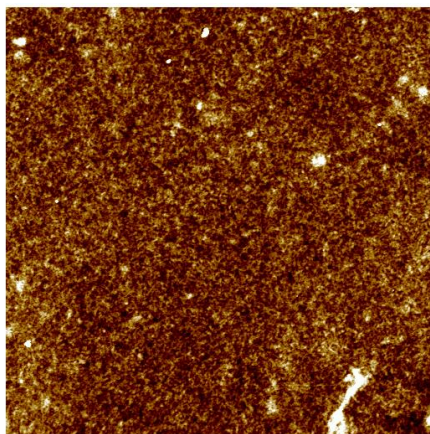


2.0 μm

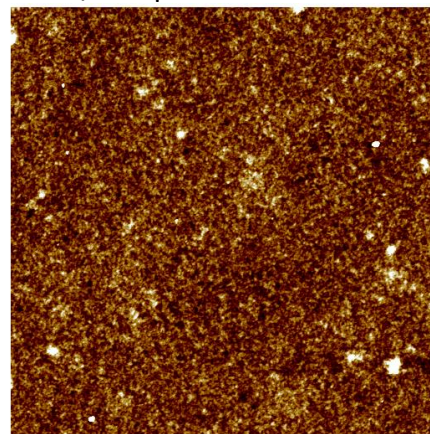


2.0 μm

Functionalised thin-film after S/D deposition



2.0 μm



2.0 μm

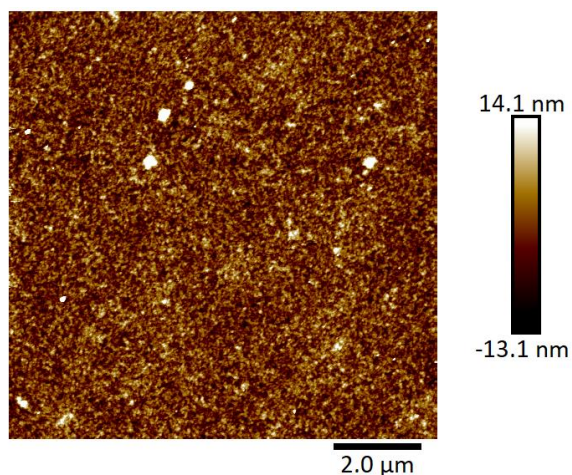
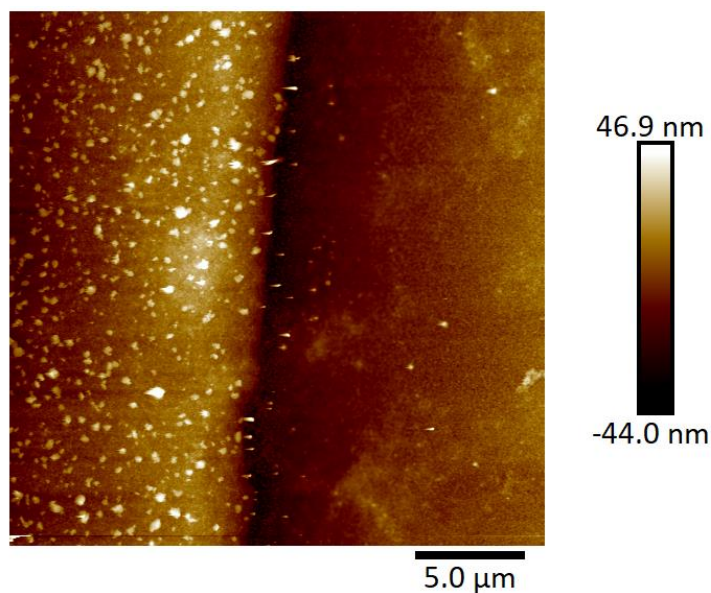
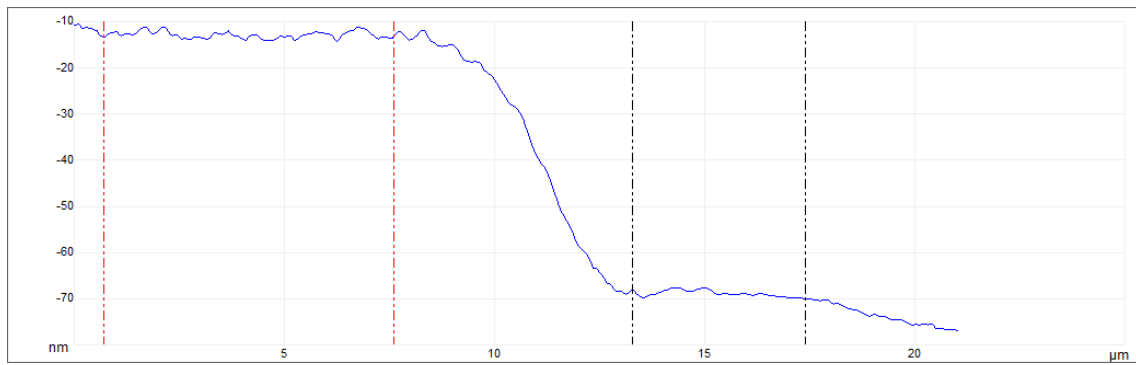


Figure 123 AFM topographical images ($10\ \mu\text{m} \times 10\ \mu\text{m}$) of $10\ \mu\text{M}$ aptamer functionalised DPP-DTT:GA thin-films before and after S/D deposition.

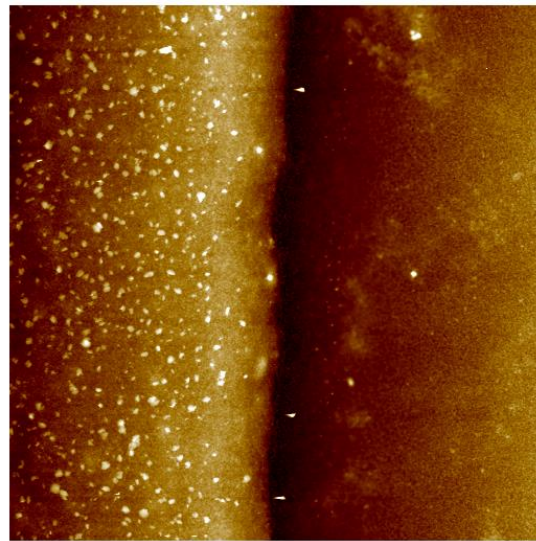
Conditions	Ra		Rq	
	Average nm	STD nm	Average nm	STD nm
DPP-DTT:GA thin-film after S/D deposition	2.98	0.037	3.74	0.040
Functionalised before S/D deposition	3.17	0.028	3.99	0.043
Functionalised thin-film after S/D deposition	3.12	0.034	3.92	0.047

Table 59 AFM averaged roughness values Ra and Rq of $10\ \mu\text{M}$ aptamer functionalised DPP-DTT:GA thin-films before and after S/D deposition.

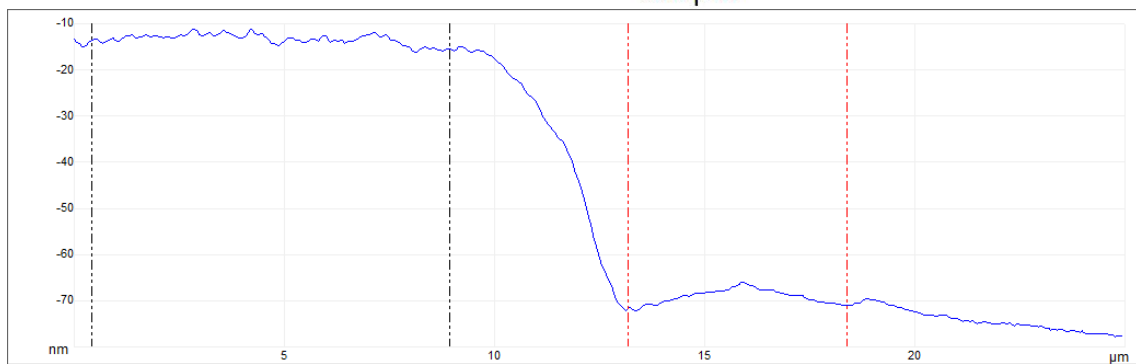




56.0 nm

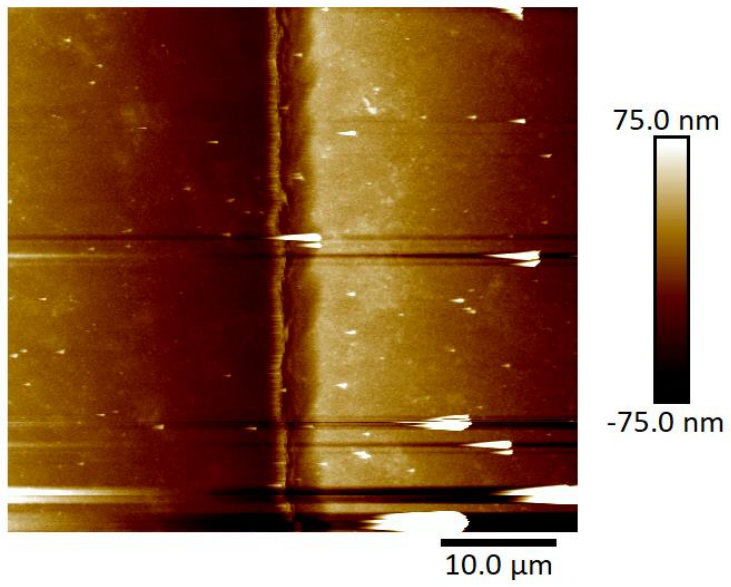
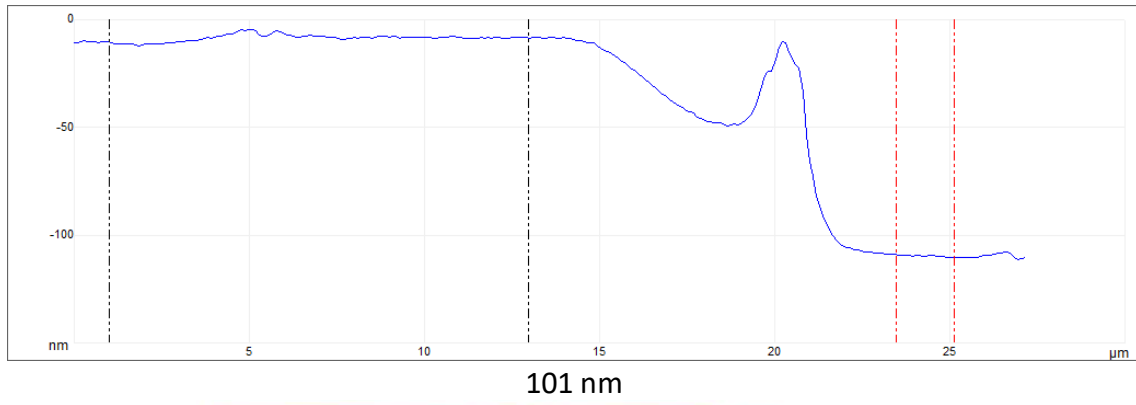
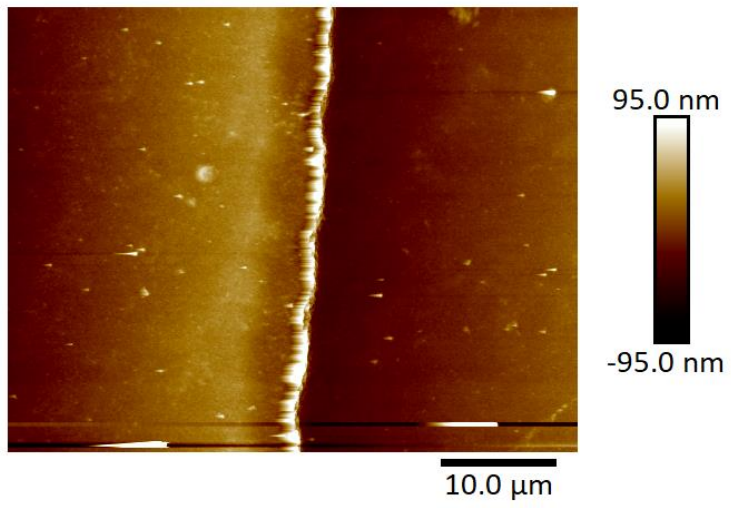


5.0 μm



55.8 nm

Figure 124 AFM topological image and cross section of DPP-DTT:GA OFET with molybdenum trioxide (50 nm) and gold (50 nm) source-drain electrodes.



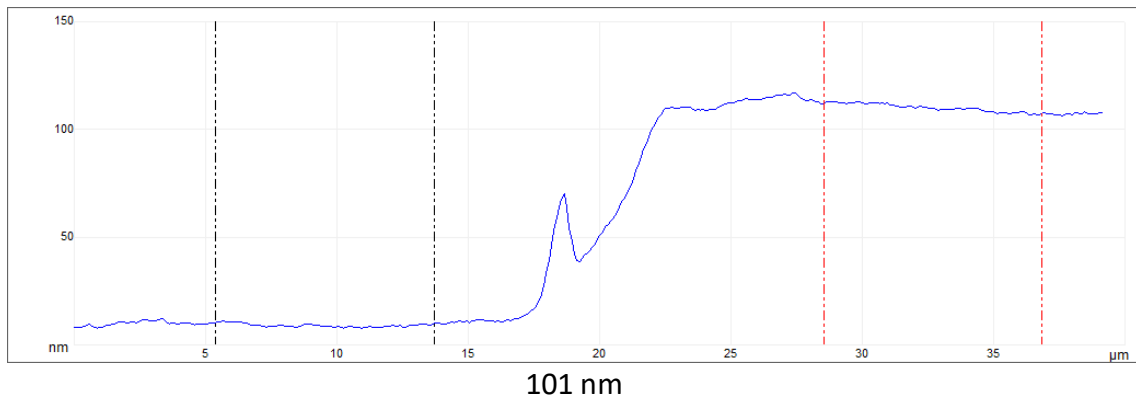


Figure 125 AFM topographical image and cross section of DPP-DTT:GA OFET with gold (50 nm) and silicon monoxide (50 nm) source-drain electrodes.

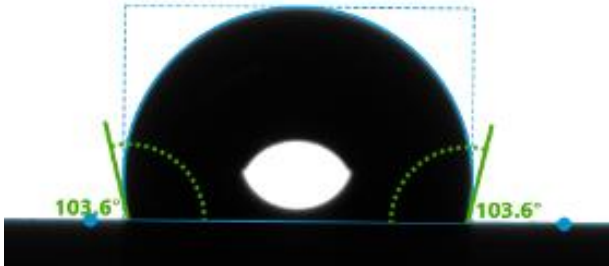
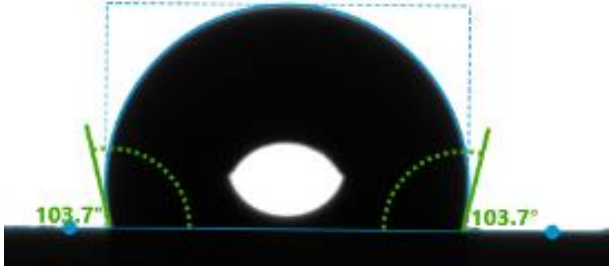
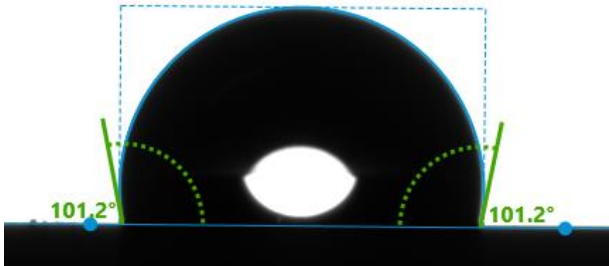
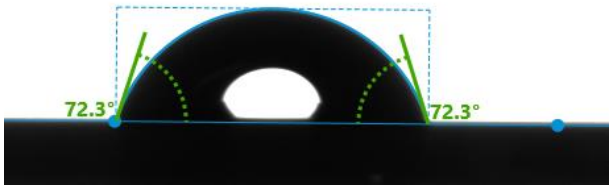
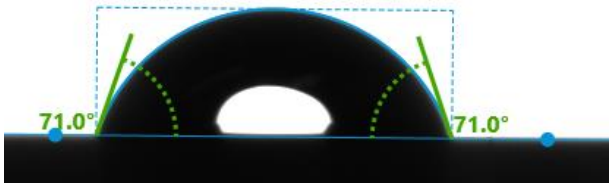
7.2.2 DPP-DTT:GA Water contact angle measurements

Conditions	1	2	3
DPP-DTT:GA			
1 μM			
5 μM			
10 μM			

Figure 126 Water contact angle measurements of DPP-DTT:GA thin-film and $\text{NH}_2\text{-CBA}$ functionalised ($1 \mu\text{M}$, $5 \mu\text{M}$ and $10 \mu\text{M}$) thin-films.

Conditions	1 (°)	2 (°)	3 (°)	Average (°)	STD (°)
DPP-DTT:GA	102.6	101.1	101.2	101.6	0.84
1 μM	82.4	95.0	82.4	86.6	7.27
5 μM	82.1	94.2	82.0	86.1	7.01
10 μM	72.3	71.0	76.6	73.3	2.93

Table 60 Water contact angle measurement pristine, 1 μM , 5 μM and 10 μM functionalised DPP-DTT:GA thin-films.

Conditions	WCA image
DPP-DTT:GA thin-film after S/D deposition	
	
	
Functionalised thin-film before S/D deposition	
	

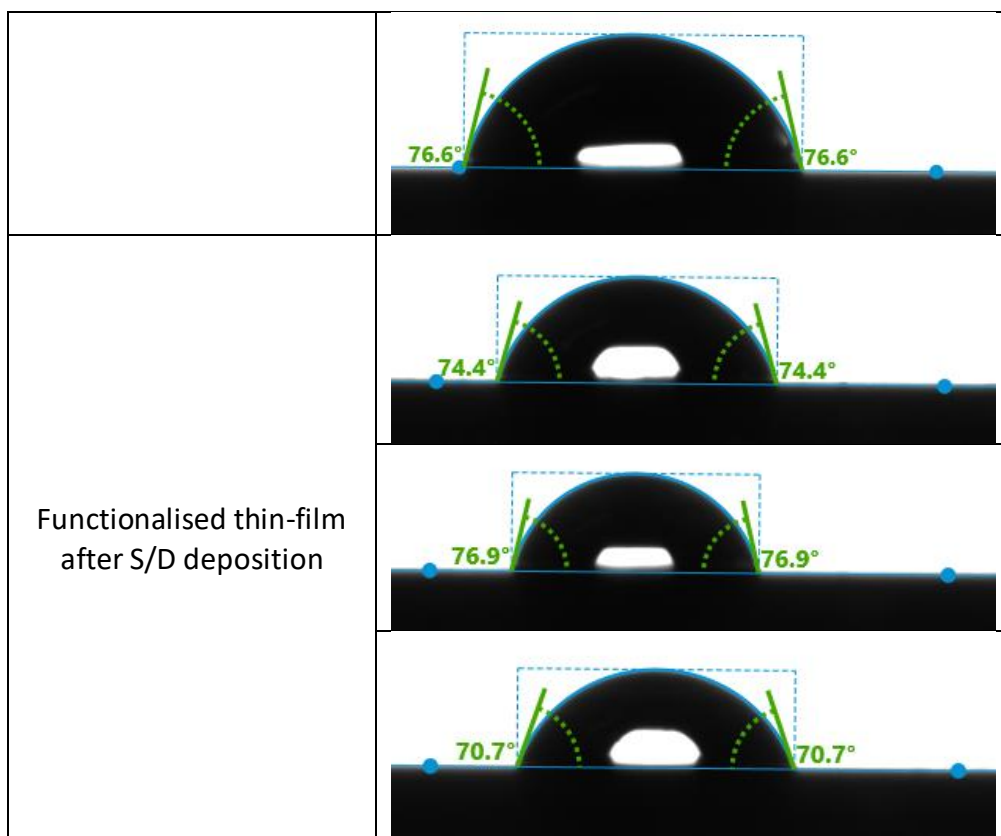


Figure 127 Water contact angle measurements of 10 μM aptamer functionalised DPP-DTT:GA thin-films before and after S/D deposition.

Conditions	1 (°)	2 (°)	3 (°)	Average (°)	STD (°)
DPP-DTT:GA thin-film after S/D deposition	103.6	103.7	101.2	102.8	1.42
Functionalised thin-film before S/D deposition	72.3	71.0	76.6	73.3	2.93
Functionalised thin-film after S/D deposition	74.4	76.9	70.7	74.0	3.12

Table 61 Water contact angle measurements of 10 μM aptamer functionalised DPP-DTT:GA thin-films before and after S/D deposition.

7.2.3 DPP-DTT:GA epifluorescence microscopy

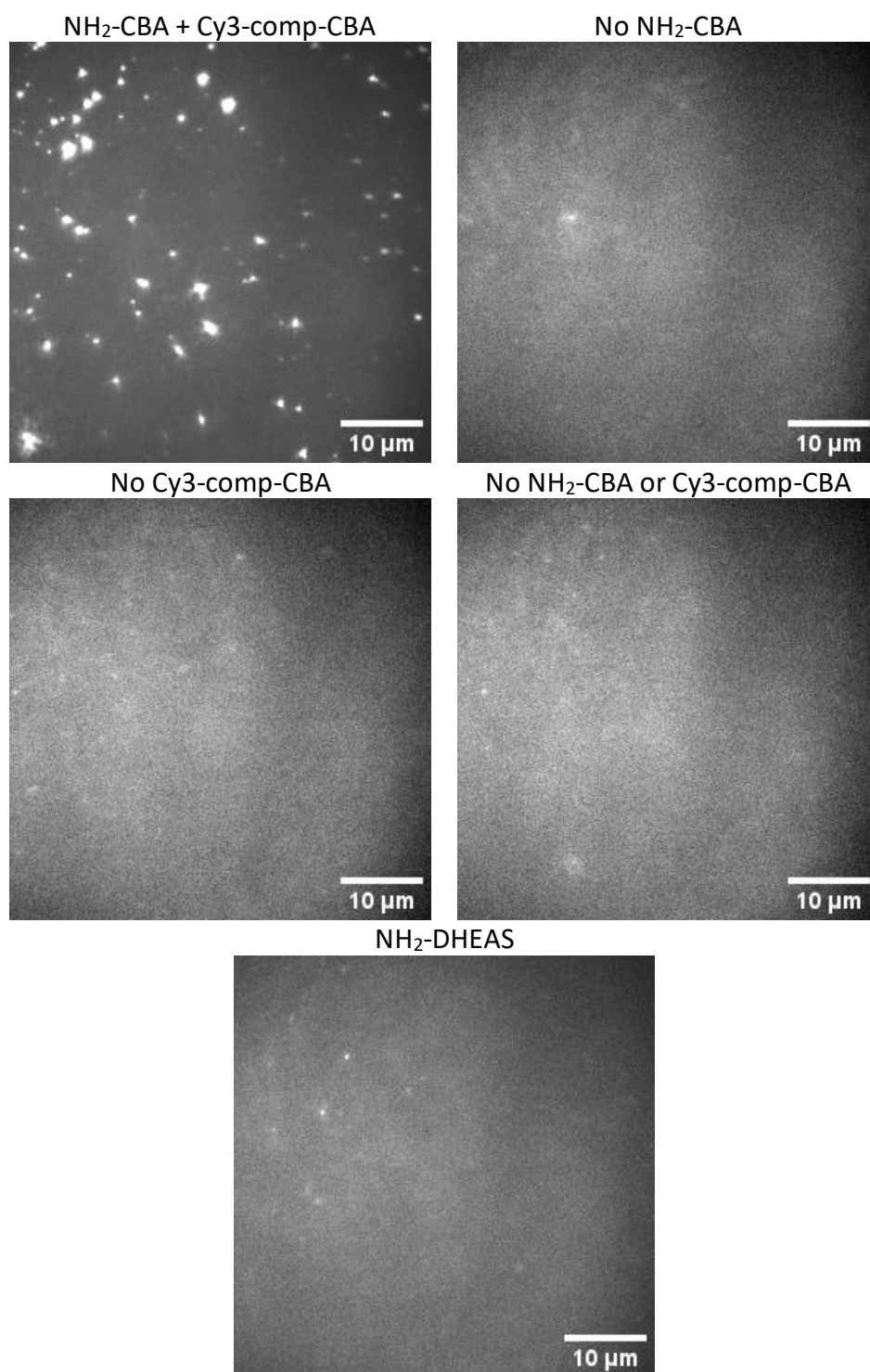


Figure 128 Epifluorescence microscopy images: DPP-DTT:GA thin-film functionalised with NH₂-CBA (10 μM) and hybridised with Cy3-comp-CBA (1 μM), and thin-film controls (51.2 μm x 51.2 μm).

Conditions	Average pixel value (Abs)
NH ₂ -CBA + Cy3-comp-CBA	12669.32
No NH ₂ -CBA	6499.687
No Cy3-comp-CBA	6113.873
No NH ₂ -CBA or Cy3-comp-CBA	5737.425
NH ₂ -DHEAS	5716.521

Table 62 Epifluorescence microscopy image pixel values: DPP-DTT:GA thin-film functionalised with NH₂-CBA (10 μ M) and hybridised with Cy3-comp-CBA (1 μ M), and thin-film controls (51.2 μ m x 51.2 μ m).

7.2.4 DPP-DTT:GA X-ray photoelectron spectroscopy

High resolution scan	Control %	STD %	1 μ M %	STD %	5 μ M %	STD %	10 μ M %	STD %
O1s	12.87	0.15	15.94	0.06	17.18	0.11	17.36	0.27
N1s	3.97	0.07	4.71	0.80	5.30	0.09	5.48	0.06
P2p	0.00	0.00	0.34	0.24	0.5	0.01	0.52	0.02

Table 63 XPS relative atomic % of DPP-DTT:GA control, 1 μ M, 5 μ M and 10 μ M thin-films.

7.2.5 Preliminary sensing of Cortisol

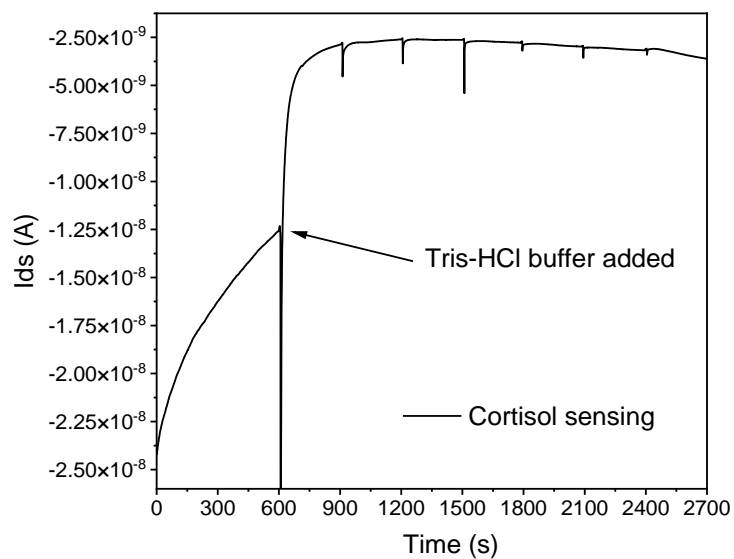


Figure 129 Scaled real-time current response of functionalised DPP-DTT:GA OFET, $V_{gs} -1$ V, $V_{ds} -0.5$ V to cortisol (2 nM to 2 mM).

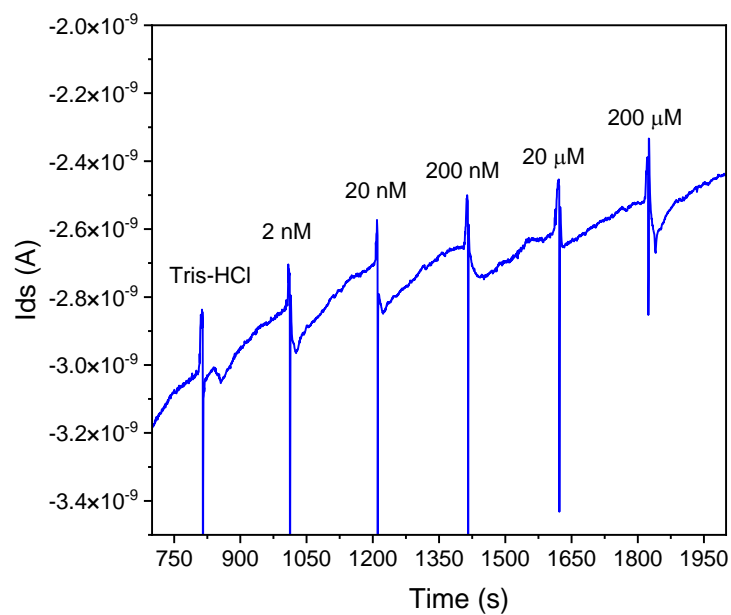


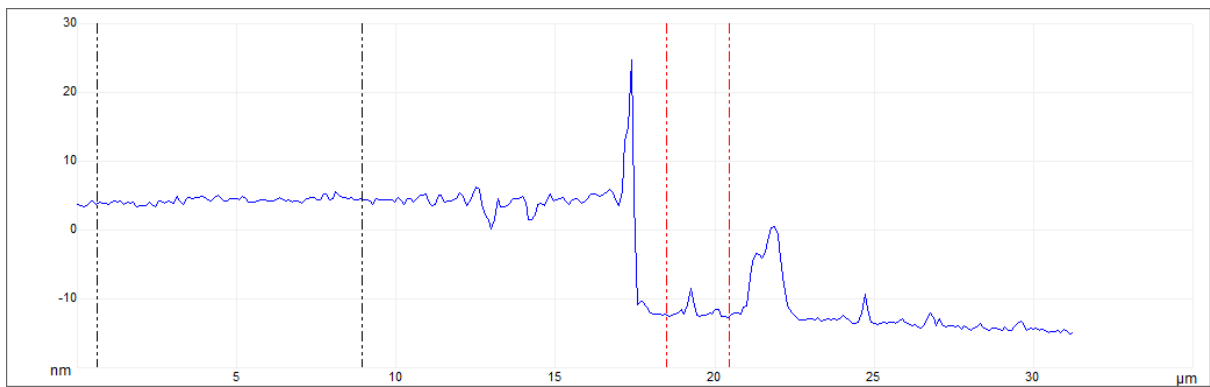
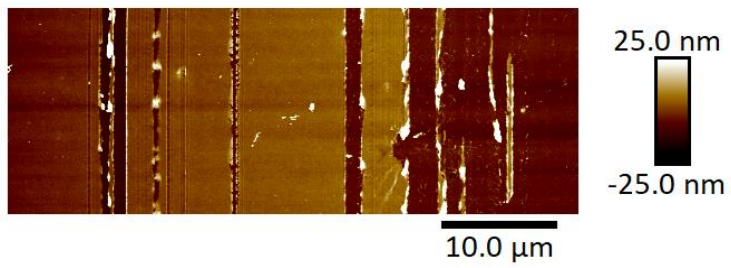
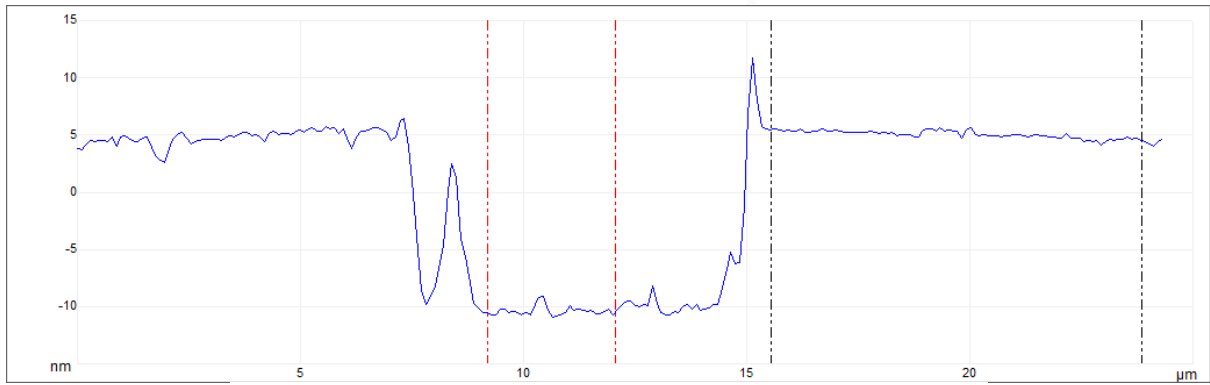
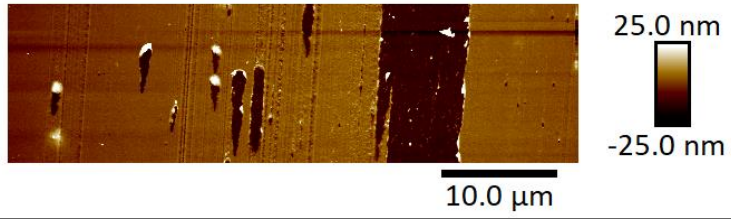
Figure 130 Real-time current response of non-functionalised DPP-DTT:GA OFET, $V_{gs} -1$ V, $V_{ds} -0.5$ V to cortisol (2 nM to 200 μ M).

7.3 Investigation of chemically modified organic semiconducting materials for aptamer functionalisation and organic transistor fabrication appendix

7.3.1 N₃-DPP AFM

Rq					
Sample	1 nm	2 nm	3 nm	Average nm	STD nm
1	1.01	1.00	1.00	0.99	0.021
2	1.00	0.95	0.97		
Ra					
Sample	1 nm	2 nm	3 nm	Average nm	STD nm
1	0.80	0.79	0.80	0.78	0.016
2	0.79	0.76	0.77		

Table 64 Roughness Rq and Ra values of N₃-DPP thin-film via FFT from chlorobenzene (5 mg mL⁻¹). Polymer solution probe sonicated.



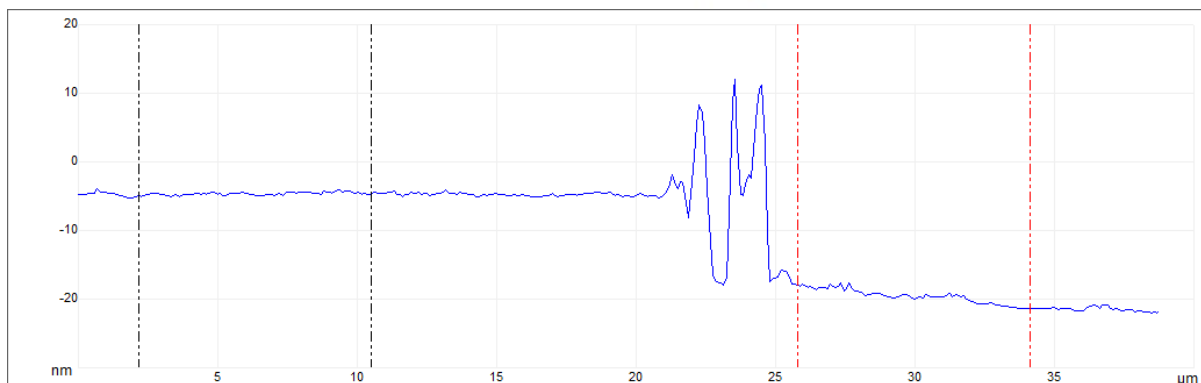
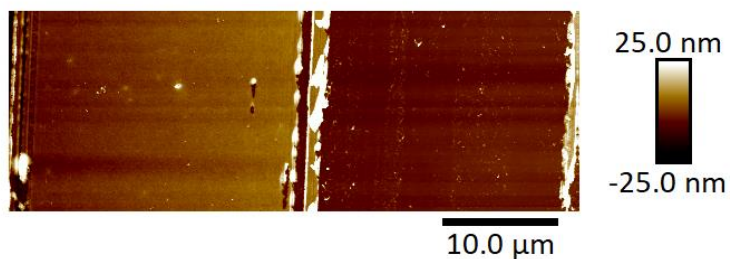


Figure 131 AFM thickness images ($50\ \mu\text{m} \times 50\ \mu\text{m}$) of N_3 -DPP thin-film via FFT from chlorobenzene ($5\ \text{mg mL}^{-1}$). Polymer solution probe sonicated.

1 nm	2 nm	3 nm	Average nm	STD nm
15.4	16.2	14.9	15.5	0.54

Table 65 Thin-film thicknesses of N_3 -DPP thin-film via FFT from chlorobenzene ($5\ \text{mg mL}^{-1}$). Polymer solution probe sonicated.

7.3.2 N₃-DPP water contact angle

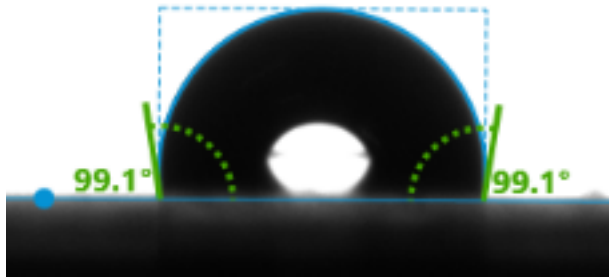
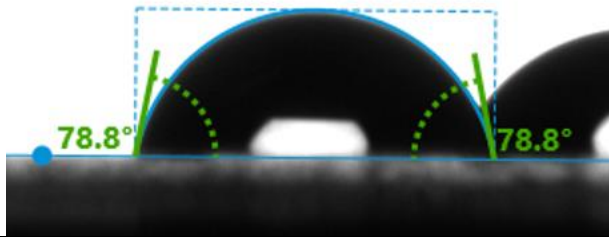
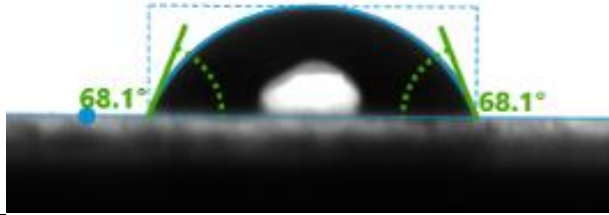
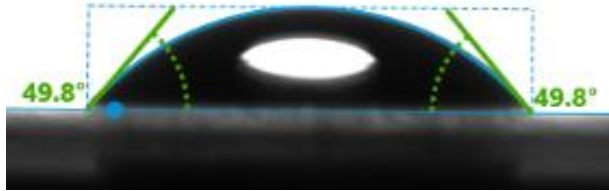
Sample conditions	Image	WCA (°)
N ₃ -DPP		99.1
Cy3-comp-CBA		78.8
DBCO-CBA		68.1
DBCO-CBA + Cy3-comp-CBA		49.8

Figure 132 Water contact angle measurements. N₃-DPP thin-films incubated with: Cy3-comp-CBA (1 μm), DBCO-CBA (1 μm) and DBCO-CBA (1 μm) + Cy3-comp-CBA (1 μm).

7.3.3 DTP-C4-acid AFM

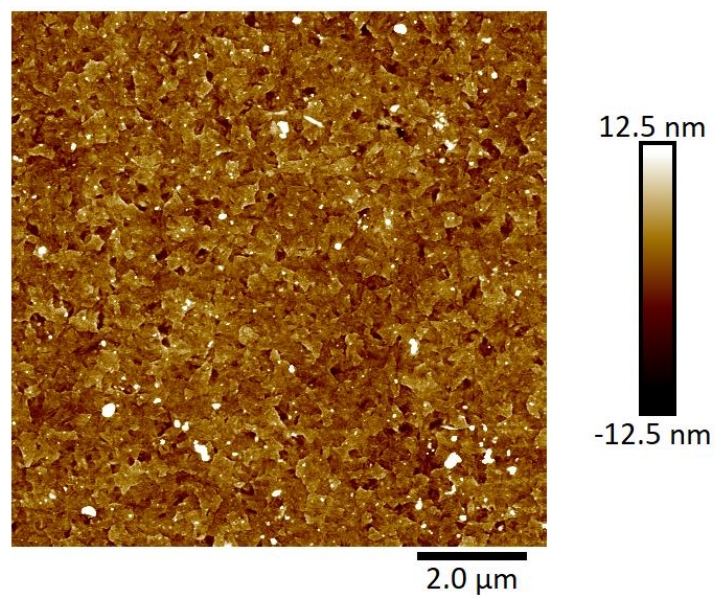


Figure 133 AFM topographical images (10 μm x 10 μm) of ITO substrate.

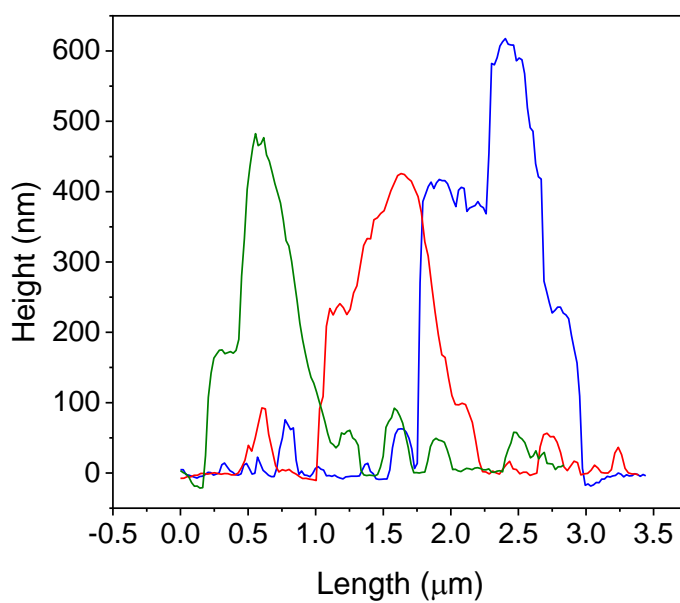
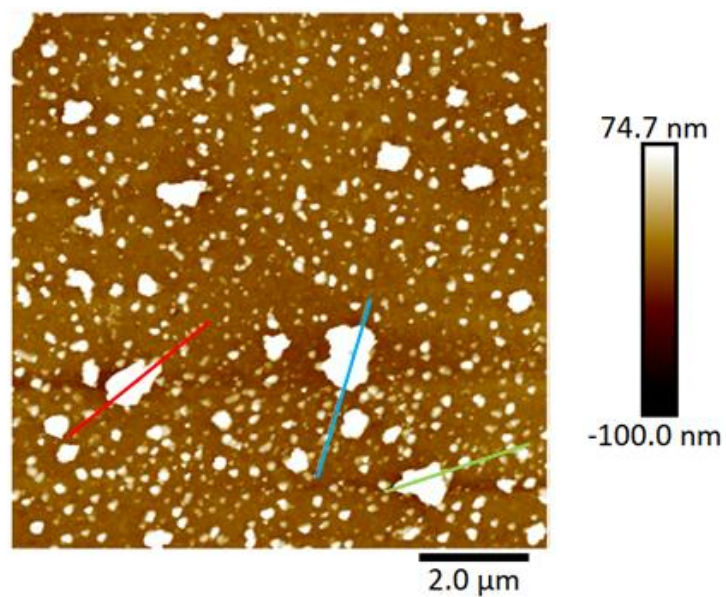


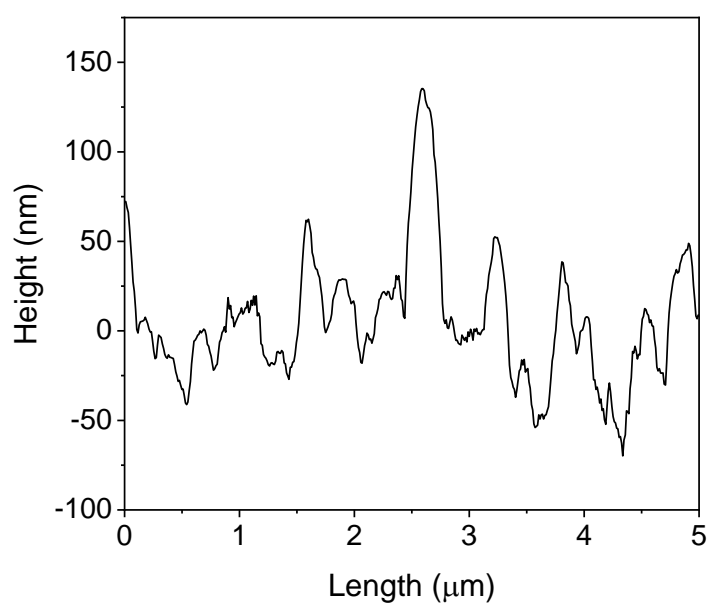
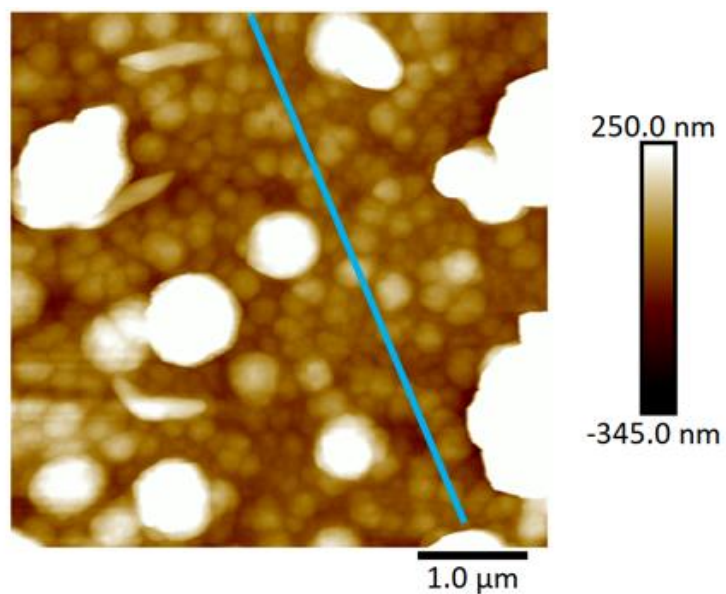
Figure 134 AFM topographical image (10 μm x 10 μm) and height profiles of DTP-C4-acid thin-film deposited via chronoamperometry on ITO substrate.

Section line	Vertical distance nm
Green	525
Red	424
Blue	621

Table 66 AFM height profiles: vertical distance of masses on DTP-C4-acid thin-film deposited via chronoamperometry on ITO substrate.

Roughness	1	2	3	4	Average nm	STD nm
Rq	1.61	1.63	2.10	1.91	1.81	0.236
Ra	1.29	1.27	1.67	1.56	1.45	0.199

Table 67 AFM roughness values Rq and Ra of DTP-C4-acid thin-film deposited via chronoamperometry on ITO substrate. Thin-film roughness measured at 250 nm x 250 nm areas, avoiding large masses.



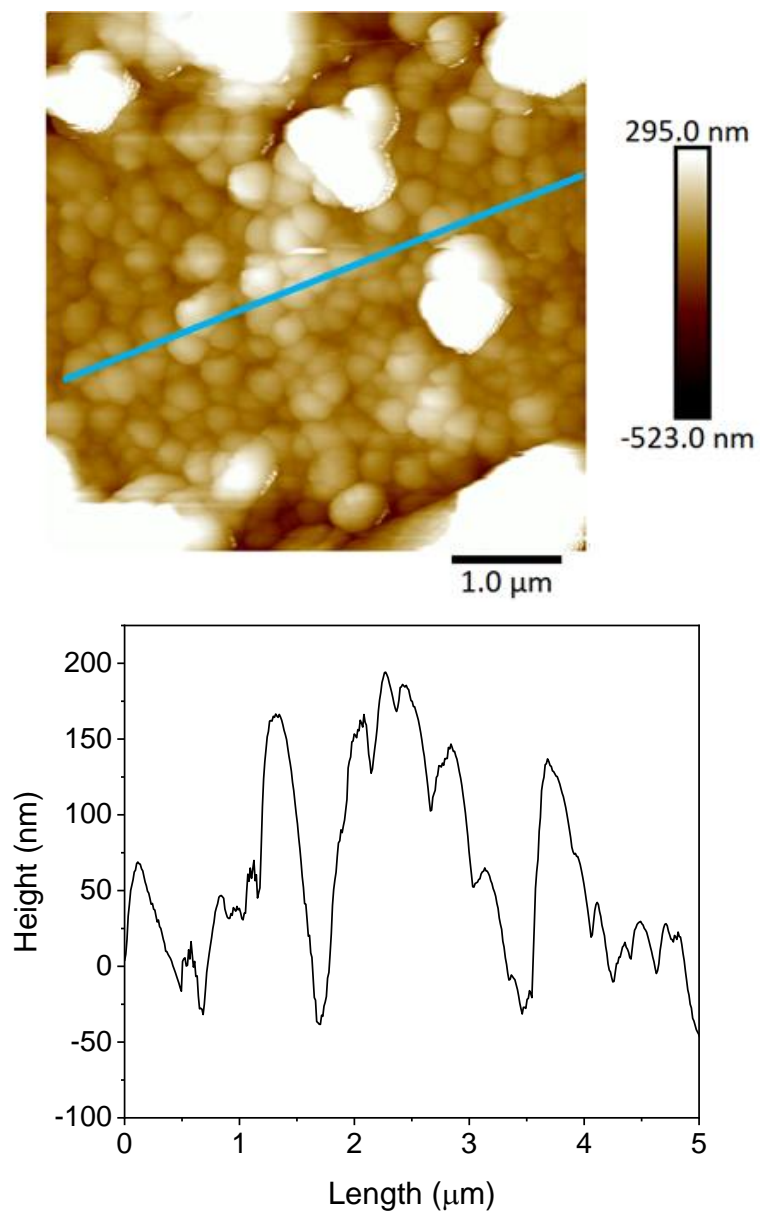
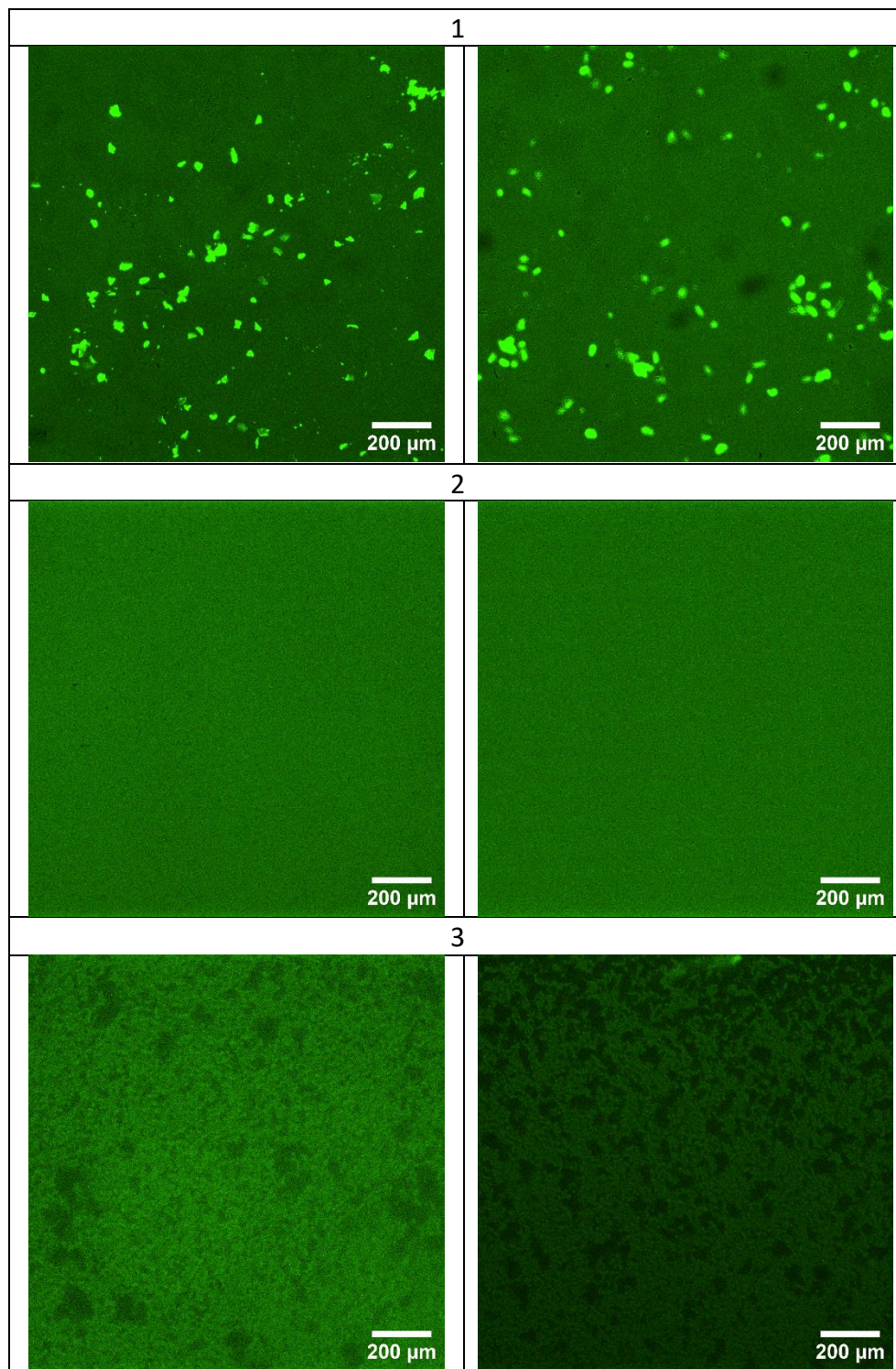
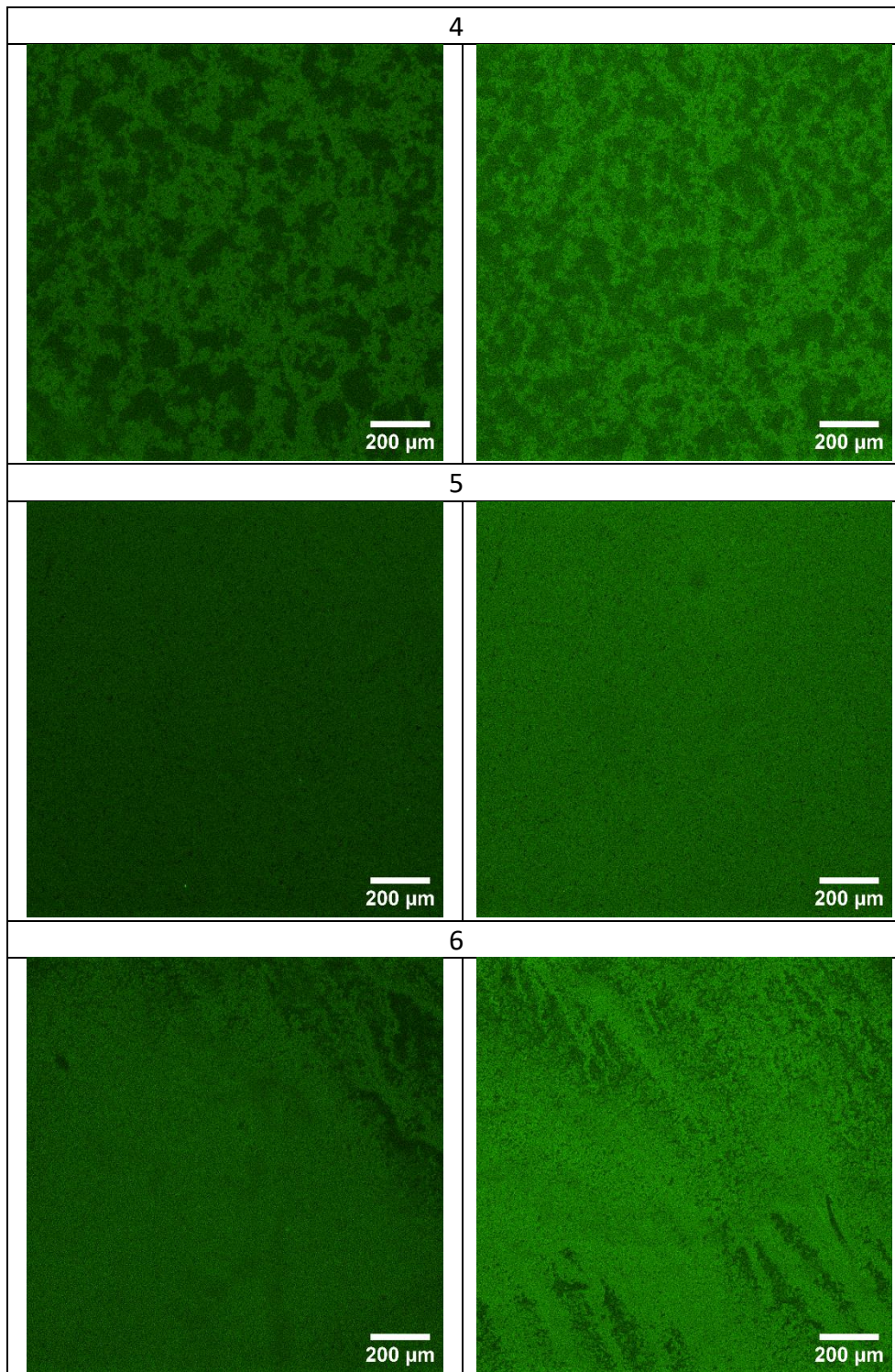


Figure 135 AFM topographical images and section height profiles (5 μm x 5 μm) of PDTP-C4-acid thin-film deposited via chronoamperometry onto gold electrodes on a polyimide substrate (50 μm channel length), white line indicates section analysed.

7.3.4 DTP-C4-acid epifluorescence microscopy





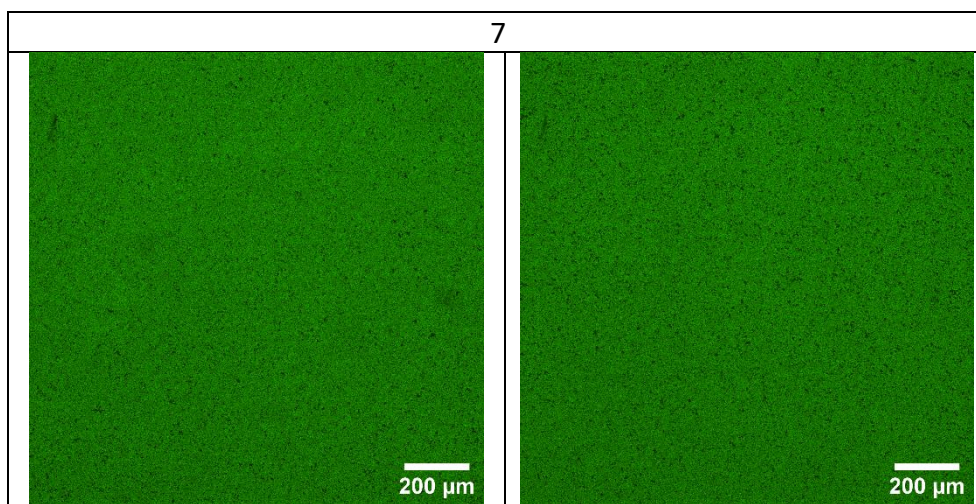


Figure 136 Epifluorescence microscopy images: DTP-C4-acid thin-films functionalised with $\text{NH}_2\text{-CBA}$ ($10 \mu\text{M}$) and hybridised with Cy3-comp-CBA ($1 \mu\text{M}$), and thin-film controls ($1.39 \text{ mm} \times 1.39 \text{ mm}$).

Sample No.	Incubation conditions	Average pixel value (Abs)	STD (Abs)
1	EDC/sulfo-NHS, $\text{NH}_2\text{-CBA}$ and Cy3-comp-CBA	191.0	2.79
2	No EDC/sulfo-NHS, $\text{NH}_2\text{-CBA}$ or Cy3-comp-CBA	126.9	0.29
3	No Cy3-comp-CBA	136.3	0.24
4	No $\text{NH}_2\text{-CBA}$	127.1	2.50
5	No $\text{NH}_2\text{-CBA}$ or Cy3-comp-CBA	149.2	2.96
6	No EDC/sulfo-NHS	141.6	0.96
7	No EDC/sulfo-NHS or $\text{NH}_2\text{-CBA}$	168.1	2.16

Table 68 Epifluorescence microscopy average image pixel values: DTP-C4-acid thin-films functionalised with $\text{NH}_2\text{-CBA}$ ($10 \mu\text{M}$) and hybridised with Cy3-comp-CBA ($1 \mu\text{M}$), and thin-film controls ($1.39 \text{ mm} \times 1.39 \text{ mm}$).

8 References

1. H. Ling, S. Liu, Z. Zheng, F. Yan, Organic Flexible Electronics. *Small Methods*. **2**, 1–33 (2018).
2. Q. Ma, J. Wang, X. Dong, W. Yu, G. Liu, Flexible ribbon-shaped coaxial electrical conductive nanocable array endowed with magnetism and photoluminescence. *RSC Adv*. **5**, 2523–2530 (2015).
3. D. R. Lide, *CRC Handbook of Chemistry and Physics, 2009–2010, 90th ed.* (CRC Press, 2009), vol. 131.
4. C. K. Chiang, C. R. Fincher, Y. W. Park, A. J. Heeger, H. Shirakawa, E. J. Louis, S. C. Gau, A. G. MacDiarmid, Electrical Conductivity in Doped Polyacetylene. *Phys. Rev. Lett.* **39**, 1098–1101 (1977).
5. H. Shirakawa, The discovery of polyacetylene film: The dawning of an era of conducting polymers. *Synth. Met.* **125**, 3–10 (2001).
6. J. Zhao, P. Ji, Y. Li, R. Li, K. Zhang, H. Tian, K. Yu, B. Bian, L. Hao, X. Xiao, W. Griffin, N. Dudeck, R. Moro, L. Ma, W. A. de Heer, Ultrahigh-mobility semiconducting epitaxial graphene on silicon carbide. *Nature*. **625**, 60–65 (2024).
7. J. Paloheimo, H. Isotalo, J. Kastner, H. Kuzmany, Conduction mechanisms in undoped thin films of C60 and C60/70. *Synth. Met.* **56**, 3185–3190 (1993).
8. R. H. Baughman, A. A. Zakhidov, W. A. de Heer, Carbon Nanotubes--the Route Toward Applications. *Science (80-.)*. **297**, 787–792 (2002).
9. S. Wan, F. Gándara, A. Asano, H. Furukawa, A. Saeki, S. K. Dey, L. Liao, M. W. Ambrogio, Y. Y. Botros, X. Duan, S. Seki, J. F. Stoddart, O. M. Yaghi, Covalent Organic Frameworks with High Charge Carrier Mobility. *Chem. Mater.* **23**, 4094–4097 (2011).
10. A. Facchetti, Semiconductors for organic transistors. *Mater. Today*. **10**, 28–37 (2007).
11. M. Geoghegan, G. Hadziioannou, *Polymer Electronics* (Oxford University Press, First

- Edit., 2013).
12. Y. Karpov, T. Erdmann, I. Raguzin, M. Al-Hussein, M. Binner, U. Lappan, M. Stamm, K. L. Gerasimov, T. Beryozkina, V. Bakulev, D. V. Anokhin, D. A. Ivanov, F. Günther, S. Gemming, G. Seifert, B. Voit, R. Di Pietro, A. Kiriya, High Conductivity in Molecularly p-Doped Diketopyrrolopyrrole-Based Polymer: The Impact of a High Dopant Strength and Good Structural Order. *Adv. Mater.* **28**, 6003–6010 (2016).
 13. Z. A. Lamport, H. F. Haneef, S. Anand, M. Waldrip, O. D. Jurchescu, Tutorial: Organic field-effect transistors: Materials, structure and operation. *J. Appl. Phys.* **124**, 071101 (2018).
 14. B. Li, H. Yu, E. C. Montoto, Y. Liu, S. Li, K. Schwieter, J. Rodríguez-López, J. S. Moore, C. M. Schroeder, Intrachain Charge Transport through Conjugated Donor–Acceptor Oligomers. *ACS Appl. Electron. Mater.* **1**, 7–12 (2019).
 15. M. Kim, S. U. Ryu, S. A. Park, K. Choi, T. Kim, D. Chung, T. Park, Donor–Acceptor-Conjugated Polymer for High-Performance Organic Field-Effect Transistors: A Progress Report. *Adv. Funct. Mater.* **30**, 1–25 (2020).
 16. B. Kumar, B. K. Kaushik, Y. S. Negi, Organic Thin Film Transistors: Structures, Models, Materials, Fabrication, and Applications: A Review. *Polym. Rev.* **54**, 33–111 (2014).
 17. C. Wang, H. Dong, W. Hu, Y. Liu, D. Zhu, Semiconducting π -Conjugated Systems in Field-Effect Transistors: A Material Odyssey of Organic Electronics. *Chem. Rev.* **112**, 2208–2267 (2012).
 18. B. X. Dong, J. K. Wenderott, P. F. Green, Charge carrier transport in thin conjugated polymer films: influence of morphology and polymer/substrate interactions. *Colloid Polym. Sci.* **299**, 439–456 (2021).
 19. C. Wang, X. Zhang, H. Dong, X. Chen, W. Hu, Challenges and Emerging Opportunities in High-Mobility and Low-Energy-Consumption Organic Field-Effect Transistors. *Adv. Energy Mater.* **10**, 1–7 (2020).

20. H. Un, J. Wang, J. Pei, Recent Efforts in Understanding and Improving the Nonideal Behaviors of Organic Field-Effect Transistors. *Adv. Sci.* **6**, 1900375 (2019).
21. L. M. Cowen, J. Atoyo, M. J. Carnie, D. Baran, B. C. Schroeder, Review—Organic Materials for Thermoelectric Energy Generation. *ECS J. Solid State Sci. Technol.* **6**, N3080–N3088 (2017).
22. A. J. Heeger, Semiconducting polymers: the Third Generation. *Chem. Soc. Rev.* **39**, 2354 (2010).
23. I. Kymissis, *Organic Field Effect Transistors: Theory, Fabrication and Characterization* (Springer US, Boston, MA, 2009; <http://link.springer.com/10.1007/978-0-387-92134-1>), *Integrated Circuits and Systems*.
24. B. Kumar, B. K. Kaushik, Y. S. Negi, Perspectives and challenges for organic thin film transistors: materials, devices, processes and applications. *J. Mater. Sci. Mater. Electron.* **25**, 1–30 (2014).
25. L. Chua, J. Zaumseil, J. Chang, E. C.-W. Ou, P. K.-H. Ho, H. Sirringhaus, R. H. Friend, General observation of n-type field-effect behaviour in organic semiconductors. *Nature.* **434**, 194–199 (2005).
26. M. Nikolka, A perspective on overcoming water-related stability challenges in molecular and hybrid semiconductors. *MRS Commun.* **10**, 98–111 (2020).
27. S. Griggs, A. Marks, H. Bristow, I. McCulloch, n-Type organic semiconducting polymers: stability limitations, design considerations and applications. *J. Mater. Chem. C.* **9**, 8099–8128 (2021).
28. J. Dong, Y. Wang, T. Mori, T. Michinobu, Improving the air-stability of n-type organic thin-film transistors by polyacrylonitrile additive. *Jpn. J. Appl. Phys.* **59**, SDDC05 (2020).
29. M. Goel, C. D. Heinrich, G. Krauss, M. Thelakkat, Principles of Structural Design of Conjugated Polymers Showing Excellent Charge Transport toward Thermoelectrics and Bioelectronics Applications. *Macromol. Rapid Commun.* **40**, 1–31 (2019).

30. Z. Bao, A. Dodabalapur, A. J. Lovinger, Soluble and processable regioregular poly(3-hexylthiophene) for thin film field-effect transistor applications with high mobility. *Appl. Phys. Lett.* **69**, 4108–4110 (1996).
31. M. Brinkmann, Structure and morphology control in thin films of regioregular poly(3-hexylthiophene). *J. Polym. Sci. Part B Polym. Phys.* **49**, 1218–1233 (2011).
32. H. Klauk, Organic thin-film transistors. *Chem. Soc. Rev.* **39**, 2643 (2010).
33. H. Huang, L. Yang, A. Facchetti, T. J. Marks, Organic and Polymeric Semiconductors Enhanced by Noncovalent Conformational Locks. *Chem. Rev.* **117**, 10291–10318 (2017).
34. T. Marszalek, M. Li, W. Pisula, Design directed self-assembly of donor–acceptor polymers. *Chem. Commun.* **52**, 10938–10947 (2016).
35. D. Pei, Z. Wang, Z. Peng, J. Zhang, Y. Deng, Y. Han, L. Ye, Y. Geng, Impact of Molecular Weight on the Mechanical and Electrical Properties of a High-Mobility Diketopyrrolopyrrole-Based Conjugated Polymer. *Macromolecules.* **53**, 4490–4500 (2020).
36. Y. Lei, P. Deng, M. Lin, X. Zheng, F. Zhu, B. S. Ong, Enhancing Crystalline Structural Orders of Polymer Semiconductors for Efficient Charge Transport via Polymer-Matrix-Mediated Molecular Self-Assembly. *Adv. Mater.* **28**, 6687–6694 (2016).
37. H. J. Cheon, T. K. An, Y.-H. Kim, Diketopyrrolopyrrole (DPP)-Based Polymers and Their Organic Field-Effect Transistor Applications: A Review. *Macromol. Res.* **30**, 71–84 (2022).
38. W. W. Bao, R. Li, Z. C. Dai, J. Tang, X. Shi, J. T. Geng, Z. F. Deng, J. Hua, Diketopyrrolopyrrole (DPP)-Based Materials and Its Applications: A Review. *Front. Chem.* **8**, 1–6 (2020).
39. Q. Liu, S. E. Bottle, P. Sonar, Developments of Diketopyrrolopyrrole-Dye-Based Organic Semiconductors for a Wide Range of Applications in Electronics. *Adv. Mater.* **1903882**,

- 1–46 (2019).
40. L. Shi, Y. Guo, W. Hu, Y. Liu, Design and effective synthesis methods for high-performance polymer semiconductors in organic field-effect transistors. *Mater. Chem. Front.* **1**, 2423–2456 (2017).
 41. S. Chen, B. Sun, W. Hong, H. Aziz, Y. Meng, Y. Li, Influence of side chain length and bifurcation point on the crystalline structure and charge transport of diketopyrrolopyrrole-quaterthiophene copolymers (PDQTs). *J. Mater. Chem. C.* **2**, 2183–2190 (2014).
 42. N. Luo, P. Ren, Y. Feng, X. Shao, H. L. Zhang, Z. Liu, Side-Chain Engineering of Conjugated Polymers for High-Performance Organic Field-Effect Transistors. *J. Phys. Chem. Lett.* **13**, 1131–1146 (2022).
 43. I. Ohnishi, K. Hashimoto, K. Tajima, Synthesis of diketopyrrolopyrrole-based polymers with polydimethylsiloxane side chains and their application in organic field-effect transistors. *R. Soc. Open Sci.* **5** (2018), doi:10.1098/rsos.172025.
 44. Y. Li, S. P. Singh, P. Sonar, A High Mobility P-Type DPP-Thieno[3,2- b]thiophene Copolymer for Organic Thin-Film Transistors. *Adv. Mater.* **22**, 4862–4866 (2010).
 45. J. Li, Y. Zhao, H. S. Tan, Y. Guo, C.-A. Di, G. Yu, Y. Liu, M. Lin, S. H. Lim, Y. Zhou, H. Su, B. S. Ong, A stable solution-processed polymer semiconductor with record high-mobility for printed transistors. *Sci. Rep.* **2**, 754 (2012).
 46. O. Knopfmacher, M. L. Hammock, A. L. Appleton, G. Schwartz, J. Mei, T. Lei, J. Pei, Z. Bao, Highly stable organic polymer field-effect transistor sensor for selective detection in the marine environment. *Nat. Commun.* **5**, 2954 (2014).
 47. P. A. Gilhooly-Finn, I. E. Jacobs, O. Bardagot, Y. Zaffar, A. Lemaire, S. Guchait, L. Zhang, M. Freeley, W. Neal, F. Richard, M. Palma, N. Banerji, H. Sirringhaus, M. Brinkmann, C. B. Nielsen, Interplay between Side Chain Density and Polymer Alignment: Two Competing Strategies for Enhancing the Thermoelectric Performance of P3HT

- Analogues. *Chem. Mater.* **35**, 9029–9039 (2023).
48. Z. Genene, W. Mammo, E. Wang, M. R. Andersson, Recent Advances in n-Type Polymers for All-Polymer Solar Cells. *Adv. Mater.* **31**, 1807275 (2019).
 49. L. Bai, Y. Zhang, Y. Han, S. Wang, Z. Zhuo, Y. Zheng, M. Li, W. Chen, N. Yu, L. Sun, X. An, B. Liu, Q. Wei, J. Lin, W. Huang, Large-Area Printed Display Based on Green Solvent Processable Blue Light-Emitting Conjugated Polymer. *Adv. Mater. Technol.* **2300312**, 1–8 (2023).
 50. J. Yang, Z. Zhao, S. Wang, Y. Guo, Y. Liu, Insight into High-Performance Conjugated Polymers for Organic Field-Effect Transistors. *Chem.* **4**, 2748–2785 (2018).
 51. X. Guo, A. Facchetti, T. J. Marks, Imide- and Amide-Functionalized Polymer Semiconductors. *Chem. Rev.* **114**, 8943–9021 (2014).
 52. R. G. Arns, The other transistor: early history of the metal-oxide semiconductor field-effect transistor. *Eng. Sci. Educ. J.* **7**, 233–240 (1998).
 53. A. Tsumura, H. Koezuka, T. Ando, Macromolecular electronic device: Field-effect transistor with a polythiophene thin film. *Appl. Phys. Lett.* **49**, 1210–1212 (1986).
 54. H. Chen, W. Zhang, M. Li, G. He, X. Guo, Interface Engineering in Organic Field-Effect Transistors: Principles, Applications, and Perspectives. *Chem. Rev.* **120**, 2879–2949 (2020).
 55. H. Sirringhaus, 25th Anniversary Article: Organic Field-Effect Transistors: The Path Beyond Amorphous Silicon. *Adv. Mater.* **26**, 1319–1335 (2014).
 56. R. A. Street, Thin-Film Transistors. *Adv. Mater.* **21**, 2007–2022 (2009).
 57. Y. Yan, Y. Zhao, Y. Liu, Recent progress in organic field-effect transistor-based integrated circuits. *J. Polym. Sci.* **60**, 311–327 (2022).
 58. Z. Zhu, Y. Guo, Y. Liu, Application of organic field-effect transistors in memory. *Mater. Chem. Front.* **4**, 2845–2862 (2020).

59. S. G. Surya, H. N. Raval, R. Ahmad, P. Sonar, K. N. Salama, V. R. Rao, Organic field effect transistors (OFETs) in environmental sensing and health monitoring: A review. *TrAC Trends Anal. Chem.* **111**, 27–36 (2019).
60. J. Bae, I. T. Kim, J. Hur, Field-Effect Transistors Based on Organic and Carbon-Based Materials for Chemical and Biological Sensors. *Curr. Org. Chem.* **19**, 1176–1190 (2015).
61. Y. Wang, Q. Gong, Q. Miao, Structured and functionalized organic semiconductors for chemical and biological sensors based on organic field effect transistors. *Mater. Chem. Front.* **4**, 3505–3520 (2020).
62. L. Janasz, M. Borkowski, P. W. M. Blom, T. Marszalek, W. Pisula, Organic Semiconductor/Insulator Blends for Elastic Field-Effect Transistors and Sensors. *Adv. Funct. Mater.* **32** (2022), doi:10.1002/adfm.202105456.
63. H. Yue, Z. Wang, Y. Zhen, Recent Advances of Self-Healing Electronic Materials Applied in Organic Field-Effect Transistors. *ACS Omega.* **7**, 18197–18205 (2022).
64. W.-Y. Lee, J. Mei, Z. Bao, "OFETs: BASIC CONCEPTS AND MATERIAL DESIGNS" in (2016; http://www.worldscientific.com/doi/abs/10.1142/9789813148611_0002), pp. 19–83.
65. P. W. M. Blom, Polymer Electronics: To Be or Not to Be? *Adv. Mater. Technol.* **5**, 1–14 (2020).
66. K. D. Deshmukh, K. Reuter, H. Kempa, J. E. West, H. E. Katz, Tuning of threshold voltage in organic field-effect transistors with hydrophobic gate dielectric using monoenergetic low-energy electron beams and triode corona. *Appl. Phys. Lett.* **95** (2009), doi:10.1063/1.3222854.
67. S. Park, S. H. Kim, H. H. Choi, B. Kang, K. Cho, Recent Advances in the Bias Stress Stability of Organic Transistors. *Adv. Funct. Mater.* **30**, 1904590 (2020).
68. M. Y. Lee, H. R. Lee, C. H. Park, S. G. Han, J. H. Oh, Organic Transistor-Based Chemical Sensors for Wearable Bioelectronics. *Acc. Chem. Res.* **51**, 2829–2838 (2018).
69. A. S. Sharova, M. Caironi, Sweet Electronics: Honey-Gated Complementary Organic

- Transistors and Circuits Operating in Air. *Adv. Mater.* **33**, 2103183 (2021).
70. F. Torricelli, D. Z. Adrahtas, Z. Bao, M. Berggren, F. Biscarini, A. Bonfiglio, C. A. Bortolotti, C. D. Frisbie, E. Macchia, G. G. Malliaras, I. McCulloch, M. Moser, T.-Q. Nguyen, R. M. Owens, A. Salleo, A. Spanu, L. Torsi, Electrolyte-gated transistors for enhanced performance bioelectronics. *Nat. Rev. Methods Prim.* **1**, 66 (2021).
 71. N. Mohammadian, L. A. Majewski, "High Capacitance Dielectrics for Low Voltage Operated OFETs" in *Integrated Circuits/Microchips* (IntechOpen, 2020; <https://www.intechopen.com/books/integrated-circuits-microchips/high-capacitance-dielectrics-for-low-voltage-operated-ofets>).
 72. M. J. Iqbal, M. Z. Iqbal, T. Afzal, M. A. Raza, K. Saghir, M. A. Raza, S. Atiq, S. Riaz, S. Naseem, Impact of interfacial trap states on achieving bias stability in polymer field-effect transistors. *Microelectron. Eng.* **247**, 111602 (2021).
 73. D. Simatos, I. E. Jacobs, I. Dobryden, M. Nguyen, A. Savva, D. Venkateshvaran, M. Nikolka, J. Charmet, L. J. Spalek, M. Gicevičius, Y. Zhang, G. Schweicher, D. J. Howe, S. Ursel, J. Armitage, I. B. Dimov, U. Kraft, W. Zhang, M. Alsufyani, I. McCulloch, R. M. Owens, P. M. Claesson, T. P. J. Knowles, H. Sirringhaus, Effects of Processing-Induced Contamination on Organic Electronic Devices. *Small Methods.* **7**, 1–14 (2023).
 74. C. Guo, Z. Yang, L. Qin, J. Man, T. Zhang, D.-K. Wang, Z.-H. Lu, Q. Zhu, Improving bias-stress stability of p-type organic field-effect transistors by suppressing electron injection. *J. Mater. Sci. Mater. Electron.* **33**, 3726–3737 (2022).
 75. J. Noh, S. Jeong, J.-Y. Lee, Ultrafast formation of air-processable and high-quality polymer films on an aqueous substrate. *Nat. Commun.* **7**, 12374 (2016).
 76. X. Gu, L. Shaw, K. Gu, M. F. Toney, Z. Bao, The meniscus-guided deposition of semiconducting polymers. *Nat. Commun.* **9**, 534 (2018).
 77. K. Kim, S. H. Kim, H. Cheon, X. Tang, J. H. Oh, H. Jhon, J. Jeon, Y.-H. Kim, T. K. An, Electrohydrodynamic-Jet (EHD)-Printed Diketopyrrolopyroole-Based Copolymer for

- OFETs and Circuit Applications. *Polymers (Basel)*. **11**, 1759 (2019).
78. J. Y. Na, B. Kang, S. G. Lee, K. Cho, Y. D. Park, Surface-Mediated Solidification of a Semiconducting Polymer during Time-Controlled Spin-Coating. *ACS Appl. Mater. Interfaces*. **9**, 9871–9879 (2017).
79. N.-K. Kim, S.-Y. Jang, G. Pace, M. Caironi, W.-T. Park, D. Khim, J. Kim, D.-Y. Kim, Y.-Y. Noh, High-Performance Organic Field-Effect Transistors with Directionally Aligned Conjugated Polymer Film Deposited from Pre-Aggregated Solution. *Chem. Mater.* **27**, 8345–8353 (2015).
80. R. Venkatesh, Y. Zheng, A. L. Liu, H. Zhao, C. Silva, C. J. Takacs, M. A. Grover, J. C. Meredith, E. Reichmanis, Overlap concentration generates optimum device performance for DPP-based conjugated polymers. *Org. Electron.* **117**, 106779 (2023).
81. J. Deng, Y. Guo, W. Li, Z. Xie, Y. Ke, R. A. J. Janssen, M. Li, Tuning the nanostructure and molecular orientation of high molecular weight diketopyrrolopyrrole-based polymers for high-performance field-effect transistors. *Nanoscale*. **15**, 553–561 (2023).
82. N.-K. Kim, E.-S. Shin, Y.-Y. Noh, D.-Y. Kim, A selection rule of solvent for highly aligned diketopyrrolopyrrole-based conjugated polymer film for high performance organic field-effect transistors. *Org. Electron.* **55**, 6–14 (2018).
83. H. Phan, M. J. Ford, A. T. Lill, M. Wang, G. C. Bazan, T.-Q. Nguyen, Electrical Double-Slope Nonideality in Organic Field-Effect Transistors. *Adv. Funct. Mater.* **28**, 1707221 (2018).
84. T. Afzal, M. J. Iqbal, M. Z. Iqbal, A. Sajjad, M. A. Raza, S. Riaz, M. A. Kamran, A. Numan, S. Naseem, Effect of post-deposition annealing temperature on the charge carrier mobility and morphology of DPPDTT based organic field effect transistors. *Chem. Phys. Lett.* **750**, 137507 (2020).
85. G. Zuo, M. Linares, T. Upreti, M. Kemerink, General rule for the energy of water-induced traps in organic semiconductors. *Nat. Mater.* **18**, 588–593 (2019).

86. M. Pandey, N. Kumari, S. Nagamatsu, S. S. Pandey, Recent advances in the orientation of conjugated polymers for organic field-effect transistors. *J. Mater. Chem. C*. **7**, 13323–13351 (2019).
87. H. Heil, T. Finnberg, N. Von Malm, R. Schmechel, H. Von Seggern, The influence of mechanical rubbing on the field-effect mobility in polyhexylthiophene. *J. Appl. Phys.* **93**, 1636–1641 (2003).
88. B. Wang, W. Huang, L. Chi, M. Al-Hashimi, T. J. Marks, A. Facchetti, High- k Gate Dielectrics for Emerging Flexible and Stretchable Electronics. *Chem. Rev.* **118**, 5690–5754 (2018).
89. M. Geiger, R. Acharya, E. Reutter, T. Ferschke, U. Zschieschang, J. Weis, J. Pflaum, H. Klauk, R. T. Weitz, Effect of the Degree of the Gate-Dielectric Surface Roughness on the Performance of Bottom-Gate Organic Thin-Film Transistors. *Adv. Mater. Interfaces*. **7** (2020), doi:10.1002/admi.201902145.
90. S. Casalini, C. A. Bortolotti, F. Leonardi, F. Biscarini, Self-assembled monolayers in organic electronics. *Chem. Soc. Rev.* **46**, 40–71 (2017).
91. Y. Lei, B. Wu, W.-K. E. Chan, F. Zhu, B. S. Ong, Engineering gate dielectric surface properties for enhanced polymer field-effect transistor performance. *J. Mater. Chem. C*. **3**, 12267–12272 (2015).
92. P. Zhang, Y. Guo, K. Cao, M. Yi, L. Huang, W. Shi, J. Zhu, W. Huang, An organic field effect transistor memory adopting octadecyltrichlorosilane self-assembled monolayer. *J. Phys. D: Appl. Phys.* **54**, 095106 (2021).
93. B. Nketia-Yawson, Y. Y. Noh, Recent Progress on High-Capacitance Polymer Gate Dielectrics for Flexible Low-Voltage Transistors. *Adv. Funct. Mater.* **28**, 1–27 (2018).
94. Y. Wang, X. Huang, T. Li, L. Li, X. Guo, P. Jiang, Polymer-Based Gate Dielectrics for Organic Field-Effect Transistors. *Chem. Mater.* **31**, 2212–2240 (2019).
95. W. Shi, Y. Zheng, J. Yu, "Polymer Dielectric in Organic Field-Effect Transistor" in

- Properties and Applications of Polymer Dielectrics* (InTech, 2017; <https://www.intechopen.com/books/advanced-biometric-technologies/liveness-detection-in-biometrics>), vol. i, p. 13.
96. X. Wu, R. Jia, J. Pan, X. Zhang, J. Jie, Roles of interfaces in the ideality of organic field-effect transistors. *Nanoscale Horizons*. **5**, 454–472 (2020).
 97. Y. Yang, Z. Liu, J. Chen, Z. Cai, Z. Wang, W. Chen, G. Zhang, X. Zhang, L. Chi, D. Zhang, SI A Facile Approach to Improve Interchain Packing Order and Charge Mobilities by Self-Assembly of Conjugated Polymers on Water. *Adv. Sci.* **5** (2018), doi:10.1002/advs.201801497.
 98. M. Waldrip, O. D. Jurchescu, D. J. Gundlach, E. G. Bittle, Contact Resistance in Organic Field-Effect Transistors: Conquering the Barrier. *Adv. Funct. Mater.* **30**, 1904576 (2020).
 99. A. Kahn, Fermi level, work function and vacuum level. *Mater. Horizons*. **3**, 7–10 (2016).
 100. Y. Cao, M. L. Steigerwald, C. Nuckolls, X. Guo, Current Trends in Shrinking the Channel Length of Organic Transistors Down to the Nanoscale. *Adv. Mater.* **22**, 20–32 (2010).
 101. T. Yang, Q. Wu, F. Dai, K. Huang, H. Xu, C. Liu, C. Chen, S. Hu, X. Liang, X. Liu, Y. Y. Noh, C. Liu, Understanding, Optimizing, and Utilizing Nonideal Transistors Based on Organic or Organic Hybrid Semiconductors. *Adv. Funct. Mater.* **1903889**, 1–39 (2019).
 102. Z. Bao, J. Locklin, *Organic Field-Effect Transistors* (CRC Press, 2018).
 103. Y. Sung, E.-Y. Shin, Y.-Y. Noh, J.-Y. Lee, Flexible Bottom-Gated Organic Field-Effect Transistors Utilizing Stamped Polymer Layers from the Surface of Water. *ACS Appl. Mater. Interfaces*. **12**, 25092–25099 (2020).
 104. Y. Huang, H. Chen, J. Yang, W. Tian, W. Wang, 3D-Printed OFETs of the 1,4-bis(3-phenylquinoxalin-2-yl)benzene-based polymer semiconductors. *Polym. Chem.* **8**, 4878–4886 (2017).
 105. B. Lyu, S. Im, H. Jing, S. Lee, S. H. Kim, J. H. Kim, J. H. Cho, Work Function Engineering of Electrohydrodynamic-Jet-Printed PEDOT:PSS Electrodes for High-Performance

- Printed Electronics. *ACS Appl. Mater. Interfaces*. **12**, 17799–17805 (2020).
106. B. Nagel, H. Dellweg, L. M. Gierasch, Glossary for chemists of terms used in biotechnology (IUPAC Recommendations 1992). *Pure Appl. Chem.* **64**, 143–168 (1992).
 107. L. Torsi, M. Magliulo, K. Manoli, G. Palazzo, Organic field-effect transistor sensors: a tutorial review. *Chem. Soc. Rev.* **42**, 8612 (2013).
 108. K. Strimbu, J. A. Tavel, What are biomarkers? *Curr. Opin. HIV AIDS*. **5**, 463–466 (2010).
 109. E. R. Kim, C. Joe, R. J. Mitchell, M. B. Gu, Biosensors for healthcare: current and future perspectives. *Trends Biotechnol.* **41**, 374–395 (2023).
 110. P. Mehrotra, Biosensors and their applications - A review. *J. Oral Biol. Craniofacial Res.* **6**, 153–159 (2016).
 111. R. Etzioni, N. Urban, S. Ramsey, M. McIntosh, S. Schwartz, B. Reid, J. Radich, G. Anderson, L. Hartwell, The case for early detection. *Nat. Rev. Cancer*. **3**, 243–252 (2003).
 112. M. Jackson, L. Marks, G. H. W. May, J. B. Wilson, The genetic basis of disease. *Essays Biochem.* **62**, 643–723 (2018).
 113. J. Tu, R. M. Torrente-Rodríguez, M. Wang, W. Gao, The Era of Digital Health: A Review of Portable and Wearable Affinity Biosensors. *Adv. Funct. Mater.* **1906713**, 1906713 (2019).
 114. H. Teymourian, A. Barfidokht, J. Wang, Electrochemical glucose sensors in diabetes management: an updated review (2010–2020). *Chem. Soc. Rev.* **49**, 7671–7709 (2020).
 115. J. Budd, B. S. Miller, N. E. Weckman, D. Cherkaoui, D. Huang, A. T. Decruz, N. Fongwen, G.-R. Han, M. Broto, C. S. Estcourt, J. Gibbs, D. Pillay, P. Sonnenberg, R. Meurant, M. R. Thomas, N. Keegan, M. M. Stevens, E. Nastouli, E. J. Topol, A. M. Johnson, M. Shahmanesh, A. Ozcan, J. J. Collins, M. Fernandez Suarez, B. Rodriguez, R. W. Peeling, R. A. McKendry, Lateral flow test engineering and lessons learned from COVID-19. *Nat. Rev. Bioeng.* **1**, 13–31 (2023).

116. V. R. Samuel, K. J. Rao, A review on label free biosensors. *Biosens. Bioelectron. X.* **11**, 100216 (2022).
117. S. Sang, Y. Wang, Q. Feng, Y. Wei, J. Ji, W. Zhang, Progress of new label-free techniques for biosensors: a review. *Crit. Rev. Biotechnol.* **36**, 1–17 (2015).
118. J. Kim, A. S. Campbell, B. E. F. de Ávila, J. Wang, Wearable biosensors for healthcare monitoring. *Nat. Biotechnol.* **37**, 389–406 (2019).
119. B. A. Prabowo, P. D. Cabral, P. Freitas, E. Fernandes, The Challenges of Developing Biosensors for Clinical Assessment: A Review. *Chemosensors.* **9**, 299 (2021).
120. M. J. Schöning, A. Poghossian, Recent advances in biologically sensitive field-effect transistors (BioFETs). *Analyst.* **127**, 1137–1151 (2002).
121. Y.-C. Syu, W.-E. Hsu, C.-T. Lin, Review—Field-Effect Transistor Biosensing: Devices and Clinical Applications. *ECS J. Solid State Sci. Technol.* **7**, Q3196–Q3207 (2018).
122. Y. H. Lee, M. Jang, M. Y. Lee, O. Y. Kweon, J. H. Oh, Flexible Field-Effect Transistor-Type Sensors Based on Conjugated Molecules. *Chem.* **3**, 724–763 (2017).
123. T. Minamiki, T. Minami, Y. Sasaki, S. Wakida, R. Kurita, O. Niwa, S. Tokito, Label-Free Detection of Human Glycoprotein (CgA) Using an Extended-Gated Organic Transistor-Based Immunosensor. *Sensors.* **16**, 2033 (2016).
124. M. D. Angione, S. Cotrone, M. Magliulo, A. Mallardi, D. Altamura, C. Giannini, N. Cioffi, L. Sabbatini, E. Fratini, P. Baglioni, G. Scamarcio, G. Palazzo, L. Torsi, Interfacial electronic effects in functional bilayers integrated into organic field-effect transistors. *Proc. Natl. Acad. Sci.* **109**, 6429–6434 (2012).
125. C. Di, H. Shen, F. Zhang, D. Zhu, Enabling Multifunctional Organic Transistors with Fine-Tuned Charge Transport. *Acc. Chem. Res.* **52**, 1113–1124 (2019).
126. E. Macchia, L. De Caro, F. Torricelli, C. Di Franco, G. F. Mangiatordi, G. Scamarcio, L. Torsi, Why a Diffusing Single-Molecule can be Detected in Few Minutes by a Large Capturing Bioelectronic Interface. *Adv. Sci.* **9**, 2104381 (2022).

127. M. Berto, C. Diacci, R. D'Agata, M. Pinti, E. Bianchini, M. Di Lauro, S. Casalini, A. Cossarizza, M. Berggren, D. Simon, G. Spoto, F. Biscarini, C. A. Bortolotti, EGOFET Peptide Aptasensor for Label-Free Detection of Inflammatory Cytokines in Complex Fluids. *Adv. Biosyst.* **2**, 1700072 (2018).
128. C. Diacci, M. Berto, M. Di Lauro, E. Bianchini, M. Pinti, D. T. Simon, F. Biscarini, C. A. Bortolotti, Label-free detection of interleukin-6 using electrolyte gated organic field effect transistors. *Biointerphases.* **12**, 05F401 (2017).
129. J. Pallu, M. Avci-Adali, P. Mackeben, L. Mohammadnejad, G. Mattana, V. Noël, B. Piro, A DNA hydrogel gated organic field effect transistor. *Org. Electron.* **75**, 105402 (2019).
130. R. Kubota, Y. Sasaki, T. Minamiki, T. Minami, Chemical Sensing Platforms Based on Organic Thin-Film Transistors Functionalized with Artificial Receptors. *ACS Sensors.* **4**, 2571–2587 (2019).
131. T. Minamiki, Y. Hashima, Y. Sasaki, T. Minami, An electrolyte-gated polythiophene transistor for the detection of biogenic amines in water. *Chem. Commun.* **54**, 6907–6910 (2018).
132. M. L. Hammock, A. N. Sokolov, R. M. Stoltenberg, B. D. Naab, Z. Bao, Organic Transistors with Ordered Nanoparticle Arrays as a Tailorable Platform for Selective, In Situ Detection. *ACS Nano.* **6**, 3100–3108 (2012).
133. M. L. Hammock, O. Knopfmacher, B. D. Naab, J. B.-H. Tok, Z. Bao, Investigation of Protein Detection Parameters Using Nanofunctionalized Organic Field-Effect Transistors. *ACS Nano.* **7**, 3970–3980 (2013).
134. H. Shen, Y. Zou, Y. Zang, D. Huang, W. Jin, C. Di, D. Zhu, Molecular antenna tailored organic thin-film transistors for sensing application. *Mater. Horizons.* **5**, 240–247 (2018).
135. R. A. Picca, K. Manoli, E. Macchia, L. Sarcina, C. Di Franco, N. Cioffi, D. Blasi, R. Österbacka, F. Torricelli, G. Scamarcio, L. Torsi, Ultimately Sensitive Organic

- Bioelectronic Transistor Sensors by Materials and Device Structure Design. *Adv. Funct. Mater.* **30**, 1–23 (2020).
136. C. Sun, G. Feng, Y. Song, S. Cheng, S. Lei, W. Hu, Single Molecule Level and Label-Free Determination of Multibiomarkers with an Organic Field-Effect Transistor Platform in Early Cancer Diagnosis. *Anal. Chem.* **94**, 6615–6620 (2022).
 137. J. Ko, C. K. Ng, Arramel, A. T. S. Wee, T. L. D. Tam, W. L. Leong, Water robustness of organic thin-film transistors based on pyrazino[2,3- g]quinoxaline-dione conjugated polymer. *J. Mater. Chem. C* **8**, 4157–4163 (2020).
 138. Y. Zang, D. Huang, C. Di, D. Zhu, Device Engineered Organic Transistors for Flexible Sensing Applications. *Adv. Mater.* **28**, 4549–4555 (2016).
 139. E. Macchia, F. Torricelli, P. Bollella, L. Sarcina, A. Tricase, C. Di Franco, R. Österbacka, Z. M. Kovács-Vajna, G. Scamarcio, L. Torsi, Large-Area Interfaces for Single-Molecule Label-free Bioelectronic Detection. *Chem. Rev.* **122**, 4636–4699 (2022).
 140. E. Stern, R. Wagner, F. J. Sigworth, R. Breaker, T. M. Fahmy, M. A. Reed, Importance of the debye screening length on nanowire field effect transistor sensors. *Nano Lett.* **7**, 3405–3409 (2007).
 141. B. M. Lowe, K. Sun, I. Zeimpekis, C. K. Skylaris, N. G. Green, Field-effect sensors-from pH sensing to biosensing: Sensitivity enhancement using streptavidin-biotin as a model system. *Analyst.* **142**, 4173–4200 (2017).
 142. J. Wang, D. Ye, Q. Meng, C. Di, D. Zhu, Advances in Organic Transistor-Based Biosensors. *Adv. Mater. Technol.* **5**, 1–17 (2020).
 143. N. Nakatsuka, K.-A. Yang, J. M. Abendroth, K. M. Cheung, X. Xu, H. Yang, C. Zhao, B. Zhu, Y. S. Rim, Y. Yang, P. S. Weiss, M. N. Stojanović, A. M. Andrews, Aptamer–field-effect transistors overcome Debye length limitations for small-molecule sensing. *Science (80-.)*. **362**, 319–324 (2018).
 144. C.-A. Vu, W.-Y. Chen, Predicting Future Prospects of Aptamers in Field-Effect Transistor

- Biosensors. *Molecules*. **25**, 680 (2020).
145. M. Witt, J.-G. Walter, F. Stahl, Aptamer Microarrays—Current Status and Future Prospects. *Microarrays*. **4**, 115–132 (2015).
 146. N. Nakatsuka, H. H. Cao, S. Deshayes, A. L. Melkonian, A. M. Kasko, P. S. Weiss, A. M. Andrews, Aptamer Recognition of Multiplexed Small-Molecule-Functionalized Substrates. *ACS Appl. Mater. Interfaces*. **10**, 23490–23500 (2018).
 147. H. U. Khan, M. E. Roberts, O. Johnson, R. Förch, W. Knoll, Z. Bao, In Situ, Label-Free DNA Detection Using Organic Transistor Sensors. *Adv. Mater.* **22**, 4452–4456 (2010).
 148. N. Saraf, E. R. Woods, M. Pepler, S. Seal, Highly selective aptamer based organic electrochemical biosensor with pico-level detection. *Biosens. Bioelectron.* **117**, 40–46 (2018).
 149. Y. C. Lim, A. Z. Kouzani, W. Duan, Aptasensors: A Review. *J. Biomed. Nanotechnol.* **6**, 93–105 (2010).
 150. X. Xu, P. Clément, J. Eklöf-Österberg, N. Kelley-Loughnane, K. Moth-Poulsen, J. L. Chávez, M. Palma, Reconfigurable Carbon Nanotube Multiplexed Sensing Devices. *Nano Lett.* **18**, 4130–4135 (2018).
 151. L. Li, S. Wang, Y. Xiao, Y. Wang, Recent Advances in Immobilization Strategies for Biomolecules in Sensors Using Organic Field-Effect Transistors. *Trans. Tianjin Univ.* **26**, 424–440 (2020).
 152. X. Wu, J. Zhou, J. Huang, Integration of Biomaterials into Sensors Based on Organic Thin-Film Transistors. *Macromol. Rapid Commun.* **39**, 1–10 (2018).
 153. M. Magliulo, K. Manoli, E. Macchia, G. Palazzo, L. Torsi, Tailoring Functional Interlayers in Organic Field-Effect Transistor Biosensors. *Adv. Mater.* **27**, 7528–7551 (2015).
 154. Y. Wang, S. Cheng, C. Sun, T. Wang, Organic Thin Film Transistor for Effective Biomarker Detection in Early Disease Diagnosis. *Chemosensors*. **11**, 202 (2023).

155. N. Li, Y. Dai, Y. Li, S. Dai, J. Strzalka, Q. Su, N. De Oliveira, Q. Zhang, P. B. J. St. Onge, S. Rondeau-Gagné, Y. Wang, X. Gu, J. Xu, S. Wang, A universal and facile approach for building multifunctional conjugated polymers for human-integrated electronics. *Matter*. **4**, 3015–3029 (2021).
156. G. E. Fenoy, R. Hasler, F. Quartinello, W. A. Marmisollé, C. Lorenz, O. Azzaroni, P. Bäuerle, W. Knoll, “Clickable” Organic Electrochemical Transistors. *JACS Au*. **2**, 2778–2790 (2022).
157. G. E. Fenoy, R. Hasler, C. Lorenz, J. Movilli, W. A. Marmisollé, O. Azzaroni, J. Huskens, P. Bäuerle, W. Knoll, Interface Engineering of “Clickable” Organic Electrochemical Transistors toward Biosensing Devices. *ACS Appl. Mater. Interfaces* (2023), doi:10.1021/acsami.2c21493.
158. J. Aerathupalathu Janardhanan, Y. Chen, C. Liu, H. Tseng, P. Wu, J. She, Y. Hsiao, H. Yu, Sensitive Detection of Sweat Cortisol Using an Organic Electrochemical Transistor Featuring Nanostructured Poly(3,4-Ethylenedioxythiophene) Derivatives in the Channel Layer. *Anal. Chem.* **94**, 7584–7593 (2022).
159. E. Y. Poimanova, P. A. Shaposhnik, D. S. Anisimov, E. G. Zavyalova, A. A. Trul, M. S. Skorotetcky, O. V. Borshchev, D. Z. Vinnitskiy, M. S. Polinskaya, V. B. Krylov, N. E. Nifantiev, E. V. Agina, S. A. Ponomarenko, Biorecognition Layer Based On Biotin-Containing [1]Benzo[thieno[3,2- b][1]benzothiophene Derivative for Biosensing by Electrolyte-Gated Organic Field-Effect Transistors. *ACS Appl. Mater. Interfaces*. **14**, 16462–16476 (2022).
160. C. Sun, M. V. Vinayak, S. Cheng, W. Hu, Facile Functionalization Strategy for Ultrasensitive Organic Protein Biochips in Multi-Biomarker Determination. *Anal. Chem.* **93**, 11305–11311 (2021).
161. C. Sun, R. Li, Y. Song, X. Jiang, C. Zhang, S. Cheng, W. Hu, Ultrasensitive and Reliable Organic Field-Effect Transistor-Based Biosensors in Early Liver Cancer Diagnosis. *Anal. Chem.* **93**, 6188–6194 (2021).

162. G. Palazzo, D. De Tullio, M. Magliulo, A. Mallardi, F. Intranuovo, M. Y. Mulla, P. Favia, I. Vikholm-Lundin, L. Torsi, Detection Beyond Debye's Length with an Electrolyte-Gated Organic Field-Effect Transistor. *Adv. Mater.* **27**, 911–916 (2015).
163. S. Wustoni, T. C. Hidalgo, A. Hama, D. Ohayon, A. Savva, N. Wei, N. Wehbe, S. Inal, In Situ Electrochemical Synthesis of a Conducting Polymer Composite for Multimetabolite Sensing. *Adv. Mater. Technol.* **5**, 1900943 (2020).
164. B. Piro, D. Wang, D. Benaoudia, A. Tibaldi, G. Anquetin, V. Noël, S. Reisberg, G. Mattana, B. Jackson, Versatile transduction scheme based on electrolyte-gated organic field-effect transistor used as immunoassay readout system. *Biosens. Bioelectron.* **92**, 215–220 (2017).
165. B. Kang, W. H. Lee, H. H. Choi, Y. D. Park, K. Cho, Built-in water resistance in organic transistors modified with self-assembled monolayers. *RSC Adv.* **4**, 45082–45087 (2014).
166. G. Binnig, C. F. Quate, C. Gerber, Atomic Force Microscope. *Phys. Rev. Lett.* **56**, 930–933 (1986).
167. G. Buscarino, "Atomic Force Microscopy and Spectroscopy" in *Spectroscopy for Materials Characterization* (Wiley, 2021; <https://onlinelibrary.wiley.com/doi/10.1002/9781119698029.ch15>), pp. 425–460.
168. T. Degousée, W. G. Neal, Z. Edwards, S. Singh, J. Selvarajah, T. Talha-Dean, M. Palma, B. C. Schroeder, J. A. Mol, One hour road to high-quality arrays of gold nanoparticles coated with organic ligands. *J. Mater. Chem. C.* **11**, 16518–16526 (2023).
169. L. M. Cowen, P. A. Gilhooly-Finn, A. Giovannitti, G. LeCroy, H. Demetriou, W. Neal, Y. Dong, M. Westwood, S. Luong, O. Fenwick, A. Salleo, S. Heutz, C. B. Nielsen, B. C. Schroeder, Critical analysis of self-doping and water-soluble n-type organic semiconductors: structures and mechanisms. *J. Mater. Chem. C.* **10**, 8955–8963 (2022).
170. S. Caponi, C. Canale, O. Cavalleri, M. Vassalli, "Characterization Tools for Mechanical Probing of Biomimetic Materials" in *Nanotechnology Characterization Tools for Tissue*

- Engineering and Medical Therapy* (Springer Berlin Heidelberg, Berlin, Heidelberg, 2019; http://link.springer.com/10.1007/978-3-662-59596-1_2), pp. 69–111.
171. G. Greczynski, L. Hultman, A step-by-step guide to perform x-ray photoelectron spectroscopy. *J. Appl. Phys.* **132** (2022), doi:10.1063/5.0086359.
 172. F. A. Stevie, C. L. Donley, Introduction to x-ray photoelectron spectroscopy. *J. Vac. Sci. Technol. A Vacuum, Surfaces, Film.* **38**, 063204 (2020).
 173. C. D. Easton, C. Kinnear, S. L. McArthur, T. R. Gengenbach, Practical guides for x-ray photoelectron spectroscopy: Analysis of polymers. *J. Vac. Sci. Technol. A Vacuum, Surfaces, Film.* **38**, 023207 (2020).
 174. G. H. Major, N. Fairley, P. M. A. Sherwood, M. R. Linford, J. Terry, V. Fernandez, K. Artyushkova, Practical guide for curve fitting in x-ray photoelectron spectroscopy. *J. Vac. Sci. Technol. A Vacuum, Surfaces, Film.* **38**, 061203 (2020).
 175. D. J. Webb, C. M. Brown, "Epi-Fluorescence Microscopy" in, D. J. Taatjes, J. Roth, Eds. (Humana Press, Totowa, NJ, 2012; <http://www.springerlink.com/index/10.1007/978-1-62703-056-4>), vol. 931 of *Methods in Molecular Biology*, pp. 29–59.
 176. C. Stewart, J. Giannini, Inexpensive, Open Source Epifluorescence Microscopes. *J. Chem. Educ.* **93**, 1310–1315 (2016).
 177. Y. Xu, Y. Li, S. Li, F. Balestra, G. Ghibaud, W. Li, Y. Lin, H. Sun, J. Wan, X. Wang, Y. Guo, Y. Shi, Y. Noh, Precise Extraction of Charge Carrier Mobility for Organic Transistors. *Adv. Funct. Mater.* **30**, 1–23 (2020).
 178. P. Lin, F. Yan, Organic Thin-Film Transistors for Chemical and Biological Sensing. *Adv. Mater.* **24**, 34–51 (2012).
 179. J. Borges-González, C. J. Kousseff, C. B. Nielsen, Organic semiconductors for biological sensing. *J. Mater. Chem. C.* **7**, 1111–1130 (2019).
 180. K. Kim, H. Yoo, E. K. Lee, New Opportunities for Organic Semiconducting Polymers in Biomedical Applications. *Polymers (Basel).* **14**, 2960 (2022).

181. A. Koklu, D. Ohayon, S. Wustoni, V. Druet, A. Saleh, S. Inal, Organic Bioelectronic Devices for Metabolite Sensing. *Chem. Rev.* **122**, 4581–4635 (2022).
182. H. Shen, C.-A. Di, D. Zhu, Organic transistor for bioelectronic applications. *Sci. China Chem.* **60**, 437–449 (2017).
183. D. T. Simon, E. O. Gabrielsson, K. Tybrandt, M. Berggren, Organic Bioelectronics: Bridging the Signaling Gap between Biology and Technology. *Chem. Rev.* **116**, 13009–13041 (2016).
184. H. Li, W. Shi, J. Song, H.-J. Jang, J. Dailey, J. Yu, H. E. Katz, Chemical and Biomolecule Sensing with Organic Field-Effect Transistors. *Chem. Rev.* **119**, 3–35 (2019).
185. X. Zhang, Z. Pu, X. Su, C. Li, H. Zheng, D. Li, Flexible organic field-effect transistors-based biosensors: progress and perspectives. *Anal. Bioanal. Chem.* **415**, 1607–1625 (2023).
186. L.-Y. Ma, N. Soin, S. N. Aidit, F. A. Md Rezali, S. F. Wan Muhamad Hatta, Recent advances in flexible solution-processed thin-film transistors for wearable electronics. *Mater. Sci. Semicond. Process.* **165**, 107658 (2023).
187. E. Macchia, K. Manoli, C. Di Franco, R. A. Picca, R. Österbacka, G. Palazzo, F. Torricelli, G. Scamarcio, L. Torsi, Organic Field-Effect Transistor Platform for Label-Free, Single-Molecule Detection of Genomic Biomarkers. *ACS Sensors.* **5**, 1822–1830 (2020).
188. E. Macchia, K. Manoli, B. Holzer, C. Di Franco, M. Ghittorelli, F. Torricelli, D. Alberga, G. F. Mangiatordi, G. Palazzo, G. Scamarcio, L. Torsi, Single-molecule detection with a millimetre-sized transistor. *Nat. Commun.* **9**, 3223 (2018).
189. L. Sarcina, F. Viola, F. Modena, R. A. Picca, P. Bollella, C. Di Franco, N. Cioffi, M. Caironi, R. Österbacka, I. Esposito, G. Scamarcio, L. Torsi, F. Torricelli, E. Macchia, A large-area organic transistor with 3D-printed sensing gate for noninvasive single-molecule detection of pancreatic mucinous cyst markers. *Anal. Bioanal. Chem.* **414**, 5657–5669 (2022).
190. J.-P. Booth, M. Mozetič, A. Nikiforov, C. Oehr, Foundations of plasma surface

- functionalization of polymers for industrial and biological applications. *Plasma Sources Sci. Technol.* **31**, 103001 (2022).
191. T. Desmet, R. Morent, N. De Geyter, C. Leys, E. Schacht, P. Dubruel, Nonthermal plasma technology as a versatile strategy for polymeric biomaterials surface modification: A review. *Biomacromolecules.* **10**, 2351–2378 (2009).
 192. K. S. Siow, L. Britcher, S. Kumar, H. J. Griesser, Plasma Methods for the Generation of Chemically Reactive Surfaces for Biomolecule Immobilization and Cell Colonization - A Review. *Plasma Process. Polym.* **3**, 392–418 (2006).
 193. A. Kyzioł, K. Kyzioł, "Surface Functionalization With Biopolymers via Plasma-Assisted Surface Grafting and Plasma-Induced Graft Polymerization—Materials for Biomedical Applications" in *Biopolymer Grafting: Applications* (Elsevier, 2018; <https://linkinghub.elsevier.com/retrieve/pii/B9780128104620000041>), pp. 115–151.
 194. D. Hetemi, J. Pinson, Surface functionalisation of polymers. *Chem. Soc. Rev.* **46**, 5701–5713 (2017).
 195. C. Alemán, G. Fabregat, E. Armelin, J. J. Buendía, J. Llorca, Plasma surface modification of polymers for sensor applications. *J. Mater. Chem. B.* **6**, 6515–6533 (2018).
 196. M. Magliulo, B. R. Pistillo, M. Y. Mulla, S. Cotrone, N. Ditaranto, N. Cioffi, P. Favia, L. Torsi, PE-CVD of Hydrophilic-COOH Functionalized Coatings on Electrolyte Gated Field-Effect Transistor Electronic Layers. *Plasma Process. Polym.* **10**, 102–109 (2013).
 197. C. Zhai, X. Yang, S. Han, G. Lu, P. Wei, A. Chumakov, E. Erbes, Q. Chen, S. Techert, S. V. Roth, P. Zhang, L. Bu, Surface Etching of Polymeric Semiconductor Films Improves Environmental Stability of Transistors. *Chem. Mater.* **33**, 2673–2682 (2021).
 198. Z. Hu, D. Li, W. Lu, Z. Qin, Y. Ran, X. Wang, G. Lu, In situ tuning of the performance of polymer field-effect transistors by soft plasma etching. *Mater. Adv.* **4**, 2811–2820 (2023).
 199. J. Wang, D. Chen, W. Huang, N. Yang, Q. Yuan, Y. Yang, Aptamer-functionalized field-

- effect transistor biosensors for disease diagnosis and environmental monitoring. *Exploration*. **3** (2023), doi:10.1002/EXP.20210027.
200. H. F. Haneef, A. M. Zeidell, O. D. Jurchescu, Charge carrier traps in organic semiconductors: a review on the underlying physics and impact on electronic devices. *J. Mater. Chem. C*. **8**, 759–787 (2020).
201. F. J. Zhang, C. A. Di, N. Berdunov, Y. Hu, Y. Hu, X. Gao, Q. Meng, H. Sirringhaus, D. Zhu, Ultrathin film organic transistors: Precise control of semiconductor thickness via spin-coating. *Adv. Mater.* **25**, 1401–1407 (2013).
202. W. Niu, H.-C. Wu, J. R. Matthews, A. Tandia, Y. Li, A. L. Wallace, J. Kim, H. Wang, X. Li, K. Mehrotra, Z. Bao, M. He, Synthesis and Properties of Soluble Fused Thiophene Diketopyrrolopyrrole-Based Polymers with Tunable Molecular Weight. *Macromolecules*. **51**, 9422–9429 (2018).
203. M. Pandey, S. S. Pandey, S. Nagamatsu, S. Hayase, W. Takashima, Controlling Factors for Orientation of Conjugated Polymer Films in Dynamic Floating-Film Transfer Method. *J. Nanosci. Nanotechnol.* **17**, 1915–1922 (2017).
204. Y. Yang, Z. Liu, J. Chen, Z. Cai, Z. Wang, W. Chen, G. Zhang, X. Zhang, L. Chi, D. Zhang, A Facile Approach to Improve Interchain Packing Order and Charge Mobilities by Self-Assembly of Conjugated Polymers on Water. *Adv. Sci.* **5**, 1801497 (2018).
205. F. J. M. Colberts, M. M. Wienk, R. Heuvel, W. Li, V. M. Le Corre, L. J. A. Koster, R. A. J. Janssen, Bilayer–Ternary Polymer Solar Cells Fabricated Using Spontaneous Spreading on Water. *Adv. Energy Mater.* **8**, 1–12 (2018).
206. A. Nawaz, A. C. B. Tavares, T. Trang Do, B. B. Patil, P. Sonar, I. A. Hümmelgen, Experimental and modeling study of low-voltage field-effect transistors fabricated with molecularly aligned copolymer floating films. *Flex. Print. Electron.* **3**, 015006 (2018).
207. S. Kim, H. Yoo, Self-Assembled Monolayers: Versatile Uses in Electronic Devices from Gate Dielectrics, Dopants, and Biosensing Linkers. *Micromachines*. **12**, 565 (2021).

208. S. Yuvaraja, A. Nawaz, Q. Liu, D. Dubal, S. G. Surya, K. N. Salama, P. Sonar, Organic field-effect transistor-based flexible sensors. *Chem. Soc. Rev.* **49**, 3423–3460 (2020).
209. M. Devynck, P. Tardy, G. Wantz, Y. Nicolas, L. Hirsch, Organic field-effect transistor with octadecyltrichlorosilane (OTS) self-assembled monolayers on gate oxide: effect of OTS quality. *Eur. Phys. J. Appl. Phys.* **56**, 34106 (2011).
210. Y. Wang, M. Lieberman, Growth of Ultrasmooth Octadecyltrichlorosilane Self-Assembled Monolayers on SiO₂. *Langmuir*. **19**, 1159–1167 (2003).
211. G. Choi, K. Lee, S. Oh, J. Seo, C. Kim, T. K. An, J. Lee, H. S. Lee, Understanding Marangoni flow-driven solidification of polymer semiconducting films on an aqueous substrate. *J. Mater. Chem. C*. **8**, 10010–10020 (2020).
212. K. P. Goetz, O. D. Jurchescu, "Conductivity measurements of organic materials using field-effect transistors (FETs) and space-charge-limited current (SCLC) techniques" in *Handbook of Organic Materials for Electronic and Photonic Devices* (Elsevier, ed. 2, 2019; <http://dx.doi.org/10.1016/B978-0-08-102284-9.00014-0>), pp. 453–487.
213. H. J. Lee, G. M. Fernandes-Cunha, I. Putra, W.-G. Koh, D. Myung, Tethering Growth Factors to Collagen Surfaces Using Copper-Free Click Chemistry: Surface Characterization and in Vitro Biological Response. *ACS Appl. Mater. Interfaces*. **9**, 23389–23399 (2017).
214. S. Balamurugan, A. Obubuafo, S. A. Soper, D. A. Spivak, Surface immobilization methods for aptamer diagnostic applications. *Anal. Bioanal. Chem.* **390**, 1009–1021 (2008).
215. V. Podzorov, E. Menard, A. Borissov, V. Kiryukhin, J. A. Rogers, M. E. Gershenson, Intrinsic Charge Transport on the Surface of Organic Semiconductors. *Phys. Rev. Lett.* **93**, 086602 (2004).
216. X. Yu, J. Yu, W. Huang, L. Zhang, H. Zeng, Source/drain electrodes contact effect on the stability of bottom-contact pentacene field-effect transistors. *AIP Adv.* **2** (2012),

doi:10.1063/1.4707164.

217. F. Bussolotti, S. Kera, K. Kudo, A. Kahn, N. Ueno, Gap states in Pentacene Thin Film Induced by Inert Gas Exposure. *Phys. Rev. Lett.* **110**, 267602 (2013).
218. M. Egginger, S. Bauer, R. Schwödiauer, H. Neugebauer, N. S. Sariciftci, Current versus gate voltage hysteresis in organic field effect transistors. *Monatshefte für Chemie - Chem. Mon.* **140**, 735–750 (2009).
219. S. Kim, H. Yoo, J. Choi, Effects of Charge Traps on Hysteresis in Organic Field-Effect Transistors and Their Charge Trap Cause Analysis through Causal Inference Techniques. *Sensors.* **23**, 2265 (2023).
220. H.-M. Liao, T.-C. Huang, G.-Y. Huang, M.-S. Chen, W.-M. Huang, P-62: Organic Surface of a TFT Array Treated with Nitrogen Plasma. *SID Symp. Dig. Tech. Pap.* **39**, 1421 (2008).
221. A. Vesel, M. Mozetic, Surface modification and ageing of PMMA polymer by oxygen plasma treatment. *Vacuum.* **86**, 634–637 (2012).
222. J. A. Martin, J. L. Chávez, Y. Chushak, R. R. Chapleau, J. Hagen, N. Kelley-Loughnane, Tunable stringency aptamer selection and gold nanoparticle assay for detection of cortisol. *Anal. Bioanal. Chem.* **406**, 4637–4647 (2014).
223. M. Freeley, R. E. A. Gwyther, D. D. Jones, M. Palma, DNA-Directed Assembly of Carbon Nanotube–Protein Hybrids. *Biomolecules.* **11**, 955 (2021).
224. L.-H. Chou, Y. Na, C.-H. Park, M. S. Park, I. Osaka, F. S. Kim, C.-L. Liu, Semiconducting small molecule/polymer blends for organic transistors. *Polymer (Guildf).* **191**, 122208 (2020).
225. Y. Pan, G. Yu, Multicomponent Blend Systems Used in Organic Field-Effect Transistors: Charge Transport Properties, Large-Area Preparation, and Functional Devices. *Chem. Mater.* **33**, 2229–2257 (2021).
226. M. Wright, R. Lin, M. J. Y. Tayebjee, G. Conibeer, Effect of Blend Composition on Bulk Heterojunction Organic Solar Cells: A Review. *Sol. RRL.* **1**, 1–31 (2017).

227. G. Zuo, H. Abdalla, M. Kemerink, Conjugated Polymer Blends for Organic Thermoelectrics. *Adv. Electron. Mater.* **5**, 1–20 (2019).
228. J. E. Cochran, M. J. N. Junk, A. M. Glauddell, P. L. Miller, J. S. Cowart, M. F. Toney, C. J. Hawker, B. F. Chmelka, M. L. Chabynyc, Molecular Interactions and Ordering in Electrically Doped Polymers: Blends of PBTTT and F4TCNQ. *Macromolecules.* **47**, 6836–6846 (2014).
229. Y. Karpov, N. Kiriya, M. Al-Husseini, M. Hamsch, T. Beryozkina, V. Bakulev, S. C. B. Mannsfeld, B. Voit, A. Kiriya, Hexacyano-[3]-radialene anion-radical salts: a promising family of highly soluble p-dopants. *Chem. Commun.* **54**, 307–310 (2018).
230. S. Yoon, E.-Y. Shin, N.-K. Cho, S. Park, H. Y. Woo, H. J. Son, Progress in morphology control from fullerene to nonfullerene acceptors for scalable high-performance organic photovoltaics. *J. Mater. Chem. A.* **9**, 24729–24758 (2021).
231. K. M. Cheung, K. A. Yang, N. Nakatsuka, C. Zhao, M. Ye, M. E. Jung, H. Yang, P. S. Weiss, M. N. Stojanović, A. M. Andrews, Phenylalanine Monitoring via Aptamer-Field-Effect Transistor Sensors. *ACS Sensors.* **4**, 3308–3317 (2019).
232. X. Fan, W. Nie, H. Tsai, N. Wang, H. Huang, Y. Cheng, R. Wen, L. Ma, F. Yan, Y. Xia, PEDOT:PSS for Flexible and Stretchable Electronics: Modifications, Strategies, and Applications. *Adv. Sci.* **6** (2019), doi:10.1002/advs.201900813.
233. H. Zhong, J. Smith, S. Rossbauer, A. J. P. White, T. D. Anthopoulos, M. Heeney, Air-Stable and High-Mobility n-Channel Organic Transistors Based on Small-Molecule/Polymer Semiconducting Blends. *Adv. Mater.* **24**, 3205–3211 (2012).
234. C.-K. Chen, Y.-C. Lin, E. Ercan, P.-J. Yu, J.-C. Ho, M. Ueda, W.-C. Chen, Functionalized Poly(phenylene ether) with high thermal stability as flexible dielectrics and substrates for organic field-effect transistors. *Org. Electron.* **96**, 106225 (2021).
235. H. Ren, Y. Tong, M. Ouyang, J. Wang, L. Zhang, Y. Fu, Q. Tang, Balancing the trade-off between the mechanical and electrical properties of conjugated polymer blend films

- for organic field-effect transistors. *J. Mater. Chem. C.* **10**, 14921–14928 (2022).
236. D. G. Koo, D. Lee, J. Noh, Y. H. Lee, S. Jang, I. Nam, T. J. Shin, J. Park, Impact of Intermolecular Interactions Between a Diketopyrrolopyrrole-Based Conjugated Polymer and Bromobenzaldehyde on Field-Effect Transistors. *Macromol. Res.* **29**, 89–97 (2021).
237. S. Han, X. Zhuang, W. Shi, X. Yang, L. Li, J. Yu, Poly(3-hexylthiophene)/polystyrene (P3HT/PS) blends based organic field-effect transistor ammonia gas sensor. *Sensors Actuators B Chem.* **225**, 10–15 (2016).
238. J. Jeong, M. Essafi, C. Lee, M. Haoues, M. F. Diouani, H. Kim, Y. Kim, Ultrasensitive detection of hazardous reactive oxygen species using flexible organic transistors with polyphenol-embedded conjugated polymer sensing layers. *J. Hazard. Mater.* **355**, 17–24 (2018).
239. C.-C. Wu, Y. B. Manga, M.-H. Yang, Z.-S. Chien, K.-S. Lee, Label-Free Detection of BRAF V599E Gene Mutation Using Side-Gated Nanowire Field Effect Transistors. *J. Electrochem. Soc.* **165**, B576–B581 (2018).
240. Z. Wang, Y. Jia, Graphene solution-gated field effect transistor DNA sensor fabricated by liquid exfoliation and double glutaraldehyde cross-linking. *Carbon N. Y.* **130**, 758–767 (2018).
241. I. Migneault, C. Dartiguenave, M. J. Bertrand, K. C. Waldron, Glutaraldehyde: behavior in aqueous solution, reaction with proteins, and application to enzyme crosslinking. *Biotechniques.* **37**, 790–802 (2004).
242. D. W. Schubert, Spin coating as a method for polymer molecular weight determination. *Polym. Bull.* **38**, 177–184 (1997).
243. R. Shivhare, T. Erdmann, U. Hörmann, E. Collado-Fregoso, S. Zeiske, J. Benduhn, S. Ullbrich, R. Hübner, M. Hamsch, A. Kiriya, B. Voit, D. Neher, K. Vandewal, S. C. B. Mannsfeld, Alkyl Branching Position in Diketopyrrolopyrrole Polymers: Interplay

- between Fibrillar Morphology and Crystallinity and Their Effect on Photogeneration and Recombination in Bulk-Heterojunction Solar Cells. *Chem. Mater.* **30**, 6801–6809 (2018).
244. W. Li, K. H. Hendriks, A. Furlan, W. S. C. Roelofs, M. M. Wienk, R. A. J. Janssen, Universal Correlation between Fibril Width and Quantum Efficiency in Diketopyrrolopyrrole-Based Polymer Solar Cells. *J. Am. Chem. Soc.* **135**, 18942–18948 (2013).
245. K. Keren, R. S. Berman, E. Braun, Patterned DNA Metallization by Sequence-Specific Localization of a Reducing Agent. *Nano Lett.* **4**, 323–326 (2004).
246. K. Hemminki, R. Suni, Sites of reaction of glutaraldehyde and acetaldehyde with nucleosides. *Arch. Toxicol.* **55**, 186–190 (1984).
247. H. Hantsche, High Resolution XPS of Organic Polymers: The Scienta ESCA300 Database (Beamson, G.; Briggs, D.). *J. Chem. Educ.* **70**, A25 (1993).
248. N. Saraf, E. R. Woods, M. Peppler, S. Seal, Highly selective aptamer based organic electrochemical biosensor with pico-level detection. *Biosens. Bioelectron.* **117**, 40–46 (2018).
249. H. O. Ham, Z. Liu, K. H. A. Lau, H. Lee, P. B. Messersmith, Facile DNA Immobilization on Surfaces through a Catecholamine Polymer. *Angew. Chemie.* **123**, 758–762 (2011).
250. I. Kubo, T. Eguchi, Study on Electrochemical Insulin Sensing Utilizing a DNA Aptamer-Immobilized Gold Electrode. *Materials (Basel)*. **8**, 4710–4719 (2015).
251. P. Qi, W. Yan, Y. Yang, Y. Li, Y. Fan, J. Chen, Z. Yang, Q. Tu, N. Huang, Immobilization of DNA aptamers via plasma polymerized allylamine film to construct an endothelial progenitor cell-capture surface. *Colloids Surfaces B Biointerfaces.* **126**, 70–79 (2015).
252. A. Kuznetsov, N. Komarova, M. Andrianova, V. Grudtsov, E. Kuznetsov, Aptamer based vanillin sensor using an ion-sensitive field-effect transistor. *Microchim. Acta.* **185**, 3 (2018).
253. R. Raveendran, M. A. G. Namboothiry, Bias Stress Stability and Hysteresis in

- Elastomeric Dielectric Based Solution Processed OFETs. *Mater. Res. Bull.* **146**, 111596 (2022).
254. T. Minami, T. Sato, T. Minamiki, K. Fukuda, D. Kumaki, S. Tokito, A novel OFET-based biosensor for the selective and sensitive detection of lactate levels. *Biosens. Bioelectron.* **74**, 45–48 (2015).
255. S. Sheibani, L. Capua, S. Kamaei, S. S. A. Akbari, J. Zhang, H. Guerin, A. M. Ionescu, Extended gate field-effect-transistor for sensing cortisol stress hormone. *Commun. Mater.* **2**, 10 (2021).
256. A. Kaushik, A. Vasudev, S. K. Arya, S. K. Pasha, S. Bhansali, Recent advances in cortisol sensing technologies for point-of-care application. *Biosens. Bioelectron.* **53**, 499–512 (2014).
257. A. Idili, F. Ricci, A. Vallée-Bélisle, Determining the folding and binding free energy of DNA-based nanodevices and nanoswitches using urea titration curves. *Nucleic Acids Res.* **45**, 7571–7580 (2017).
258. M. E. Belowich, J. F. Stoddart, Dynamic imine chemistry. *Chem. Soc. Rev.* **41**, 2003 (2012).
259. R. F. Borch, M. D. Bernstein, H. D. Durst, The Cyanohydrinborate Anion as a Selective Reducing Agent. *J. Am. Chem. Soc.* **93**, 2897–2904 (1971).
260. B. Wang, C. Zhao, Z. Wang, K.-A. Yang, X. Cheng, W. Liu, W. Yu, S. Lin, Y. Zhao, K. M. Cheung, H. Lin, H. Hojajji, P. S. Weiss, M. N. Stojanović, A. J. Tomiyama, A. M. Andrews, S. Emaminejad, Wearable aptamer-field-effect transistor sensing system for noninvasive cortisol monitoring. *Sci. Adv.* **8**, 1–16 (2022).
261. M. Nikolka, I. Nasrallah, B. Rose, M. K. Ravva, K. Broch, A. Sadhanala, D. Harkin, J. Charmet, M. Hurhangee, A. Brown, S. Illig, P. Too, J. Jongman, I. McCulloch, J. L. Bredas, H. Sirringhaus, High operational and environmental stability of high-mobility conjugated polymer field-effect transistors through the use of molecular additives.

- Nat. Mater.* **16**, 356–362 (2017).
262. H. F. Iqbal, Q. Ai, K. J. Thorley, H. Chen, I. McCulloch, C. Risko, J. E. Anthony, O. D. Jurchescu, Suppressing bias stress degradation in high performance solution processed organic transistors operating in air. *Nat. Commun.* **12**, 2352 (2021).
263. G. Zhou, S. Zhou, Q. Zhu, N. Zhao, Improving Operational Stability of p-Type Field-Effect Transistors by Charge Selective Electrodes: a General Strategy. *Adv. Electron. Mater.* **5**, 1900055 (2019).
264. C. J. Kousseff, Conjugated polymers for sensing biologically relevant molecules (2021) (available at <https://qmro.qmul.ac.uk/xmlui/handle/123456789/77233>).
265. B. W. H. Saes, M. M. Wienk, R. A. J. Janssen, The Effect of α -Branched Side Chains on the Structural and Opto-Electronic Properties of Poly(Diketopyrrolopyrrole- alt - Terthiophene). *Chem. – A Eur. J.* **26**, 14221–14228 (2020).
266. C. J. Kousseff, F. E. Taifakou, W. G. Neal, M. Palma, C. B. Nielsen, Controlling morphology, adhesion, and electrochromic behavior of <sc>PEDOT</sc> films through molecular design and processing. *J. Polym. Sci.* **60**, 504–516 (2022).
267. A. Giovannitti, D. T. Sbircea, S. Inal, C. B. Nielsen, E. Bandiello, D. A. Hanifi, M. Sessolo, G. G. Malliaras, I. McCulloch, J. Rivnay, Controlling the mode of operation of organic transistors through side-chain engineering. *Proc. Natl. Acad. Sci. U. S. A.* **113**, 12017–12022 (2016).
268. A. Giovannitti, I. P. Maria, D. Hanifi, M. J. Donahue, D. Bryant, K. J. Barth, B. E. Makdah, A. Savva, D. Moia, M. Zetek, P. R. F. Barnes, O. G. Reid, S. Inal, G. Rumbles, G. G. Malliaras, J. Nelson, J. Rivnay, I. McCulloch, The Role of the Side Chain on the Performance of N-type Conjugated Polymers in Aqueous Electrolytes. *Chem. Mater.* **30**, 2945–2953 (2018).
269. Z. S. Parr, J. Borges-González, R. B. Rashid, K. J. Thorley, D. Meli, B. D. Paulsen, J. Strzalka, J. Rivnay, C. B. Nielsen, From p- to n-Type Mixed Conduction in Isoindigo-

- Based Polymers through Molecular Design. *Adv. Mater.* **34** (2022), doi:10.1002/adma.202107829.
270. Z. Wang, Z. Liu, L. Ning, M. Xiao, Y. Yi, Z. Cai, A. Sadhanala, G. Zhang, W. Chen, H. Sirringhaus, D. Zhang, Charge Mobility Enhancement for Conjugated DPP-Selenophene Polymer by Simply Replacing One Bulky Branching Alkyl Chain with Linear One at Each DPP Unit. *Chem. Mater.* **30**, 3090–3100 (2018).
271. C. J. Mueller, T. Klein, E. Gann, C. R. McNeill, M. Thelakkat, Azido-Functionalized Thiophene as a Versatile Building Block To Cross-Link Low-Bandgap Polymers. *Macromolecules.* **49**, 3749–3760 (2016).
272. S. Schmid, J. Gačanin, Y. Wu, T. Weil, P. Bäuerle, Synthesis and bioconjugation of first alkynylated poly(dithieno[3,2-b:2',3'-d]pyrrole)s. *Polym. Chem.* **8**, 7113–7118 (2017).
273. L. Kergoat, B. Piro, M. Berggren, M.-C. Pham, A. Yassar, G. Horowitz, DNA detection with a water-gated organic field-effect transistor. *Org. Electron.* **13**, 1–6 (2012).
274. J. Escorihuela, A. T. M. Marcelis, H. Zuilhof, Metal-Free Click Chemistry Reactions on Surfaces. *Adv. Mater. Interfaces.* **2**, 1–42 (2015).
275. A. Jawalekar, S. Malik, J. Verkade, B. Gibson, N. Barta, J. Hodges, A. Rowan, F. van Delft, Oligonucleotide Tagging for Copper-Free Click Conjugation. *Molecules.* **18**, 7346–7363 (2013).
276. S. C. Rasmussen, S. J. Evenson, Dithieno[3,2-b:2',3'-d]pyrrole-based materials: Synthesis and application to organic electronics. *Prog. Polym. Sci.* **38**, 1773–1804 (2013).
277. Y. Geng, A. Tang, K. Tajima, Q. Zeng, E. Zhou, Conjugated materials containing dithieno[3,2-b:2',3'-d]pyrrole and its derivatives for organic and hybrid solar cell applications. *J. Mater. Chem. A.* **7**, 64–96 (2019).
278. Y. Bandera, H. W. Jones, B. Grant, S. Mell, S. H. Foulger, Synthesis, electropolymerization and functionalization via click chemistry of N -alkynylated

- dithieno[3,2-b:2',3'-d]pyrrole. *RSC Adv.* **12**, 29187–29196 (2022).
279. M. Mohammedture, N. Rajput, A. I. Perez-Jimenez, Z. Matouk, S. AlZadjali, M. Gutierrez, Impact of probe sonication and sulfuric acid pretreatment on graphene exfoliation in water. *Sci. Rep.* **13**, 18523 (2023).
280. J. T. Han, J. I. Jang, H. Kim, J. Y. Hwang, H. K. Yoo, J. S. Woo, S. Choi, H. Y. Kim, H. J. Jeong, S. Y. Jeong, K.-J. Baeg, K. Cho, G.-W. Lee, Extremely Efficient Liquid Exfoliation and Dispersion of Layered Materials by Unusual Acoustic Cavitation. *Sci. Rep.* **4**, 5133 (2014).
281. A. C. Gouget-Laemmel, J. Yang, M. A. Lodhi, A. Siriwardena, D. Aureau, R. Boukherroub, J.-N. Chazalviel, F. Ozanam, S. Szunerits, Functionalization of Azide-Terminated Silicon Surfaces with Glycans Using Click Chemistry: XPS and FTIR Study. *J. Phys. Chem. C.* **117**, 368–375 (2013).
282. H. Runfang, Y. Yangfan, L. Leilei, J. Jianlong, Z. Qiang, D. Lifeng, S. Shengbo, L. Qiang, P3HT-based organic field effect transistor for low-cost, label-free detection of immunoglobulin G. *J. Biotechnol.* **359**, 75–81 (2022).
283. F. Li, S. Wang, Y. Zhang, J. L. Lutkenhaus, Electrochemical Energy Storage in Poly(dithieno[3,2-b:2',3'-d]pyrrole) Bearing Pendant Nitroxide Radicals. *Chem. Mater.* **30**, 5169–5174 (2018).
284. H. Azak, S. Kurbanoglu, H. B. Yildiz, S. A. Ozkan, Electrochemical glucose biosensing via new generation DTP type conducting polymers/gold nanoparticles/glucose oxidase modified electrodes. *J. Electroanal. Chem.* **770**, 90–97 (2016).
285. F. Mariani, I. Gualandi, M. Tessarolo, B. Fraboni, E. Scavetta, PEDOT: Dye-Based, Flexible Organic Electrochemical Transistor for Highly Sensitive pH Monitoring. *ACS Appl. Mater. Interfaces.* **10**, 22474–22484 (2018).
286. X. Zheng, A. Calò, E. Albisetti, X. Liu, A. S. M. Alharbi, G. Arefe, X. Liu, M. Spieser, W. J. Yoo, T. Taniguchi, K. Watanabe, C. Aruta, A. Ciarrocchi, A. Kis, B. S. Lee, M. Lipson, J.

- Hone, D. Shahrjerdi, E. Riedo, Patterning metal contacts on monolayer MoS₂ with vanishing Schottky barriers using thermal nanolithography. *Nat. Electron.* **2**, 17–25 (2019).
287. Y. Liang, C. Wu, G. Figueroa-Miranda, A. Offenhäusser, D. Mayer, Amplification of aptamer sensor signals by four orders of magnitude via interdigitated organic electrochemical transistors. *Biosens. Bioelectron.* **144**, 111668 (2019).